Technical Report

TR-10-11

THM modelling of buffer, backfill and other system components

Critical processes and scenarios

Mattias Åkesson, Ola Kristensson,
Lennart Börgesson, Ann Dueck
Clay Technology AB

Jan Hernelind, 5T-Engineering AB

March 2010

Svensk Kärnbränslehantering AB
Swedish Nuclear Fuel
and Waste Management Co

Box 250, SE-101 24 Stockholm
Phone +46 8 459 84 00

ISSN 1404-0344
SKB TR-10-11
ID 1245316
Updated 2015-08

THM modelling of buffer, backfill and other system components

Critical processes and scenarios

Mattias Åkesson, Ola Kristensson,
Lennart Börgesson, Ann Dueck
Clay Technology AB

Jan Hernelind, 5T-Engineering AB

March 2010

Update notice

The original report, dated March 2010, was found to contain editorial errors which have been corrected in this updated version.

Abstract

A number of critical thermo-hydro-mechanical processes and scenarious for the buffer, tunnel backfill and other filling components in the repository have been identified. These processes and scenarious representing different aspects of the repository evolution have been pinpointed and modelled. In total, 22 cases have been modelled.

Most cases have been analysed with finite element (FE) calculations, using primarily the two codes Abaqus and Code_Bright. For some cases analytical methods have been used either to supplement the FE calculations or due to that the scenario has a character that makes it unsuitable or very difficult to use the FE method.

Material models and element models and choice of parameters as well as presumptions have been stated for all modelling cases. In addition, the results have been analysed and conclusions drawn for each case. The uncertainties have also been analysed. Besides the information given for all cases studied, the codes and material models have been described in a separate so called data report.

Sammanfattning

Ett antal kristiska termo-hydro-mekaniska processer och scenarier avseende buffert, tunnelåterfyllning och andra återfyllningskomponenter i slutförvaret har identifierats. Dessa processer och scenarier som representerar olika spekter på slutförvarets gradvisa utveckling har preciserats och modellerats. Totalt har 22 olika fall modellerats.

De flesta fallen har analyserats med finita-element(FE)-beräkningar varvid främst två olika koder Abaqus och Code_Bright har använts. För några fall har analytiska metoder använts antingen för att komplettera FE-beräkningarna eller på grund av att scenariet har en karaktär som gör det olämpligt eller mycket svårt att använda FE-metoden.

För varje modelleringsfall anges alla förutsättningar, vilka materialmodeller och elementmodeller som använts och parameterval. Dessutom analyseras reultaten och slutatser av varje fall drages. En analys av osäkerheter görs också. Koder och materialmodeller beskrivs även i en separat så kallad datarapport.

Contents

Introduction

A number of critical THM processes and scenarious for the buffer, backfill and other filling components in the repository have been identified in the process description of the process reports for SR-Site. These processes and scenarious representing different aspects of the repository evolution have been pinpointed and modelled as a number of different modelling tasks. In total, 22 modelling tasks have been identified. The overall topics and objectives of these models are summarized in Table 1 together with a note on where they were treated in SR-Can. The tasks are described in more detail in the following sections.

Table 1. Overview of modelling tasks and where corresponding problems were treated in SR-Can.

	Objective	SR-Can model
T	1. Peak temperature calculations	/Hedin 2004/
H	2. Analysis of time-scale of backfill hydration	/Börgesson et al. 2006/
TH	3. Analysis of time-scale of buffer hydration	/Börgesson and Hernelind 1999/ /Börgesson et al. 2006/
	4. Analysis of moisture-redistribution in dry rock	No
THM	5. Buffer homogenisation	No
HM	6. Homogenisation of erosion damages	/Börgesson and Hernelind 2006c/
	7. Backfill homogenisation	No
	8. Buffer upward swelling	/Börgesson et al. 2006/ /Börgesson and Johannesson 2006/
	9. Canister sinking	/Börgesson and Hernelind 2006b/
	10. Rock shear through a deposition hole	/Börgesson and Hernelind 2006a/
	11. Piping and erosion	Brief description
H	12. Analysis of time-scale of tunnel plug hydration	No
	13. Hydraulic modelling of the sealing ability of the tunnel plug	No
	14. Analysis of time-scale of central area etc and top seal hydration	No
	15. Analysis of time-scale of borehole seal hydration	No
HM	16. Homogenisation of tunnel plug	No
	17. Backfill swelling after tunnel plug disintegration 1	No
	18. Bottom plate 1 Lifting of package	No
	19. Bottom plate 2 Buffer swelling after concrete disintegration	No
	20. Homogenization of bore hole seals	No
	21. Homogenization of bore hole seals after loss of bentonite	No
	22. Backfill swelling after tunnel plug disintegration 2 Omitted filling outside the plug	No

1 Peak temperature calculations

1.1 Introduction

For the buffer there is a specified temperature criterion, the temperature must not exceed 100°C at any time. This criterion will be an important factor for determining the dimensions of the repository, i.e. tunnel spacing and canister spacing. In the report "Strategy for thermal dimensioning of the final repository for spent nuclear fuel" (the STD-report /Hökmark et al. 2009/) a strategy for how the peak temperature criterion should be considered when designing the repository has been developed. The strategy is translated into layout instructions to be followed when designing the repository at some chosen site. The SR-Site safety assessment will be based on layout step D2 for which the following design premises apply:

1. Maximum allowed peak temperature in the bentonite buffer in all deposition holes; 100°C.
2. Maximum thermal power in the canister: 1,700 W.
3. Distance between deposition tunnels: c-c = 40 m.
4. Distance between deposition holes: c-c ≥ 6 m.

Figure 1-1 shows the principles of calculating peak buffer temperature as described in the strategy report (three steps):

1. Calculation of the rock wall temperature, taken into account the spatial variability in thermal rock properties.
2. Calculation of the temperature difference between the rock wall and the canister/bentonite interface at the top of the canister.
3. Addition of the rock wall temperature and the temperature difference to get the bentonite temperature at the hottest point.

1.2 Thermal dimensioning

The layout instructions will vary between the different rock domains identified at the sites such that the hottest canisters in each domain will determine the minimum canister spacing in that individual domain. These canisters will be found in deposition holes that are:

1. Completely dry. Since there is no water uptake and buffer swelling in dry holes, the initial gap between canister and buffer is not closed or reduced. This gives a high heat transport resistance and high canister temperatures. The bentonite blocks and the pellets-filled annular space between the blocks and the walls of the deposition holes remain in the initial, unsaturated state with initial, low values of the heat transport parameters. This, too, will tend to give high canister temperatures.
2. Located in the central parts of the deposition areas, i.e. with several neighbour canisters in all directions. This gives higher canister temperatures compared to the conditions in the peripheral parts of the repository.
3. Located in volumes dominated by low conductive rock. Low conductive rock surrounding an individual canister will tend to increase the temperature contribution from that particular canister and, depending on the size of the volume, also from nearby canisters.

For dry deposition holes the 10 mm clearance between canister and bentonite blocks will remain open and the 50 mm pellets-filled gap between bentonite blocks and rock wall will remain unsaturated. The heat transport resistance of these gaps will tend to raise the temperature of the canister surface and the temperature of the bentonite that is actually in direct contact with the canister, i.e. the bentonite on top of and below the canister. Knowing the canister power and assuming typical parameter values of the heat transport properties of the gaps and the buffer, it is possible to establish a reference evolution of the total difference $\Delta T_{tot}(t)$ between the rock wall temperature at canister mid-height and the temperature at the top of the canister /Hökmark et al. 2009/.

$$\Delta T_{tot}(t) = \Delta T_1(t) + \Delta T_2(t) = 0.02213 \cdot Q(t) \qquad (1\text{-}1)$$

Here ΔT_1 is the temperature drop across the buffer material and ΔT_2 the effects of the open canister-buffer gap.

This reference evolution is independent of the rock properties. Adding this difference to the rock wall temperature $T_{wall}(t)$ at canister mid-height will give the maximum bentonite temperature.

Calculating the rock wall temperature at canister mid-height is a much more complicated problem. For the idealized case of homogenous rock with one distinct value of the thermal conductivity (and the heat capacity), an analytical solution can be used to find the rock wall temperature as function of the canister and tunnel spacing.

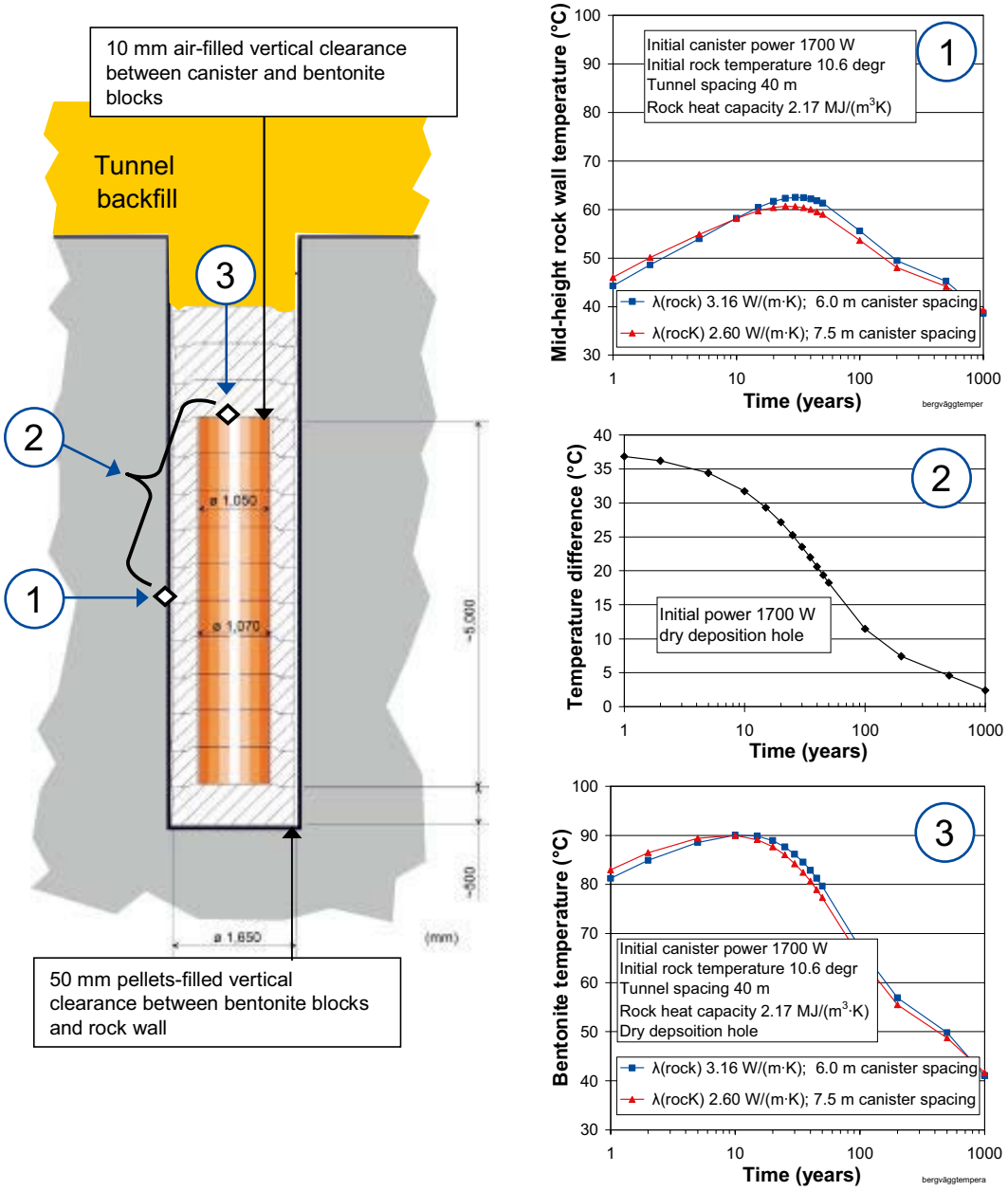

Figure 1-1. *Principle of peak buffer temperature calculation. The rock wall temperature at canister mid-height (1) is added to the temperature difference (2) between rock wall and the top of the canister to find the maximum bentonite temperature (3). The difference (2) is due to the heat resistance over buffer and gaps (local solution) whereas the rock wall temperature (1) depends on layout and rock thermal properties. The example curves shown here were calculated by use of the analytical method.*

In the real case of heterogeneous rock it is necessary to take the spatial variability of thermal conductivity and heat capacity into account. For this reason a numerical code is used that takes the spatial variability and the anisotropy in the geology directly into account, i.e. with automatic, or implicit, inclusion of all scale aspects. The numerical code has been applied (together with reference evolution (see Equation (1-1)) in the layout work to establish the Layout D2 canister spacing in the different rock domains identified at the Forsmark and Laxemar sites (cf. Site Engineering Reports). The canister spacing at Fosrmark is 6.0 m in rock domain RFM029 and 6.8 m in rock domain RFM045.

It is important to note that there are uncertainties in all input data (for instance effects of drying and moisture redistribution in dry deposition holes). Therefore the canister spacing has been established with account of a margin to the 100°C threshold.

The following observations made in the strategy report may be relevant for the present report:

- The largest uncertainties relate to the interior of the deposition holes, .i.e. to the reference evolution.
- Effects of open gaps make out about 50% of the reference evolution.
- The peak buffer temperature occurs some 5–15 years after deposition.
- The peak rock wall temperature occurs some 25–35 years after deposition.
- Provided that the deposition is made in a reasonably orderly fashion, i.e. tunnel by tunnel from one edge of the repository to the other, the sequence approximation made in the layout work (i.e. that all canisters are deposited simultaneously) is valid.

2 Analysis of time scale of backfill hydration

2.1 Introduction and objectives

The objective of this task was to analyze the time-scale to saturate the backfill.

2.2 Approach

The task was modelled with different hydraulic Code_Bright models. In the *primary* variation, four different geometries was used: a 1D axisymmetric geometry, two 2D axisymmetric geometries with different fracture distances (6 m and 24 m), and one 2D plane geometry (PS). Two different tunnel sections were considered: a theoretical section (Th) and a maximum fallout (MF) section. Two different approached were considered for the filling of the tunnels: with block and pellets materials (B&P), and with homogenized (Hom) material. Finally a number of fracture transmissivities were considered. In the *secondary variation*, the effect of an EDZ, tunnel ventilation, alternative rock and bentonite properties and the absence of a fracture was investigated. A summary of the investigated variations is given in Table 2-1.

The presentation of this task begins with a general description of the hydraulic representation on the near-field rock and a specification of fracture transmissivities in Section 2.3. Thereafter follows a description of the models in Section 2.4; and a presentation of the results from these models is given in Section 2.5. A discussion of the different variations and features is given in Section 2.6. Finally, the conclusions and uncertainties are presented in Section 2.7.

2.3 Hydraulic representation of near-field rock

The near-field rock in the 2D models is represented by un-fractured rock with low hydraulic conductivity, and intersecting fractures with defined transmissivities. These models thus largely rely on their fractures for the water supply. Three features are sought in the representation of these fractures:

- They should be fed with hydrostatic pressure in order to enable a final state with hydrostatic pressure.
- They should provide a relevant inflow into the cavity. One extreme is an inflow of 0.1 litres per minute, which is the maximum allowed inflow into a deposition hole. Another relevant extreme can be set to two orders of magnitude lower.
- The influence of the fracture on the pressure in the matrix rock should be relevant, i.e. the pressure at no-flow boundaries, intersected by the fracture, should reflect the actual draw-down around the tunnel.

Table 2-1. Summary primary and secondary variations.

Variation		
Primary	Tunnel section area	Two different tunnel sections
	Backfill representation	Two and in some cases three different representations
	Fracture distance and orientation	Two different orientations: vertical and horizontal Two different distances for the vertical orientation
	Fracture transmissivity	Two different transmissivities
Secondary	Rock permeability	Several cases with different rock permeabilities
	Presence of EDZ	Two cases with EDZ
	Absence of fractures	Five cases with no fracture
	Rock retention	Two cases with different retention curve
	Bentonite permeability	Four cases with different permeabilities
	Bentonite relative permeability	Two cases with different relative permeabilities
	Thermal evolution	One case with thermal evolution
	Hydromechanical processes	One case with hydromechanical processes
	Bentonite retention	Two cases with steeper retention curve
	Tunnel ventilation	One case with 10 years of RH 70%

The vertical plane 2D model has a pressure boundary on the upper boundaries, whereas no-flow boundaries are used on the sides and the lower boundary (Figure 2-1 and Figure 2-2). The cavities are fed through fractures, which are modelled as folded slabs; a horizontal board connected to a vertical board. The distance from the tunnel to the upper boundary corresponds to the distance to the high permeability rock, i.e. 60 m (see Chapter 3). For convenience, the same distance is chosen for the distance to the lower boundary. The distance between the symmetry line and the vertical boundary is given as half of the tunnel spacing. The used fracture simply consists of two boards in right angle. The length of the horizontal and the vertical fractures are 17.5 m and 60 m respectively. A fracture with a flow of 5 l/min along the entire tunnel length of 300 m will thus correspond to a transmissivity of approx. $5 \cdot 10^{-8}$ m^2/s. This value is divided by 2 due to the symmetry line through the tunnel.

The horizontal axisymmetric 2D models have no-flow boundaries on all sides (Figure 2-1 and Figure 2-2). The cavities are fed through fractures, which are modelled as folded slabs, i.e. as a circular disk connected to a cylinder in right angle. The axial length of the backfill model is determined by the investigated fracture distance. The radial distance to the outer boundary is chosen together with a target boundary pressure to provide the same inflow as in the true problem with interfering tunnels (see Figure 2-3 left). It can be shown that a very large radius has to be chosen in order to obtain the same inflow for the same pressure difference. Instead a realistic target pressure at the intersection of the no-flow boundaries can be calculated as:

$$\left.\begin{aligned} Q &\approx \frac{B \cdot T \cdot \Delta h}{H} \\ Q &= \frac{2\pi \cdot T \cdot \Delta h_{ax}}{\ln\left(\frac{r_o}{r_i}\right)} \end{aligned}\right\} \Rightarrow \quad \Delta h_{ax} = \Delta h \cdot \frac{B \cdot \ln\left(\frac{r_o}{r_i}\right)}{2\pi \cdot H} \qquad (2\text{-}1)$$

Q is the inflow, B is the tunnel spacing, H is the distance to the hydraulic boundary, r_i and r_o are the inner and outer radii in the axisymmetric representation, Δh and Δh_{ax} are the head differences in the plane and axisymmetric representation, and T is the transmissivity.

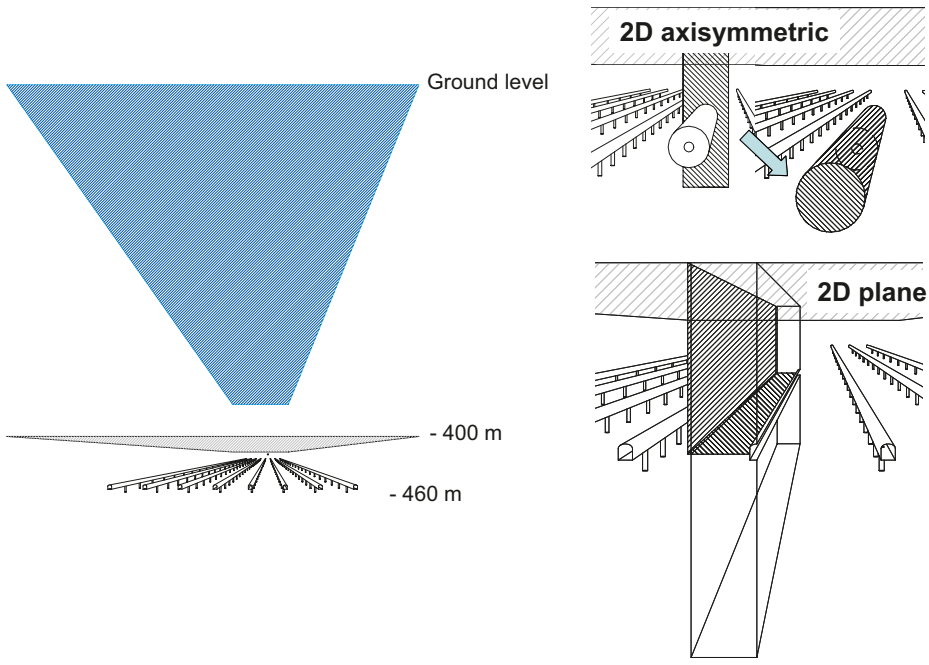

Figure 2-1. *Schematic outline of repository with hydrostatic pressure at –400 m (left). 2D axisymmetric and 2D plane representations of tunnels (right).*

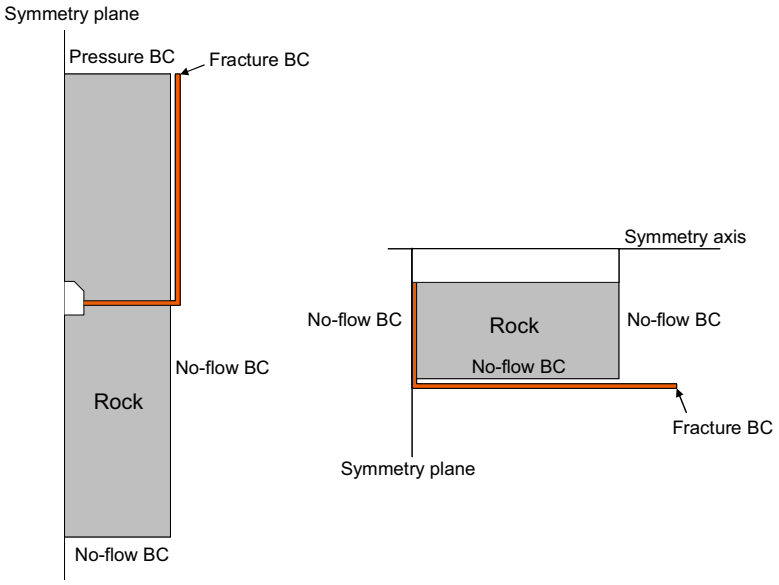

Figure 2-2. *Schematic model geometries with applied hydraulic boundaries. Plane backfill model (left) and axisymmetric backfill model (right).*

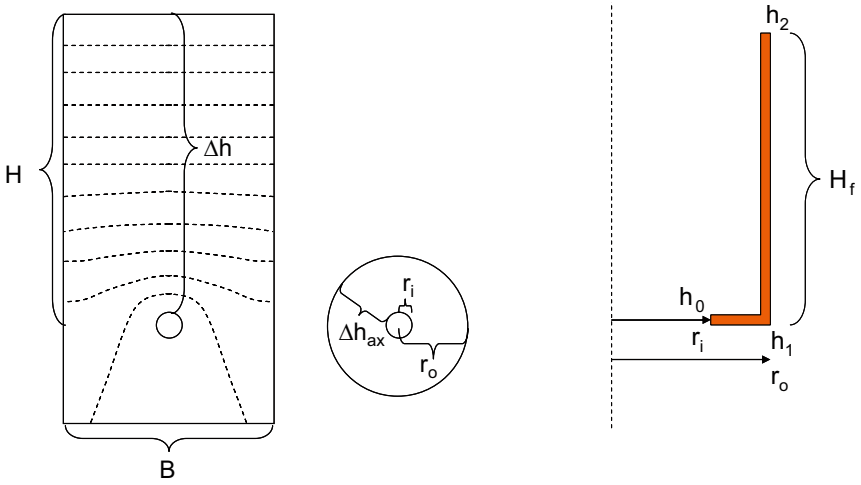

Figure 2-3. *Comparison of pressure distribution at true conditions and with axisymmetric representation (left). Fracture geometry (right).*

It can be noted that the accuracy of the first relation is approx. 10% for the investigated geometry. These relations show that the target head at the outer boundary is approx. 70 m with an outer radius of 10 m.

The use of a folded fracture, with a circular disk connected to a cylinder (Figure 2-3 right), implies a certain pressure at the interface. If the transmissivity in the disk and the cylinder is the same, this pressure (h_1) can be calculated as:

$$\left.\begin{aligned} Q &= T \cdot \frac{h_2 - h_1}{H_f} \cdot 2\pi \cdot r_o \\ Q &= 2\pi \cdot T \cdot \frac{h_1 - h_0}{\ln\left(\frac{r_o}{r_i}\right)} \end{aligned}\right\} \Rightarrow \quad h_1 = \frac{\ln\left(\frac{r_o}{r_i}\right) \cdot \frac{h_2}{H_f} \cdot r_o + h_0}{\ln\left(\frac{r_o}{r_i}\right) \cdot \frac{r_0}{H_f} + 1} \qquad (2\text{-}2)$$

H_f is the length of the fracture cylinder, whereas h_0, h_1 and h_2 are the heads at the tunnel, the disk/cylinder connection and the hydraulic boundary, respectively.

This relation is illustrated for different cases in Figure 2-4 (left).

In order to obtain a relevant head at the intersection of the no-flow boundary the relation provided by Equation (2-1) should be taken into account. An expression for the length of the fracture cylinder (H_f) as a function of the outer radius can be derived, if both Equations (2-1) and (2-2) are taken together. A rearrangement of (2-2) yields:

$$H_f = \frac{h_2 - h_1}{h_1 - h_0} \cdot r_o \cdot \ln\left(\frac{r_o}{r_i}\right) \tag{2-3}$$

The ratio of the head differences is identified as ($\Delta h/\Delta h_{ax}$-1) with the notation of Equation (2-1). The length of the fracture can thus be expressed as:

$$H_f = \left(\frac{2\pi \cdot H}{B} - \ln\left(\frac{r_o}{r_i}\right)\right) \cdot r_o \tag{2-4}$$

This relation is illustrated in Figure 2-4 together with the calculated head at the intersection. It can be noticed that an outer radius of 10 m yields a fracture length (H_f) of 80 m and a head at intersection of approx. 70 m. A fracture with a flow of 0.1 l/min will thus correspond to a transmissivity of approx. $5 \cdot 10^{-9}$ m^2/s. This value is also divided by 2 due to the symmetry plane through the tunnel.

It should be noted that the horizontal axisymmetric models can not be modelled with gravity and the length of the cylindrical fracture should not be mistaken for the real distance between the tunnel and the high permeability rock.

All fractures are modelled as slabs with a thickness (d) of 0.1 m. The intended transmissivity (T) is attained by a certain hydraulic conductivity of the slab (K = T/d).

2.4 Model description

Geometries and densities are modelled in accordance with the Backfill production line report. Parameter data for backfill blocks, pellets and rock materials are used in accordance with the Buffer THM Data report /Åkesson et al. 2010/.

2.4.1 Geometry and mesh

Four different geometries were used: an axisymmetric 1D geometry (Figure 2-5); two axisymmetric 2D geometries with fracture distances 6 and 24 m (Figure 2-6) and a plane 2D geometry (Figure 2-7). The tunnel sections, i.e. the radii of the rock wall, were adjusted in order to compensate for the void space in the slots between the backfill blocks, which otherwise was not explicitly represented.

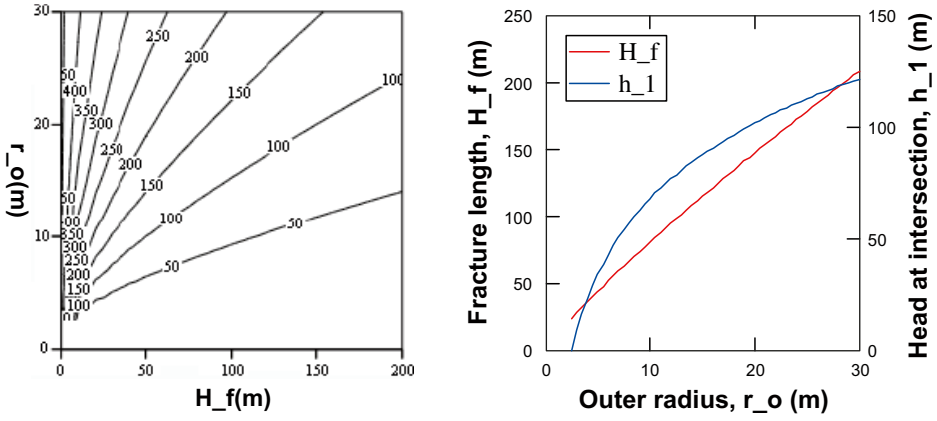

Figure 2-4. *Calculated values of head at intersection of no-flow boundary (h_1) as a function of H_f and r_o. Head at feed of fracture (h_2) is 460 m; head at cavity (h_0) is zero; r_i=2.5 (left). Horizontal backfill models. Fracture length and head at intersection as a function of the outer radius (right).*

The 2D geometries include representations of a fracture. These representations are treated as half a fracture due to the symmetry planes in these geometries. For each geometry two different tunnel sections were investigated: a theoretical section and a maximum fallout.

Gravity was included in the 2D plane models, which thereby exhibit a hydrostatic pressure distribution.

The mesh for each model is shown in Figure 2-5– Figure 2-7. The number of nodes and elements are compiled in Table 2-2.

2.4.2 Initial and boundary conditions

The models are purely hydraulic, and therefore are only the liquid pressure specified in the initial (Figure 2-8) and the boundary conditions (Figure 2-9). The initial liquid pressure for all backfill materials were –45.9 MPa. The initial liquid pressure for the rock materials (matrix and fracture) in the 2D axisymmetric models was set to a linear distribution from 0.1 to 0.8 MPa with increasing radius, and linear from 0.8 to 4.6 MPa along the cylindrical fracture. The reason for this approach is that the code only allows linear distributions for the initial conditions. The corresponding distribution for the 2D plane strain models were from 4.0 MPa at the top to 5.2 MPa at the bottom, thereby representing the hydrostatic pressure distribution. Boundary pressures were applied in the outer boundary of the 1D models (atmospheric or hydrostatic). The 2D axisymmetric models were fed with 4.6 MPa at the outer boundary of the cylindrical fracture. The 2D plane models were fed from the top boundaries (both matrix and fracture) with 4.0 MPa.

All calculations were made for a constant temperature of 20°C, in order to adhere to the hydraulic conductivity values evaluated in the Data report /Åkesson et al. 2010/. The expected temperatures are however higher and the influence of this on the water viscosity is addressed in the secondary variations.

2.4.3 Material properties

The properties for all modelled material are compiled in Table 2-3. All data were taken from the Buffer THM Data report /Åkesson et al. 2010/. Special emphasis was given to the rock matrix permeability. The significance of this property was investigated in the secondary variation. For the base cases a value of 5E–20 m^2 (representative for core samples) was used.

In some of the primary variation the pellets material was modelled with an alternated representation with the aim to mimic the phenomena of piping. With this approach the pellets were modelled with significantly higher flow coefficients ($k = 1E–17\ m^2$; $k_r = 1$) during the hydration of the pellets filling. As soon as the filling reached saturation, the flow coefficients were set to their listed values.

Table 2-2. Number of nodes and elements in different geometries.

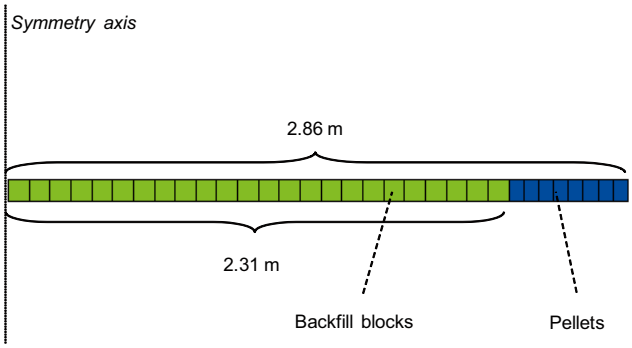

Figure 2-5. *Geometry 1. 1D axisymmetric model with maximum fallout. In the theoretical section the outer radius is 2.5 m.*

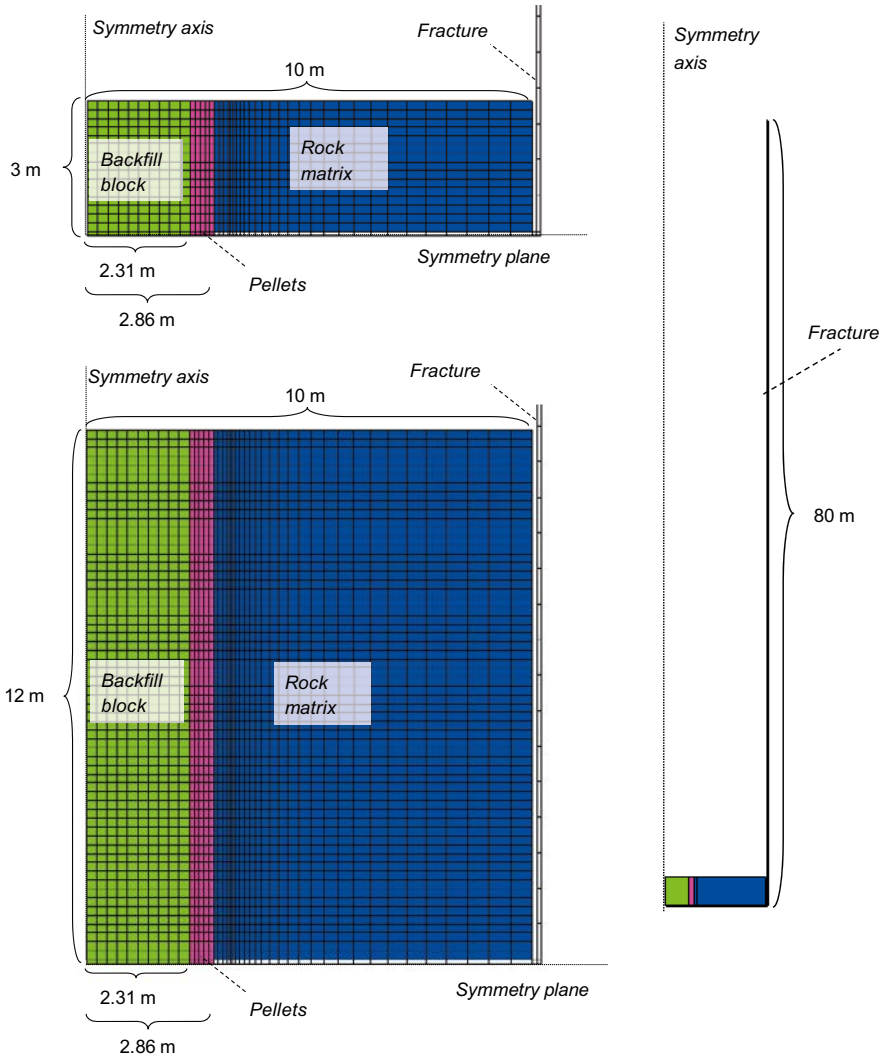

Figure 2-6. *Geometries 2 and 3. 2D axisymmetric models with maximum fallout. 6 and 24 m fracture distances. In the theoretical section, the outer radius of the pellets-filled slot is 2.5 m.*

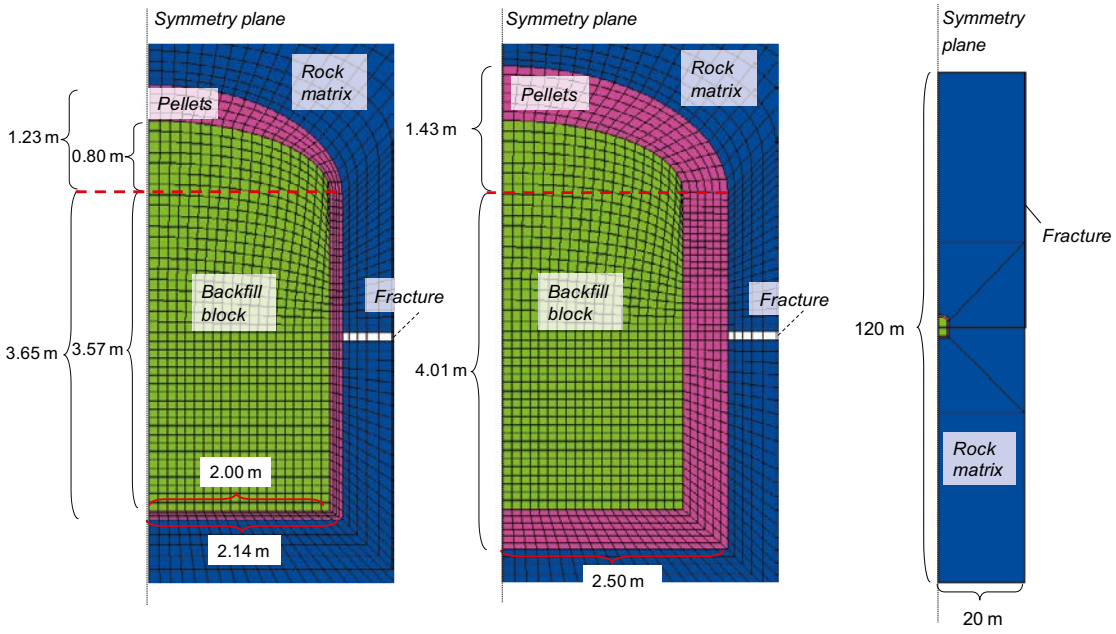

Figure 2-7. *Geometry 4. 2D plane models. Full outline (right); Details: theoretical section (left) and maximum fallout (middle).*

Geometry	Tunnel section	Number of nodes	Number of elements
1	Theoretical	56	27
	Maximum fallout	66	32
2	Theoretical	918	758
	Maximum fallout	952	790
3	Theoretical	2,808	2,603
	Maximum fallout	2,932	2,725
4	Theoretical	4,594	4,416
	Maximum fallout	4,758	4,578

Table 2-3. Material properties for modelled materials.

Parameter		Backfill block e=0.635 w=17%	Backfill pellets e=1.780 w=17%	Homog. packfill e=0.74 w=17%	Homog. backfill e=0.91 w=17%	Rock matrix	Fracture material	EDZ
Porosity	n (–)	0.388	0.64	0.425	0.476	0.003	0.003	0.003
Intrinsic permeability	k (m^2)	2.1E–21	5.2E–19	4.8E–21	1.5E–20	5E–20	*	1E–15
Relative permeability	k_r (–)	S_r^3	S_r^3	S_r^3	S_r^3	vG†: λ = 0.6	vG†: λ = 0.6	vG†: λ = 0.6
Water retention curve	P_0 (MPa) λ (–)	37.2 0.34	0.162 0.19	11.6 0.23	3.45 0.20	1.74 0.6	1.74 0.6	1.74 0.6

* Geometry 2 and 3: 2.5 E–15 m^2 (0.1 l/min) and 2.5 E–17 m^2 (0.001 l/min); Geometry 4: 2.5 E–14 m^2 (5 l/min á 300 m) and 2.5 E–16 m^2 (0.05 l/min á 300 m).

† vG: van Genuchten relative permeability law.

2.4.4 Variations

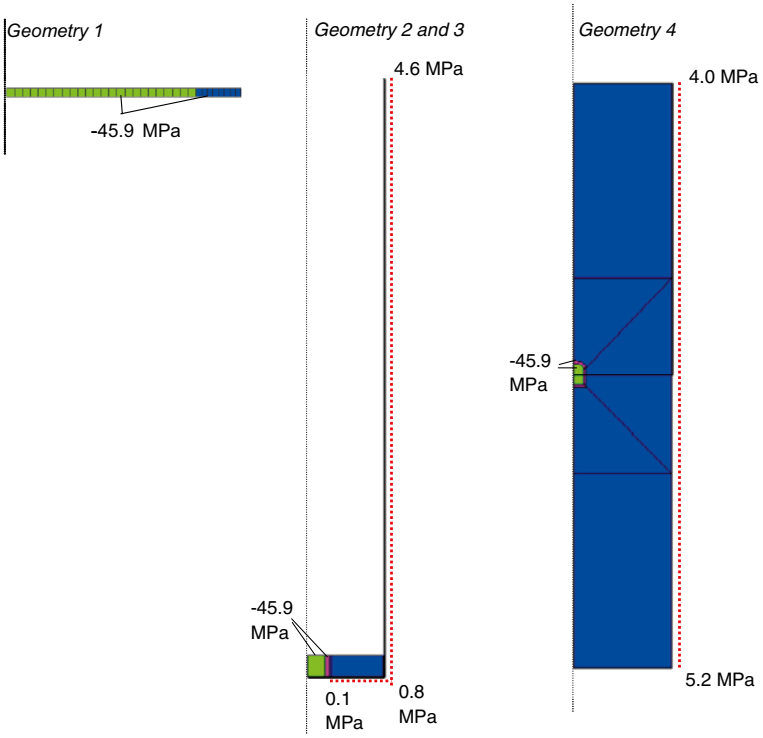

Figure 2-8. *Initial liquid pressures in different geometries. Red lines show linear distributions.*

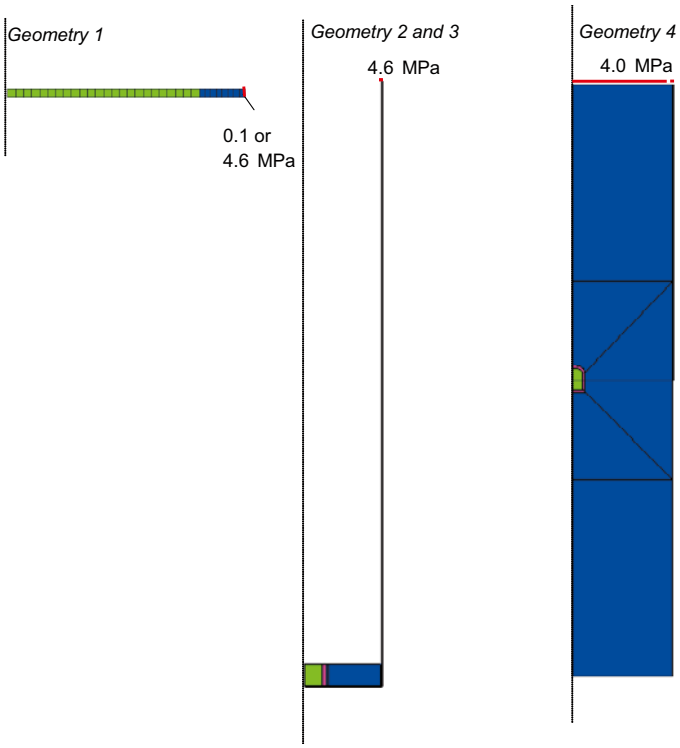

Figure 2-9. *Boundary liquid pressures in different geometries. Gravity is only included in Geometry 4.*

40 different models were investigated in the primary variation. The combination of tunnel sections, backfill representations, and fracture inflow (or boundary pressure) are shown in Table 2-4–Table 2-7.

25 different modes were investigated in the secondary variations. The used base case models and the modified features: inclusion of EDZ, removal of fractures as well as modified permeabilities and retention properties are shown in Table 2-8. The uncertainty of the backfill permeability was tested in accordance with the data report /Åkesson et al. 2010/. The influence of the retention curve for the backfill was investigated with a case with steeper retention curves for blocks and pellets in accordance with the model by /Dueck 2004/, see Figure 2-10. The effects of changing the relative permeability relation was tested for the two cases: Sr^2 and Sr^4. The influence of the thermal evolution, as shown in Figure 2-11, and the temperature dependence of the viscosity of water was

Table 2-4. Primary variation for axisymmetric 1D models.

Model	Tunnel section		Backfill representation			Boundary pressure	
	Theoretical	Maximum fallout	Block/ pellets	Block/ pellets (alt.)	Homog.	Atmospheric (0.1 MPa)	Hydrostatic (4.6 MPa)
T2G1TDA2	X		X			X	
T2G1TDH2	X		X				X
T2G1TAA2	X			X		X	
T2G1TAH2	X			X			X
T2G1THA2	X				X	X	
T2G1THH2	X				X		X
T2G1MDA2		X	X			X	
T2G1MDH2		X	X				X
T2G1MAA2		X		X		X	
T2G1MAH2		X		X			X
T2G1MHA2		X			X	X	
T2G1MHH2		X			X		X

tested in one case. Finally, the effects of taking the hydromechanical processes into account was made in accordance with the work presented in Chapter 7, but with adhering to the use of a boundary pressure of 4.6 MPa along the outer boundary.

The influence of the retention curve for the rock was investigated with a modified case with the retention curve and relative permeability used by /Börgesson and Hernelind 1999/. A second variation was made with a very low retention curve accoding to /Jarsjö et al. 2009/ for the fracture.

2.5 Results

Table 2-5. Primary variation for axisymmetric 2D models with 6 m fracture distance.

Model	Tunnel section		Backfill representation			Fracture inflow	
	Theoretical	Maximum fallout	Block/ pellets	Block/ pellets (alt.)	Homog.	0.1 l/min	0.001 l/min
T2G2TDL2	X		X			X	
T2G2TDS2	X		X				X
T2G2TAL2	X			X		X	
T2G2TAS2	X			X			X
T2G2THL2	X				X	X	
T2G2THS2	X				X		X
T2G2MDL2		X	X			X	
T2G2MDS2		X	X				X
T2G2MAL2		X		X		X	
T2G2MAS2		X		X			X
T2G2MHL2		X			X	X	
T2G2MHS2		X			X		X

Table 2-6. Primary variation for axisymmetric 2D models with 24 m fracture distance.

Model	Tunnel section		Backfill representation		Fracture inflow	
	Theoretical	Maximum fallout	Block/ pellets	Homog.	0.1 l/min	0.001 l/min
T2G3TDL	X		X		X	
T2G3TDS	X		X			X
T2G3THL	X			X	X	
T2G3THS	X			X		X
T2G3MDL		X	X		X	
T2G3MDS		X	X			X
T2G3MHL		X		X	X	
T2G3MHS		X		X		X

Table 2-7. Primary variation for plane 2D models.

Model	Tunnel section		Backfill representation		Fracture inflow	
	Theoretical	Maximum fallout	Block/ pellets	Homog.	5 l/min (á 300 m)	0.05 l/min (á 300 m)
T2G4TDL3	X		X		X	
T2G4TDS3	X		X			X
T2G4THL3	X			X	X	
T2G4THS2	X			X		X
T2G4MDL3		X	X		X	
T2G4MDS2		X	X			X
T2G4MHL2		X		X	X	
T2G4MHS2		X		X		X

Table 2-8. Secondary variations.

Model	BaseCase	Modification							
		EDZ	Frac.	Intrinsic permeability (m^2)			Retention, P0 (MPa) and λ (–)		
				Rock	Block	Pellet	Rock	Block	Pellet
T2G1BK2	T2G1MDH2				4.2E–21	1.0E–18			
T2G1BK06					1.3E–21	3.1E–20			
T2G1BR								17.4 0.2	0.0251 0.15
T2G1T		Prescribed temperature protocol							
T2G1Sr2		kr=Sr^2							
T2G1Sr4		kr=Sr^4							
T2G1HM		Hydromechanical processes included							
T2G2E	T2G2MDS2	Yes							
T2G2RK20				1E–27					
T2G3E	T2G3MDS	Yes							
T2G3RK20				1E–27					
T2G4RK14	T2G4MDS2			5E–21					
T2G4RK11				1E–18					
T2G4RK20				1E–27					
T2G4RR							4.0 0.65 k_r:S_r^3		
T2G4RR2							Frac. 5E–3 0.55		
T2G4NF13			No	1E–20					
T2G4NFD			No						
T2G4NF12			No	1E–19					
T2G4NF11			No	1E–18					
T2G4NF10			No	1E–17					
T2G4BK2					4.2E–21	1.0E–18			
T2G4BK06					1.3E–21	3.1E–20			
T2G4BR								17.4 0.2	0.0251 0.15
T2G4V3		10 years of ventilation of tunnel with RH 70% before insallation							

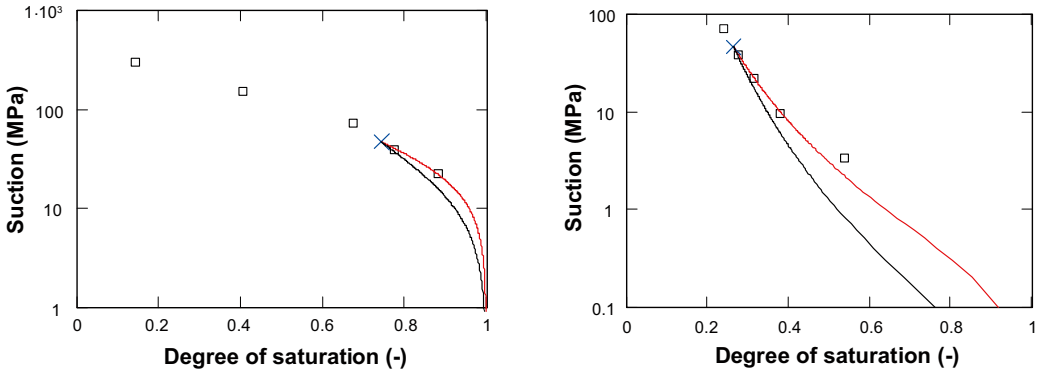

Figure 2-10. *Backfill retention curves in secondary variations: blocks (left) and pellets (right). Red lines are original and black lines are modified curves.*

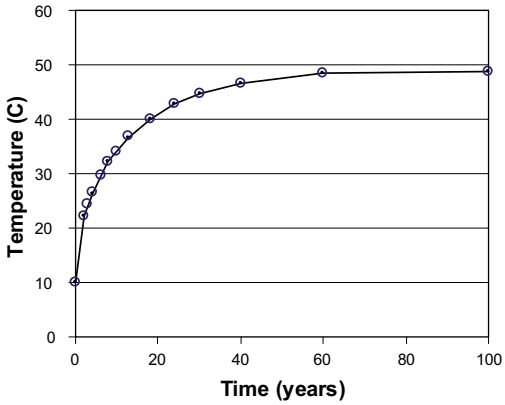

Figure 2-11. *Temperatures in tunnels. Average values of temperature at tunnel floor and tunnel roof for two positions: 0.2 m and 3 m, respectively, from the axis of the nearest canister (data from Process report).*

2.5.1 Evaluation of results

The main result of each model is the time to fully saturate the backfill. The models are therefore evaluated as history plots of the last saturated nodes. Such nodes are primarily located in the inner part of the backfill blocks, far from the mouth of fracture, but in some cases the hydration of the pellets filling may be even slower. The evolution of the degree of saturation at nodes in the blocks, and in some cases, in the pellets is shown as graphs in Figure 2-12–Figure 2-26. A number of contour plots are also included in order to show the location of the nodes. It can be noted that it would be more relevant to evaluate the elements, but it is not possible to extract history plots for elements with the available interface.

A value of the saturation time was evaluated as the time to reach a certain degree of saturation. The time for the degree of saturation to reach 95% and 99% have been evaluated and results are compiled in Table 2-9 and Table 2-10. The value for the latter level (99%) is used in the evaluation of the variations in the next section.

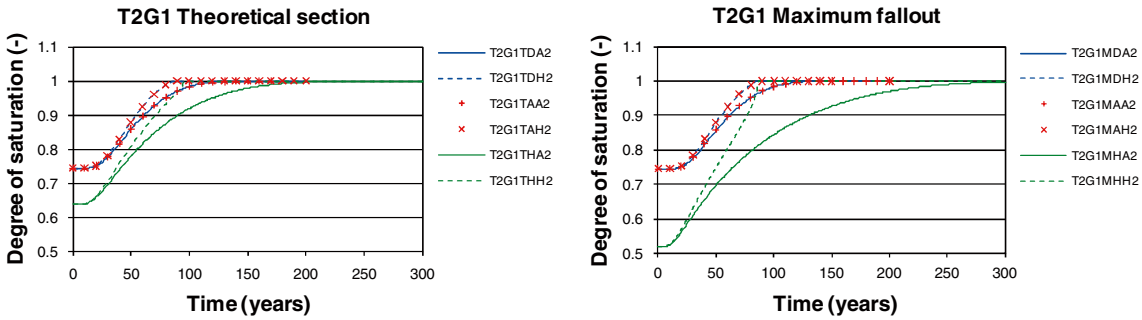

Figure 2-12. *Result from primary variations. Axisymmetric 1D models. Evolution of degree of saturation at inner nodes in backfill.*

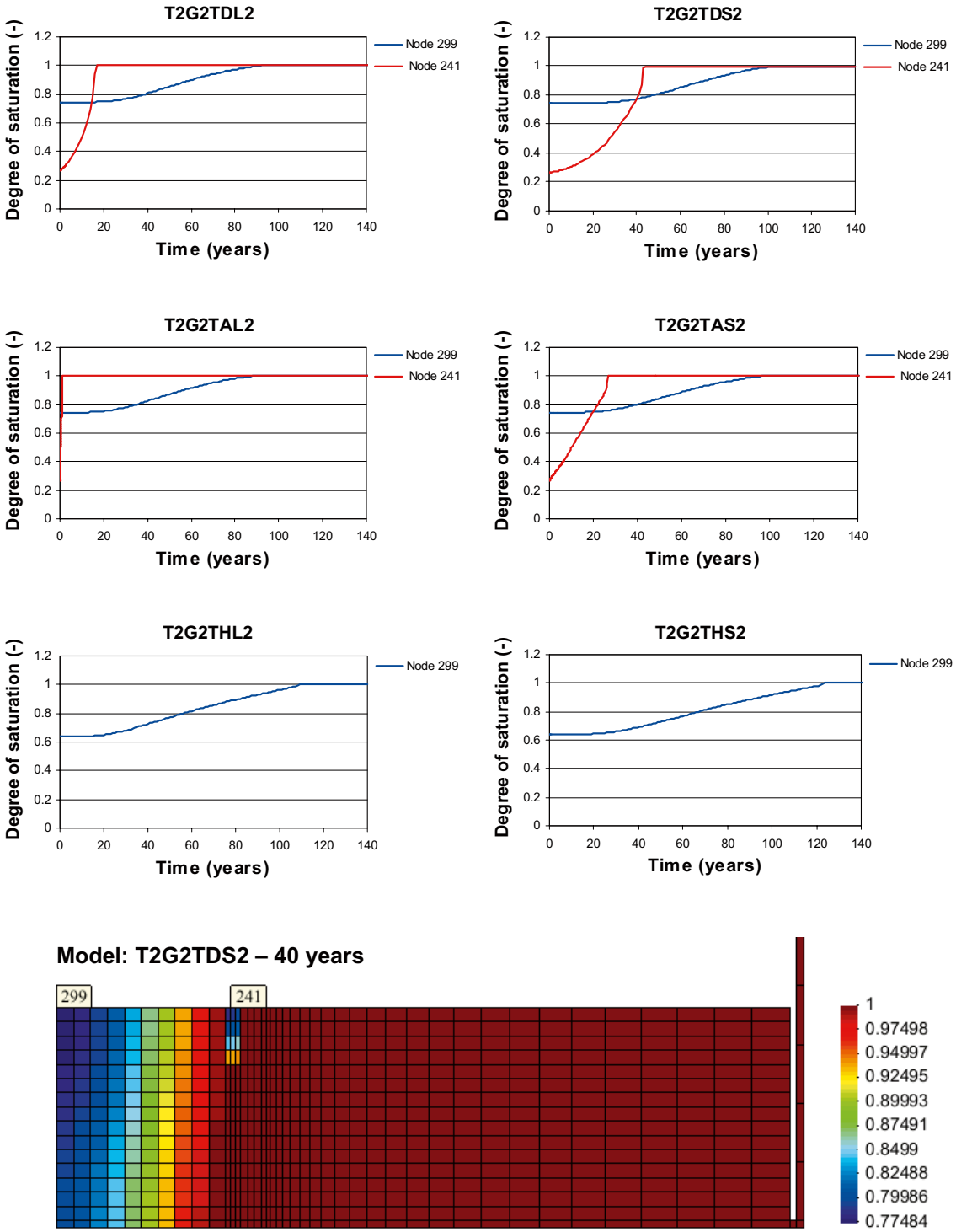

Figure 2-13. *Result from primary variations. Axisymmetric 2D models, 6 m and theoretical section. Evolution of degree of saturation at last hydrated nodes in blocks and pellets.*

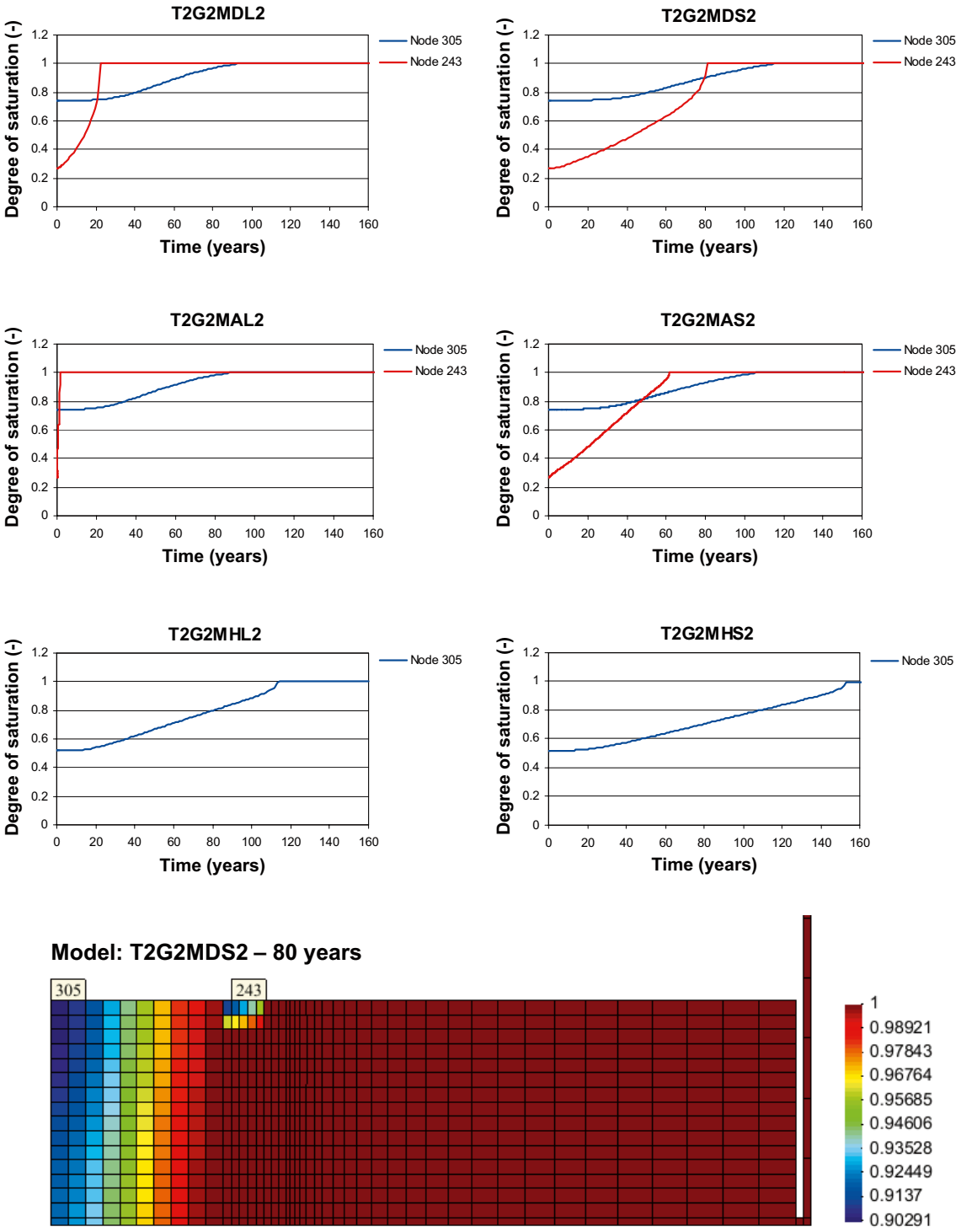

Figure 2-14. *Result from primary variations. Axisymmetric 2D models, 6 m and maximum fallout. Evolution of degree of saturation at last hydrated nodes in blocks and pellets.*

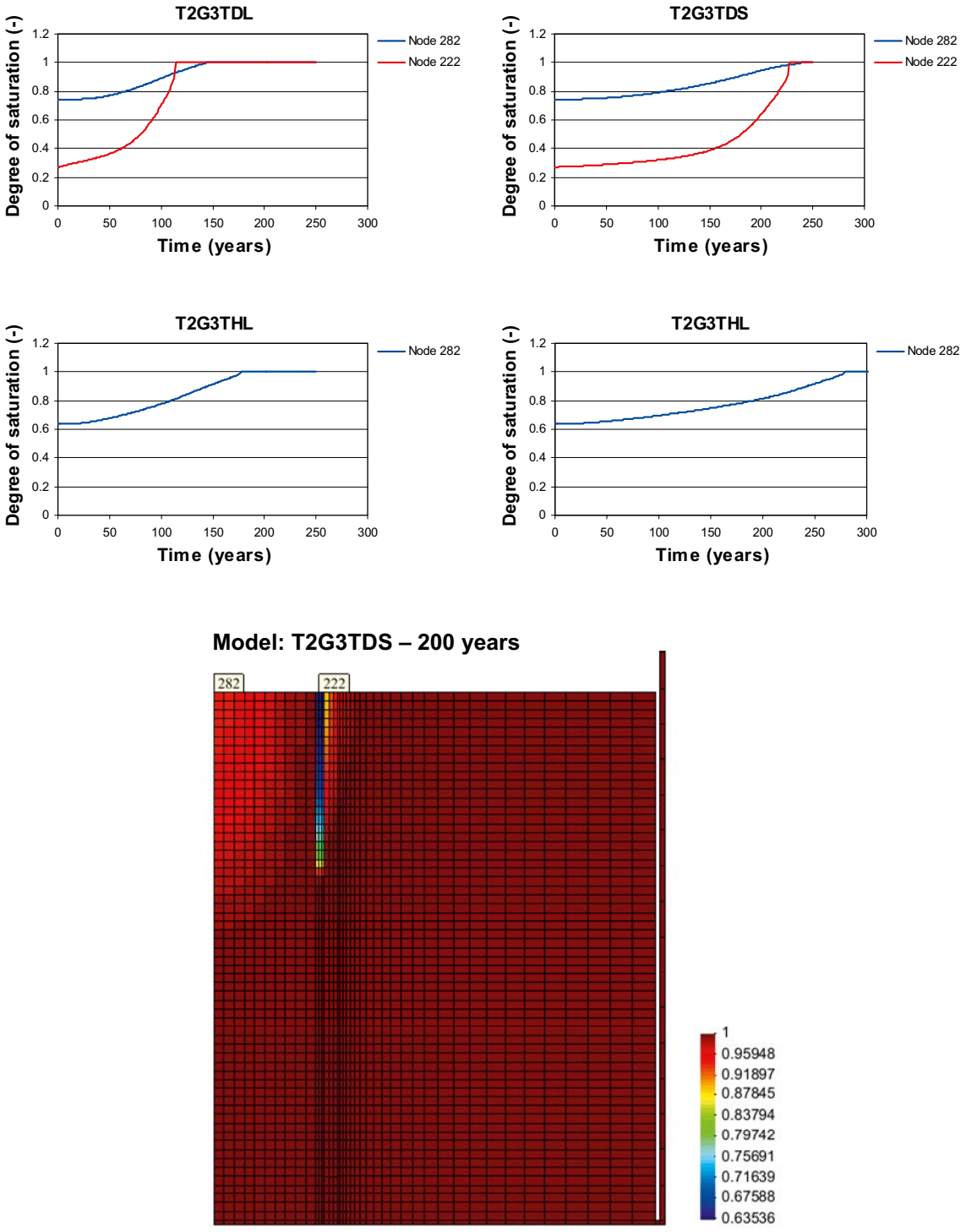

Figure 2-15. *Result from primary variations. Axisymmetric 2D models, 24 m and theoretical section. Evolution of degree of saturation at last hydrated nodes in blocks and pellets.*

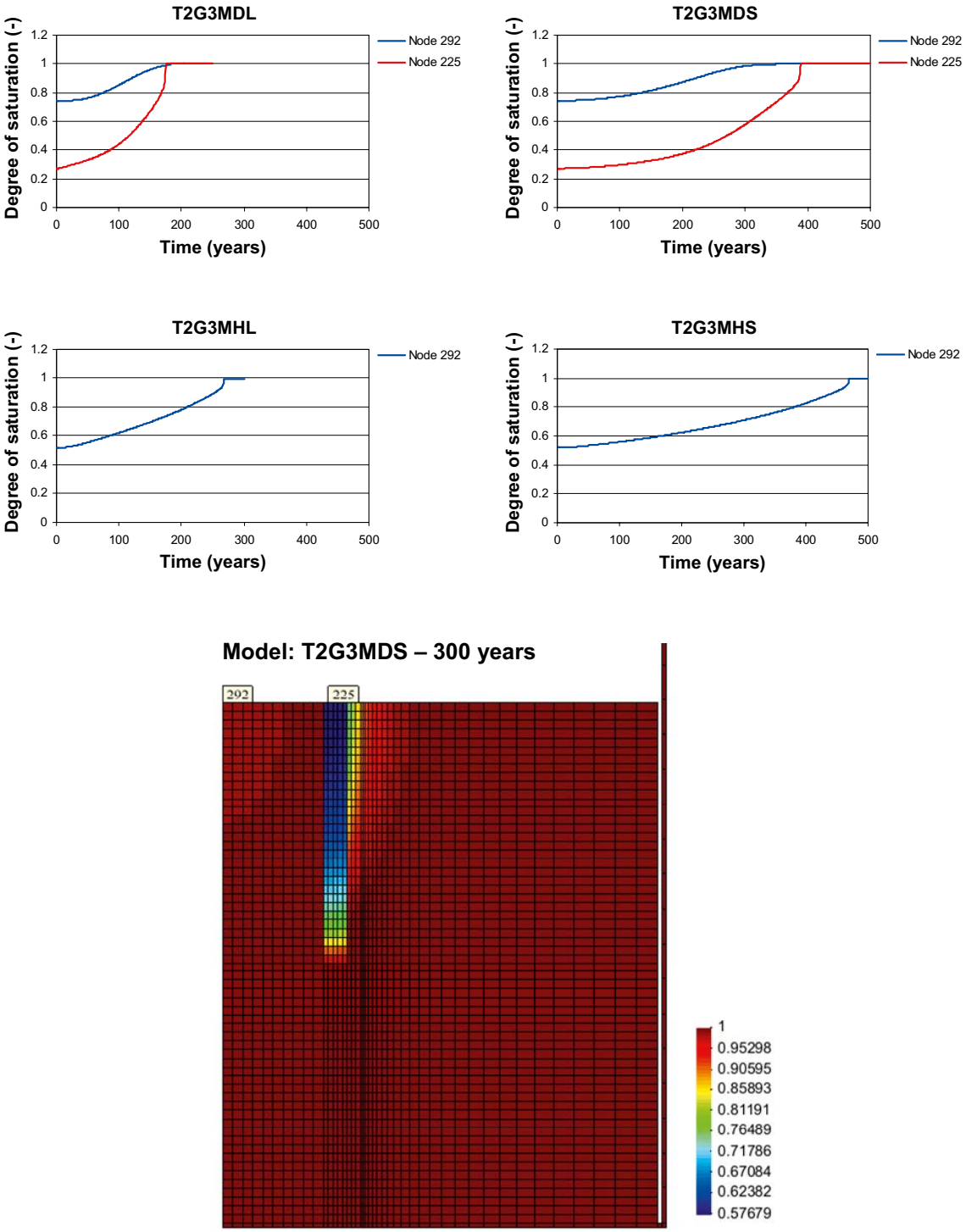

Figure 2-16. *Result from primary variations. Axisymmetric 2D models, 24 m and maximum fallout. Evolution of degree of saturation at last hydrated nodes in blocks and pellets.*

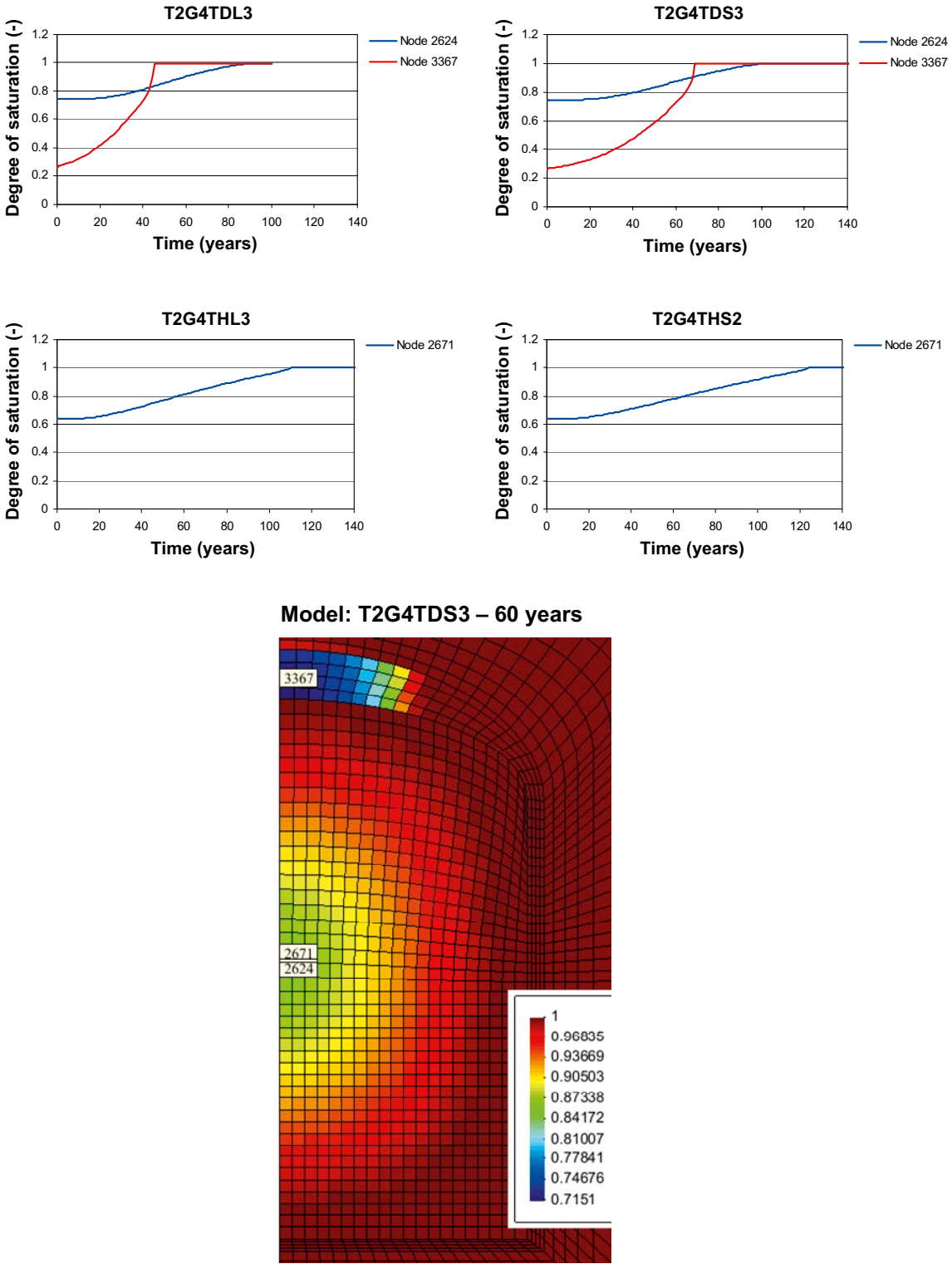

Figure 2-17. *Result from primary variations. Plane strain 2D models and theoretical section. Evolution of degree of saturation at last hydrated nodes in blocks and pellets.*

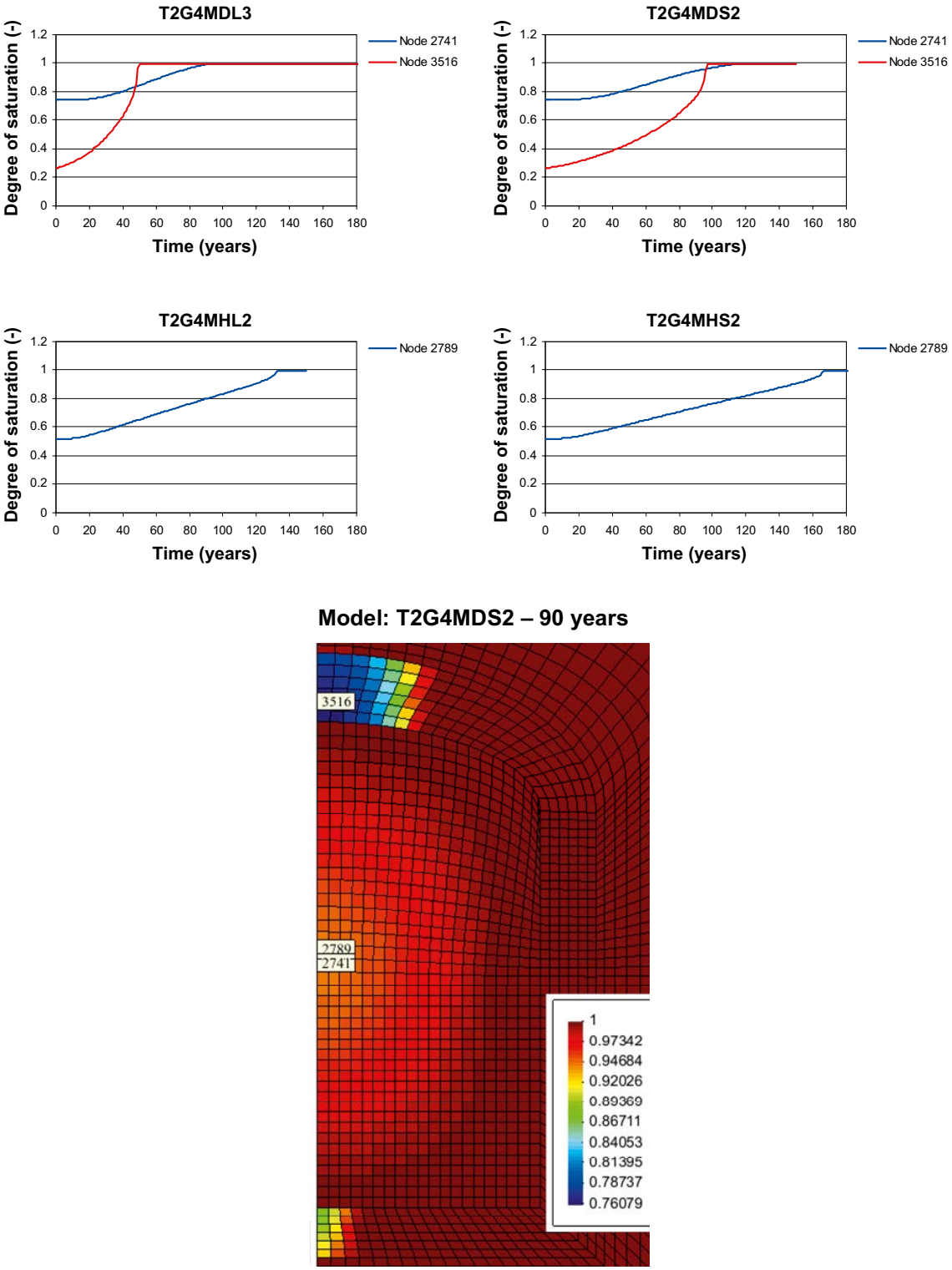

Figure 2-18. *Result from primary variations. Plane strain 2D models and maximum fallout. Evolution of degree of saturation at last hydrated nodes in blocks and pellets.*

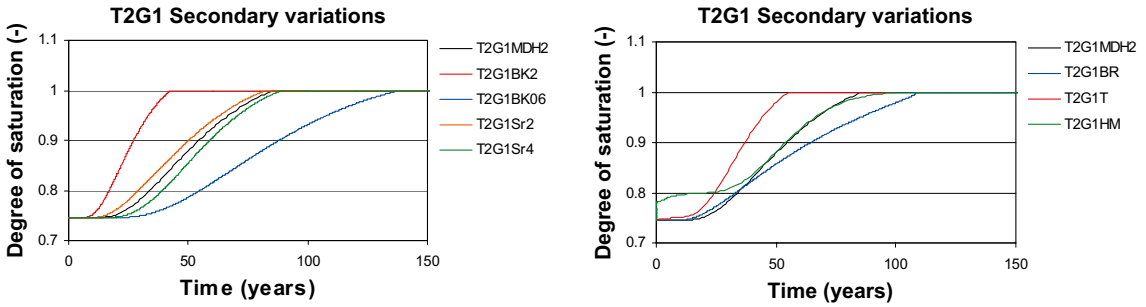

Figure 2-19. *Result from secondary variations. Axisymmetric1D models and maximum fallout. Evolution of degree of saturation at inner nodes in backfill.*

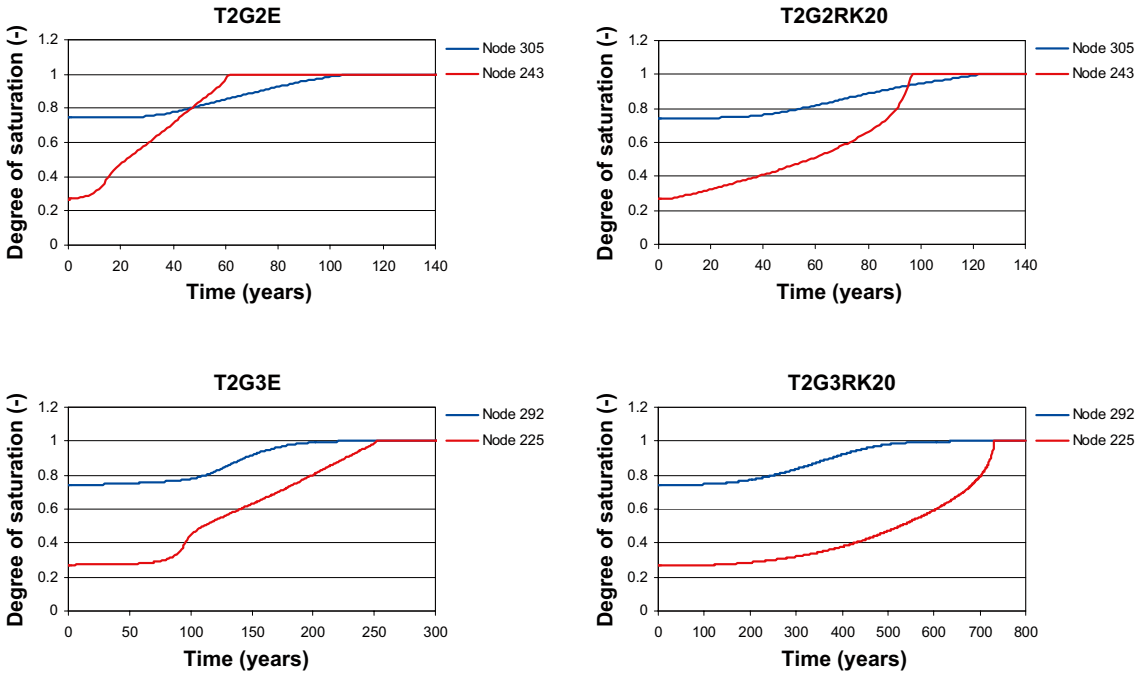

Figure 2-20. *Result from secondary variations. Axisymmetric 2D models and maximum fallout. Evolution of degree of saturation at last hydrated nodes in blocks and pellets. Location of nodes shown in Figure 2-14 and Figure 2-16.*

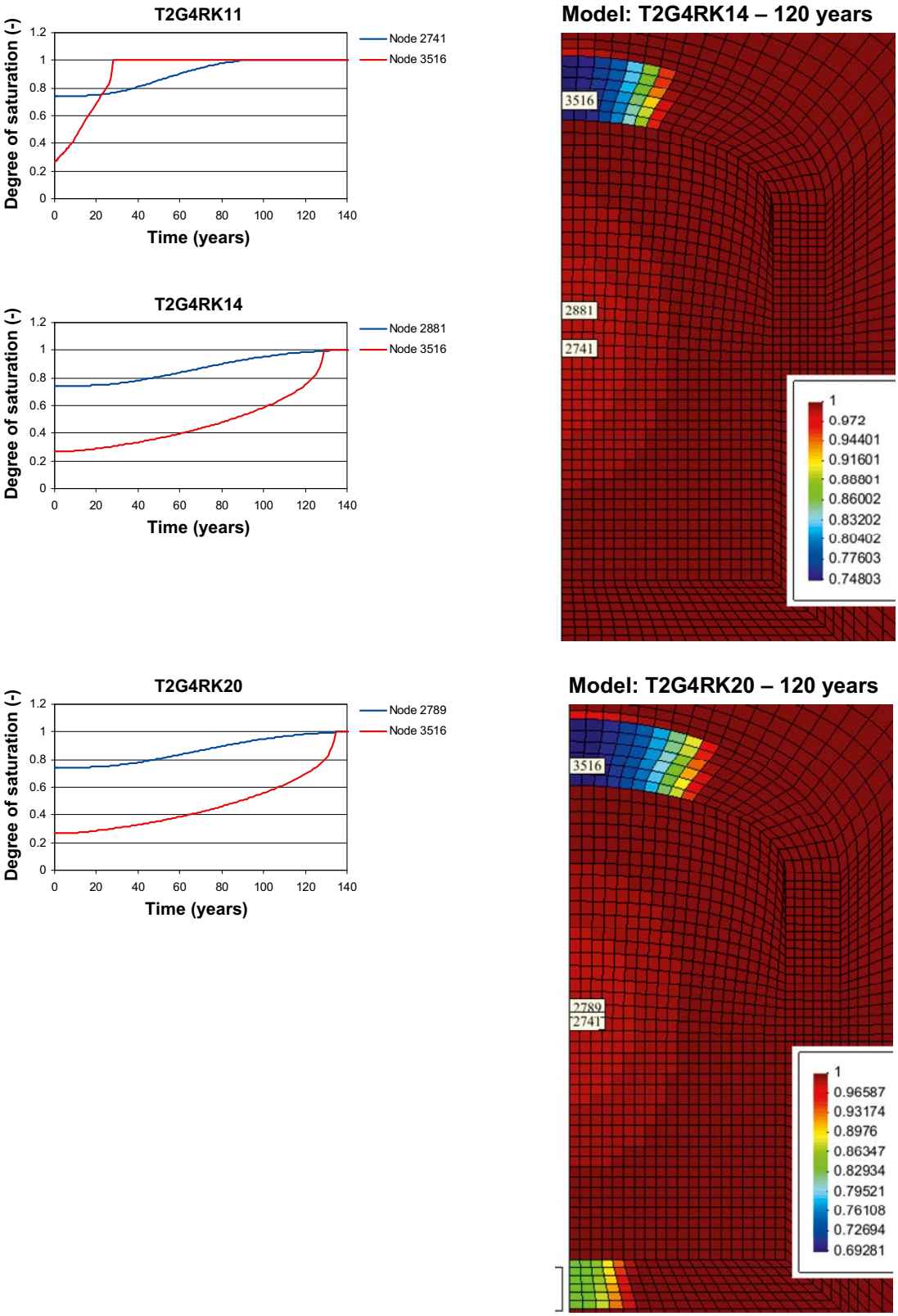

Figure 2-21. *Result from secondary variations. Plane 2D models and maximum fallout. Evolution of degree of saturation at last hydrated nodes in blocks and pellets.*

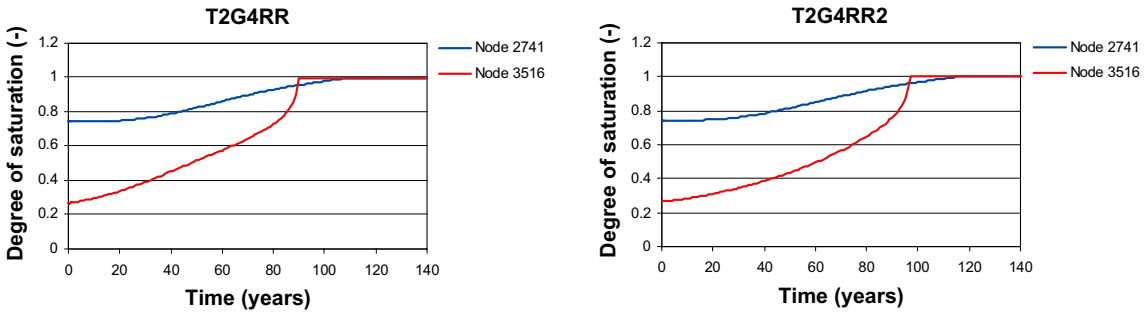

Figure 2-22. Result from secondary variations. Plane 2D models and maximum fallout. Evolution of degree of saturation at last hydrated nodes in blocks and pellets.

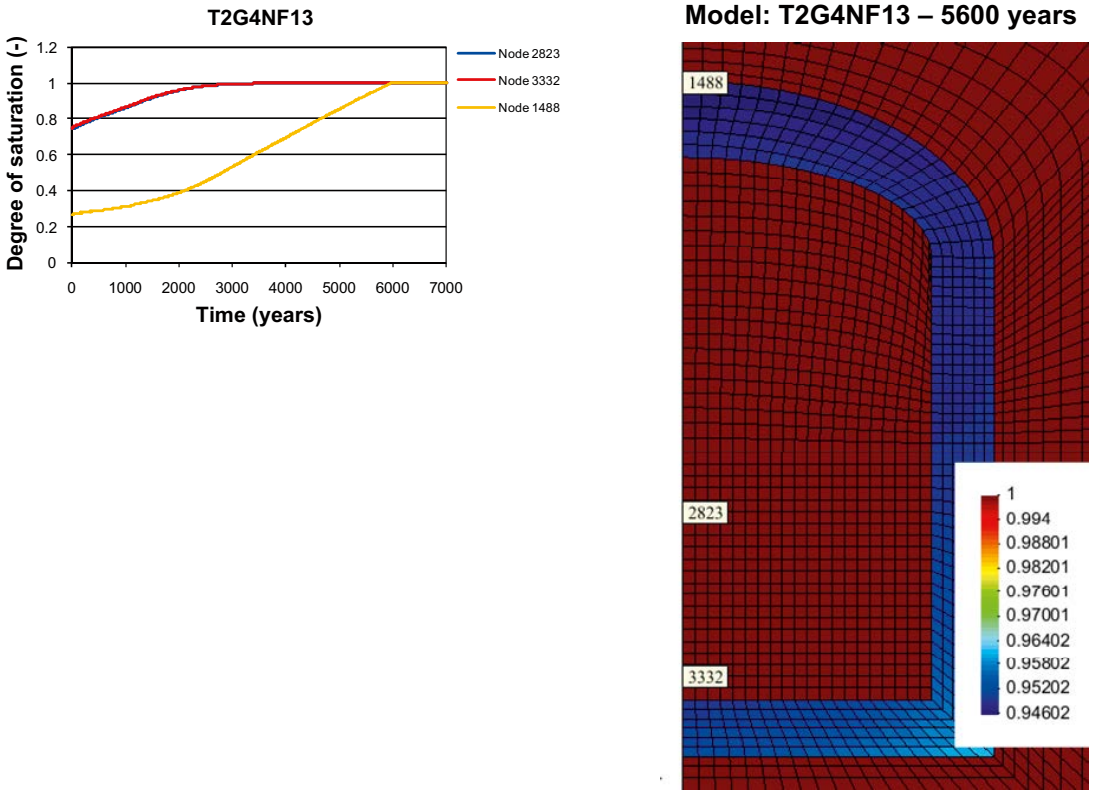

Figure 2-23. Result from secondary variations. Plane 2D models and maximum fallout. Evolution of degree of saturation at last hydrated nodes in blocks and pellets.

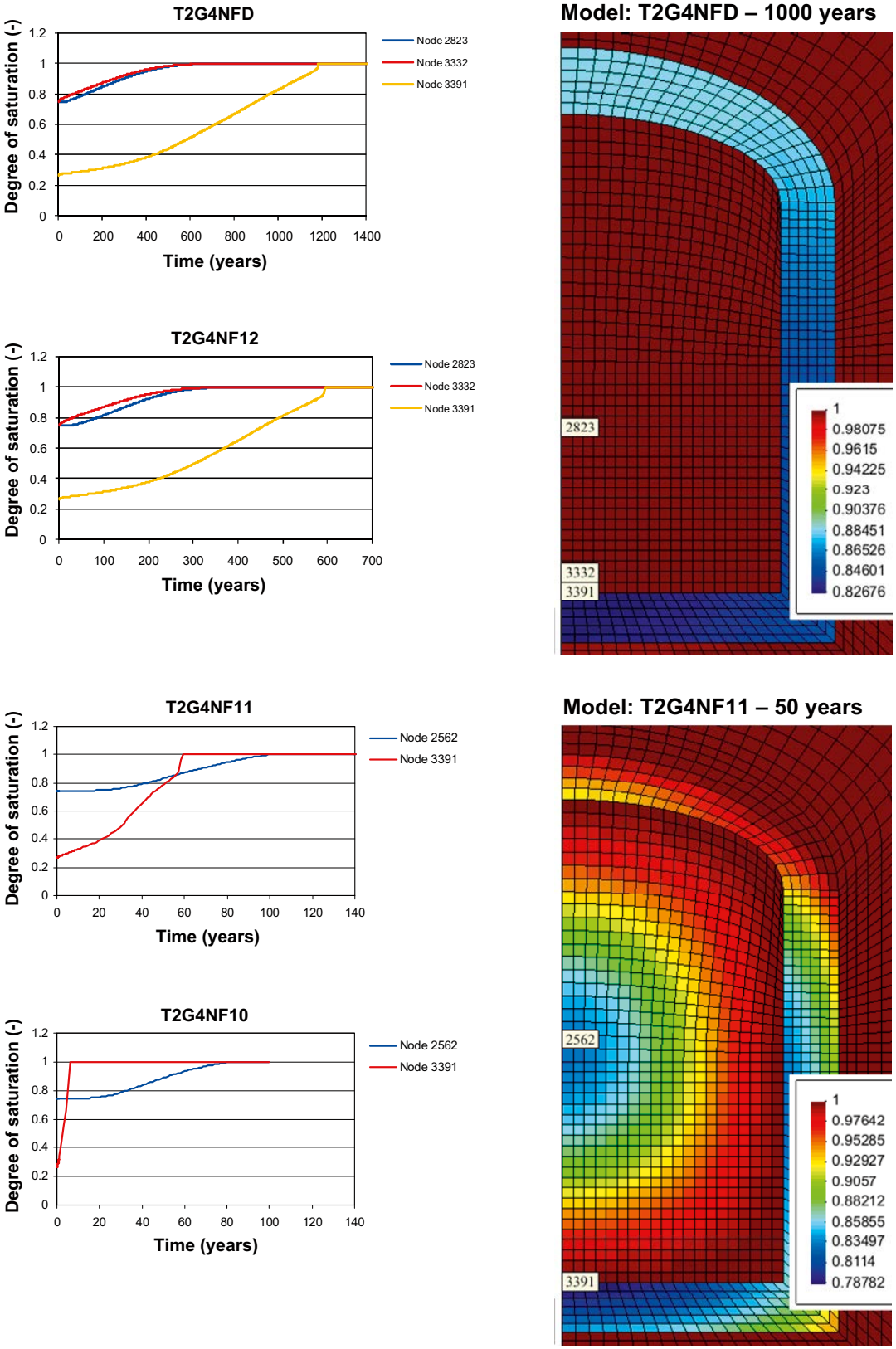

Figure 2-24. *Result from secondary variations. Plane 2D models and maximum fallout. Evolution of degree of saturation at last hydrated nodes in blocks and pellets.*

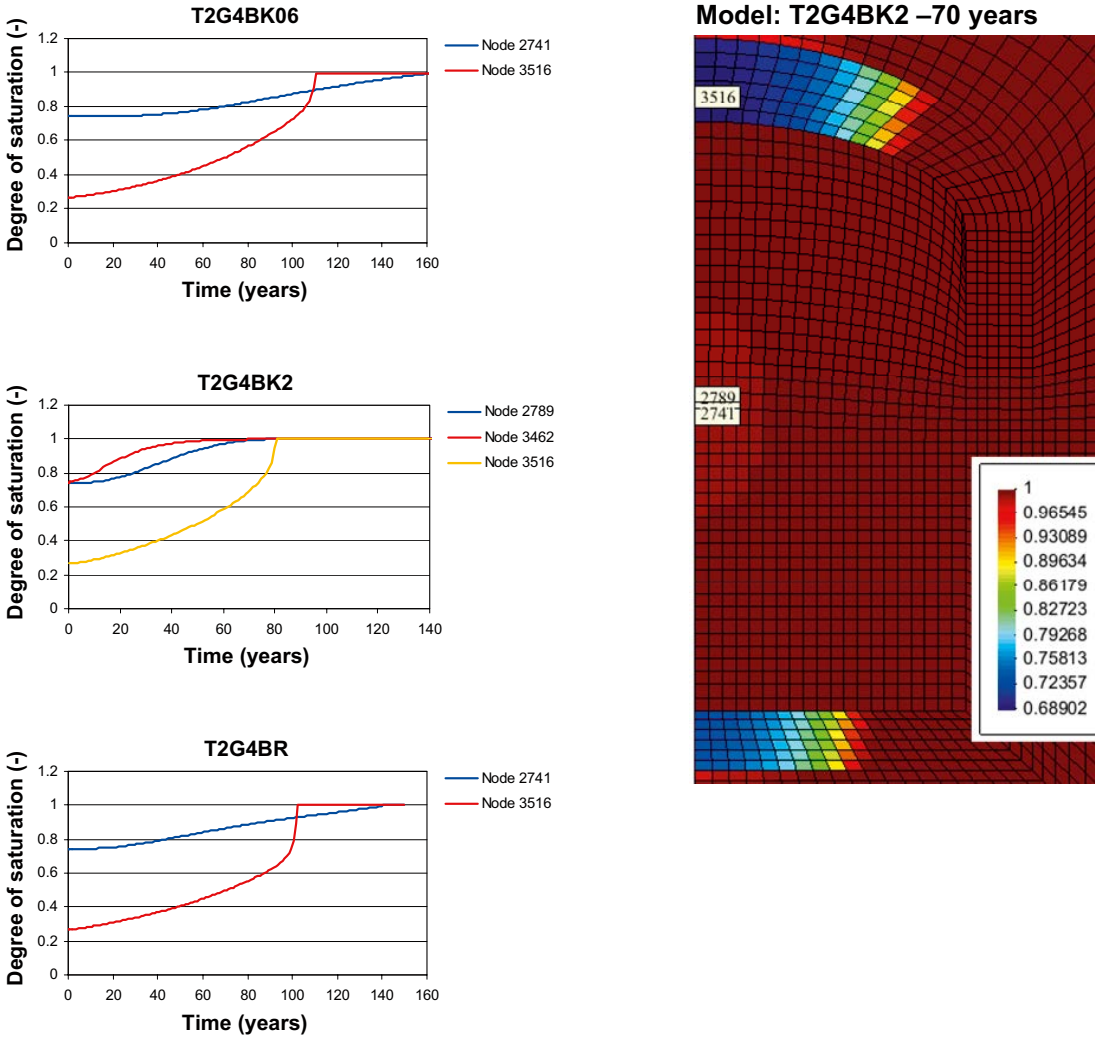

Figure 2-25. *Result from secondary variations. Plane 2D models and maximum fallout. Evolution of degree of saturation at last hydrated nodes in blocks and pellets.*

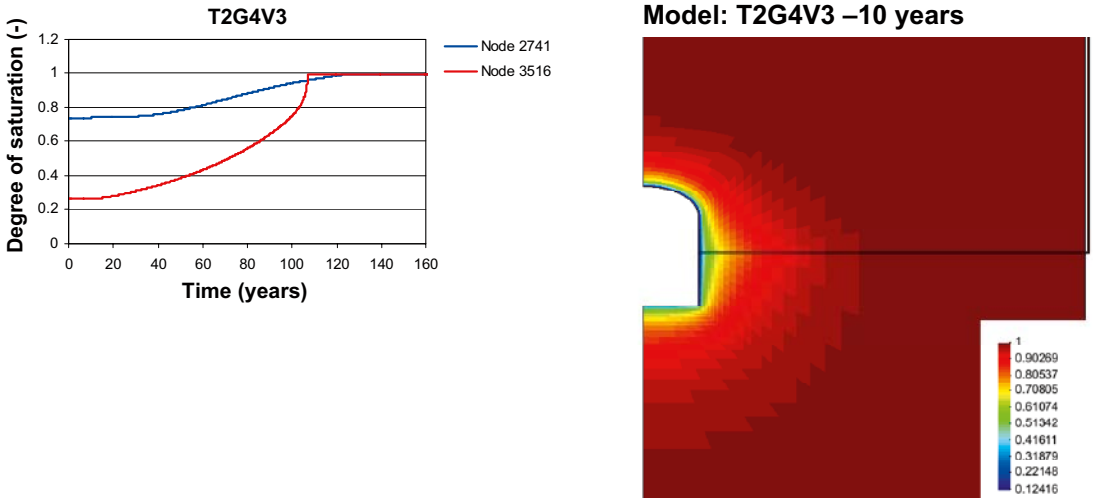

Figure 2-26. *Result from secondary variations. Plane 2D models and maximum fallout. Evolution of degree of saturation at last hydrated nodes in blocks and pellets. Dehydration of rock after 10 years of ventilation (right).*

Table 2-9. Hydration times (years) for primary variation models. Bold numbers indicate cases in which the pellets reach the 95/99% levels at a later stage than in the blocks.

Model	Backfill		Pellets	
	95%	99%	95%	99%
T2G1TDA2	79	107		
T2G1TDH2	67	81		
T2G1TAA2	79	107		
T2G1TAH2	67	81		
T2G1THA2	120	172		
T2G1THH2	84	95		
T2G1MDA2	80	108		
T2G1MDH2	67	81		
T2G1MAA2	79	107		
T2G1MAH2	67	81		
T2G1MHA2	173	251		
T2G1MHH2	84	86		
T2G2TDL2	73	87	16	17
T2G2TDS2	84	98	43	43
T2G2TAL2	69	84	1,1	1,1
T2G2TAS2	77	92	26	27
T2G2THL2	96	107		
T2G2THS2	110	122		
T2G2MDL2	75	89	22	23
T2G2MDS2	96	111	80	81
T2G2MAL2	69	83	1,5	1,5
T2G2MAS2	86	102	60	62
T2G2MHL2	111	113		
T2G2MHS2	150	153		
T2G3TDL	122	140	114	114
T2G3TDS	203	233	**226**	227
T2G3THL	163	176		
T2G3THS	264	277		
T2G3MDL	144	176	**175**	175
T2G3MDS	260	309	**388**	**389**
T2G3MHL	266	269		
T2G3MHS	466	469		
T2G4TDL3	72	86	45	46
T2G4TDS3	81	96	68	69
T2G4THL3	98	109		
T2G4THS2	111	123		
T2G4MDL3	75	89	49	50
T2G4MDS2	92	110	**96**	97
T2G4MHL2	128	132		
T2G4MHS2	161	166		

Table 2-10. Hydration times (years) for secondary variation models. Bold numbers indicate cases in which the pellets reach the 95/99% levels at a later stage than in the blocks.

Model	Backfill		Pellets	
	95%	99%	95%	99%
T2G1BK2	33	41		
T2G1BK06	108	131		
T2G1BR	85	106		
T2G1T	44	52		
T2G1Sr2	63	78		
T2G1Sr4	71	84		
T2G1HM	66	85		
T2G2E	87	102	59	61
T2G2RK20	101	118	96	97
T2G3E	164	195	240	250
T2G3RK20	440	535	728	730
T2G4RK14	99	123	128	129
T2G4RK11	71	85	28	28
T2G4RK20	101	126	134	135
T2G4RR	87	105	89	90
T2G4RR2	92	110	96	97
T2G4NF13	1,881	2,732	5,630	5,903
T2G4NFD	407	571	1,163	1,181
T2G4NF12	231	311	593	594
T2G4NF11	81	95	58	59
T2G4NF10	64	78	6	6
T2G4BK2	54	68	80	81
T2G4BK06	135	158	110	110
T2G4BR	115	137	102	102
T2G4V3*	92	111	97	97

* 10 years of ventilation has been subtracted from results.

2.5.2 Verification of mesh and fracture representation

The relevance of the chosen mesh was investigated by a re-run of one model (T2G2TDL2) with a model (T2G2TDLM3) with finer elements. Each element was divided in four elements, so the number of elements increased from 758 to 3,032. A comparison of the evolution of saturation at two different nodes shows that the result did not change due to the refined mesh (Figure 2-27). The chosen mesh size can therefore be regarded to be sufficient.

The relevance of the fracture representation was investigated with two models (T2G2TDL2 and T2G4TDL3). These were modified (T2G2TFT2 and T2G4TFT2) in order to maintain an atmospheric pressure in the tunnel and to minimize the transport through the rock matrix ($k = 1E{-}27$ m^2). The inflow of 0.1 l/min corresponds to 1.67E–6 m^3/s. At radiuses of 2.5 m and 10 m, and for a model fracture width of 0.1 m, half of this flow corresponds to fluxes of 5.3E–7 and 1.3E–7 m/s, respectively. Similarly, an inflow of 5 l/min into a 300 m tunnel corresponds to 2.8E–7 m^2/s. For a model fracture width of 0.1 m, half of this flow corresponds to a flux of 1.4E–6 m/s. This is approximately within 10% of what is given by the models, see Figure 2-28.

An examination of pressures and fluxes in the rock indicated that the maximum allowed time step in some models (T2G4NF12 and T2G4NF13) was high. These models were therefore re-run with significantly shorter time-steps. This modification only influenced the final saturation time with less than 0.5%.

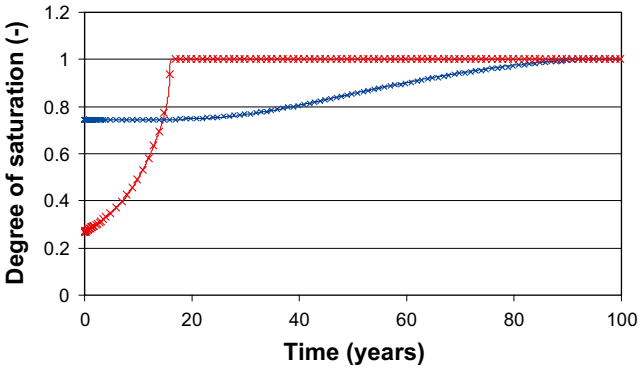

Figure 2-27. *Verification of mesh. Evolution of degree of saturation in last hydrated nodded in blocks (blue) and pellets (red). Symbols show result from employed mesh, lines show results from mesh with quadrupled number of elements.*

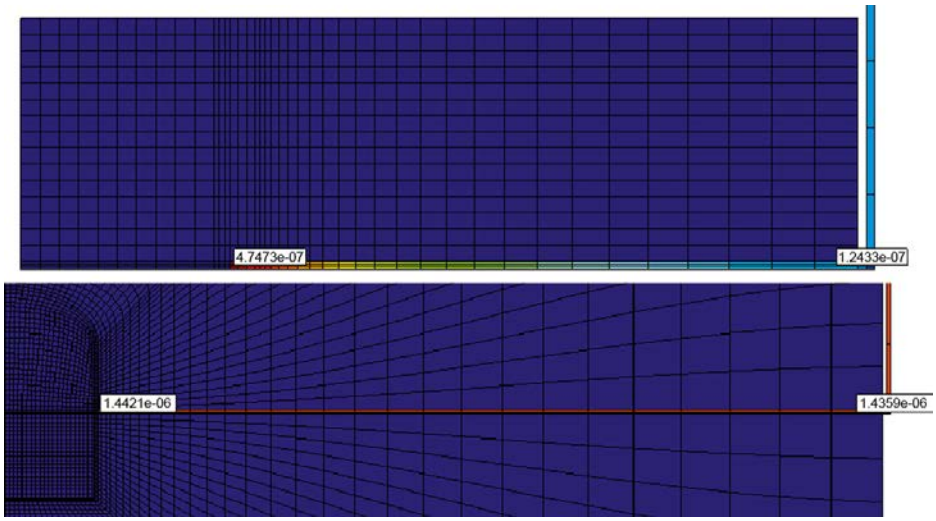

Figure 2-28. *Verification of fracture representations. Steady-state fluxes (m/s) in models.*

2.6 Discussion

2.6.1 Introduction

The time needed for the last node to reach 99% degree of saturation has been regarded as the saturation time. The effects of different variations and features of the models on the saturation time are discussed below. In general, either the backfill or the rock system can be regarding as the limiting factor for the rate of hydration. The results from the 1D models, with hydration times of approx. 80 to 100 years, therefore represents the time needed for the backfill with free access of water. Time scales higher than this represents cases in which the rock system is limiting, either directly through a high homogenous flow resistance, or indirectly through a localized water entry in the tunnel wall, which implies a water transport through the backfill along the tunnel axis. In the latter case, the backfill can therefore also for some configurations be regarded as rate limiting.

The approach with primary variations was largely an attempt to map the effects of different combinations of different section areas, backfill representations, and fracture inflows (or boundary pressure) for different geometries. The secondary variations were initially mainly performed with large plane geometries with fractues. During the course of the work it was noticed that more information could be gained through clear-cut cases with 1D models with altered bentonite properies. A more systematic investigation of the influence of the rock permeability was also performed for geometries without fractures.

2.6.2 Primary variations

Results from all models in the primary variations are compiled in Figure 2-29.

Different *tunnel sections* imply different available pore volumes (or areas). If the rock system limits the rate of hydration, then the pore area will influence the time of filling. This can be clearly seen for a geometry with 24 m fracture distance and with a low fracture transmissivity (see Figure 2-29). With the block/pellets backfill representation, the saturation time is 233 years for a theoretical section, whereas it is 389 years with a section with maximum fallout.

The saturation time for the different *backfill representation* falls in the following order of precedence: the alternated representation (mimicking piping) display the fastest hydration. This is closely followed by the block/pellets representation. Finally, the homogenized representation displays the slowest hydration. The difference between the alternated and block/pellets representation is minor.

The 2D axisymmetric model with 6 m *fracture distance* and the 2D plane geometries display very similar saturation times. This can be expected due to the adopted transmissivities in the model. An inflow of 0.1 l/min over a tunnel length of 6 m is equal to 5 l/min over a tunnel length of 300 m. An increased fracture distance, e.g. from 6 to 24 meters, will obviously tend to increase the saturation time. The extent of influence is, however, not very clear cut. If the rock system is limiting and the pressure condition at the mouth of the fracture is similar, then the time of hydration should be proportional to available pore volume between the fractures, and ultimately the distance between the fracture. This appears to be the case for the low flow block/pellets maximum fallout models, which displayed saturation times of 111 and 389 years for the 6 and 24 m distance, respectively.

An increased *fracture transmissivity* will obviously decrease the saturation time. The observed relation in the models is however far from being proportional, since the backfill clearly is rate limiting in the modelling cases with high transmissivity.

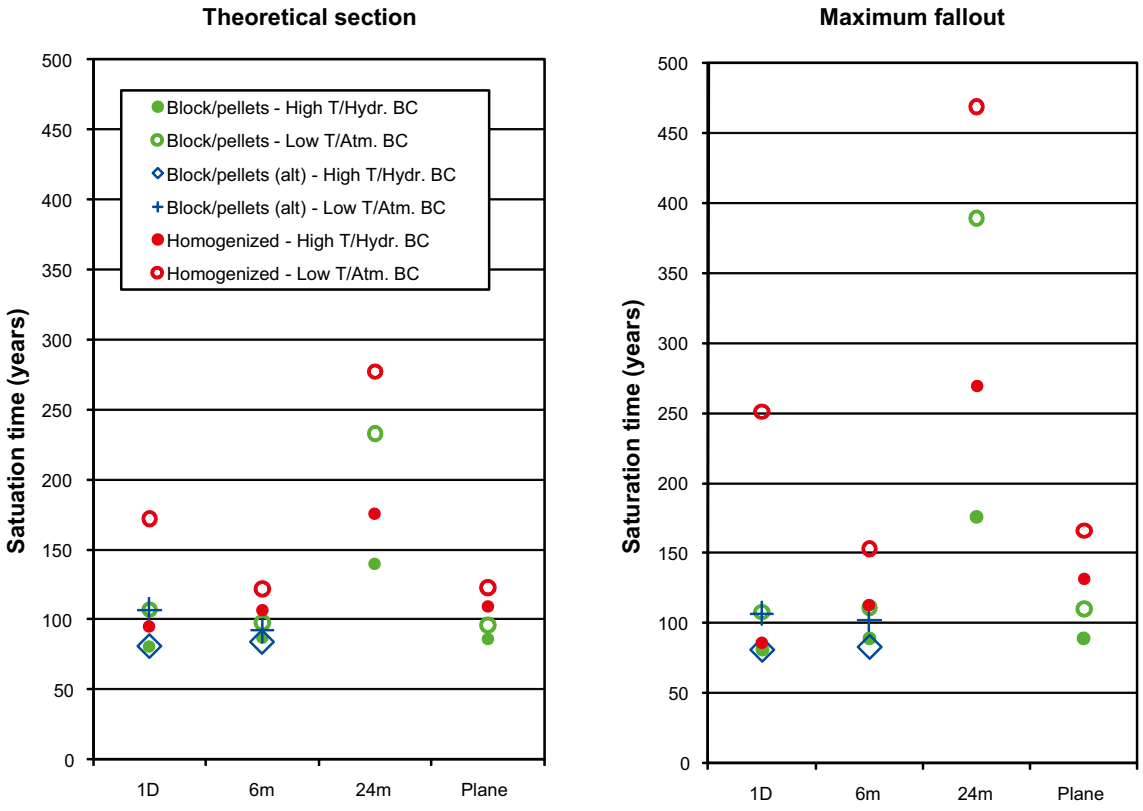

Figure 2-29. *Compilation of saturation times for all primary variations. Legend indicates 1D models with either hydrostatic or atmospheric boundary pressure, and 2D models with either high or low fracture transmissivity.*

2.6.3 Secondary variations

The effects of varied *backfill properties* were investigated with seven 1D models. The associated base case model (T2G1MDH2) yielded a saturation time of 81 years. Enhanced hydration was observed in three of the secondary variation models: with doubled backfill permeability (41 years), taking thermal evolution and temperature dependence of the viscosity into account (52 years), Sr^2 relative permeability (78 years). Slower hydration was observed in four of the models: with 40% lower backfill permeability (131 years), adoption of a steeper retention curve (106 years), taking hydromechanical processes into account (85 years), Sr^4 relative permeability (84 years). It can be noticed that the variation of the permeability displayed the largest influence and that the saturation time is inverse proportional to the permeability. The variation in relative permeabity displayed, in contrast, only a minor influence. The steeper retention curve yielded a slower hydration and this can be expected by evaluating the moisture diffusivity:

$$D(S_r) = \frac{k \cdot k_r(S_r)}{n \cdot \mu} \cdot \frac{dP_l}{dS_r} \qquad (m^2 / s) \tag{2-5}$$

This is generally lower at high saturation degrees for the case of the steeper retention curve (see Figure 2-30). The low influence of the hydromechanical processes is probably due to the rapid hydration of the pellets filled slot in both cases. Finally, the inclusion of the thermal evolution, i.e. the impact of a temperature field on the viscosity, will reduce the saturation time with 30–40%.

The variation of backfill permeabilty were also tested for the plane geometry and the inverse proportionality is shown in Figure 2-31. It can be noted that the for case with doubled permeability, the calculated time (81 yr) is quite close to the limit of the fracture (67 yr). The steeper backfill retention curve was also tested for the plane geometry. In this case the saturation time (137 years) was slightly longer than for the base case (110 years).

In *cases with no fractures*, the permeability of the intact rock will have a strong influence on the time of hydration. For the base case rock permeability, the hydration time will increase to 1,200 years, whereas the time is only 95 years for a hydraulic conductivity of 10^{-11} m/s. A confirmation of this influence can be obtained with a simple analytical calculation (see Figure 2-32).

$$t_{sat} = \frac{A_{pore} \cdot H}{B \cdot K \cdot \Delta h} \tag{2-6}$$

A_{pore} is the available pore area (3.0 m^2 for theoretical section; 5.9 m^2 for maximum fallout), H is the height to hydrostatic pressure (60 m), B is the tunnel distance (40 m), K is the hydraulic conductivity and Δh is the difference in head (460 m).

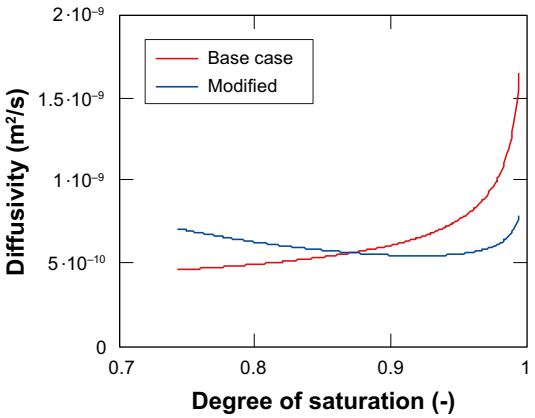

Figure 2-30. *Influence of backfill retention. Water diffusivity versus degree of saturation. Comparison of two parameter sets.*

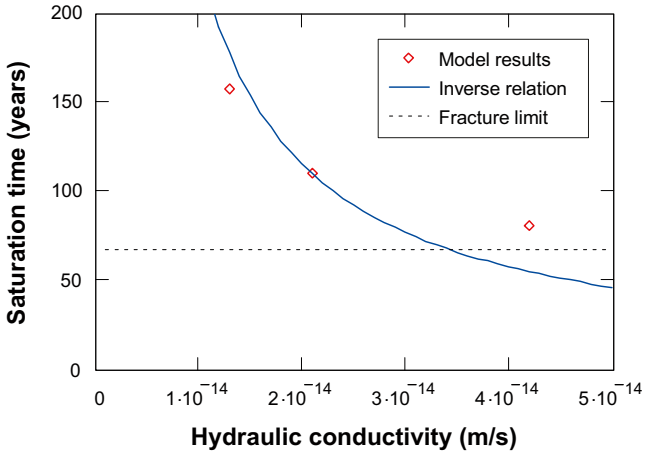

Figure 2-31. *Influence of backfill permeability.*

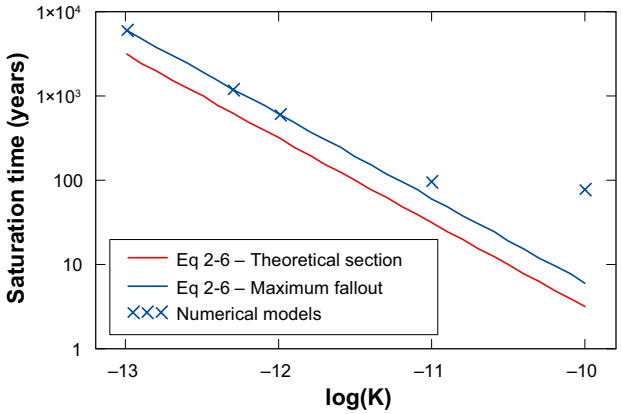

Figure 2-32. *Models without fractures. Comparison of simple analytical expression with numerical models.*

In *cases with representation of fractures* the rock matrix clearly contributes to the hydration process and reduces the saturation time. The contribution diminishes however with decreasing rock permeability. The geometry of the rock appears to determine the extent of the contribution. In the 2D axisymmetric model with 6 m fracture distance and the 2D plane geometry, the saturation time does not increase very much if the rock permeability is set very low (see Figure 2-33). In contrast, the saturation time is doubled in the geometry the 24 m fracture distance.

If the backfill is rate limiting for the hydration process, then *the presence of a high permeable EDZ* would effectively bring about a one dimensional problem. In the case with 6 m fracture distance, the saturation time reduces from 111 to 102 years. If the rock system on the other hand is rate limiting, then the EDZ will reduce the saturation time to the time scale given by fracture and the available the pore volume. In the cases with 24 m fracture distance, a low fracture inflow, a maximum fallout tunnel section, and a block/pellets backfill representation the saturation time will decrease with the inclusion of an EDZ, from 389 to 250 years. The latter value is close to the time needed to fill the available pore volume at a free inflow of 0.001 l/min. An available pore area of 5.9 m^2 and the tunnel length of 24 m yield a filling time of 268 years.

The influence of the *retention curve for the rock* was investigated with a modified case with the retention curve and relative permeability used by /Börgesson and Hernelind 1999/. The time of hydration (105 years) was slightly shorter than for the base case (110 years). This could be expected due to the higher relative permeability in the case (see Figure 2-34). A second variation was made with a very low retention curve for the fracture. This gave the same saturation time as for the base case. It can be remarked that this parameter set yields a very limited dehydration. Since the flow coefficient is very low, then the pressure gradient will be very high (see evaluation in Section 4.3).

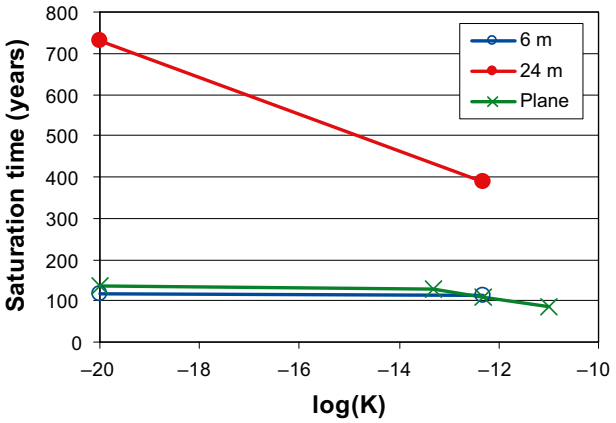

Figure 2-33. *Compilation of saturation times for secondary variations with varied rock permeability.*

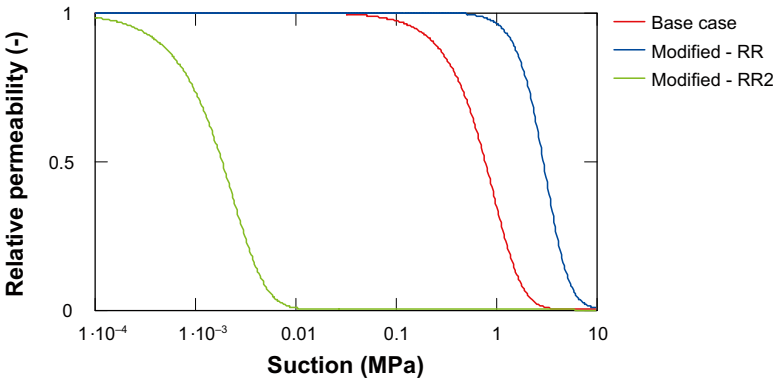

Figure 2-34. *Influence of rock retention and relative permeability. Relative permeability versus suction. RR: first variation, applied to matrix and fracture; RR2: second variation, applied to fracture.*

Finally, a case with ten years of ventiation of tunnel was tested. This gave only marginally longer saturation time (111 years) than the base case (110 years).

2.6.4 Synthesis of results

A selection of the calculated saturation times is compiled in Figure 2-35. Results from three types of models is included: i) all secondary variation 1D models with the associated base case model (only maximum fallout section, and hydrostatic boundary pressure); ii) all 2D axisymmetric fracture models with block/pellets representation (both theoretical and maximum fallout sections, and both high and low transmissivity); and iii) all secondary variation 2D plane models without fractures (only maximum fallout section). The dotted lines in Figure 2-35 represent the base case properties and two different fracture transmissivities. The diagram illustrates the effects of changing the bentonite properties on one hand, and the effects of changing the rock properties and fracture distance on the other.

2.7 Conclusions and uncertainties

The problem of the time-scale of backfill hydration is fundamentally two-parted, so that the time-scale is determined by the backfill material, if the rock is highly permeable, and that the time-scale is determined by the rock, if the rock has a low permeability. Figure 2-35 illustrates these influences as well as the uncertainties of the material properties and the influence of fractured rock. The effects of different bentonite properties and other variations are shown for a situation with free access of water in the top row. The dependence of the rock matrix permeability at a fracture-free condition is shown on the lower row, while the middle rows show results from two different fracture distances.

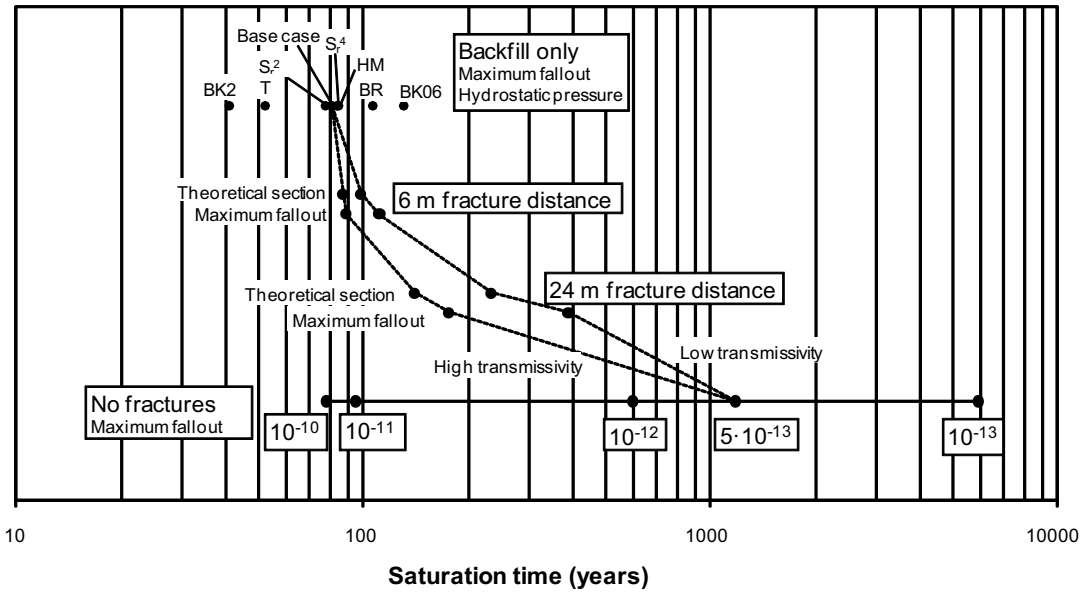

Figure 2-35. *Compilation of backfill saturation times for different geometries and cases. Results from 1D models with free access of water shown on top row (BK2: with doubled backfill permeability; T: with thermal evolution and temperature dependence of the viscosity; S_r^2 and S_r^4: with square and 4th power saturation dependent backfill relative permeability relations – the base case has a cubic dependence; HM: with hydromechanical processes; BR: with steeper backfill water retention curve; BK06: with 40% lower backfill permeability). Results from 2D axisymmetric models with different fracture representations shown in the middle rows. Results from plane 2D models without fractures shown on bottom row (numbers indicate rock hydraulic conductivity). The dotted lines represent the base case properties and two different fracture transmissivities.*

The figure thus demonstrates that the overall influence of the rock on the hydration rate is much higher than the uncertainties related to the bentonite. The calculations for backfill with free access of water result in time-scales of approx. 80 years. A case with no fracture and a matrix hydraulic conductivity of 10^{-13} m/s result in time-scales of approx. 6,000 years.

The presence of EDZ has been shown to be of relevance at geometries with high fracture distance, and this will reduce the influence of the rock. The phenomenon of piping should have a similar effect although this has not been fully demonstrated.

The uncertainty related to the bentonite is associated with scatter in data for the permeability of MX-80 (–40% to +100%), and that the data for the reference material may also differ from the data that has been used. All calculations have been performed at a constant temperature of 20°C, which should imply that the time-scale for the hydration at conditions with free access of water can be approx. 30–40% lower than the calculated values. These effects would in general tend to shorten the time-scale. On the other hand, the influences of a steeper slope of the retention curve and the hydro-mechanical interactions would tend to increase the time-scale.

All secondary variations were performed with geometries with a maximum fallout section. The hydration time for an average section area in the fracture free plane models with low rock permeability would therefore probably be 25% lower than for a maximum fallout section (see Figure 2-32).

The possible influence of gases, such as air in the installed backfill and dissolved gas in the pore water in the rock, has not been investigated. The representation of the rock, with its permeability and a pressure boundary 60 m above the repository, also constitutes an uncertainty. And although efforts have been made to assign relevant fracture transmissivities, the overall representation of fractures has been quite simple.

Finally, the slots between the blocks have not been explicitly modelled. The effect of this simplification is regarded to be of minor importance, but it is uncertain if this implies an enhancement or a reduction in the hydration rate.

3 Analysis of time scale of buffer hydration

3.1 Introduction

The water saturation process and the time scale of the buffer (the bentonite material within the deposition hole) hydration is here investigated.

The buffer water saturation process is externally influenced by the wetting/drying from the rock and backfill and the heating from the canister.

Inwards in the buffer, from the rock side, liquid water is transported by “advective” flow in the buffer (the actual mechanism of liquid flow through the bentonite “matrix” is not totally clear but the term advection is here used since the models uses an advective transportation law) and outwards, from the canister, vapor is transported by diffusion. The advective flow is driven by the water pressure gradient and the diffusive flow is driven by the vapor concentration gradient.

The transportation properties are dependent on the state of the materials in terms of degree of saturation and temperature. The different retention properties of the buffer constituents (cylinder- and ring-shaped blocks and the pellet filled slot) will also influence the water transportation in the buffer.

3.2 Model description

3.2.1 Geometry

2D axisymmetric TH-models were used to study the buffer hydration in a deposition hole. The geometry of the axisymmetric representation of the deposit hole and backfilled tunnel used in this study is shown in Figure 3-1, where the right picture shows a case where a fracture is intersecting the hole wall at canister mid height. The geometry of the deposition hole, tunnel section and the constituents within are designed with respect to what is given in the Buffer production report /SKB 2010a/ and the Backfill production report /SKB 2010b/.

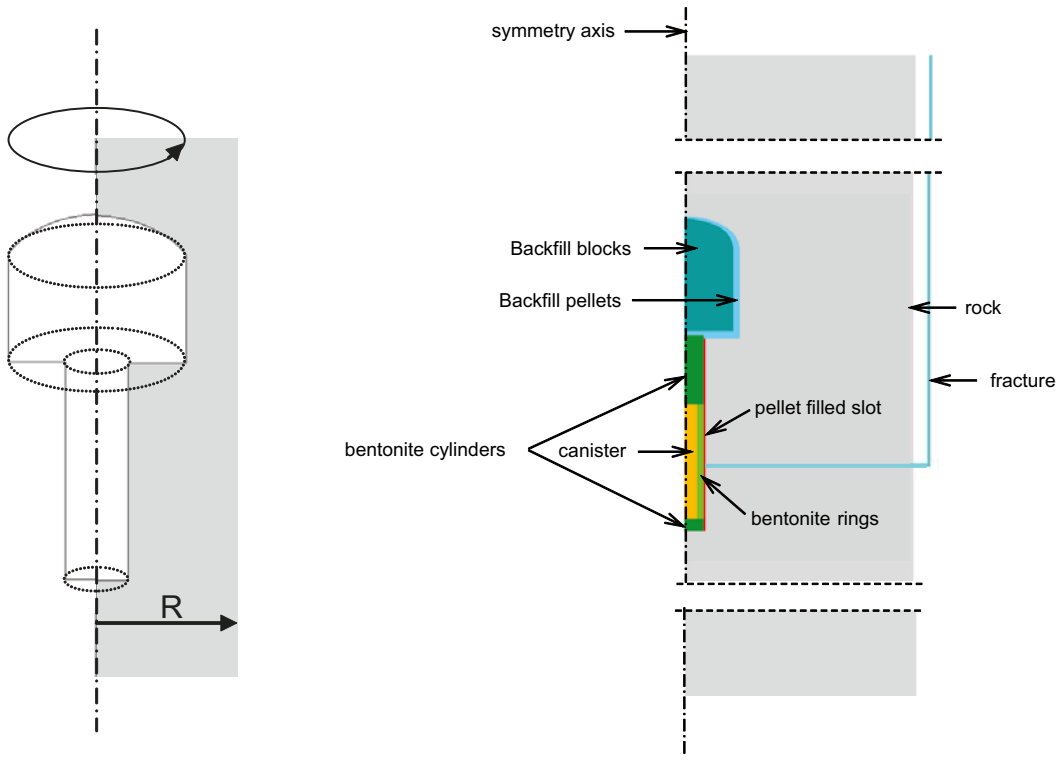

Figure 3-1. *Buffer hydration model geometry. The left figure shows a model where a fracture at canister mid-height is present.*

When designing the axisymmetric model geometrically, considerations of the conditions at the boundaries were made. Therefore, in the following discussion of the geometric dimensions of the model, the boundary conditions are referred to.

The position of the vertical boundary (the outer radius R of the model) was chosen so that the base area of the axisymmetric representation equals the area "belonging" to one deposition hole in a periodic representation of the repository, see Figure 3-2. In this way the deposition hole is allotted with a suitable rock volume in which the hydraulic process contributes to the buffer hydration. The obtained radius following this line of reasoning (assuming 40 m tunnel spacing and 7 m canister spacing as show in Figure 3-2) becomes R = 9.44 m.

The position of the upper and lower boundary (60 m above/below the tunnel floor respectively) was decided from studying a large hydraulic model incorporating an entire repository, described in the Data Report. This model is also discussed in Section 3.2.3 and Appendix A.

The geometry of the constituents in the deposition hole and tunnel are given in Figure 3-3. Models with homogenized buffer and backfill are also used. In these models the combinations:

1. backfill blocks and backfill pellets,
2. cylinder-shaped buffer blocks and surrounding pellet slot,
3. cylinder-shaped buffer blocks and surrounding pellet slot,

are represented with corresponding homogenized materials.

3.2.2 Constitutive laws and parameter values

In the poro-mechanical formulation Code_Bright is based on, an additive split of a material volume element, dv, in a solid volume element, dv_s, and a pore volume element, dv_p is used. Furthermore the pore volume element, dv_p, is additively split into a liquid volume element, dv^l, and a gas volume element, dv^g. The liquid volume element is divided into a liquid water volume element dv_w^l and a liquid air volume element dv_a^l (dissolved air into the liquid).

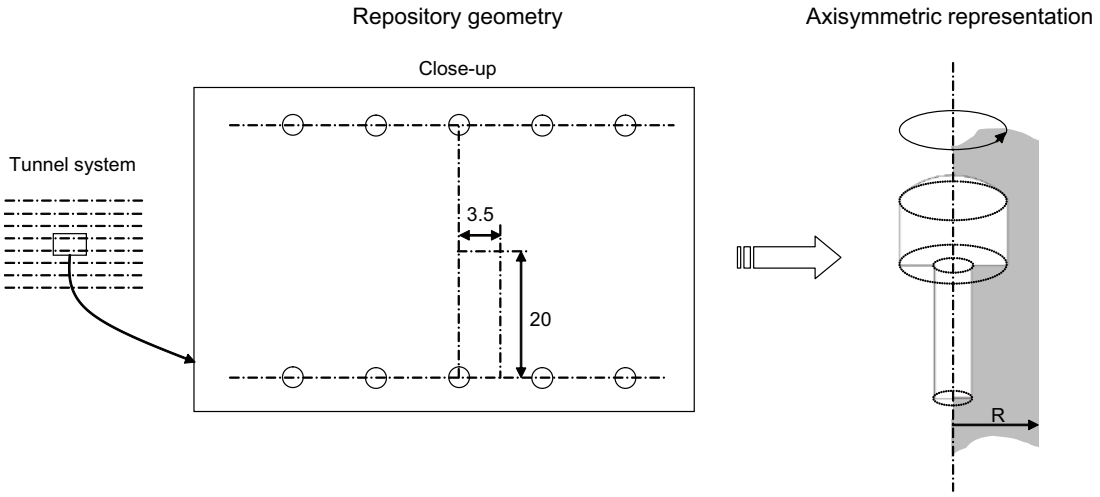

Figure 3-2. *Schematic geometry of the repository (left) and an axisymmetric representation of one deposition hole with an associated tunnel volume (right).*

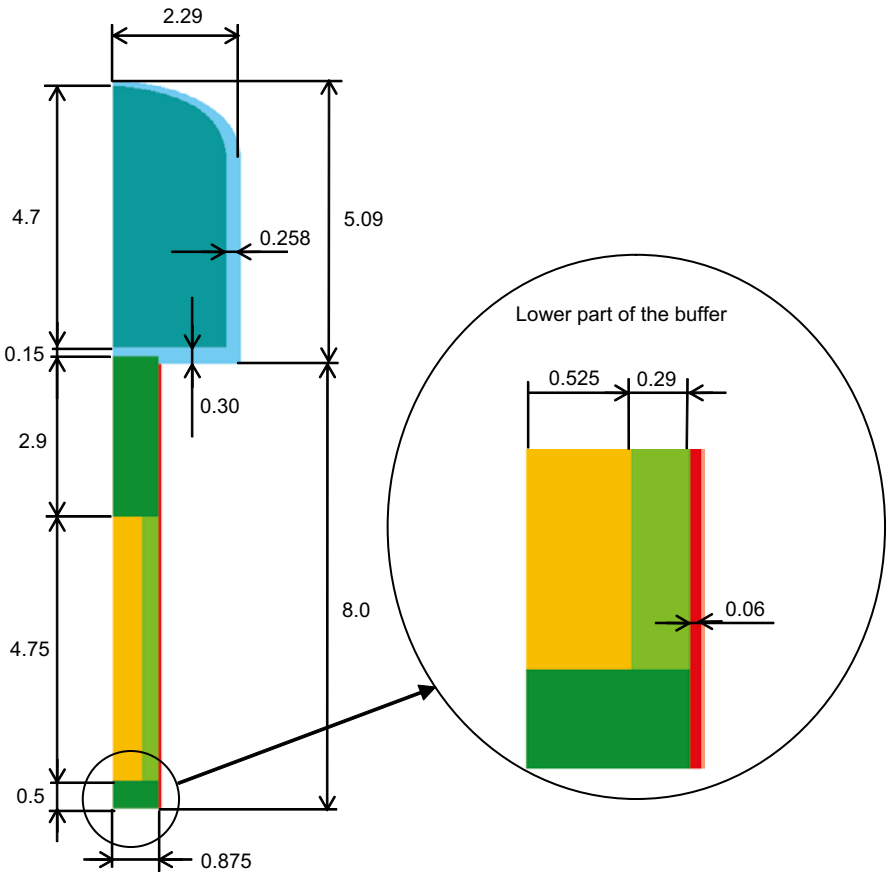

Figure 3-3. *Geometry of the model constituents in the deposition hole and tunnel.*

Using the defined volume elements above, or the corresponding mass elements, the following variables are defined: $w = dm_w^l/dm_s$, $S_l = dv_w^l/dv_p$, $e = dv_p/dv_s$, $n = dv_p/dv$, being the water ratio, water saturation, void ratio and porocity, respectively.

In the THM model, balance laws of; solid mass (which gives the evolution of porosity), water mass, energy for the system and momentum for the system are considered. The gas pressure is constant, 0.1 MPa, in the model. The psycrometric law,

$$\omega_g^w = (\omega_g^w)_0 \frac{RH}{100}$$
$$(\omega_g^w)_0 = f(T) \qquad (3\text{-}1)$$
$$\frac{RH}{100} = \exp\left(\frac{-(p_g - p_l)\, M_w}{R(273.15+T)\rho_l}\right)$$

is used as an equilibrium constraint between the liquid phase and vapour phase of water.

Below the constitutive laws used in the models and the parameter values for the different materials are specified. The setup for the base cases is shown. When constitutive laws or parameter values are used in the models they are specified.

The calibration of the rock thermal conductivity and fracture transmissivity is discussed in the end of this section.

Liquid and gas densities

$$\rho_l = 1002.6\exp(4.5\cdot10^{-4}(p_l - p_{l0}) - 3.4\cdot10^{-4}T)$$

$$\rho_g = \frac{0.018\,p_v}{8.3143(273.15+T)}\cdot RH$$

$$RH = \exp\left(\frac{-(p_g - p_l)\,0.018}{8.3143(273.15+T)\rho_l}\right) \qquad (3\text{-}2)$$

$$p_v = 136075\exp\left(-\frac{5239.7}{273.15+T}\right)$$

Conductive heat flux

$$\mathbf{i}_c = -\lambda\nabla T$$

$$\lambda = \lambda_{sat}S_l + \lambda_{dry}(1-S_l) \qquad (3\text{-}3)$$

Retention behavior, Van Genuchten

$$S_l = \left(1+\left(\frac{S}{p_0}\right)^{1/(1-\lambda)}\right)^{-\lambda} \qquad (3\text{-}4)$$

$$S = p_g - p_l$$

Flow through porous medium

$$\boldsymbol{q}_l = -\frac{kk_{rl}}{\mu_l}\nabla p_l$$

$$k_{rl} = S_l^{\,3}$$

$$k_{rl} = \sqrt{S_l}\left(1-(1-S_l^{\,1/\lambda})^{\lambda}\right)^2 \quad \text{for Rock} \qquad (3\text{-}5)$$

$$\mu_l = 2\cdot10^{-12}\exp\left(\frac{1808.5}{273.15+T}\right)$$

Vapor diffusion

$$\mathbf{i}_g^w = -(n\rho_g(1-S_l)D_m^w)\nabla\omega_g^w$$

$$D_m^w = \tau 5.9\cdot10^{-6}\frac{(273.15+T)^{2.3}}{p_g} \qquad (3\text{-}6)$$

Table 3-1. Data used for initial state MX-80 materials.

Parameter		Buffer ring n=0.36 w=17%	Buffer cylinder n=0.61 w=17%	Buffer pellets n=0.61 w=17%	Backfill block n=0.39 w=17%	Backfill pellets n=0.61 w=17%
Thermal conductivity	λ_{dry} λ_{sat} (W/mK)	0.7 1.3	0.7 1.3	0 1.3	0.7 1.3	0 1.3
Specific heat, density for solid	C (J/kgK) ρ_s (kg/m^3)			800 2,780		
Intrinsic permeability	k (m^2)	1.2E–21	2.0E–21	5.2E–19	2.1E–21	5.2E–19
Relative permeability	k_{rl} (–)			S_r^3		
Vapour diffusion tortuosity	τ (–)			1		
Water retention curve	P_0 (MPa) λ (–)	67.2 0.48	43.5 0.38	0.508 0.26	37.2 0.34	0.162 0.19

Table 3-2. Data used for homogenized MX-80 materials.

Parameter		Homog. buffer cylinder n=0.419 w=17%	Homog. buffer ring n=0.435 w=17%	Homog. backfill n=0.454 w=17%
Thermal conductivity	λ_{dry} λ_{sat} (W/mK)		0.7 1.3	
Specific heat, density for solid	C (J/kgK) ρ_s (kg/m^3)		800 2,780	
Intrinsic permeability	k (m^2)	4.2E–21	6.0E–21	8.9E–21
Relative permeability	k_{rl} (–)		S_r^3	
Vapour diffusion tortuosity	τ (–)		1	
Water retention curve	P_0 (MPa) λ (–)	15.19 0.25	8.93 0.22	5.85 0.21

To obtain the properties of the Homogenized Backfill, a representative tunnel geometry was obtained as an average of the measures of the "Theoretical section" geometry and the "Maximum fall out" geometry defined in the Backfill production report /SKB 2010b/. The "Averaged" geometry had to be considered when suitable properties of the homogenized tunnel backfill materials, backfill blocks and the pellet slot, were evaluated.

Knowing the dimensions of the tunnel, the backfill blocks and an estimate of the slot volume between the blocks made it possible to calculate the pellet volume. The known volumes and densities gave a homogenized void ratio of 0.83. The properties of the homogenized tunnel backfill (retention and permeability) were produced using the same procedure used in the Data report /Åkesson et al. 2010/.

The thermal properties of the Canister have been obtained by considering the canister dimensions (radius = 0.525 m, height = 4.8 m) and calculating volume averages of the properties of the steel inset and the 5 cm thick surrounding copper. The hydraulic properties of the canister have not been specified above, the values were set so that the hydraulic process became insignificant.

For the Rock different values of intrinsic permeability have been used, the two specified are the settings of the base cases. The Van Genuchten law of the relative permeability was used for the rock mass.

Table 3-3. Data used for the rock, fracture and canister materials.

Parameter		Rock n=0.003	Fracture n=0.99	Canister n=0.0001
Thermal conductivity	$\lambda_{dry} = \lambda_{sat}$ (W/mK)	2.8	2.8	90
Specific heat density for solid	C (J/kgK) ρ_s (kg/m^3)	770 2,277	770 2,277	480 7,500
Intrinsic permeability	k (m^2)	1.0E–18 1.0E–19	4.3E–15 4.3E–17	–
Relative permeability	k_{rl} (–)	λ = 0.6*	S_r^3	–
Vapour diffusion tortuosity	τ (–)	1	1	–
Water retention curve	P_0 (MPa) λ (–)	1.74 0.6	1.74 0.6	–

* Van Genuchten is used, see Equation (3-5.c).

Rock thermal conductivity

The thermal rock conductivity is calibrated by matching the temperature evolution at the deposition hole rock wall at canister mid-height of a thermal model with the result obtained by an analytical solution /Hökmark et al. 2009/, see Figure 3-4. In the analytical model a canister spacing of 6 m, tunnel spacing of 40 m and a thermal rock conductivity of 3.57 W/(m·K) has been used. The obtained thermal rock conductivity for the FE-model that matches the analytical solution is 2.8 W/(m·K).

The Code_Bright model could therefore, in a thermal sense, be considered to have the approximate thermal rock conductivity 3.57 W/(m·K), a canister spacing of 6 m, tunnel spacing of 40 m and implicit consider the heat contribution from the surrounding canisters.

Fracture transmissivity

A suitable fracture transmissivity was produced by using the constraint that the total inflow from the fracture $Q = A_f\, q = 0.1$ l/min. This is the maximum permissible inflow into a deposition hole. An expression of the flux inflow q from a water bearing fracture into an open deposition hole in an axisymmetric model was derived. The derivation is shown in Appendix. The fracture is assumed to have the geometry shown in Figure 3-5 below, where (r_0,z_1) are the coordinates of the fracture outlet into the deposition hole, and (r_1,z_0) are the position where the fracture is pressurized. z is aligned with the symmetry axis.

The obtained expression of the inflowing water flux at the hole wall q is,

$$q_r(r_0) = \left(\frac{r_0}{r_1}\frac{z_1 - z_0}{K_a} - \frac{r_0}{K_r}\ln\left(\frac{r_1}{r_0}\right) \right)^{-1} \left(h(z_0) - h(r_0) - z_1 + z_0 \right) \qquad (3\text{-}7)$$

Inserting the geometry data of the model together with the boundary pressures $p(h(z_0)) = 4$ MPa, $p(h(r_0)) = 0.1$ MPa and choosing $K_a = K_r = 4.2\cdot10^{-8}$ m/s gives an inflow of $Q = 0.1$ l/min. The corresponding transmissivity (obtained from knowing the fracture width, $w = 0.125$ m, used in the model) and permeability are $T = 5.25\cdot10^{-9}$ m²/s and $k = 4.31\cdot10^{-15}$ m², respectively.

3.2.3 Boundary conditions and thermal load

Below a motivation for the boundary conditions, thermal and hydraulic, which are applied to the axisymmetric deposition hole model, follows. The applied boundary conditions are shown schematically in Figure 3-6.

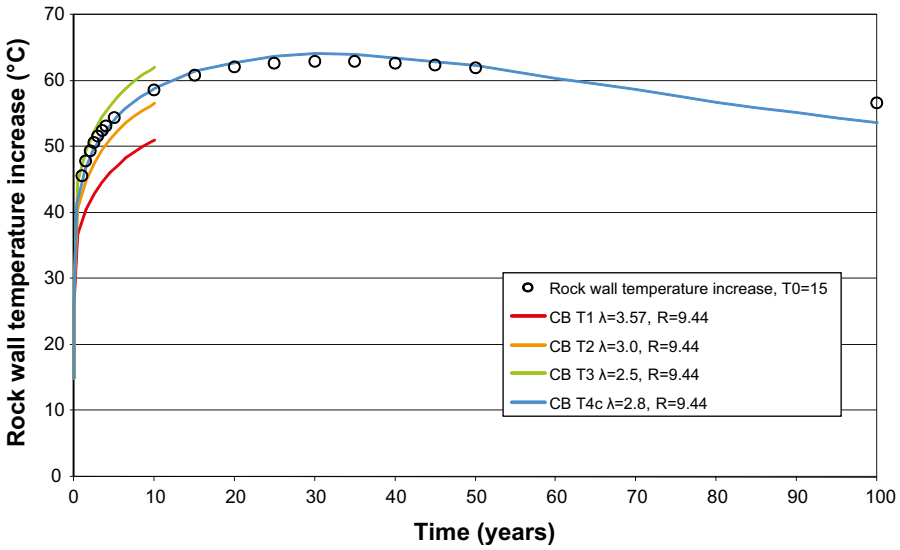

Figure 3-4. *Rock wall temperature evolution at canister mid height. Analytical solution and numerical solutions using different thermal conductivities.*

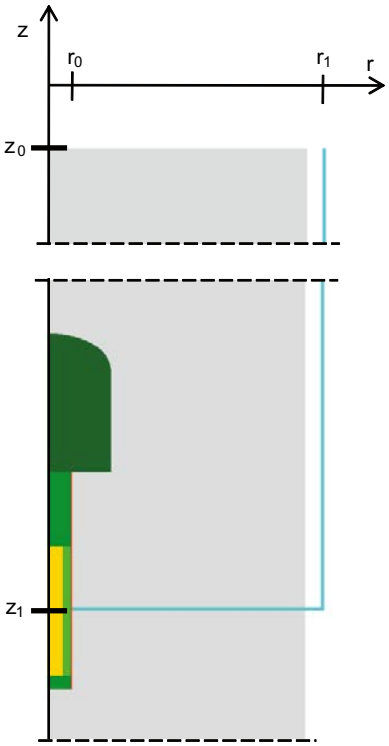

Figure 3-5. *Fracture geometry.*

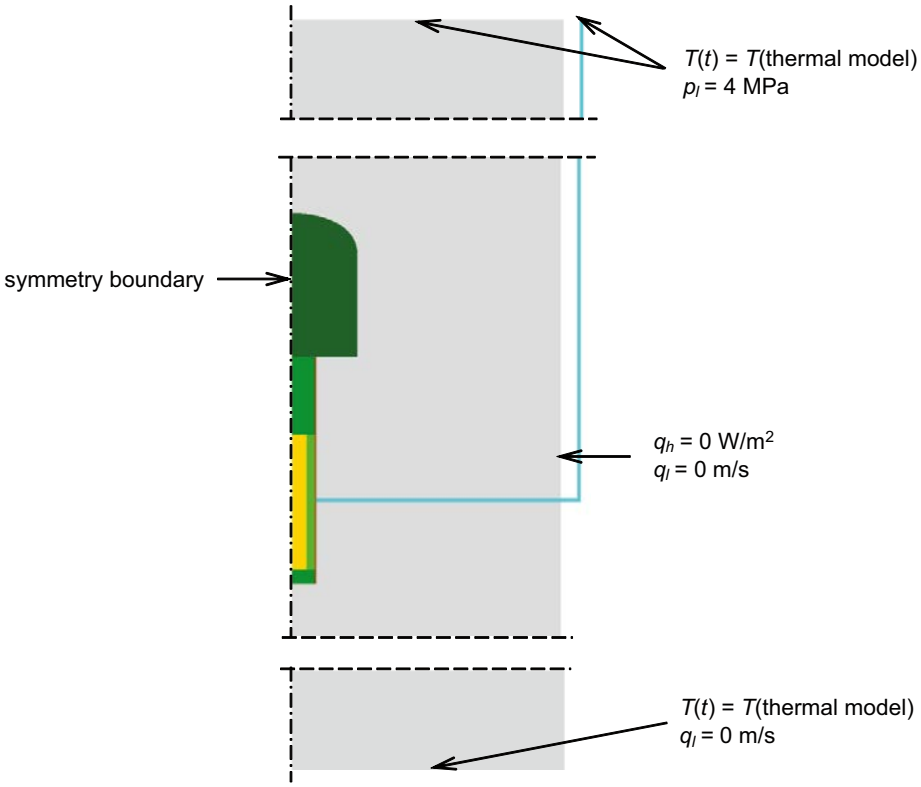

Figure 3-6. *Applied boundary conditions.*

Heat load and thermal boundary conditions

The heat load (the canister power) is prescribed according to the expression reported in /Hökmark et al. 2009/,

$$P(t) = P(0)\sum_{i=1}^{i_{max}} a_i \exp(-t/t_i) \qquad (3\text{-}8)$$

where $P(0)$ = 1,700 W, i_{max} = 7 and the parameters a_i and t_i have the values shown in Table 3-4.

The canister power is prescribed on two concentric vertically orientated cylinders within the canister material. 1/3 of the total heat load is prescribed at the radial distance r = 0.105 m and 2/3 of the total heat load at r = 0.315 m. This approach is used in order to consider that 4 fuel elements and 8 fuel elements are placed at these approximate radial distances, respectively.

On the vertical boundary an adiabatic thermal condition is prescribed.

The thermal boundary conditions at the upper and lower boundaries are represented by prescribed temperature evolutions obtained from a thermal model, used in the THM report concerning the geosphere /Hökmark et al. 2010/, where the entire repository with the surrounding rock mass is considered, see Figure 3-7. In the thermal model the canister spacing is 6 m or 6.8 m, dependent on the location within the repository, and the thermal conductivity is 3.57 W/(m·K).

Table 3-4. Decay function coefficients and the corresponding canister power graph.

i	t_i	a_i
1	20	0.060
2	50	0.705
3	200	–0.055
4	500	0.250
5	2,000	0.025
6	5,000	–0.009
7	20,000	0.024

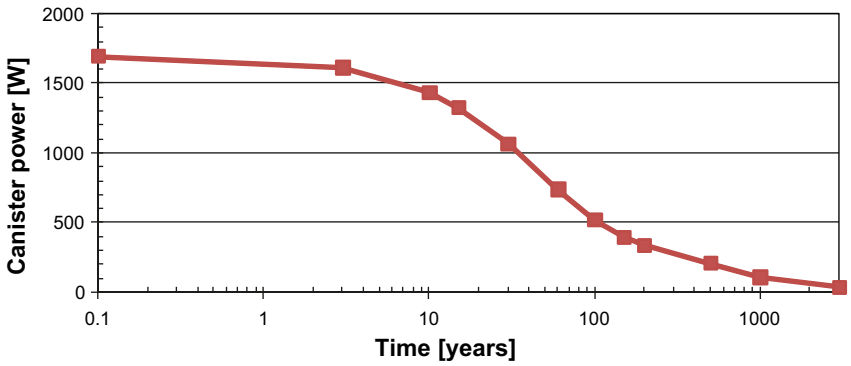

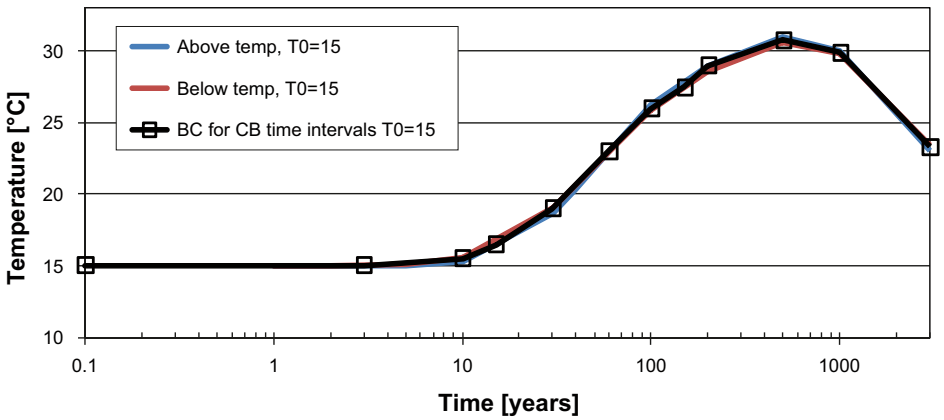

Figure 3-7. *Temperature change at the upper and lower boundary obtained from the thermal model of an entire repository presented in /Hökmark et al. 2010/.*

Hydraulic boundary conditions

In a cylindrical large scale hydraulic model (Height = 1,000 m, Radius = 3,057 m) the repository is represented by a disc centered at –460 m depth with a height of h_r = 6 m (approximately the tunnel height) and the radius r_r = 1,000 m. The disk models the repository in a homogeneous way, where the backfilled tunnels and the surrounding rock are averaged according to the description in Appendix A. The geometry and applied boundary conditions of the large model is shown in Figure 3-8. The hydraulic conductivity of the rock was prescribed according to the values shown in Table 3-5. The values in Table 3-5 correspond to field-measurements from Forsmark /Follin et al. 2007/.

In the large H-model the repository acts as a sink for water, and the water pressure evolution may be recorded at suitable depths (above and below the repository). As mentioned when describing the geometry, the depths 400 m and 520 m (60 m above/below the repository) were here chosen. Since there is a significant change in hydraulic conductivity at 400 m depth, the water pressure will not be significantly affected at this depth. Choosing the upper boundary position at 400 m therefore seems convenient. For symmetry reasons the lower boundary was then decided to be situated at 520 m depth.

Thus, these depths define the position of the upper and lower boundary in the smaller TH-model of the deposition hole only, and the recorded water pressure evolutions at these depths were thought to be used as boundary conditions in the deposition hole model. This approach, with respect to the hydraulic conditions of the lower boundary, was however later on abandoned in favour for a simplified approach where a zero water flux boundary condition was used at the lower boundary.

The hydraulic boundary conditions of the upper and lower boundaries were considered to be taken as the water pressures obtained from the large H-model. It was however found from comparing the model responses from a 1,000 m deep model with a 520 m deep model (i.e. large H-models), both with closed lower boundaries, that no significant difference in time until saturation in the repository material occurred, see Appendix. Therefore, in the deposition hole model, a zero water flux boundary condition is adopted over the vertical boundary.

Table 3-5. Rock conductivities used in the large hydraulic model.

Rock conductivity m/s	Position m
$K = 1.44 \cdot 10^{-7}$	depth < 200
$K = 5.18 \cdot 10^{-10}$	depth > 200 and radius > 1,600
$K = 6.04 \cdot 10^{-12}$	depth > 400 and radius < 1,600

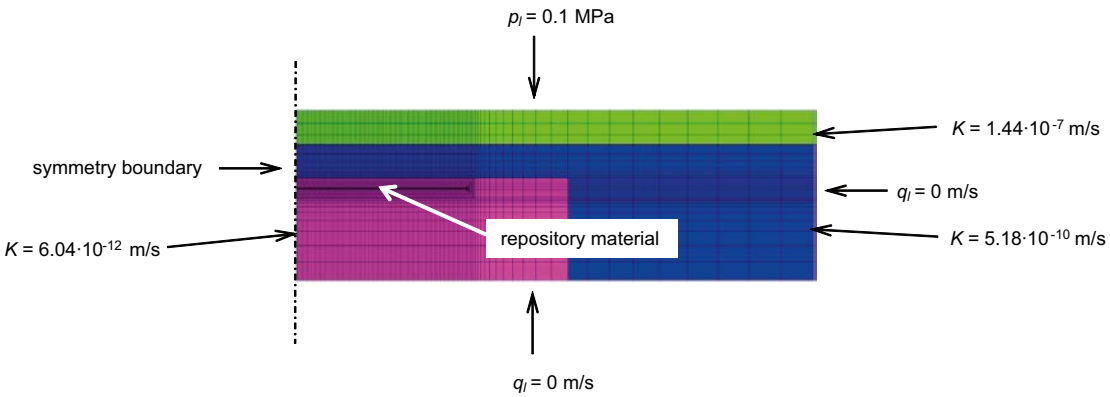

Figure 3-8. *Large hydraulic axisymmetric repository model.*

3.3 Investigations and models

Here a brief overview of the investigations made is given. The models used for performing the investigations are also characterized.

The models have been divided in two different sets. The first set contains what could be called the base case models and the second set contains models with special features.

3.3.1 Evaluation of the saturation times obtained for initial and homogenized state TH models

No mechanical behaviour has been included in the models used for this task. A mechanical homogenization will however take place between the bentonite blocks and the pellet filling. To account for the effect of the homogenization, two extreme cases are analyzed. The saturation time is calculated for 1) a model where the initial state (I) void ratios are adopted and 2) a model where a fully developed homogenized state (H) is assumed. Using this approach the actual saturation time is assumned to be bounded by the I-model and H-model saturation times.

To validate the approach, comparisons between THM-models of the Canister Retrieval Test (CRT) experiment (used in the Natural Buffer Homogenization task) and corresponding TH-models using the initial state or homogenized state representation have been made.

3.3.2 Overview of the buffer water saturation process

A general overview of the saturation process in the buffer is given by studying two models (1I, 1H).

3.3.3 Estimate of buffer saturation time for unfractured rock

An estimate of the saturation time of the buffer in models with unfractured rock is given. The estimated saturation time is given as a range, where the bounds are obtained from studying the responses of four different models (1I, 1H, 2I and 2H).

3.3.4 Estimate of buffer saturation time for fractured rock

Two different vertical fracture positions are analyzed. Either the fracture intersects with the hole wall at the canister mid-height (CMH) or the fracture intersects with the tunnel wall (T). For each fracture position, the estimated saturation time is given as a range, where the bounds are obtained from studying the responses of four different models (3I, 3H, 4I, 4H for CMH and 5I, 5H, 6I, 6H for T).

3.3.5 The effect of extremely low rock permeability

The model with unfractured rock is equipped with an extremely low rock conductivity, $K = 10^{-13}$ m/s. The saturation time in the buffer, the saturation evolution in critical points and the peak temperature in the buffer and at the deposition hole rock wall are given. Two models are used (8I and 8H).

3.3.6 Rock permeability dependence

The influence of rock permeability on saturation time is investigated for models with unfractured rock. The results obtained from eight models are used (1I, 2I, 7I, 8I, 1H, 2H, 7H, 8H).

3.3.7 The effect of higher rock retention

The effect from using higher rock retention as compared to the ordinary setting is investigated. Two models with different permeability are used (11I-high and 11I-low).

3.3.8 The effect of an initially ventilated tunnel

The effect of ventilation of the tunnel prior to the buffer and backfill installation is investigated. The tunnel ventilation is modeled using an empty hydraulic model (no material in the tunnel or deposit hole) with a prescribed *RH* on the internal boundary. Two different values of *RH* are used which gives two different pre installation models (preA and preB).

Approximate representations of the pressure fields obtained from the pre installation models are prescribed as an initial condition onto models where the buffer and backfill are represented. The pre installation pressure fields are prescribed onto high and low permeable models. Four post installation models are used (14I A-high, 14I A-low, 14I B-high, 14I B-low).

3.3.9 The effect of altered block retention

An alternative bentonite block retention curve is used. Two models with different rock permeability are used (12I-high and 12I-low).

3.3.10 The effect of altered buffer permeability

The effect from changing the bentonite buffer permeability (block and pellet slot) is investigated by using two different permeability setups (the choices are denoted by A and B). Four different models are used (15I A-high, 15I A-low, 15I B-high and 15I B-low).

3.3.11 Description of the first set of models

Mechanical representation

As described above, mechanically, two extreme cases are analyzed to simplify the simulations by allowing excluding the mechanical logic in the models.

- The first case (initial state model denoted I) uses initial densities for block and pellets (for both buffer and backfill).
- The second case (homogenized state model denoted H) uses three homogenized densities: (1) cylinder shaped buffer block and surrounding pellets, (2) ring shaped buffer blocks and surrounding pellets and (3) backfill block and surrounding pellets.

This approach makes it possible to consider the influence from the mechanical process explicitly, using TH-models only, since the used extreme cases bounds the “actual” evolving mechanical state.

Rock hydraulic conductivity

Two cases with representations having different properties in terms of permeability are investigated. This is achieved by altering the hydraulic conductivity in the rock material. In the more permeable case a higher value of hydraulic conductivity (10^{-11} m/s) is used, which corresponds approximately to a sparsely fractured rock mass at the present size scale. In the less permeable representation the rock mass is allotted with a low hydraulic conductivity (10^{-12}), estimated to correspond to a close to non-fractured rock mass at this size scale.

Fracture position

Two different vertical fracture positions are analyzed. Either the fracture intersects with the hole wall at the canister mid-height (CMH) or the fracture intersects with the tunnel wall (T). Also, the case with no fracture is studied (NF).

Fracture transmissivities

The fracture is also allotted with two different transmissivities. The first transmissivity is calibrated to give the maximum allowed deposition hole inflow (Q = 0.1 l/min) and the second choice is one percent of the first choice.

The variations of the models in the first set are compiled in Table 3-6 below.

Table 3-6. Variations in the first set of models.

Mechanical representation	Initial state (I)		Homogenized state (H)
Rock conductivity	$K = 10^{-11}$ m/s (K-high)		$K = 10^{-12}$ m/s (K-low)
Fracture position	No Fracture (NF)	Canister Mid Height (CMH)	Tunnel (T)
Fracture transmissivity	$T = T_{0.1} = 5.3 \cdot 10^{-9}$ m²/s (T-high)		$T = T_{0.1}/100 = 5.3 \cdot 10^{-11}$ m²/s (T-low)

Beforehand, for all of the fracture options (NF, CMH and T), the cases with a highly permeable rock (K-high) and a high fracture transmissivity (T-high) are known to produce the most rapid saturation process. These cases, simulated for both buffer/backfill representations (I and H), give bounds of how long the saturation process will take in the fastest case. The models are denoted 1(I, H), 3(I, H), 5(I, H) in Table 3-7.

Similarly, the cases with a lower permeable rock representation (K-low) and a lower fracture transmissivity (T-low) give together with the different buffer/backfill representations (I and H) bounds for how long the saturation process will take in the slowest case. These models are denoted 2(I, H), 4(I, H), 6(I, H) in Table 3-7.

3.3.12 Description of the second set of models

The models in the second set are based on models in the first set, but equipped with a special feature see Table 3-8.

- extremely low hydraulic rock conductivity
- extremely high hydraulic rock conductivity
- high rock retention
- altered initial condition
- altered block retention
- altered buffer permeability.

Table 3-7. Compilation of the first set of models. I:Initial state, H:Homogenized state, NF:No Fracture, CMH:Canister Mid-Height fracture, T:Tunnel fracture.

Model		Buffer/Backfill representation		Rock conductivity		Fracture position			Fracture transmissivity	
		I	H	K-high	K-low	NF	CMH	T	T-high	T-low
1	I	X		X		X				
1	H		X	X		X				
2	I	X			X	X				
2	H		X		X	X				
3	I	X		X			X		X	
3	H		X	X			X		X	
4	I	X			X		X			X
4	H		X		X		X			X
5	I	X		X				X	X	
5	H		X	X				X	X	
6	I	X			X			X		X
6	H		X		X			X		X

Table 3-8. Compilation of the second set of models. I:Initial state, H:Homogenized state, NF:No Fracture, CMH:Canister Mid-Height fracture, T:Tunnel fracture.

Model		Basic setup	Special feature	
8	I	NF, I, K-low (2I)	Extremely low rock conductivity New buffer thermal conductivity law	$K = 10^{-13}$
8	H	NF, H, K-low (2H)	Extremely low rock conductivity New buffer thermal conductivity law New buffer retention law	$K = 10^{-13}$
7	I	NF, I, K-high (1I)	Extremely high rock conductivity	$K = 10^{-10}$
7	H	NF, H, K-high (1H)	Extremely high rock conductivity	$K = 10^{-10}$
11 I	high	NF, I, K-high (1I)	Higher rock retention	
11 I	low	NF, I, K-low (2I)		
14 I	preA		Initial ventilation simulation Prescribed initial water pressure field	$RH_A = 100\%$
14 I	A-high	NF, I, K-high (1I)		
14 I	A-low	NF, I, K-low (2I)		
14 I	preB			$RH_B = 70\%$
14 I	B-high	NF, I, K-high (1I)		
14 I	B-low	NF, I, K-low (2I)		
12 I	high	NF, I, K-high (1I)	Lower block retention for $S_l > S_{l0}$	
12 I	low	NF, I, K-low (2I)		
15 I	A-high	NF, I, K-high (1I)	Altered buffer permeability	$k_A = 0.6 \cdot k$
15 I	A-low	NF, I, K-low (2I)		
15 I	B-high	NF, I, K-high (1I)		$k_B = 2 \cdot k$
15 I	B-low	NF, I, K-low (2I)		

3.4 Evaluation of the saturation times obtained for initial and homogenized state TH models

3.4.1 CRT models

Here follows an investigation of how well the saturation times of TH models adopting the initial state or homogenized state representation coincide with THM models for rapid saturation conditions. A THM simulation (THM CRT) performed for the Canister Retrieval Test (CRT) experiment has been used as the basis for the evaluation.

Two TH models were developed by excluding the mechanical part. In the first model (TH CRT I) the void ratio field is identical to the initial void ratio field in THM CRT and in the second model (TH CRT H) a totally homogenized void ratio was used. TH CRT I has properties identical to THM CRT and TH CRT H has been equipped with a retention curve and permeability that corresponds to the homogenized void ratio.

The boundary conditions are identical for the three different models and the water pressure in the outer part of the "pellet slot" section (there is no pellet slot in the homogenized representation) is prescribed from –45.9 to 0.1 Mpa during the first day of the simulation. This might lead to difficulties when comparing the saturation process between TH CRT H and the two other models since there is much less available volume for additional water in the "pellet slot" section in the homogenized model. However, for a first comparison the three described models have been used.

In Figure 3-9 the water saturation history is shown for all models at three radial positions (r = 585, 685 and 785 mm).

Table 3-9. CRT models in the TH evaluation.

Model	Character
THM CRT	Thermo Hydraulic Mechanical
TH CRT I	Thermo Hydraulic, Initial state
TH CRT H	Thermo Hydraulic, Homogenized state

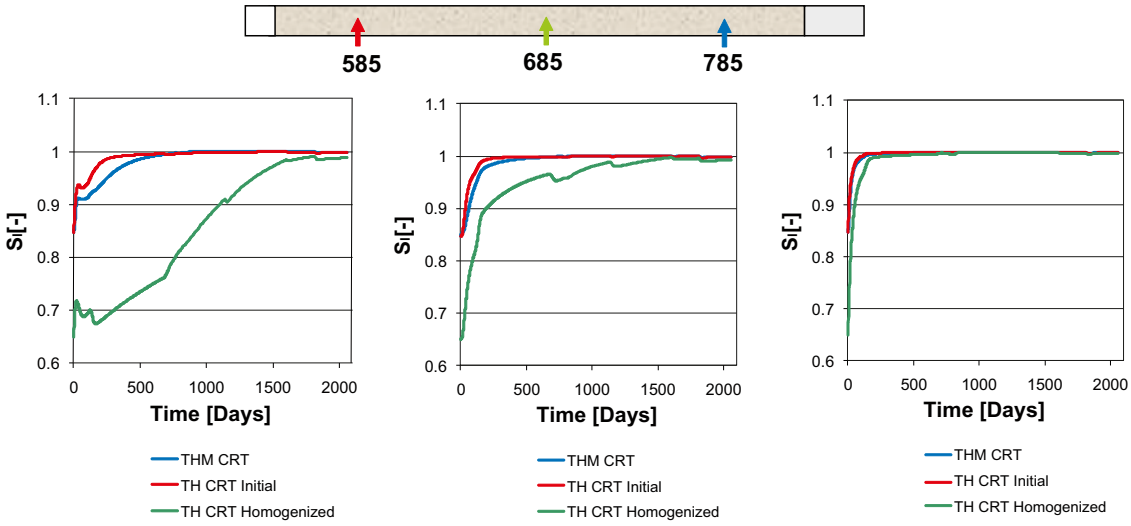

Figure 3-9. *Water saturation evolution at three different radii (585, 685 and 785 mm).*

The figures show that the THM solution is situated between the solution of the initial void ratio model and the homogenized void ratio model. TH CRT I gives faster water saturation and TH CRT H gives slower water saturation. The response for TH CRT H at r = 585 mm differs significantly from the other simulations.

To quantify the difference in time until saturation for the three models, the times when S_l = 0.99 are given in the diagram and table below. To enable a clear picture of the differences between the THM and TH simulations the time until saturation is also scaled with the saturation times obtained for the THM simulation, see Figure 3-10.

The difference in time until saturation is evident when studying Figure 3-10. Note that, the homogenized model has not reached S_l = 0.99 at the position 585 mm after 2,052 days.

The initial state model gives times until S_l = 0.99 that are 0.48–0.76 of the THM model saturation time and the homogenized state model gives 1.71–4.38 as long time as the THM model.

3.4.2 Simplified CRT models

As mentioned earlier, the comparison above might be too hard on the homogenized model. In order to obtain a more fair comparison the models are "simplified" somewhat by ignoring the inner slot at the canister and applying the initial water pressure condition (going from –45.9 to 0.1 Mpa during the first day simulated) at the rock wall boundary instead for over the outer part of the pellet slot.

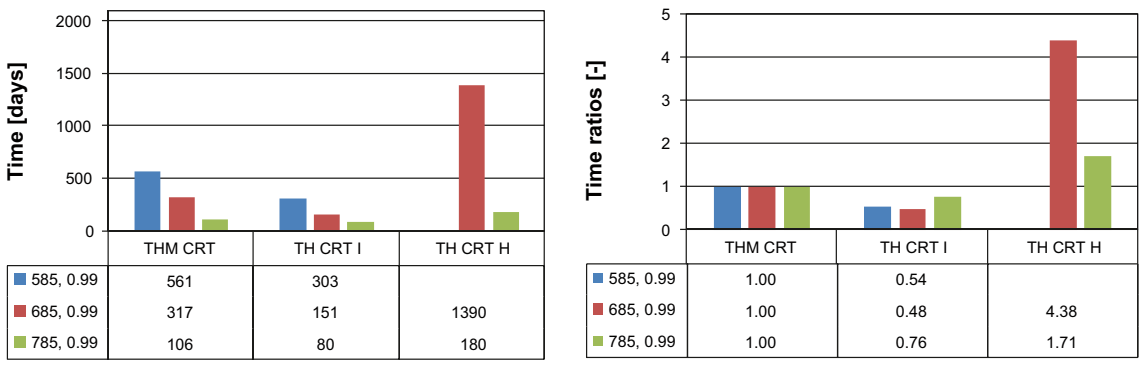

	THM CRT	TH CRT I	TH CRT H
585, 0.99	561	303	
685, 0.99	317	151	1390
785, 0.99	106	80	180

	THM CRT	TH CRT I	TH CRT H
585, 0.99	1.00	0.54	
685, 0.99	1.00	0.48	4.38
785, 0.99	1.00	0.76	1.71

Figure 3-10. *Saturation times (left) saturation time ratios (right).*

Table 3-10. Simplified CRT models in the TH evaluation.

Model	Characterization
THM (CRT 8)	“simplified” CRT THM model
TH I (TH 1c)	Corresponding initial state TH model
TH H (TH 2c2)	Corresponding homogenized state TH model
TH H filled (TH 2c3)	Corresponding homogenized state TH model, filled

Also, the initial water saturation (or suction) in TH H has been calibrated so that the total initial gas volume is close to the other models. Since the pellet slot material starts from a suction of 46 Mpa in the TH I model instead of 100 Mpa (which corresponds to the actual initial water ratio of 0.1), the initial suction in TH H becomes 36.7 Mpa to obtain the correct initial gas volume. (The lower pellet slot suction used in the TH I model makes the numerical solution easier and does not significantly affect the result.)

The times and the time ratios, saturation time normalized with the THM saturation time, are shown in Figure 3-11.

The situation with longer saturation times for the homogenized model remains even though all the models now are comparable.

When comparing THM CRT and THM it is found that the saturation times (when $S_l = 0.99$) for the “cleaned up” THM model are 1.30–1.44 times the “original” THM model saturation times. The longer saturation times in the “cleaned up” THM-model are expected since the water in the inner slot has been removed and that the supplied water from the rock wall side is prescribed at the boundary also during the first day.

The time ratios for both TH-models are closer to unity (i.e. the saturation times are closer to the THM-models’) for this set of models as compared to the former set. The initial state model gives time ratios (when $S_l = 0.99$) in the range 0.81–0.89 and the homogenized model gives ratios in the range 1.47–3.28.

To investigate the origin of the differences in the water saturation process for the two TH models, the added water volume (ΔV_w) is calculated at a number of times for the initial state model and homogenized state model. The added water volume: in the total geometry (RED), in the inner part where $r < 825$ mm (GREEN) and in the outer part where $r > 825$ mm (BLUE), are shown in Figure 3-12 below. The available volume for additional water in the initial state (the initial gas volume V_g^0) is also shown for the different parts.

It can be seen that in TH I the pellet slot (blue curve) is filled rapidly and also that the initial gas volume for $r > 0.825$ m is significantly larger as compared to TH H. Thus, a considerable part of the available total volume is filled at an early stage in the saturation process for TH I.

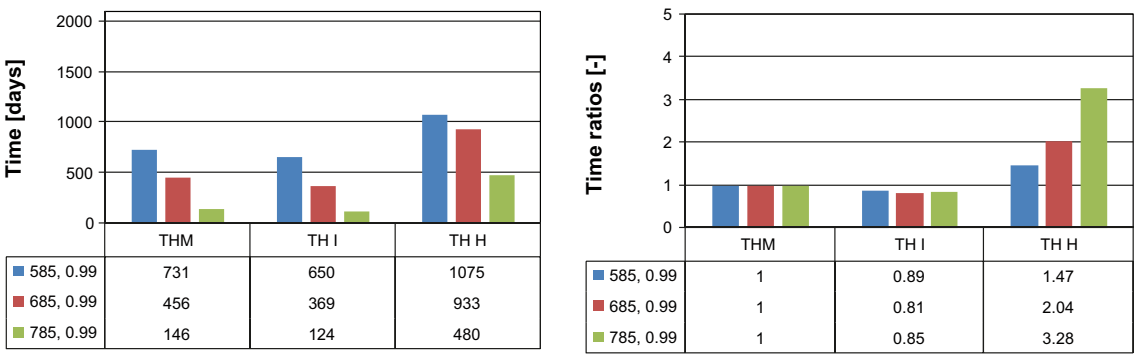

Figure 3-11. *Saturation times (left) saturation time ratios (right).*

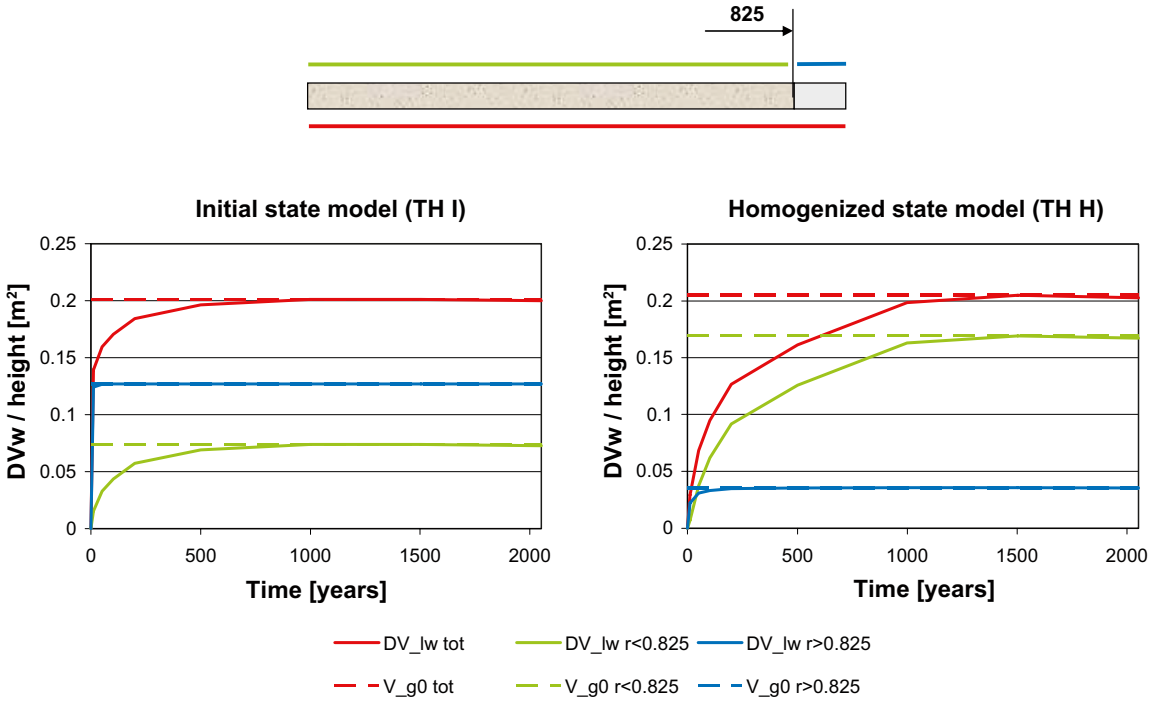

Figure 3-12. *Added water volume evolution in different section for the I and H model.*

This makes the inner, more impermeable material (the bentonite block), "available" for saturation at an earlier stage as compared to the homogenized model. The pressure gradient subjected to the inner material in the initial phase will be steeper, which promotes a larger water flux, for the initial state model.

After the initial phase the rate of the water filling is faster in the homogenized model since the permeability is higher. The inner volume ($r < 825$ mm) to fill up is however significantly larger for TH H as compared to TH I, and as a consequence the homogenized model demands longer time until saturation.

Another aspect that makes the homogenized model slower in terms of water saturation is that the lower initial water saturation gives a lower thermal conductivity which in turn enhances the vapor transportation from the part close to the canister.

3.4.3 Filled pellet slot representation

A homogenized state TH-model has been compared with the THM-model. In other studies homogenized models with initial hydraulic conditions corresponding to a water filled pellet slot have been used /Börgesson and Hernelind 1999, Börgesson et al. 2006/. To accomplish this, the homogenized material is allotted full water saturation in an outer band, between the rock wall interface and a radius calculated so that the water volume in the band matches the water volume of a fully saturated pellet slot. The calculated radius in this case becomes 798 mm, i.e. the band width becomes 77 mm.

The times until saturation and the time ratios for the THM-model the homogenized TH-model and the initially filled homogenized TH-model are shown in Figure 3-13 below.

The initial water filling of the outer part of the buffer has an effect on the saturation times. The effect is however not very significant. The filled homogenized TH-model has saturation times ($S_l = 0.99$) 1.38–3.05 of the THM-model as compared to 1.47–3.28 for the initially "dry" homogenized model.

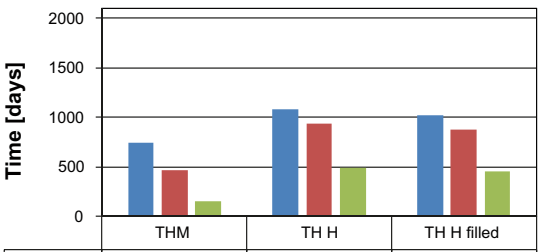

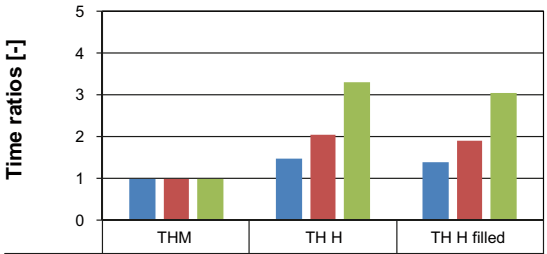

Figure 3-13. *Saturation times (left) saturation time ratios (right).*

3.5 Results and discussion

3.5.1 Overview of the buffer water saturation process

Here an overview of the saturation process in the buffer is given for the first two models (1I, 1H).

Sequences of maps over the water saturation are given below in Figure 3-14 to show the saturation process in the buffer, backfill and surrounding rock mass. Sequences are given for both models to show the differences between them. (The water saturation in the white rectangular shape in the center of the tunnel is not shown due to limitations of the post processor.)

It can be seen that the initial saturation conditions differ between the models. The initial state model has higher saturated material in the buffer and backfill blocks as compared to the corresponding sections in the homogenized buffer. The pellet slot material in turn has less initial water saturation as compared to the homogenized buffer.

After one year water has transported from the rock into the buffer and backfill due to the water pressure gradient. As a consequence the rock close to the tunnel and deposition hole becomes dryer. The rock mass close to the edge formed by the intersection of the tunnel and deposition hole becomes very dry since water is transported both horizontally into the buffer and vertically into the backfill. The buffer material on top of and below the canister has dried. The heat generated by the nuclear waste induces a temperature gradient that makes the vapor concentration vary which activates the vapor diffusion process in the outward direction from the canister.

The water transportation processes explained above continue as the simulations proceed to five years. Here it can be seen that the lower part of the buffer blocks in the initial state model is highly saturated but the corresponding section in the homogenized model is not. The pellet slots, in both tunnel and deposit hole, are however clearly not saturated in the initial state model.

When looking at the 10 year maps the same situation as was found for the five year maps still prevails. The initial state model has more saturated block sections and the pellet slots are still not as saturated as the corresponding sections in the homogenized model.

After 20 years the buffer seems to be completely saturated in the initial state model (in fact, the very top part of the buffer pellet slot has not reached $S_l > 0.99$), but there still are unsaturated parts in the tunnel backfill and tunnel pellet slot. The homogenized model on the other hand still has a slight unsaturated part in the very top of the buffer (hardly visible with the chosen saturation interval) and the backfill has a large part that is unsaturated.

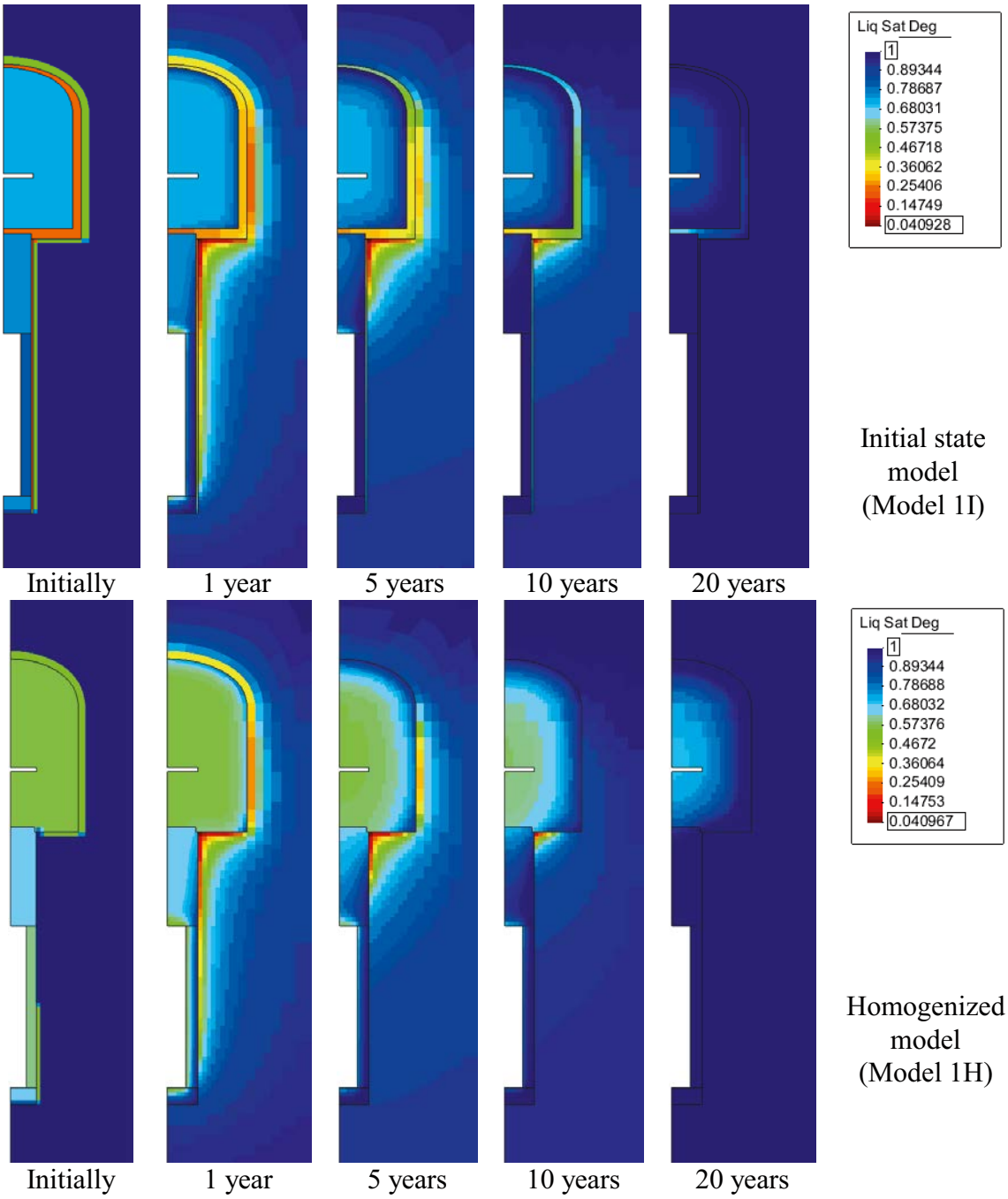

Figure 3-14. *Sequence of maps of the water saturation for both models.*

In the following the time until 99% saturation in some chosen key points are used to describe the character of the water saturation process in the buffer. The chosen points, with the used notation, are shown and described in Figure 3-15 below.

The obtained water saturation times (where $S_l = 0.99$) for the chosen points in models 1I and 1H are shown in Figure 3-16 below.

Studying the saturation times above gives that the initial state model has a more "axial" saturation process in contrast to the more "radial" saturation process obtained for the homogenized state model. *pt*(last) = *pt*(2) for model 1I and *pt*(last) = *pt*(1) for model 1H.

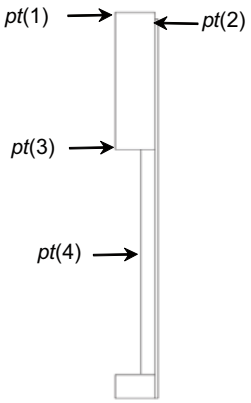

pt(1): The center point upper most in the buffer

pt(2): The upper most point in the pellet slot

pt(3): The center point on top of the canister

pt(4): The point at canister mid-height close to the canister

pt(last): Last saturated point in the buffer

Figure 3-15. *Chosen point position and notation.*

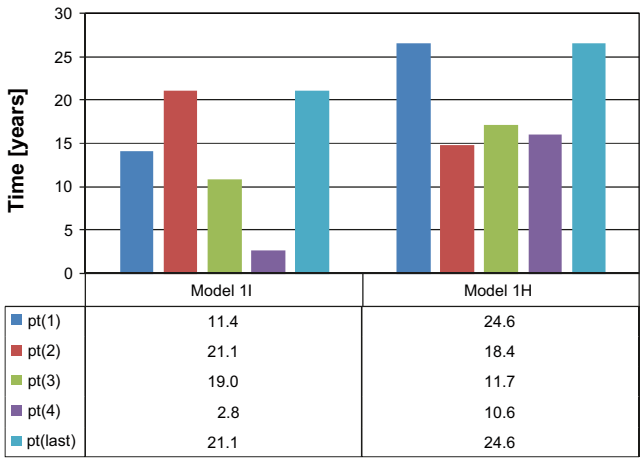

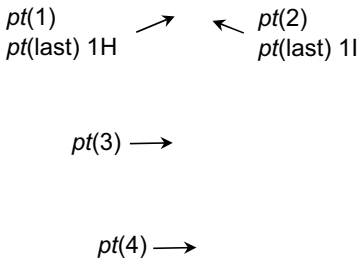

Figure 3-16. *Saturation times for the indicated points.*

3.5.2 Estimate of buffer saturation time for unfractured rock

An estimate of the saturation time of the buffer in a model with unfractured rock is here produced. The estimated saturation time is given as a range, where the bounds are obtained from studying the responses of four different models (1I, 1H, 2I and 2H).

In Figure 3-17 the time until 99% saturation in the chosen points as well as the time until the entire buffer has water saturation ≥ 99% is given for all four models. *Pt*(last) is indicated in the right figure.

The difference in saturation times between the models 1 and models 2 is significant. The obtained range in saturation time for the buffer surrounded by an unfractured rock is 21.1–177.2 years.

The saturation process for 1I and 2I is however the same when studying the sequence of saturation of the chosen points. The pellet slot saturation is significantly slower as compared to the other points for both initial state models.

The saturation sequence has changed slightly when going from 1H to 2H, but *pt*(1) is the last to be saturated in both models.

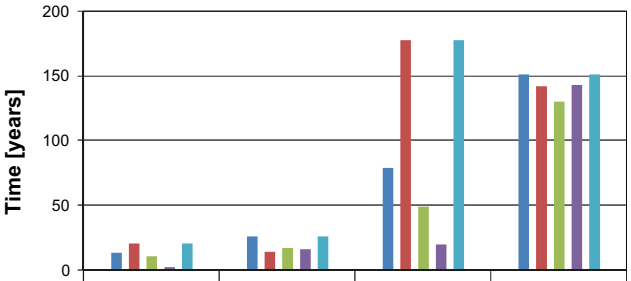

	Model 1I	Model 1H	Model 2I	Model 2H
pt(1)	14.1	26.4	79.0	150.9
pt(2)	21.1	14.8	177.2	141.7
pt(3)	10.9	17.1	49.1	130.1
pt(4)	2.8	16.0	19.7	142.6
pt(last)	21.1	26.4	177.2	150.9

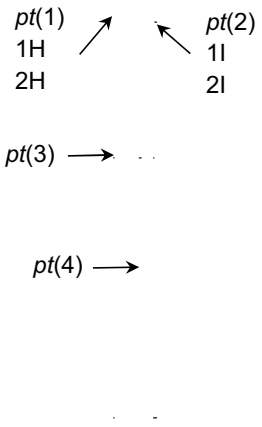

Figure 3-17. *Saturation times for the indicated points in the unfractured models.*

3.5.3 Estimate of buffer saturation time for fractured rock

Models with two different vertical fracture positions are analyzed. Either the fracture intersects with the hole wall at the canister mid-height (CMH) or the fracture intersects with the tunnel wall (T). For each fracture position, the estimated saturation time is given as a range, where the bounds are obtained from studying the responses of four different models (3I, 3H, 4I, 4H for CMH and 5I, 5H, 6I, 6H for T)

Canister mid-height fracture

In Figure 3-18 the time until 99% saturation in the chosen points as well as the time until the entire buffer has water saturation ≥ 99% is given for all four CMH models. *pt*(last) is indicated in the right figure.

There is a clear difference in saturation times for models 3 and models 4. It can also be seen that the saturation process (the sequence of saturation in the points) changes when going from models 3 to models 4. The obtained range in saturation time for the buffer surrounded by rock fractured at canister mid-height is 7–35.4 years.

In 3I the pellet slot is not the last saturated point as was found for 1I and 2I. In 3I the pellet slot is fed with water from the highly transmissive fracture and highly permeable rock. (The water pressure in the fracture generates a pressure gradient field in the rock that drives the water transportation into the pellet slot.) In 4I the saturation process resembles what was found in 1I and 2I, i.e. *pt*(2) becomes

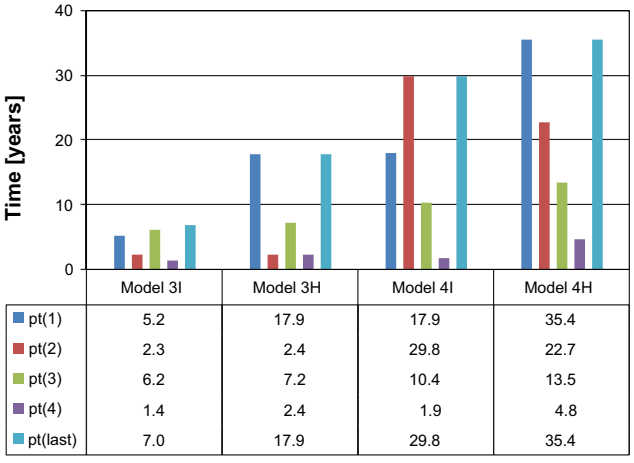

	Model 3I	Model 3H	Model 4I	Model 4H
pt(1)	5.2	17.9	17.9	35.4
pt(2)	2.3	2.4	29.8	22.7
pt(3)	6.2	7.2	10.4	13.5
pt(4)	1.4	2.4	1.9	4.8
pt(last)	7.0	17.9	29.8	35.4

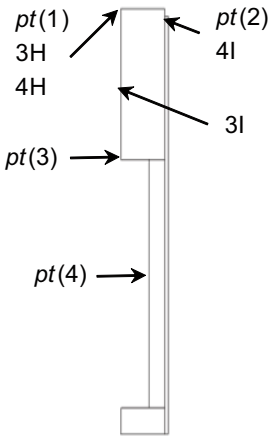

Figure 3-18. *Saturation times for the indicated points in the models with a CMH fracture.*

saturated last. The transmissivity of the fracture and the permeability of the rock are not high enough to feed the pellet slot efficiently enough to retain the saturation process seen in 3I.

The homogenized state models 3H and 4H reflects what was found in the initial state models. The saturation process changes when going from the highly permeable model to the lower permeable model. In 3H *pt*(2) is efficiently fed from the rock and in 4H the same point is not. For both models *pt*(1) is the last that becomes saturated.

Tunnel fracture

In Figure 3-19 the time until 99% saturation in the chosen points as well as the time until the entire buffer has water saturation ≥ 99% is given for all four T models. *Pt*(last) is indicated in the right figure.

All tunnel fracture models and their relation to each other are very much like the CMH fracture cases. The saturation process changes between case 5 and case 6 models in the same way. The obtained range in saturation time for the buffer surrounded by rock fractured at the tunnel is 6.9–30.0 years.

If comparing the tunnel fracture cases with the corresponding CMH fracture cases it is seen that *pt*(3) and *pt*(4) are saturated simultaneously or earlier in the CMH fracture cases due to the closer distance to the fracture. The opposite is found for *pt*(2) which is closer to the fracture in the tunnel fracture models.

Comparing the unfractured and fractured models

In order to evaluate the differences of the models, ratios between the average total saturation times are used. Below in Table 3-11 all possible ratios (numerator/denominator) are given.

Table 3-11. Averaged time ratios.

Numerator averge of:						Denominator average of:
Models 1: 23.7	**Models 2: 164.0**	**Models 3: 12.4**	**Models 4: 32.6**	**Models 5: 12.2**	**Models 6: 26.7**	
1.0	6.9	0.5	1.4	0.5	1.1	Models 1: 23.7
	1.0	0.1	0.2	0.1	0.2	Models 2: 164.0
		1.0	2.6	1.0	2.1	Models 3: 12.4
			1.0	0.4	0.8	Models 4: 32.6
				1.0	2.2	Models 5: 12.2
					1.0	Models 6: 26.7

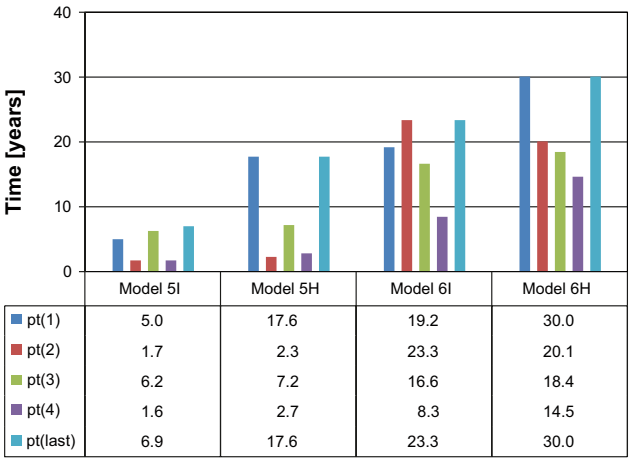

	Model 5I	Model 5H	Model 6I	Model 6H
pt(1)	5.0	17.6	19.2	30.0
pt(2)	1.7	2.3	23.3	20.1
pt(3)	6.2	7.2	16.6	18.4
pt(4)	1.6	2.7	8.3	14.5
pt(last)	6.9	17.6	23.3	30.0

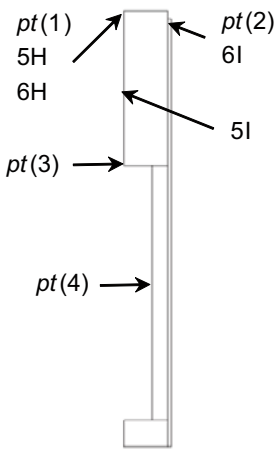

Figure 3-19. *Saturation times for the indicated points in the models with a tunnel fracture.*

Effect from changing permeability (and trasmissivity) (t_{low} / t_{high}):
No fracture: $t_2 / t_1 = 6.9$
Fracture at CMH: $t_4 / t_3 = 2.6$
Fracture at tunnel: $t_6 / t_5 = 2.2$

The effect from changing permeability (and transmissivity in the fractured models) is significantly greater in the case of unfractured rock as compared to the fractured cases. The fracture position is not as significant.

Effect from introducing the CMH fracture (t_{fract} / $t_{unfract}$):
High permeability models: $t_3 / t_1 = 0.5$
Low permeability models: $t_4 / t_2 = 0.2$

The effect from introducing a CMH fracture is greater in the low permeable model.

Effect from introducing the tunnel fracture (t_{fract} / $t_{unfract}$):
High permeability models: $t_5 / t_1 = 0.5$
Low permeability models: $t_6 / t_2 = 0.2$

The effect from introducing a tunnel fracture is also greater in the low permeable model. The effect is the same, for both high and low permeable models, as for the CMH models.

3.5.4 The effect of extremely low rock permeability

Here the rock permeability is set to 10^{-20} m^2 to investigate the saturation times, saturation evolution and peak temperature in the buffer and rock.

Since this case may give rise to very low degrees of water saturation, two of the constitutive laws (thermal conductivity dependence on saturation and the retention curves in the homogenized state model) have been altered in order to give a better representation for low saturation levels.

Another dependence of thermal conductivity on saturation for the buffer blocks (in the initial state model) and homogenized blocks and pellet slot (in the homogenized state model) has been used to improve the representation of the law to lower degree of saturation. The ordinary law and the new law is shown as expressions and graphs in Figure 3-20.

In the homogenized model another water retention law is used to enable more accurate representation at lower degrees of water saturation of the homogenized buffer material. Below the ordinary and new retention formulation are shown in equations, used parameter values and graphically in Figure 3-21.

Ordinary law:

$$\lambda(S_l) = \lambda_{sat} S_l + \lambda_{dry}(1 - S_l)$$

λ_{sat} = 1.3 W/(m·K)
λ_{dry} = 0.7 W/(m·K)

New law:

$$\lambda(S_l) = \lambda_{sat}^{\,S_l^n} \lambda_{dry}^{\,(1-S_l)^{\frac{1}{n}}}$$

λ_{sat} = 1.3 W/(m·K)
λ_{dry} = 0.33 W/(m·K)
n = 0.5

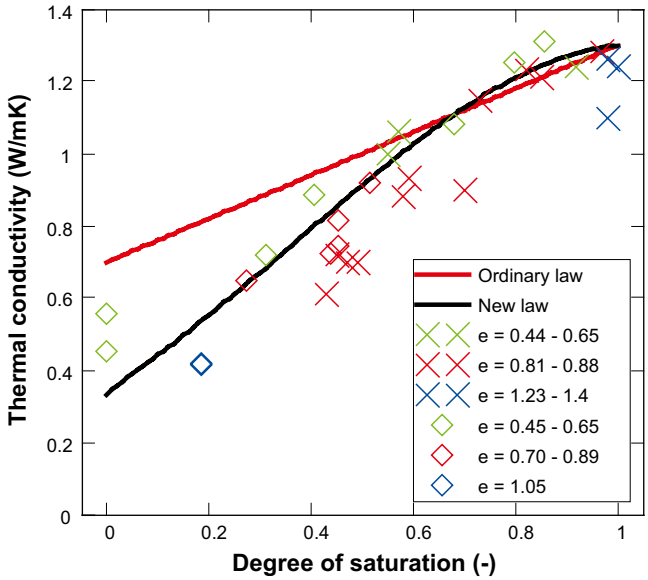

Figure 3-20. *Ordinary and new water saturation dependence of the thermal conductivity.*

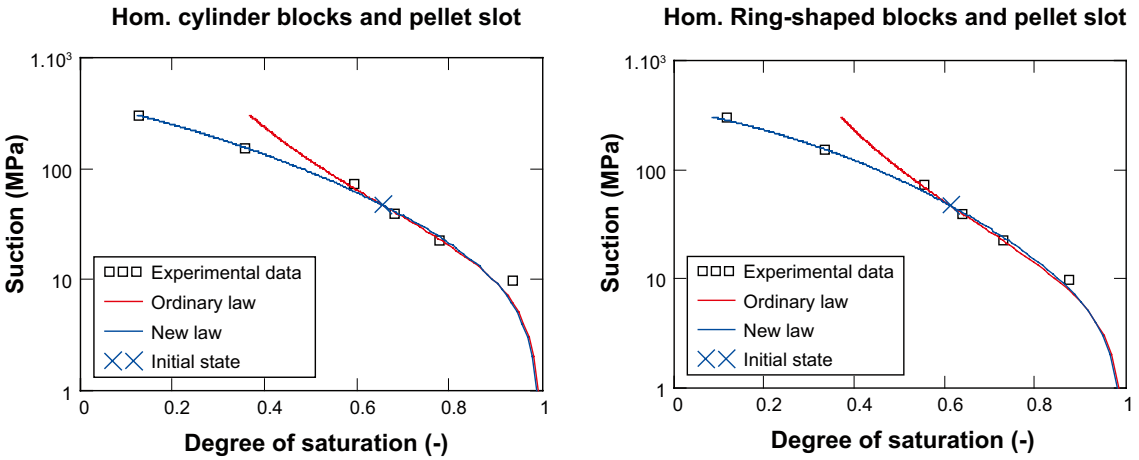

Figure 3-21. *Ordinary and new retention curves together with experimental data.*

Ordinary law: $$S_l(S) = \left(1 + \left(\frac{S}{p}\right)^{\frac{1}{1-\lambda}}\right)^{-\lambda} \tag{3-9}$$

Table 3-12. Parameter values in the ordinary retention curve.

Hom. Cylinder blocks and pellet slot	Hom. ring-shaped blocks and pellet slot
p = 15.191 Mpa	p = 11.551 Mpa
λ = 0.25	λ = 0.22

New law: $$S_l(S) = \left(1 + \left(\frac{S}{p(T)}\right)^{\frac{1}{1-\lambda}}\right)^{-\lambda} \left(1 - \frac{S}{p_1}\right)^{\lambda_1}$$
$$p(T) = p_0 \frac{\sigma(T)}{\sigma_0} \tag{3-10}$$
$$\sigma(T) = \left(1 - 0.625\frac{374.15 - T}{647.3}\right)\left(0.2358\left(\frac{374.15 - T}{647.3}\right)^{1.256}\right)$$

Table 3-13. Parameter values in the new retention curve.

Hom. Cylinder blocks and pellet slot	Hom. Ring-shaped blocks and pellet slot
p_0 = 15.56 Mpa	p_0 = 8.176 Mpa
p_1 = 400 Mpa	p_1 = 350 Mpa
λ = 0.19	λ = 0.165
λ_1 = 1	λ_1 = 0.9
σ_0 = 0.072 N/m	σ_0 = 0.072 N/m

The histories of water saturation for the chosen points are given in Figure 3-22 and the time until 99% saturation is given in Figure 3-23 below.

Clearly, in general the water saturation process follows what was found for models 2 (no fracture, low permeability). It takes a long time to saturate the pellet slot in the initial state model as compared to all other points. This clearly shows when studying the saturation times for the models below in Figure 3-23.

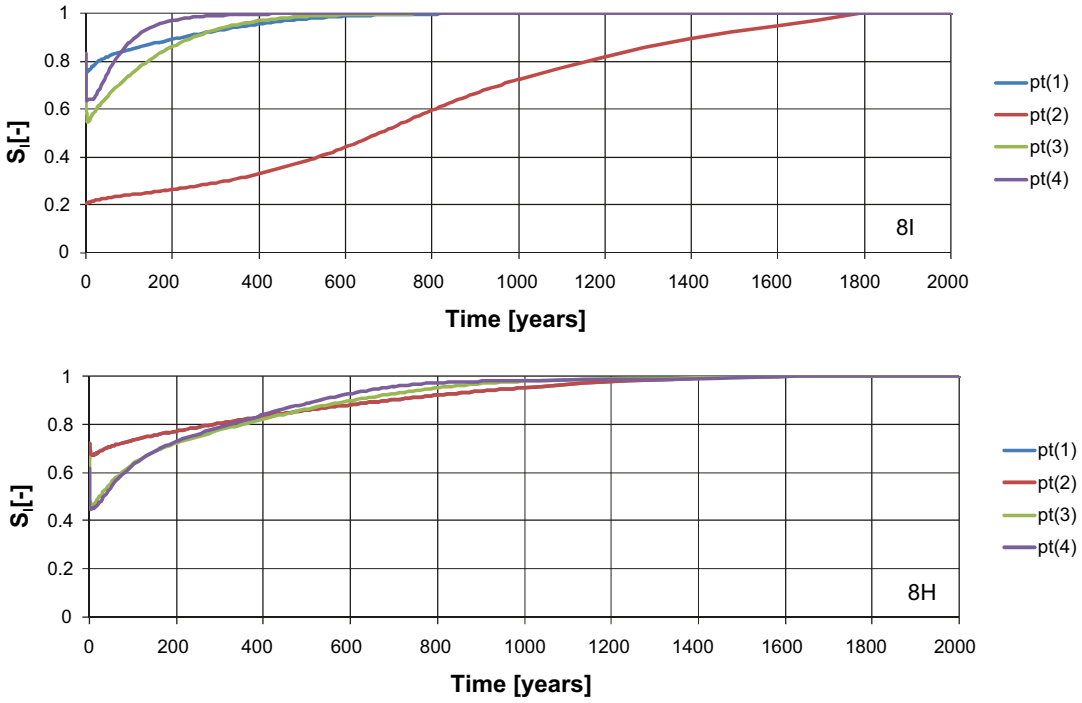

Figure 3-22. *Water saturation evolution in the chosen points for both TH models (upper) Initial state model (lower) Homogenized state model.*

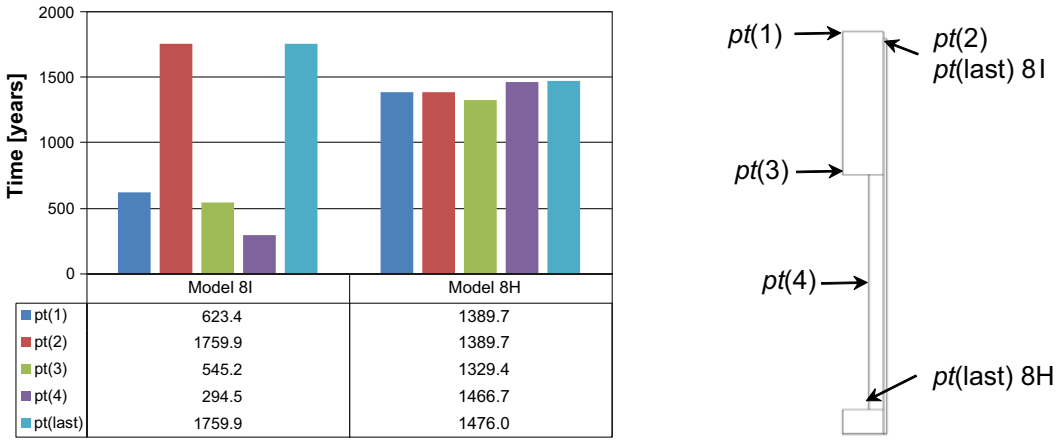

Figure 3-23. *Times until 0.99 water saturation in the points indicated to the right.*

The initial state model shows the same sequence of saturation as was found for case 2. In the homogenized model however, the saturation sequence has changed somewhat from what was found in case 2. Here, it is not *pt*(1) that becomes saturated last (as was the case in the case 2 model). Instead, a point close to the canister lower end is saturated last.

A case with extremely low rock permeability (the same value as used in this model, 10^{-20} m^2) has also been investigated in /Rutqvist and Tsang 2008/. /Rutqvist and Tsang 2008/ scrutinized SKB's work related to THM modelling within the SR-Can project. The model setup used in SR-Can was therefore also utilized in models developed for the Rocmas solver used in /Rutqvist and Tsang 2008/.

For a model containing extremely low rock permeability, very low degrees of water saturation were found in the buffer in /Rutqvist and Tsang 2008/. Also, the maximum temperature in the buffer was close to 100°C, a design criterion not to be exceeded.

Below, in Figure 3-24, the history of temperature in the points where the maximum temperature is reached in the bentonite and at the rock wall of the deposition hole are given in the left graph (for both models, 8I and 8H). In the right graph the water saturation histories of the central point on top of the canister, *pt*(3), and the point at canister mid-height close to the canister, *pt*(4), are given.

These results were also shown in /Rutqvist and Tsang 2008/ and are here repeated below in Figure 3-25 and Figure 3-26 for comparison. In /Rutqvist and Tsang 2008/ two different values of thermal vapour diffusion coefficients were used. In Figure 3-25 the results from using a lower coefficient are shown and in Figure 3-26 the results obtained from using a higher coefficient are shown. The results produced with the "Forsmark" model are here shown, since this model agree better with the Code_Bright model setup in terms of: canister spacing (6 m in both models) and thermal conductivity (3.46 W/(m·K) in the Forsmark model and 3.57 W/(m·K) in the Code_Bright model).

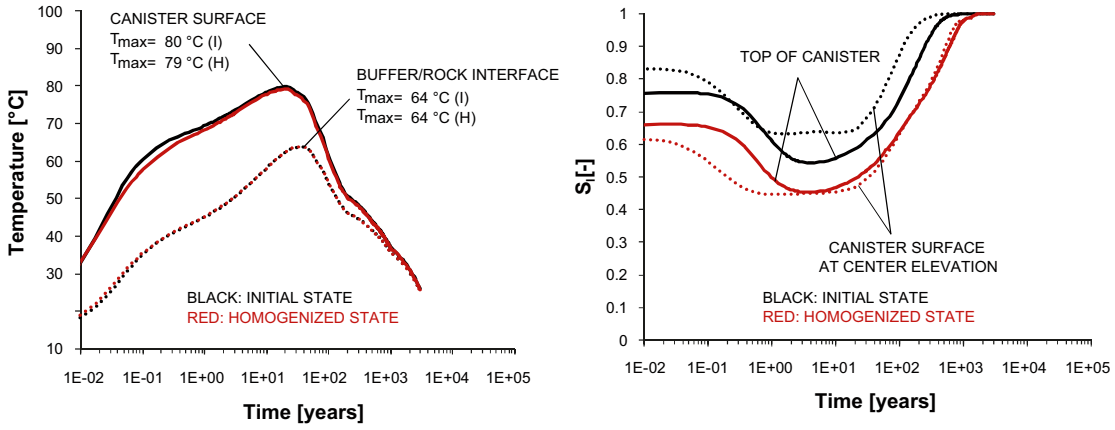

Figure 3-24. *Temperature and water saturation evolution for the I and h model in the case with extremely low rock permeability.*

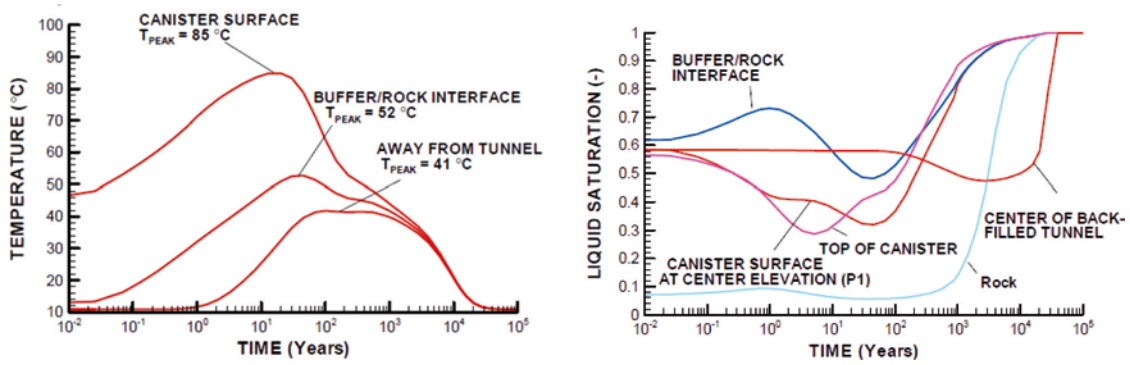

Figure 3-25. *Extremely low rock permeability and low thermal diffusion coefficient (Forsmark Rocmas model) from /Rutqvist and Tsang 2008/ (Figures 4.5-1a and 4.5-2a).*

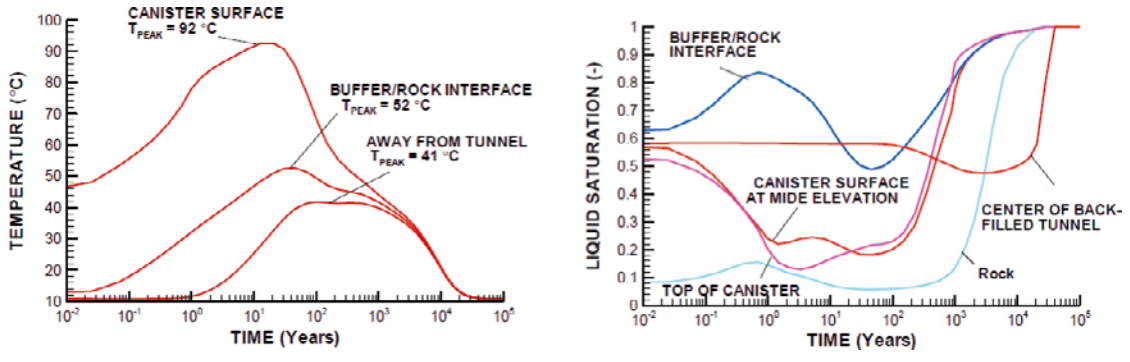

Figure 3-26. *Extremely low rock permeability and high thermal diffusion coefficient (Forsmark Rocmas model) from /Rutqvist and Tsang 2008/ (Figures 4.11-1a and 4.11-2a).*

The temperature drop over the buffer has been evaluated in /Hökmark et al. 2009/ for the same canister heat evolution used here and an adopted effective thermal buffer conductivity of 1.0 W/(m·K). Below in Figure 3-27 the contribution from the temperature drop over the barrier (the bentonite buffer) and in an inner slot between the canister and bentonite ring are shown. The inner slot is not considered in the Code_Bright or the Rocmas model, so that contribution should be disregarded.

The peak temperature occurs approximately after 20 years in both the Rocmas and Code_Bright models. If the barrier temperature drop is evaluated at 20 years from Figure 3-27 a value around 16°C is obtained. In the Code_Bright models a temperature drop of 15 or 16°C is obtained and the Rocmas model gives a considerable larger temperature drop of 33 or 40°C. Thus, in the Code_Bright models, the effective thermal conductivity of the buffer is close to what was used in /Hökmark et al. 2009/ (1.0 W/(m·K)) and in the Rocmas model the effective thermal conductivity is significantly lower.

Below, possible reasons for the different results produced with the Code_Bright model and Rocmas model are given.

To begin with, the dimensions of the models are different. The Rockmas model is a 3D model, where a quarter of a deposition hole is modelled with assumed symmetry boundaries at half the canister spacing (3 m) and half the tunnel spacing (20 m). The Rocmas model also stretches up to the ground level where the hydraulic water pressure boundary condition (0.1 Mpa) is situated (400 m above the repository depth) and down to 1,000 m depth. The extremely tight rock is thus assumed to stretch entirely up to the ground level. In the Code_Bright model the tight rock section is only assumed to stretch 60 m above the repository depth, where the water pressure boundary condition (4 MPa) is present (at 400 m depth). The motivation for this is found in the presentation of the model in Section 3.2.3.

In the Rockmas model, a pre-installation phase, where the repository is open (represented by a 0.1 MPa water pressure boundary), is also considered. This result in a drained rock, where the water pressure field is lower as compared to the hydrostatic condition assumed in the Code_Bright model. In a following study in this report, however, this effect is also evaluated for the Code_Bright model and the impact on the water saturation times is found to be slim, see Section 3.5.7.

The retention curves adopted in the buffer are quite different as can be seen in Figure 3-28.

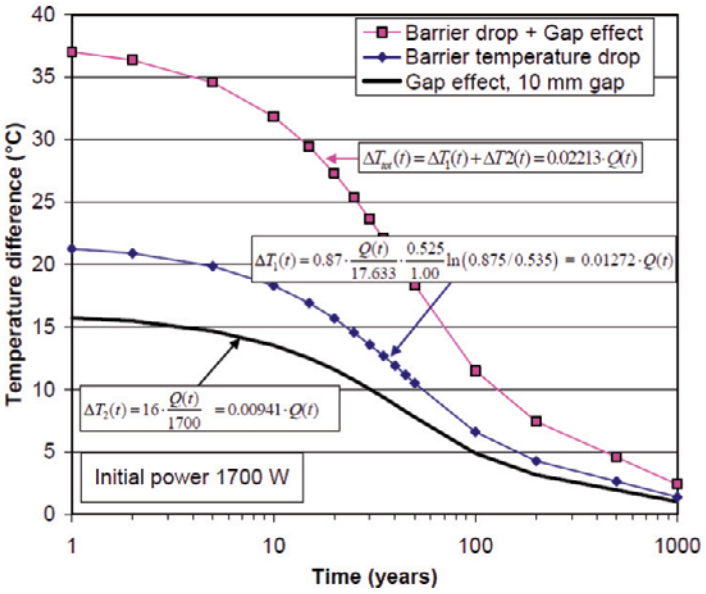

Figure 3-27. *The temperature drop between the canister and rock wall. (Figure 4-13 in /Hökmark et al. 2009/).*

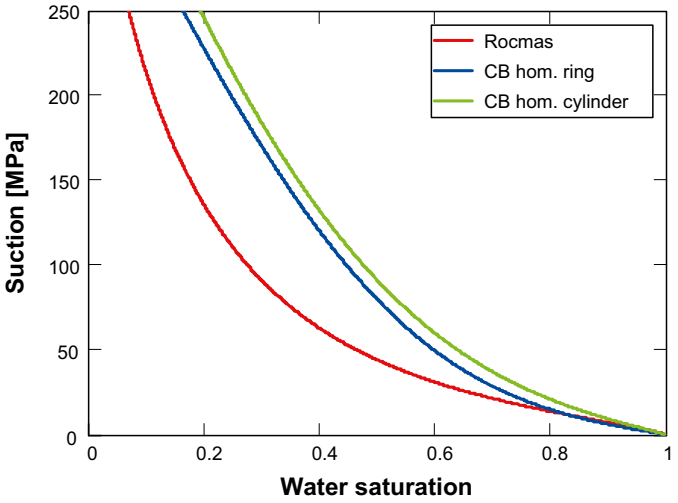

Figure 3-28. *Buffer retention curves used in the Rocmas and Code_Bright model.*

The Rocmas model has a significantly lower retention curve as compared to the curves adoped in the Code_Bright model. Thus, for a given suction value the Rocmas model produces lower water saturation values as compared to the Code_Bright model. The retention curves used in the Code_Bright model are fitted against experimental retention data obtained for an initial water ratio of 0.175 as described in the Data Report. The retention curve used in the Rocmas model is fitted against data presented in /Börgesson and Hernelind 1999/, which was developed considering swelling pressure data presented in /Börgesson and Hernelind 1999/ and pure adsorption data starting from completely dry conditions presented in /Kahr et al. 1990/.

The assumed thermal conductivity dependence on water saturation in the homogenized buffer is rather different in the two models. As can be seen in Figure 3-29, the thermal conductivity is lower in the Rocmas model at lower degrees of water saturation (< 0.7).

At lower water saturations (< 0.7) this result in higher thermal gradient in the buffer (given the same heat load) and therefore higher temperatures in the buffer. The relation used in the Code_Bright model has been obtained considering all experimental data shown in Figure 3-29 whereas the relation used in the Rocmas simulations were developed considering the data indicated with the X-symbols /Börgesson and Hernelind 1999/.

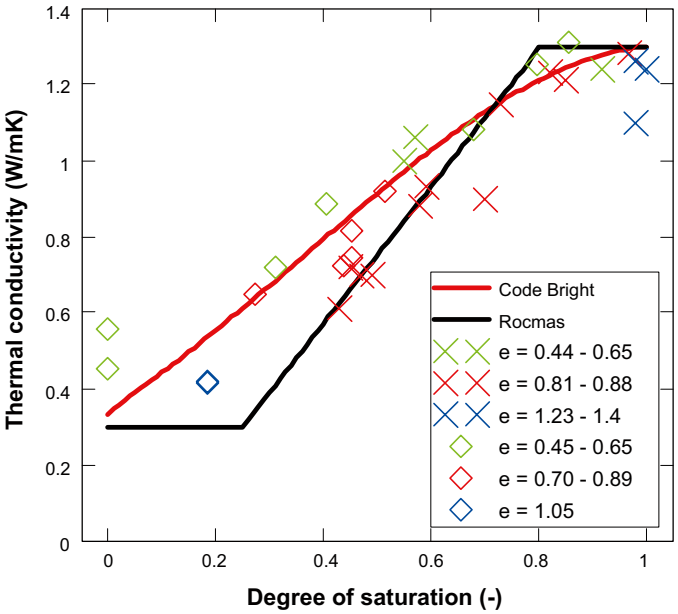

Figure 3-29. *Water saturation dependence on thermal conductivity in the Rocmas and Code_Bright model.*

Somewhat different formulations have also been used when it comes to vapor transport. To evaluate if this is a cause of the different saturation levels, the transport coefficients are compared. Code_Bright uses a direct diffusion formulation on the format,

$$\boldsymbol{q}_v = -\rho_g D_v \frac{\partial}{\partial \boldsymbol{x}}\left(\frac{\rho_v}{\rho_g}\right) \tag{3-11}$$

whereas Rocmas normally uses the format,

$$\begin{aligned} &\boldsymbol{q}_v = -\rho_l\left(D_{pv}\frac{\partial p_l}{\partial \boldsymbol{x}} + D_{Tv}\frac{\partial T}{\partial \boldsymbol{x}}\right) \\ &D_{pv} = \frac{D_v}{\rho_l}\frac{\partial \rho_v}{\partial p_l} \quad , \quad D_{Tv} = f_{Tv}\frac{D_v}{\rho_l}\frac{\partial \rho_v}{\partial T} \end{aligned} \tag{3-12}$$

obtained from (3-11) with the assumption that ρ_g is constant in the material. In the Rocmas simulations producing the results shown above however, the two vapor diffusion coefficients in the Rocmas model are prescribed as,

$$D_{pv} = 0$$

$$D_{Tv} = \begin{cases} D_{Tv0} & \text{for } 0.3 < S_l < 0.7 \\ D_{Tv0}\cos^6\left(\dfrac{S_l - 0.7}{0.3}\dfrac{\pi}{2}\right) & \text{for } S_l > 0.7 \\ D_{Tv0}\sin^6\left(\dfrac{S_l}{0.3}\dfrac{\pi}{2}\right) & \text{for } S_l < 0.3 \end{cases} \tag{3-13}$$

where $D_{Tv0} = 0.7 \cdot 10^{-11}$ or $1.5 \cdot 10^{-11}$ (m²/s/°C). To compare the setups, an effective thermal vapor diffusion coefficient D_{Tv}^{eff} is calculated using the Code_Bright homogenized buffer ring representation and the obtained responses in the 8H simulation at canister mid-height. D_{Tv}^{eff} is obtained from considering that the vapor is driven by a temperature gradient only according to,

$$\boldsymbol{q}_v = -\rho_l\left(D_{pv}\frac{\partial p_l}{\partial \boldsymbol{x}} + D_{Tv}\frac{\partial T}{\partial \boldsymbol{x}}\right) = -\rho_l\left(D_{pv}\frac{\partial p_l}{\partial \boldsymbol{x}}\frac{\partial T}{\partial \boldsymbol{x}}^{-1} + D_{Tv}\right)\frac{\partial T}{\partial \boldsymbol{x}} = -\rho_l D_{Tv}^{\ eff}\frac{\partial T}{\partial \boldsymbol{x}} \tag{3-14}$$

Comparing the above with the Rocmas setup it can be seen that D_{Tv}^{eff} may be compared with the specified D_{Tv}. D_{Tv}^{eff} depends on temperature, pressure and the corresponding gradients.

Below in Figure 3-30 the effective thermal vapor diffusion coefficient obtained at three different radii in the 8H simulation is given as a function of the water saturation at the considered radius. In the computation, the enhancement factor f_{Tv} has been set to unity and approximated averages and gradients of the variables at the three radii have been used.

As can be seen, there is not a large difference in D_{Tv}^{eff} obtained from evaluating the Code_Bright simulation at canister mid-height and D_{Tv} as specified in the Rocmas models. At high water saturation however, (> 0.8) D_{Tv}^{eff} is higher as compared to D_{Tv} which should promote more vapor diffusion (given the same temperature gradient) in the Code_Bright model as compared to the Rocmas model. The vapor transportation is therefore not considered to be a factor that gave the different saturation levels in the two models.

3.5.5 Rock permeability dependence

Here the influence from rock permeability on time until water saturation (99%) in the buffer is investigated. The results obtained from eight unfractured models are used (1I, 1H, 2I, 2H, 7I, 7H, 8I, 8H).

The buffer saturation time is shown as a function of rock hydraulic conductivity in Figure 3-31. The graphs contain results for the initial state models, the homogenized state models and the average of the results of the I and H models.

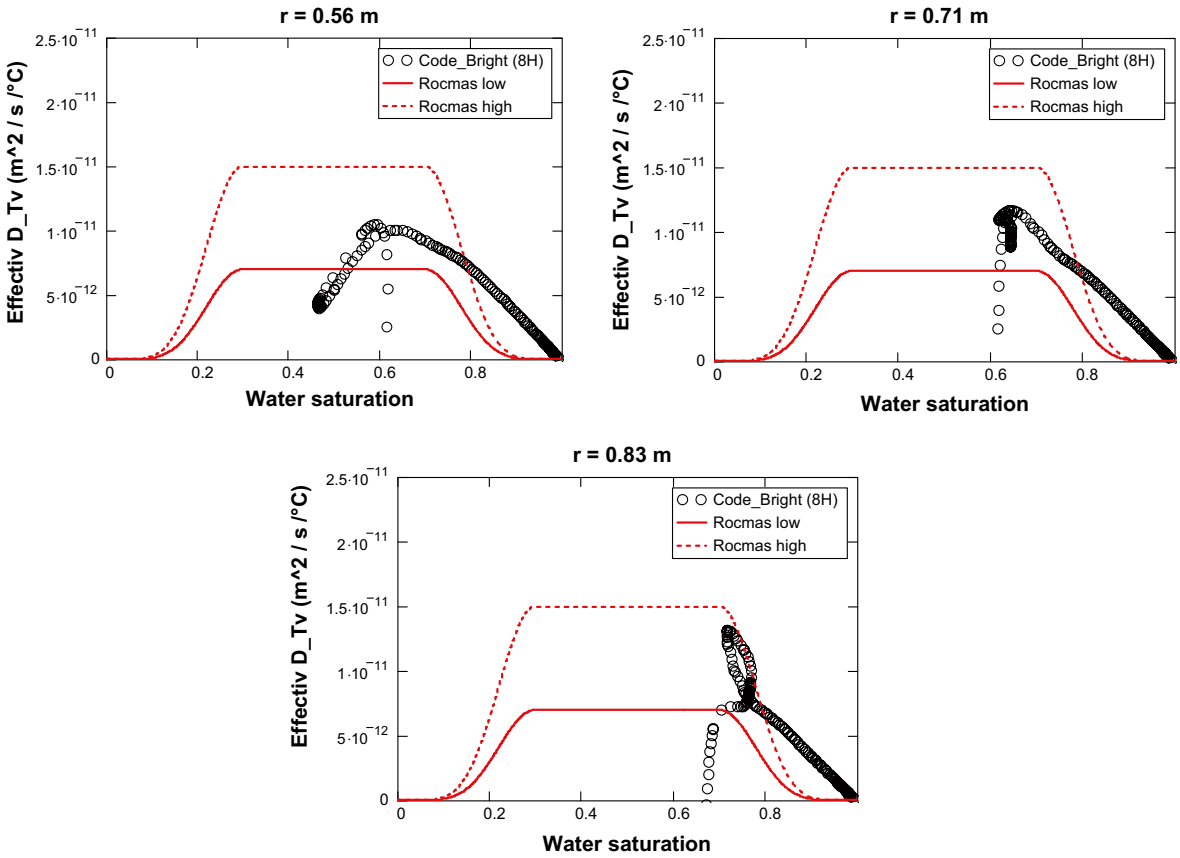

Figure 3-30. *Effective thermal vapor diffusion coefficient. The expression used in the Rocmas model and evaluated from the 8H Code_Bright model.*

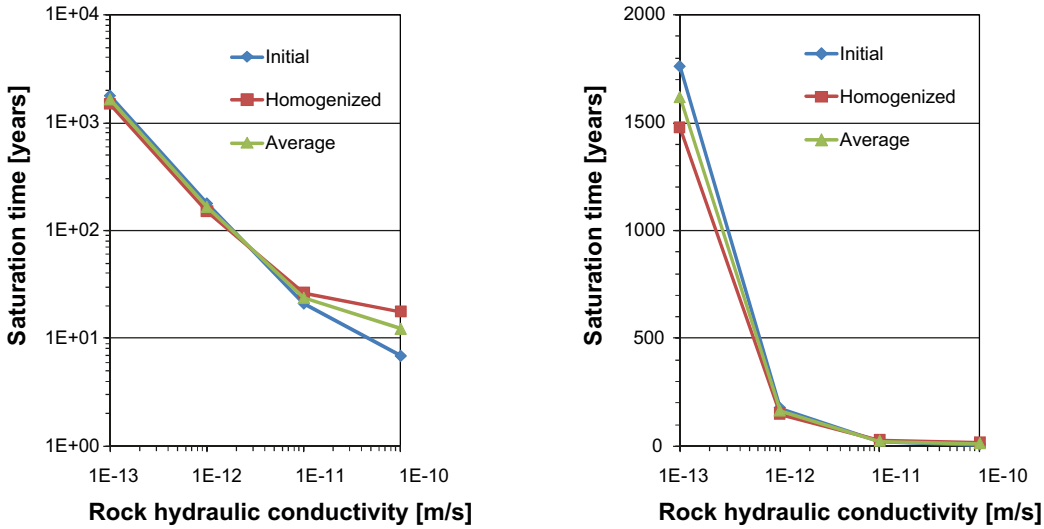

Figure 3-31. *Time until full water saturation in the buffer as a function of rock conductivity.*

The effect of increasing the rock permeability on the saturation time becomes relatively insignificant when $K>10^{-11}$. The saturation times for I and H representations agree well but diverges somewhat for $K<10^{-12}$.

Below in Figure 3-32 the effect of changing rock permeability on saturation time for the different point can be studied for the initial state models and the homogenized state models.

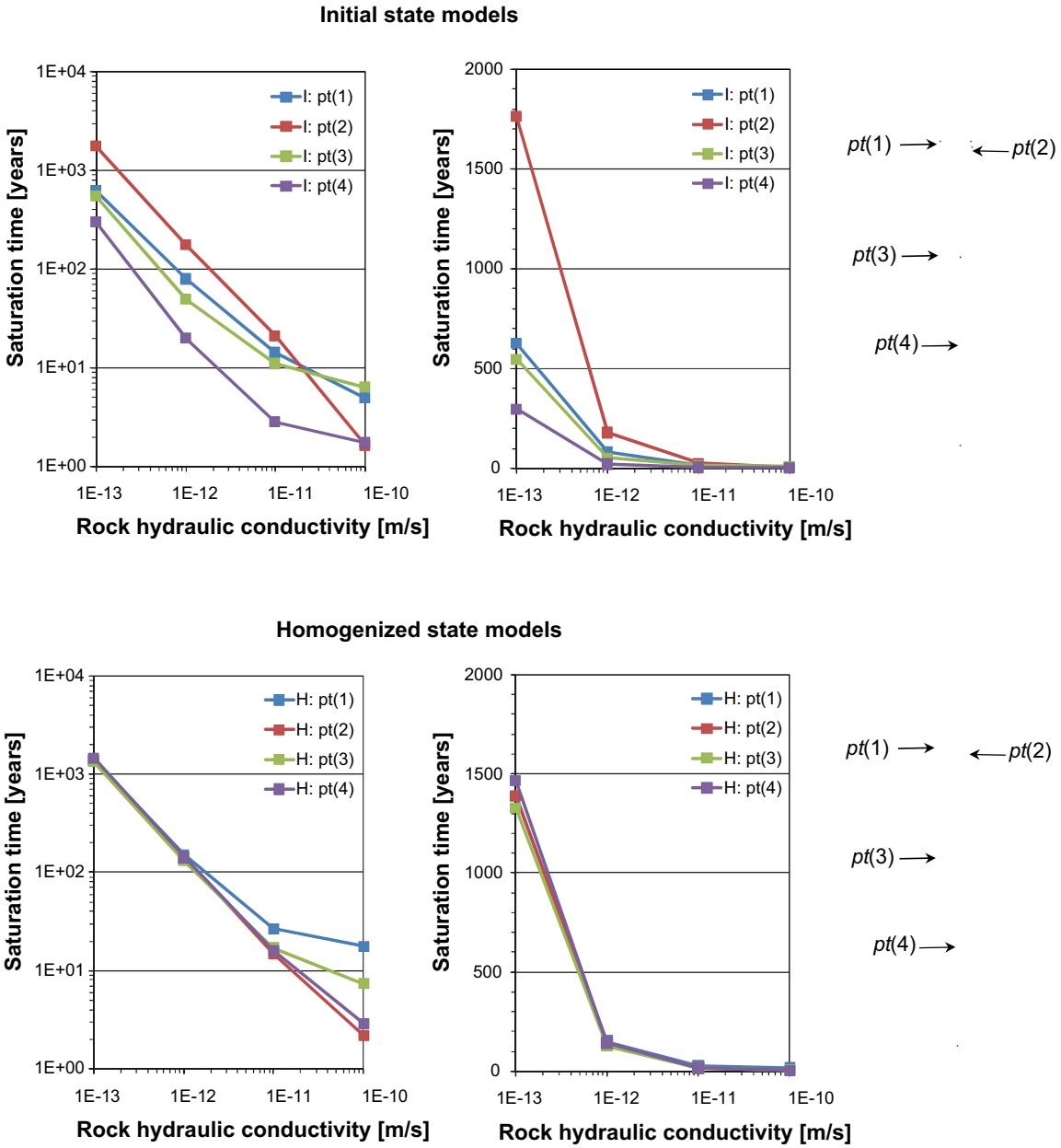

Figure 3-32. *Water saturation time as a function of rock conductivity in the indicated points.*

The saturation times for the different points in the initial state models diverges with decreasing permeability. The saturation time of *pt*(2) (topmost in the pellet slot) has a considerable increase when going from $K = 10^{-12}$ to $K = 10^{-13}$.

For the homogenized state model the saturation times for the different points are close to each other when changing permeability. There is a slight divergence when going from $K = 10^{-12}$ to $K = 10^{-13}$.

3.5.6 The effect of higher rock retention

Here the effect from altering the rock retention on the saturation process is studied. The standard rock retention was modeled by the Van Genuchten law with a parameter setting identical to that used by /Finsterle and Pruess 1995/ ($p_0 = 1.74$ Mpa and $\lambda = 0.60$). The altered retention is obtained as a fitting of the Van Genuchten model to the model used by /Börgesson and Hernelind 1999/. The parameters obtained by the fitting are $p_0 = 4$ MPa and $\lambda = 0.65$. Thus, the altered models have a higher rock retention curve as compared to the standard setup.

The initial state models with unfractured rock (1I and 2I) are equipped with the new rock retention curve. The new models are denoted 11I-high and 11I-low. Below, in Figure 3-33, the saturation times ($S_l = 0.99$) of the points are shown for all four models.

The effect from raising the retention curve of the rock is not dramatic. The sequence of saturation is not changed and the time until full saturation changes from 21.1 years to 19.5 years in the high permeable models and 177.2 years to 160.1 years in the models with low permeability.

The saturation time of *pt*(1) is however shortened significantly from 14.1 years to 9.4 years and 79.0 years to 56.7 years in the high and low permeable models, respectively.

3.5.7 The effect of an initially drained/ventilated tunnel

This investigation is performed in two steps to simplify the models. In the first step, an empty model where the materials within the tunnel and deposition hole have been removed is prescribed with a *RH*, (A) 100% or (B) 70%, on the inner boundary. The empty condition is simulated for 30 years. The obtained water pressure in the rock at 30 years is then evaluated and a suitable representation of the water pressure field is prescribed on a filled model (containing buffer and backfill) as an initial condition.

To specify the *RH* in the empty models it is translated into a water pressure by using,

$$S = p_g - p_l = -\frac{R(273.15+T)\rho_w}{M_w}\ln(RH) \qquad (3\text{-}15)$$

where $p_l(RH = 100\%) = 0.1$ MPa and $p_l(RH = 70\%) = -47.4$ MPa.

Profiles of the obtained water pressure are shown in Figure 3-34 where also the chosen water pressure profiles are shown. For $RH = 100\%$ the chosen pressure field are obtained by simply fitting a pricewise linear function to the model response. For $RH = 70\%$ the water pressure is not independent on radius in the indicated mid-section. To obtain a representative constant pressure in this section, the volume average of the water saturation is calculated and translated into a water pressure using the retention curve for rock. Above/below the mid section the pressure profile is obtained by fitting a linear function to the responses.

The chosen water pressure profiles are prescribed as an initial condition of model 1I and 2I. The new models are denoted 14I A-high and 14I A-low for $RH = 100\%$, and 14I B-high and 14I B-low for $RH = 70\%$.

For the models where $RH = 100\%$ in the tunnel during the ventilation the saturation times (when $S_l = 0.99$) for the points indicated are shown in Figure 3-35 below.

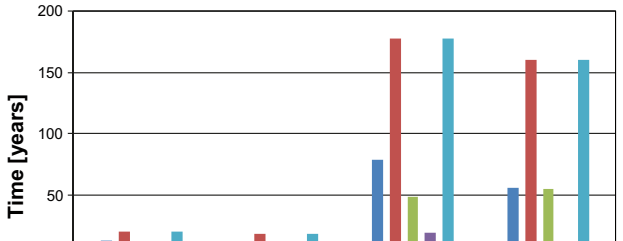

	Model 1I	Model 11I-high	Model 2I	Model 11I-low
pt(1)	14.1	9.4	79.0	56.7
pt(2)	21.1	19.5	177.2	160.1
pt(3)	10.9	10.4	49.1	55.7
pt(4)	2.8	2.5	19.7	10.7
pt(last)	21.1	19.5	177.2	160.1

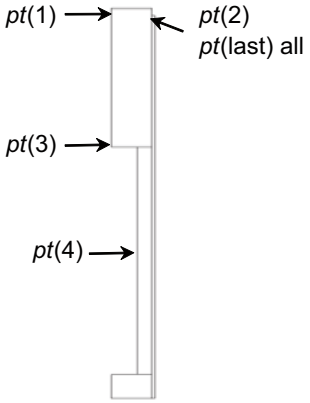

Figure 3-33. *Time until water saturation in the indicated points.*

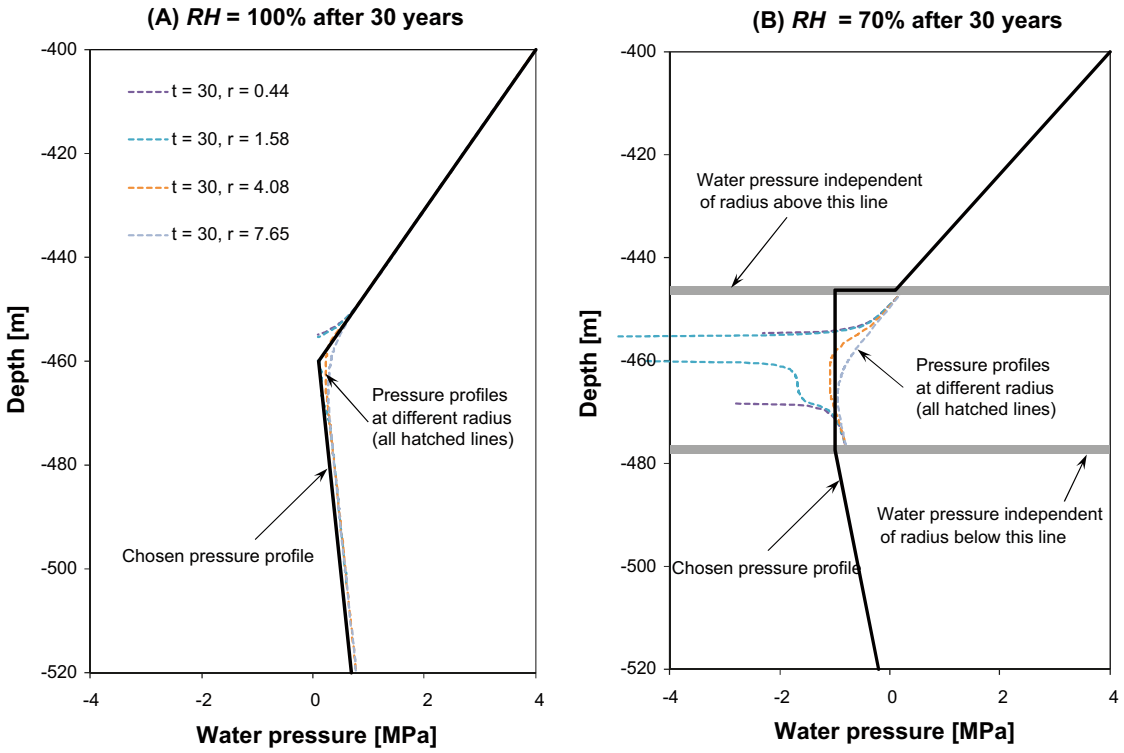

Figure 3-34. *Vertical water pressure profiles in the case of a drained (RH = 100%) and ventilated (RH = 70%) erpository.*

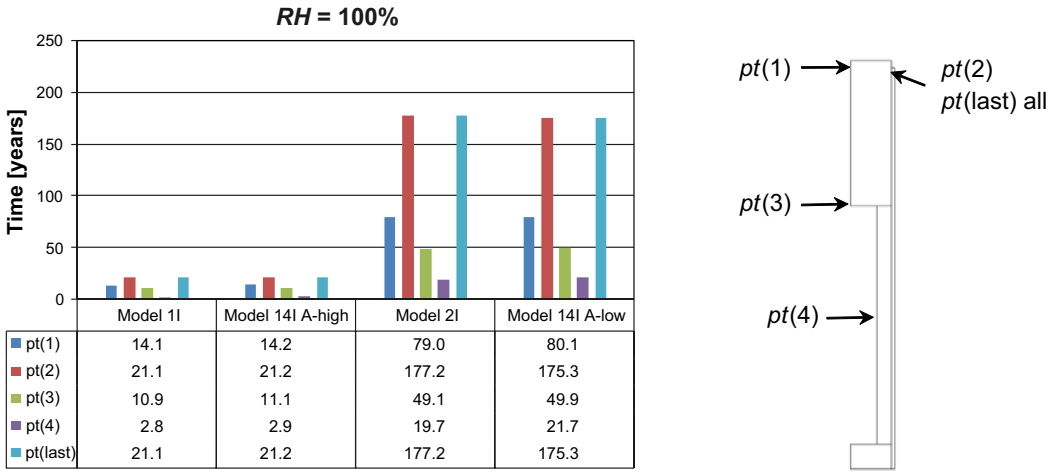

	Model 1I	Model 14I A-high	Model 2I	Model 14I A-low
pt(1)	14.1	14.2	79.0	80.1
pt(2)	21.1	21.2	177.2	175.3
pt(3)	10.9	11.1	49.1	49.9
pt(4)	2.8	2.9	19.7	21.7
pt(last)	21.1	21.2	177.2	175.3

Figure 3-35. *Saturation times in the indicated points for an initially drained (RH = 100%) and undrained deposition hole.*

Comparing the saturation times shows that the effect from considering the initial ventilation, where *RH* = 100%, is insignificant.

Below, in Figure 3-36, the saturation times (when $S_l = 0.99$) are given for the *RH* = 70% models.

For this case the change in saturation times are significant. For the highly permeable models the saturation time has increased from 21.1 years to 28.2 years. When lower rock permeability is used the saturation time increases from 177.2 years to 232.5 years. As low mean value as 70% RH over a 30 year period is however very unlikely to occur in Sweden (even at the ground level).

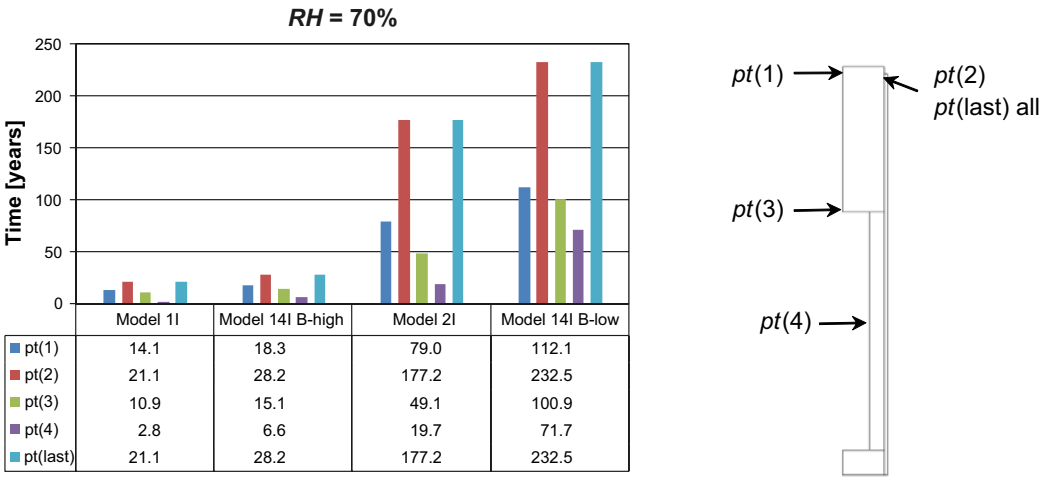

Figure 3-36. *Saturation times in the indicated points for an initially ventilated (RH = 70%) and unventilated deposition hole.*

3.5.8 The effect of altered block retention

The effect from altering the block retention curve is here investigated. The extended Van Genuchten model is used with the parameters shown in Table 3-14 below.

$$S_l(S) = \left(1 + \left(\frac{S}{p(T)}\right)^{\frac{1}{1-\lambda}}\right)^{-\lambda}\left(1 - \frac{S}{p_1}\right)^{\lambda_1}$$

$$p(T) = p_0 \frac{\sigma(T)}{\sigma_0} \qquad (3\text{-}16)$$

$$\sigma(T) = \left(1 - 0.625\frac{374.15 - T}{647.3}\right)\left(0.2358\left(\frac{374.15 - T}{647.3}\right)^{1.256}\right)$$

The shape of the retention curves has been altered so that the new curves are below the corresponding standard setup at water saturations above the initial state. For degrees of saturations less than the initial, the new curves are close to the original retention curves. This shape of the retention curves is more in line with what is reported in /Dueck 2004/. The ordinary and new retention curves are shown in Figure 3-37, where also experimental data are shown.

The effect of altering the block retention curve as described above on the saturation times is clearly visible in Figure 3-38.

The time until full buffer saturation has changed significantly:

- 21.1 and 26.3 years in 1I and 12I-high, respectively.
- 177.2 and 191.9 years in 2I and 12I-low, respectively.

Table 3-14. Parameters used in the extended Van Genuchten model.

Cylinder blocks	Ring-shaped blocks
p_0 = 5.222 Mpa	p_0 = 47.651 Mpa
p_1 = 280 Mpa	p_1 = 320 Mpa
λ = 0.05	λ = 0.05
λ_1 = 0.9	λ_1 = 1.0
σ_0 = 0.072 N/m	σ_0 = 0.072 N/m

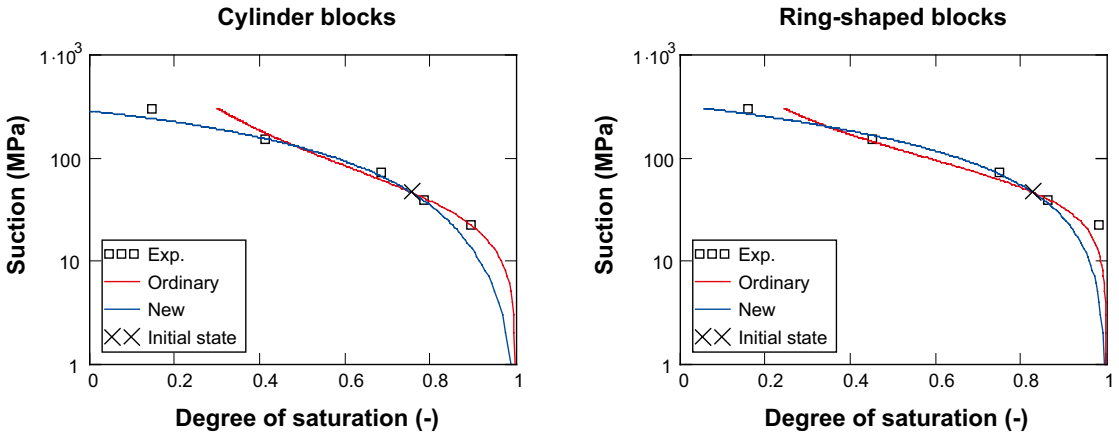

Figure 3-37. Ordinary and new retention curves together with experimental data and the initial state.

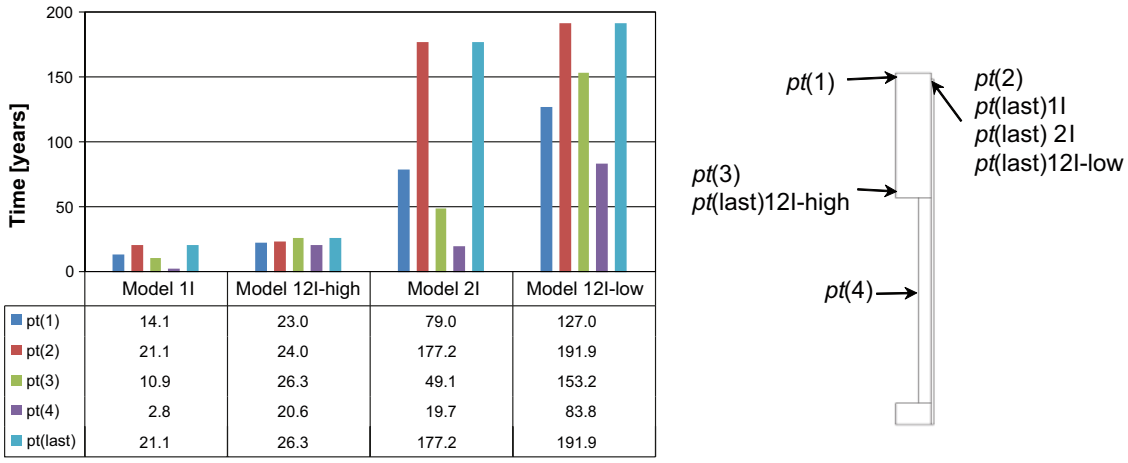

	Model 1I	Model 12I-high	Model 2I	Model 12I-low
pt(1)	14.1	23.0	79.0	127.0
pt(2)	21.1	24.0	177.2	191.9
pt(3)	10.9	26.3	49.1	153.2
pt(4)	2.8	20.6	19.7	83.8
pt(last)	21.1	26.3	177.2	191.9

Figure 3-38. Saturation times in the indicated points.

The saturation times for all points are significantly longer in models 12I. There is also a change in saturation sequence between the models and for 12I-high the final saturation of the buffer occurs in a different point as compared to 1I.

3.5.9 The effect of altered buffer permeability

The block permeability has here been altered for both block materials (cylinder and ring) and the pellet slot in the initial state models with high (10^{-18}) and low (10^{-19}) rock permeability. In the first case (A) the new permeability is taken as 0.6 times the original permeability and in the second case (B) the new permeability is taken as 2 times the original permeability.

The resulting saturation times are shown in Figure 3-39 and Figure 3-40, where also the basic models (1I and 2I) results are shown.

For the highly permeable rock model the A setup (0.6 the original permeability in the block and pellet slot) results in somewhat longer saturation times in all indicated points. The difference in saturation time (compared to the original model) is however not large. When turning to the B setup (2.0 the original permeability in the block and pellet slot) all points except for *pt*(2) (the last saturated point) becomes saturated earlier as compared to the original model. The small increase in saturation time (which intuitively seems peculiar when a more permeable buffer has been used) might come from the obtained variation in the interplay between the host rock water supply and the flow resistance in the buffer.

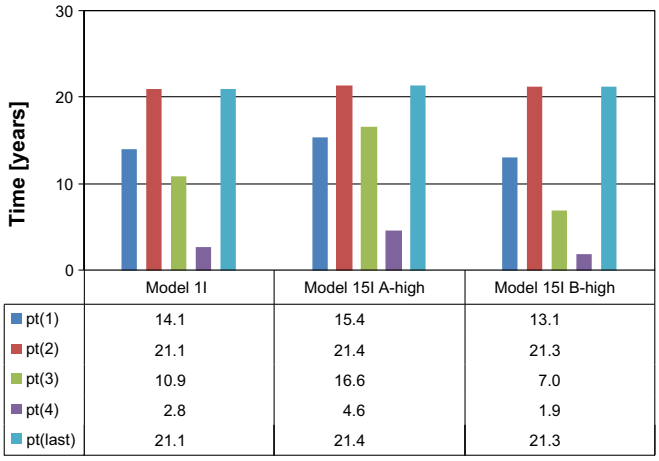

	Model 1I	Model 15I A-high	Model 15I B-high
pt(1)	14.1	15.4	13.1
pt(2)	21.1	21.4	21.3
pt(3)	10.9	16.6	7.0
pt(4)	2.8	4.6	1.9
pt(last)	21.1	21.4	21.3

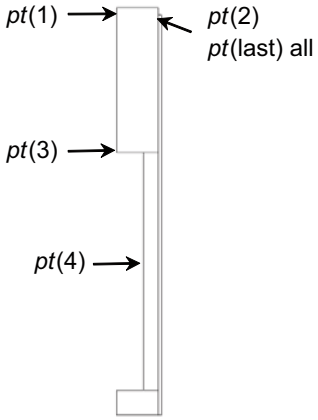

Figure 3-39. *Saturation times in the indicated points.*

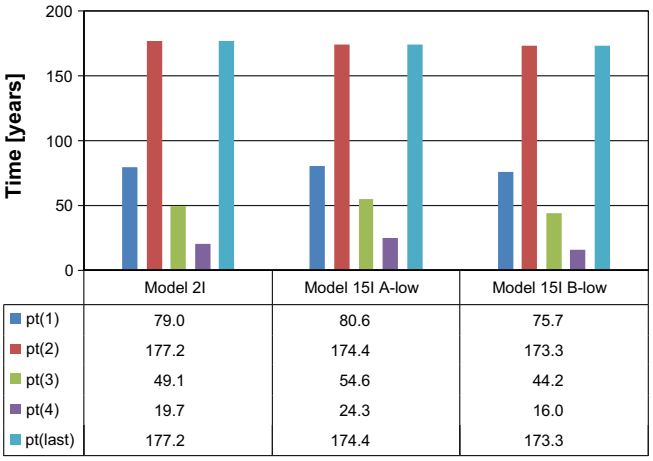

	Model 2I	Model 15I A-low	Model 15I B-low
pt(1)	79.0	80.6	75.7
pt(2)	177.2	174.4	173.3
pt(3)	49.1	54.6	44.2
pt(4)	19.7	24.3	16.0
pt(last)	177.2	174.4	173.3

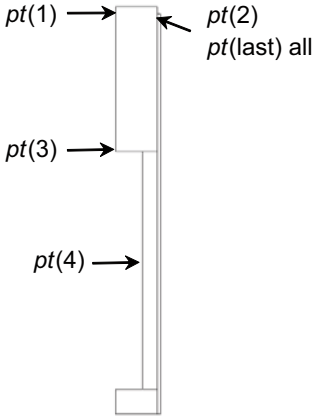

Figure 3-40. *Saturation times in the indicated points.*

The low permeable rock model equipped with the A setup produces somewhat longer saturation times in all points except for the last saturated point which is unexpected. The B setup results show no surprises since all points become saturated earlier as compared to the original model.

3.6 Conclusions

The buffer saturation times (the time where $S_l \geq 0.99$ in the entire buffer), for all TH-simulations of a deposition hole made in this work, are shown in Figure 3-41. The horizontal lines represent the cases indicated to the right of the line where also the "mechanical assumption" (Homogenized state or Initial state) is indicated. Below the lower line (Init. Unfractured rock) the rock conductivity used are indicated. The hatched lines connect models with identical rock conductivities. Close to the lower line, the positions of the models where the buffer was altered are given (unfilled circles).

3.6.1 Evaluation of the saturation times obtained for initial and homogenized state TH models

Using an axisymmetric model geometry the saturation time for a THM model was compared to the saturation times of two corresponding TH models. Two different assumptions concerning the void ratio field where made: initial state void ratios (I) or homogenized state void ratios (H).

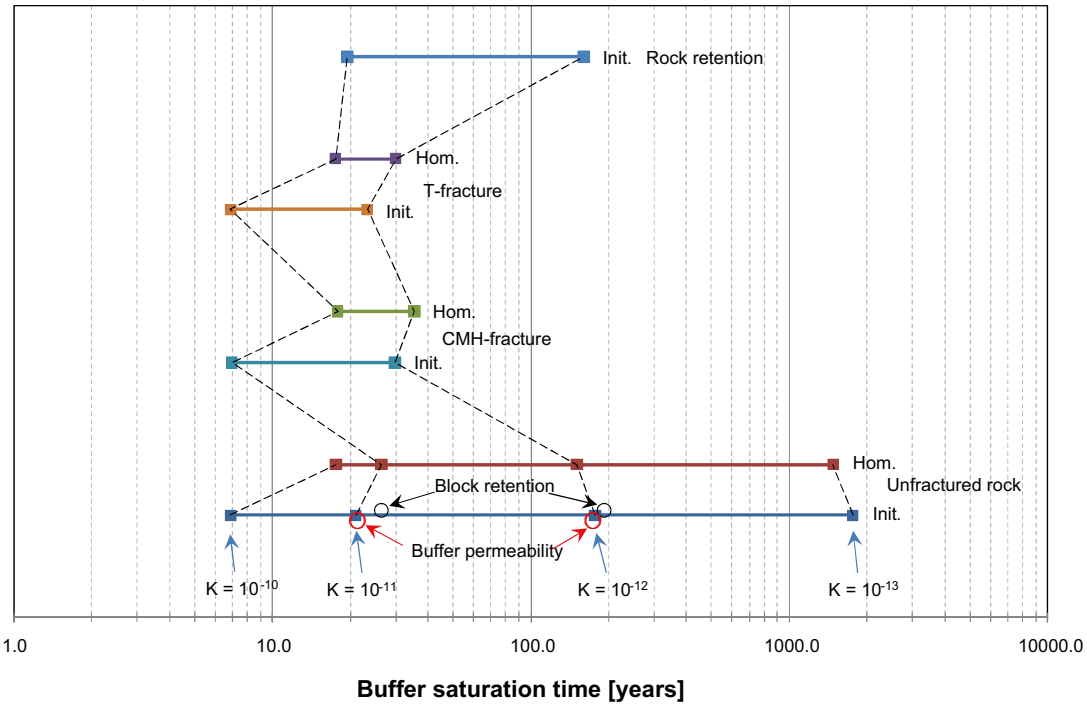

Figure 3-41. *Compilation of the buffer saturation times (the time when Sl = 0.99 in the entire buffer) for all TH-simulations of a deposition hole. The text rightmost of the lines indicates the representation of the rock: Unfractured rock, CHM-fracture (fracture at canister mid-height), T-fracture (fracture at tunnel) and Rock retention (changed rock water retention curve). In the three first cases (from the bottom up) the buffer has been represented as in the initial state (Init.), where blocks and pellet slot are present, and as in a fully homogenized state (Hom.) as indicated to the left of the corresponding horizontal line. In the Rock retention representation case has only the Init. buffer representation been used. The results obtained using the same rock conductivity, indicated below the bottom line, are connected by hatched lines. The results from changing the Buffer permeability or Block retention are indicated by red or black circles, respectively.*

The THM model was originally developed for investigating the Canister Retrieval Test, in which the water saturation process was rapid.

The study show that the I model gives faster saturation as compared to the THM model and the H model give slower saturation as compared to the THM model. It is concluded that this depends on the inflow rate and the difference in available pore volumes in the buffer geometry.

It should be noted that the conclusion above is valid for rapid wetting processes. In the case of a slow wetting process (c.f. when saturation times for cases of low rock permeabilty is studied) the H model is found to give faster buffer saturation as compared to the I model.

3.6.2 Estimate of buffer saturation time for unfractured rock

Two different rock conductivities were used in this study, a high conductivity of 10^{-11} m/s and a low rock conductivity of 10^{-12} m/s. For each rock conductivity I and H models were evaluated.

- For high rock conductivity the buffer saturation times became 21 and 26 years for the I and H model, respectively.
- For low rock conductivity the buffer saturation times became 177 and 151 years for the I and H model, respectively.

3.6.3 Estimate of buffer saturation time for fractured rock

The four models in the previous investigation were now equipped with a horizontal water bearing fracture, either intersecting with the buffer at the deposition hole wall at canister mid height or with the backfill at the tunnel rock wall. To obtain limiting cases the transmissivity of the fracture was set high for the high rock conductivity and low for the low rock conductivity.

For the canister mid height fracture it was found that:

- The high permeable models gave 7 and 18 years for the I and H model, respectively.
- The low permeable models gave 30 and 35 years for the I and H model, respectively.

For the tunnel fracture it was found that:

- The high permeable models gave 7 and 18 years for the I and H model, respectively.
- The low permeable models gave 23 and 30 years for the I and H model, respectively.

3.6.4 The effect of extremely low rock permeability

The unfractured model was equipped with an extremely low rock permeability of 10^{-20} m^2. The obtained saturation times were 1,760 and 1,476 years for the I and H model, respectively.

The peak temperature in the bentonite buffer (here equal to the peak temperature at the canister surface since no open slot is considered) was found to be 80°C. The peak temperature at the rock wall was 64°C. Thus, the obtained temperature drop in the buffer was 16°C.

The minimum degree of saturation in the buffer at the top of the canister and at canister mid height was > 0.4.

In /Rutqvist and Tsang 2008/ the temperature drop in the buffer was found to be 33–40°C using a similar model setup. A number of reasons for the difference in results of the model in the present study and in /Rutqvist and Tsang 2008/ are discussed:

- The difference in model dimensions, distance to water pressure boundary.
- Difference in buffer retention curves.
- Difference in buffer thermal conductivity.

3.6.5 Rock permeability dependence

For a rock conductivity > 10^{-11} m/s the buffer saturation time becomes effectively independent of the rock conductivity.

The saturation times for I and H agree well for a rock conductivity > 10^{-12} m/s.

3.6.6 The effect of higher rock retention

Using a higher rock water retention curve (larger suction given the same water degree of saturation) does not give a significant effect on the buffer saturation time.

3.6.7 The effect of an initially drained/ventilated tunnel

To investigate the effect of initial conditions different from hydraulic pressure, a model without buffer/backfill/canister was prescribed a RH at the internal boundary. An approximation of the obtained water pressure field after 30 years was then used as initial condition in the model where all constituents were installed. Two cases were investigated, a drained condition (RH = 100%) and a ventilated condition (RH = 70%).

For the drained condition the effect was insignificant.

For the ventilated condition the effect was significant. For high rock permeability the saturation time went from 21 to 28 years, and for low rock permeability saturation time went from 177 to 233 years, when considering a time of ventilation prior to the buffer installation. For 70% relative permeability the surrounding rock may experience desaturation. Two factors concerning the change in rock permeability will reflect the resaturation process. First, the lower the permeability the smaller the volume of rock that is subject to significant desaturation, and second, at lower permeability the resaturation of the rock is slower. The assumption of RH = 70% is, however, a very extreme case.

3.6.8 The effect of altered block retention

The block retention curve was altered by lowering the retention curve at higher degrees of saturation as compared to the initial state, for lower degrees of saturation the retention curve was chosen to be close to the original curve.

The effect of this relatively moderate altering of the retention curve was rather significant:

For the high rock permeability the saturation time increased from 21 to 26 years and in the low permeable case the saturation time increased from 177 to 192 years.

3.6.9 The effect of altered buffer permeability

No significant change in saturation time was found when adopting 0.6 or 2.0 times the original buffer permeabilities.

3.6.10 Uncertainties

The effect of the assumed axial symmetry, reducing the problem to 2D, has not been investigated. The assumption leads to that the tunnel volume associated to the deposition hole is represented by a "mushroom-shaped" volume, of half the size as compared to the real case when assuming a canister spacing of 7 m (in the real case the associated volume is canister spacing times the tunnel section area). With the axisymmetric assumption it also follows that the backfill surface subjected to wetting from the rock is 80% of the surface in the real case when assuming a canister spacing of 7 m. The mean distance to the wetted backfill surface is however shorter in the 2D model as compared to the real case. The saturation time of the backfill can therefore not be considered representative in the present model. The 2D model will produce faster saturation in the backfill as compared to 3D models. This will probably have some impact on the saturation time of the deposition hole buffer.

To obtain, numerically, more reasonable problem sizes, the inner slot (between the vertical canister boundary and the bentonite blocks), present in the buffer initially, has been omitted in the initial state models. The effect on the thermal process when incorporating an open inner slot has been investigated in /Hökmark et al. 2009/.

The saturation time for the buffer was found to be rather sensitive for changes in the buffer retention. The retention curves used have been calibrated against relevant experimental data. The accuracy in the experimental data is therefore an uncertainty factor. Since only TH simulations are carried out, there is a need for implicitly assuming a stress evolution when adopting retention curves. In fact, in Code_Bright there is always (even for THM-models) an assumption of confined conditions (i.e.a stress evolution is implicitly adopted when choosing a retention curve). The implicitly chosen stress evolution might not be representative for the material which in turn would leads to improper retention characteristics.

The relation between the saturation responses for TH-models (initial state or homogenized state) and THM-models has only been investigated for rapid saturation processes. Under these conditions the THM-results was bounded by the TH-results (faster saturation for the initial state model and slower for the homogeized state model). From studying the TH-solutions for low rock permeabilities (slow wetting) the saturation time sequence shifted (homogenized state first and initial state last). It has not been confirmed from studying THM and TH models that the saturation time for the THM model is bounded by the saturation times for the TH models for slow wetting processes.

The time until saturation in the buffer largely depends on properties of the surrounding rock. The distance to the hydraulic pressure boundary as well as the rock permeability are of importance. When it comes to the distance to the hydraulic pressure boundary, the strategy in this work has been to study data of the rock properties at the Forsmark and Laxemark site and developing a relevant representation. The rock permeability in turn, has been varied in a wide range.

The mesh dependence has not been investigated in the large model due to the complicated geometry and large problem size. The mesh dependence of the buffer in a small 1D TH model (used in the THM vs. TH study) has, however, been investigated. Doubling the number of elements in the bentonite and pellet slot material gave no significant effect on the water saturation evolution ($|S_l(t) / S_l^{fine}(t)-1| < 0.002$). The effect of a coarser buffer mesh density, as used in the large model, has been investigated by remeshing the small 1D TH model to contain the corresponding number of elements. The small model can be seen as an approximative representation of the buffer at canister mid-height in the large model. Comparing the water saturation evolutions of the fine-meshed and coarse-meshed models showed no significant differences ($|S_l^{coarse}(t) / S_l^{fine}(t)-1| < 0.013$).

4 Analysis of moisture redistribution in dry rock scenario

4.1 Introduction

Here the moisture redistribution in a deposition hole buffer is studied for a case of a dry surrounding rock mass. The result of this investigation (a water saturation field translated into thermal conductivities) is used in /Hökmark et al. 2009/, where a strategy for designing the repository with respect to the thermal evolution in the buffer and rock is developed.

The simulations in this Task were performed before the Data Report /Åkesson et al. 2010/ was written. At the time the backfill material was thought to have higher retention as compared to the buffer blocks. The initial state of the backfill was also thought to be considerable dryer ($w = 0.1$) as compared to the buffer material ($w = 0.17$). Finally, in the design at this time, the topmost block in the deposition hole belonged to the backfill and therefore consisted of backfill material.

Despite the differences between the design at that time and currently, the results are considered relevant. With the used model setup the results should be conservative but it is believed not to be over-conservative. One of the additional cases investigated within this work has buffer material in the entire deposition hole, which makes only the backfill material different from the current design.

4.2 Modelling strategy

In this section the modelling strategy is discussed. Assumptions and an overview of the solution scheme used for the analyses are discussed. First the TH-modelling strategy used in this work is described. It is divided in two different analyses, 1) investigation of the dehydration of the rock mass surrounding the deposition tunnels and 2) water redistribution in the buffer in a deposition hole.

Next, the connection between the resulting thermal conductivities, obtained from using the TH-solutions in this work, and the following purely thermal modelling, in /Hökmark et al. 2009/ (the STD-report), is described in order to facilitate an easier understanding of the analysis.

4.2.1 Thermo-Hydraulic modelling strategy in this work

The first investigation considers dehydration of the rock mass around a deposition tunnel due to venting of the tunnels prior to installing buffer in the deposition holes and backfilling the tunnel. A 1D axisymmetric hydraulic model is used for this purpose where the liquid pressures at the tunnel boundary and the outer boundary are prescribed. The outcome of the analysis is the available gas filled pore volume which potentially could host water transported from the buffer. The gas filled pore volume is calculated for varying parameter settings to investigate the sensibility.

When investigating the water-redistribution in the buffer of a deposition hole a TH-model is used. The developed axisymmetric geometry models one deposition hole and the near-field rock mass, see Figure 4-1.

In the model, hydraulic processes are active only in the buffer, i.e. the hydraulic influence from the surrounding rock mass on the buffer is assumed insignificant. The first investigation considering dehydration of the rock mass around a deposition tunnel due to venting, which is discussed above, shows that this assumption is valid.

Thermally the influence from all the surrounding canisters is considered indirectly in the used TH-model by prescribing adiabatic conditions at the outer vertical boundary. The outer radius and initial temperature of the model is varied. The obtained rock wall temperature at canister mid-height is compared with an analytical solution where heat contributions from all canisters are considered.

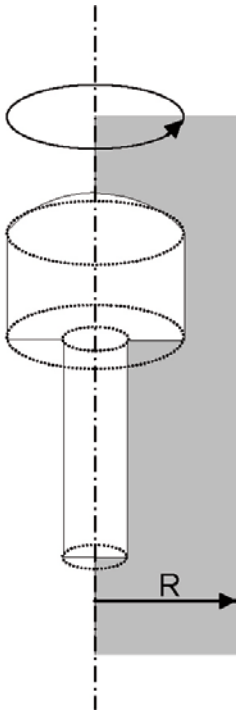

Figure 4-1. *The axisymmetric geometry of the TH-model.*

The model will when following this strategy have a temperature field that is a representative approximation of the canister near-field temperatures using a geometrically relative small model.

When using this strategy a number of problematic issues are avoided. Since the geometrical size of the problem can be kept moderate (in contrast to if the entire repository was to be modeled), it becomes possible to obtain a high resolution of the solution without being forced to solve huge equation systems (which would require huge memory capacity) and the CPU time-consumption will also as a consequence be reasonable. If the heat contribution from all canisters was to be considered by imposing more "sophisticated" thermal boundary conditions on a smaller sized model, the degree of complexity when developing the model would be serious.

4.2.2 Thermal modelling strategy in /Hökmark et al. 2009/

One of the main reasons of the present study is to investigate the effect of the water redistribution in the buffer of a dry deposition hole on the thermal conductivities in different parts of the buffer. These conductivities are to be used in a purely thermal analysis, /Hökmark et al. 2009/, where the maximum peak bentonite temperature, T_b, is evaluated. The maximal bentonite temperature is an important design criterion of the repository.

It has been found that the maximum bentonite temperature occurs at the top of the canister, see Figure 4-2.

As the figure also shows, the canister top temperature may be considered via a superposition of the rock wall temperature at canister mid-height T_{rw} and the temperature difference between the canister top and the rock wall temperature at canister mid-height $\Delta T_{b\text{-}rw}$.

$$T_b = T_{rw} + \Delta T_{b\text{-}rw} \tag{4-1}$$

In the same fashion $\Delta T_{b\text{-}rw}$ (obtained from considering the *total* heat source contribution) may be considered via a superposition of the temperature differences when either; only the contribution from the *local* canister is considered, or, only the contribution from all other canisters (here denoted the *global* contribution) are considered. In Figure 4-3 the different heat source definitions (total, global, and local) are schematically draw.

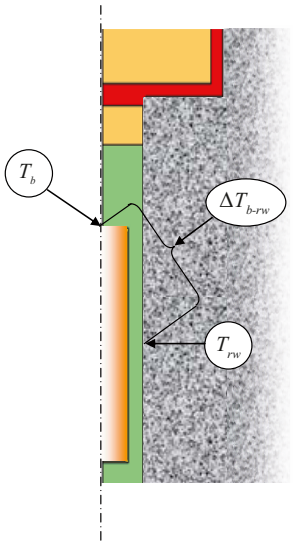

Figure 4-2. *Temperatures at different positions in the buffer.*

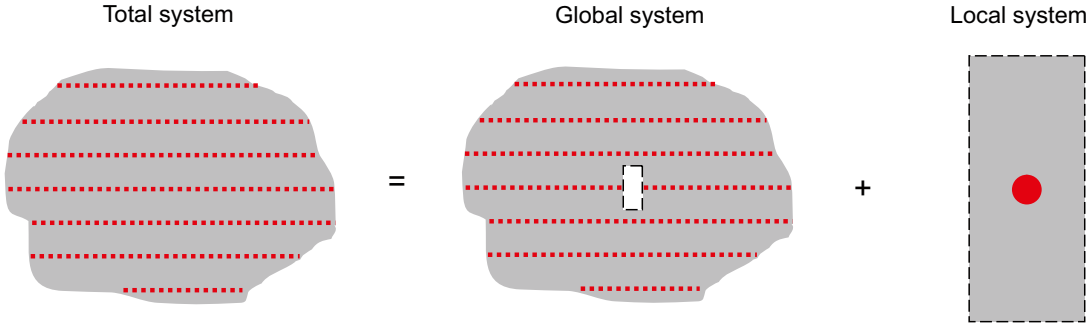

Figure 4-3. *Schematic drawing of the definitions of the total, global and local systems (heat contribution sources).*

The temperature difference produced by the global heat source is however significantly smaller in magnitude as compared to what the local heat source (canister) gives rise to. I.e. a model considering only the heat from the local canister will produce a good approximation of the total temperature difference.

$$\Delta T_{b\text{-}rw} = \Delta T_{b\text{-}rw}^{local} + \Delta T_{b\text{-}rw}^{global} \approx \Delta T_{b\text{-}rw}^{local} \quad (4\text{-}2)$$

Thus, a good approximation of the maximum bentonite temperature can be evaluated from:

$$T_b \approx T_{rw} + \Delta T_{b\text{-}rw}^{local} \quad (4\text{-}3)$$

where T_{rw} is obtained from an analytical solution where all canisters in the repository are accounted for and $\Delta T_{b\text{-}rw}^{local}$ is obtained from a local model of the near-field of the considered canister.

There is however one problem when calculating the local contribution to the temperature difference between the canister top and the rock wall at canister mid-height using a model where no other heat sources but the local canister are accounted for. The local temperature field T^{local} depends on the total temperature field T^{total}.

This is easily understood if one considers that the local temperature field T^{local} depends on the thermal conductivity λ, which in turn depends on the water saturation S_l, which in turn is dependent on the total temperature field T^{total}, i.e.

$$T^{local} = T^{local}(\lambda(S_l(T^{total}))). \quad (4\text{-}4)$$

This issue can be solved by using the solution of the TH-model in this work, where $S_l(T^{total})$ is a part of the solution. The obtained water saturation may be translated into a corresponding heat conductivity $\lambda(S_l(T^{total}))$ by using a suitable relation. Thereafter the pure thermal problem can be solved for the local temperature field, from which the desired temperature difference can be calculated.

4.3 Investigation of the dehydration of the surrounding rock

The venting of deposition tunnels during significant time spans (prior to filling of the deposition holes and the tunnels) may imply that the surrounding rock can dehydrate. This air-filled pore-space in the rock could potentially constitute a sink for the water that is associated with the buffer at installation. If a significant amount of this water would migrate into the rock, then this could potentially imply a significant increase of peak temperatures at the canister surfaces. The aim of this study is to investigate the extent of dehydration as a function of the rock properties.

4.3.1 Model geometry and conditions

The water transport in the rock is modeled as a 1D axisymmetric problem (Figure 4-4). The tunnel is thus regarded as an infinite cylinder with the radius r_T and with a constant negative liquid pressure p_T, which corresponds to the relative humidity during ventilation of the tunnel. A low relative humidity, corresponding to a liquid pressure of –60 MPa, was chosen as a base case value. A boundary liquid pressure (p_{BC}) is held constant at some distant radius (r_{BC}). This pressure represents the hydrostatic pressure at the depth of the repository. A steady-state condition is assumed, implying that the total liquid flow is the same at all radii between the tunnel and the outer boundary. The resulting pressure profile corresponds to a gas saturation profile. The gas-filled pore volume along the distance (L) between two deposition holes can thus be calculated and compared to the available water volume in each installed buffer, i.e. approx. 3 m^3.

Table 4-1. Model geometry and conditions.

Parameter	Description	Base case value	Interval
r_T	Tunnel radius	2.5 m	–
r_{BC}	Boundary radius	30 m	30 → 300 m
p_T	Tunnel pressure	–60 MPa	–60 → 0 MPa
p_{BC}	Boundary pressure	5 MPa	–
L	Distance between deposition holes	7 m	–

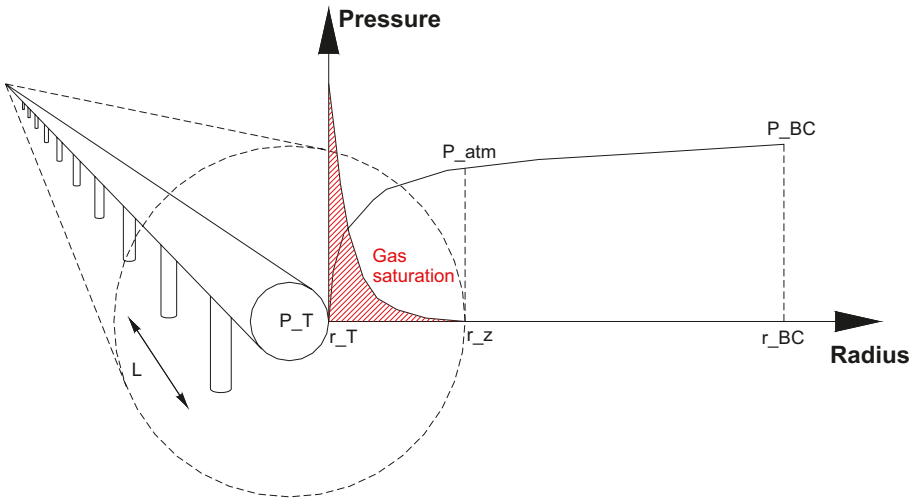

Figure 4-4. *Axis symmetric representation of dehydration of rock surrounding tunnel.*

Table 4-2. Rock properties.

Parameter	Description	Base case value	Interval
n	Porosity	0.003 (–)	–
p_0	van Genuchten parameter	4 (MPa)	0.1 → 100 (MPa)
λ	van Genuchten parameter	0.65 (–)	0.2 → 0.8 (–)
K	Hydraulic conductivity at saturation	10^{-13} (m/s)	10^{-14} →10^{-9} (m/s)
ð	Relative permeability parameter	3 (–)	2 → 10 (–)

4.3.2 Rock properties

The rock is characterized by three main properties: the porosity, the retention properties and the hydraulic conductivity. The porosity (n) is fairly well known, whereas the remaining properties are less known (Table 4-2).

The retention properties, i.e. the relation between the degree of liquid saturation (S_l) and the liquid pressure (p), are described by the van Genuchten function:

$$S_l(p) = \left(1 + \left(\frac{p_g - p}{p_0} \right)^{\frac{1}{1-\lambda}} \right)^{-\lambda} \qquad (p < p_g) \tag{4-5}$$

The gas pressure (p_g) is kept at atmospheric level (p_{atm}) throughout the analysis. The retention property is thus described by two parameters (p_0 and λ). The hydraulic conductivity consists of two factors: the hydraulic conductivity *at saturation* (K); and the relative permeability, which is a function of the liquid degree of saturation:

$$k_r(S_l) = (S_l)^{\delta} \tag{4-6}$$

The hydraulic conductivity is thus described by two parameters (K and δ).

4.3.3 Mathematical description

The water flow per unit length of tunnel is at a specified radius given as:

$$q = 2\pi \cdot r \cdot \frac{k_r(p) \cdot K}{\gamma} \cdot \frac{dp}{dr} \qquad (m^3/s, m) \tag{4-7}$$

The unit weight of water (γ = 0.01 MPa/m) is required since p denote pressure rather than head.

Under the assumption of steady-state conditions, the flow can be calculated as:

$$q = \frac{\frac{K}{\gamma} \int_{p_T}^{p_{BC}} k_r(p) dp}{\frac{1}{2\pi} \cdot \ln\left(\frac{r_{BC}}{r_T} \right)} \tag{4-8}$$

With the knowledge of q, the radius with atmospheric pressure can be derived as:

$$r_z = r_T \cdot \exp\left(\frac{2\pi \cdot K}{q \cdot \gamma} \cdot \int_{p_T}^{p_{atm}} k_r(p) dp \right) \tag{4-9}$$

Finally the gas filled pore volume corresponding to the distance between deposition holes can be evaluated as:

$$V = \int_{r_T}^{r_z} 2\pi \cdot r \cdot n \cdot L \cdot (1 - S_l(p(r))) dr \tag{4-10}$$

To do this calculation it is necessary to determine a relation between the pressure and the radius. This can be made through root solving of the following function:

$$f(p,r) = \int_{p_T}^{p} \frac{k_r(p)\cdot K}{\gamma} dp - \frac{q}{2\pi}\cdot \ln\left(\frac{r}{r_T}\right) \qquad (4\text{-}11)$$

These relations can be readily implemented in an advanced mathematical spread-sheet. Moreover, they can easily be modified to facilitate parameter analyses.

The calculated gas volume can be compared to the available water volume in each installed buffer, i.e. approx. 3 m^3.

4.3.4 Parameter analysis

Parameter analyses have been performed for a number of parameters and conditions. A common base case setting as well as analyzed intervals is shown in Table 4-1 and Table 4-2. For base case conditions, the gas volume is 0.16 m^3. This volume thus represents only 5% of the available water volume in each installed buffer.

Contour plots of the gas filled pore volume are shown for combinations of varied parameters and conditions in Figure 4-5. In the first plot, the effect of the retention parameters is analyzed. It can be noticed that the volume increases strongly with decreasing values of λ and increasing values of p_0. There is apparently a domain in p_0-λ-space in which the dehydration could be extensive. In the second plot, the effect of the conductivity parameters (K and δ) is analyzed. It can be noticed that the volume appears to be independent of the saturated conductivity and that the volume decreases with increasing δ-value. Nevertheless, it can be anticipated that the K value has large influence on the time-scale to reach the steady-state condition. In the third plot, the effect of the boundary conditions (p_T and r_{BC}) is analyzed. It can be noticed that the volume appears to be independent of the tunnel pressure, exception for pressures close to zero which corresponds to zero gas volume. The volume tends to increase with increasing boundary radius. This variation illustrates the limitation of the used method.

4.3.5 Coupled retention and relative permeability

In several reported works, the relative permeability is described as a van Genuchten-relation:

$$k_r(S_l) = \sqrt{S_l}\left(1-\left(1-S_l^{1/\lambda}\right)^{\lambda}\right)^2 \qquad (4\text{-}12)$$

The parameter λ is in this relation the same as the one used in the retention curve (Equation (4-5)). The influence of this parameter is the opposite as δ in Equation (4-6), in that the relative permeability decreases with decreasing λ value. The combined effect on the gas-filled pore volume is shown in Figure 4-6. Here it can be seen that the volume is quite independent of the λ value, and in order to get a significant increase of volume the p_0 would have to exceed 10 MPa. In fact, the maximum volume is in this case only 0.3 m^3, i.e. only twice as high as the base case value in the parameter analysis.

4.3.6 Calculations for reported rock properties

Finally, the gas volume has been calculated for specific rock properties reported in the literature. A compilation of retention parameters and relative permeability parameters is given in Table 4-3. The retention curves are shown in Figure 4-7. Van Genuchten parameters have been adopted to the retention data applied by /Börgesson and Hernelind 1999/. The gas volume calculated from the data by /Börgesson and Hernelind 1999/ is the same as the base case value described in the parameter analysis. The other two descriptions yield significantly lower gas volume (see Table 4-3). This is clearly an effect of the low relative permeability relations used in these reports.

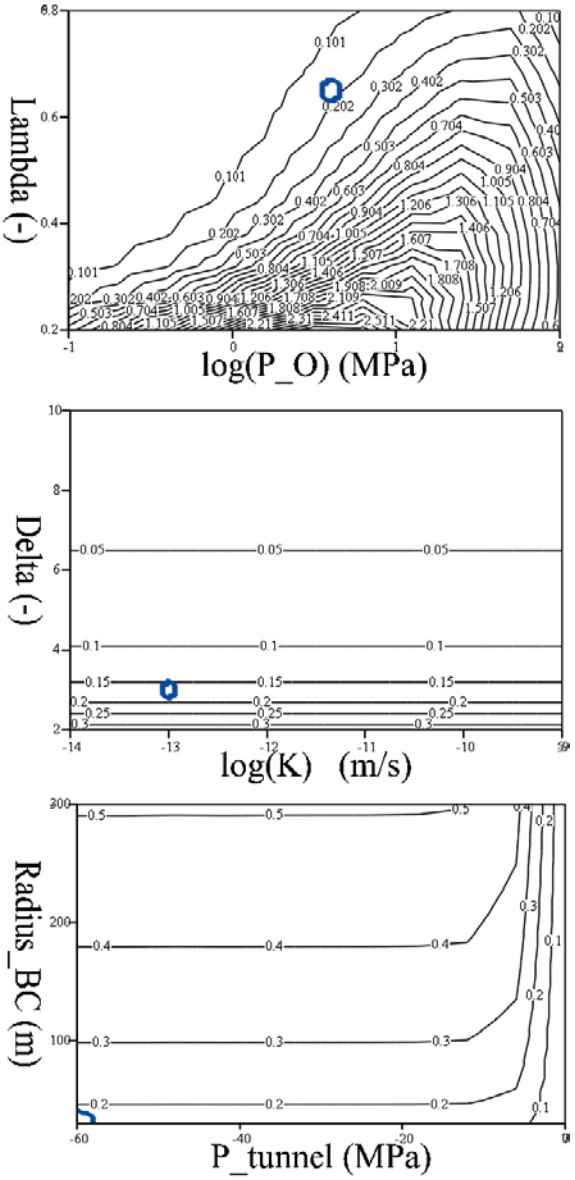

Figure 4-5. *Gas-filled pore volume (m³) corresponding to the distance between two deposition holes. Parameter analysis for retention properties (upper); hydraulic conductivity parameters (middle); and geometry and boundary conditions (lower). Blue rings correspond to base case values and retention properties reported by /Börgesson and Hernelind 1999/.*

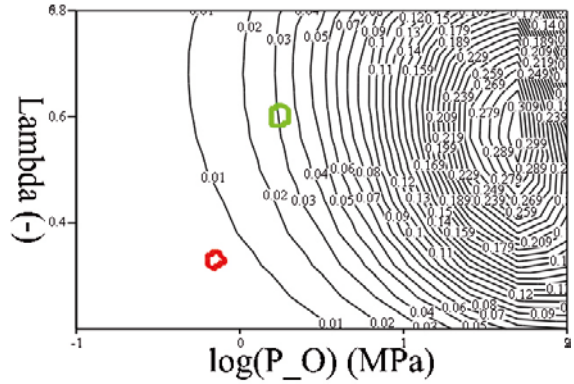

Figure 4-6. *Gas-filled pore volume (m³) corresponding to the distance between two deposition holes. Parameter analysis for retention properties coupled to relative permeability parameters. Rings correspond to retention properties reported by /Finsterle and Pruess 1995/ (green), and /Thomas et al. 2003/ (red).*

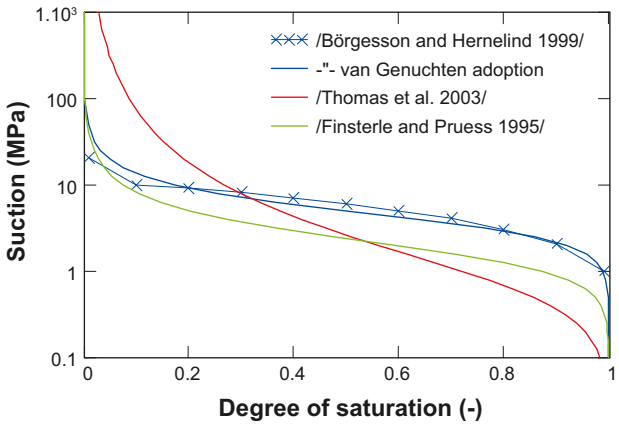

Figure 4-7. Reported retention curves for crystalline rock.

Table 4-3. Reported rock properties and calculated gas volumes.

Source	p_0 (MPa)	λ (–)	Relative permeability	Gas volume (m^3)
/Börgesson and Hernelind 1999/	4	0.65	Equation (4-6) (δ = 3)	0.16
/Thomas et al. 2003/	0.7	0.33	Equation (4-12) (λ = 0.33)	0.006
/Finsterle and Pruess 1995/	1.74	0.60	Equation (4-12) (λ = 0.60)	0.03

4.4 Investigation of the water redistribution in a dry deposition hole

4.4.1 General model description

In the left box of Figure 4-8 a schematic overview of a KBS-3V repository is shown. The repository consists of parallel horizontal tunnels, with a distance of 40 m between them, in which the canisters and buffer are placed in vertical boreholes that are positioned with a spacing of approximately 7 m.

The model used in this work represent the near-field of one deposition hole assuming axisymmetry, see the right box in Figure 4-8. Adopting this representation a small convenient problem size is obtained.

The geometry of the surrounding rock mass is shown in Figure 4-9. The top and bottom of the model is positioned 260 m from the tunnel floor and the magnitude of the outer radius, R, is discussed below. The tunnel has a height of 5.4 m and a width of 4.9 m. The borehole has a depth of 8 m and a radius of 0.875 m.

Adiabatic conditions are imposed on the outer vertical boundary of the model in order to capture heat in the model which makes the temperature increase. The obtained increase in temperature is thought of simulating the temperature contribution from all other canisters in the repository.

To obtain a representative simulated temperature field, a suitable outer radial dimension, R, of the model and a suitable initial temperature, T_0, have to be chosen. The two parameters are calibrated by performing thermal simulations with different choices and comparing the obtained temperature at the rock wall surface at canister mid-height with an analytical solution /Hökmark et al. 2009/. The set $\{R,T_0\}$ for which a representative temperature history is obtained is considered suitable. Some results when performing the calibration are shown in Figure 4-10.

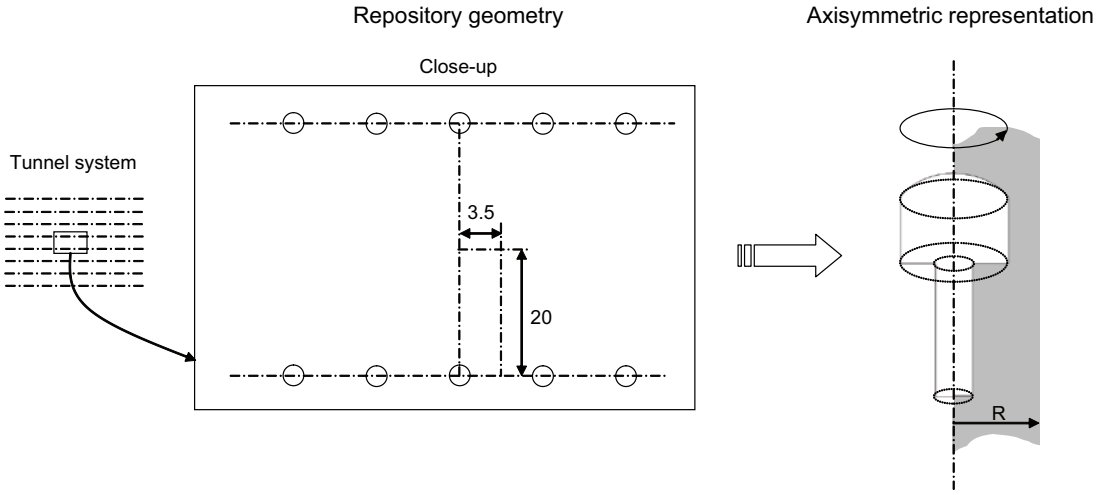

Figure 4-8. *Schematic geometry of the repository (left) and an axisymmetric representation (right).*

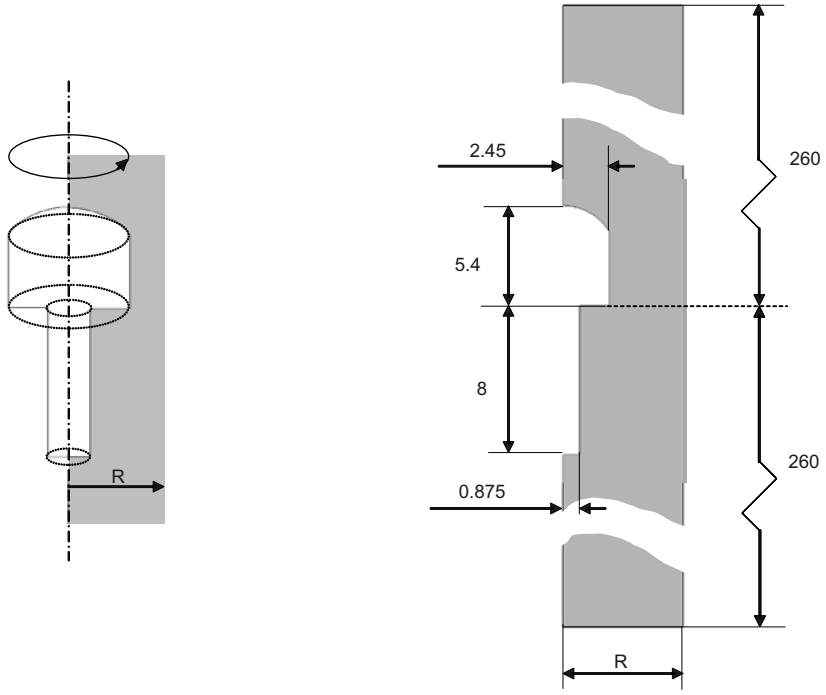

Figure 4-9. *The geometry of the surrounding rock mass in the axisymmetric representation.*

It can be seen that using R = 8 m and T_0 = 15°C gives slightly lower response and that using R = 7 m and T_0 = 15°C gives higher response as compared to the analytical solution. The most accurate temperature response is obtained using R = 8 m and T_0 = 18°C which is considered the Base Case setup. However, two of the three different setups shown in Figure 4-10 have been used in analyses in this work:

1. R = 8 m and T_0 = 18°C
2. R = 8 m and T_0 = 15°C

The first is used when studying the general picture of the water redistribution and when obtaining suitable thermal conductivities. The second one is only used when qualitative investigations between some alterations of the model are studied and no quantitative evaluations are made.

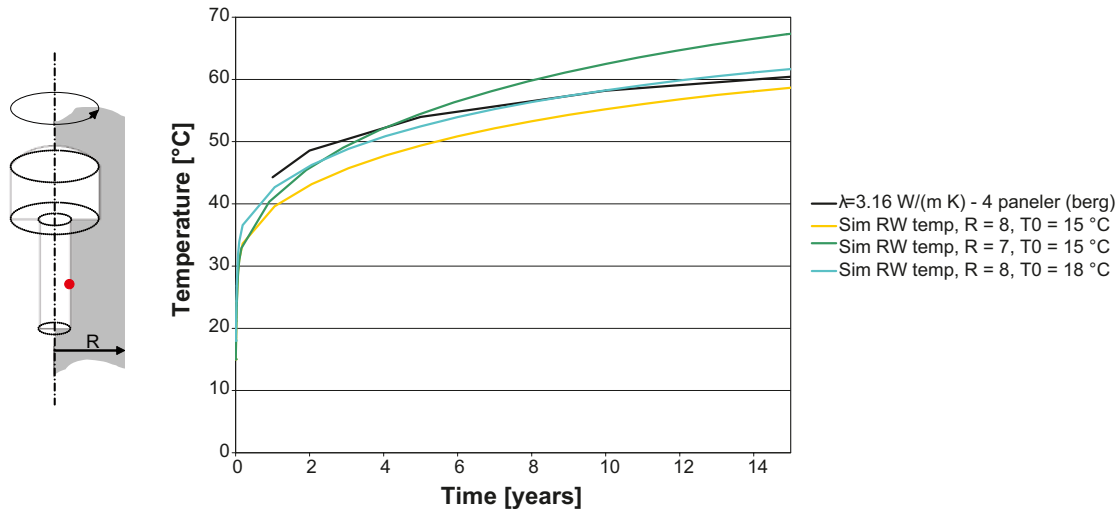

Figure 4-10. *Thermal simulations for different outer model-radii and initial temperature.*

Since the rock is assumed impermeable the hydraulic "boundary conditions" may be considered as zero flux conditions at the interface surface between the rock and the buffer/backfill.

The constituents of the entire model are shown in Figure 4-11. The TH-model of the engineered buffer, which is surrounded by the rock mass, consists of:

- The canister (consisting of a cast iron inset surrounded by a copper shield), in which the heat load is imposed.
- Bentonite blocks.
- Volumes filled with bentonite pellets.
- A backfill material.

The geometry of the engineered buffer constituents is shown in Figure 4-12.

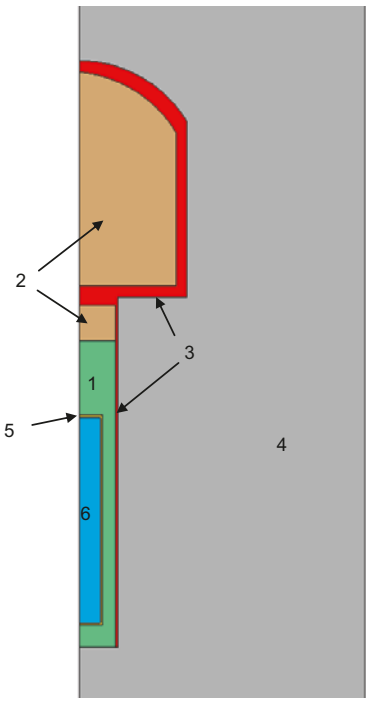

No.	Material
1	Bentonite blocks
2	Backfill
3	Pellets
4	Rock
5	Copper
6	Cast iron

Figure 4-11. *The model constituents.*

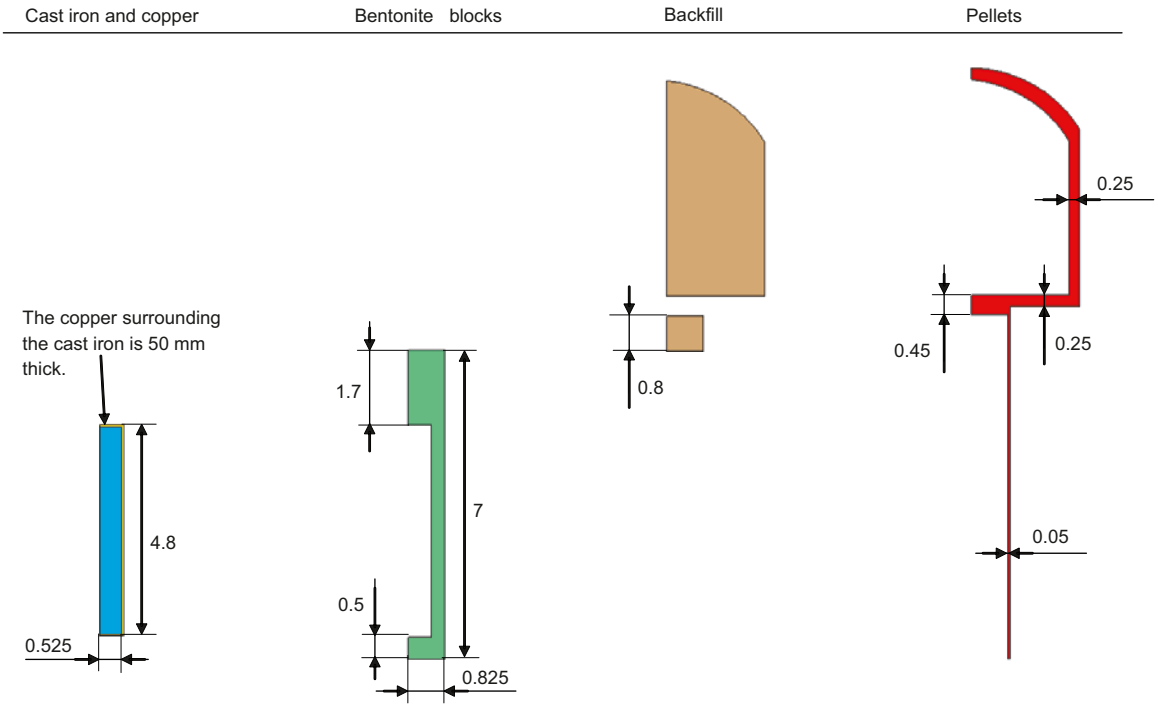

Figure 4-12. *Geometry of the constituents of the engineered buffer.*

The heat load is prescribed at two concentric vertically orientated cylinders. 1/3 of the total heat load is prescribed at the radial distance r = 0.105 m and 2/3 of the total heat load at r = 0.315 m. This approach is used in order to consider that 4 fuel elements and 8 fuel elements are placed at these approximate radial distances respectively. The cylinders where the thermal load is imposed have the height 4.4 m and are symmetrically positioned in the canister, i.e. at a distance of 0.2 m from the top and bottom.

The equation describing the canister power, also used in /Hökmark et al. 2009/, is given by the expression

$$P(t) = P(0)\sum_{i=1}^{7} a_i \exp(-t/t_i) \qquad (4\text{-}13)$$

where $P(0)$ = 1,700 W and the decay function coefficients, shown in

i	t_i	a_i
1	20	0.060
2	50	0.705
3	200	–0.055
4	500	0.250
5	2,000	0.025
6	5,000	–0.009
7	20,000	0.024

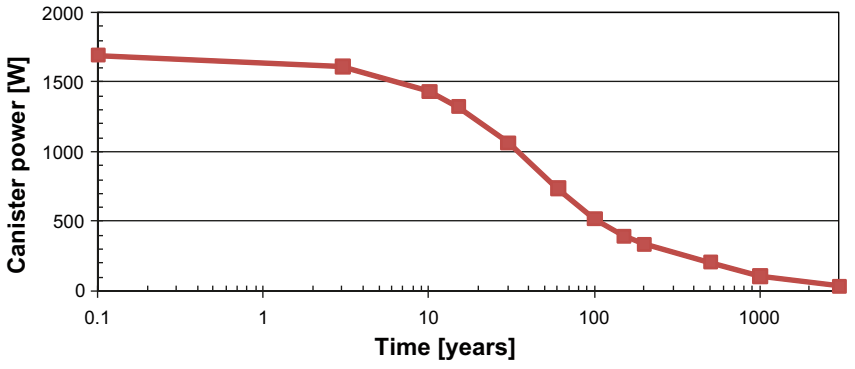

corresponds to 35 year-old fuel.

Table 4-4. Decay function coefficients and the corresponding canister power graph.

i	t_i [years]	a_i
1	20	0.060
2	50	0.705
3	200	–0.055
4	500	0.250
5	2,000	0.025
6	5,000	–0.009
7	20,000	0.024

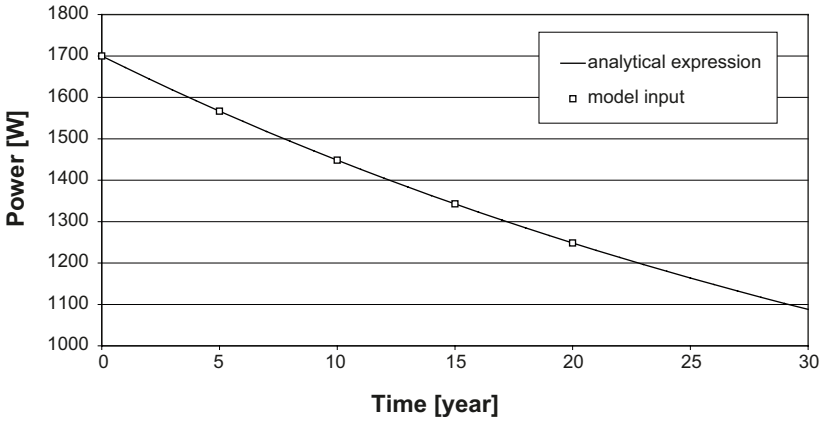

4.4.2 Parameters of the base case model

In the poro-mechanical formulation Code_Bright is based on, an additive split of a material volume element, dv, in a solid volume element, dv_s, and a pore volume element, dv_p is used. Furthermore the pore volume element, dv_p, is additively split into a liquid volume element, dv^l, and a gas volume element, dv^g. The liquid volume element is divided into a liquid water volume element dv_w^l and a liquid air volume element dv_a^l (dissolved air into the liquid).

Using the defined volume elements above, or the corresponding mass elements, the following variables are defined: $w = dm_w^l/dm_s$, $S_l = dv_w^l/dv_p$, $e = dv_p/dv_s$, $n = dv_p/dv$, being the water ratio, water saturation, void ratio and porocity, respectively.

In the THM model, balance laws of; solid mass (which gives the evolution of porosity), water mass, energy for the system and momentum for the system are considered. The gas pressure is constant, 0.1 MPa, in the model. The psycrometric law,

$$\omega_g^w = (\omega_g^w)_0 \frac{RH}{100}$$
$$(\omega_g^w)_0 = f(T) \qquad (4\text{-}14)$$
$$\frac{RH}{100} = \exp\left(\frac{-(p_g - p_l)\, M_w}{R(273.15+T)\rho_l} \right)$$

is used as an equilibrium constraint between the liquid phase and vapour phase of water.

Initial state

Table 4-5. Initial state.

Material	T (C)	p_g (MPa)	p_l (MPa)	n (–)
Buffer	18	0.1	–46.893	0.364
Backfill	18	0.1	–109.847	0.415
Pellets	18	0.1	–109.847	0.64
Rock	18	0.1	–109.847	10^{-4}
Copper	18	0.1	–46.893	10^{-4}
Cast iron	18	0.1	–46.893	10^{-4}

Material parameters

$$\rho_l = 1002.6\exp(4.5\cdot 10^{-4}(p_l - p_{l0}) - 3.4\cdot 10^{-4}T)$$
$$\rho_g = \frac{0.018 p_v}{8.3143(273.15+T)}\cdot RH$$
$$RH = \exp\left(\frac{-(p_g - p_l)\,0.018}{8.3143(273.15+T)\rho_l}\right) \qquad (4\text{-}15)$$
$$p_v = 136075\exp\left(-\frac{5239.7}{273.15+T}\right)$$

Table 4-6. Heat capacity and solid density.

Material	C_s (J/kgK)	ρ_s (kg/m³)
Buffer	800	2,780
Backfill	800	2,780
Pellets	800	2,780
Rock	770	2,770
Copper	390	8,930
Cast iron	500	7,200

Conductive heat flux

$$\mathbf{i}_c = -\lambda\nabla T$$
$$\lambda = \lambda_{sat}S_l + \lambda_{dry}(1 - S_l) \qquad (4\text{-}16)$$

Table 4-7. Conductive heat flow parameters.

Material	λ_{dry} (W/mK)	λ_{sat} (W/mK)
Buffer	0.3	1.2
Backfill	0.3	1.2
Pellets	0.3	1.2
Rock	3.63	3.63
Copper	390	390
Cast iron	40	40

Retention behavior, Van Genuchten

$$S_l = \left(1 + \left(\frac{S}{p_0}\right)^{1/(1-\lambda)}\right)^{-\lambda} \qquad (4\text{-}17)$$
$$S = p_g - p_l$$

Table 4-8. Retention parameters.

Material	p_0 (MPa)	λ
Buffer	65.77	0.43
Backfill	20.2	0.35
Pellets	0.307	0.24
Rock	10^{-4}	0.5
Copper	10^{-4}	0.5
Cast iron	10^{-4}	0.5

Flow through porous medium

$$\mathbf{q}_l = -\frac{kk_{rl}}{\mu_l}\nabla p_l$$
$$k_{rl} = AS_l^{\,3} \qquad (4\text{-}18)$$
$$\mu_l = 2\cdot 10^{-12}\exp\left(\frac{1808.5}{273.15+T}\right)$$

Table 4-9. Advective water flow parameters.

Material	*k* (m²)	A
Buffer	$2.2\cdot10^{-21}$	1
Backfill	$6.1\cdot10^{-21}$	1
Pellets	$4.4\cdot10^{-19}$	1
Rock	10^{-30}	10^{-10}
Copper	10^{-30}	10^{-10}
Cast iron	10^{-30}	10^{-10}

Vapor diffusion

$$\mathbf{i}_g^w = -(n\rho_g(1-S_l)D_m^w)\nabla\omega_g^w$$
$$D_m^w = \tau 5.9\cdot10^{-6}\frac{(273.15+T)^{2.3}}{p_g} \qquad (4\text{-}19)$$

Table 4-10. Vapor diffusion parameters.

Material	Vapor *τ*
Buffer	1
Backfill	1
Pellets	1
Rock	10^{-5}
Copper	10^{-5}
Cast iron	10^{-5}

4.4.3 Water redistribution in the Base Case

Below, in Figure 4-13, contour plots of the water saturation are given for: the initial state, 5, 10 and 15 years. It can be seen that the water has been transported away from the canister. It is however hard to discover any difference between the three last saturation maps.

In order to study the evolution of the water saturation more in detail, profiles of water saturation are given along some chosen scan-lines in the buffer. The first scan-line is vertically oriented, going from the top of the canister to a point in the backfilled tunnel 2 m above the tunnel floor. In Figure 4-14 the scan-line and the corresponding water saturation profiles at times 0, 1, 5, 10 and 15 years are shown.

There is not a significant change of the water saturation in and above the tunnel floor pellet filling. The backfill block in the deposit hole has gained some water and the buffer has lost water, mostly close to the canister top and some in the area close to the backfill block. When studying the succession of profiles, the state in the backfill block seems quite static and the buffer shows a process of slow desaturation. The lowest value of saturation in the buffer occurs at the top of the canister and is approximately 45% after 15 years.

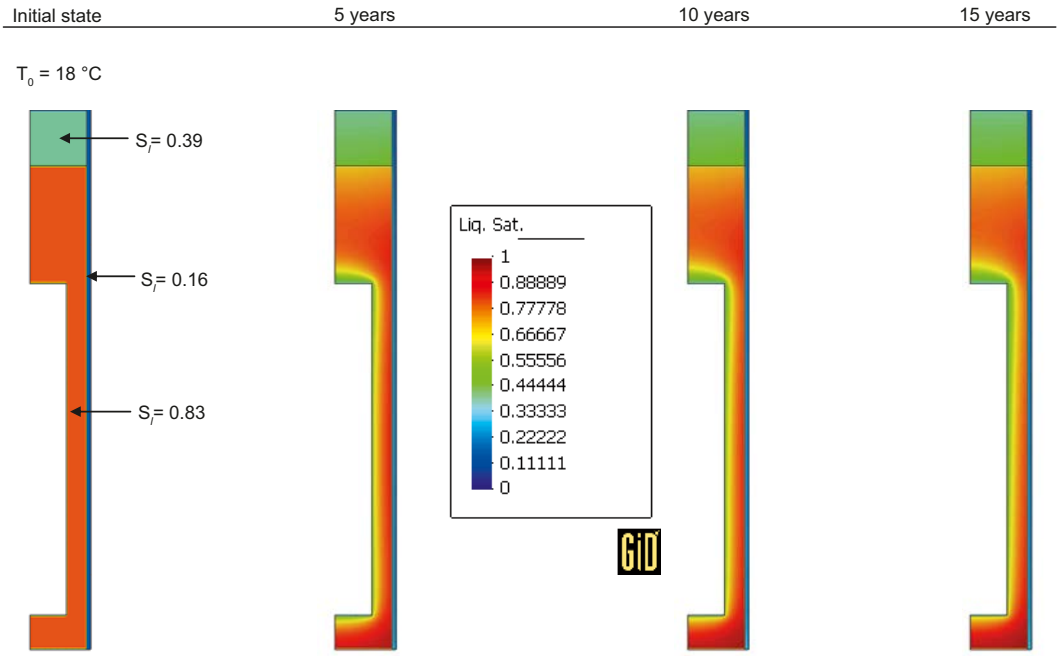

Figure 4-13. *Water saturation after 0, 5, 10 and 15 years.*

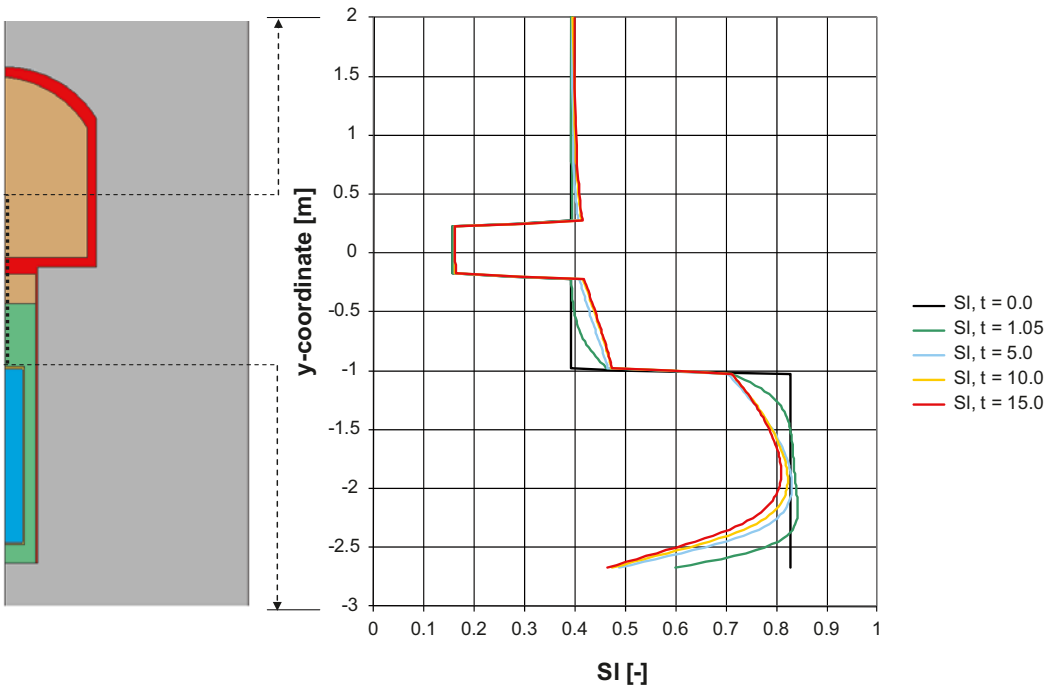

Figure 4-14. *Water saturation profiles at the indicated vertical scan line above the canister.*

The next scan line is vertically oriented in the pellet slot. In Figure 4-15 the scan line is indicated and the corresponding water saturation profiles are shown for 0, 1, 5, 10 and 15 years.

Here the water saturation has increased from the initial state all along the scan line. The change in the succession of the profiles indicates that the water is first quickly transported into the pellet slot, and then the water slowly migrates vertically from the canister mid-height. In the model, the water is not allowed to propagate out in the surrounding rock and therefore the region close to the hole floor is becoming more saturated. In the upward direction there is no obstacle for the water migration and the "saturation front" therefore propagates in this direction.

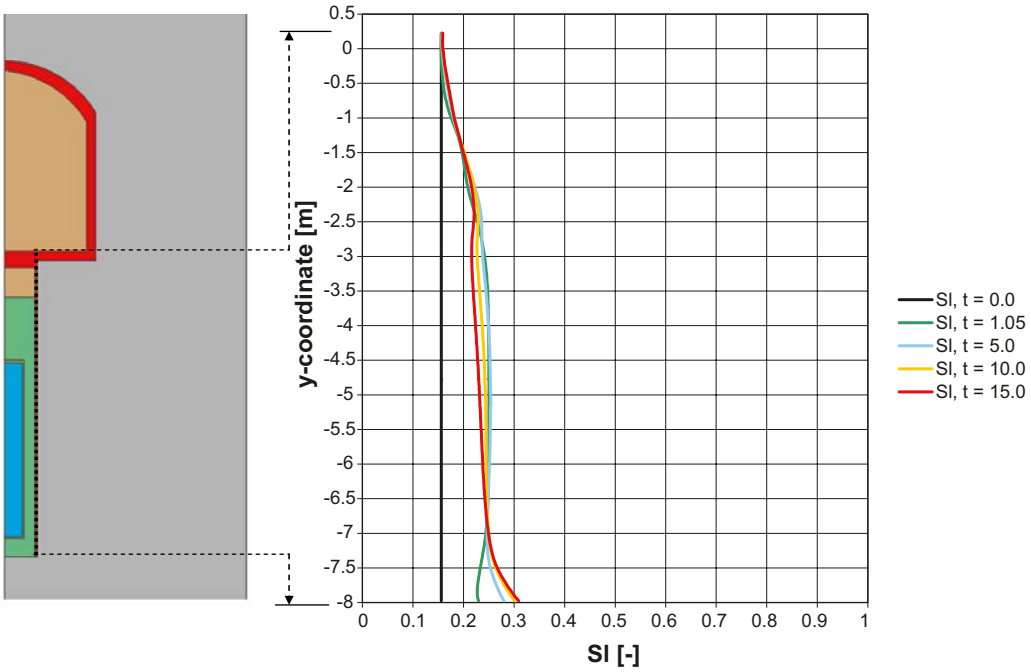

Figure 4-15. *Water saturation profiles at the indicated vertical scan line in the pellet slot.*

Next, a horizontally oriented scan-line, just above the canister top, is considered. The corresponding water saturation profiles are shown for 0, 1, 5, 10 and 15 years in Figure 4-16.

As the first scan line indicated, the buffer material on top of the canister is considerably desaturated. The evolution is however slow when studying the successive profiles. The pellet slot is more saturated as compared to the initial saturation and a slow desaturation can be seen to occur from this higher value.

The next scan line to consider is horizontally oriented, at the canister mid-height. The results are shown in Figure 4-17.

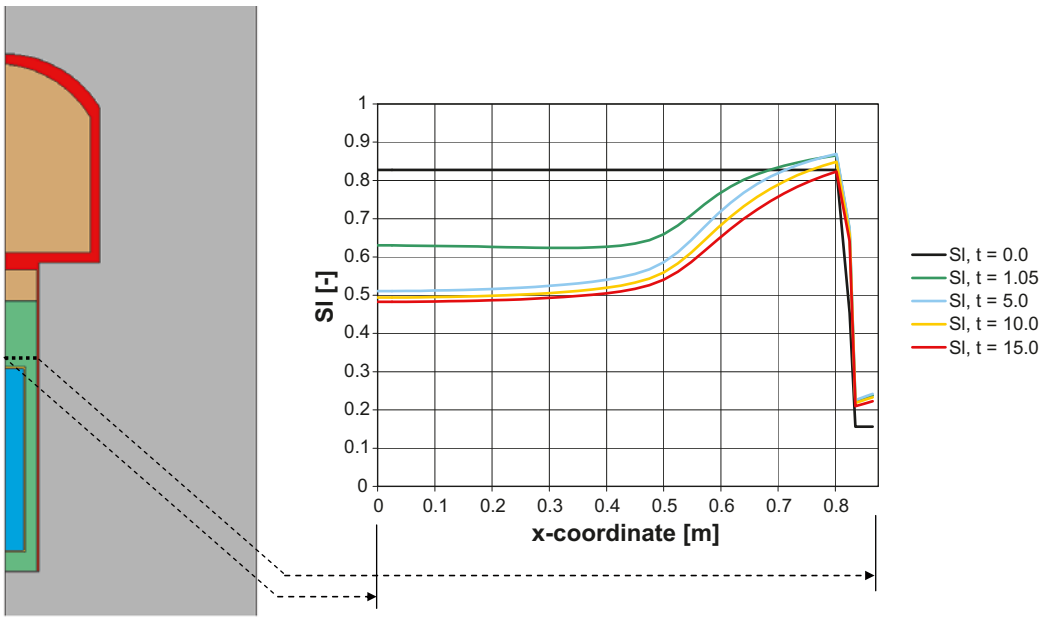

Figure 4-16. *Water saturation profiles at the indicated horizontal scan line above the canister.*

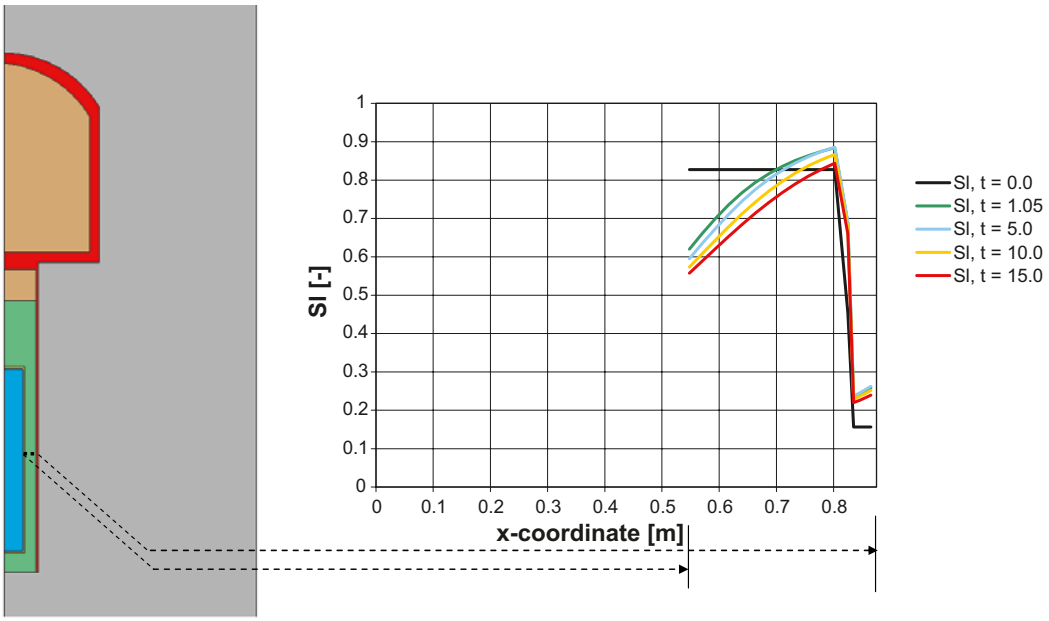

Figure 4-17. *Water saturation profiles at the indicated horizontal scan line at canister mid-height.*

Here the water saturation process is very close to what was found in the previous analysis in the same region. In the buffer material close to the canister the water saturation is considerably lower as compared with the initial value. The pellet-slot and the buffer close to the pellet-slot have gained some water which is slowly migrating vertically.

The last scan-line is horizontally oriented just below the canister. The successive water saturation profiles are shown in Figure 4-18.

The water saturation process is similar to the two other horizontal scan-lines, the buffer close to the canister is less saturated as compared to the initial state and the material in and close to the pellet slot is more saturated. But there is one big difference. The water saturation is increasing over the entire scan line. As mentioned before, in the model the vertical water transportation is stopped by the tunnel floor and therefore the water saturation in the section close to the tunnel floor will increase.

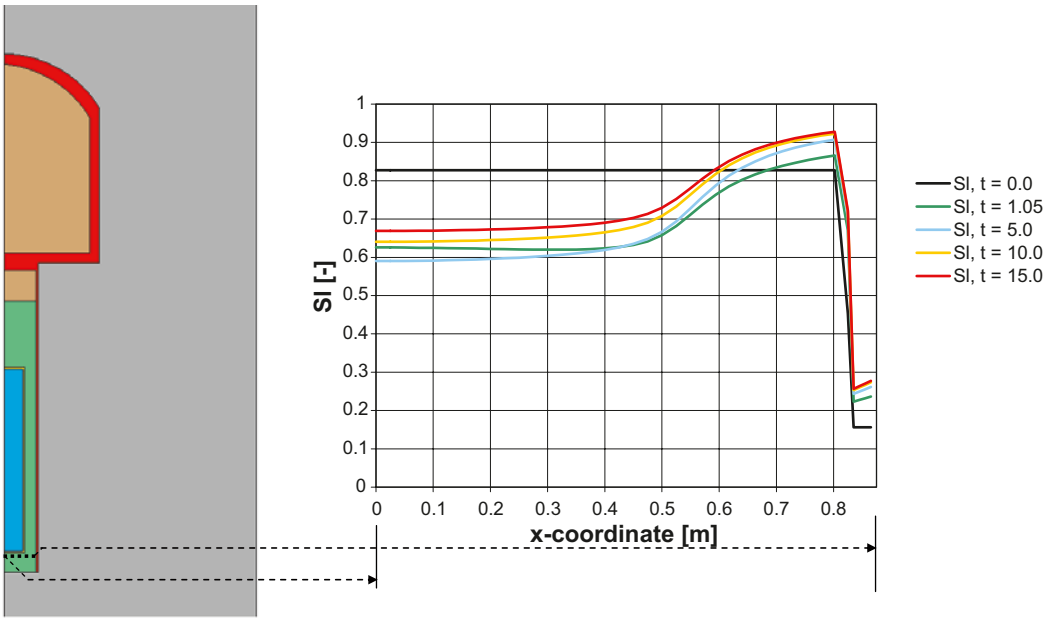

Figure 4-18. *Water saturation profiles at the indicated horizontal scan line below the canister.*

4.4.4 Water redistribution in additional cases

Three more different cases are simulated to investigate the influence of different aspects on the water saturation. For these cases models with R = 8 m, T_0 = 15°C have been used, i.e. there is a difference in initial temperature as compared to the base case. The three different additional cases are:

1. The system is closed hydraulically above the block section (1 m below the tunnel floor) and the upper part of the hole is filled with backfill material.
2. The system is hydraulically open and the upper part of the hole is filled with backfill material. (Same set-up as the base case except for the initial temperature.)
3. The system is hydraulically open and the upper part of the hole is filled with block material.

Contour plots of the water saturation situation initially and after 15 years (for each of the three different cases) are shown in Figure 4-19.

It can clearly be seen in Figure 4-19 that the state after 15 years differs considerably from the initial state for all three cases. The two cases that differs most after 15 years are case 1 (Closed, Backfill) and case 2 (Open, Backfill). In case 1 the water has been trapped at the upper part of the buffer and thereby saturates this part of the buffer. In case 2 the water has been allowed to migrate upwards and is "pulled" by the backfill block to a greater extent as compared to what the buffer block does due to the difference in initial suction for the two materials.

In order to get a more clear view of the differences between the three cases, an estimation of the average saturation at a given height is shown for the block (Figure 4-20) and the pellets (Figure 4-21) after 15 years. As can be seen in Figure 4-20 the block material is sub-structured into three parts:

1) Side, all material outside the canister radius.
2) Top, the material above the canister.
3) Bottom, the material below the canister.

Figure 4-20 shows that the water saturation profiles at the top of the buffer are significantly affected by the different hydraulic conditions and materials on top of the buffer. The lower part of the buffer (below –3.5 m) is not significantly different for the three cases. The water profile of case 3 is between the profiles of case 1 and case 2. At the top of the buffer (–1 m) the water saturations are approximately 92% for case 1, 72% for case 2 and 78% for case 3.

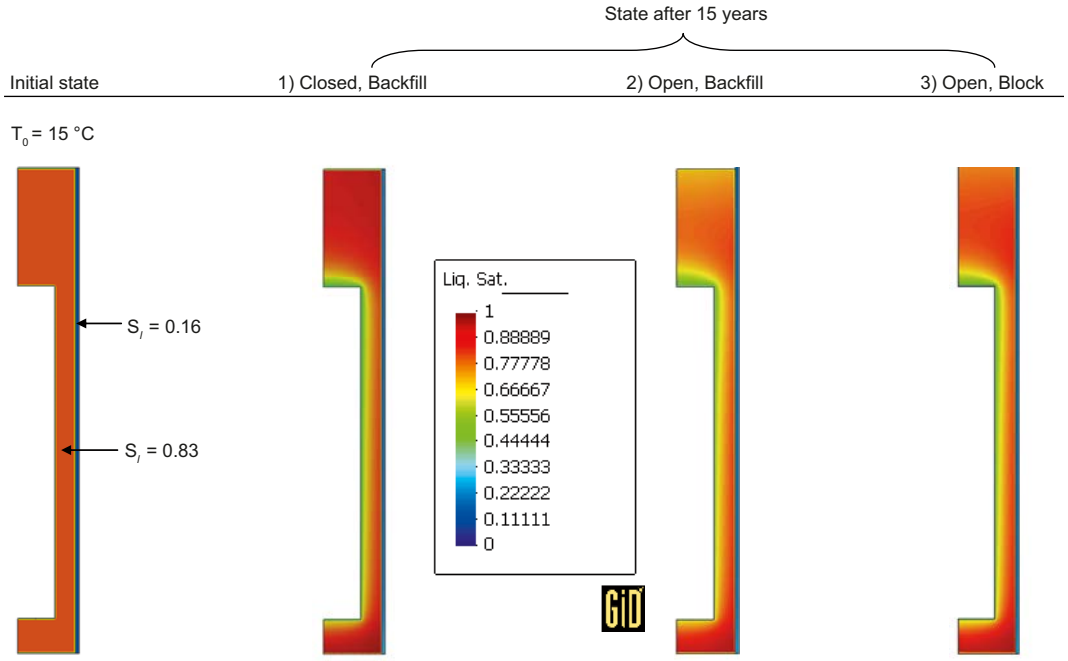

Figure 4-19. *Water saturation contour plots for the initial state (leftmost) and after 15 years for the three different cases.*

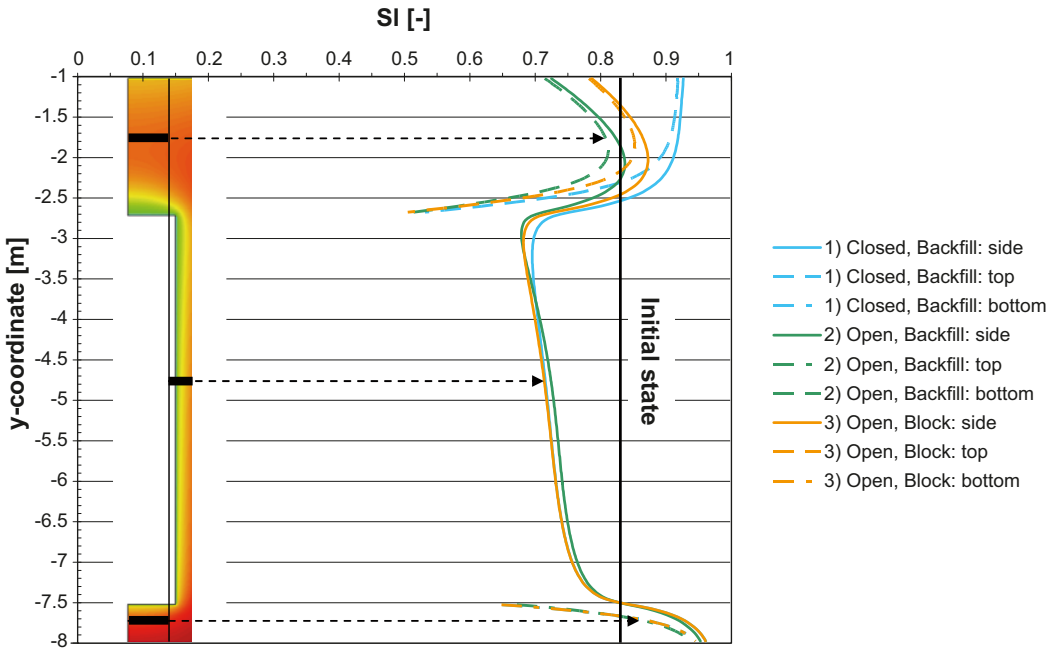

Figure 4-20. *Estimated average water saturation after 15 years at a given height in the three subsections: side, top, bottom.*

Figure 4-21 shows that all parts of the pellet slot have gained in water saturation for all cases. Also here, it is only in the upper part of the considered material that the profiles show a significant difference between the different cases. In the upper part the water saturation profiles of the pellet slot appear in the same order as for the buffer material, with the profile of case 3 between the profiles of case 1 and case 2. At –1 m the water saturation is approximately: 25% for case 1, 18% for case 2, and 20% for case 3.

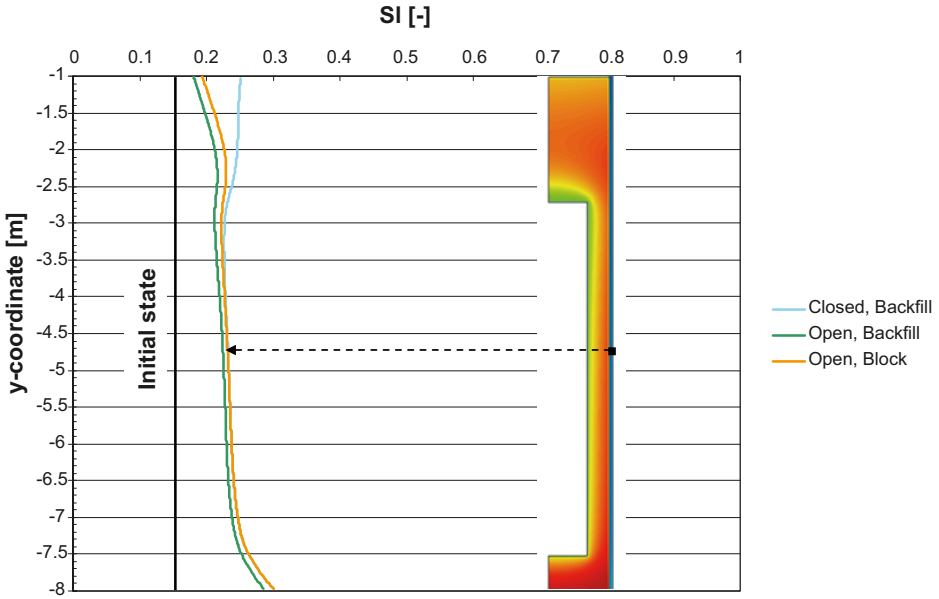

Figure 4-21. *Estimated average water saturation after 15 years at a given height in the pellet slot.*

4.4.5 Study of the diffusive heat transport in the pellet slot

In the pellet slot the water has a high mobility both as a liquid and as vapor due to the high porosity. As a consequence the heat transport might have a significant contribution from convection in the pellet slot. The diffusive transport of vapor acts as a vehicle for heat, not only by motion of the vapor but also due to the phase transition of the water. The evaporation-condensation process, where latent heat is absorbed in the water when evaporation occurs and latent heat is released when the water condensate, contribute to the heat transportation. The flux of the liquid water does not contribute as much as the diffusive flux of the vapor to the heat transportation and therefore this term is omitted. Thus, the total heat flux is considered to be an addition of the conductive heat flux and the diffusive heat flux,

$$\boldsymbol{q}_{total} = \boldsymbol{q}_{conduction} + \boldsymbol{q}_{convection} \approx \boldsymbol{q}_{conduction} + \boldsymbol{q}_{diffusive} \tag{4-20}$$

In pure thermal models the only heat transport mechanism is by conduction. When considering experimental temperature measurements an effective thermal conduction is evaluated where all contributions from other heat transport mechanisms are included.

The relative magnitude of diffusive heat transport in the pellet slot can be evaluated by studying Figure 4-22, where the total heat flux (assuming radial heat flow only) and the conductive heat flux are shown for the model where $R = 8$ m $T_0 = 15$°C. It is the heat flux at canister mid-height that is shown in Figure 4-22.

The relative magnitude of the radial diffusive heat transport in the pellet slot is obtained from

$$\frac{q_{diffusive}}{q_{total}} \approx 1 - \frac{q_{conduction}}{q_{total}} = 1 - 0.89 = 0.11 \tag{4-21}$$

Thus, approximately 10% of the total heat flux is coming from diffusive heat transportation in the model.

4.4.6 The effect of water redistribution on the thermal conductivities

In order to evaluate how different water saturation states affect the thermal properties and the temperatures, the water saturation states after 15 years obtained by the TH model where $T_0 = 18$°C and $R = 8$ m are translated into thermal conductivities using the functions shown in Figure 4-23. In Figure 4-23 two alternative translation functions are shown for the bentonite block material and one is given for the pellet slot material. As can be seen, there is a lack of experimental data for the low void ratio that is used in the block material. Therefore two alternative translation functions have been suggested, alternative 1 being somewhat optimistic and alternative 2 being more pessimistic if considering an estimation of the peak temperature. Using the two alternatives will give upper and lower bound results with respect to the uncertainty in the relation between water saturation and thermal conductivity.

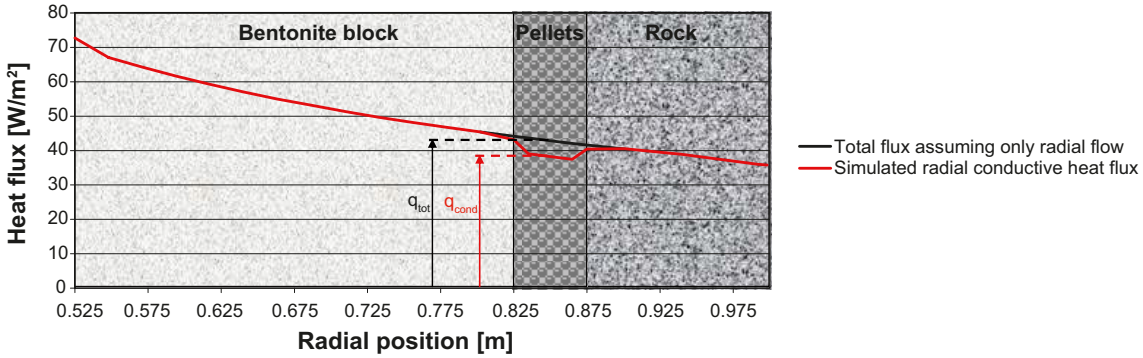

Figure 4-22. *Total and conductive radial heat flux at canister mid-height.*

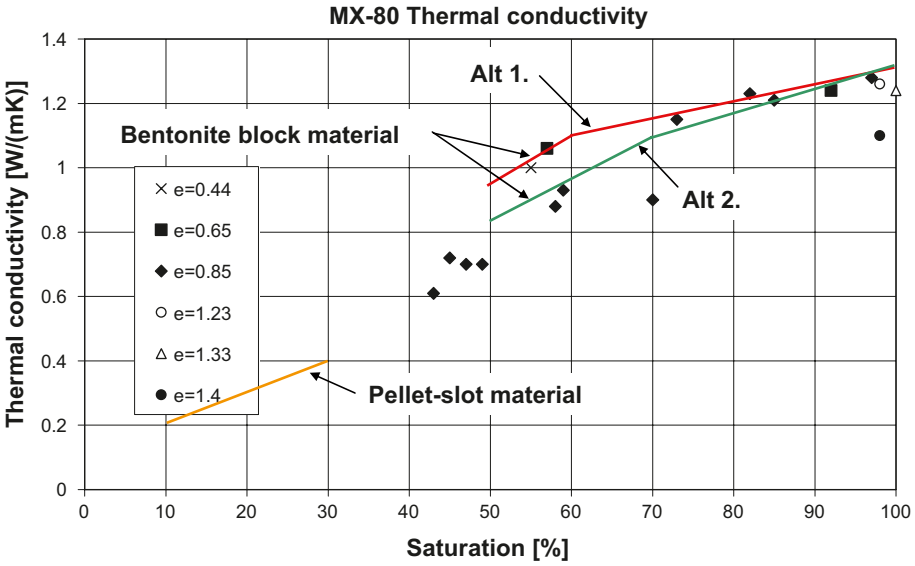

Figure 4-23. *Thermal conductivity: experimental data and the functions used.*

When allotting the thermal model with suitable conductivities, the bentonite block material is sub-structured into B(lock)C(entral parts) 1–3 and B(lock)O(uter parts) 1–5. The pellet slot is sub-structured into P(ellet slot) 1–5. The substructures can be seen in Figure 4-24.

Each substructure is equipped with an individual thermal conductivity. The thermal conductivity is obtained by mapping the average water saturation in each substructure using the different alternatives shown in Figure 4-23. The resulting conductivities for the different cases are also shown in Figure 4-24.

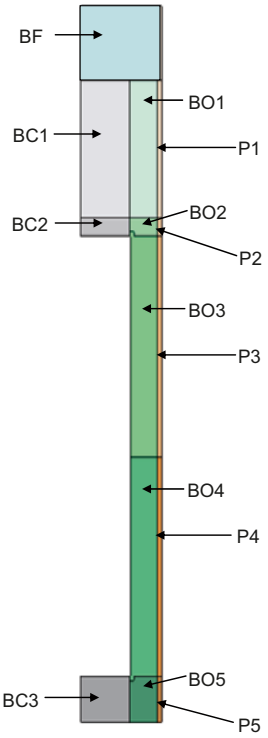

Old case conductivities

Material ID	Conductivity W/(m·K)
BF	1.50
BCx	1.10
BOx,Px	1.00

Initial state conductivities

Material ID	Conductivity W/(m·K)
BF	0.70
BCx, BOx	1.21
Px	0.26

Conductivities based on the 15-year-state of the TH modelwith T_0= 18 °C

	Conductivity W/(m·K)	
Material ID	Alt. 1	Alt. 2
BF	0.75	0.75
BC1	1.19	1.15
BC2	1.03	0.92
BC3	1.21	1.18
BO1	1.20	1.17
BO2	1.17	1.13
BO3	1.14	1.08
BO4	1.17	1.13
BO5	1.26	1.25
P1	0.31	0.31
P2	0.32	0.32
P3	0.32	0.32
P4	0.34	0.34
P5	0.39	0.39

Figure 4-24. *The introduced substructures of the buffer and the obtained conductivities.*

4.5 Conclusions

4.5.1 Investigation of the dehydration of the surrounding rock

The used method can apparently identify domains in p_0-λ-space with potentially extensive dehydration following from venting of deposition tunnels. For reported retention and relative permeability parameters the analysis shows that the gas-filled pore volume is significantly smaller than the available water volume in the installed buffer. This is even more pronounced if a van Genuchten relation is used for the relative permeability.

4.5.2 Water redistribution for the Base Case

For the base case the water redistribution was investigated by plotting water saturation profiles along chosen scan lines. When studying the profiles it was found that the water was transported from the canister and outwards. Below some of the saturation levels are given 15 years after installation.

Directly above the canister the water saturation level decreased from the initial value of 0.83 to 0.45. The backfill block present at the top of the buffer gained water in the outward transportation.

The pellet slot increased its degree of water saturation at all vertical positions. At canister mid-height the water saturation increased from 0.16 to 0.25.

The buffer block close to the canister at canister mid height decreased its degree of water saturation from 0.83 to 0.55 and the outer part of the buffer block at the same height slightly increased the saturation level.

4.5.3 Water redistribution in additional cases

The water distribution was studied in three additional cases (all having the initial temperature 15°C) characterized by:

1. Hydraulically closed at 1 m below the tunnel floor.
2. Hydraulically open, backfill block from 1 m below the tunnel floor and upwards.
3. Hydraulically open, buffer block in the entire deposition hole.

The significant difference in water saturation is only occurring in the top-part of the buffer. The following could be concluded studying the results of the three models.

1. Gives highest saturation levels since the water is trapped and cannot escape upwards.
2. Gives lowest saturation levels. The dry backfill block at the top of the buffer “pulls” the water upwards.
3. Has saturation levels in between the two other cases. Water is allowed to escape upward, but the buffer block material has less suction as compared to the backfill block material used in case 2.

4.5.4 Diffusive heat transport in the pellet slot

It is found that in the Base Case model approximately 10% of the total heat flux origins from diffusive heat transport.

4.5.5 Translation of the water saturation field into thermal conductivities

In order to translate the saturation field into thermal conductivities the buffer was substructured according to what is shown in Figure 4-24, and the averages of the water saturation within the substructures was calculated. The substructure saturations were then translated into thermal conductivity by using higher and lower alternative functions shown in Figure 4-24.

4.5.6 Uncertainties

Since the simulations in this task are very similar to those in the general buffer hydration task (Task 3 shown in the previous chapter) much of the uncertainties discussed concerning Task 3 also apply here. The main difference between the two simulations is that the rock has been closed hydraulically in this task and therefore the issues concerning the rock discussed in Task 3 may be disregarded here.

The main outcome of this work has been to produce thermal conductivities that may be applied in a pure thermal simulation. Therefore the translation process from the obtained field of water saturation into thermal conductivities is of high importance.

In this translation process the buffer has to be substructured in a suitable manner in order to capture relevant features of the water saturation field (so that relevant thermal conductivities may be produced). As can be seen from studying the subtructuring and the obtained water saturation profiles, when large differences (gradients) in the water saturation field are present the substructures are small (at the top and bottom of the canister). It is believed that the used substructuring of the buffer are relevant and produces a representative discretized water saturation field, but the effect from using a different substructuring has not been investigated.

Moreover, when translating the discretized water saturation field into a discretized thermal conductivity field a representative function has to be used. Here, two alternative functions have been used, an upper “optimistic” and a lower “pessimistic” function. Using the two alternative translation functions two sets of thermal conductivities are obtained, which may be used for bounding the thermal process.

The mesh dependence has not been investigated in the large model geometry due to the complicated geometry and large problem size. In Task 3, where a similar model was used, the mesh dependence in the buffer was studied by using small radial models. The discussion in Task 3 about this issue is also valid here.

5 Buffer homogenisation

5.1 Introduction

Many models of the buffer material assume a completely homogeneous bentonite with the average density at saturation 2,000 kg/m^3 everywhere. However, the initial state of the buffer after placement is unsaturated bentonite blocks and rings with much higher density than the average and one empty slot at the canister surface and a pellet filled slot with very low density at the rock surface. Due to mainly to friction within the material, but also due to hysteresis effects, the swelling and homogenisation that comes with the wetting of the bentonite is not complete and there will remain density differences and swelling pressure differences in the buffer.

The remaining inhomogeneities in the buffer material have been studied with different approaches. One full scale test (the Canister Retrieval Test) that simulated a deposition hole with canister and buffer material according to the reference design of a KBS-3V deposition hole was run for more than 5 years and excavated with extensive sampling and determination of the density and water ratio of the buffer material. The buffer material was completely water saturated between the canister and the rock and the results represent the expected final density distribution. The results can also be used to compare modelling results in order to evaluate the capability of the codes to accurately model the saturation and homogenisation process.

The test was equipped with a plug in the top of the deposition hole that simulated a compressible backfill by flexible anchors. When the test was interrupted the buffer material above the canister was not water saturated so the sampling results represent a hydro-mechanical state at a certain time. The results of the sampling with complete presentation of the distribution of density and water ratio are described by /Johannesson 2007/.

Three different analyses of the natural homogenisation process in the buffer have been done. In the first analysis analytical solutions have been studied. In the second analysis the finite element code Code_Bright has been used. In the third analysis the finite element code Abaqus has been used. The analystical analysis and the Code_Bright analysis are presented in Sections 5.2–5.8 while the Abaqus analysis is presented in Sections 5.9–5.18.

Code Bright is used for studying the process in more detail, for example the influence of slot width etc in a section between the canister and the rock. Abaqus is used for modelling the entire deposition hole.

5.2 Analytical and Code Bright analyses (Sections 5.2–5.9)

The objective is to investigate the mechanical homogenization process in the buffer system containing high density bentonite blocks, a pellet filled slot of lower density and an initially open inner slot close to the canister. When the buffer absorbs water, the bentonite blocks swell which leads to filling the inner slot and compression of the pellet filled slot. The homogenization is however not complete, which would lead to a homogeneous density at full saturation. Different influences on the homogenization and the remaining heterogeneity in the buffer at full saturation are studied.

The Canister Retrieval Test (CRT) is used as an example, since sensor data is present from this test and the final state (after excavation) of the experiment is also known. The CRT geometry was designed according to the KBS-3 specifications and is therefore a suitable case to study. The water inflow was controlled by filter-mats at the deposition hole wall and within the canister, an arrangement of heaters are used to simulate the thermal response of the spent fuel elements. When the outer slot was filled with pellets the slot was subsequently filled with water. Sensor data from positions in the bentonite block close to the canister shows that the water, used when filling the pellet slot, penetrated trough the block-interfaces and therefore the inner slot has some water initially.

The mechanisms of homogenization are first studied by using an idealized analytical model, with its basis in thermodynamics. The effect of adopting different wetting processes and assuming different pressures in the block and pellet slot are investigated. The CRT-experiment is used as a reference in the investigations.

The next step is to develop a Finite Element (FE) model of the buffer (open slot, bentonite block and pellet slot) at canister mid-height, where the processes to the greatest extent are radial. First an axisymmetric 1D THM model of the canister mid-height section of the CRT-experiment is developed for the Code_Bright solver. The solution is compared to experimental data to study the validity of the model. Next, the geometry of the CRT-model is altered by changing the pellet slot width, and the effect of having different pellet slot widths is investigated. Finally, the idealized wetting processes used in the analytical model are applied to the CRT-model in order to study the response of the FE-model.

5.3 Analytical investigation of the heterogeneity

Here follows an investigation of processes that gives rise to a remaining heterogenic density profile as found for the CRT experiment.

It is stressed upon that the highly idealized model only considers averages of the buffer. In a horizontal section close to the canister mid-height the entire block and pellet slot are represented by two materials equipped with homogeneous properties which are subjected to homogeneous processes. This is of course a huge simplification since different parts of the block and pellet slot will be subjected to different processes. For identifying the processes that have effect on the remaining heterogeneity, the model is, however, considered to be useful.

Analyzing the free energy difference for pure water and soil water, in a closed system where pure water is connected to moist soil via a semi-permeable membrane /Low and Anderson 1957, Kahr et al. 1990/, gives the relation,

$$-\frac{\rho_w R\theta}{m_w}\ln(RH(w)) = p \tag{5-1}$$

where ρ_w is the water density, R the universal gas constant, θ the absolute temperature, m_w the molecular mass of water vapour, RH the relative humidity and $p = (\sigma_1 + \sigma_2 + \sigma_3)/3$ the swelling pressure (σ_1, σ_2 and σ_3 being the principal stresses). It is indicated that the relative humidity can be expressed as a function of the water ratio, $w = dm_w^l/dm_s$, where dm_w^l is a mass element of liquid water and dm_s is a mass element of compacted solid material. The relation $RH(w)$ can be obtained from experiments (e.g. /Dueck 2004/) and may be considered as defining the water retention property of the material. The left hand side of (5-1) defines the suction under free swelling conditions,

$$s_{free}(w) = -\frac{\rho_w RT}{m_w}\ln(RH(w)) \tag{5-2}$$

Combining the two equations above gives the relation,

$$s_{free}(w) = p \tag{5-3}$$

which is valid at fully water saturated conditions. Thus, from considering thermodynamic basic theory, a relation between swelling pressure and suction under free and saturated conditions is obtained.

This relation is also arrived at if using the experimentally motivated relation presented in /Croney et al. 1958/ and /Kassiff and Shalom 1971/, where it is shown that the suction for a material subjected to pressure may be expressed,

$$s = s_{free}(w) - \beta\, p \tag{5-4}$$

where s is the suction of the pressurized material. If considering saturated conditions, $s = 0$, and adopting a unity compressibility factor, $\beta = 1$, Equation (5-3) reappears. The choice $\beta = 1$ can be motivated by the findings in /Dueck 2004/ concerning MX-80 properties and statements made in /Croney et al. 1958/ and /Kassiff and Shalom 1971/ concerning heavy clays.

Taking the volume averages of (5-3), over the pellet slot volume v^p and the block volume v^p, produces the expressions,

$$\frac{1}{v^p}\int_{v^p} s_{free}(w)dv = \frac{1}{v^p}\int_{v^p} pdv$$
$$\frac{1}{v^b}\int_{v^b} s_{free}(w)dv = \frac{1}{v^b}\int_{v^b} pdv \qquad (5\text{-}5)$$

To simplify the left hand side of the equations above, the water ratio w is approximated as being constant in v^p and v^b and the free retention curve $s_{free}(w)$ is also taken as independent of the position in v^p and v^b. Thus, $w = w^b$ and $s_{free}(w) = s_{free}{}^b(w)$ in the block and $w = w^p$ and $s_{free}(w) = s_{free}{}^p(w)$ in the pellet slot. The right hand side defines the volume average of the pressure field in the pellet slot, p^p, and the bentonite block, p^b, respectively. Using the above in the expressions gives,

$$s_{free}{}^p(w^p) = p^p$$
$$s_{free}{}^b(w^b) = p^b \qquad (5\text{-}6)$$

The pressure averages at full water saturation are not likely to be equal since there are no conditions that constrain the axial and tangential stresses to be similar in the block and pellet slot (the radial stresses are expected to be similar due to force balance). Therefore, a pressure ratio, $\alpha = p^p / p^b$, is introduced.

The water ratios at full water saturation can be expressed in terms of: water density ρ_w (here taken as 1,000 kg/m^3), solid density ρ_s (here taken as 2,780 kg/m^3), and the void ratios e^p and e^b (also being constant in v^p and v^b due to the assumption made for the water ratio).

$$w^p = \frac{\rho_w}{\rho_s} e^p$$
$$w^b = \frac{\rho_w}{\rho_s} e^b \qquad (5\text{-}7)$$

The void ratio e, extensively used in this study, is defined and related to other variables according to,

$$e = \frac{dv_p}{dv_s} = \frac{\rho_s}{\rho_d} - 1 = \frac{n}{1-n} \qquad (5\text{-}8)$$

where dv_p denotes the pore volume within a material volume element, dv_s denotes the volume of solid material within a material volume element, ρ_s is the solid mass density, ρ_d is the dry mass density and n denotes the porosity the ratio of pore volume in a material volume element.

Using the conditions that are assumed to prevail at full water saturation in (5-6) gives,

$$s_{free}{}^p\left(\frac{\rho_w}{\rho_s} e^p\right) - \alpha\, s_{free}{}^p\left(\frac{\rho_w}{\rho_s} e^b\right) = 0 \qquad (5\text{-}9)$$

which may be solved for the pellet slot void ratio if the $s_{free}(w)$ functions are specified.

The chosen functions, developed from considering experimental measurements (the same choice is made in /Kahr et al. 1990/) have following form,

$$s_{free}(w) = \exp(a - b\,w) \qquad (5\text{-}10)$$

where the parameter set (a,b) is determined from calibrating the expression against relevant experimental measurements. Below, in Figure 5-1, experimental data is shown for different *referential* (here initial) water saturations indicated in the legend.

If the parameters a and b are evaluated between the high and low limits shown in Figure 5-1 and are plotted vs. the referential water saturation in Figure 5-2.

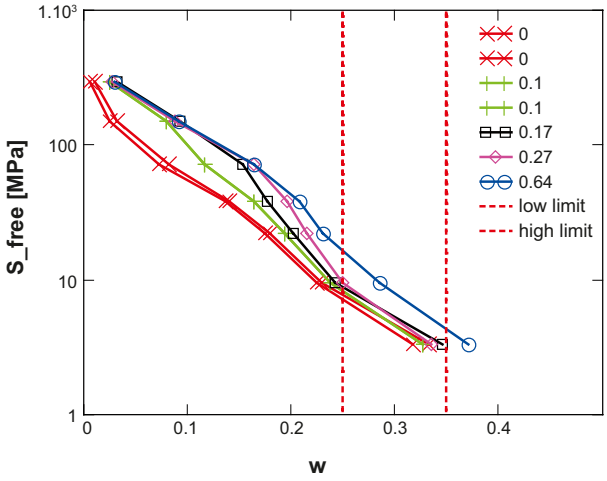

Figure 5-1. *Retention data for free swelling MX-80.*

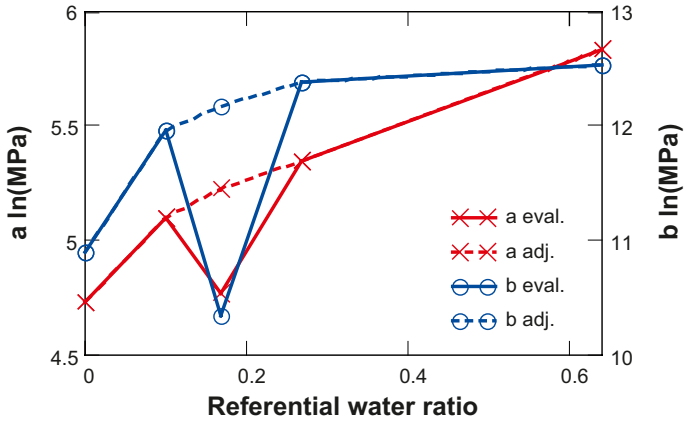

Figure 5-2. *Parameters in the expression of free retention as a function of the referential water ratio.*

It can be seen that the values of the parameters for a referential degree of water saturation of 0.17 deviates largely from the trend of the other results. An adjusted set (a,b) has therefore been developed for w_{ref} = 0.17 to match the trend of the other results.

With the expression of the free retention inserted in (5-9) the resulting expression, valid at full water saturation under the assumptions made, reads,

$$e^p = \frac{\rho_s}{\rho_w}\frac{a^p - a^b - \ln(\alpha)}{b^p} + \frac{b^b}{b^p}e^b \qquad (5\text{-}11)$$

where (a^p,b^p) and (a^b,b^b) are the specified parameter sets for the pellet slot material and the bentonite block material, respectively. Using the relation above gives an opportunity to investigate how retention and pressure difference affects the heterogeneity in void ratio.

To evaluate the relation, the average pellet slot void ratio is calculated for different combinations of average referential water saturation (for both block and pellet slot) and average pressure ratio when the average block void ratio is 0.75. The result is presented in the three iso-maps shown in Figure 5-3.

As an example, the referential water ratio of the block is assumed to be 0.2 and α = 1 (the leftmost graph). A line parallel to the horizontal axis (starting at 0.2 on the vertical axis) gives the dependence of the pellet slot void ratio on the referential pellet slot water ratio. If for example w_{ref} *pellets* = 0.2, $e^p = e^b$ = 0.75, i.e. the homogenization process gives a totally homogenized buffer since there is no difference in pressures and referential void ratio. But if w_{ref} *pellets* < w_{ref} *block* → $e^p < e^b$ and if w_{ref} *pellets* > w_{ref} *block* → $e^p > e^b$.

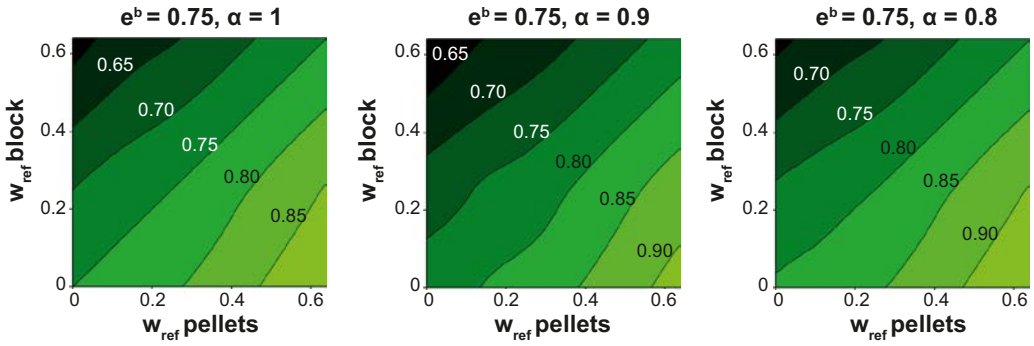

Figure 5-3. *Maps of pellet void ratio obtained for different referential water ratios in block and pellet slot assuming a block void ratio (0.75) and three different pressure ratios: (left) 1, (middle) 0.9 and (right) 0.8.*

If now the assumed referential water ratio of the block is kept (w_{ref} *block* = 0.2) and the pressure ratio is changed to 0.9 it can be seen in the middle graph that $e^p > 0.75$ for w_{ref} *pellets* = 0.2. Thus, the pressure difference increases the pellet void ratio. It can also be seen that the value of w_{ref} *pellets* where $e^p < e^b$ is shifted to the right (≈ 0.1).

All combinations of (w_{ref} *pellets*, w_{ref} *block,* α) that are represented in the graphs above are however not likely to occur in a deposition hole buffer. Below, some cases are studied more in detail with special emphasis on the CRT experiment.

5.3.1 Serial wetting with retention hysteresis effect (CRT)

In the CRT experiment the outer pellet filled slot was water filled directly after the pellet filling. The initial water ratio was $w^p_0 = 0.1$ and if it is assumed that the pellet filled slot was totally water filled (both pores outside and inside the pellets) and had approximately constant dry density (it is assumed that the swelling pressure of the loose pellet slot was not able to move the stiffer block material significantly), the water ratio became $w^p = 0.64$. At this point the bentonite block has begun to absorb water and swelled which led to compression of the pellet slot. This went on until the entire buffer system was water saturated. Due to the sequential wetting process that occurred in the CRT experiment it may be characterized as a *serial wetting*.

In the CRT experiment the water saturation process in the pellet slot and bentonite block may be viewed as a sequence 0-1-2 in terms of water ratio w and suction at free swelling conditions s_{free}, which is shown graphically in Figure 5-4.

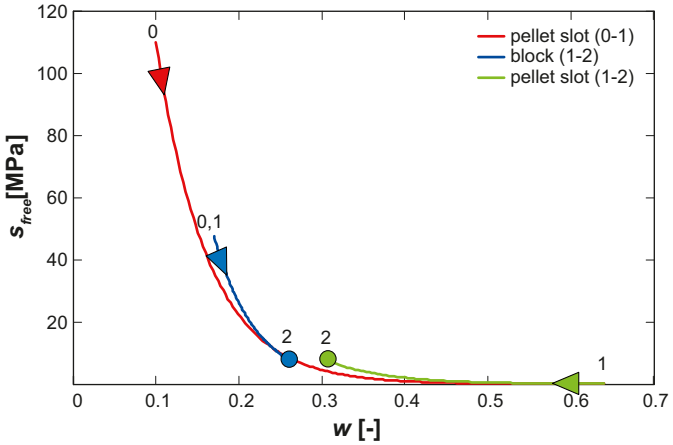

Figure 5-4. *Serial wetting process in free retention.*

(0-1) The pellet slot is rapidly saturated during approximately constant volume from $w^p_0 = 0.1$ to $w^p_1 = 0.64$ and nothing happens with the bentonite block. The pellet slot will follow a wetting curve during (0-1).

(1-2) The bentonite block absorb water from the initial state $w^b_0 = 0.17$ and compress the pellet slot during the water uptake due to swelling of the block material. Since the pellet slot is compressed it will follow a drying curve, not equal to the wetting curve that was followed during (0-1). This is an effect of the hysteresis of the retention curve.

In this first investigation, focusing on the influence from retention, the pressure ratio is set to unity and the effect from following different retention paths (in this serial wetting origin from the retention hysteresis) for the block and pellet slot is investigated.

The parameters *a* and *b,* for the block and the pellet slot, are taken from the adjusted parameter set shown in Figure 5-2.

- Block: $a^b = 5.22$ ln(MPa) and $b^b = 12.17$ ln(MPa) for $w_{ref} = 0.17$
- Pellet slot: $a^p = 5.83$ ln(MPa) and $b^p = 12.52$ ln(MPa) for $w_{ref} = 0.64$

The result from using the chosen parameter values is shown in Figure 5-5, where also the CRT average values are indicated.

If the average block void ratio is taken as 0.74, which equals the volume average of the CRT experimental void ratios for $r \leq 830$ mm in ring R6 and ring R7, the corresponding average pellet slot void ratio becomes:

- 0.86

The result above can be compared with the homogenized CRT experimental void ratios for $r > 830$ mm, which are:

- 0.86 for R6
- 0.85 for R7

The experimental and calculated average pellet slot void ratios, shown in Figure 5-6 (Block R6) and Figure 5-7 (Block R7), agree well.

As can be seen, the experimental measurements show a large variation at the same radial distance. Especially the void ratio measurements in the pellet slot and the block close to the pellet slot covers a wide range.

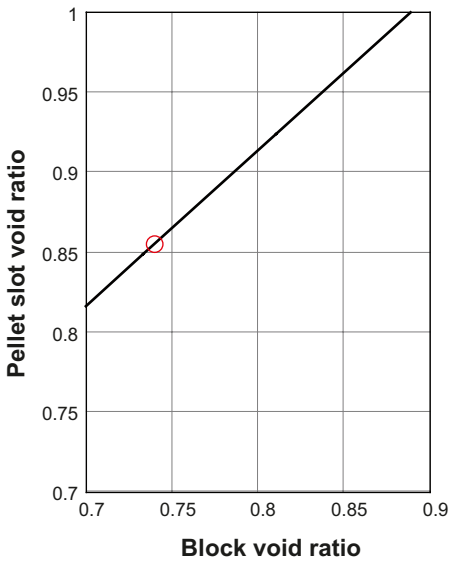

Figure 5-5. *Obtained void ratio relation for the serial wetting process assuming equal pressures.*

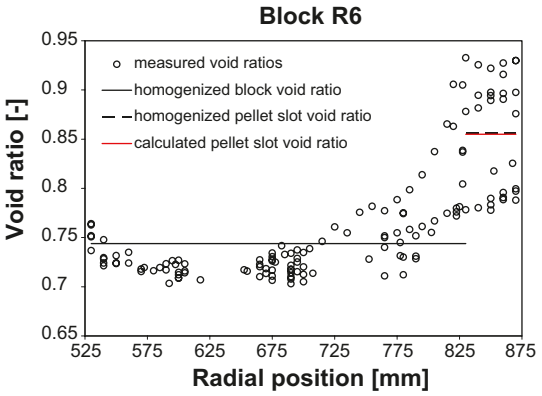

Figure 5-6. *Experimental data of the void ratios in block R6 and average values calculated from the experimental data and the analytical serial wetting model.*

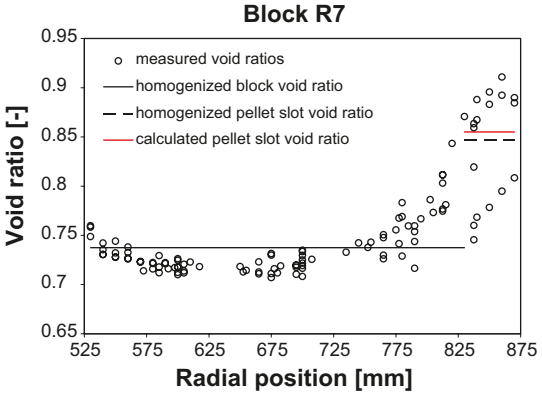

Figure 5-7. *Experimental data of the void ratios in block R7 and average values calculated from the experimental data and the analytical serial wetting model.*

From the obtained results above it might seem like the difference in retention path for the block and pellet slot is solely responsible for all void ratio heterogeneity. It must however be remembered that in the analysis above the system is highly idealized where only the "average behavior" of the block and pellet slot is considered.

In reality, different parts of the materials will undergo different processes, some parts of the block will for instance undergo compression, and therefore the adopted "average behavior" does not agree well with what really takes place in some parts of the material.

The assumption that the pellet slot is fully water saturated, $S_l = 1 \rightarrow w_{ref} = 0.64$, after the water filling of the outer slot is probably also exaggerated. Less extreme would be to assume that only the volume between the pellets is water filled, which would lead to $w_{ref} = 0.57$.

Taking all this into account, the obtained results above probably overestimates the effect of the serial wetting process as compared to what occurred in the CRT experiment.

Thus, the results show that the different paths in retention have significant influence on the remaining void ratio heterogeneity fund in the CRT experiment, but the exact magnitude of this effect might be hard to estimate with this model.

5.3.2 A parallel wetting process

The serial wetting process studied above (suitable for analyzing the CRT-experiment) is a special case. Another case would be if the entire buffer, both block and pellet slot, is water saturated at the same time (*parallel wetting*). In such a case the retention paths for the buffer and pellet slot are

concurrently tracing from the initial points until full water saturation, see Figure 5-8. Thus, the difference from the serial wetting is that the pellet slot now starts the concurrent tracking with the block material along the retention path from the very beginning.

Since the pellet slot will undergo both wetting (which leads to swelling) and compression (the material is subjected to pressure induced by the swelling of the block material) at the same time, the retention path is expected to become more complex in this case. The path could be seen as a sequence of wetting-drying processes. The overall path would then be drifting from a pure wetting curve towards the pure drying curve due to retention hysteresis. How large this drift would be is however hard to estimate.

The approach here is to obtain a limiting case and therefore the pellet slot is assumed to stay close to the pure wetting curve. To account for some drift, at full saturation, the pellet slot retention curve is assumed to be equal to the retention curve of the block material ($a^p = a^b$ and $b^p = b^b$). I.e. the resulting analytical expression becomes,

$$e^p = e^b - \frac{\rho_s}{\rho_w}\frac{1}{b^b}\ln(\alpha) \tag{5-12}$$

Thus, it is only the pressure difference that gives raise to any difference between e^p and e^b. The pressure difference is discussed in the next chapter.

This parallel wetting process could represent a case when the buffer becomes water saturated at a very slow rate. In such a case the suction would be equal in the entire buffer during saturation since there would be plenty of time for the water to be transported in the buffer and all uneven concentrations in suction would disipate.

5.3.3 The pressure difference

If now, solely the effect from considering different pressures in the block and pellets is to be studied, the retention curves for the block and pellet slot are set equal.

The pressure ratio is set to $\alpha = \{1, 0.9, 0.8, 0.7, 0.6\}$. With $a^p = a^b = a$ and $b^p = b^b = b$ the resulting relation $e^p = e^p$ (e^b) becomes,

$$e^p = e^b - \frac{\rho_s}{\rho_w}\frac{1}{b}\ln(\alpha) \tag{5-13}$$

Using $b = b^p$ or $b = b^b$ does not give any significant difference. The result is shown in Figure 5-9, where also the combination of average void ratios in CRT is indicated.

It can be seen that if only the pressure ratio should be the cause of all heterogeneity, it would have to be as low as 0.6 to match the CRT average void ratios.

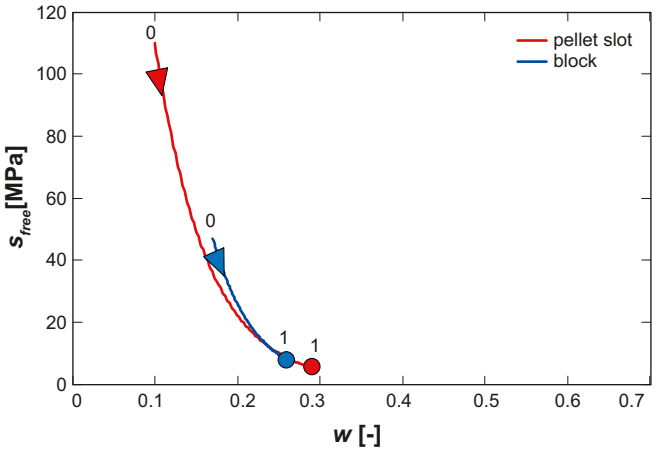

Figure 5-8. *Parallel wetting process in free retention.*

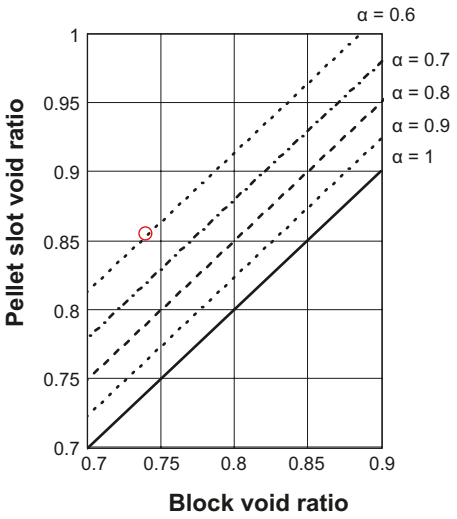

Figure 5-9. *The void ratio relation assuming identical retention representations and different pressure rations.*

To evaluate the lower limit of α in the buffer, the simplified system shown in Figure 5-10 is studied.

It is assumed that the radial stress, σ_r, is equal in the block and pellet slot due to force balance. The pressure in the two materials can be expressed as,

$$p^b = \frac{\sigma_1{}^b + \sigma_2{}^b + \sigma_r}{3}, \quad p^p = \frac{\sigma_r + \sigma_2{}^p + \sigma_3{}^p}{3} \tag{5-14}$$

The lower limit of α occurs when $p^b = p^b{}_{\max} \rightarrow \sigma_a{}^b = \sigma_t{}^b = \sigma_1{}^b$ and $p^p = p^p{}_{\min} \rightarrow \sigma_d{}^p = \sigma_t{}^p = \sigma_3{}^p$. Thus, following relations are adopted,

$$p^b = \frac{2\sigma_1{}^b + \sigma_r}{3}, \quad p^p = \frac{\sigma_r + 2\sigma_3{}^p}{3} \tag{5-15}$$

where obviously $\sigma_1{}^b = \sigma_1{}^b{}_{max}$ and $\sigma_3{}^p = \sigma_3{}^p{}_{min}$ produces $p^b = p^b{}_{\max}$ and $p^p = p^p{}_{\min}$, respectively. $\sigma_1{}^b{}_{max}$ and $\sigma_3{}^p{}_{min}$ are obtained from evaluating the maximum of the deviator stress parameter q. The maximum of this parameter is recognized as occurring at the state of failure $q_{max} = q_f$, *i.e.*

$$\begin{aligned} q^b{}_{\max} &= \sigma_1{}^b{}_{\max} - \sigma_r, \quad q^b{}_{\max} = q^b{}_f \\ q^p{}_{\max} &= \sigma_r - \sigma_3{}^p{}_{\min}, \quad q^p{}_{\max} = q^p{}_f \end{aligned} \tag{5-16}$$

Thus, to obtain the lower limit pressure ratio, the stress state of the two materials is at failure, $q = q_f(p)$, where,

$$q_f(p) = ap^b \tag{5-17}$$

(a = 0.5 (MPa)$^{1-b}$ and b = 0.77) is a function calibrated against experimental measurements. Using all relations above give $\alpha = \alpha(\sigma_r)$ which is plotted below in Figure 5-11.

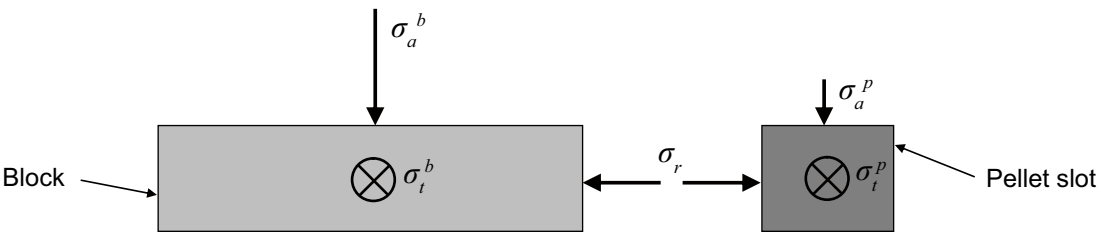

Figure 5-10. *Simplified system used for evaluating the minimum pressure ratio.*

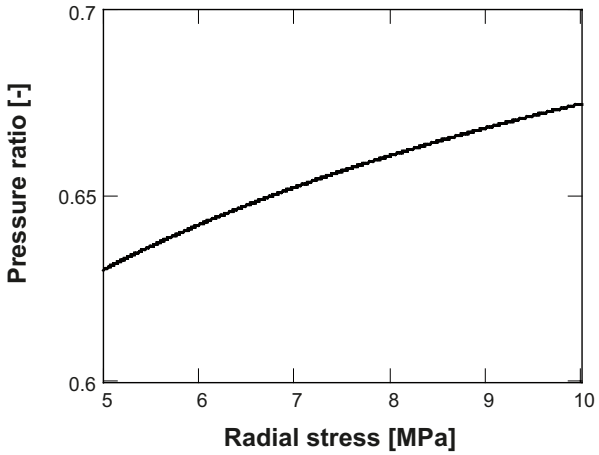

Figure 5-11. *The obtained minimum pressure ratio as a function of radial stress.*

It can be seen that for the used interval in radial stress, {5,10} MPa, the pressure ratio does not attain the value 0.6 which was necessary for reproducing the CRT void ratios with the pressure difference only. FE solutions of the CRT experiment produces radial stress which is approximately 7 MPa and this would give $\alpha = 0.65$ using the relation above. Also, it must be remembered that the stress state that gave the relation in Figure 5-11 is extreme with both materials at failure.

When analyzing FE solutions of the CRT problem, pressure ratios in the range 0.8–0.9 are obtained. Therefore the pellet slot void ratios are calculated using $\alpha = 0.8$ and $\alpha = 0.9$ in the following. With the block void ratio taken as 0.74 (which equals the volume average of the CRT experimental void ratios for $r \leq 830$ mm in ring R6 and ring R7) the obtained corresponding pellet slot void ratios are:

- 0.79 for $\alpha = 0.8$
- 0.76 for $\alpha = 0.9$

The results above can be compared with the homogenized CRT experimental void ratios for $r > 830$ mm, which are:

- 0.86 for R6
- 0.85 for R7

The results are also shown in Figure 5-12 for block R6 and in Figure 5-13 for block R7.

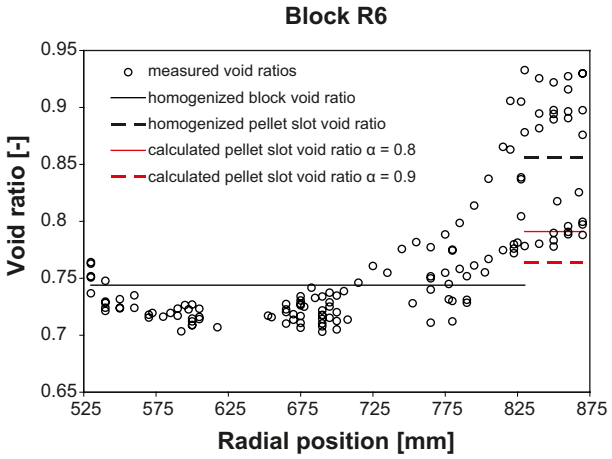

Figure 5-12. *Experimental data of the void ratios in block R6 and average values calculated from the experimental data and the analytical model only considering different pressures.*

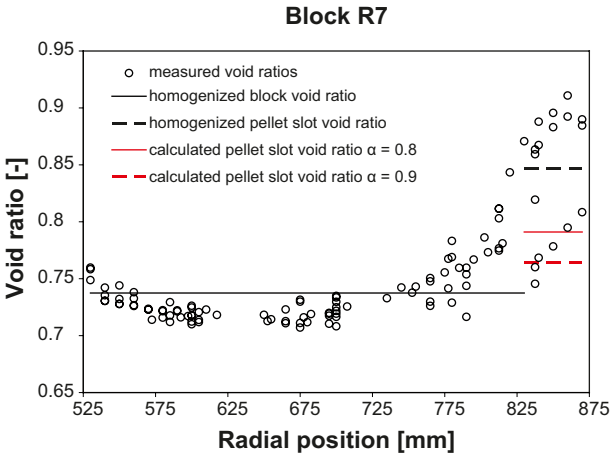

Figure 5-13. *Experimental data of the void ratios in block R7 and average values calculated from the experimental data and the analytical model only considering different pressures.*

Again, it must be remembered that the problem formulation is highly idealized and therefore the exact magnitude of the effect from considering a pressure difference in the block and pellet slot cannot be determined from the analysis above. However, the pressure difference can be said to have a significant contribution to the void ratio heterogeneity found in the CRT experiment, but seems to be of less magnitude as compared to the effect from adopting different retention curves for the block and pellet slot.

5.3.4 Compilation of the results from the analytical investigation

Below in Figure 5-14 the relation between the average void ratios of the pellet slot and block are plotted for both serial wetting (rapid pellet slot water saturation) and parallel wetting (concurrent water saturation of block and pellet slot). The pressure ratio has been set to $\alpha = \{1, 0.9, 0.8, 0.7\}$ for both cases of wetting. The average void ratio combination obtained from analyzing the CRT experiment is also indicated (red circle) for comparison. The relation obtained for an assumption of constant volume (as compared to the measured state in the CRT experiment) in the radial system is also shown.

Figure 5-14 shows possible void ratio states at full water saturation when different wetting processes and different pressure ratios are given. Examples of obtained "void ratio profiles" when assuming different combinations of wetting process and pressure ratio are shown to the right in the figure (the combinations are indicated with A, B, C and D along the constant volume assumption relation in the graph). As mentioned before, the serial wetting process could represent a rapid saturation process starting in the pellet slot and the parallel wetting process may represent a slow wetting process.

If the analytical model is to produce a void ratio combination that equals the average void ratios in the CRT experiment ($e^b = 0.74$ and $e^p = 0.855$) admissible combinations of w_{ref}, for the block and pellet slot, and α may be calculated. If e^b, e^p, $w_{ref}{}^b$ (the referential water ratio of the block) and α are specified, $w_{ref}{}^p$ (the referential water ratio of the pellet slot) may be calculated according to:

$$e^p = \frac{\rho_s}{\rho_w}\frac{a(w_{ref}{}^p) - a(w_{ref}{}^b) - \ln(\alpha)}{b(w_{ref}{}^p)} + \frac{b(w_{ref}{}^b)}{b(w_{ref}{}^p)}e^b \Rightarrow w_{ref}{}^p(e^b, e^p, w_{ref}{}^b, \alpha) \qquad (5\text{-}18)$$

As can be seen, the parameters in the free retention curves, a and b, are here taken as functions of the referential water ratio. These are given by the piecewise linear functions shown in Figure 5-2.

In Figure 5-15 below, the admissible combinations are shown as an iso-map where the parameter value ranges: $w_{ref}{}^b = \{0.17, 0.25\}$, $\alpha = \{0.8, 0.9\}$ have been adopted and $w_{ref}{}^p$ is given by solving the analytical expression where $e^b = 0.74$ and $e^p = 0.855$.

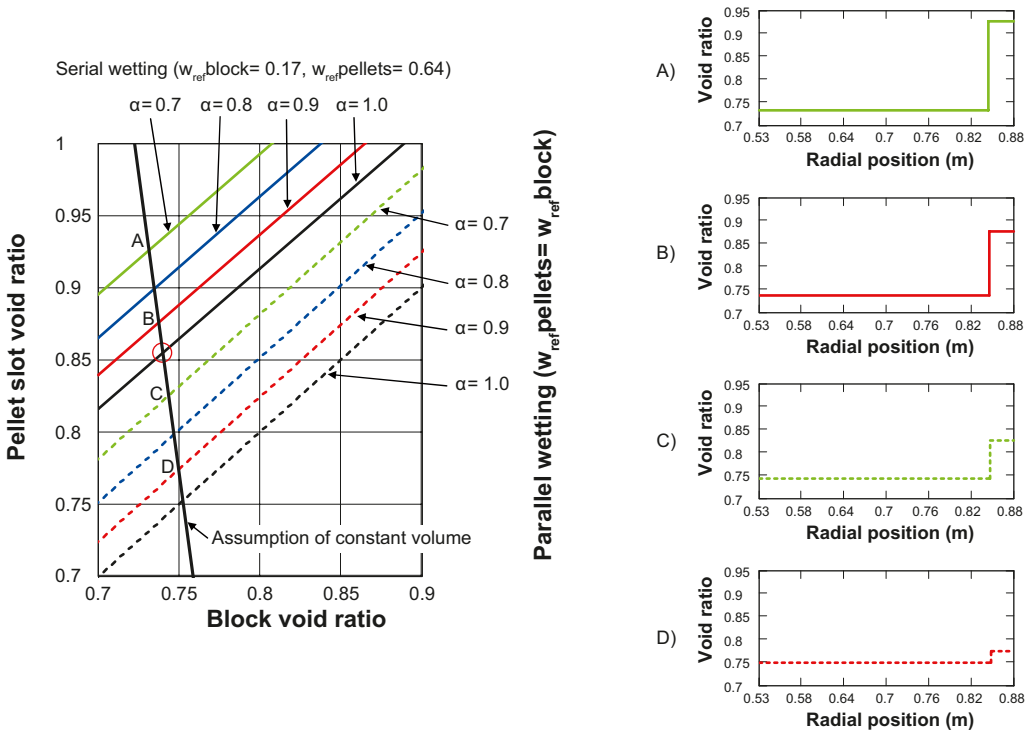

Figure 5-14. *Compilation of the analytical model results for serial (solid lines) and parallel wetting (hatched lines) assuming different pressure ratios. The obtained average void ratio profiles are shown for four different choices in wetting process and pressure ratio along the constant volume assumption with the CRT state as a reference.*

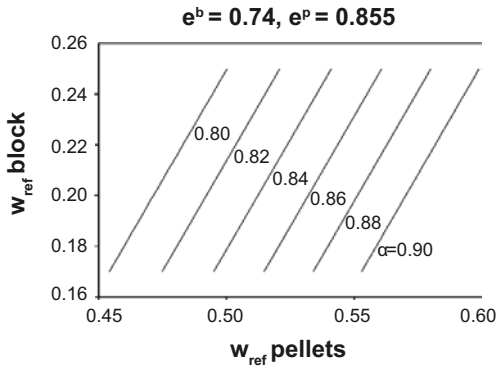

Figure 5-15. *Admissible referential water ratios for different pressure ratios given the void ratio state in CRT.*

For example, if $\alpha = 0.8$, all combinations of (w_{ref}^p, w_{ref}^b) along the leftmost diagonal line produces the sought void ratio combination. The result above indicates that if $\alpha = \{0.8, 0.9\}$ the referential average water ratios cannot be chosen as they were when studying the serial wetting previously. $w_{ref}^b = 0.17$ and $w_{ref}^p = 0.64$ is not an admissible combination according to the solution above.

As mentioned before, heterogeneity in the wetting process within the materials and deviations from the pure wetting/drying process makes the average retention curve drift from the adopted pure representations.

The analytical investigations above show that the wetting process (serial, parallel or in between these) and the pressure difference between the materials in the system have significant effect on the final void ratio heterogeneity.

5.4 CRT FE-model description and calibration

In the poro-mechanical formulation Code_Bright is based on, an additive split of a material volume element, dv, in a solid volume element, dv_s, and a pore volume element, dv_p is used. Furthermore the pore volume element, dv_p, is additively split into a liquid volume element, dv^l, and a gas volume element, dv^g. The liquid volume element is divided into a liquid water volume element dv_w^l and a liquid air volume element dv_a^l (dissolved air into the liquid).

Using the defined volume elements above, or the corresponding mass elements, the following variables are defined: $w = dm_w^l/dm_s$, $S_l = dv_w^l/dv_p$, $e = dv_p/dv_s$, $n = dv_p/dv$, being the water ratio, water saturation, void ratio and porocity, respectively.

In the THM model, balance laws of; solid mass (which gives the evolution of porosity), water mass, energy for the system and momentum for the system are considered. The gas pressure is constant, 0.1 MPa, in the model. The psycrometric law,

$$\omega_g^w = (\omega_g^w)_0 \frac{RH}{100}$$
$$(\omega_g^w)_0 = f(T) \qquad (5\text{-}19)$$
$$\frac{RH}{100} = \exp\left(\frac{-(p_g - p_l)\, M_w}{R(273.15+T)\rho_l}\right)$$

is used as an equilibrium constraint between the liquid phase and vapour phase of water.

5.4.1 Geometry

The model is axisymmetric and incorporates three constituents:

1. Bentonite block (0.535 < r < 0.825)
2. Pellet filled outer slot (0.825 < r < 0.875)
3. Empty inner slot (0.525 < r < 0.535)

as shown in Figure 5-16 below.

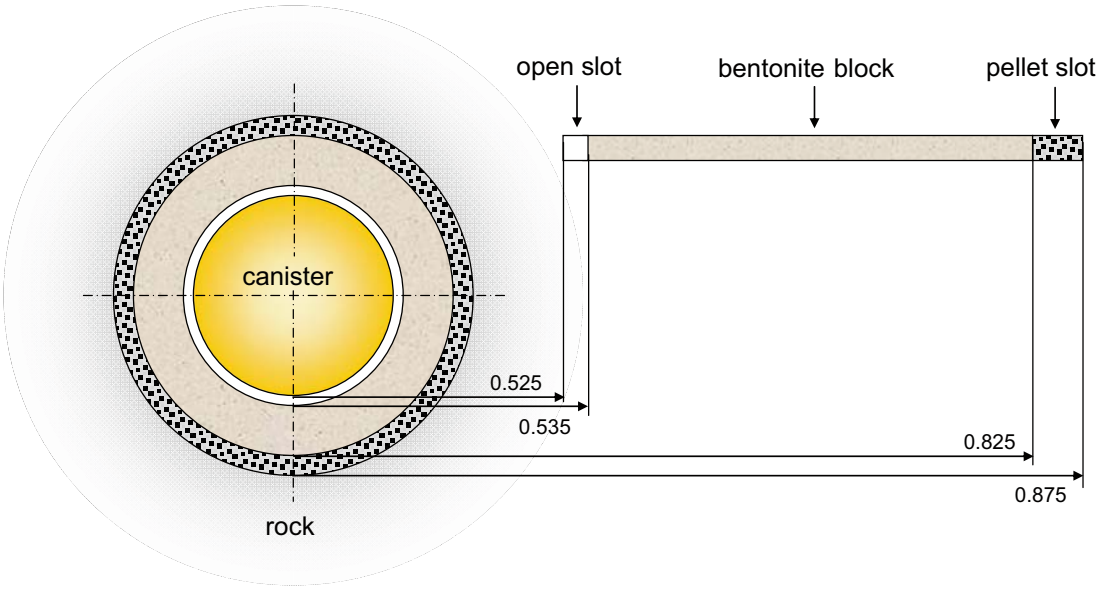

Figure 5-16. *Code_Bright model geometry and constituents.*

5.4.2 Material properties

In the following tables, Table 5-1 to Table 5-9 the constitutive laws and the parameters used for representing the different materials are shown.

Table 5-1. Material parameters.

Parameter	Block	Pellets	Slot
ρ_s [kg/m³]		2,780	
c [J/(kg K)]		800	

Table 5-2. Conductive heat transportation law.

Constitutive law	Parameter	Block	Pellets	Slot
Conductive heat flux	λ_{dry} [Wm/K]	0.7	0	0.04
$\boldsymbol{i}_c = -\lambda \nabla T$ $\lambda = \lambda_{sat} S_l + \lambda_{dry}(1 - S_l)$	λ_{sat} [Wm/K]	1.3	1.3	0.6

Table 5-3. Retention law.

Constitutive law	Parameter	Block	Pellets	Slot
Retention curve	p_0 [MPa]	73.412 37.273	0.558	0.558
$S_l = \left(1 + \left(\frac{S}{p_0}\right)^{1/(1-\lambda)}\right)^{-\lambda}$	λ	0.48 0.2	0.26	0.26
$S = p_g - p_l$				

Table 5-4. Advective water transportation law.

Constitutive law	Parameter	Block (1) *	Pellets (2)	Slot (2) **
Flow through porous medium	k [m²]	$1.09 \cdot 10^{-21}$ $2.18 \cdot 10^{-21}$	$5.19 \cdot 10^{-19}$ $1.04 \cdot 10^{-18}$	$1 \cdot 10^{-10}$/$1 \cdot 10^{-30}$
$\boldsymbol{q}_l = -\frac{k k_{rl}}{\mu_l} \nabla p_l$	B		21.3	0
(1) $k = k_0 \frac{n^3}{(1-n)^2} \frac{(1-n_0)^2}{n_0^3}$	λ	3	3	0
(2) $k = k_0 \exp(B(n - n_0))$				
$k_{rl} = S_l^{\lambda}$				
$\mu_l = 2 \cdot 10^{-12} \exp\left(\frac{1808.5}{273.15 + T}\right)$				

* Convergence problems occurred when adopting (2) for the block material, therefore (1) was used instead. (1) gives lower k-values as compared to (2) when n_0 is unaltered which leads to somewhat lower fluxes.

** When the slot closed (became small enough) water transportation was prevented in the slot material.

Table 5-5. Vapor diffusion law.

Constitutive law	Parameter	Block	Pellets	Slot *
Vapor diffusion $\boldsymbol{i}_g^w = -(n\rho_g S_g D_m^w)\nabla\omega_g^w$ $S_g = 1 - S_l$ $D_m^w = \tau 5.9\cdot 10^{-6}\,\frac{(273.15+T)^{2.3}}{p_g}$	τ	1	1	1/0.001

* When the slot closed (became small enough) water transportation was prevented in the slot material.

Table 5-6. Elastic strain increment in modified BBM.

Constitutive law	Parameter	Block	Pellets
"Elastic strain increment" $d\boldsymbol{\varepsilon}^e = -1/3\ d\varepsilon_v^e \boldsymbol{I} + d\boldsymbol{e}^e$ $d\varepsilon_v^e = \frac{dp'}{K},\ K = \max\left\{\frac{(1+e)p'}{\kappa_i(s)}, K_{\min}\right\}$ $\kappa_i(s) = \kappa_{i0}[1+\alpha_i s]$ $d\boldsymbol{e}^e = \frac{d\boldsymbol{s}}{2G},\ G = \frac{3(1-2\nu)}{2(1+\nu)}K$	κ_{i0}	0.13	0.15
	α_i	–0.021	–0.02
	ν	0.2	0.2
	K_{min} [MPa]	20	2

Table 5-7. Plastic strain increment in modified BBM.

Constitutive law	Parameter	Block	Pellets
"Plastic strain increment" $d\boldsymbol{\varepsilon}^p = d\Lambda\frac{\partial g}{\partial \boldsymbol{\sigma}}$ $f = q^2 - M^2(p'+p_s)(p_0-p')$ $g = \alpha q^2 - M^2(p'+p_s)(p_0-p')$ $M(p_0,p_s) = 0.5\left(\frac{p_0+p_s}{2}\right)^{-0.23}$ $p_0(s,p_0^*) = p^c\left(\frac{p_0^*}{p^c}\right)^{\frac{\lambda_0-\kappa_{i0}}{\lambda(s)-\kappa_{i0}}}$ $\lambda(s) = \lambda_0((1-r)\exp(-\beta s)+r)$ $dp_0^* = \frac{1+e}{\lambda_0-\kappa_{i0}}p_0^* d\varepsilon_v^p$	M	0.236 $M(p_0,p_s)$ *)	0.589 $M(p_0,p_s)$ *)
	α	0.5	0.5
	p_0* [MPa] **)	16.9	0.242
	p_c [MPa]	1	1
	λ_0	0.184	0.243
	p_s [MPa]	2.5	0.05

*) A constant value or the expression shown was used for *M*.

**) p_0*, which is containing the hardening information, is really a state variable and the value given above is a part of the initial conditions.

Table 5-8. Hydraulic strain increment in modified BBM.

Constitutive law	Parameter	Block	Pellets
"Hydraulic strain increment"	κ_{s0}	0.3	0.2
$d\boldsymbol{\varepsilon}^h = -1/3\ d\varepsilon_v{}^h \boldsymbol{I}$			
$d\varepsilon_v{}^h = \dfrac{\kappa_s(p',e)}{(1+e)(s+p_{atm})} ds$	p_{ref} [MPa]	1	0.1
$\kappa_s(p',e) = \kappa_{s0} f(p',e)$			
$f(p',e) = \begin{cases} 1 & \text{if } p' < p_{ref} \\ 10^{-20} & \text{if } p' > p_{swell}(e) \\ 1 - \dfrac{\ln p' - \ln p_{ref}}{\ln(p_{swell}(e)) - \ln p_{ref}} & \text{otherwise} \end{cases}$			
$p_{swell}(e) = 10^{\left[-4.741+4.117\cdot10^{-3}\frac{\rho_s}{1+e}-3.94\cdot10^{-7}\left(\frac{\rho_s}{1+e}\right)^2\right]}$			

Table 5-9. Nonlinear elastic strain increment used for representing the inner slot.

Constitutive law	Parameter	Slot
Strain increment	$-a_1$	1
$d\boldsymbol{\varepsilon} = -1/3\ d\varepsilon_v \boldsymbol{I} + d\boldsymbol{e}$		
$d\varepsilon_v = \dfrac{1}{K} dp'$	v	0.2
$K = \dfrac{p'}{-a_1}$		
$d\boldsymbol{e} = \dfrac{d\boldsymbol{s}}{2G},\ G = \dfrac{3(1-2v)}{2(1+v)} K$		

5.4.3 Initial conditions

The initial conditions, shown in Table 5-10, are here given in terms of the temperature, T, the water ratio, w, (or the corresponding water saturation, S_l), the void ratio, e, (or the corresponding porosity, n), and the total stress tensor, $\boldsymbol{\sigma}$. As mentioned in the former section, the hardening parameter p_0^* is also part of the initial conditions.

The initial water ratio of the pellet slot was 0.1 in the experiment. Directly after installing the pellet filling in the outer slot the slot was water filled using hoses installed before the pellet filling. In the simulations, the initial water ratio is taken as 0.136, which give the same level of suction as the block material has initially. This makes the problem more suitable numerically and does not deviate significantly from the conditions in the experiment.

Sensors that measured the hydraulic conditions in the block close to the canister showed that water had penetrated trough the buffer when the outer slot was water filled initially. Therefore, the slot material is initially taken as fully water saturated.

Table 5-10. Initial conditions used in the models.

Material	T [°C]	w/S_l	e/n	σ [MPa]
Block	15	0.171 / 0.849	0.56 / 0.359	$-0.1\boldsymbol{1}$
Pellets		0.136 / 0.212	1.78 / 0.64	
Slot		359 / 1	999 / 0.999	

5.4.4 Boundary conditions

The boundary conditions used in the model are shown in Figure 5-17.

Thermal boundary conditions

The heat flux evolution, prescribed at the canister boundary, is taken from a thermal 3D FE model where both CRT and TBT are considered, see 0. The heat flux boundary condition in the small THM model is obtained from evaluating the horizontal heat flux response of the 3D model at the canister surface at canister mid-height. As can be seen, the abrupt spikes in the heat flux (the heater elements were shut off) have not been incorporated in the boundary condition. This was done in order to simplify the numerical solution of the problem.

The temperature boundary condition at the rock wall boundary is obtained from fitting a function to relevant temperature sensor data, see Figure 5-19. Also here the spikes in the temperature have not been incorporated in the boundary condition.

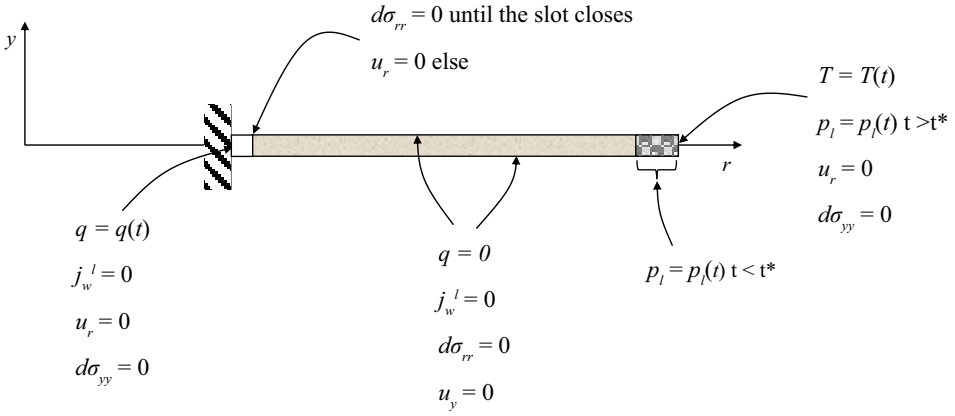

Figure 5-17. *Schematic picture of the boundary conditions used in the model.*

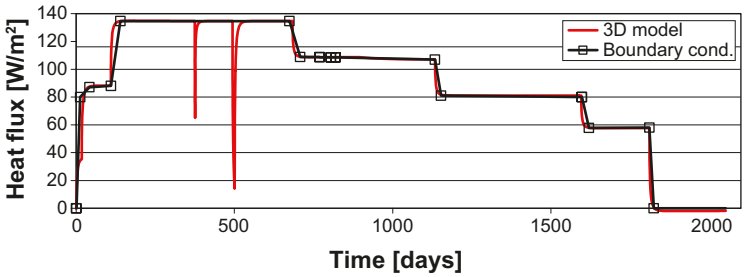

Figure 5-18. *Heat flux prescribed at the canister boundary.*

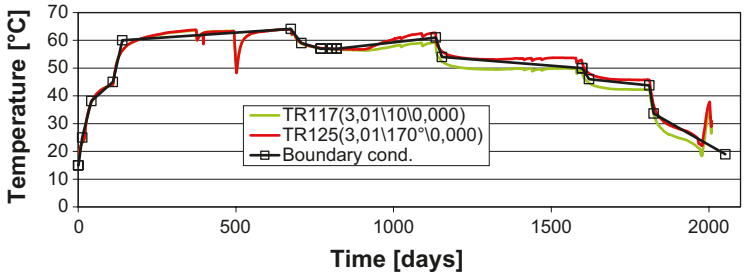

Figure 5-19. *Temperature prescribed at the rock wall boundary.*

Hydraulic boundary conditions

The water pressure condition at the pellet slot side is first prescribed as a surface condition over the outer part of the pellet slot ($0.835 < r < 0.875$) to mimic the fast water filling of the pellet slot when hoses were used. The water pressure is in this first step increased from –45.9 MPa to 0.1 MPa. After the initial water filling a water pressure boundary condition is prescribed at the rock wall side of the model. The prescribed water pressure follows the filter pressure protocol shown in Figure 5-20.

Mechanical boundary conditions

Since there is not any contact elements present in the current version of Code_Bright, the inner slot closure has to be considered in another way. The inner slot is modeled using a soft material. A first simulation is made where the displacement of the inner slot/block interface is studied for a model where the tangential traction is zero at all times. The time where the inner slot is sufficiently small is identified. In the next simulation (the actual simulation) the node displacements are locked at the interface at the identified time.

5.5 Mechanical investigation

Here the mechanical behaviour of the model is investigated when prescribing a constant or variable *M* parameter (the slope of the critical state line). The variable *M* parameter formulation is described in Appendix 5.3.

5.5.1 Void ratio

Below the void ratio profiles obtained at the end of the simulation are compared with the void ratio profiles obtained from analyzing the excavation-data (shown in Figure 5-6, Figure 5-7, Figure 5-12 and Figure 5-13). To facilitate a clear comparison an "averaged" void ratio profile has been calculated using data from the excavation, i.e. the data has been filtered by calculating the volume average of the void ratio for a chosen increment in radius.

Also, the excavation-data has been adjusted (lowered) so that the total volume average of the void ratio concurs with the homogenized initial void ratio. This has been done in order to enable a fair comparison between simulations and experiment. The total volume average of the excavation data show that either; 1) the initial conditions at block R6 and R7 differed from the overall conditions, or, that 2) the buffer has swollen some amount in the axial direction. Since the model is restricted to radial deformation only, the excavation data has to be adjusted in order to obtain a fair comparison.

Table 5-11. Models used in this section.

Model ID	Hydraulic				Mechanical		
	S_l		k		M		
	high	low	high	low	high	low	$M(p_0,p_s)$
CRT 1	x			x	x		
CRT 3	x			x			x

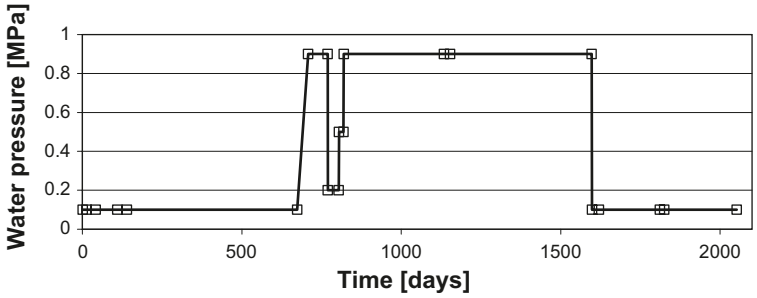

Figure 5-20. *Filter water pressure protocol.*

As can be seen in Figure 5-21 below, the void ratio profiles for both models match the adjusted experimental measurements well. No significant difference can be found in the void ratio profiles of the two models.

5.5.2 Axial stress

There is no significant difference between the axial stresses obtained from the two models, see Figure 5-22. The calculated stresses are larger as compared to the measured. The measured stress is however small to the expected swelling pressure. This probably comes from a higher porosity around the sensor tip as compared to the porosity in the block material.

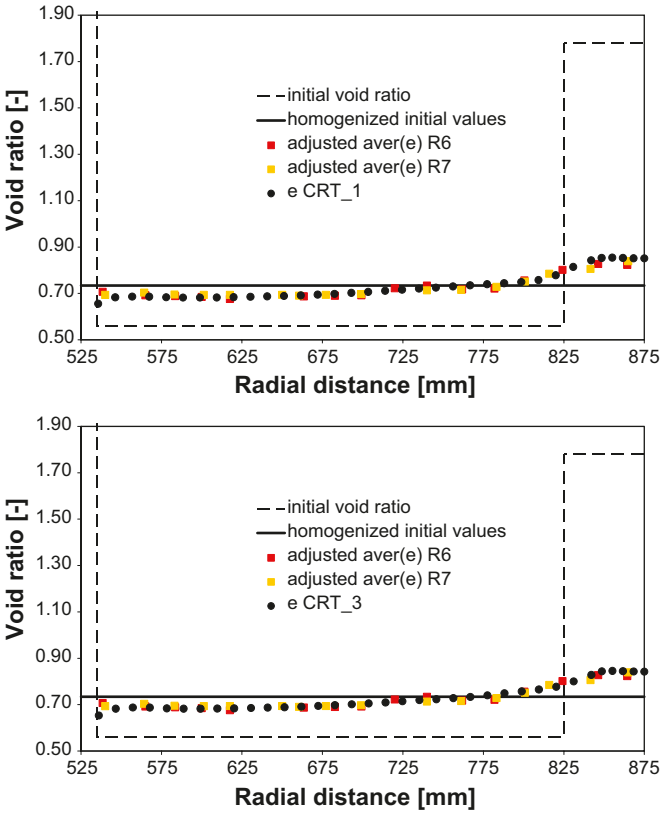

Figure 5-21. *Void ratio profiles for both models.*

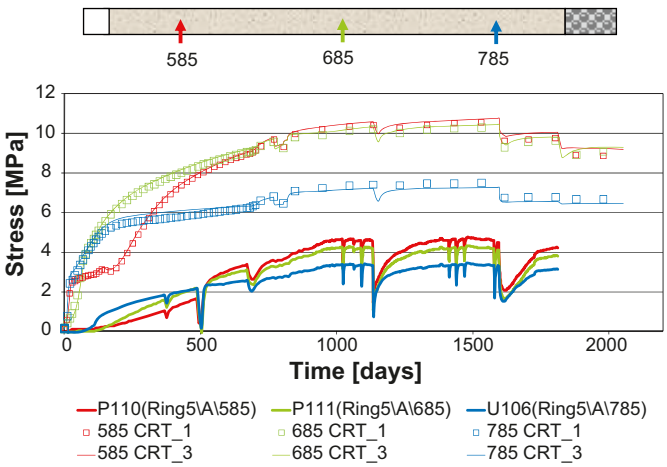

Figure 5-22. *Axial stress responses at r = 585, 685 and 785 mm.*

When the sensors were installed, in holes drilled in the block, the match between the holes and the sensors was not perfect. In order to obtain a tight fit, bentonite powder was compacted in the hole both at the sensor tip and as backfill at the opposite side of the sensor. The measurements do, however, indicate that pores remained at the sensor tips and/or that the density in the packed powder was less than the density in the block material.

5.5.3 Mechanical process

The mechanical process is here viewed as traces in the $e - \ln(p')$ space for five chosen points in the buffer, see Figure 5-23. Points 1 and 2 are located in the pellet slot and 3, 4 and 5 in the block material. The approximate location of the points is indicated at the top of Figure 5-23.

The obtained void ratio – net mean stress relations, $e - \ln(p')$, show no large differences for the two models. The overall features of the $e - \ln(p')$ graphs are in correspondence with what is expected for the buffer system.

The pellet slot material (pt(1) and pt(2), where pt(1) is obscured by pt(2)) obtains a higher void ratio as compared to the buffer material (pt(3), pt(4) and pt(5)) at the same level of net mean stress. The point in the block material close to the pellet slot, pt(3), undergoes a swelling – compression process and therefore obtains a higher void ratio.

It can be seen that the pellet slot material attains a state which corresponds to the higher swelling pressure curve, indicated with p'_{swell} high, and the block material, not undergoing a compressive phase, attains a state more in correspondence with the lower swelling pressure curve (p'_{swell}). This is in accordance with what was discussed in the analytical investigation of the homogenization process. As mentioned the swelling pressure curve is linked to the free suction curve and in serial-like wetting processes the swelling pressure curve for the pellet slot will attain a higher value as compared to the block material.

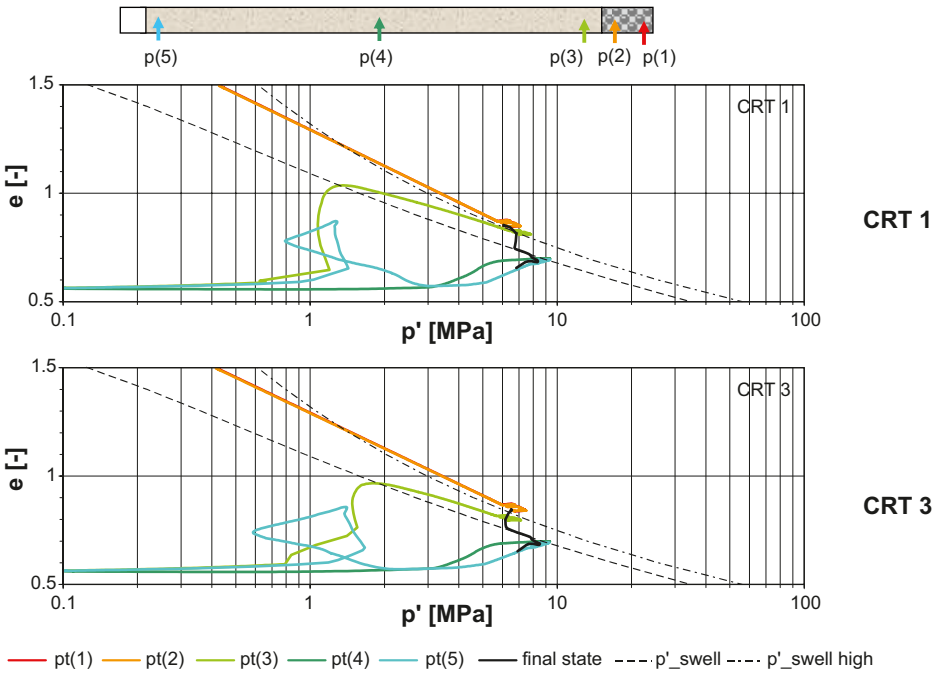

Figure 5-23. *Traces in void ratio – net mean stress space for the five points indicated in the figure above the graphs.*

Figure 5-24 show the stress state history in the five selected points, pt(1)–pt(5). The stress state is here expressed in terms of the net mean stress *p'* and the deviator stress variable *q*. The final stress state of the buffer system is also indicated (black, solid line), as well as the initial yield surface of the block material (black, dashed line) and the failure stress at the final state (circular symbols).

It can be seen that the stress paths are quite complicated due to the varying boundary conditions over time.

The overall picture is quite similar for the both solutions. There are however significant differences. The pellet slot stress paths, pt(1) and pt(2), are steeper in CRT 1, and the final deviatoric failure stresses, $q_f = M\,p'_{mid} = M\,(p_0 + p_s)/2$, are also in CRT 1 larger in the pellet slot as compared to the block material. This comes from the use of a constant value of *M*.

If the obtained deviatoric failure stress profile at the end of the simulation is plotted together with the result from using the expression found from analyzing experimental data the graphs in Figure 5-25 are obtained.

The constant *M* solution (CRT 1) underestimates the deviatoric failure stress in the block material and overestimates the deviatoric failure stress in pellet slot material. From the figure showing the results from CRT 3 it is seen that the two solutions concur. It is so because this solution calculates the value of *M* from the material specific failure stress curve. It should be noted that for CRT 1, one have to specify two constant values of *M* (which according to experiments should be variable) but for CRT 3, the material specific failure stress curve is implemented in the code and no pellet slot or block parameters have to be given by the user.

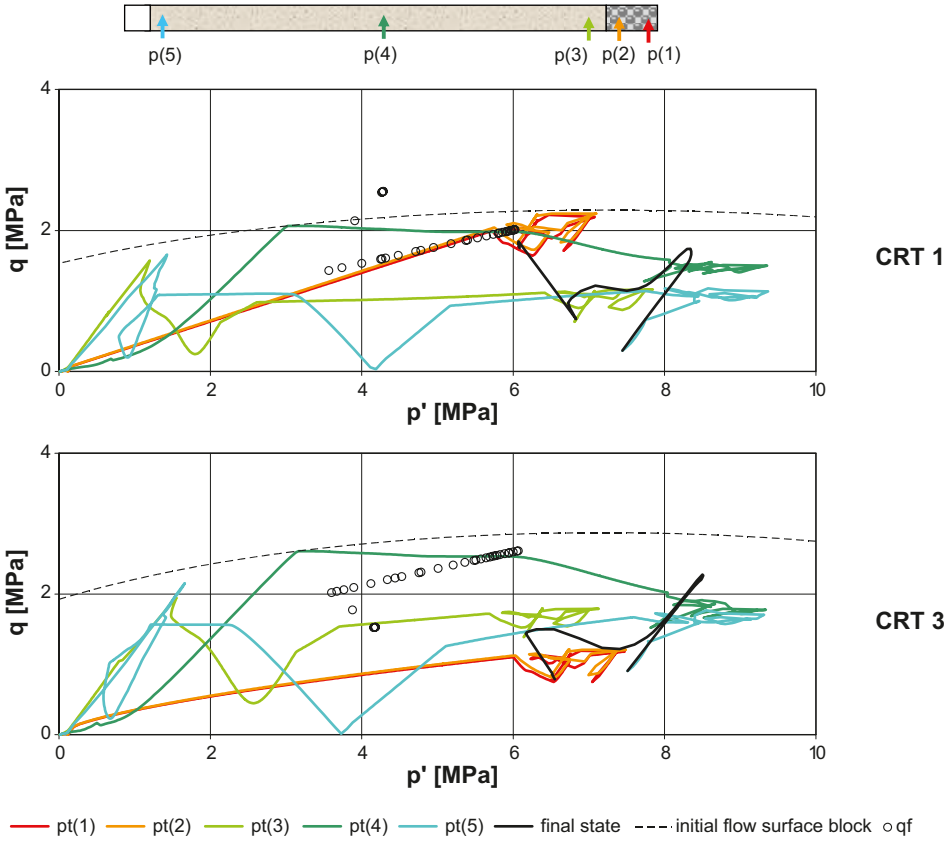

Figure 5-24. *Stress state evolution expressed in q and p'.*

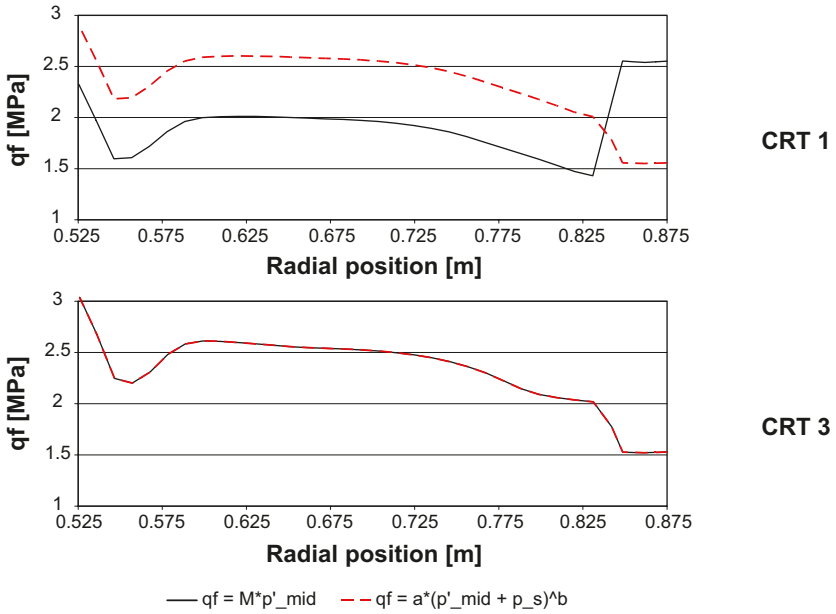

Figure 5-25. *Deviatoric failure stress calculated from the BBM model and the experimentally validated expression.*

5.6 Hydraulic investigation

In Figure 5-26 suction responses from the three THM-models, with differences in the hydraulic representation, are shown. The solutions are shown at three different radial positions (r = 585, 685 and 785 mm) for which experimental measurements also are shown.

The overall behavior for all three models is in agreement with the experimental measurements. The decrease in suction is more rapid closer to the rock wall and there is a saturation-desaturation process at r = 585 mm.

The effect from increasing the permeability (in CRT 4 and CRT 6b) brings the solution closer to the experiment, the saturation becomes more rapid. One reason why CRT 3 underpredicts the rate of saturation as compared to the sensor data probably comes from that Kozeny's law, ((1) in Table 5-4), is used for the buffer material instead of the exponential law, ((2) in Table 5-4).

When lowering the retention curve (CRT 6b) the initial saturation becomes more rapid but after some time the saturation slows down as compared to the higher retention solution (CRT 4). This comes from the relation between the slopes of the different retention curves. The lower retention curve has a higher slope at lower water saturation and lower slope at higher water saturation when compared to the high retention curve. CRT 6b is considered to be the model that most accurately mimics the water saturation process in the CRT–experiment.

Table 5-12. Models used in this section.

Model ID	Hydraulic				Mechanical		
	S_l		k		M		
	high	low	high	low	high	low	$M(p_0,p_s)$
CRT 3	x			x			x
CRT 4	x		x				x
CRT 6b		x	x				x

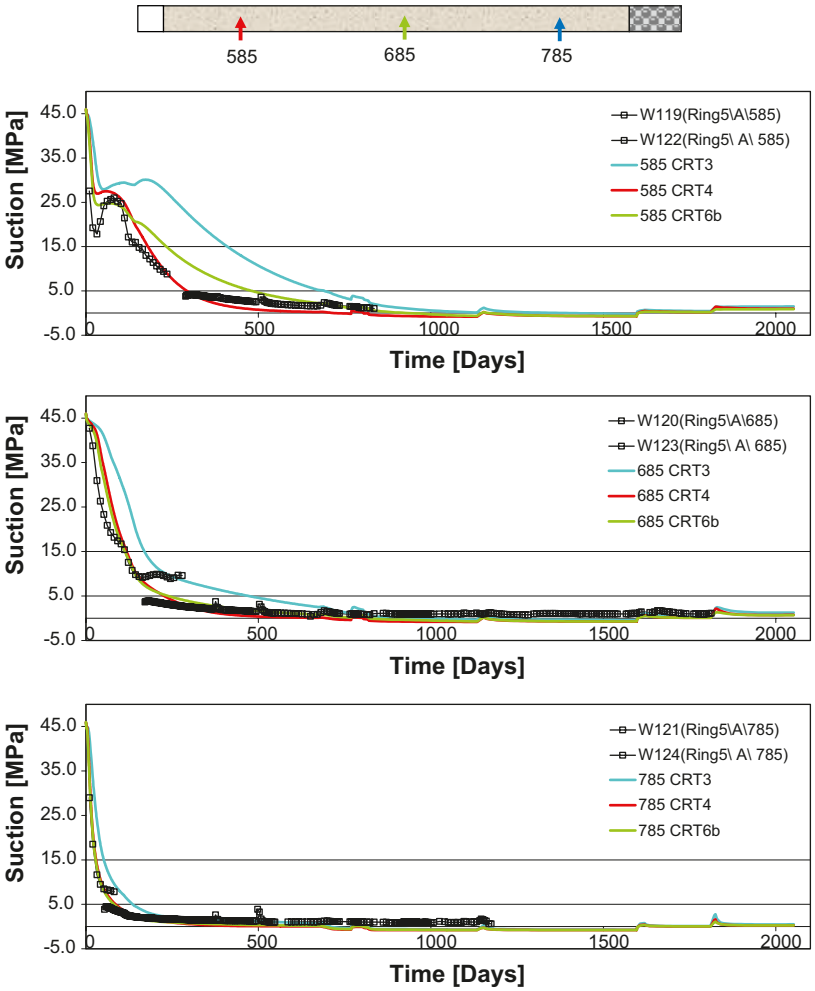

Figure 5-26. *Suction responses for all three models at r = 585, 685 and 785 mm.*

5.7 Investigation of pellet slot width variation

Since there will be variations of the hole diameter in the repository, the pellet slot width will vary. This gives rise to different void ratio profiles at full water saturation and also different total pressures. To investigate the effect from having different pellet slot widths two models with 9 cm (CRT 9b4) and 3 cm (CRT 10b) pellet slot width are developed. In addition to the pellet slot width, the models differ in some of the plastic parameters due to different expected target void ratios. The differing plastic parameters are shown in Table 5-14.

Table 5-13. Models used in this section.

Model ID	Pellet slot width [cm]
CRT 10b	3
CRT 6b	5 (CRT)
CRT 9b4	9

Table 5-14. Altered plastic parameters.

Parameter	3 cm model		9 cm model	
	Block	Pellet slot	Block	Pellet slot
λ	0.18	0.238	0.191	0.253
p_0^* [MPa]	22.046		11.144	

Below in Figure 5-27 the void ratio profiles at day 2,052 (the last simulated day) are given. Together with the model solution, experimental measurements for CRT, the interfaces (inner slot – block, block – pellet slot and pellet slot – rock wall) and the homogenized initial void ratios are given.

As expected, the larger slot gives higher void ratios and the smaller slot gives lower void ratios.

To get an overview of the void ratio results the volume average of the void ratios are calculated in the pellet slot, the block and the total model. The obtained values are shown in Figure 5-28. When performing the calculation the end point, closest to the inner slot, has been disregarded since the result for this point is not representative. In the following the variable name is used instead of "the volume average of" in order to improve the readability.

The block void ratio is slightly less then the total void ratio for all three models and the pellet slot void ratio is significantly higher. Figure 5-29 below shows the pellet slot and block void ratios normalized against the total void ratio.

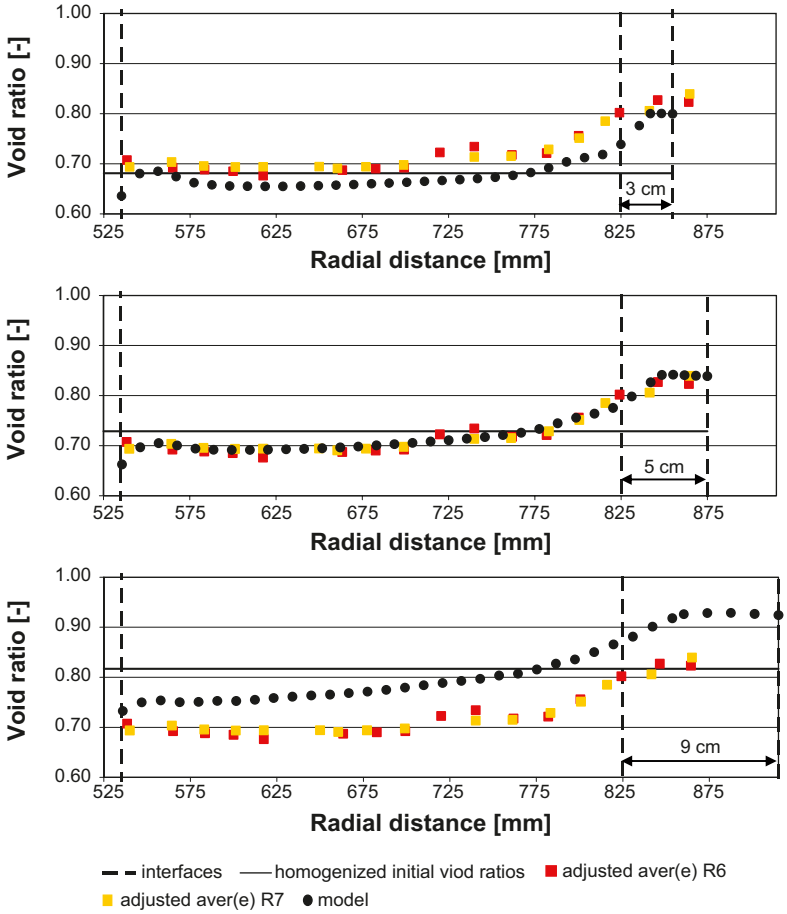

Figure 5-27. *Void ratio profiles obtained for 3, 5 and 9 cm pellet slot.*

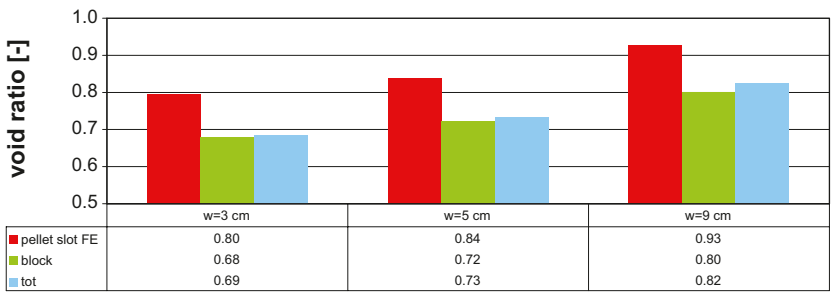

Figure 5-28. *Averages of void ratio for 3, 5 and 9 cm pellet slot.*

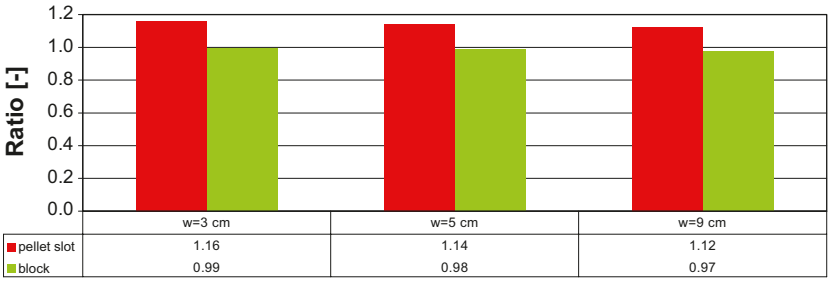

Figure 5-29. *Averaged void ratios in the pellet slot and block normalized against the average total void ratio for 3, 5 and 9 cm pellet slot.*

It can be seen that the three models produce ratios of the void ratios that are very similar despite the difference in homogenized void ratio (or pellet slot width). There is however a slight decrease in the ratios of the void ratios with increasing homogenized void ratio (or pellet slot width). Conditions different from the ones that prevail in this problem might change this character.

The history plot in the log(*p'*) – *e* space given in Figure 5-30 for five selected points in the system show the mechanical process that takes place. Again, a lower swelling pressure curve (hydration curve) and a higher swelling pressure curve (dehydration curve) are also shown.

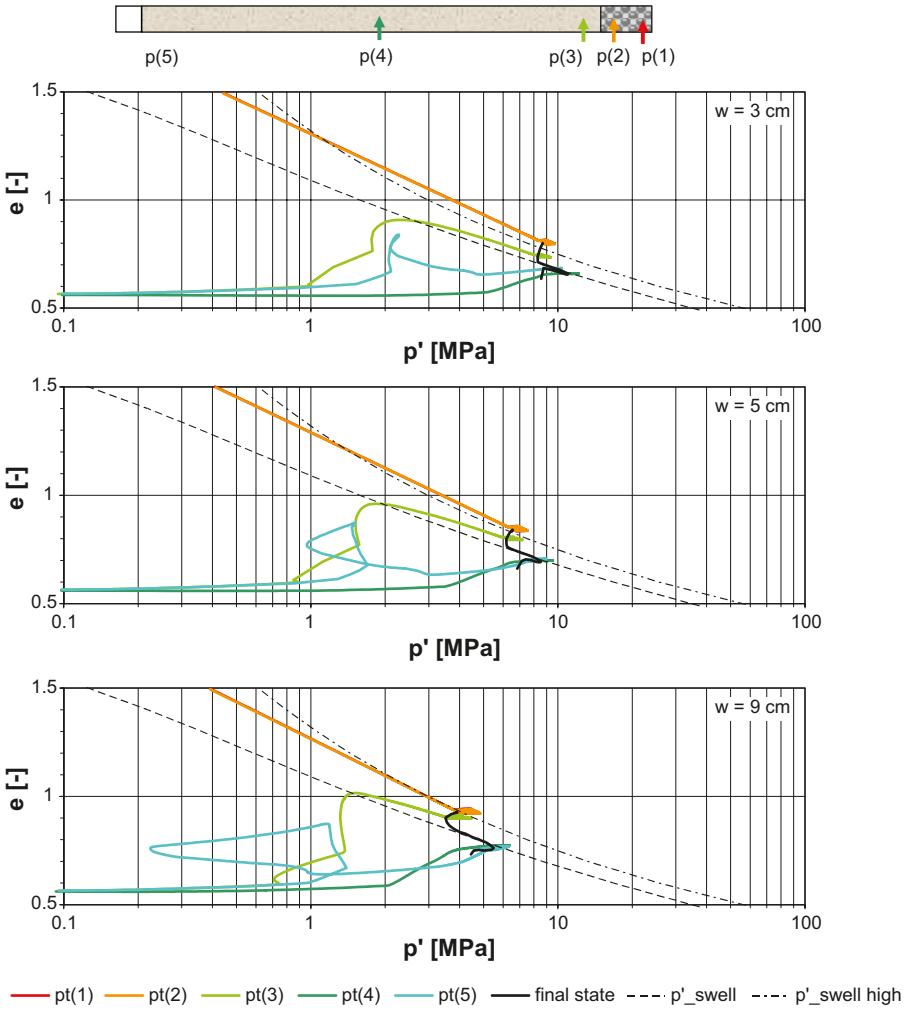

Figure 5-30. *Traces in void ratio – net mean stress space for the five points indicated in the figure above the graphs.*

The three models behave in a very similar manner. The pellet slot, pt(1–2), compresses and therefore ends up close to the dehydration curve. The material in the block, close to the pellet slot, pt(3), has a expansion-compression cycle and therefore shifts towards the dehydration curve. The material in the center of the block "torus", pt(4), has a rather uncomplicated history and simply swells until full "hydration" swelling pressure is reached. The point close to the inner slot, pt(5), has a swelling – compression cycle, where the pressure also drops. The swelling is however not as large as for the block material close to the pellet slot and the point ends up close to the hydration curve.

To evaluate the swelling pressures at the end of the simulation, the volume average of the total pressures in the pellet slot, block and the total model are calculated. The obtained values are shown in Figure 5-31 below.

The pressures reflect the void ratios in the corresponding section. The pellet slot is subjected to less pressure as compared to the block.

When performing the analytical evaluation of the pressure difference dependence on heterogeneity a variable $\alpha = p^p / p^b$ was introduced. In Figure 5-32 the obtained pressure ratio α is shown for the three models.

The pressure ratios are similar for all models, ranging from 0.82–0.85. By using the obtained pressure ratios and the block void ratios in the analytical expression it is possible to evaluate the analytical expression.

In Figure 5-33 the pellet slot void ratio obtained from the FE-formulation and the analytical formulation are shown together with the ratio between the two void ratios, i.e. $e_{analytic} / e_{FE}$.

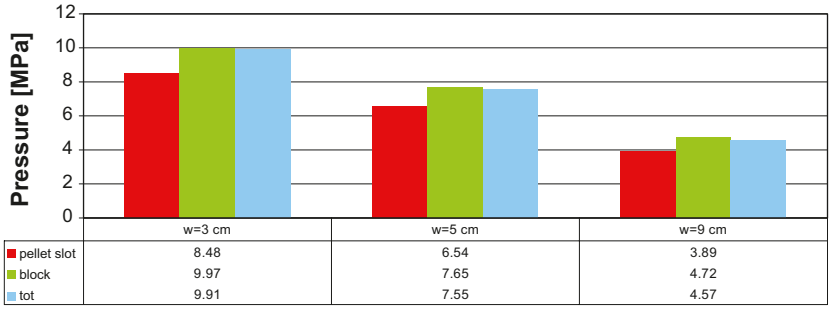

Figure 5-31. *Averages of pressure for 3, 5 and 9 cm pellet slot.*

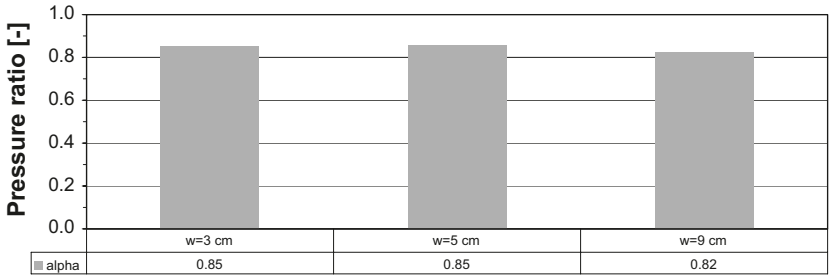

Figure 5-32. *Pressure ratio for 3, 5 and 9 cm pellet slot.*

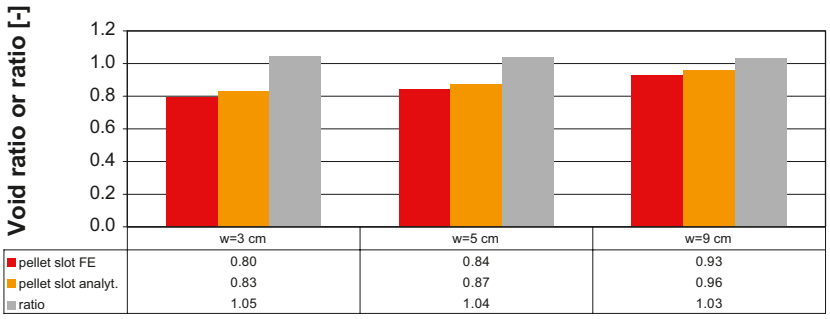

Figure 5-33. *Average pellet slot void ratio obtained for the FE-model and the analytical model for 3, 5 and 9 cm pellet slot. The ratio between the analytical and FE-model solution is also shown.*

The analytical expression produces solutions that are close to the FE-solutions. The maximal deviation of 5% from the FE-solution occurs for the 3 cm slot model.

Since the analytical expression seems useful for evaluating the present problem, the normalized void ratios of the pellet slot and block are addressed once more. If the normalized block void ratio is assumed to be equal to or 0.97 times the totally homogenized void ratio (based on the findings when studying Figure 5-29) the normalized pellet slot void ratio might be calculated using the analytical expression. The result form this is shown in Figure 5-34 below, where also the pressure ratio α has been prescribed to either 0.9 or 0.8 (based from the findings of Figure 5-32). In Figure 5-34 the normalized pellet slot void ratio is plotted against the homogenized void ratio. The results from using: the block void ratio, the totally homogenized void ratio and the pressure ratio obtained from the FE solution in the analytical expression are also indicated as well as the FE solution results.

As can be seen, when assuming a constant normalized block void ratio and pressure ratio, the analytical expression predicts slightly higher void ratio dependence of the normalized pellet slot void ratio as compared to what the FE solution shows.

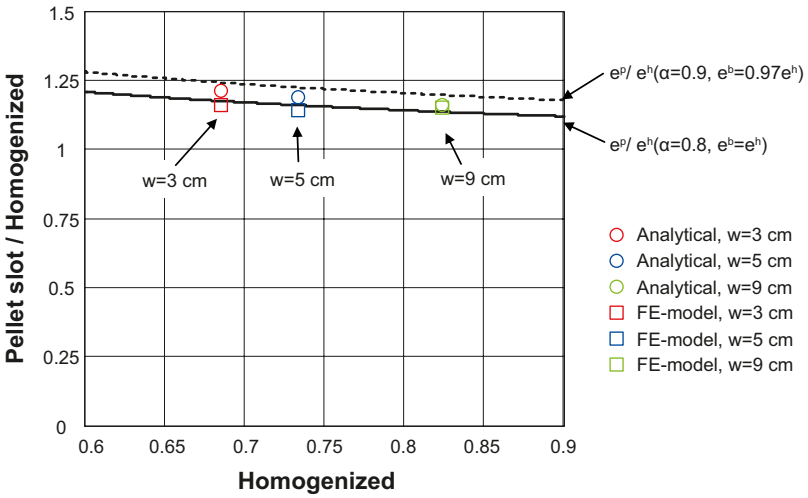

Figure 5-34. *Normalized pellet void ratio given as a function of totally homogenized void ratio using the FE-model and analytical model for 3, 5 and 9 cm pellet slot.*

5.8 Modelling pure serial and parallel wetting

To evaluate the capabilities of the FE code utilized (Code_Bright) simplified wetting processes are prescribed to the model used for simulating the CRT experiment.

It was found that in order to obtain reasonable results for the parallel wetting process $\kappa_i = \kappa_{i0}$ in the pellet slot. This is obtained by setting the parameter $\alpha_i = 0$. By doing this, the pellet material compression is controlled by the flexibility parameter λ when the material has a plastic behavior.

Pure serial and parallel wetting processes are here simulated by prescribing the suction field evolution in the block and pellet slot. The serial wetting process is accomplished by first prescribing a suction decrease from the initial value (46 MPa) to 0.1 MPa in the pellet slot and thereafter prescribing an identical suction decrease in the block. The parallel wetting process is given by prescribing a simultaneous decrease in both pellet slot and block. Using this approach the transient flow of water within the model is not considered and the model becomes time independent

The obtained void ratio profiles are given in Figure 5-35.

The pure serial wetting gives a larger heterogeneity in the void ratio field as compared to the CRT measurements (and what the CRT model gave). The parallel wetting process in turn produces less heterogeneity as compared to the CRT measurements.

This is what is expected from the analytical investigation which showed that the different wetting processes should give different void ratio profiles due to different saturation paths (which give rise to different retention curves) in the two cases.

In Code_Bright, however, there is no such direct coupling between the stress state and the retention curve as in the analytical model. The reason for the obtained difference in void ratios is found in the coefficient $\kappa_s(p',e)$ that determines the suction increment contribution to the void ratio increment. The implemented pressure dependence of $\kappa_s(p',e)$ includes the expression of the swelling pressure $p_{swell}(e)$ (a function of the current void ratio). When the pressure is larger then the swelling pressure the coefficient is set extremely 1ow (10^{-20}) and effectively no swelling occurs. When no swelling occurs and the material behaves plastic (the pellet slot does) the plastic flexibility λ determines the $e - \ln(p')$ relation.

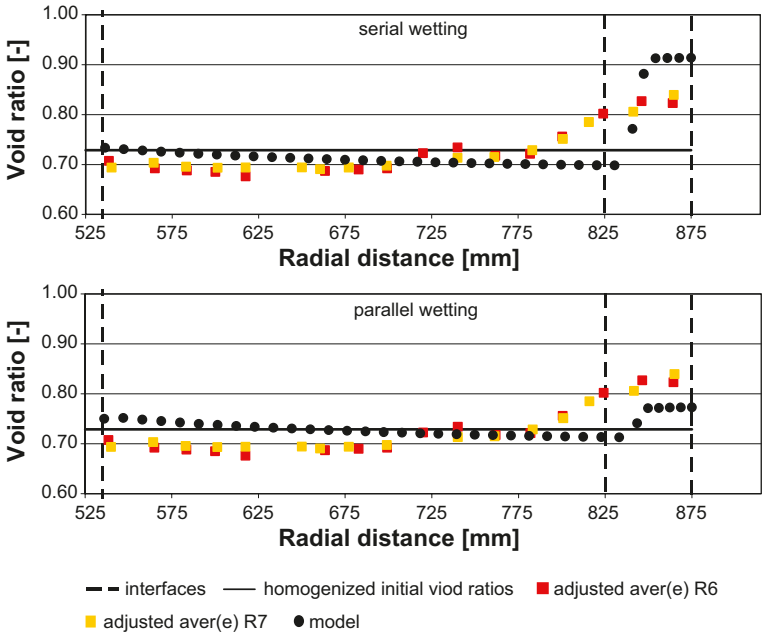

Figure 5-35. *Void ratio profiles obtained for serial and parallel wetting.*

The evolution in $e - \ln(p')$ of the five indicated points is shown in Figure 5-36 for both wetting processes.

The pellet slot evolution (point 1 and 2) has for serial wetting an initial increase in void ratio (actually not seen in the logarithmic plot above since the void ratio increase occurs at very low pressures) and at pressures between 0.1–0.2 MPa the slope is lower as compared to the evolution for parallel wetting. The slope of the $e - \ln(p')$ curve is at higher pressures determined by the value of the λ parameter only. This is clearly seen since the both wetting processes produce the same slope in $e - \ln(p')$.

As a result, the serial wetting process gives rise to a final state of the pellet slot that overshoots the adopted swelling pressure curve and the parallel wetting process produces a final pellet slot state that coincides with the swelling pressure curve. Thus, the obtained final state in the FE simulations depends on the adopted swelling pressure curve and the adopted λ parameter value.

To make the numerical mechanism described above more clear the "time" (the models are time independent) evolution of the void ratio and the net mean pressure are given in Figure 5-37 together with the adopted swelling pressure curve $p_{swell}(e)$ for both wetting processes.

The initial increase of the void ratio in the serial wetting process model (during the pellet slot wetting) is clearly visible in this plot. When the pressure is below the swelling pressure curve expansion takes place. Thus the function $\kappa_s(p',e)$ has a significant magnitude.

The initial void ratio evolution of the pellet slot in the parallel process model is instead decreasing from the very start. In this case the pressure does very rapidly overshoot the swelling pressure curve which gives insignificant $\kappa_s(p',e)$ magnitudes.

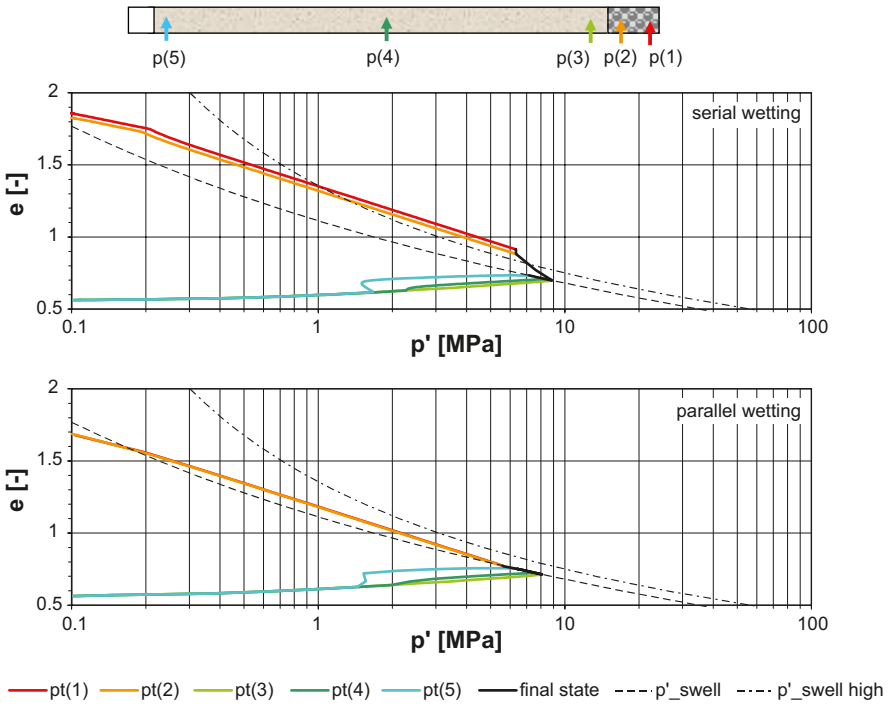

Figure 5-36. *Traces in void ratio – net mean stress space for the five points indicated in the figure above the graphs.*

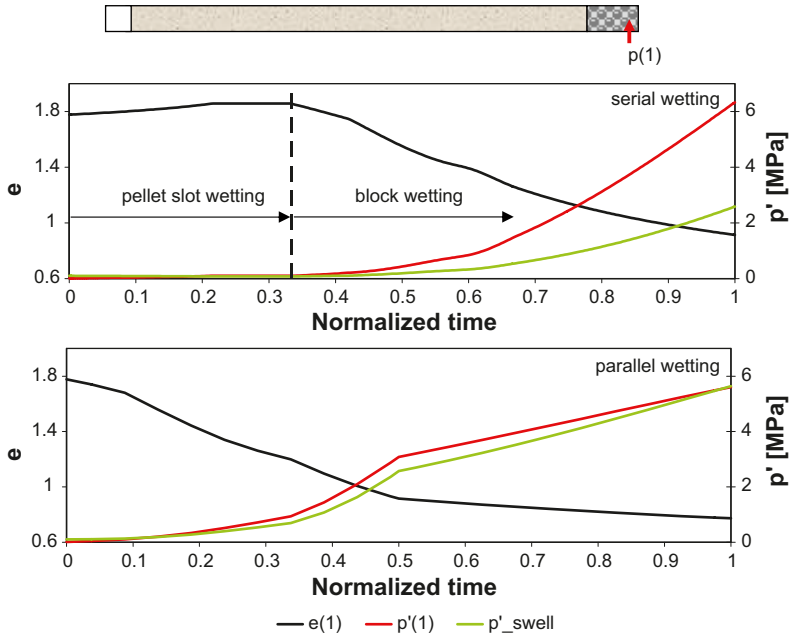

Figure 5-37. *Evolution of void ratio and net mean stress at the point indicated in the picture above the graphs.*

5.9 Conclusions

5.9.1 Analytical investigation

An analytical model of the homogenization at full saturation in a block/pellet slot system has been derived. The basis is an expression of the free energy difference for pure water and soil water in a system where the pure water is in connection with moist soil via a semi-permeable membrane. The resulting expression, relating the suction under free swelling conditions to the swelling pressure, is averaged over a block and pellet slot volume. Thus, the analytical model concerns averages in the block and pellet slot.

The analytical expression gives (for fully saturated conditions) a relation between:

- The pellet slot void ratio.
- The block void ratio.
- A referential water ratio for the pellet slot.
- A referential water ratio for the block.
- And the ratio between the pressure in the pellet slot and block.

Using the analytical expression a serial wetting process (where the pellet slot is saturated first and thereafter the saturation of the block begins) has been analysed. Also, a parallel wetting process (where both materials are simultaneously saturated) is analyzed.

5.9.2 Finite element calculations

Here, the CRT experiment is used as a suitable problem to model. The calculated responses can be compared to the sensor data recorded during the experiment and the data obtained at excavation. In this way the THM models (mainly the laws and parameters used) can be validated against an experiment.

Mechanical investigation

In the mechanical investigation, two models, where different representations of the parameter *M* setting the slope of the state line, is used. In the first model the parameter M is constant (ordinary Code_Bright setting) and must to be calibrated and set differently in different materials (i.e. block or pellet slot). In the second model, an in-house developed and implemented variable *M* formulation, with basis in an experimentally calibrated function of the deviatoric failure stress, is used. Using the variable *M* formulation, the user does not have to set any parameter, the parameters of the expression for the deviatoric failure stress are implemented directly in the source code.

When void ratio profiles and axial stress evolutions are investigated for the two models no significant difference can be found. The models produce void ratio profiles that agree well with excavation data in CRT. The axial stress response differs from the experimental sensor data. The sensor data is, however, not believed to be representative for the block material due to pores or low density around the sensors.

When the mechanical process (in terms of void ratio and net mean stress) and the stress state evolution were studied, however, the variable *M* formulation was thought to produce more realistic stress evolution and yield surface evolution as compared to the constant *M* formulation.

Hydraulic investigation

When studying the hydraulic behaviour, three different models are used. All models uses the variable *M* formulation discussed previously, but differs in the hydraulic representation in terms of retention curve and permeability.

Comparing the solutions of the three models with hydraulic sensor data shows that the models produce responses that agree well with the process in the experiment. The model equipped with a lower retention curve and a higher permeability is considered to agree best with the experimental data.

Pellet slot width variation in the CRT model

Three different pellet slot widths have been studied: 3, 5 (the CRT model) and 9 cm. The obtained average void ratios in the pellet slot, block and the total buffer is shown in Figure 5-28, repeated below in Figure 5-38.

The average pressures obtained in the three models are shown in Figure 5-31, repeated below in Figure 5-39.

The analytical solution is compared with the FE-models and is found to agree well.

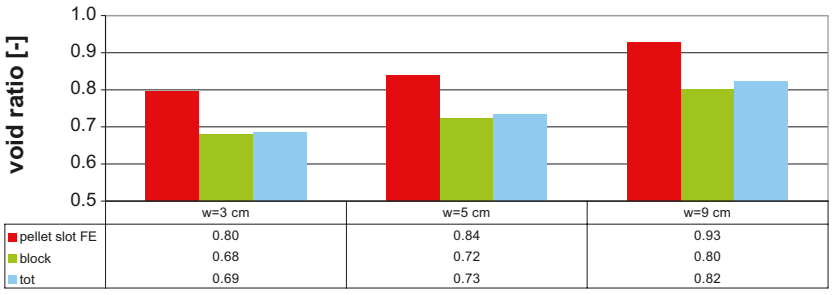

Figure 5-38. *Averages of void ratio for 3, 5 and 9 cm pellet slot.*

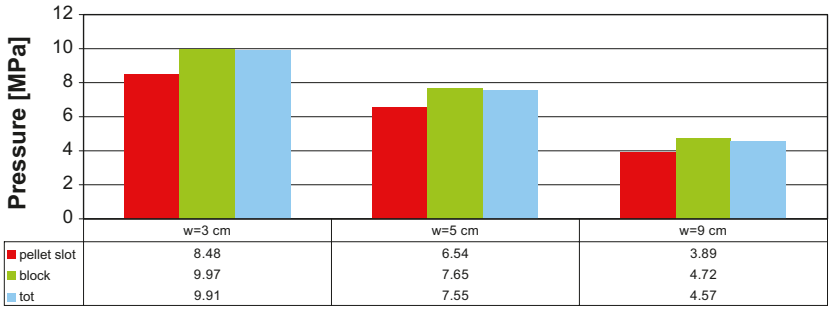

Figure 5-39. *Averages of pressure for 3, 5 and 9 cm pellet slot.*

Modelling pure serial and parallel wetting

To evaluate the generality of the formulation used by FE-solver (Code_Bright), two extreme cases with either pure serial or pure parallel wetting are modelled. To obtain reasonable results for the parallel wetting process without large modifications of the parameter setup the elastic flexibility was reformulated as constant. When this had been done the results agreed surprisingly well with what was expected for the two wetting processes.

The mechanism in the formulation that give rise to the nice results is however not dependent on any hysteresis in the retention curves, as expected from the analytical investigation. Instead, the reason is believed to originate in the mechanical formulation of the material. Expressed more explicit, in the expression of the volumetric strain increment generating the swelling during wetting, a modulus is formulated as dependent on the swelling pressure curve and this comes into play differently in the serial and parallel wetting processes.

5.9.3 Uncertainties

Analytical model

Due to the concept used, working with averages over the bentonite and pellet slot, the validity of the solutions depends on how well the properties can be represented by averages in the two materials.

The model heavily relies on that the expression of free retention is representative. The water ratio dependency of the parameters, *a* and *b*, obtained from evaluating experimental data, had a continuous appearance except for a water ratio of 0.17. An adjusted set of parameters were therefore used.

FE-model

Significant uncertainties are related to the mechanical part of the model. What is believed to be characteristic properties of bentonite clay, found from analyzing experimental data, are sometimes hard to mimic with the used mechanical constitutive law (a slightly modified BBM).

BBM also has a rather extensive number of parameter values to specify and due to lack of experimental data (or rather, data of specific dedicated experiments needed) the uncertainties in the adopted parameter values might be significant. When data is available, dependencies of the parameters are sometimes found that are not supported in the model. In these cases a suitable value of the parameter has to be estimated with the model behaviour in mind for the specific process considered.

This might stem from that BBM has a general phenomenological basis, valid for a broad range of geomaterials, but that bentonite, in a sense, is not a typical geomaterial. It seems like the underlying mechanisms, governing the material characteristics, work on a rather different scale (the montmorillonite mineral layers have interlayer distances on the nm-scale) as compared to typical geomaterials (sand, silt etc). As a consequence, phenomenological models developed with typical geomaterials in mind, might have shortcomings when simulating bentonite clay. A more suitable path might be if a model was developed from thermodynamical considerations.

As have been discussed in this task, there is a coupling between retention and the stress state for the bentonite clay. The retention curve formulations available in Code_Bright are based on an assumption of contained conditions, i.e. a stress evolution is implicitly adopted when specifying the retention curve. The implicitly adopted stress evolution might be close to or far from what the material is subjected to in the model. A more theoretically and experimentally correct formulation should be based on the retention for free swelling and the current stress state, as shown in the analytical model.

One issue that is not very influential for the geometry used here, but that might be significant for more unconstrained deformations, is that Code_Bright uses a small strain formulation. The small strain assumption is based on that second order terms in the displacement gradient are neglectable as compared to first order terms.

It has not been possible to study the mesh dependency of the THM-models due to covergency problems in the stress integration when using finer meshes. In Task 3, however, the mesh dependency of the TH-model was studied for the same mesh density as used here and for a model where the nuber of elements was doubled. The water saturation evolutions obtained with the two models were compared which indicated that the mesh dependency was insignificant. The influence from incorporate the mechanical process on the mesh dependency has not been studied and must therefore be taken as an uncertainity.

5.10 Abaqus analysis (Sections 5.10–5.19)

The following sections present the modelling work that has been done with the finite element code Abaqus /Abaqus Manuals 2008/.

5.11 Problem description

Most of the work for modelling CRT is done for the Task Force for Engineered Barrier Systems (TF-EBS), where the test is used as a modelling task. A detailed description of the results from this modelling will be reported in a separate report for the TF-EBS. The most relevant parts of this work regarding homogenisation are described in this chapter. The following calculations will be described:

1. 1D axisymmetric THM modelling of the 5 years period to the end of the test in a horizontal axisymmetric section through the center of the canister with correct initial conditions of the bentonite ring and all slots.
2. 2D axisymmetric THM modelling of the entire test with an axisymmetric mesh that includes also the deformable plug, the rock and the canister in addition to the bentonite rings, blocks and slots.
3. Continuation of the calculation of the test until full water saturation and homogenisation is reached in the entire buffer.

The reasons for continuing the calculation until full saturation is to predict the expected homogenised buffer in a real deposition hole.

The Canister Retrieval Test is described in several reports. The installation is described by /Thorsager et al. 2002/ and the dismantling, the sampling and the results of the density and water ratio determinations are described by /Johannesson 2007/. The detailed modelling results will be described in a future report.

A schematic view of the test layout is shown in Figure 5-40. The buffer material was artificially wetted along the rock surface up to 0.75 m from the plug/buffer interface and the filter pressurised with 800 kPa during about half the test period. The canister was equipped with heaters and the power 2.6 kW applied during about two years and then successively reduced. The neighbouring test (TBT) was also heated, which increased the temperature in the buffer of CRT with up to 10 degrees. Figure 5-41 shows the power and water pressure protocols of the tests.

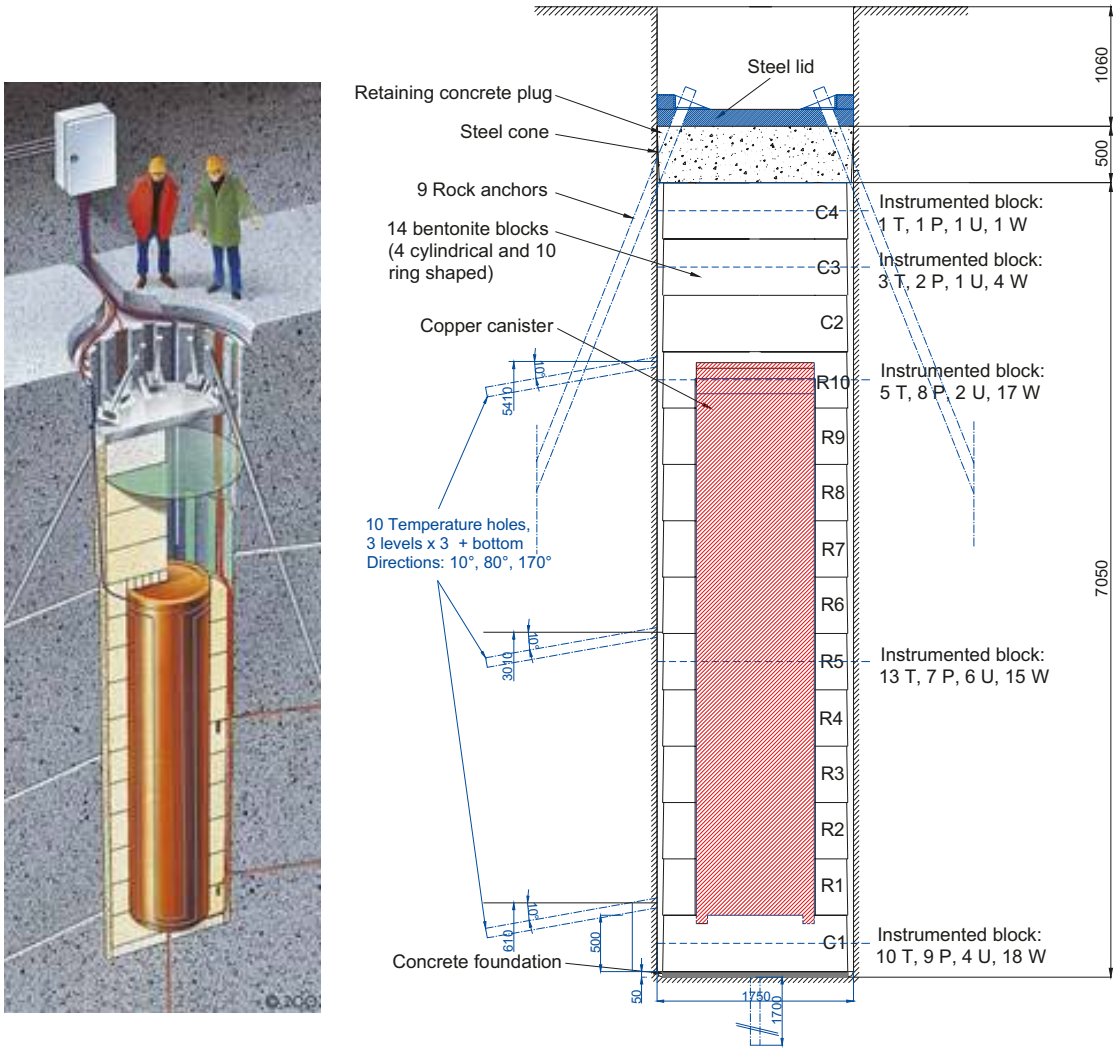

Figure 5-40. *Illustration of the Canister Retrieval Test. Sampling of the bentonite occurred down to the level of the upper surface of block R5. The bentonite below this level was removed using a non-mechanical retrieval technique. The drawing also shows the number and positions of the installed sensors (T=temperature, P=total pressure, U=pore pressure and W=relative humidity).*

5.12 Finite element models

The finite element program Abaqus has been used for the described calculations. Two element models, one that is a 1D axisymmetric model and one that is a 2D axisymmetric model have been used.

5.12.1 1D model

Figures 5-42 shows the geometry of the 1D model. The mesh consists of 350 axisymmetric elements with 1 mm thickness. The model represents a horizontal section located close to the centre of the canister. The canister and rock are not modelled but are represented by mechanical and hydraulic boundaries. Three materials with different properties are used to model the empty slot, the bentonite ring and the pellets filling.

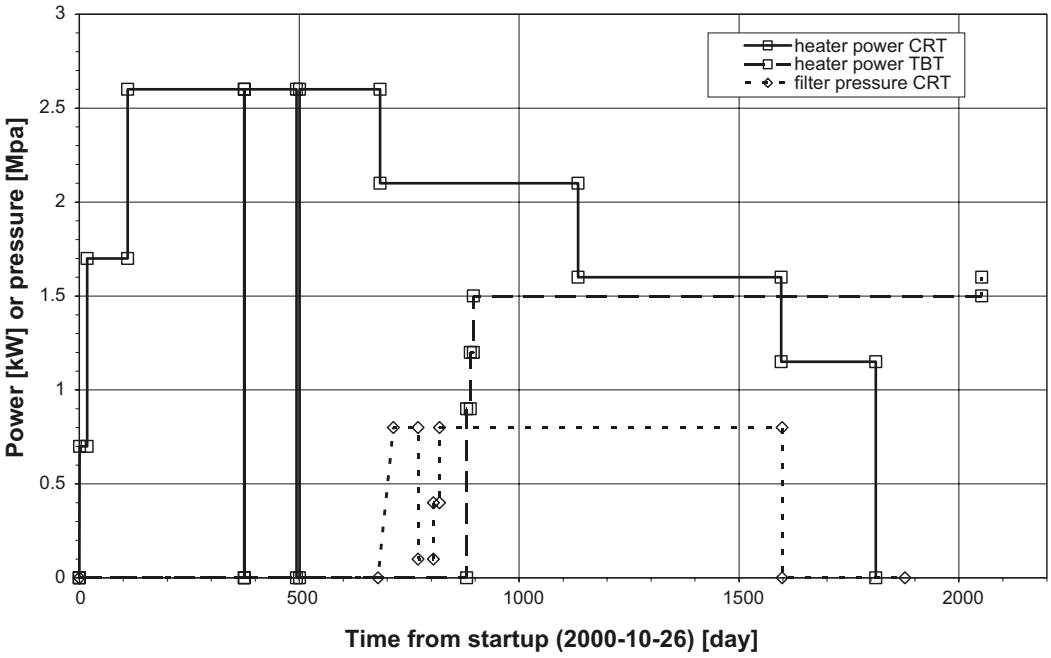

Figure 5-41. *Graph of the power protocols of CRT and TBT and the filter pressure of CRT.*

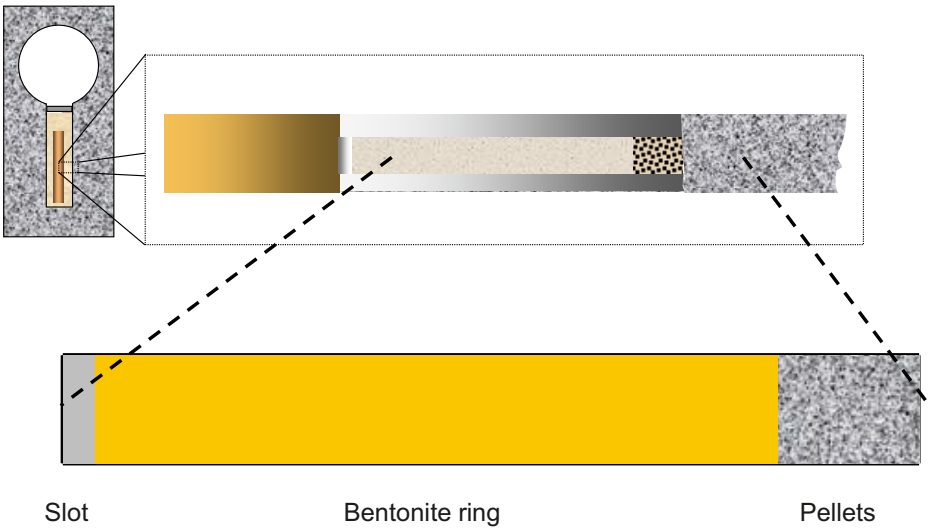

Figure 5-42. *The 1D model represents an axisymmetric cross section through the centre of the canister with the following dimensions*

- *Canister r=0.525 m*
- *Slot Δr=0.01 m*
- *Buffer ring Δr=0.285 m*
- *Pellets Δr=0.055*
- *Rock r>0.875 m*

5.12.2 2D model

Figure 5-43 shows the geometry and the element mesh of the 2D model. The model includes altogether five different bentonite materials (ring shaped blocks, solid blocks, bricks, pellets and the empty slot) and four other materials (canister, rock, concrete plug and steel lid).

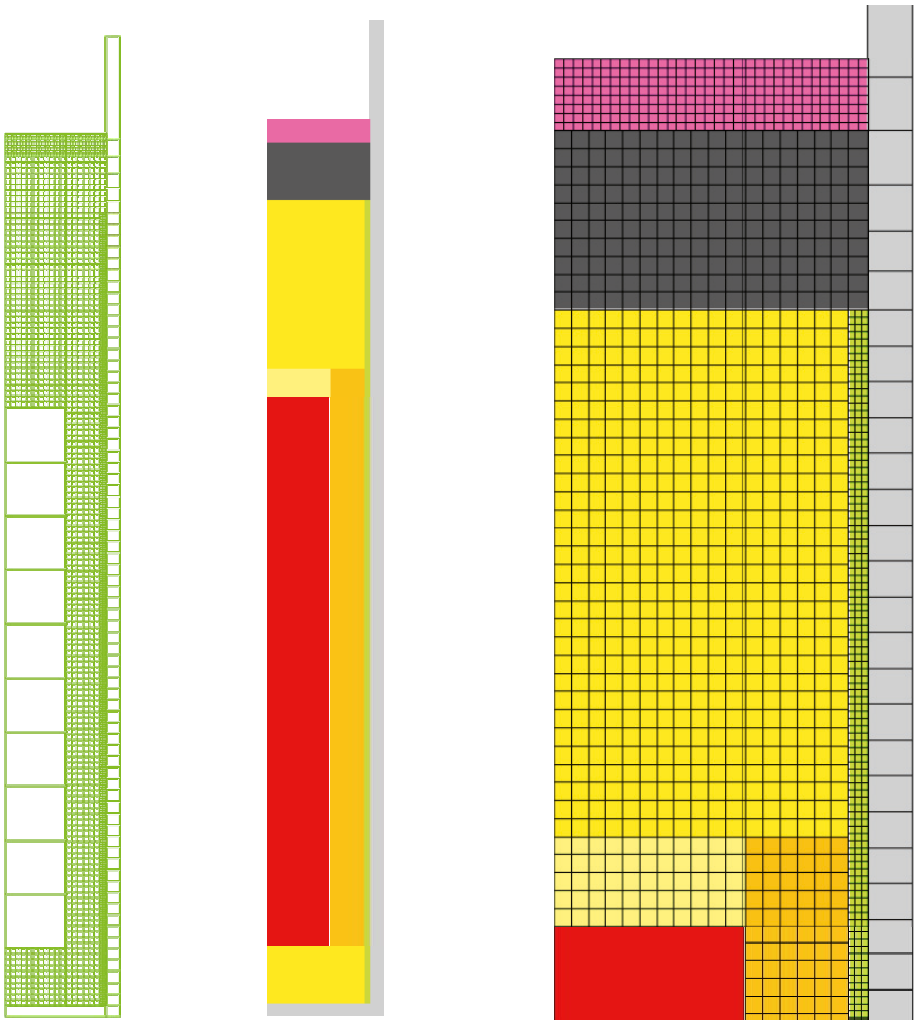

Figure 5-43. *Element mesh and property areas of the 2D model. The model is axial symmetric around the left boundary.*

5.13 Material properties

5.13.1 General

The model is composed of nine different materials, of which five are different bentonite models. The bentonite material MX-80 is used for all bentonite parts but with different densities and water contents, resulting in the same material model but different initial conditions. Table 5-15 shows the basic properties for four of the five bentonite parts. Pellets I refer to the pellets filled slot before water filling and Pellets II after water filling.

Table 5-15. Basic properties of four of the five bentonite parts.

Section	Density (kg/m³)	Water ratio	Dry density (kg/m³)	Void ratio	Degr. of saturation
Solid block	1,991	0,172	1,699	0,636	0,751
Ring shaped block	2,087	0,171	1,782	0,560	0,849
Bricks	1,883	0,165	1,616	0,720	0,637
Pellets I (dry)	1,101	0,100	1,001	1,778	0,156
Pellets II (water filled)	1,574	0,572	1,001	1,778	0,895

The three types of blocks are modelled as water unsaturated bentonite with the models developed for Abaqus. The pellets filling will change its density significantly during the wetting due to the swelling of the blocks. Since the model of unsaturated bentonite is not well suited for large volume changes and since the degree of saturation after the water filling is very high the pellets filling has been modelled as completely water saturated.

In addition there is a slot of 1 cm between the canister and the bentonite rings that has been assumed to be filled during the water filling of the pellets filling. This slot is modelled as a water filled space between two contact surfaces.

The other materials in the test are not modelled. Instead contact surfaces and boundary conditions are applied in order to yield a proper boundary to the buffer material.

5.13.2 Bentonite blocks

General

This chapter contains a description of the material models for the three types of bentonite blocks and the parameters included in the models.

The following processes are modelled:

Thermal

- Thermal flux from conduction

Hydraulic

- Water liquid flux
- Water vapour flux
- Hydraulic coupling between the pore water and the pore gas

Mechanical

- Mechanical behaviour of the structure
- Thermal expansion
- Mechanical behaviour of the separate phases
- Mechanical coupling between the structure and the pore water

The model includes complete coupling between all processes. The processes may be a function of the following variables:

- Temperature
- Degree of water saturation
- Void ratio

Required parameters

The required input parameters for the described THM model in Abaqus are the following:

Thermal

- Tables of thermal conductivity λ and specific heat c as function of void ratio e, degree of saturation S_r. and temperature (not used).

Hydraulic

- Table of the hydraulic conductivity of water saturated material K as function of void ratio e and temperature T.
- Influence of degree of saturation S_r on the hydraulic conductivity K_p expressed as the factor δ in Equation (5-21).

- The basic water vapour flow diffusivity D_{vTb} and the parameters a and b in Equations (5-24) to (5-25).
- The retention curve (table of the matric suction u_w as a function of the degree of saturation S_r).

Mechanical

- Porous bulk modulus κ according to Equation (5-28) and Poisson's ratio ν.
- Drucker Prager plasticity parameters β, d, Ψ, and the **yield function**.
- Bulk modulus and coefficient of thermal expansion of water (B_w, α_w) and bulk modulus solids (B_s).
- Bishops parameter χ in Equation (5-29) (usual assumption $\chi = S_r$).
- The volume change correction ε_v as a function of the degree of saturation S_r (the "moisture swelling" procedure).

Initial conditions

The following initial conditions of the elements in the structure need to be specified:

- void ratio e
- degree of saturation S_r
- pore pressure u (kPa)
- average effective stress p (kPa)
- temperature T (°C)

Material models of the ring-shaped blocks, solid blocks and the bricks

The models and data used for the buffer are essentially the same as used for modelling the wetting of KBS-3V for SR-Can /Börgesson et al. 2006/, but the parameters used are mainly valid for the void ratios 0.7–0.9. In the CRT the initial void ratio is 0.56–0.72 (except for the pellets filling), which requires recalibration of some of the data.

Thermal flux from conduction

The only thermal flux that is included in the model is thermal conduction with the following parameters:

λ = thermal conductivity
c = specific heat

The *thermal conductivity* has been measured as a function of the degree of saturation and density /Börgesson et al. 1994/. The parameter values for the Abaqus model are shown in Table 5-16 (linear interpolation between the values).

Table 5-16. Thermal conductivity λ of the buffer material as a function of the degree of saturation S_r and the void ratio e.

S_r	λ W/m,K		
	e=0.5	e=0.78	e=1.0
0	0.4	0.3	0.2
0.2	0.4	0.3	0.2
0.3	0.5	0.4	0.3
0.4	0.65	0.55	0.45
0.5	0.85	0.75	0.65
0.6	1.05	0.95	0.85
0.7	1.2	1.1	1.0
0.8	1.3	1.2	1.1
0.9	1.35	1.25	1.15
1.0	1.4	1.3	1.2

The *specific heat* has been calculated as the weight average of the specific heat of water and particles according to Equation (5-20).

$$c = 800/(1+w)+4{,}200w/(1+w) \quad (5\text{-}20)$$

Equation (5-20) yields the input parameters shown in Table 5-17 (linear interpolation).

Water liquid flux

The water flux in the liquid phase is modelled to be governed by Darcy's law with the water pressure difference as driving force in the same way as for water saturated clay.

The magnitude of the hydraulic conductivity K_p of partly saturated clay is a function of the void ratio, the degree of saturation and the temperature. K_p is assumed to be a function of the hydraulic conductivity K of saturated clay and the degree of saturation S_r according to Equation (5-21).

$$K_p = (S_r)^{\delta} K \quad (5\text{-}21)$$

where

K_p = hydraulic conductivity of partly saturated soil (m/s)
K = hydraulic conductivity of completely saturated soil (m/s)
δ = parameter (usually between 3 and 10)

For the MX-80 the standard value

$\delta = 3$

has been found to be satisfactory according to the calibration calculations.

Water transport driven by gravity and density gradients is included in the model as well.

The *hydraulic conductivity* of water saturated bentonite has been measured at different temperatures and void ratios /Börgesson et al. 1995/. Table 5-18 shows the values for the model.

Table 5-17. Heat capacity *c* of the buffer material as a function of the water ratio *w*.

w	c Ws/m,kg
0	800
0.1	1,109
0.2	1,367
0.3	1,585
1.0	2,500

Table 5-18. Hydraulic conductivity *K* as a function of void ratio *e* and temperature *T*.

T °C	e	*K* m/s
20	0.4	$0.035 \cdot 10^{-13}$
20	0.6	$0.2 \cdot 10^{-13}$
20	0.8	$0.65 \cdot 10^{-13}$
20	1.0	$1.75 \cdot 10^{-13}$
40	0.4	$0.05 \cdot 10^{-13}$
40	0.6	$0.31 \cdot 10^{-13}$
40	0.8	$1.0 \cdot 10^{-13}$
40	1.0	$2.75 \cdot 10^{-13}$
60	0.4	$0.07 \cdot 10^{-13}$
60	0.6	$0.44 \cdot 10^{-13}$
60	0.8	$1.45 \cdot 10^{-13}$
60	1.0	$3.85 \cdot 10^{-13}$
80	0.4	$0.1 \cdot 10^{-13}$
80	0.6	$0.55 \cdot 10^{-13}$
80	0.8	$1.8 \cdot 10^{-13}$
80	1.0	$4.9 \cdot 10^{-13}$

Water vapour flux

The water vapour flux is modelled as a diffusion processes driven by the temperature gradient and the water vapour pressure gradient (at isothermal conditions) according to Equation (5-22).

$$q_v = -D_{Tv}\nabla T - D_{pv}\nabla p_v \qquad (5\text{-}22)$$

where

q_v = vapour flow
D_{Tv} = thermal vapour flow diffusivity
T = temperature
D_{pv} = isothermal vapour flow diffusivity
p_v = vapour pressure

The isothermal vapour flow is neglected and thus $D_{pv} = 0$.

The thermal water vapour diffusivity D_{Tv} can be evaluated from moisture redistribution tests by calibration calculations. The following relations were found to yield acceptable results:

$$D_{Tv} = D_{Tvb} \qquad 0.3 \le S_r \le 0.7 \qquad (5\text{-}23)$$

$$D_{Tv} = D_{Tvb} \cdot \cos^{a}\left(\frac{S_r - 0.7}{0.3}\cdot\frac{\pi}{2}\right) \qquad S_r \ge 0.7 \qquad (5\text{-}24)$$

$$D_{Tv} = D_{Tvb} \cdot \sin^{b}\left(\frac{S_r}{0.3}\cdot\frac{\pi}{2}\right) \qquad S_r \le 0.3 \qquad (5\text{-}25)$$

a and b are factors that regulates the decreased vapour flux at high and low degree of saturation.

The diffusivity is thus constant with a basic value D_{Tvb} between 30% and 70% degree of saturation. It decreases strongly to $D_{Tv} = 0$ at 0% and 100% saturation. The influence of temperature and void ratio on the diffusivity is not known and not considered in the model.

The *thermal vapour flow diffusivity* D_{Tvb} and the parameters a and b according to Equations (5-23) to 5-25 have originally been evaluated for the void ratio 0.8 with calibration calculations of moisture redistribution tests. New tests have been performed at lower void ratios and those results confirm the following value:

$\boldsymbol{D}_{Tvb} = 0.7 \cdot 10^{-11}$ m^2/s,K
$a = 6$
$b = 6$

Hydraulic coupling between the pore water and the pore gas

The pore pressure u_w of the unsaturated buffer material, which is always negative, is modelled as being a function of the degree of saturation S_r independent of the void ratio (*water retention curve*).

$$u_w = f(S_r) \qquad (5\text{-}26)$$

The pore air pressure is not modelled.

The water retention curves have been evaluated according to a method developed by /Dueck and Börgesson 2007/. The evaluation is described in Appendix E. Since the void ratio differs in the different buffer blocks different curves are required. Figure 5-44 shows the evaluated retention curves.

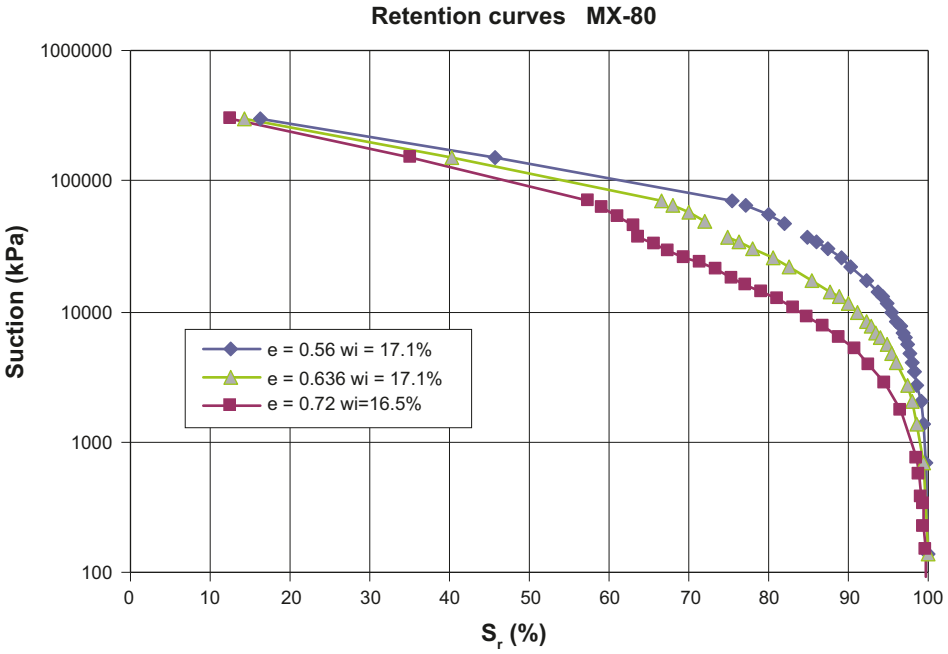

Figure 5-44. *Retention curve of MX-80 at the void ratio 0.56 (rings), 0.636 (blocks) and 0.72 (bricks).*

Since the water transport in Abaqus is governed by the pore water pressure (u_w) but the measurements are in relative humidity (R_h) a conversion from calculated negative pore water pressure to relative humidity has also been done. The conversion according to Equation (5-27), which is derived from thermodynamic considerations (see e.g. /Dueck 2004/), has been used.

$$R_h = exp(u_w/462T) \quad (5\text{-}27)$$

where T = absolute temperature (t+273)

Mechanical behaviour of the structure

The mechanical behaviour has been modelled with a non-linear Porous Elastic Model and Drucker-Prager Plasticity model. The effective stress theory is applied and adapted to unsaturated conditions and the shortcomings of this theory are compensated for by a correction called moisture swelling (see below).

The *Porous Elastic Model* implies a logarithmic relation between the void ratio e and the average effective stress p according to Equation (5-28).

$$\Delta e = \kappa \Delta \ln p \quad (5\text{-}28)$$

where κ = porous bulk modulus

Poisson's ratio v is also required.

Drucker Prager Plasticity model contains the following parameters:

β = friction angle in the p-q plane
d = cohesion in the p-q plane
ψ = dilation angle
q = $f(\varepsilon^d_{pl})$ = yield function

The yield function is the relation between Mises' stress q and the plastic deviatoric strain ε^d_p at a specified stress path. The dilation angle determines the volume change during shear.

The following data has been used for the *Porous Elastic* model:

$\kappa = 0.20$
$\nu = 0.4$

The value of κ has been derived from oedometer and swelling pressure tests /Börgesson et al. 1995/.

The following data was used for the *Drucker Prager Plasticity* model:

$\beta = 0.001°$
$d = 3{,}000$ kPa
$\psi = 2°$
yield function: Ideally plastic (no hardening)

The low friction angle and high cohesion are motivated by evidence that the strength is mainly a function of the void ratio, independently of the degree of saturation, and not the effective stress /Börgesson and Johannesson 1995/.

Thermal expansion

The volume change caused by the thermal expansion of water and particles can be modelled with the parameters

α_s = coefficient of thermal expansion of solids
α_w = coefficient of thermal expansion of water

Only the expansion of the separate phases is taken into account. The possible change in volume of the structure by thermal expansion (not caused by expansion of the separate phases) is not modelled. However, a thermal expansion in water volume will change the degree of saturation which in turn will change the volume of the structure. The following values have been used:

$\alpha_w = 3.0 \cdot 10^{-4}$
$\alpha_s = 0$

Mechanical behaviour of the separate phases

The water and the particles are mechanically modelled as separate phases with linear elastic behaviour. The pore air is not mechanically modelled. The following standard values have been used for the *properties of the water and solid phases*:

$B_w = 2.1 \cdot 10^6$ kPa (bulk modulus of water)
$B_s = 2.1 \cdot 10^8$ kPa (bulk modulus of solids)
$\rho_w = 1{,}000$ kg/m^3 (density of water)
$\rho_s = 2{,}780$ kg/m^3 (density of solids)

Mechanical coupling between the structure and the pore water

The mechanical behaviour is modelled to be governed by the effective stress theory and a procedure called moisture swelling.

Effective stress theory

The effective stress concept according to Bishop is used for modelling the mechanical behaviour of the water-unsaturated buffer material:

$$s_e = (s - u_a) + \chi(u_a - u_w) \qquad (5\text{-}29)$$

Equation (5-29) is simplified in the following way:

$u_a = 0$ (no account is taken to the pressure of enclosed air)
$\chi = S_r$

Moisture swelling

The shortcomings of the effective stress theory can be compensated in Abaqus by a correction called "*moisture swelling*". This procedure changes the volumetric strain ε_v by adding a strain that can be made a function of the degree of saturation S_r.

The effective stress theory decomposes the total stress into pore pressure and effective stress (which only depends on deviatoric strains). However, the effective strain can be made dependent on saturation by using the concept of *moisture swelling* which modify the effective strain by this user defined saturation dependent volumetric strain (*moisture swelling*). In this application the moisture swelling contribution is calibrated by using the measured swelling pressure and assuming that the effective strain (after adding the moisture swelling) should be zero. Neglecting moisture swelling will imply an effective strain defined by the elastic material (porous elastic) and thus the moisture swelling strain can be calculated from Equations (5-30) and (5-31).

$$\Delta\varepsilon_v = f(S_r) = \ln(p_0/p)\cdot\kappa/(1+e_0) \quad (5\text{-}30)$$

$$p = p_{tot} - u_w\cdot S_r \quad (5\text{-}31)$$

where

ε_v = volumetric strain
p_0 = initial effective stress taken from the initial conditions
p = actual effective stress
κ = porous bulk modulus (from Equation (5-28))
e_0 = initial void ratio
p_{tot} = actual total stress
u_w = pore water pressure
S_r = degree of water saturation

The moisture swelling relation (*M.S.*) that is needed as input is the logarithmic volumetric strain according to Equation (5-32) where $\Delta\varepsilon_v$ is taken from Equation (5-30).

$$M.S. = \ln(1+\Delta\varepsilon_v) \quad (5\text{-}32)$$

The data for the *moisture swelling procedure* is derived from the assumption that the relation between total stress and degree of saturation of a confined sample (constant volume) is linear when the degree of saturation is increased from its initial value to 100% /Dueck and Börgesson 2007/. This relation is linked to the retention curve. The derivation of the retention curve and the moisture swelling relation is described in Appendix E.

The derived moisture swelling relations are shown in Figure 5-45 for all three bentonite block types.

In order to check that the different bentonite block types behave according to the description in Appendix E one element tests of drying and wetting have been simulated. The volume was kept constant and the degree of saturation stepwise changed from the initial conditions to 100% and to 0%. Figure 5-46 shows the calculated average stress in the element as a function of the degree of saturation.

Figure 5-46 shows that the bentonite block types behave according to the model. From the stress-less initial state the total average stress increases linearly with increasing degree of saturation until the swelling pressure at full saturation is reached at the degree of saturation 100%. The behaviour at decreasing degree of saturation is identical but merely theoretical since real samples cannot keep their original volumes but will shrink instead of having negative stress. In the real model high tensile average stresses will be kept but if they are transferred to the boundary the contact elements will open up, which leads to shrinkage of the buffer, since the contacts have no cohesion.

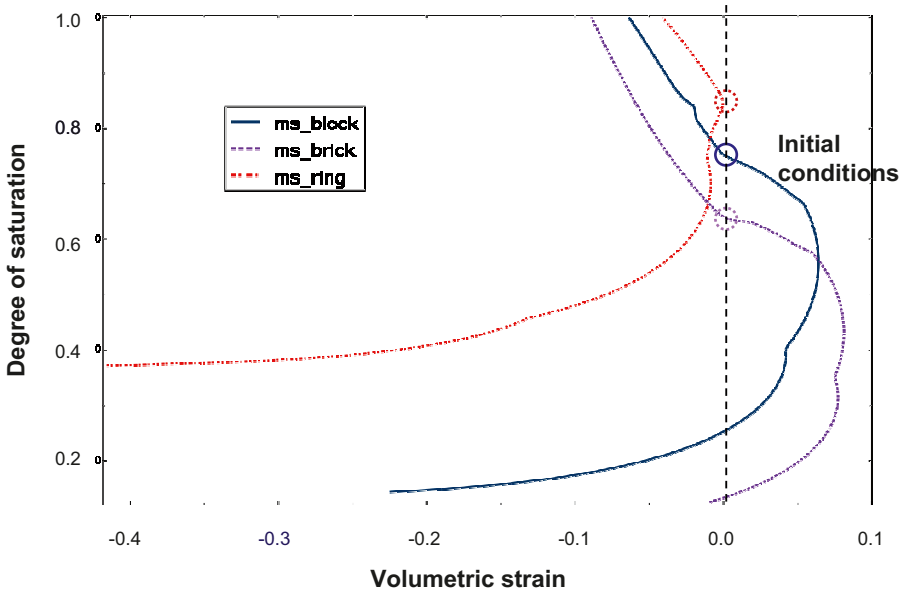

Figure 5-45. *Volume change correction $\Delta\varepsilon_v$ used in the moisture swelling procedure for the three different bentonite block types. The initial conditions are also noted in the figure.*

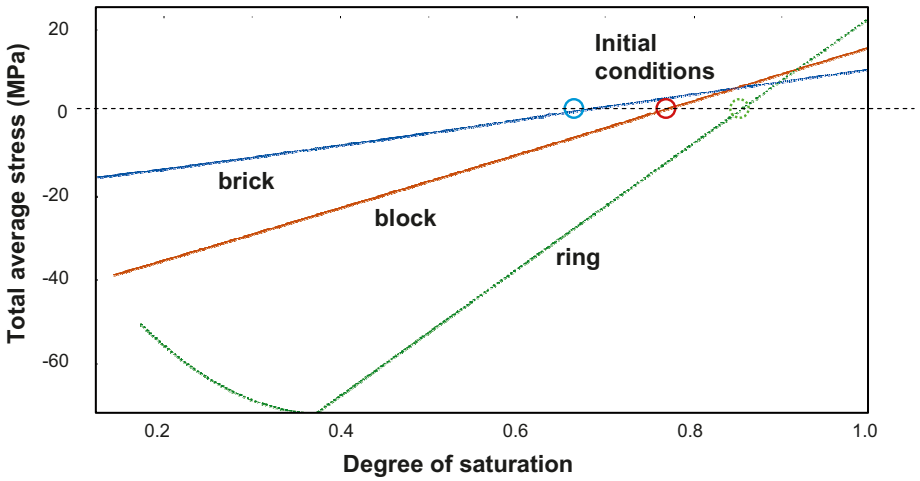

Figure 5-46. *One element tests of confined samples of the three different block types.*

5.13.3 Other buffer parts

The bentonite pellets and the gap between the rings and the canister are modelled as water saturated bentonite since the slot with pellets was artificially filled with water at the start of the experiment.

Bentonite pellets

Thermal: Thermal conductivity λ according to Table 5-19 and specific heat c according to Table 5-17 (above).

Hydraulic: See Table 5-18.

Mechanical: Porous elastic and Drucker Prager plasticity with the same properties as the bentonite blocks

Gap between rings and the canister

Thermal:

λ = 0.5 W/m,K
c = 4,200 Ws/m,kg

Hydro-mechanical:

The gap has been mechanically modelled by using contact definitions between the buffer and the canister where the initial gap volume is assumed to be filled with water.

For the themal analysis the gap has been modelled by using elements with thermal properties specified as above.

5.13.4 Other materials

The other parts of the CRT than the bentonite parts have been modelled in a very simplified way, mostly as boundary conditions. Since the thermal calculations have been simplified and use the calculation described in Appendix E as boundary conditions for the bentonite parts no description of the thermal properties will be made.

Canister

The canister has been modelled as an permeable elastic material with the following properties:

E = $2.1 \cdot 10^9$ kPa
v = 0.3
λ = 1.0 W/m,K
c = 1.0 Ws/m,kg
K = 1.0

Rock

The rock has been modelled as an impermeable material with the following properties:

E = $1.85 \cdot 10^7$ kPa
v = 0.25
λ = 1.0 W/m,K
c = 1.0 Ws/m,kg

Concrete plug

The concrete plug has been modelled as an impermeable elastic material with the following properties:

E = $1.85 \cdot 10^7$ kPa
v = 0.25

Table 5-19. Relation between thermal conductivity λ and void ratio e for the pellets filling.

e	λ W/m,K
0.78	1.3
1.0	1.2
1.4	1.1
1.78	1.0

Steel lid

The steel plug is made of a 20 cm thick steel plate. It is anchored by 9 anchor rods fixed to the top of the steel plate. In order for the plug to simulate a deformable backfill the anchor rods were fixed about 5 m deep into the anchor holes leaving about 5 m rods that elastically can be lengthened. Measurements of the force in the anchors and the displacement of the plug have showed that the plug was displaced 17 mm at the total force of 8,000 kN.

In order to simulate the elasticity in the rods the steel plate was made with an E-modulus that gives the same deformation as the lengthening of the rods. Back-calculation of 17 mm displacement from the force 8,000 kN along a 20 cm thick plate with the diameter 1.75 m gives the following E-modulus that was applied for the plate:

$E = 3.9 \cdot 10^4$ kPa
$\nu = 0.3$ (standard value for steel)
$\lambda = 1.0$ W/m,K
$c = 1.0$ Ws/m,kg

5.14 Initial conditions

The following initial conditions have been applied for the bentonite parts:

Buffer rings

$e = 0.56$
$u = -37{,}000$ kPa
$S_r = 0.849$
$p = 31{,}413$ kPa
$T = 17$°C

Buffer blocks

$e = 0.636$
$u = -37{,}000$ kPa
$S_r = 0.751$
$p = 27{,}787$ kPa
$T = 17$°C

Buffer bricks

$e = 0.72$
$u = -37{,}500$ kPa
$S_r = 0.637$
$p = 23{,}888$ kPa
$T = 17$°C

Pellets

$e = 1.78$
$u = -50$ kPa
$S_r = 1.0$
$p = 50$ kPa
$T = 17$°C

5.15 Boundary conditions and couplings

The structure is axisymmetric around the centre line of the deposition hole. The following boundary conditions were applied:

Mechanical

- Fixed outer boundaries of the rock.
- Common nodes between bentonite materials.
- Contact surfaces with friction at the boundaries between the buffer and the canister (ϕ_c=11.3°).
- Contact surfaces with friction at the boundaries between the buffer and the rock (ϕ_c= 0°).
- The steel lid top surface locked (the lid simulates the anchor stiffness).
- Canister free to move.

Thermal

- Temperature history on canister and rock surfaces according to the results from the modelling shown in Appendix B.

Hydraulic boundaries of the buffer

- Inner: no flow.
- Outer: in filters according to water pressure protocol.
- No flow in buffer/rock contact.

The water pressure protocol for the filters is shown in Table 5-20 (see also Figure 5-41).

5.16 Calculation cases and sequences

Two models with totally three main calculations have been made:

- 1D axisymmetric model of a horizontal section through the centre of the canister.
  - Until start excavation (1,919 days).
- 2D axisymmetric model of the entire test geometry.
  - Until start excavation (1,919 days).
  - Until full saturation and homogenisation has been reached in the entire buffer.

Detailed description and evaluation of the modelling results will be made in another report. In the present report the results of the saturation and homogenisation histories of the 1D model and only the results after full saturation in the 2D model will be shown.

Table 5-20. Water pressure protocol for the filters in CRT.

Date	Day	Water pressure (MPa)	Comments
00-10-26	0	0	
02-09-05	679	0	Gradual increase water pressure
02-10-10	714	0.8	
02-12-05	770	0.1	
03-01-09	805	0.4	
03-01-23	819	0.8	
05-03-12	1,598	0	Probably dry after this date
05-12-16	1,877	0	Air flushed

All calculations have been done in the following steps:

1. Thermal calculation with the initial conditions of the materials.
   – Boundary conditions: Evolution of canister and rock temperature according to the temperature model in Appendix B.
2. Hydro-Mechanical calculation.
   – Establishment of equilibrium at initial conditions.
   – HM-calculation with temperature results according to step 1 and hydraulic boundary conditions according to the water pressure protocol.
3. Repetition of 1 and 2 until the results are identical.

5.17 Results from the 1D calculation

Complete water saturation does not mean that the homogenisation process is completed but the pore water pressure has also to be equalised in the entire section. Both measurements and calculations show that the buffer between the canister and the rock was completely water saturated and had finished its homogenisation process at the end of the test.

The modelled evolution of temperature and degree of saturation in some points in the cross section between the canister and the rock is shown in Figure 5-47. Figure 5-48 shows corresponding diagrams of the pore water pressure and dry density.

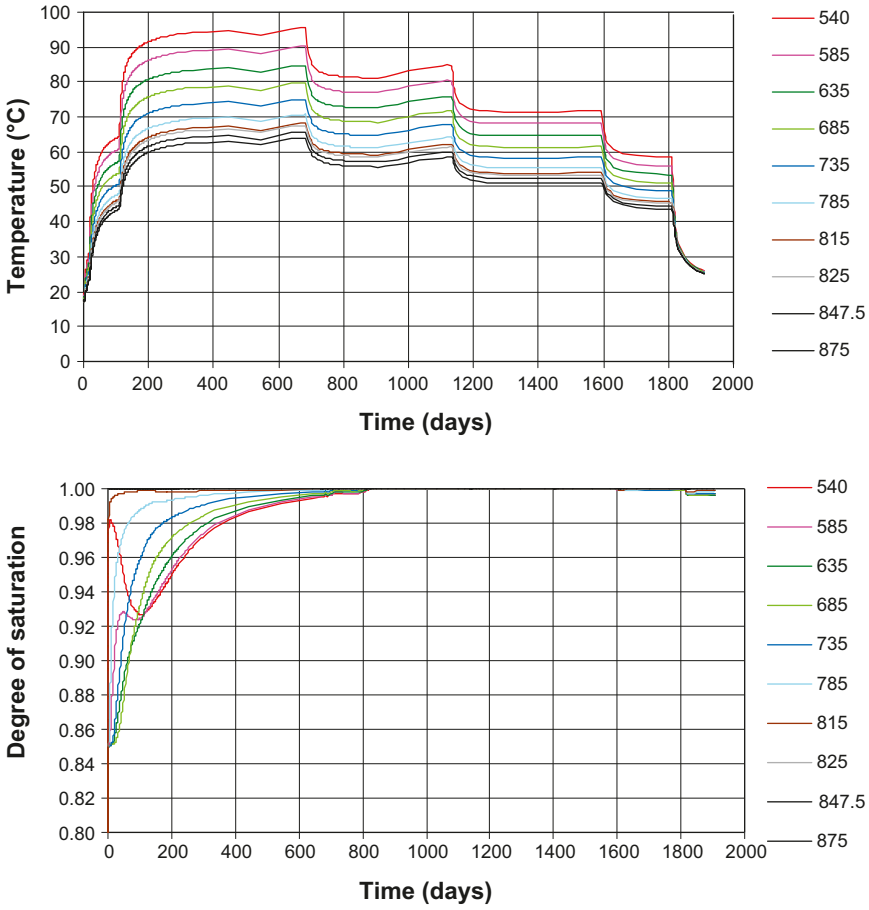

Figure 5-47. *Calculated evolution of temperature and degree of saturation in the central section of the buffer in the CRT. The legend shows the radial distance from the centre line (mm). The canister/buffer interface is located at r=525 mm and the buffer/rock interface is located at r=875 mm.*

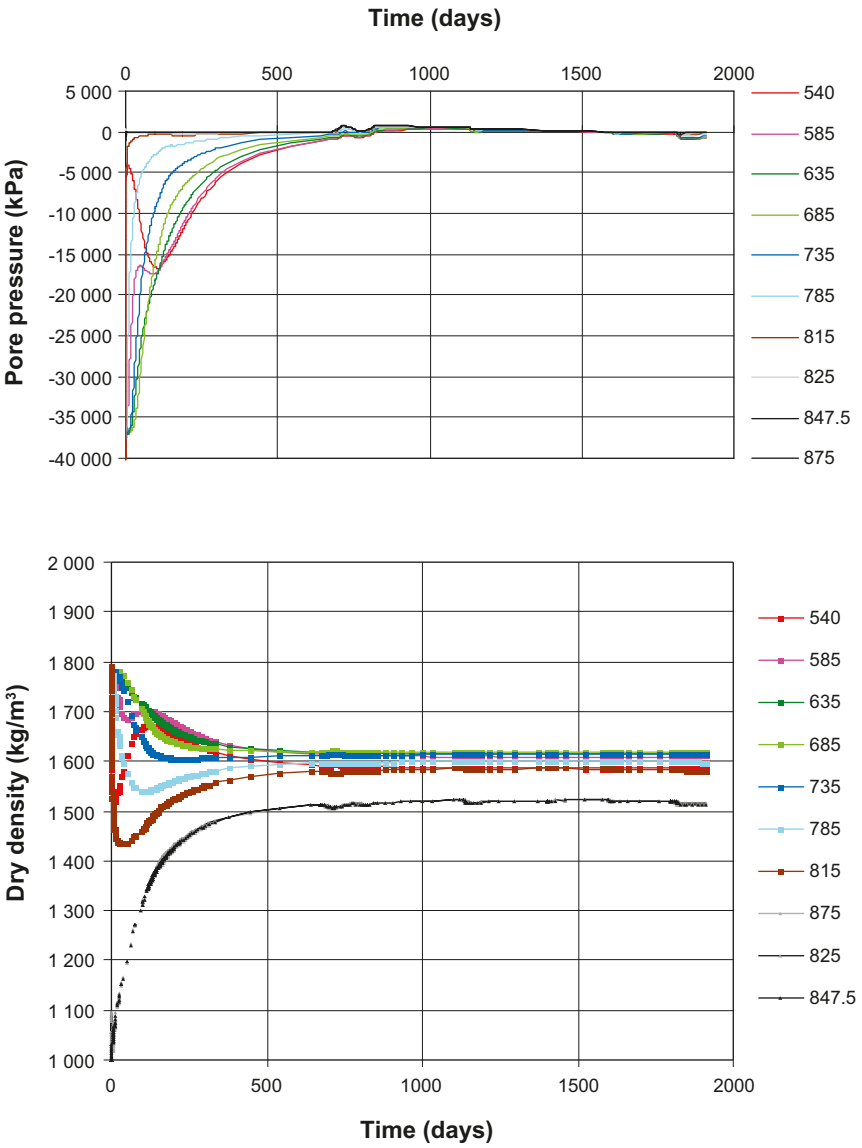

Figure 5-48. *Calculated evolution of pore water pressure and dry density in the central section of the buffer in the CRT. The legend shows the radial distance from the centre line (mm). The canister/buffer interface is located at r=525 mm and the buffer/rock interface is located at r=875 mm.*

The figures clearly show that the homogenisation is completed at the end of the test. The saturation and the pore pressure equalisation as well as the swelling/compression seem to be finished after about 1,000 days or slightly less than 3 years although there are some small effects caused by the change in water pressure and temperature also later.

The evolution of suction, pore water pressure, total pressure and temperature in the buffer was continuously measured with a large number of instruments. Figure 5-49 shows results from suction measurements in three different positions between the rock and the canister and comparisons with modelling results. Two different types of transducers were used; Wescor psychrometers for suction values below 5 MPa and Vaisala RH sensors of capacity type for higher suction. The comparison shows that the modelling results and the measurements agree very well with exception of the final remaining measured suction of about 1.5 MPa that is not modelled (part of which is caused by the salt concentration in the ground water).

The measurements thus confirm that the buffer in this region is water saturated a long time before the end of the test and thus also has had time to complete the homogenisation process.

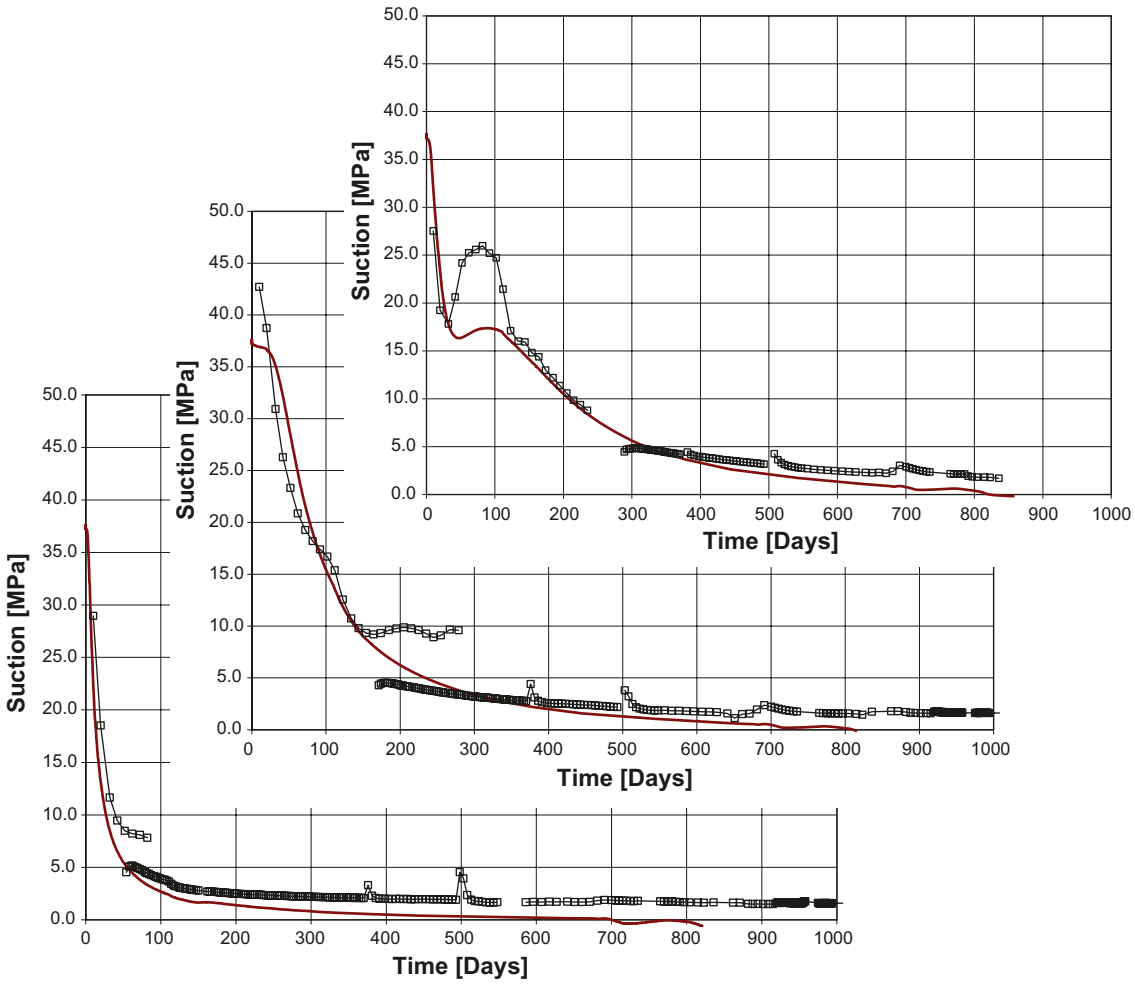

Figure 5-49. *Measured and modelled (red line) suction at the radius 785 mm (left), 685 mm (middle) and 585 mm (right) in a central section of the buffer.*

It is thus relevant to compare the modelled and measured density distribution at the end of the test in order to evaluate if the homogenisation of the buffer is well modelled. Figure 5-50 shows a comparison between modelled and measured density distribution at the end of the test. The density distribution was measured after careful sampling /Johannesson 2007/.

Figure 5-50 shows that there is a very good agreement between measured and modelled dry density distribution. The swelling of the bentonite ring from the dry density of almost 1,800 kg/m^3 to slightly higher than 1,600 kg/m^3 is well modelled as well as the compression of the pellets filling from the dry density 1,000 kg/m^3 to about 1,500 kg/m^3. The 1 cm gap has been closed but there is still a slightly lower density at the canister contact both according to the model and the measurements. The measured density of the pellets filled slot varies somewhat between the different directions, which probably is caused be a difference in initial slot width due to that the ring is placed somewhat off centre. The average value though seems to fit the modelled value well.

The results from the 1D calculation thus verify the material model of the unsaturated backfill at least regarding the final stage of the homogenisation. The modelled stresses in the bentonite were generally about 2 times larger than the measured ones, but those measurements could not be used for verification since the stress measurement gauges were not suitable. Calibration of the sensors afterwards indicated that the sensors measured about half the actual stress in the bentonite.

It is worth mentioning that the modelled results are not derived after parameter adaptation in order to reach the best agreement. On the contrary, the parameter values have been derived directly from laboratory tests and used in the calculation without any changes.

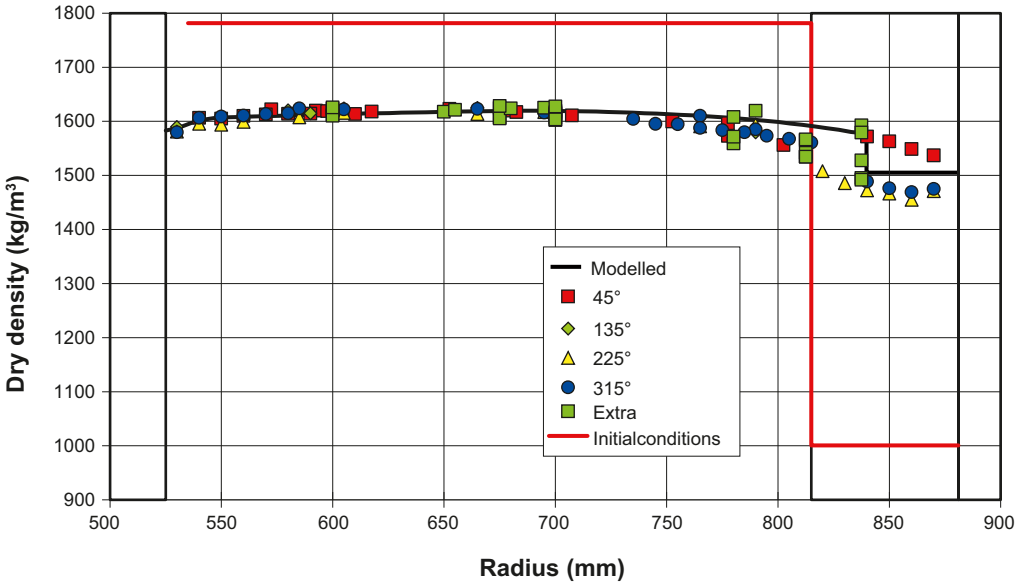

Figure 5-50. *Measured and modelled (black line) density distribution at the end of the test. The initial conditions are shown as a red line. The measurements have been done along radiuses with four different directions marked as different angles.*

5.18 Results from the 2D calculation

As reported earlier the entire CRT has been modelled with a 2D axisymmetric model. The results from this modelling will not be shown in this report since the bentonite outside the section modelled with the 1D model (above and below the canister) was far from water saturated at the end of the test. Instead the calculation has been continued with wetting until complete saturation was reached in the entire test. This is done in order to illustrate the expected final state of the buffer.

An important property for the homogenisation of the buffer above the canister is the properties of the backfill material. The plug in the CRT was made flexible in order to simulate a special stiffness of the backfill.

The calculation has been run to more than 3,000 years, which is far more than needed to reach equilibrium, which is achieved in the last saturated point on top of the canister after about 100 years.

The final state is shown in Figures 5-51 and 5-52. Figure 5-51 shows the dry density distribution and the vertical swelling. Figure 5-52 shows the radial and axial stresses.

Figure 5-51 shows the following:

- The total upwards swelling of the buffer/“backfill” interface is about 3 cm.
- The displacement of the canister is very small (< 1 mm).
- The density distribution is rather heterogeneous with high density (>1,630 kg/m^3) mainly below the canister and low density close to the rock (≈ 1,550 kg/m^3).
- Rather homogeneous density distribution between the canister and the “backfill” with the density (≈ 1,600 kg/m^3).
- Low density at the “corner” of the buffer in the contact between the “backfill” and the rock.
- No decrease in density towards the “backfill” in spite of the upwards swelling.

Figure 5-52 shows the following:

- Large difference in radial swelling pressure (≈ 7.6 MPa) and axial swelling pressure (>10 MPa) in the buffer between the canister and the rock.

- Low swelling pressure at the “corner” of the buffer in the contact between the “backfill” and the rock.
- No decrease in swelling pressure towards the “backfill” in spite of the upwards swelling.

The total axial force on the plug is 16,600 kN, which yields an average vertical stress of 6.9 MPa.

The only remarkable observation is that there is no obvious decrease in density and swelling pressure towards the “backfill” in spite of the upwards swelling of 3 cm. This results deviates from the results shown in Chapter 8 and reported by /Börgesson and Hernelind 2009/, where the mechanical buffer/backfill interaction is studied. There are several factors that in combination may explain this difference:

- The buffer material was in the swelling calculations modelled as being completely saturated and homogenised from start, which means that the swelling pressure and the friction against the rock was fully developed from start. This is not the case for the calculation made in this chapter where the initially low density of the pellets filling and initially unsaturated buffer blocks result in a lower friction between the rock and the buffer during a large part of the swelling process.
- The upper 75 cm (where no filter was applied) was wetted later, which delayed the mobilization of the friction.
- The upwards swelling of the buffer interface was only 3 cm which limits this effect.

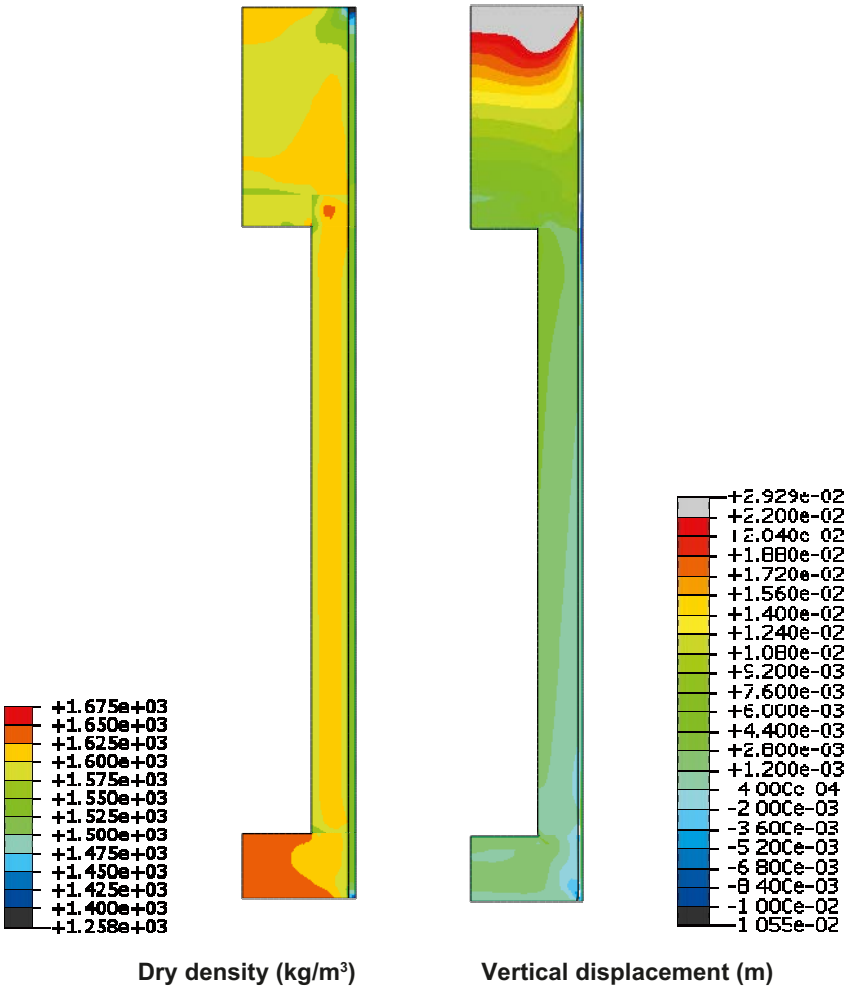

Figure 5-51. *Final state of the buffer after full saturation and completed homogenisation. The distribution of the dry density and the vertical swelling is shown.*

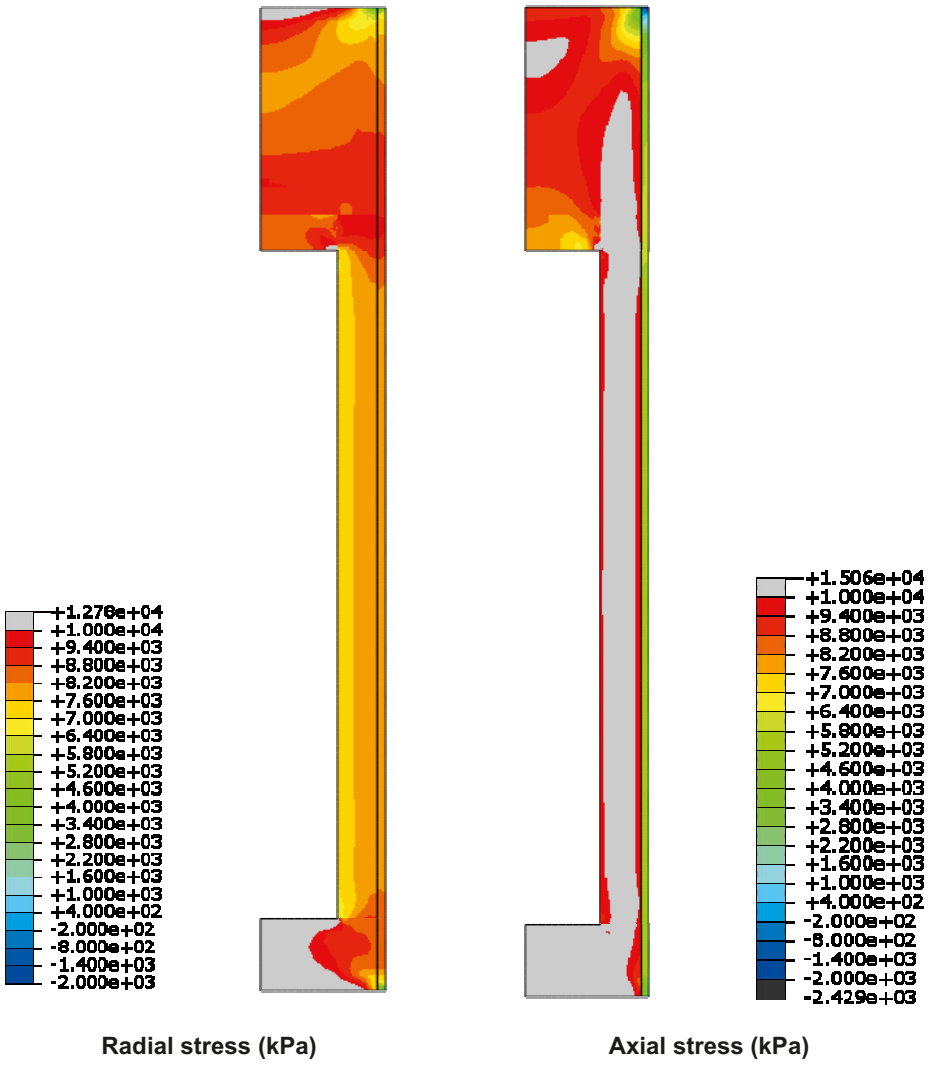

Figure 5-52. *Final state of the buffer after full saturation and completed homogenisation. The distribution of radial and axial stress is shown.*

5.19 Conclusions and uncertainties

Modelling of the Canister Retrieval Test (CRT) and comparison with measurements confirm that the material model of unsaturated bentonite blocks and the calculation technique used are relevant for modelling the homogenisation process, since the agreement between modelled and measured density distribution in the buffer between the canister and the rock after full saturation and finished homogenisation was very good. The material model and calculation technique were then used to model the homogenisation process in an entire deposition hole with identical initial conditions and boundary conditions with those in CRT. The results shown in Figures 5-51 and 5-52 gave an expected final density and stress distribution in a deposition hole covered with a backfill that is compressed about 3 cm.

Very similar results were reached with the Abaqus and the Code_Bright models but the entire test was only modelled with Abaqus.

The uncertainties are mainly the material models, which are very complicated, and the parameters values. Although they have been verified for the 1D case of swelling and homogenisation of the bentonite rings and pellets between the canister and the rock, the 2D case involves more degrees of freedom for the variables and more interactions like the friction between the bentonite and the rock or canister. The influence of the history of wetting (i.e. where and in what rate the water is available in the rock) is probably not neglectable but so far not investigated.

6 Homogenisation after loss of bentonite mass

6.1 Introduction

The swelling properties of bentonite make the buffer and backfill material swell and close open gaps or channels to form a more homogeneous buffer. These properties are important not only for homogenising the buffer and backfill after installation of the bentonite blocks but also after long time if openings in the buffer and backfill would appear.

6.2 Problem description

Except for the natural slots that exist after installation, which are treated in task 5 (natural homogenisation), such spaces may appear due to several processes:

1. The unexpected event of missing bentonite rings caused by severe mistakes during installation.
2. Erosion before closure of the repository caused by water inflow into deposition holes and deposition tunnel if the water inflow is not prevented by the bentonite until the water flow and high water pressure gradients are stopped by temporary plugs. If the erosion is strong, large openings of missing bentonite may locally be formed.
3. Long term erosion of bentonite in fractures intersecting the deposition hole or the deposition tunnel mainly caused by bentonite dispersion and subsequent colloid transportation after fresh water intrusion.
4. Small channels caused by piping and rather limited short term erosion.

6.2.1 Loss of buffer material

The swelling and sealing of bentonite cannot take place unhindered since there is a resistance to swelling caused by friction both internally in the bentonite and between the bentonite and the surrounding fixed walls represented by the rock surface and in some cases the canister.

In order to investigate how well the buffer material seals the openings resulting from the mentioned processes a number of finite element calculations with the code Abaqus have been performed. These calculations are described in this chapter.

6.2.2 Loss of backfill material

Loss of backfill material may indirect cause loss of buffer material, since the resistance to upwards swelling of the buffer, that is created by the swelling pressure and low compressibility of the backfill, may be lost if backfill above the deposition hole is lost.

The consequences of massive loss in backfill material have been investigated by simplified analytical calculations. This investigation is reported in Appendix F.

6.3 Bentonite properties

6.3.1 General

The bentonite has been modelled as completely water saturated. This is for some scenarios a simplification since e.g. erosion before closure of the repository takes place before full saturation of the buffer. The motivation for assuming full water saturation is manifold:

- The mechanical models of unsaturated bentonite are very complicated and not sufficiently good for modelling the very strong swelling that takes place after such large loss of bentonite.
- The models for water saturated bentonite are much simpler and well documented.
- The stress path and time schedule will differ if saturated instead of unsaturated bentonite is modelled but the final state will be very similar.

6.3.2 Material model

The **mechanical properties** of the buffer controlling the swelling and consolidation phase are based on the models and properties derived for MX-80 by /Börgesson et al. 1995/. *Porous Elasticity* combined with *Drucker Prager Plasticity* has been used for the swelling/consolidation mechanisms, while *Darcy's law* is applied for the **water flux** and the *Effective Stress Theory* is applied for the **interaction pore water and structure**.

Mechanical properties

The *Porous Elastic Model* implies a logarithmic relation between the void ratio e and the average effective stress p according to Equation (6-1).

$$\Delta e = \kappa/(1+e_0)\Delta \ln p \qquad (6\text{-}1)$$

where κ = porous bulk modulus, e_0 = initial void ratio.

Poisson's ratio v is also required.

Drucker Prager Plasticity model contains the following parameters:

β = friction angle in the p-q plane
d = cohesion in the p-q plane
ψ = dilation angle
$q = f(\varepsilon^d_{pl})$ = yield function

The yield function is the relation between Mises' stress q and the plastic deviatoric strain ε^d_p at a specified stress path. The dilation angle determines the volume change during shear.

The following data has been derived and used for the *Porous Elastic* model (valid for e<1.5):

κ = 0.21
v = 0.4

The following data has been derived for the *Drucker Prager Plasticity* model

β = 17°
d = 100 kPa
ψ = 2°

The yield function is shown in Table 6-1.

In some calculations the data for the *Drucker Prager Plasticity* model has been varied in order to study the influence of the friction angle, the cohesion and the dilation.

Hydraulic properties

The hydraulic conductivity is a function of the void ratio as shown in Table 6-2.

Some calculations were also done with a constant hydraulic conductivity $K = 1.0 \cdot 10^{-13}$ m/s.

Table 6-1. Yield function.

q (kPa)	ε_{pl}
113	0
138	0.005
163	0.02
188	0.04
213	0.1

Table 6-2. Relation between hydraulic conductivity and void ratio.

e	*K* (m/s)
0.45	$1.0 \cdot 10^{-14}$
0.70	$8.0 \cdot 10^{-14}$
1.00	$4.0 \cdot 10^{-13}$
1.5	$2.0 \cdot 10^{-12}$
2.00	$1.0 \cdot 10^{-11}$
3.00	$2.0 \cdot 10^{-11}$
5.00	$7.0 \cdot 10^{-11}$
10.00	$3.0 \cdot 10^{-10}$
20.00	$1.5 \cdot 10^{-9}$

Interaction pore water and structure

The effective stress theory states that the effective stress (the total stress minus the pore pressure) determines all the mechanical properties. It is modelled by separating the function of the pore water and the function of the particles. The density ρ_w and bulk modulus B_w of the pore water as well as the density ρ_s and the bulk modulus of the solid particles B_s are required parameters. The following parameters are used for Na-bentonite:

Pore water

ρ_w = 1,000 kg/m^3 (density of water)
$B_w = 2.1 \cdot 10^6$ kPa (bulk modulus of water)

Particles

ρ_s = 2,780 kg/m^3 (density of solids)
$B_s = 2.1 \cdot 10^8$ kPa (bulk modulus of solids)

6.3.3 Contact elements

The contact between *the buffer and the rock and between the buffer and the canister* has not been tied in order to allow slip. Instead interface properties with a specified friction have been applied between the different materials. The friction has been modelled with Mohr Coulomb's friction angle ϕ and without cohesion c. The following basic value has been used:

$\phi = 8.69°$

This friction angle corresponds to $\beta = 17°$ in the Drucker Prager model. The value has been changed in some calculations in order to investigate the influence of the friction.

The *surfaces of the open space* are also furnished with contact surfaces so that when the gap is closed the expansion is stopped and the surfaces cannot pass each other. Also the empty part of the rock surface is supplied with contact surfaces.

6.3.4 Initial conditions

All calculations were done with the same initial conditions of the buffer. The buffer is completely water saturated and is assumed to have an average density at saturation of ρ_m = 2,000 kg/m^3 or the void ratio $e = 0.77$ corresponding to the average density in the deposition hole. The pore pressure is set to $u = -7$ MPa in order to correspond to the effective average stress $p = 7$ MPa that yields zero total average stress. The required initial conditions of the buffer are thus:

$u = -7$ MPa
$p = 7$ MPa
$e = 0.77$

6.4 Calculations

Three different types of calculations have been performed.

- Swelling when a large part of the bentonite buffer is missing, either due to long time colloid erosion in glacial conditions or by accidental mistakes at buffer block placement.
- Swelling when local parts of the bentonite buffer are missing due to erosion caused by water inflow from either an intersecting fracture or point inflow.
- Swelling and sealing of channels produced during piping and erosion.

6.5 Large part of the bentonite buffer missing

6.5.1 General

This chapter deals with a scenario that concerns either huge loss of bentonite after extremely long time of erosion or the improbable case of one to three missing bentonite rings at the upper end of the canister. The rings are 50 cm thick and are assumed to be forgotten during the installation of the buffer, i.e. the first full block is put in place on top of the canister when only 6–8 out of 9 rings have been installed, which yield a gap of 50–150 cm at the top of the canister. This case can also represent an extreme loss of bentonite by colloid erosion after fresh water intrusion after a glaciation. The volume lost when one ring is missing is

$\Delta V = 0.77\ m^3$

and the loss of dry mass of bentonite is

$\Delta m = 1{,}200$ kg

6.5.2 Element mesh

The element meshes of two cases are shown in Figure 6-1. The meshes are axisymmetric and have contact surfaces with friction property defined between the buffer and the rock and between the buffer and the canister. The empty space at the 0.5–1.5 m gap is furnished with contact surfaces at the bentonite surfaces. Only the bentonite is modelled.

6.5.3 Calculations

The basic calculations comprise the basic cases at the empty space 0.5 m, 1.0 m and 1.5 m. One to two more calculations were also done for each case in order to investigate the influence of the friction against the rock. Table 6-3 shows the calculations. The hydraulic boundary consists of a constant water pressure at the rock surface. The empty space where bentonite is missing is supposed to be filled with water, which is modelled by applying a constant water pressure at the bentonite surface.

The last three calculations were done with a different geometry with the missing bentonite located in the centre of the buffer instead of close to the upper lid.

Table 6-3. Definition of calculations.

Calculation	Definition	Space	Remark
Case1_2c	Base case. M-C ϕ = 8.7°	1 ring – 0.5 m	
Case1_2d	Low friction. M-C ϕ = 4.36°	1 ring – 0.5 m	
Case1_2e	High friction. M-C ϕ = 17.0°	1 ring – 0.5 m	Did not converge
Case1b_2c	Base case. M-C ϕ = 8.7°	2 rings – 1.0 m	
Case1b_2c2	Low friction. M-C ϕ = 4.36°	2 rings – 1.0 m	
Case1c_2c	Base case. M-C ϕ = 8.7°	3 rings – 1.5 m	
Case1c_2c2	Low friction. M-C ϕ = 4.36°	3 rings – 1.5 m	
Case1_3c	Base case. M-C ϕ = 8.7	1 ring – 0.5 m	Additional calculation with different geometry
Case1b_3c	Base case. M-C ϕ = 8.7°	2 rings – 1.0 m	Additional calculation with different geometry
Case1c_3c	Base case. M-C ϕ = 8.7°	3 rings – 1.5 m	Additional calculation with different geometry

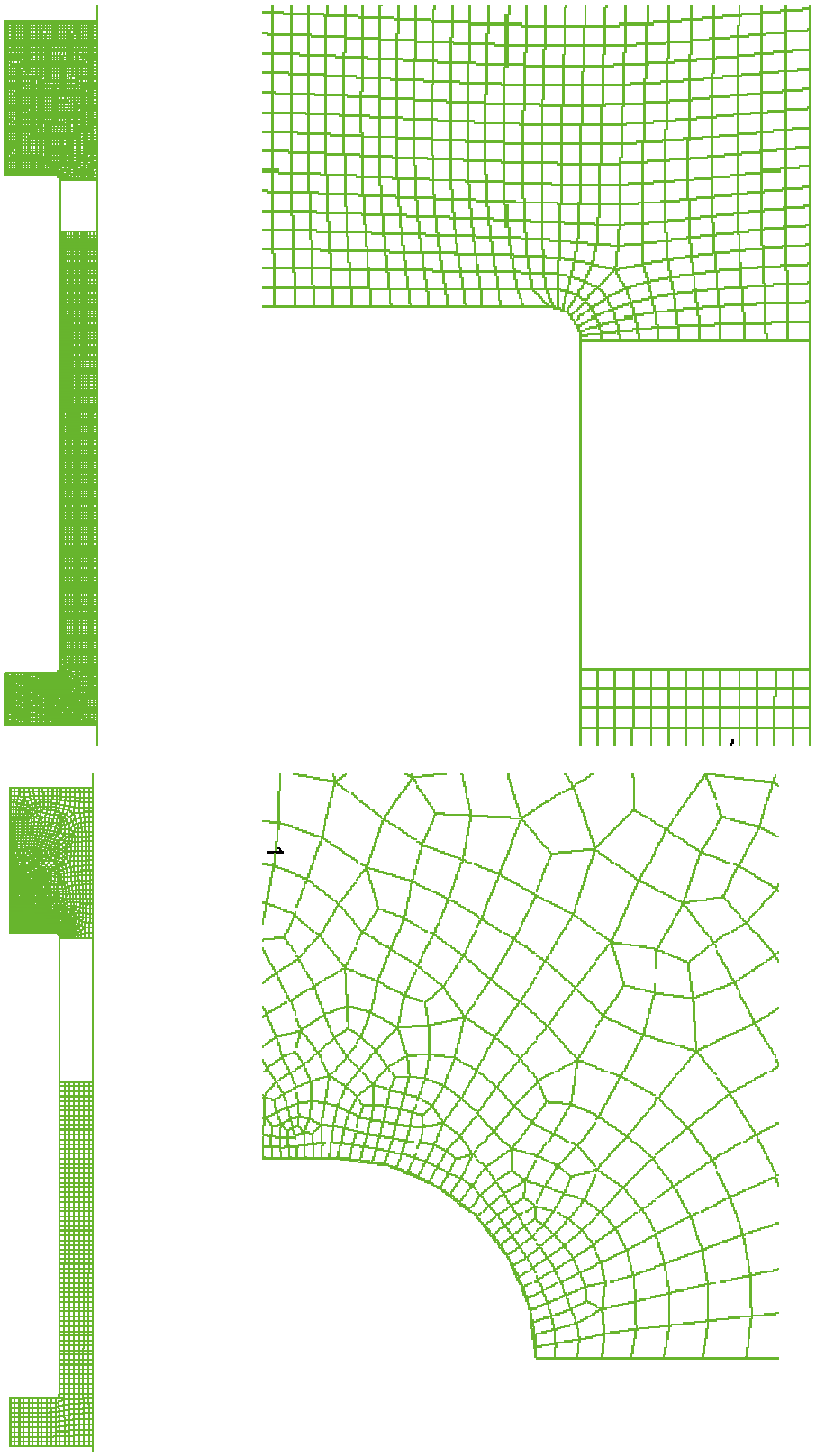

Figure 6-1. *Element meshes used for the calculations regarding missing bentonite rings by erosion or emplacement mistakes. Upper: 1 ring missing. Lower: 3 rings missing. The entire meshes and enlargements of the critical parts are shown. Axial symmetry around the left boundary.*

6.5.4 Results

Case 1 (one missing ring)

The results of the base case calculation of Case1 are shown in Figures 6-2 and 6-3.

The void ratio (Figure 6-2) increases from the initial value 0.77 up to 1.7 as a maximum during the swelling. When the open space has been closed and the two parts have come in contact after 1–2 years the swollen bentonite starts to consolidate and is compressed by the inner swelling bentonite. It then takes a very long time until complete equilibrium is reached (about 54 years). The consolidation of the bentonite is hindered by the friction in the bentonite and on the rock surface and a rather strong inhomogeneity still prevails after equilibrium. The maximum void ratio is 1.3–1.4 close to the canister and the average void ratio in the former open space is about 1.2.

The swelling pressure (average effective stress) shown in Figure 6-3 also remains very inhomogeneous. The remaining stress is below 1,000 kPa in a large part of the former open space.

The influence of the friction between the bentonite and the rock is investigated by the other two cases. The case with high friction did not converge, since the bentonite got struck to the rock wall and the elements were too much distorted. The results from the calculation with low friction are shown in Figures 6-4 and 6-5. The plots show that the gap is closed faster and that the final stage differs somewhat from the base case.

A direct comparison of the average swelling pressure in the two cases is shown in Figure 6-6. The difference is not very strong but important. In the base case the pressure is below 1 MPa in a large part of the former open space all the way between the rock and the canister, while for the low friction case the pressure is below 1 MPa only at a small ring around the canister.

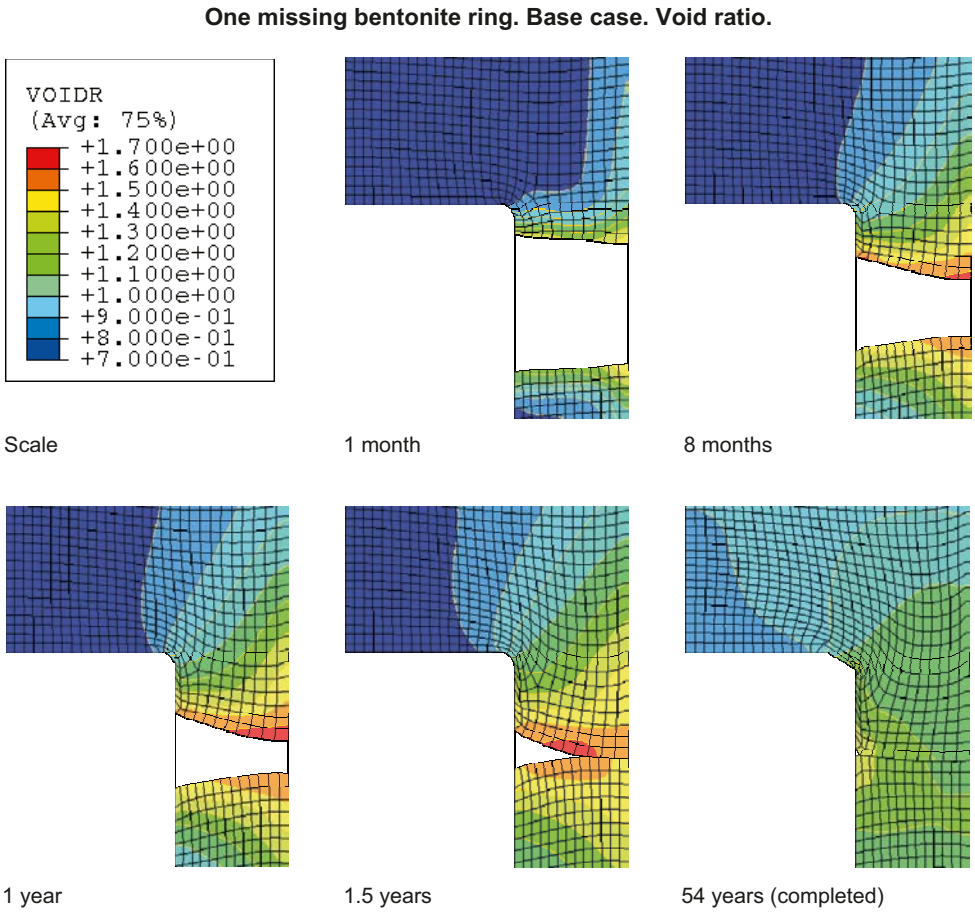

Figure 6-2. *Void ratio plotted at different times for the base case with one missing ring.*

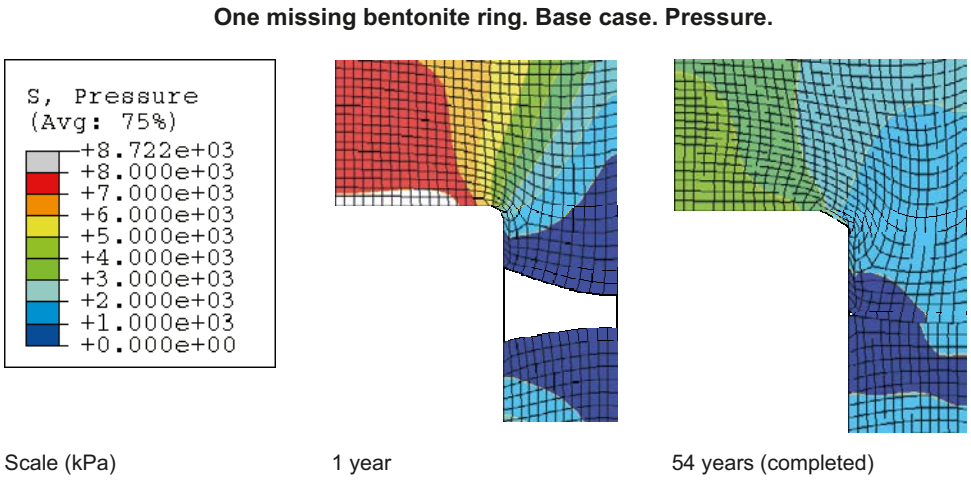

Figure 6-3. *Average stress plotted at different times for the base case of one missing ring.*

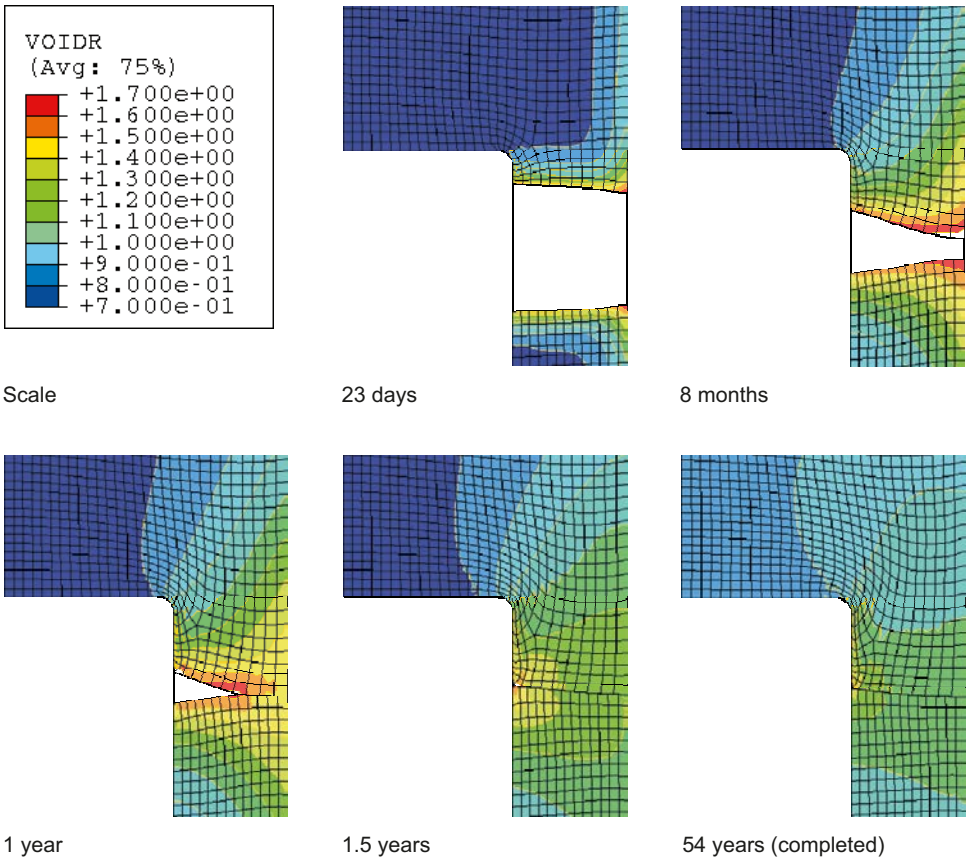

Figure 6-4. *Void ratio plotted at different times for the case with low friction.*

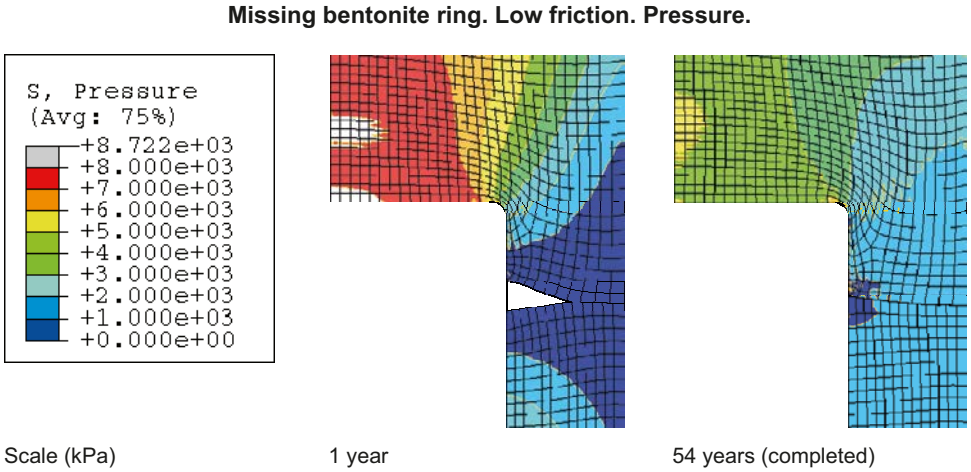

Figure 6-5. *Average stress plotted at different times for the low friction case.*

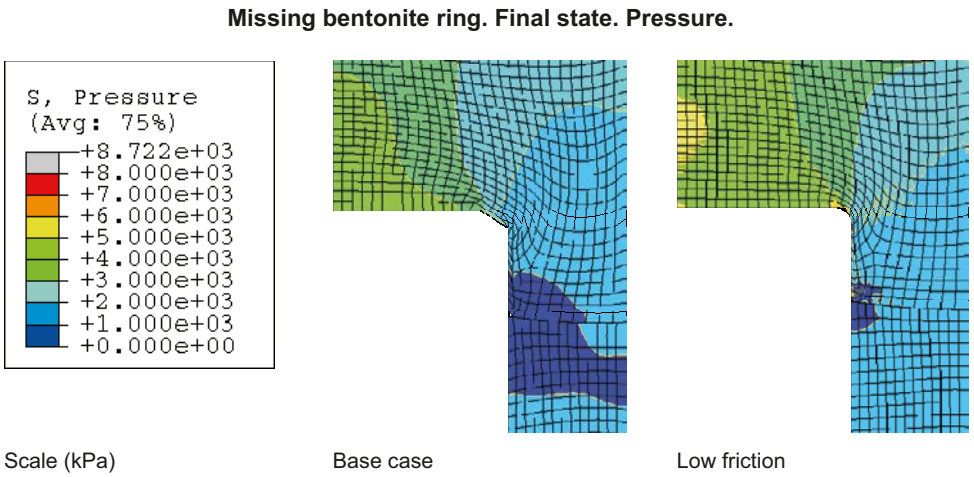

Figure 6-6. *Comparison between the final average stress of the base case (left) and the case with low friction.*

6.5.5 Case 1b (two missing rings)

The results of the calculations with two missing rings (1 m gap) are shown in Figures 6-7 to 6-10.

Figure 6-7 shows the course of swelling for the base case. After a rather long time the space is almost completely filled with bentonite but there is a small remaining final opening and the void ratio is rather high close to that opening (1.7). The existence of the open space may be caused by model simplifications, but the results anyway show that the density is so low that the expected swelling pressure might very well be below 100 kPa as illustrated in Figure 6-8.

The influence of the friction between the rock and the buffer is shown in Figures 6-9 and 6-10. Figure 6-9 shows the void ratio for the low friction case. The slot is completely closed and the void ratio varies between 1.2 and 1.5 instead of between 1.4 and more than 1.7, which was the case for the full friction case. Figure 6-10 shows a direct comparison of the swelling pressure of the two cases. Instead of an open space with no swelling pressure, the lowest swelling pressure for the low friction case is 300 kPa at the canister.

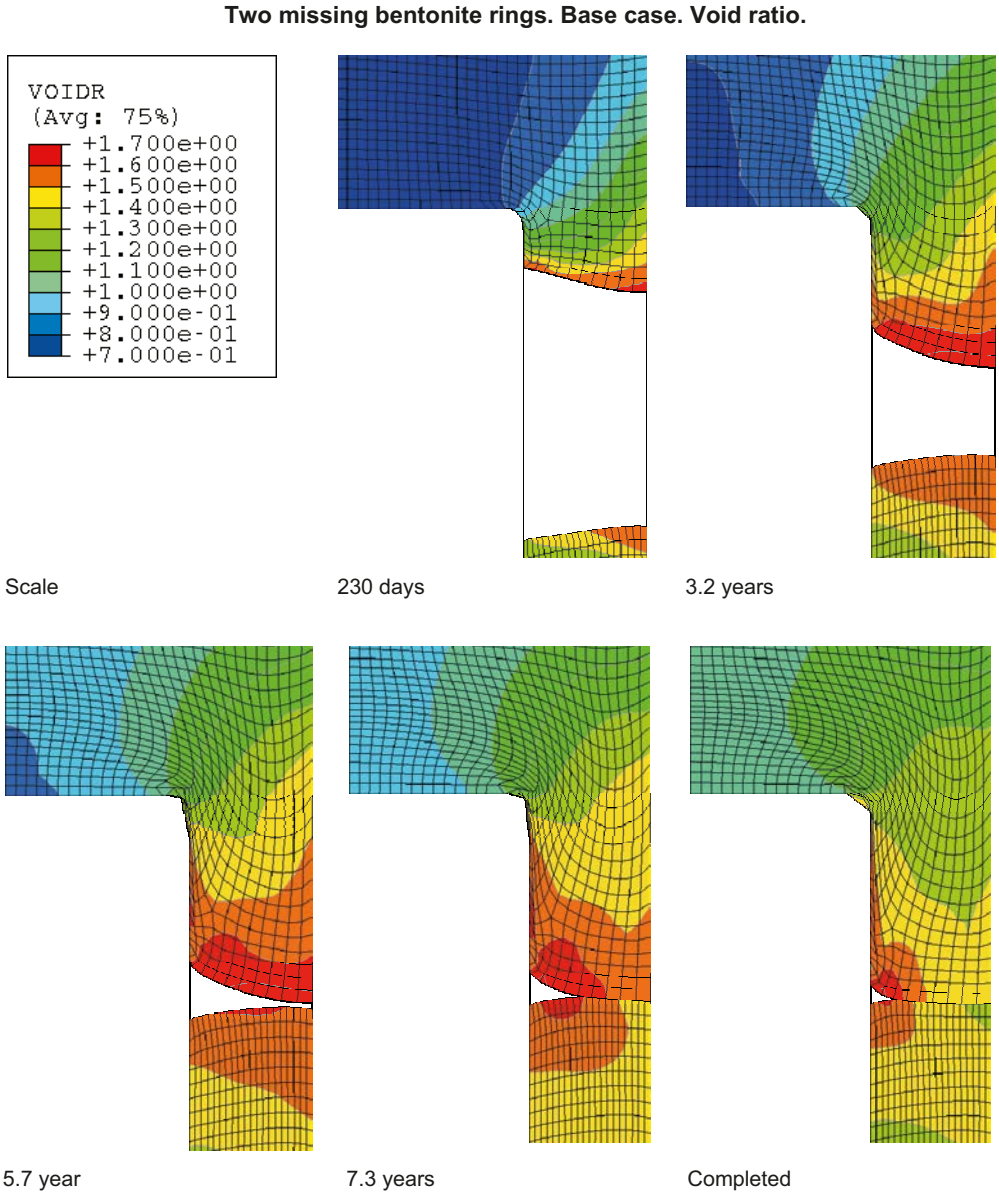

Figure 6-7. *Void ratio plotted at different times for the base case with two missing ring.*

Two missing bentonite rings. Base case. Pressure at final stage.

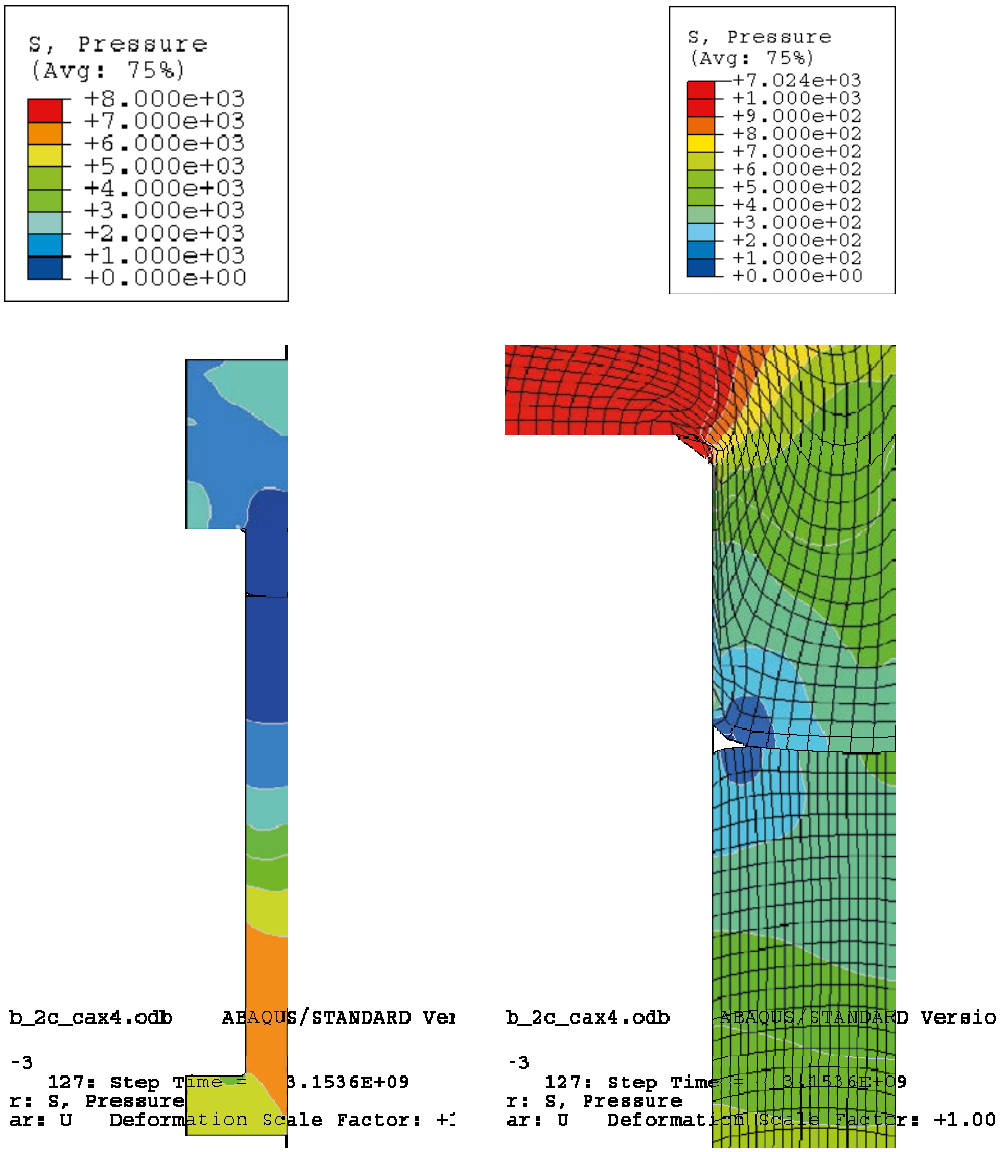

Figure 6-8. *Average stress (kPa) at final stage for the base case of two missing rings. Observe the difference in scale. 1 MPa steps in the left figure and 100 kPa in the right.*

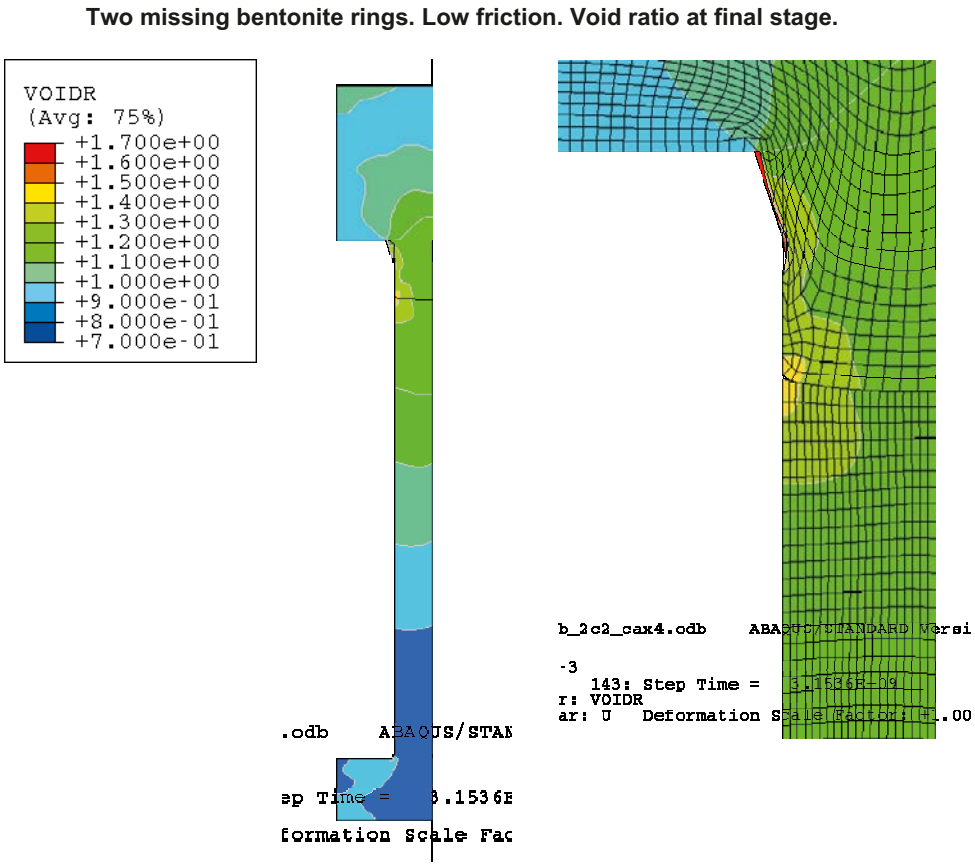

Figure 6-9. *Void ratio at final stage for the case of low friction and two missing rings.*

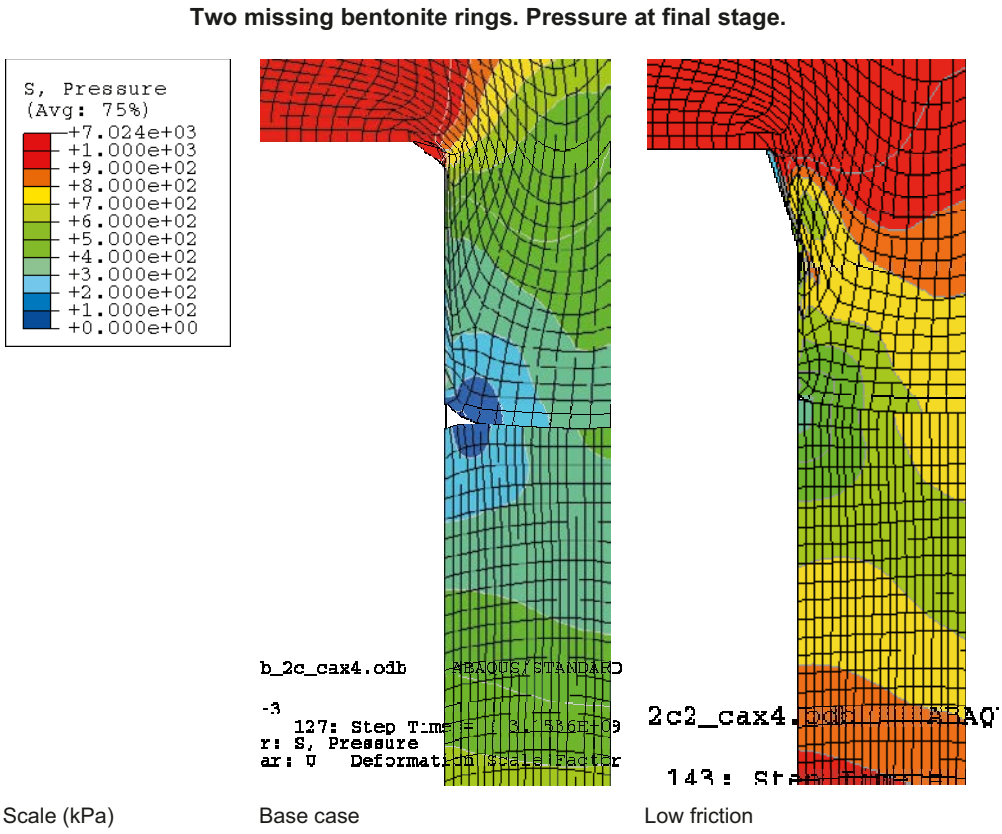

Figure 6-10. *Swelling pressure (kPa) at final stage for the case of two missing rings. Base case (left) and the case of low friction.*

6.5.6 Case 1c (three missing rings)

The results of the calculations with three missing rings (1.5 m gap) are shown in Figures 6-11 and 6-12. The final stages for the base case and the low friction case are compared concerning the void ratio (Figure 6-11) and the swelling pressure (Figure 6-12). The results show that a gap of about 20 cm is left between the upper and lower parts in the normal case, while a halved friction between the bentonite and the surroundings imply that the gap will be closed and the void ratio will vary between 1.3 and 1.7 and the swelling pressure between 100 and 400 kPa in the border between the upper and lower buffer parts.

6.5.7 Bentonite cavity located close to the centre of the canister

Three additional calculations were performed with a different simplified element mesh. The reason for doing these calculations was mainly to see if the location of the cavity had a large influence on the results. The same cavities corresponding to one, two or three missing bentonite blocks were analysed but the element meshes were simplified in such a way that the canister was prolonged so that no bentonite was modelled above or below the canister. This way no swelling and support from the bentonite below or above the canister was gained so that this case can be considered a little conservative. In addition the problems and possible errors with bentonite swelling round the canister corners were avoided.

Three missing bentonite rings. Void ratio at final stage.

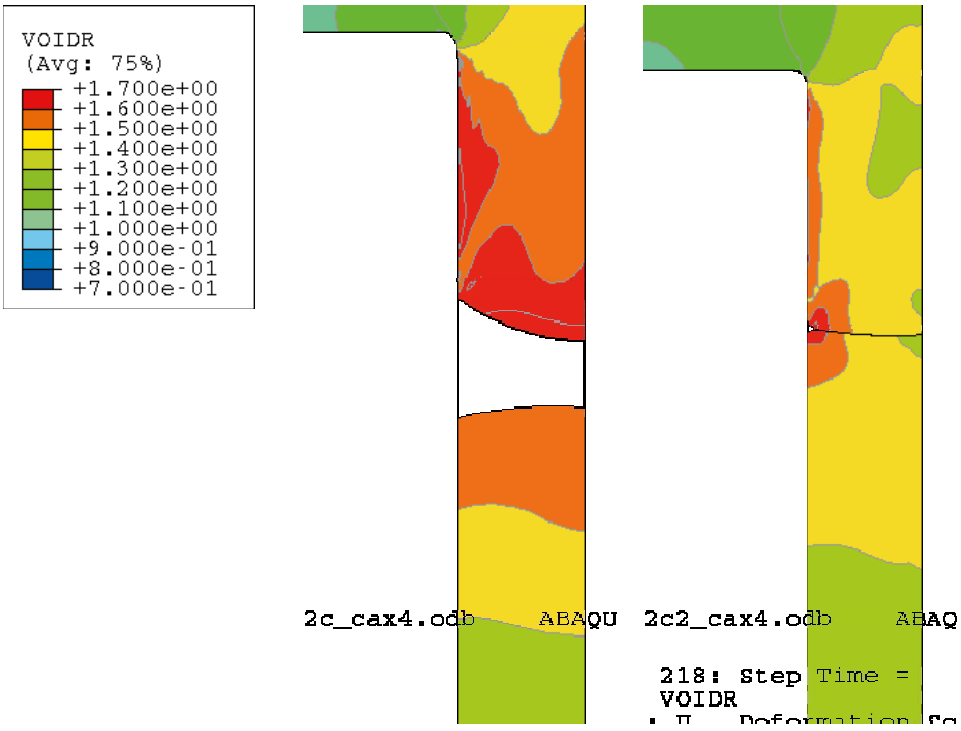

Scale (kPa) Base case Low friction

Figure 6-11. *Void ratio at final stage for the case of three missing rings. Base case (left) and the case of low friction.*

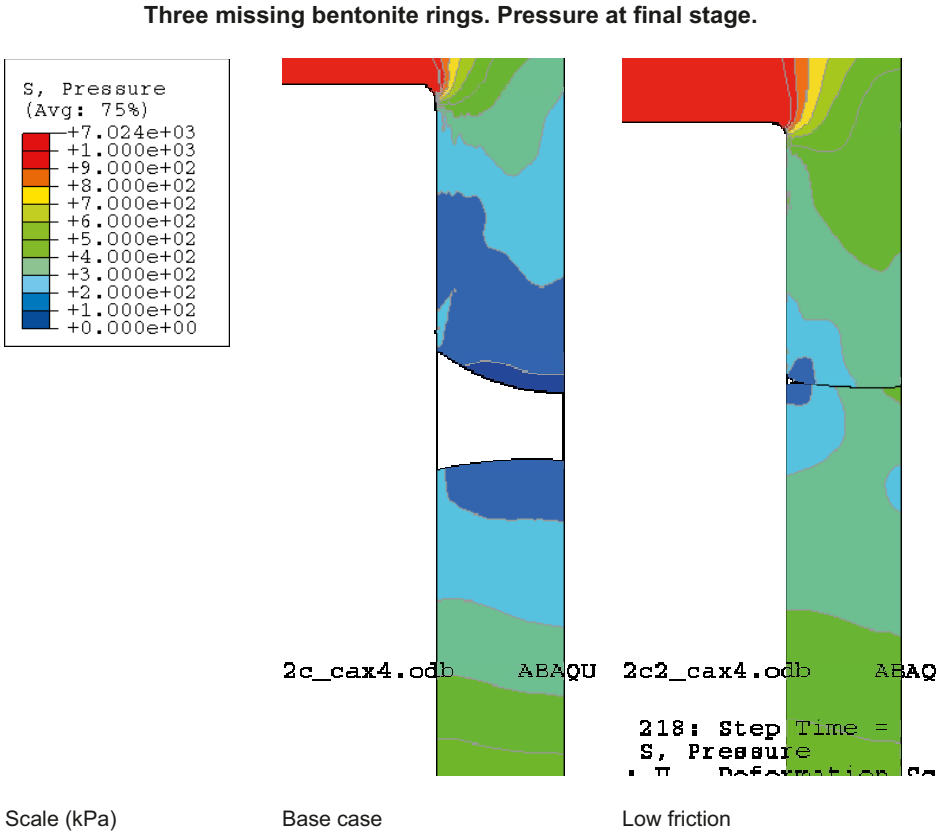

Figure 6-12. *Swelling pressure (kPa) at final stage for the case of three missing rings. Base case (left) and the case of low friction.*

Figure 6-13 shows the resulting void ratio after equilibrium at all three calculations. The figure shows the influence of the size of the cavity. The results also show that the final void ratio at this geometry is higher than at the original geometry, which is logical since in the original geometry the expansion is be helped by the swelling of the bentonite above the canister. These results thus show that the possible errors caused by elements getting stuck on the corner of the canister are of minor importance.

6.5.8 Conclusions and uncertainties

When large amounts of bentonite are lost or missing from start the bentonite swells and fills the empty space but the density and resulting swelling pressure is rather low due to the friction in the buffer and the friction against the rock surface. For 50 cm opening the swelling pressure will be in average 0.5–1 MPa in almost the entire former hole in the base case. However, if the rock surface is smooth and the resulting friction against the rock is halved the swelling pressure will be above 1 MPa in a majority of the former space.

For 100 cm opening the swelling pressure will be rather low close to the canister in the base case with pressure below 100 kPa or even an unfilled part left, while the low friction case yields a minimum swelling pressure more than 300 kPa.

If the opening is 150 cm corresponding to three missing bentonite rings the base case yields that a large volume will have a swelling pressure below 100 kPa and even be unfilled. However, the influence of the friction between the bentonite and the rock and canister is large and with halved friction almost the entire opening will be filled.

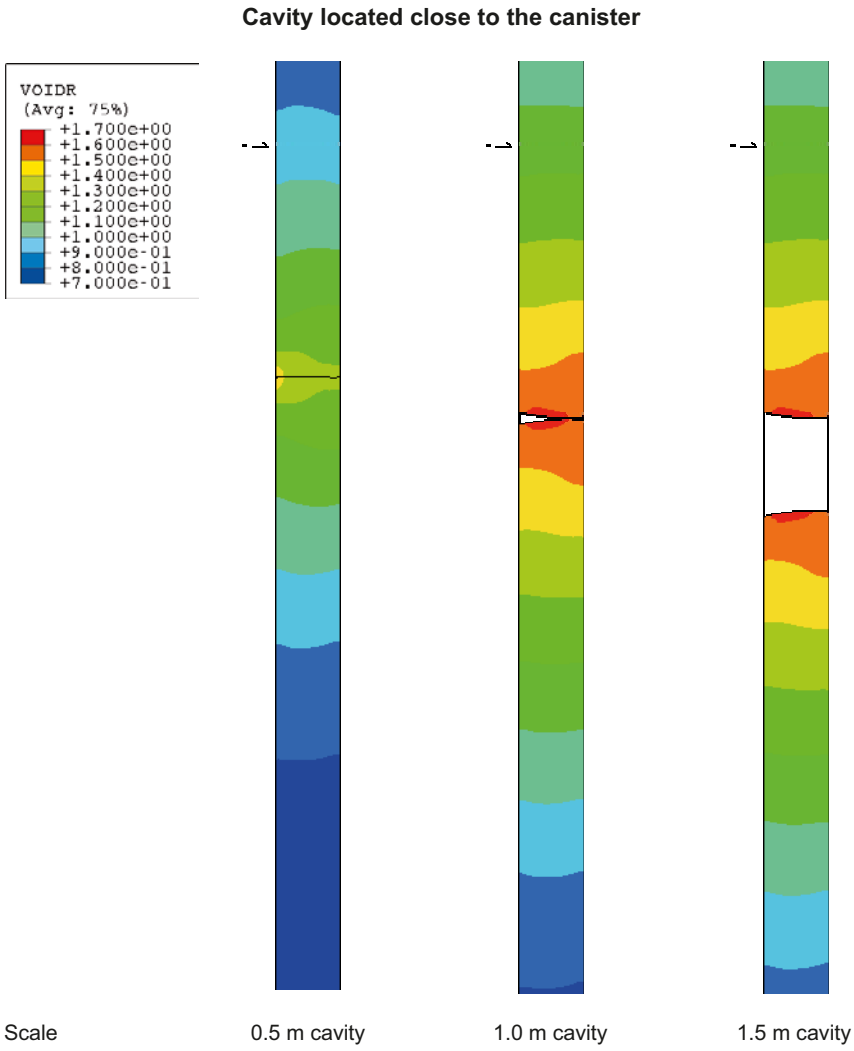

Figure 6-13. *Void ratio at final stage for the three cases of a simplified geometry with a central cavity. Base case properties.*

The swelling is gained by the swelling of the bentonite above or below the canister, which is shown by the calculations that do not include that part of the buffer.

The influence of the friction between the buffer and the surrounding rock and canister is strong as shown by the calculations done with halved friction. In the base case calculations the friction is assumed to be the same as in the bentonite but tests done on contact properties show that the friction is only about 60% if the surface is fairly smooth /Börgesson et al. 1995/. However, there are several reasons to stick to the base case:

1. There is no evidence that the deposition hole drilling can be made so that the rock surface will be without irregularities and it cannot be excluded that the interaction between the copper and the bentonite will force the slip to take place in the bentonite.
2. The friction angle of the bentonite is a function of the swelling pressure and increases with decreasing swelling pressure while the base case friction angle is valid at the initial swelling pressure 7 MPa.
3. The average friction angle in the interval 0–7 MPa is about 10 degrees which yields a friction angle of about 6 degrees if the rock and canister surfaces are smooth. The base case value 8.69 degrees thus represent some kind of average.

The following remarks regarding uncertainties in these calculations are important:

1. The material model of Na-bentonite is valid at void ratio interval 0.7–1.5 (see /Börgesson et al. 1995/), which means that the strong swelling and gel-formation that will take place at the swelling bentonite surface in non-saline water is not modelled.
2. The material parameters used represent average values and the non-linearity of friction is not taken into account.

The uncertainties about the material model at strongly swelling bentonite make the results somewhat uncertain especially at high void ratios.

6.6 Loss of bentonite from erosion

6.6.1 General

Erosion during and after installation of the buffer may cause significant loss of bentonite under unsatisfactory conditions. The erosion will stop when the plug is built and sealed and the voids in backfill pellets are filled with water. The plug is intended to function about 12 weeks after start of the installation.

As shown in Chapter 11 (task 11) the erosion may in unfavourable cases be up to a lost dry weight of 100 kg when the amount of eroding water is larger than 17 m^3. The effect of loosing 60–120 kg dry mass will be investigated.

At the dry density of the buffer $\rho_d = 1{,}570$ kg/m^3 (corresponding to the void ratio 0.77 and the density at saturation $\rho_m = 2{,}000$ kg/m^3) the volume of bentonite that will be lost is 0.038–0.077 m^3.

- Dry mass lost: 60–120 kg
- Volume lost: 0.038–0.077 m^3

Two different cases will be considered; half a donut at the rock surface and half a sphere at the rock surface.

6.6.2 Case A: Half donut

General

The first case simulates erosion that comes from an intersecting horizontal fracture that digs a hole in the form of half a donut around the buffer at the rock surface. It can also be interpreted as a 5 meter long half pipe running along an inclined or vertical fracture. This is a more realistic erosion scenario during the installation phase, while the half donut may come from long term erosion through a horizontal fracture.

The geometry of the half donut or half pipe should thus yield a total empty volume of 0.038–0.077 m^3 at the inside of or along a deposition hole. If the inner pipe radius is 0.067–0.094 m this condition is approximately fulfilled.

Calculations

The influence of the thickness or inner radius of the donut has also been investigated by varying the radius. In addition the influence of how the water is supplied to the bentonite has been investigated. In the base case water is supplied from the entire rock surface and from inside the eroded open space. In the other cases water is available from only the open space and the backfill or from only the backfill. Table 6-4 shows the different cases that have been modelled.

For these calculations the base case is defined as the case with the pipe radius 0.067 m. The element mesh of the base case is shown in Figure 6-14. The other two cases have similar meshes but other radiuses of the half donut.

The calculations were done in a similar way as the calculation of the missing bentonite ring. The bentonite properties and initial conditions of the base cases described in Section 6.3 were used.

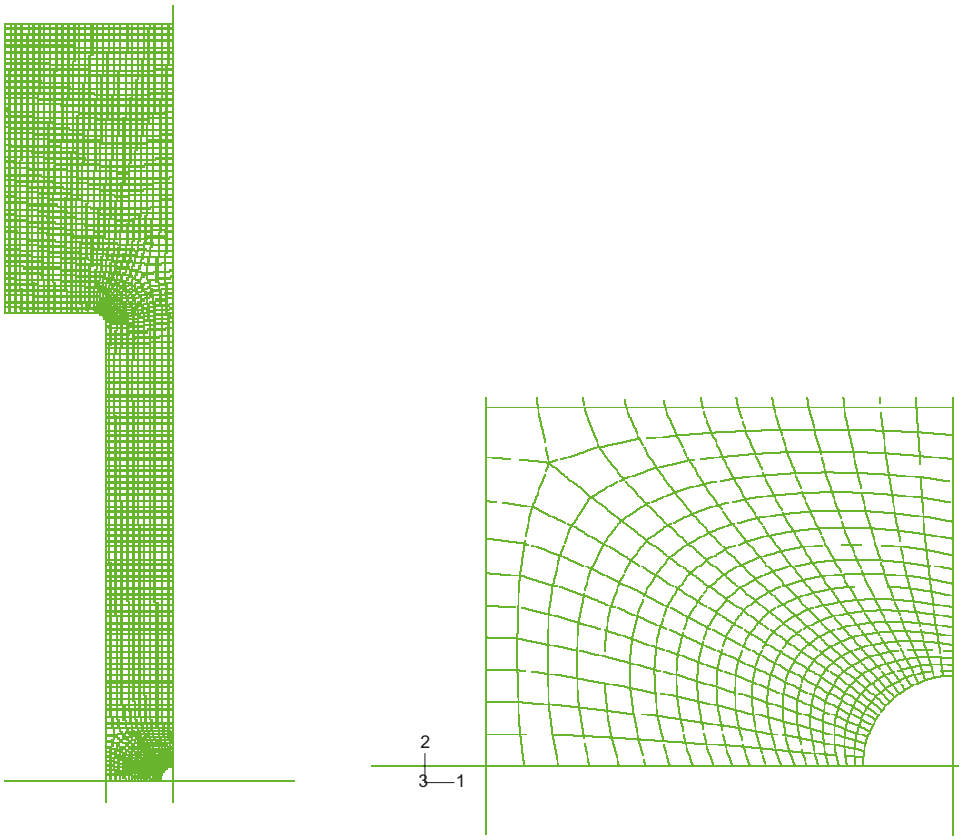

Figure 6-14. *Element mesh of the calculation of Case A with half donut and radius 0.067 (base case). The mesh is axially symmetric around the left side and the bottom plane is a symmetry plane. The whole mesh and an enlargement of the part with the empty donut are shown.*

Table 6-4. Definition of calculations of case A (half donut).

Calculation	Radius of eroded half donut (m)	Water supply from	Remark
CaseA2_2c	0.067	inside space + rock surface + backfill	
CaseA2_2c2	0.067	inside space + backfill	Base case
CaseA2_2c3	0.067	only backfill	
CaseA3_2c	0.134	inside space + rock surface + backfill	
CaseA3_2c2	0.134	inside space + backfill	Larger hole
CaseA3_2c3	0.134	only backfill	
CaseA5_2c	0.034	inside space + rock surface + backfill	Smaller hole

Results

Base case (A2)

The results of the base case calculations with water supplied from the open hole, the rock and the backfill are shown in Figures 6-15 and 6-16. The swelling is strongest at the rock surface due to the supply of water there, which yields a rather peculiar swelling pattern. The rock surface is at first covered and the hole is enclosed by bentonite in a couple of weeks. Then the rest of the empty space is filled and followed by decreased void ratio due to the swelling of the inner bentonite and subsequent compression of the gel. The maximum void ratio is above 1.7 during the swelling and then returns to a value between 1.0 and 1.5 with an average of about 1.2 in the former hole.

The minimum swelling pressure after equilibrium is higher than 1 MPa as shown in Figure 6-16.

The end state is rather “shaky” in the sense that both swelling pressure and void ratio in the former hole varies a lot in a not quite logical way. The reason for this scatter is probably the strong deformation of the elements.

Eroded half donut. Base case. Case2_2c. Void ratio.

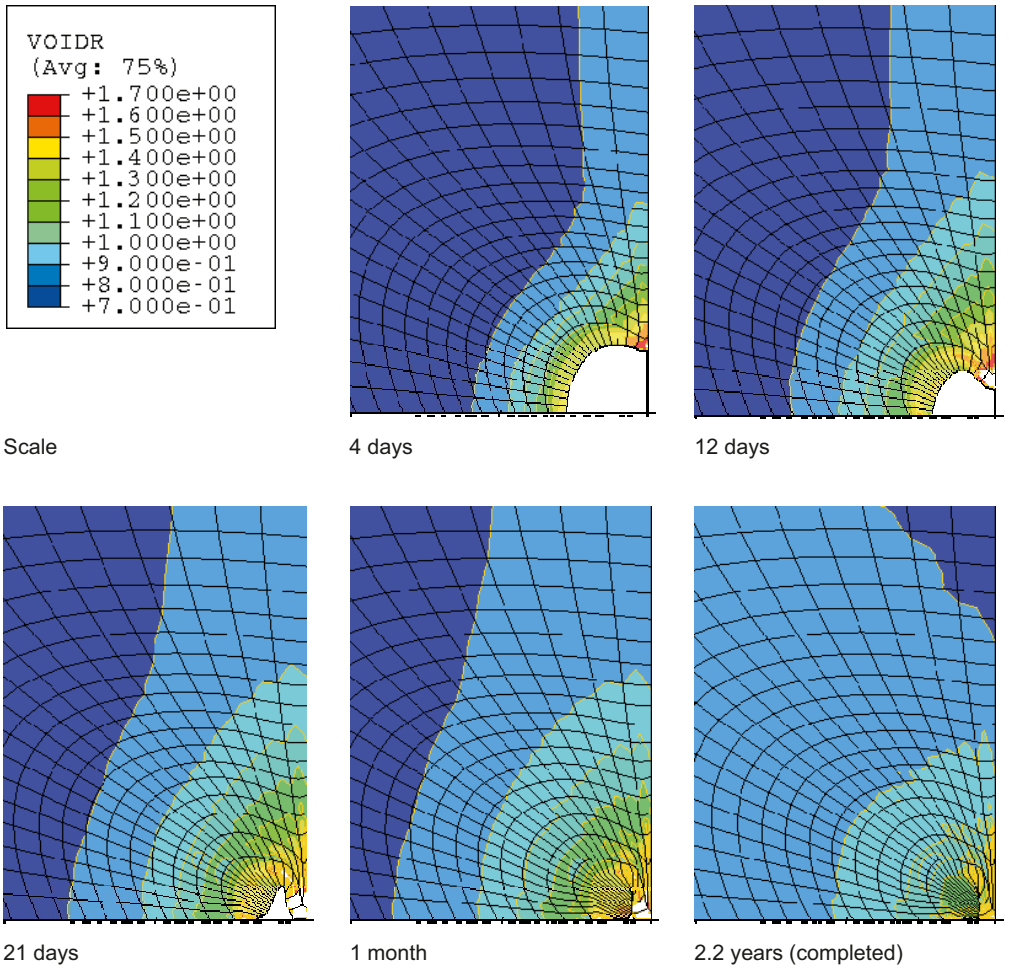

Figure 6-15. *Void ratio plotted at different times for the base case. Water supply from hole, rock and backfill.*

Eroded half donut. Base case. Case2_2c. Pressure.

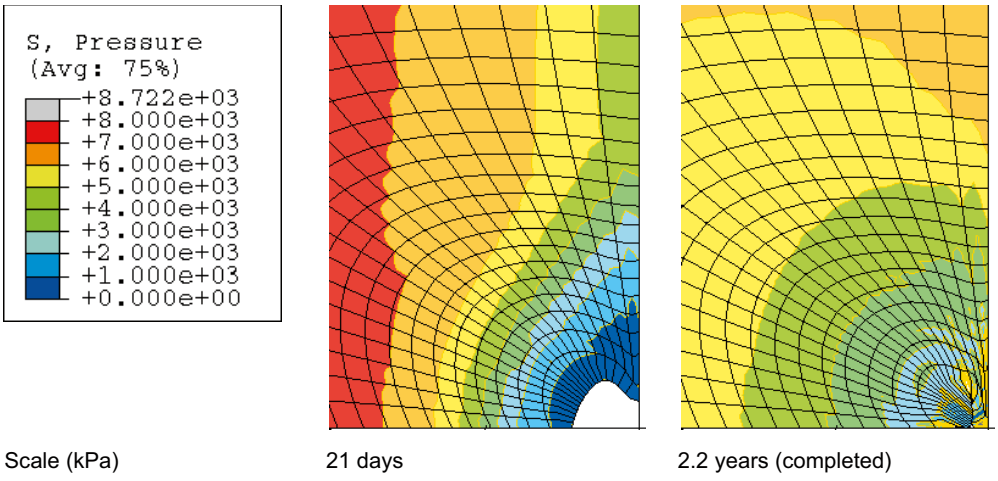

Figure 6-16. *Average stress plotted at different times for the base case. Water supply from hole, rock and backfill.*

The influence of the water supply is illustrated in Figures 6-17 and 6-18. If water is not supplied by the rock the wetting rate is much slower and the swelling process rather different. There is very little swelling along the rock surface. The swelling is instead folded along the rock surface. The time to equilibrium is also very long. If no water is supplied from the open hole itself but only from the backfill the swelling process is also quite different. No loose bentonite, which is later compressed, is formed. Instead the void ratio continues to increase during the entire swelling until the end.

In spite of the different wetting and swelling paths the end states do not differ very much. The average void ratio in the hole is about 1.1 and the minimum swelling pressure above 1 MPa.

Larger hole

The same calculations were done with half donut with double radius, i.e.13.4 cm instead of 6.7 cm, which is caused by 3–4 times more eroded bentonite mass. The element mesh is very similar to the mesh shown in Figure 6-14 but has a larger hole. Figures 6-19 and 6-20 show the final state in these calculations.

The results are very similar to the results of the base case. The swelling pressure is above 1 MPa everywhere in the former hole and the maximum void ratio is below 1.3. The solutions are in fact "better" than the solutions of the base case since there is less scatter.

Smaller hole

The calculation with a smaller hole (half radius) yielded very similar results. Only one calculation was performed.

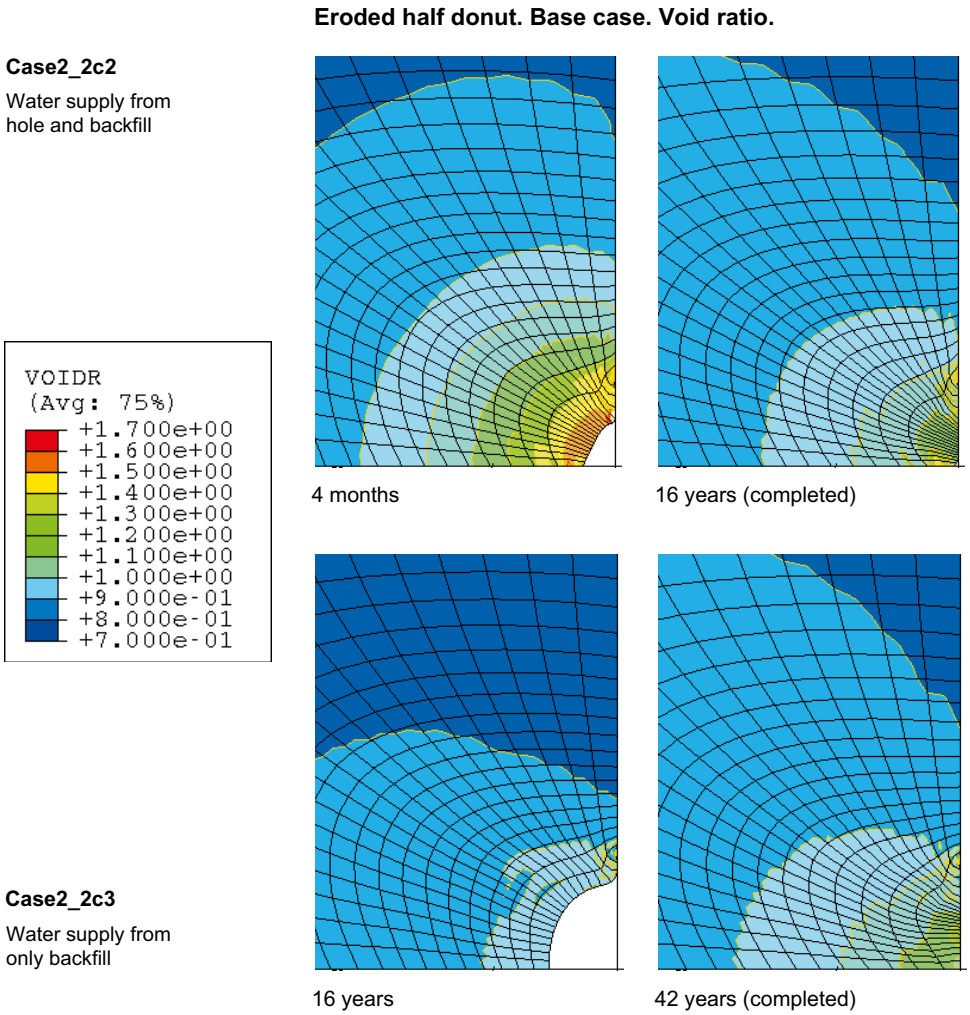

Figure 6-17. *Void ratio during and after swelling for the base case. Differing water supply.*

Eroded half donut. Base case. Pressure.

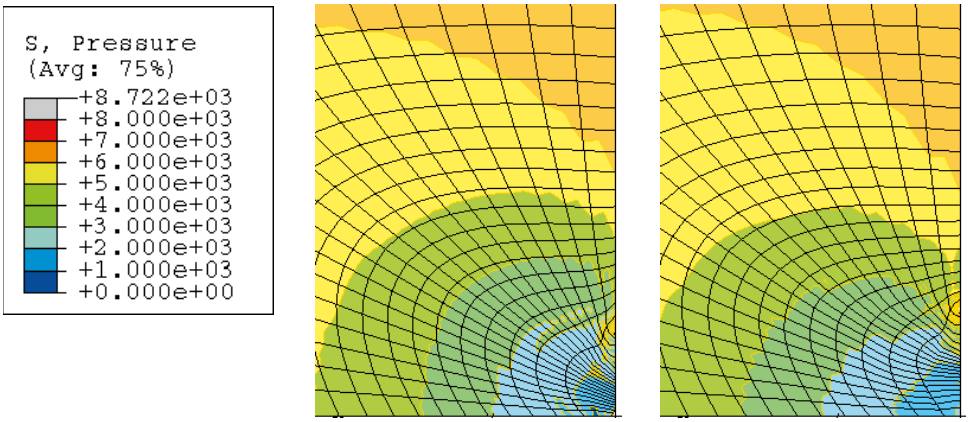

Figure 6-18. *Final average stress of the base case with deviating water supply. Water supply from the hole and the backfill (left) and from only the backfill (right)*

Eroded half donut. Large hole. Void ratio.

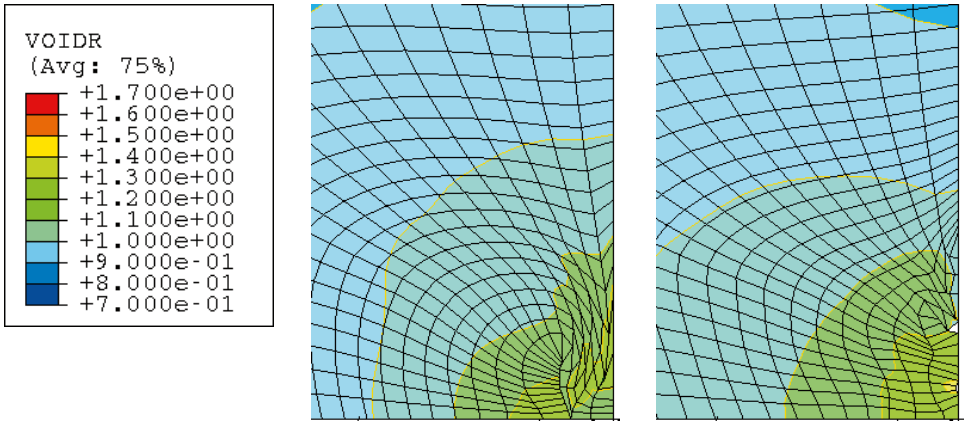

Figure 6-19. *Final void ratio in the case with a larger hole. Water supply from the hole, the rock and the backfill (left) and from only the hole and the backfill.*

Eroded half donut. Base case. Pressure.

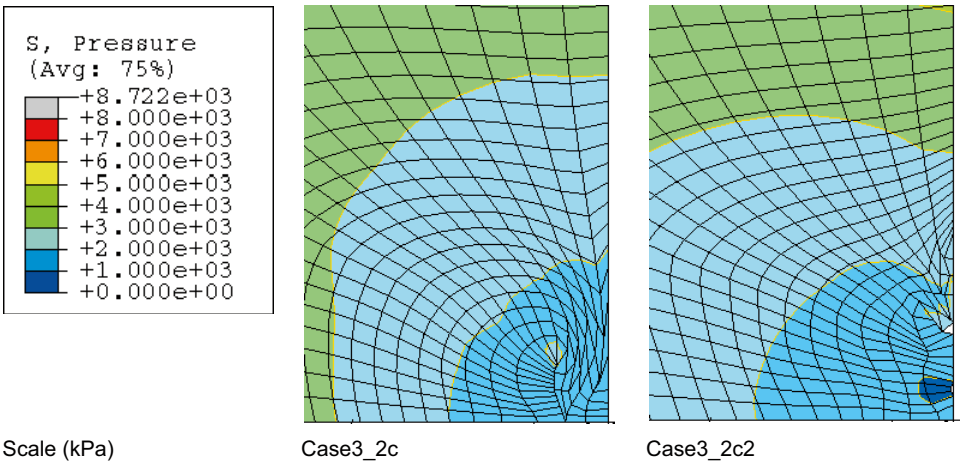

Figure 6-20. *Final swelling pressure in the case with a larger hole. Water supply from the hole, the rock and the backfill (left) and from only the hole and the backfill.*

6.6.3 Case B: Half sphere derived from point erosion

If water enters the deposition hole in one point, at e.g. a fracture intersection, the erosion may be very local around the inflow spot, which may result in a loss of bentonite in a half sphere like configuration. This is a more severe case than the donut case since the lost bentonite is local instead of distributed around the canister.

Considering the same erosion case as the base case i.e. 120 kg of dry bentonite lost the volume will be 0.077 m^3. The radius of a half sphere that yields that volume is $r = 0.333$ m. However, since half a sphere is an extreme case that is unlikely to be formed the radius 0,263 m, corresponding to 60 kg of dry bentonite lost, will be studied.

The element mesh of this model is shown in Figure 6-21.

The model is simplified in the sense that it is axisymmetric around a line that goes through the centre of the sphere, which yields that both the canister and the rock surface are modelled as planar. This is judged to have an insignificant influence on the results.

In this calculation only one wetting case was considered, namely the case that water is available only inside the hole and not at the rock surface. The bentonite model and the contact surfaces are identical to those of the previous calculations, with the friction angle 8.7 degrees. Figures 6-22 and 6-23 show the results.

The results show that the swelling process is similar to the previous cases. Due to the friction against the rock there is very little swelling along the rock surface. Instead the bentonite between the canister and the hole swells and seals the hole. Due to the rather thin buffer left between the canister and the spherical hole, the resulting void ratio after completion is rather high (>1.5), which yields a swelling pressure below 1 MPa in about 1/3 of the buffer.

6.6.4 Conclusions and uncertainties

The calculations of the swelling and homogenisation of a half donut resulting from erosion show that the swelling yields a strong decrease in density and swelling pressure due to the friction in the bentonite. However, the swelling pressure after completed homogenisation is in none of the cases

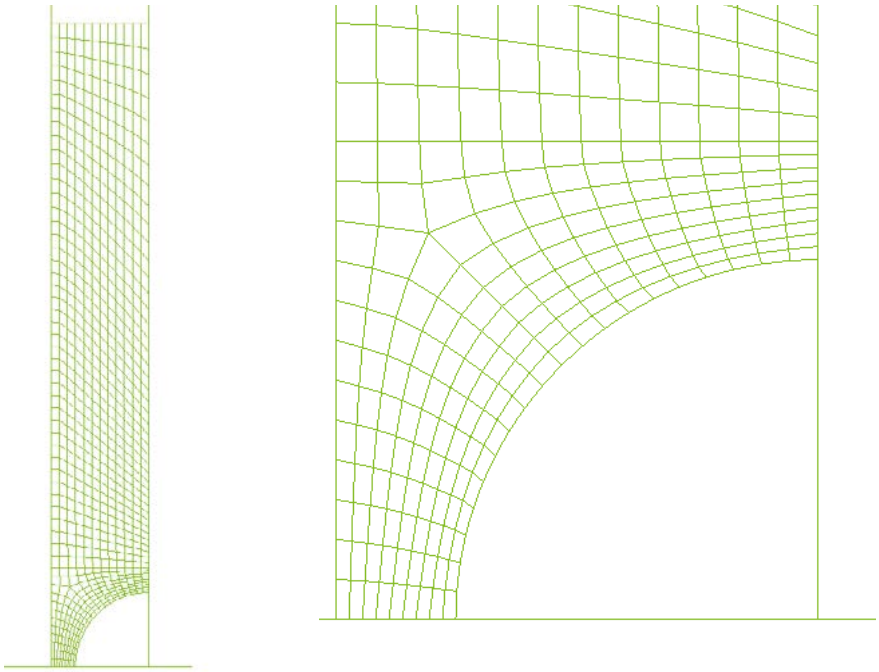

Figure 6-21. *Element mesh of the calculation of Case B with half sphere with the radius 0.263 m. The mesh is axially symmetric around the bottom side. The whole mesh and an enlargement of the empty part are shown.*

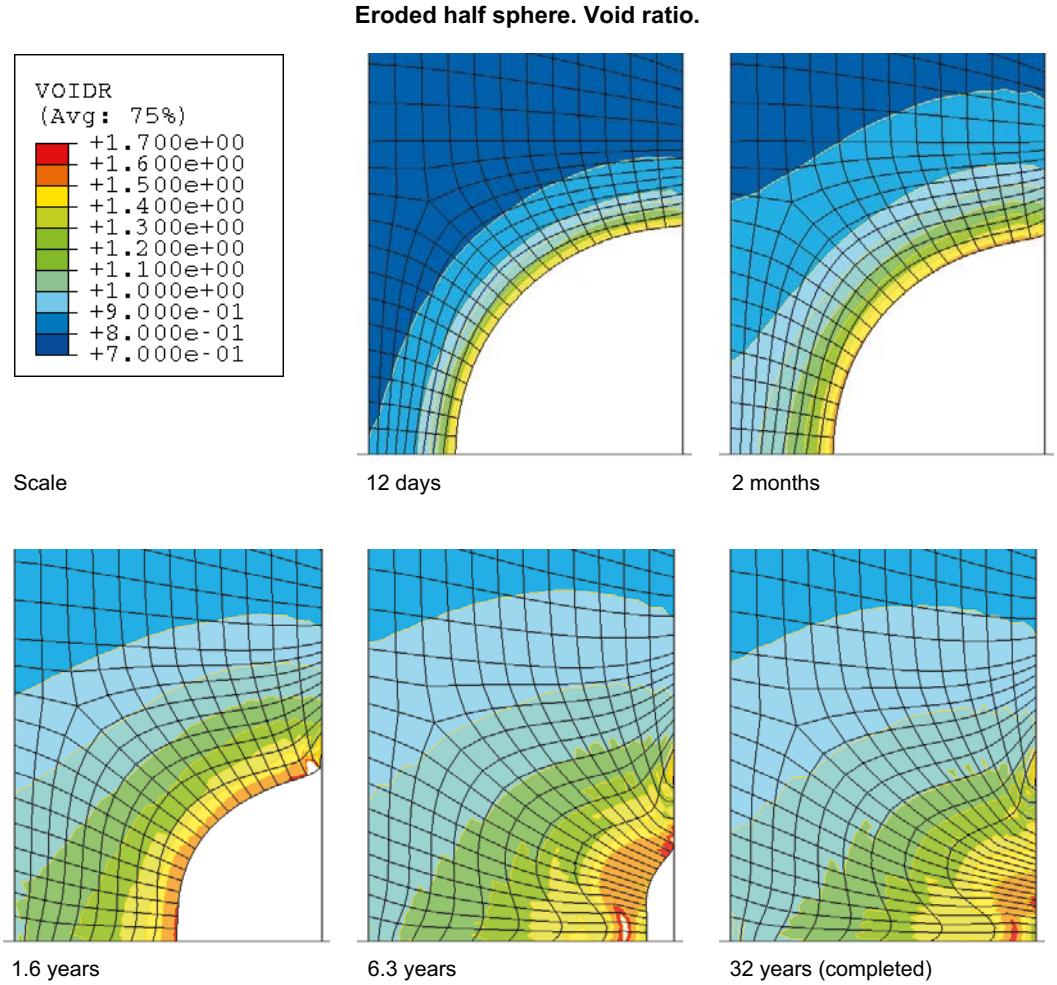

Figure 6-22. *Void ratio plotted at different times for a half sphere. Water supply from only the hole.*

with donut radius varying from 3.4 cm to 13.4 cm below 1 MPa. The influence of the radius seems to be insignificant due to the long distance to the bentonite boundaries.

If half a sphere is created instead of a donut the consequences are more severe, since the radius of the sphere is larger for the same amount of bentonite and thus the mass of bentonite left between the sphere and the canister much less. However, in 2/3 of the distance between the buffer and the rock the buffer has a swelling pressure higher than 1 MPa. The conclusion is thus that about 60 kg of dry bentonite may be lost from point erosion without jeopardizing the function of the buffer. The effect is strong but half a sphere unlikely to be formed so the conclusion is that about 100 kg may be lost as a worst case.

The same uncertainty remarks concerning the bentonite properties and the friction between the bentonite and the rock or canister surface made in Section 6.5 are valid also for the calculations presented in Section 6.6.

6.7 Self-sealing of long small channels

6.7.1 General

The consequences of piping and erosion are a small channel that leads the water and bentonite solution out through the buffer into the backfill. Such a pipe will ultimately swell up and seal when the erosion has stopped. The efficiency of that sealing has been investigated with some calculations.

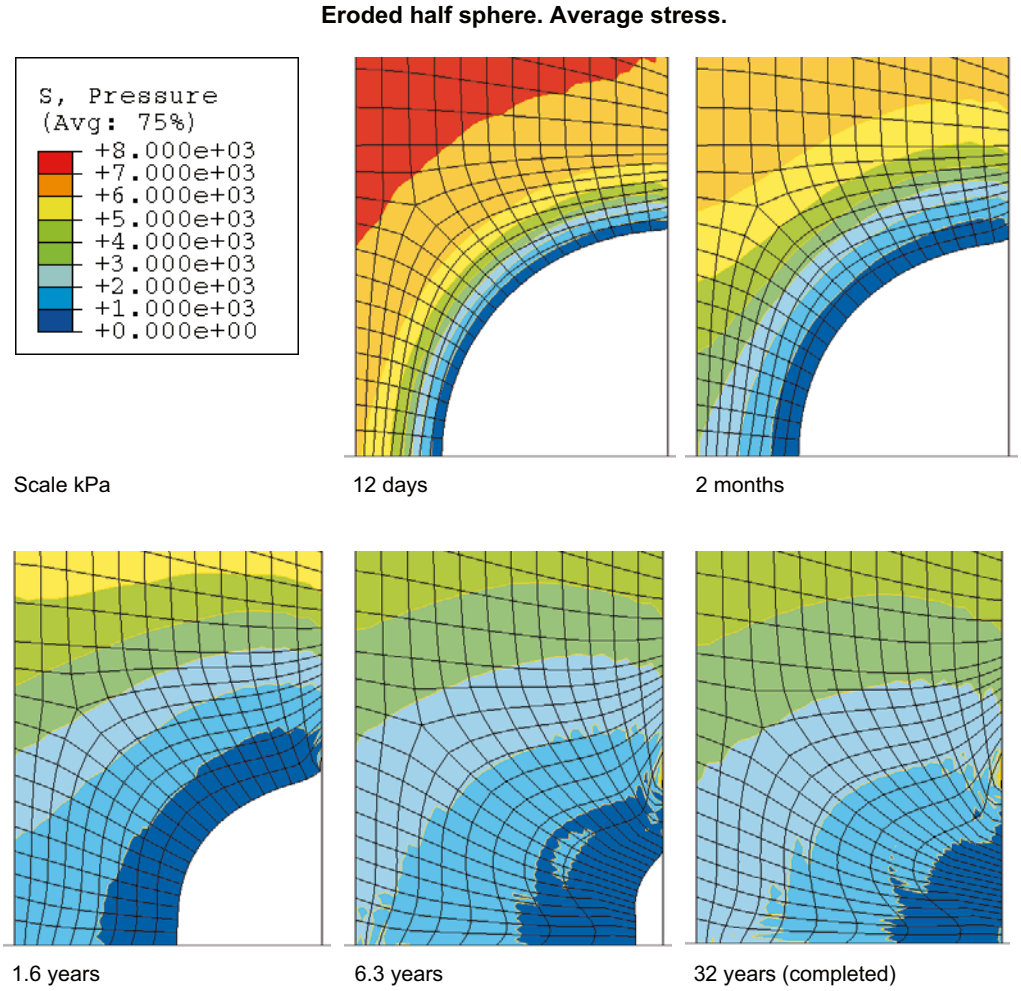

Figure 6-23. *Swelling pressure plotted at different times for a half sphere. Water supply from only the hole.*

Such calculations are also valuable in order to study the sealing in more general terms since the geometry can be simplified and the effect of a complex mesh and the element size can be studied.

6.7.2 FEM model

Geometry

One-dimensional axisymmetric elements have been used, which thus simulates an infinitely long and perfectly round hole. The base case corresponds to a pipe radius of 1 cm and a distance to the bentonite outer boundary of 10 m, but also the combination 5 cm hole and 50 m boundary was checked. The number of elements were initially 100 (see Figure 6-24) but were increased at first to 400 and finally to 800 in order to have small elements close to the hole. For the same reason the element size was reduced with decreasing distance from the hole.

Results

The calculations are compiled in Table 6-5.

For cases A–D the radius of the hole and the number of elements were varied. For cases E and F the size of the elements was strongly reduced with decreasing radius and a minimum element size of only 5 µm applied. For cases F1–F3 the influence of dilatancy and cohesion in the bentonite was studied.

Figure 6-24. 10 m element mesh with 100 elements for the modelling of long small pipes in bentonite. Axial symmetry around a vertical axis 1 cm left of the mesh.

Table 6-5. Compilation of the calculations modelling the self sealing of long small pipes in bentonite.

Case	Hole radius (m)	Outer radius (m)	Number of elements	Smallest element (m)	Largest element (m)	Remaining pipe radius after swelling (m)	Remark
A	0.01	10	100			$6.7 \cdot 10^{-3}$	No good solution
B	0.01	10	400			$3.2 \cdot 10^{-3}$	–"–
C	0.05	50	100			$33.5 \cdot 10^{-3}$	–"–
D	0.05	50	400			$16 \cdot 10^{-3}$	–"–
E	0.01	10	800	$23 \cdot 10^{-6}$	$2.7 \cdot 10^{-2}$	$162 \cdot 10^{-6}$	
F1	0.01	10	800	$5 \cdot 10^{-6}$	$2.7 \cdot 10^{-2}$	$90 \cdot 10^{-6}$	
F2	0.01	10	800	$5 \cdot 10^{-6}$	$2.7 \cdot 10^{-2}$	$85 \cdot 10^{-6}$	$\phi_d = 0$
F3	0.01	10	800	$5 \cdot 10^{-6}$	$2.7 \cdot 10^{-2}$	$40 \cdot 10^{-6}$	$\phi_d = 0$ $c = 0$

ϕ_d = dilatancy angle; c = cohesion.

All calculations yielded a remaining hole after completed swelling. Cases A–D showed that the scale is not important for the solution in the sense that the remaining hole is directly proportional to the initial hole at otherwise equal conditions. A and C yielded identical results just as B and D if the geometry is scaled. Thus, all pipe radiuses can be derived from the results of one calculation by scaling the geometry.

However, the results of calculations A–D also showed that the elements close to the pipe were too large since the final relation between the stress (or void ratio) and the radius was very irregular and strange and yielded a remaining large hole. For calculations E and F the number of elements was increased and the element sizes close to the hole strongly reduced.

The results are best illustrated with plotted relations between the void ratio or swelling pressure and the radius. Figures 6-25 and 6-26 show those relations for the last 4 calculations (E and F1–F3).

The figures show that cases E and F1 agree very well until a radius less than about 1 mm where the void ratio increases and the swelling pressure decreases more for case F1, which has smaller elements. The remaining pipe is also smaller for case F1. It thus seems as the end solution depends on the mesh resolution and that the swelling pressure goes asymptotic towards zero together with the radius.

The two final cases (F2 and F3) illustrate the sensitivity to the material model. In case F2 the dilatancy angle (2°) was removed, which yields better homogenisation with a much lower maximum void ratio but no difference in swelling pressure compared to the base case, the reason being that the bentonite does not increase in volume during pure shear. In case F3 both the dilatancy and the cohesion ($d = 100$ kPa) were removed, which yields both decreased maximum void ratio and increased minimum swelling pressure.

6.7.3 Conclusions and uncertainties

The FEM modelling of the process of self-sealing of long open circular channels in compacted bentonite have yielded some interesting results. A long open tube does not seal completely but a reduced density that decreases with decreasing radius will remain just like for the larger holes.

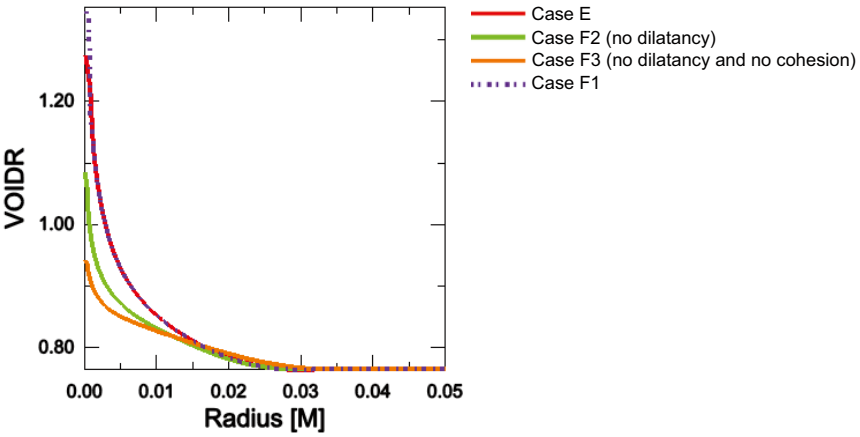

Figure 6-25. *Void ratio as function of radius after swelling and sealing of a pipe with 1 cm radius.*

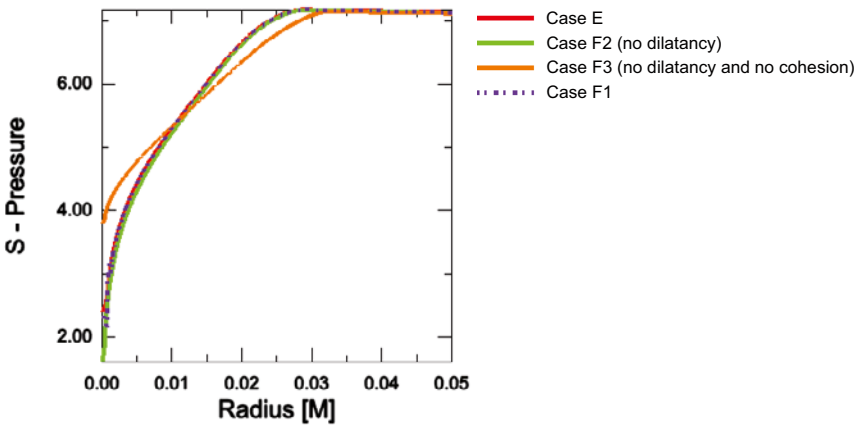

Figure 6-26. *Swelling pressure (MPa) as function of radius after swelling and sealing of a pipe with 1 cm radius.*

The following conclusions and observations were made:

- The final stage is independent of the initial radius of the hole if the geometry is scaled to the radius i.e. all the results for all initial hole radiuses can be derived from one calculation.
- All calculations yielded a remaining open pipe after completed homogenisation.
- There is a strong influence of element size on the remaining hole radius. It seems that at infinitely small elements the radius zero would correspond to a singularity with both swelling pressure and density approaching zero asymptotically. This phenomenon might be possible to investigate with analytical solutions.
- The remaining density gradient is caused by the shear resistance in the clay with the friction as dominating parameter.

The results are only valid for circular tubes. Fracture like openings will behave completely different and probably yield much better homogenisation.

The element model is idealised symmetric since it is “one-dimensional” in the sense that there is a rotational symmetry around the centre of the hole. In a real open channel there are irregularities that probably will make the pipe collapse. This may change the resulting void ratio distribution in the micro scale but probably not in the mm scale.

The same uncertainties regarding the bentonite model and the friction angle as mentioned for the other cases are valid also for this case.

6.8 Backfill material lost by collioid erosion

This case is considered in Appendix F.

7 Backfill homogenisation

7.1 Introduction and objectives

The objective of this task is to analyze the homogenisation of the backfill during hydration.

7.2 Approach

The task is modelled with a number of hydro-mechanical axisymmetric Code_Bright models: two 1D geometries and one 2D geometry. The backfill consists of block and pellets. Two tunnel sections are considered: with a theoretical section and with maximum fallout (see Figure 7-1). The hydration of the backfill is modelled with a hydraulic boundary in the pellets-filled slot.

7.3 Model description

Geometries and densities are modelled in accordance with the Backfill production line report. Backfill block and pellets material parameter data is used in accordance with the Data report /Åkesson et al. 2010/.

7.3.1 Geometry and mesh

Three different geometries were used: two 1D axisymmetric models and one 2D axisymmetric model (Figure 7-2 and Figure 7-3). The 1D models differed with respect to the size of the pellets-filled slot. The smaller representing a theoretical section and the larger representing a maximum fallout section. Both these extremes are included in the 2D model. The length of this was chosen to correspond to the canister spacing. The number of nodes and elements in the 1D theoretical section model was 102 and 50 respectively. The corresponding numbers for the 1D maximum fallout model was 116 and 57. Finally, for the 2D model the numbers were 2,201 and 2,100, respectively.

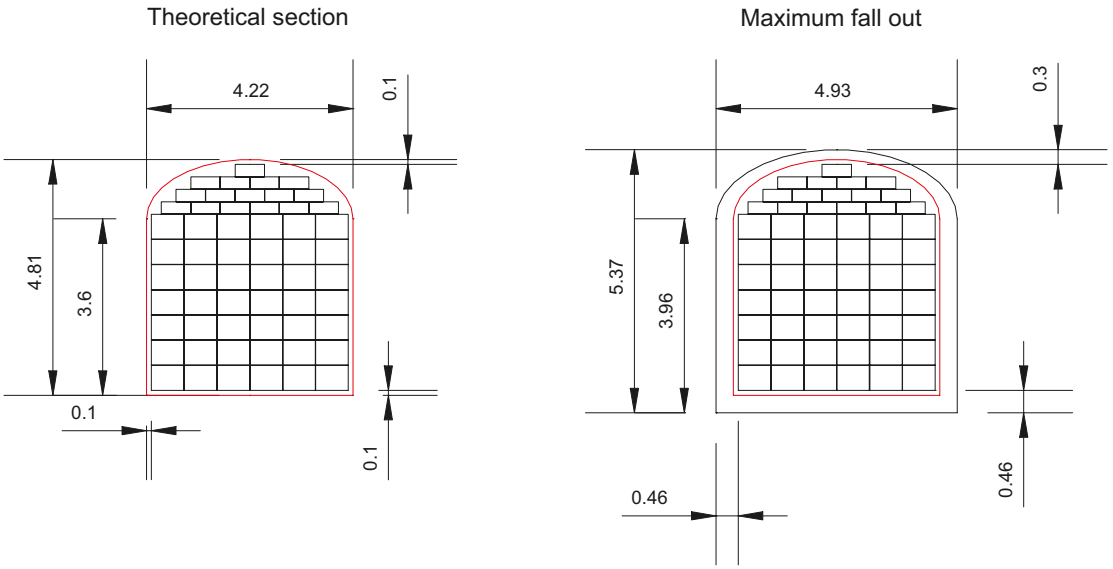

Figure 7-1. *Backfill design with arrangement of blocks and pellets filled slot. Theoretical section and maximum fallout.*

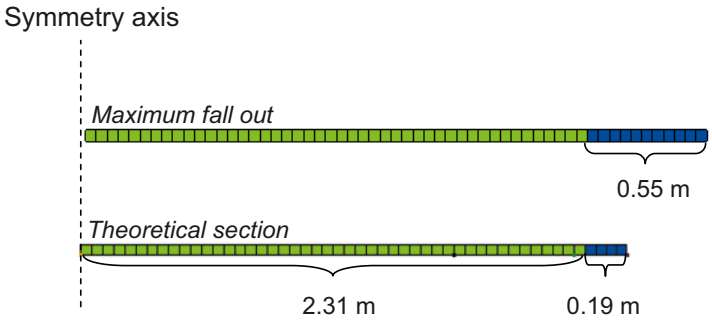

Figure 7-2. *Geometry and mesh for 1D axisymmetric models.*

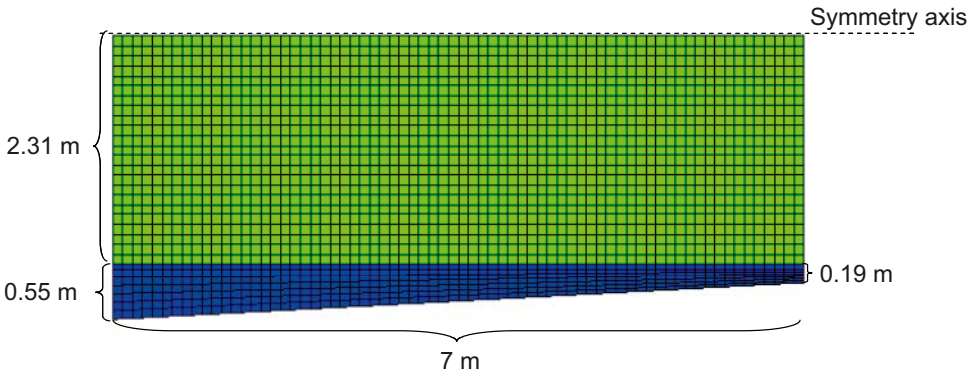

Figure 7-3. *Geometry and mesh for 2D axisymmetric model.*

7.3.2 Initial and boundary conditions

The initial liquid pressure was set to –45.9 MPa, while the initial value of all principal stress was set to –0.11 MPa corresponding to a net mean stress of 0.01 MPa.

Roller boundaries were applied to all mechanical boundaries, except for the outer boundary of the 2D model. The hydraulic boundary was implemented as a surface boundary over the pellets filling, except for the innermost elements (Figure 7-4). This boundary was increased from –45.9 to 0.1 MPa during the first 0.01 years. The reason for this approach is to avoid irreversible displacements within the pellets filling which otherwise would affect the final density profiles. All models were run at a constant temperature of 20°C and a constant gas pressure of 0.1 MPa.

7.3.3 Material properties

The properties of all modelled material are compiled in Table 7-1.The different geometries correspond to different target void ratios: the 1D model with theoretical section: 0.74; the 1D model with maximum fallout: 0.91; and the 2D model: 0.83. All data were taken from the Data report /Åkesson et al. 2010/.

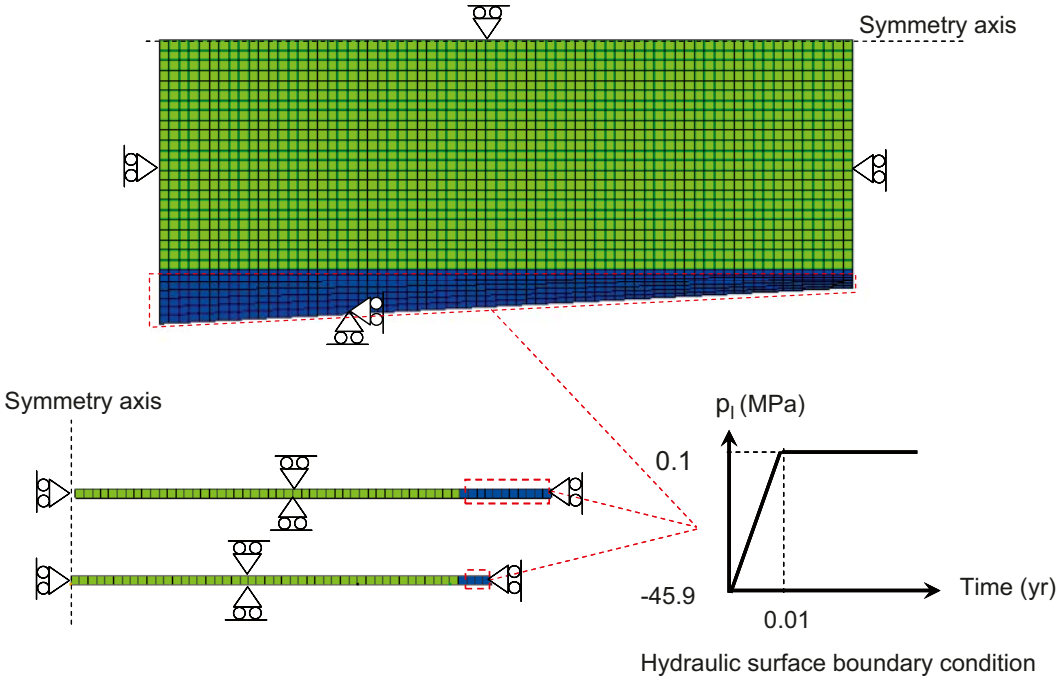

Figure 7-4. *Hydraulic and mechanical boundary conditions.*

Table 7-1. Parameter values used for different materials.

			Backfill block e=0.635 w=17%			**Backfill pellets e=1.780 w=17%**	
Intrinsic permeability	k_0 (m^2)		2.1E–21			5.2E–19	
	n_0 (–)		0.388			0.64	
	b (–)		21.3			21.3	
Relative permeability	k_r (–)		S_r^3			S_r^3	
Water retention curve	P_0 (MPa)		37.2			0.162	
	λ (–)		0.34			0.19	
Target void ratio		0.74	0.83	0.91	0.74	0.83	0.91
Porous elasticity	κ_{i0} (–)		0.14			0.15	
	α_i		–0.02			–0.02	
	α_{ils}		0			0	
	K_{min} (MPa)		20			1	
Swelling modulus	κ_{s0} (–)		0.3			0.3	
	α_{ss} (–)		0			0	
	α_{sp}		*)			*)	
	p_{ref} (MPa)		1			0.1	
Poisson's ratio	v (–)		0.2			0.2	
Plastic stress strain modulus	λ_0 (–)	0.161	0.171	0.182	0.323	0.346	0.367
	r (–)	0	0	0	0	0	0
	β (MPa^{-1})	0	0	0	0	0	0
Critical state line parameter	M (–)	0.24	0.25	0.27	0.55	0.55	0.55
Tensile strength	p_{s0} (MPa)	2.4	1.9	1.5	0.05	0.05	0.05
	k (MPa^{-1})	0	0	0	0	0	0
Non-associativity parameter	α (–)	0.5	0.5	0.5	0.5	0.5	0.5
Pre-consolidation stress	p_0* (MPa)	23	15	10	0.88	0.88	0.88
	p_c (MPa)	1	1	1	1	1	1

*) The α_{sp}-parameter is replaced with an inbuilt swelling pressure relation.

7.4 Model results

All models were allowed to hydrate for 250 years, thereby ensuring that total saturation was reached.

The mechanical evolution of the 1D models is illustrated in Figure 7-5. The void ratio is here plotted against the net mean stress at four different nodes in each model. Some general observations can be made: the inner part of the blocks expands and ends up precisely on the swelling pressure curve implemented in the kappa_s-modulus. The pellets material also reaches the swelling pressure curve when it gets water saturated. But then it gets compressed from the blocks on the inside: first elastically and subsequently plastically. The adoption of an initial p_0^* value approximately twice as high as the swelling pressure implies that the stress path apparently overshoot the swelling pressure curve. A similar behaviour can be observed for the outer part of the blocks, which initially expands, but which thereafter is compressed from the inner parts of the blocks.

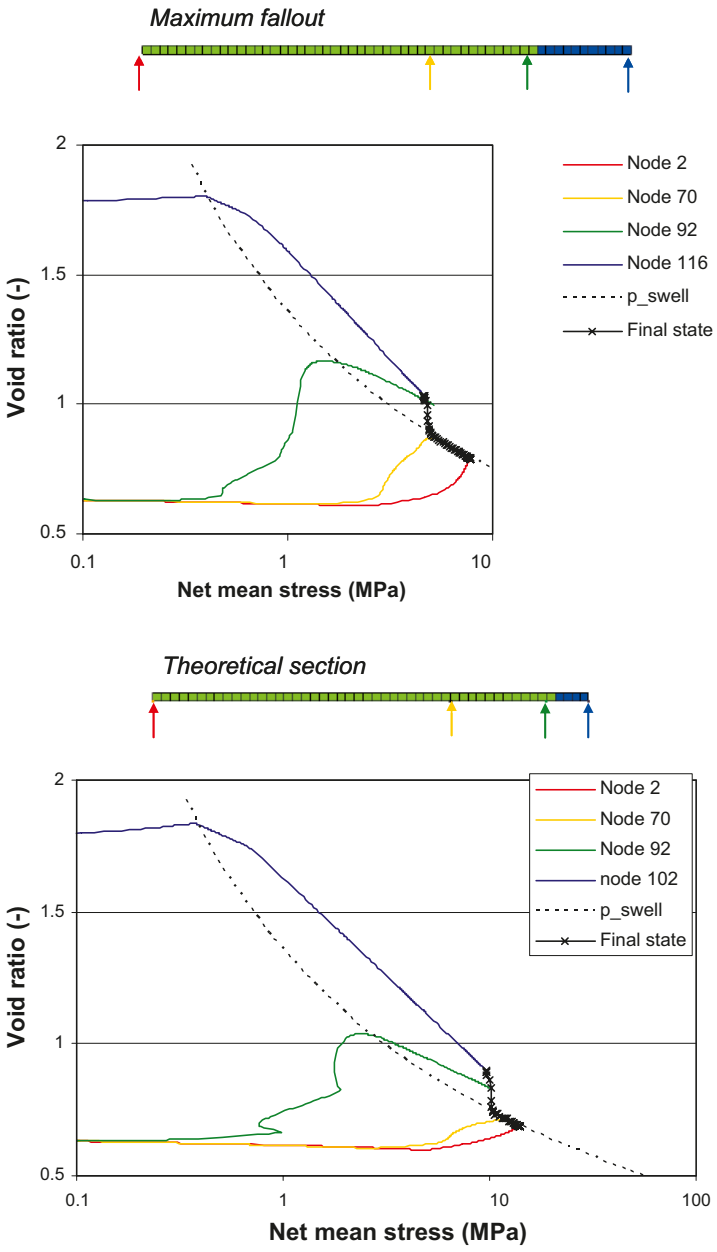

Figure 7-5. *Stress paths in for four different nodes in 1D axisymmetric models. The final state (black crosses) and swelling pressure curve (dotted line) are shown for comparison.*

The final void ratio distributions in the all the models are shown in Figure 7-6. A general difference between the inner and the outer parts of slightly more than 0.2 in void ratio can be noticed. This is generally in agreement with the experimental findings from the Canister retrieval test /Johannesson 2007/. It can be noticed that the distribution in the 2D model falls in between the two extremes sections represented by the 1D models.

The final stress state in the p'-q plane is shown in Figure 7-7. The empirical shear-strength relation presented in the Data report is shown for comparison. It can be noticed that q (the von Mises stress) in the model is generally lower than the shear strength. This is mainly due to the fact that the stress state in the model is lower than the critical state line on the "wet" side.

The final absolute displacements in the 2D model are shown in Figure 7-8. The highest occurring displacement is approx. 0.16 m.

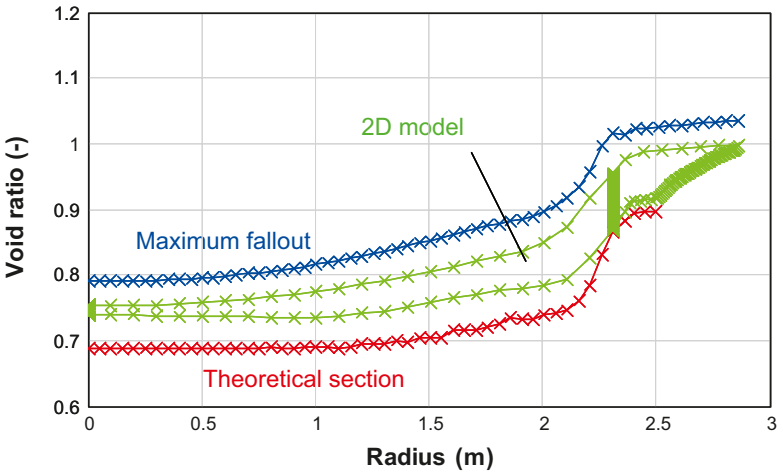

Figure 7-6. Final void ratio distributions in 1D and 2D models (the nodal radius is not modified for displacements).

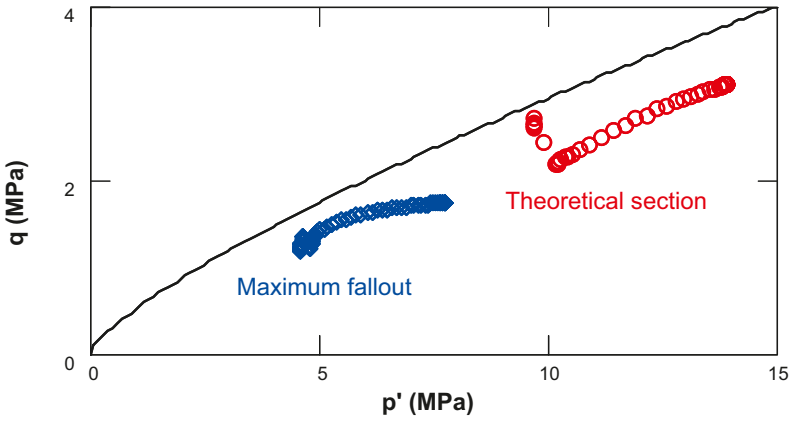

Figure 7-7. Final stress state of 1D models in p'-q plane and empirical shear strength relation (right).

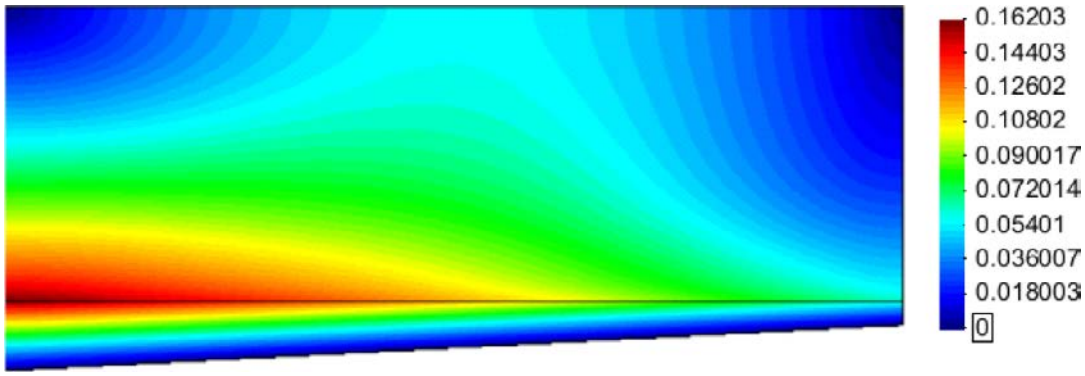

Figure 7-8. *Absolute displacements (meter) in 2D model.*

7.5 Discussion

The relevance of the results can be illustrated by comparing them with results from a saturated oedometer test reported by /Börgesson et al. 1995/. Results from one of these tests are shown in the left graph of Figure 7-9. This started with a number of increasing loading steps from 40 kPa up to 10 MPa. After this the specimen was unloaded down to 40 kPa. The corresponding net mean stresses are shown in the right graph, which shows that the net mean stress is higher during compression than during swelling for a specific void ratio. The material therefore apparently displays a hysteretic behaviour, i.e. the state depends on the path taken to achieve it.

The final stress states from the 1D models are also shown in the right graph (TheorSect and MaxFallout), and the adopted swelling pressure curve (p_{swell} – TR-06-30) is shown for comparison. The final states of the models are fairly close to the oedometer test results, which supports the notion of a remaining heterogeneity in the backfill material. Still, the model stresses is higher than in the oedometer test. The swelling pressure curve coincides with the loading curve of the oedometer test, although it appears that it would be more relevant if this curve would match the swelling curve. And this is found for the second swelling pressure curve (p_{swell} – Retention data) in Figure 7-9. The adoption of these two curves is presented in the Data report /Åkesson et al. 2010/.

These results thus suggest that the used swelling pressure curve (p_{swell} – TR-06-30) is slightly too high, and that it would be more accurate to use the one derived from the retention data. This has been done for the buffer homogenization calculations, presented in Chapter 5.

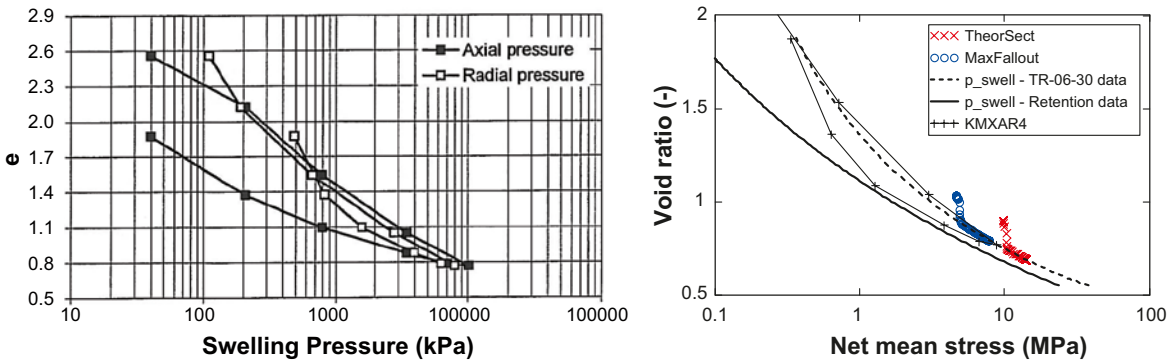

Figure 7-9. *Results from saturated oedometer test (left). Corresponding curve for net mean stress (right) with swelling pressure curve and final states from 1D models.*

7.6 Conclusions and uncertainties

The models indicate that the backfill material will not be completely homogenised. The remaining heterogeneity is of such an extent that the difference between the inner and the outer parts is slightly more than 0.2 in terms of void ratio, and the reason for this appears to be the hysteretic effects during swelling/compression cycles. This type of behaviour is analysed more in depth in Chapter 5.

The remaining heterogeneity indicates that the final void ratio can be as high as 1.03 which corresponds to a dry density of 1,370 kg/m^3. This is still higher than the dry density of 1,100 kg/m^3 that is required for Milos backfill to reach a hydraulic conductivity less than 10^{-10} m/s which is stated in the Backfill production line report.

The main uncertainty of this analysis is that the description of the material and the parameter values are based on measurements performed on MX-80. The current reference material for the backfill is Milos BF which has calcium as the dominant exchangeable cation. The qualitative behaviour of calcium bentonite regarding hysteretic swelling/compression cycles may be different than the corresponding behaviour for sodium dominated bentonite.

A second uncertainty concerns the overall treatment of the hydro-mechanical behaviour: on one hand there are the sets of data from different measurements and tests, which in general display a significant density dependency; on the other hand there is the adoption of several modules and other parameters which are used together with the constitutive laws that do not incorporate any density dependency. The predictive capabilities of the models are therefore limited. This is especially important concerning hysteretic swelling/compression behaviour.

It should also be noted that these types of hydro-mechanical models can be quite difficult to execute. The convergence aspect and the mesh dependence are therefore difficult to address, and this has not been investigated.

8 Buffer upward swelling

8.1 Introduction

One of the main design requirements of the backfill is to keep the buffer in place and prevent it from swelling upwards so that the buffer will not loose too much of its density. Some upwards swelling is expected since the backfill has a lower swelling pressure than the buffer and a certain compressibility. For SR-Can both finite element modelling and analytical calculations of this process have been performed (see e.g. /Börgesson and Johannesson 2006, Börgesson and Hernelind 2006b, Börgesson et al. 2006/ and /Johannesson and Nilsson 2006/), but the reference backfill considered in most of those calculations was an in situ compacted mixture of 30/70 bentonite/crushed rock.

For SR-Site the new reference backfill (compacted blocks and pellets of Milos backfill) is considered. This backfill behaves very different at dry and wet conditions. Preliminary modelling of both cases of this backfill has been done and the results presented in two reports /Johannesson 2008, Börgesson and Hernelind 2009/.

8.2 Problem description

Modelling of upwards swelling with both the buffer and the backfill saturated from start has been done and reported /Börgesson and Hernelind 2009/. In this report the influence of different backfill properties was investigated. For the dry case this report only considers one situation with a geometry that deviates somewhat from the reference design. The present calculations will cover some reference design cases.

The objective of this task is to do additional modelling of the dry case with some alternative geometries that were not considered in the former models and check how the final density distribution of the buffer in the deposition hole is affected by the swelling of the buffer and consequent compression of the backfill.

A schematic view of the geometry of the buffer and the backfill is shown in Figure 8-1. The actual rock contour in the deposition tunnel is not uniform since the tunnel is excavated by blasting. Instead there is a nominal cross section within which the rock contour may not appear and a maximum allowable overbreak illustrated by the two contour lines in the figure.

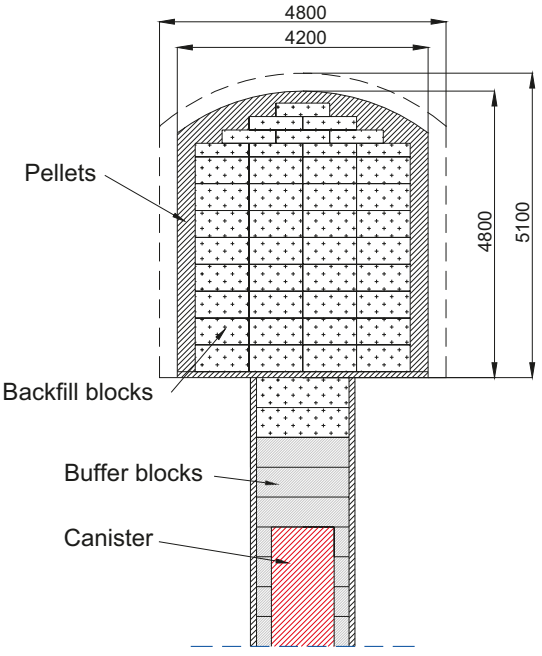

Figure 8-1. *Schematic layout of the backfill above a deposition hole.*

The rock contour has not been varied in the modelling. Instead the space between the block filling and the roof filled with pellets has been varied since for the dry case the influence of the slot width between the blocks and the walls is insignificant compared to the influence of the slot width at the roof.

The problem is simplified by assuming that the buffer material is completely water saturated and homogenised from start and that the backfill is completely unaffected by water.

8.3 Finite element model

The finite element program Abaqus has been used for the calculations. A 3D element model of a section of the tunnel with backfill and a deposition hole with buffer, canister and the bottom plate is used. The model tunnel is 4.6 m wide and 5.4 m high at the crown. Figure 8-2 shows the element mesh.

The model simulates a long tunnel with deposition holes at every 6th meter but is simplified to a quarter of a deposition hole section by using symmetry planes in three of the four vertical boundaries. There are contact surfaces in all contacts between the rock and the buffer and backfill as well as between the buffer and the canister.

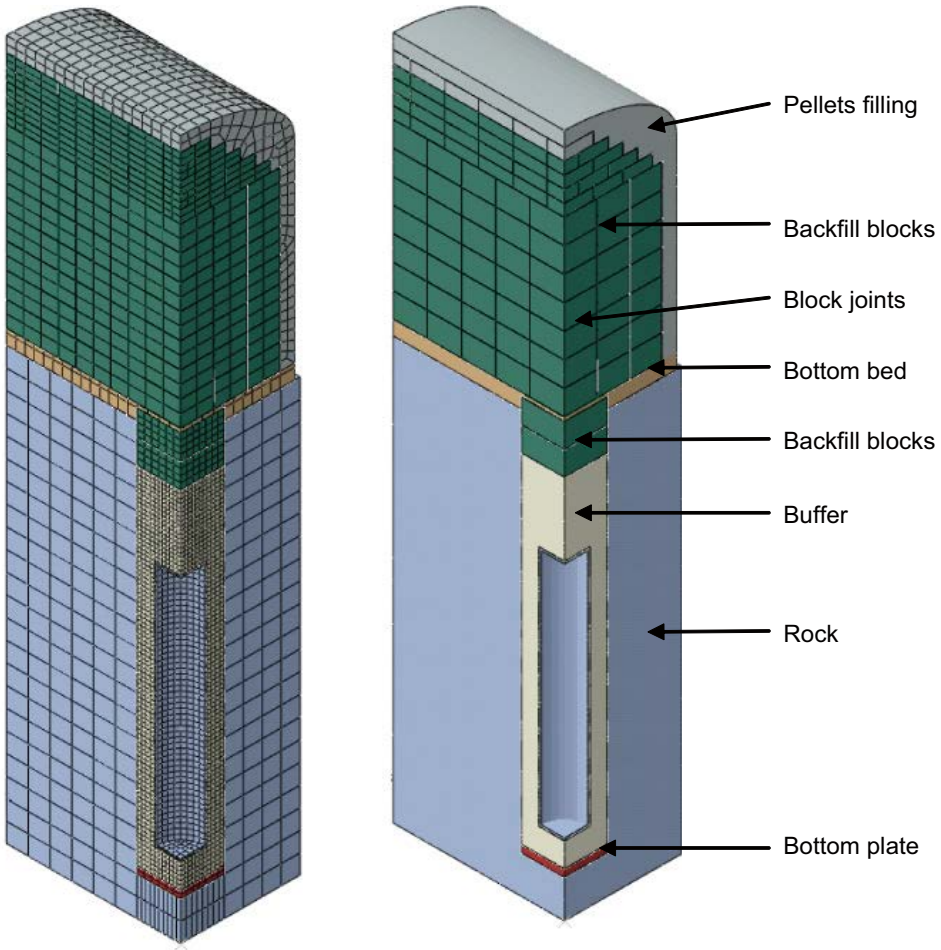

Figure 8-2. *3D element model of a deposition tunnel section with a deposition hole. The left picture shows the element mesh while the right picture shows the different property domains and all the backfill blocks separated by slots.*

The pellets filled slot at the roof is 0.3 m at the crown but a second model with the upper backfill block row replaced with pellets filling is also used yielding 0.55 m slot. The slot between the rock wall and the blocks is 0.29 m wide and the pellets filling in the floor is 0.3 m thick with exception of above the upper backfill block in the deposition hole where the pellets filling is only 0.08 m. Two block types are used; one with the dimensions 0.667×0.7×0.51 m^3 and one with the dimensions 0.6×0.7×0.25 m^3. There is a slot of 4 mm between all blocks for both horizontal and vertical slots. This slot simulates the irregularities of the backfill blocks that after piling will result in imperfect contact areas.

Altogether this geometry yields a degree of block filling of about 76%.

8.4 Material properties

8.4.1 Buffer material

The buffer material model is identical to the model used for studying the buffer homogenisation after erosion (task 6). The bentonite has been modelled as completely water saturated and homogenised from start with the average void ratio 0.77 corresponding to the density at full water saturation 2,000 kg/m^3 in the entire buffer. The motivation for assuming full water saturation and homogenisation is manifold:

- The mechanical models of unsaturated bentonite are very complicated and not sufficiently good for modelling the strong swelling that may take place.
- The models for water saturated bentonite are much more reliable and well documented.
- The stress path and time schedule will differ if saturated instead of unsaturated bentonite is modelled but the final state will be very similar.

The mechanical models of water unsaturated bentonite materials are however successively improved and some calculations could later be done with those models for comparison reason. In Task 5 (buffer homogenisation) the Canister Retrieval Test has been modelled with a complete calculation of a deposition hole with unwetted bentonite blocks and pellets filled slots and compared with an identical calculation with the same homogenised and water saturated buffer as in this task. The results showed that the resulting upwards swelling was almost identical.

The **mechanical model** of the buffer controlling the swelling and consolidation phase is identical to the models and properties derived for MX-80 by /Börgesson et al. 1995/. This model is still considered to be sufficiently good for these types of calculations and has therefore also been used in this and similar calculations for SR-Site.

Porous Elasticity combined with *Drucker Prager Plasticity* has been used for the swelling/consolidation mechanisms, while *Darcy's law* is applied for the **water flux** and the *Effective Stress Theory* is applied for the **interaction pore water and structure**.

Mechanical properties

The *Porous Elastic Model* implies a logarithmic relation between the void ratio e and the average effective stress p according to Equation (8-1).

$$\Delta e = \kappa/(1+e_0)\Delta \ln p \qquad (8\text{-}1)$$

where κ = porous bulk modulus, e_0 = initial void ratio.

Poisson's ratio ν is also required.

Drucker Prager Plasticity model contains the following parameters:

β = friction angle in the p-q plane
d = cohesion in the p-q plane
ψ = dilation angle
$q = f(\varepsilon^d_{pl})$ = yield function

The yield function is the relation between Mises' stress q and the plastic deviatoric strain ε^d_p at a specified stress path. The dilation angle determines the volume change during shear.

The following data has been derived and used for the *Porous Elastic* model (valid for $e<1.5$):

$\kappa = 0.21$
$\nu = 0.4$

The following data has been derived for the *Drucker Prager Plasticity* model

$\beta = 17°$
$d = 100$ kPa
$\psi = 2°$
yield function: see Table 8-1

In some calculations the data for the *Drucker Prager Plasticity* model has been varied in order to study the influence of the friction angle, the cohesion and the dilation.

Hydraulic properties

The hydraulic conductivity is a function of the void ratio as shown in Table 8-2.

Interaction pore water and structure

The effective stress theory states that the effective stress (the total stress minus the pore pressure) determines all the mechanical properties. It is modelled by separating the function of the pore water and the function of the particles. The density ρ_w and bulk modulus B_w of the pore water as well as the density ρ_s and the bulk modulus of the solid particles B_s are required parameters. The following parameters are used for Na-bentonite:

Pore water

$\rho_w = 1{,}000$ kg/m^3 (density of water)
$B_w = 2.1 \cdot 10^6$ kPa (bulk modulus of water)

Table 8-1. Yield function.

q (kPa)	ε_{pl}
113	0
138	0.005
163	0.02
188	0.04
213	0.1

Table 8-2. Relation between hydraulic conductivity and void ratio.

e	K (m/s)
0.45	$1.0 \cdot 10^{-14}$
0.70	$8.0 \cdot 10^{-14}$
1.00	$4.0 \cdot 10^{-13}$
1.5	$2.0 \cdot 10^{-12}$
2.00	$1.0 \cdot 10^{-11}$
3.00	$2.0 \cdot 10^{-11}$
5.00	$7.0 \cdot 10^{-11}$
10.00	$3.0 \cdot 10^{-10}$
20.00	$1.5 \cdot 10^{-9}$

Particles

ρ_s = 2,780 kg/m^3 (density of solids)

B_s = 2.1·10^8 kPa (bulk modulus of solids)

Initial conditions

Calculations with two different initial states of the buffer have been done. The buffer is completely water saturated and is assumed to have an average density at saturation of either ρ_m = 2,000 kg/m^3 or ρ_m = 1,950 kg/m^3 corresponding to the void ratio e = 0.77 or 0.87. The swelling pressure at those two densities is 7 MPa and 3.5 MPa. The pore pressure is set to u = –7 MPa and –3.5 MPa respectively in order to correspond to the effective average stress p = 7 MPa that yields zero total average initial stress. The required initial conditions of the buffer are thus:

Buffer density 2,000 kg/m^3

u_0 = –7 MPa
p_0 = 7 MPa
e_0 = 0.77

Buffer density 1,950 kg/m^3

u_0 = –3.5 MPa
p_0 = 3.5 MPa
e_0 = 0.87

8.4.2 Backfill

There are three different parts included in the dry backfill, namely the blocks, the joints between the slots and the pellets filling.

Block section

The backfill blocks will according to the reference design in the production line report be compacted with a water content of 17% to a dry density of 1,700 kg/m^3. Unfortunately no measurements of the elastic properties of the reference material Milos backfill have been done but measurements on similar materials (e.g. Asha /Johannesson 2008/ and IBECO-RWC-BF) have yielded similar results. The blocks are very stiff compared to the pellets filling and the joints so the results are rather insensitive to the elastic properties of the blocks.

The backfill blocks are modelled as a linear elastic material with the following properties:

E = 245 MPa
ν = 0.17
Initial average stress p_0 = 0 MPa

Pellet section

Also the pellets are modelled as linear elastic. There are two types of pellets filling with different properties.

Walls and roof

The pellets filling in the walls and in the roof is a loose filling with the following parameters:

E = 3.9 MPa
ν = 0.3
Initial average stress p_0 = 0 MPa

Bottom bed

The compacted pellets filling in the floor is stiffer and has been given the following parameters:

$E = 10$ MPa
$\nu = 0.3$
Initial average stress $p_0 = 0$ MPa

The compressibility of different pellets fillings have been tested and reported by /Johannesson 2008/. The E-modules used are evaluated from those measurements for an increase in stress from 0 to 1 MPa for the pellets in the roof and walls and from 0 to 3 MPa for the compacted pellets filling in the floor.

Joints between blocks

Since the bottom bed on which the blocks rest cannot be made as a completely plane or horizontal surface the backfill blocks will be placed slightly uneven in relation to each other. This means that there will be joints that are not even due to slightly inclined blocks that also have slightly different heights. The properties of these joints between the blocks are not known but they will have compression and friction properties that deviate significantly from the properties of the blocks.

As a first assumption that can be used for the calculations the joints have been assumed to have the following properties (both horizontal and vertical):

- Average joint thickness: 4 mm
- Compression properties: the joints are closed at an external pressure of 10 MPa
- Friction angle $\phi = 20°$

Figure 8-3 shows the stress-compression relation that has been used for the joints.

8.4.3 Canister

The canister is modelled as a very stiff can with the following elastic parameters:

$E = 2.1 \cdot 10^6$ MPa
$\nu = 0.3$

8.4.4 Rock

The rock is modelled as a rigid body.

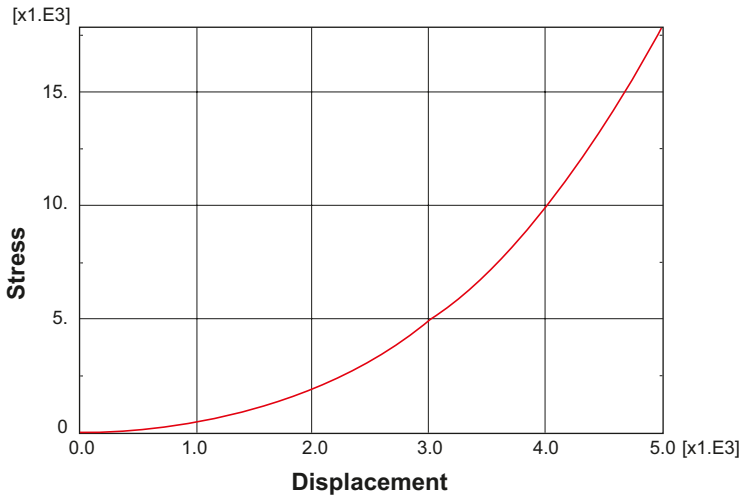

Figure 8-3. *Mechanical model of the joints between blocks. The displacement or compression (m) of the joint is plotted as a function of the total stress (kPa) perpendicular to the joint. After 4 mm compression the joint is closed.*

8.4.5 Bottom plate

The 15 cm thick bottom plate is modelled as a very stiff elastic concrete body. It does not affect these calculations but is included and used for investigating the effect of concrete disintegration in another task.

8.4.6 Contact surfaces

The contact between *the buffer and the rock* and the *pellets filling and the rock* has not been tied in order to allow slip. Instead interface properties with a specified friction have been applied between the different materials. The friction can be modelled with Mohr Coulomb's parameter friction angle ϕ and without cohesion c. The following basic value has been used:

$\phi = 8.69°$

This friction angle corresponds to $\beta = 17°$ in the Drucker Prager model.

The contact surfaces are made not to withstand tensile stress, which means that the contact may be lost and a gap formed between the surfaces.

Another property of the contact surface is the so called "slip tolerance", which describes the required slip to reach full friction. This parameter has been set to 1 mm. Below 1 mm slip the friction is proportional to the slip.

8.5 Boundary conditions

The following boundary conditions are applied:

Mechanical

The vertical planes except the one that represents the tunnel rock wall are free to move parallel with the plane and fixed perpendicular to the plane.

All other outer boundaries are fixed.

Hydraulic

Only the buffer is modelled hydraulically with pore pressure elements. The buffer boundaries to the rock have constant water pressure ($u = 0$ MPa), the boundaries to the canister are no flow boundaries and the vertical "inner" boundaries (x-y and y-z planes) are no flow boundaries.

8.6 Calculation sequence

The calculations are coupled hydro-mechanical calculations. The pore water pressure in the hydraulic boundary of the buffer is stepwise increased from the initial value –7 MPa (–3.5 MPa) to 0 MPa during 1,000 seconds. Then the actual consolidation calculation is run until complete pore water pressure equilibrium with pore pressure 0 MPa is reached in the entire buffer. The calculations were run for over 300 years but the displacements were finished and the pore pressure equalized already in less than 30 years.

8.7 Results

Three calculations have been done with different initial density of the buffer and different slot height at the roof. Table 8-3 summarises the calculations.

Table 8-3. Performed calculations.

Model	Density at saturation kg/m³	Pellets filled slot at roof cm
1	2,000	30
2	2,000	55
3	1,950	55

8.7.1 Density 2,000 kg/m³ and 30 cm slot at the roof

Figures 8-4 to 8-6 show the results for the density 2,000 kg/m³ when 30 cm is left between the roof and the blocks.

Figure 8-4 shows the total vertical displacement after completed swelling. The figure shows that the upwards swelling of the buffer at the buffer/backfill interface is 96 mm and that the major displacements are evenly distributed in the central block pile mainly due to compression of the horizontal slots. The compression of the pellets filling at the roof is about 30 mm i.e. 30% of the total compression of the backfill.

Figure 8-5 shows the end state of the buffer after completed swelling. The lowest density at saturation and corresponding lowest vertical stress at the top of the canister is 1,960 kg/m³ and about 3.8 MPa. At the buffer/backfill interface the corresponding values are consequently lower or about 1,920 kg/m³ and 2.3 MPa. Locally the values are rather low (about 1,840 kg/m³ and about 2.0 MPa) due to edge effects at the rock surface.

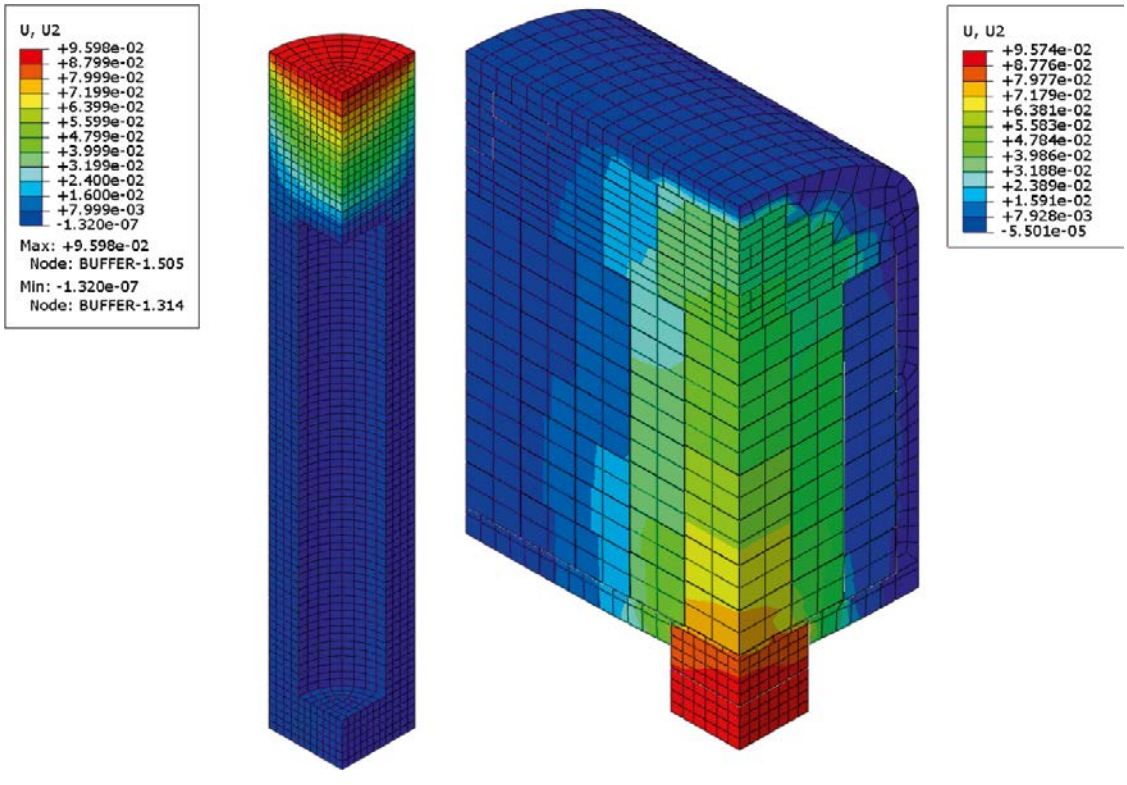

Vertical displacements (m) in the buffer

Vertical displacements (m) in the backfill

Figure 8-4. *Total vertical displacements after equilibrium.*

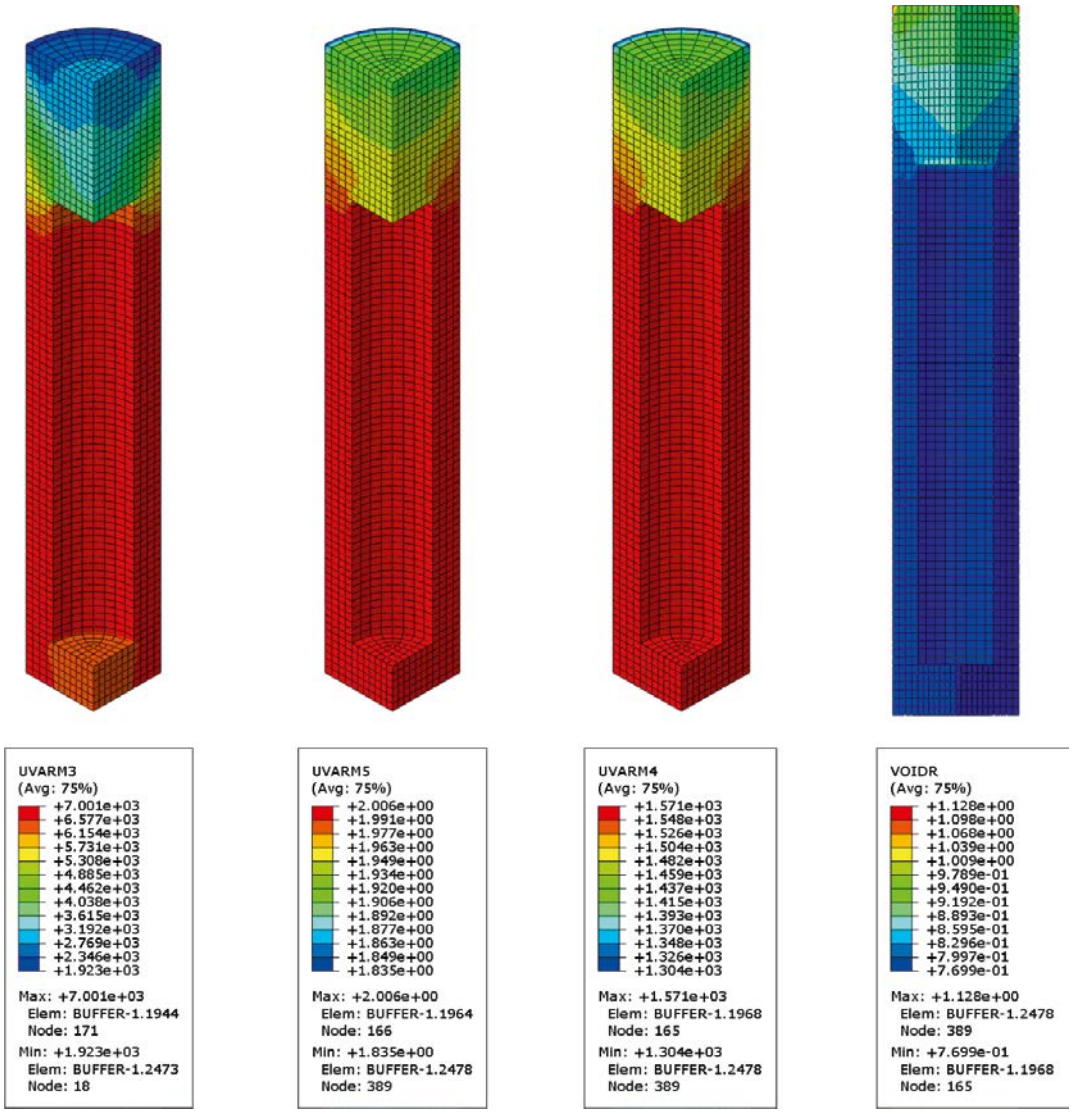

Figure 8-5. *Final state of the buffer after completed swelling.*

Since the backfill blocks are rather dry they are also brittle and have a limited strength. Figure 8-6 shows von Mises' stresses in the backfill. Measurement of the uniaxial compression strength on a similar material (Asha 230 /Johannesson 2008/) at corresponding density have shown that the blocks will fail at a Mises stress of about 3.5 MPa while old results on MX-80 indicate a failure stress of about 3.0 MPa /Börgesson and Johannesson 1995/. In Figure 8-6 Mises stresses higher than 3.0 MPa are marked in gray colour. High stresses with possible failure may thus occur in the upper backfill block in the deposition hole and some blocks resting on the pellets filling in the bottom bed.

8.7.2 Density 2,000 kg/m³ and 55 cm slot at the roof

By removing the upper backfill block row the slot will be 55 cm instead of 30 cm. Results from calculations with the density 2,000 kg/m^3 and this geometry are shown in Figures 8-7 to 8-9.

The show that influence of the larger slot is small. The upwards swelling of the buffer is 102 mm instead of 96 mm while the difference in the overall state of the buffer is insignificant.

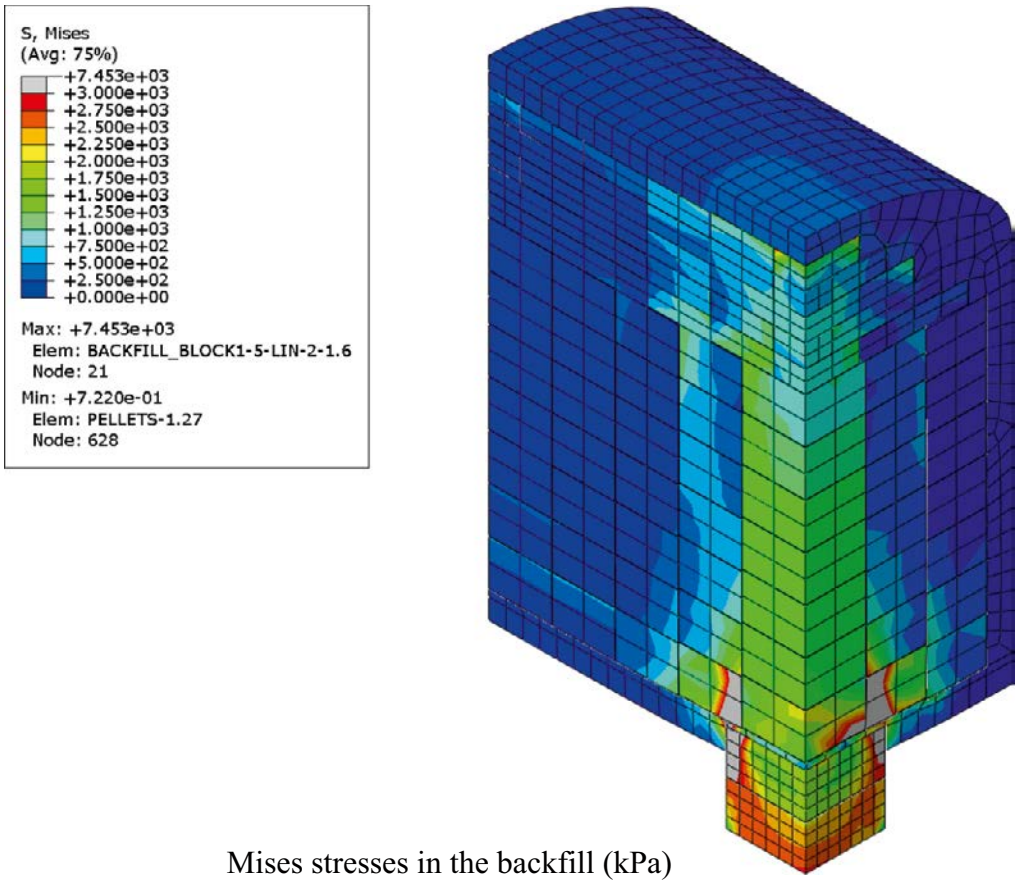

Figure 8-6. *Von Mises' stresses in the backfill after completed swelling.*

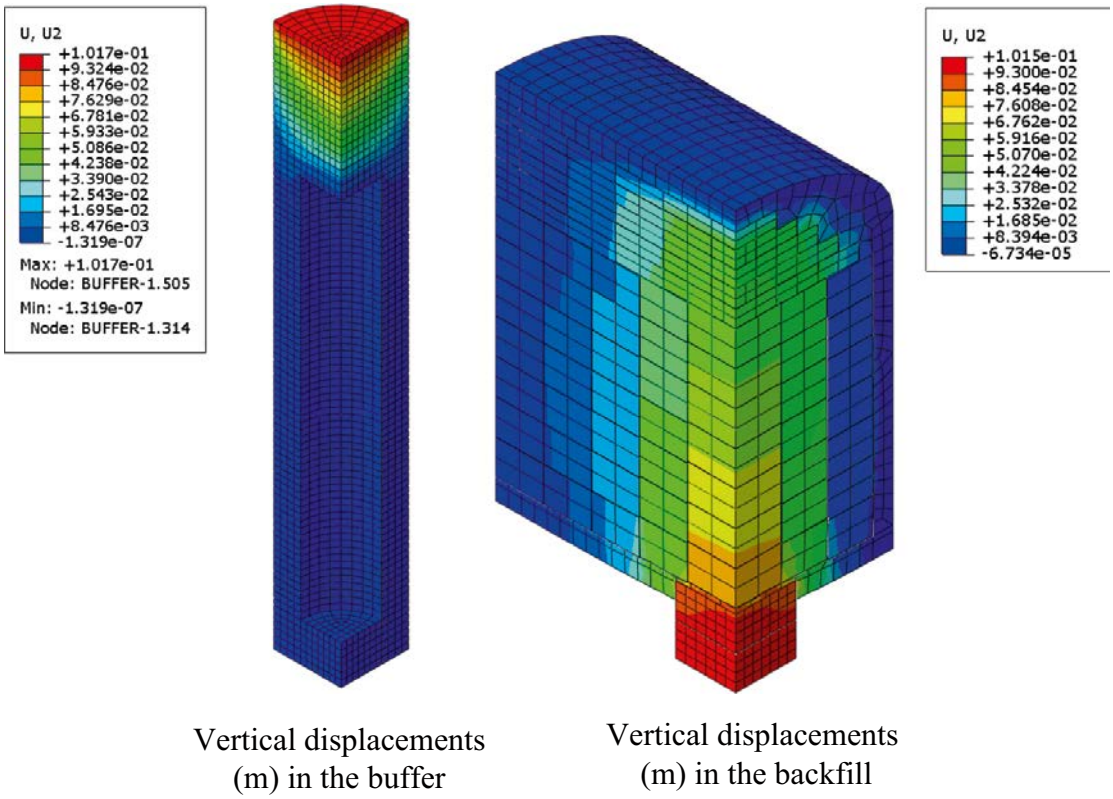

Figure 8-7. *Total vertical displacements after equilibrium.*

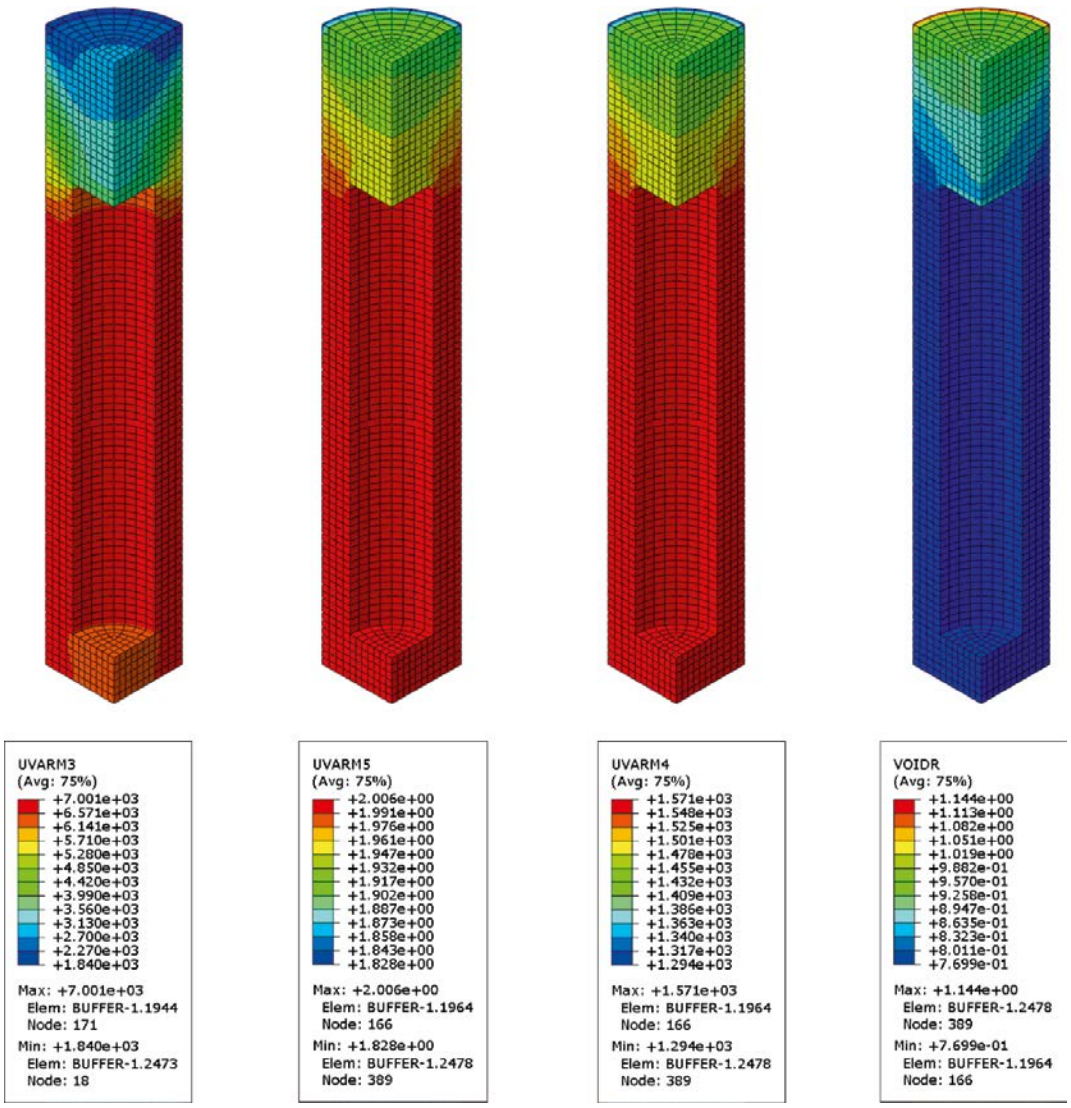

Figure 8-8. *Final state of the buffer after completed swelling.*

The reason for this small effect of increasing the slot width is probably that only 0.6 m out of the 4.6 m wide tunnel is covered by the upper removed block while the rest of the tunnel width is unchanged. As seen in Figure 8-2 the unfilled space at the roof is rather large with a distance to the roof varying from 0.55 m to more than 1.0 m, indicating that the base case represents a rather poorly filled roof section.

8.7.3 Density 1,950 kg/m³ and 55 cm slot at the roof

Figures 8-10 and 8-11 show results from the calculations with the initial buffer density 1,950 kg/m³ and 55 cm slot at the roof.

Figure 8-10 shows that the total vertical displacement is as expected much smaller for the density 1,950 kg/m³ than for the density 2,000 kg/m³. The maximum heave of the interface between the backfill and the buffer is 6.8 cm instead of 10.2 cm. Figure 8-11 shows that the density at saturation is below 1,950 kg/m³ in the entire buffer between the canister lid and the backfill and about 1,920 kg/m³ at the lid of the canister. However, the lowest axial swelling pressure is higher than 2 MPa.

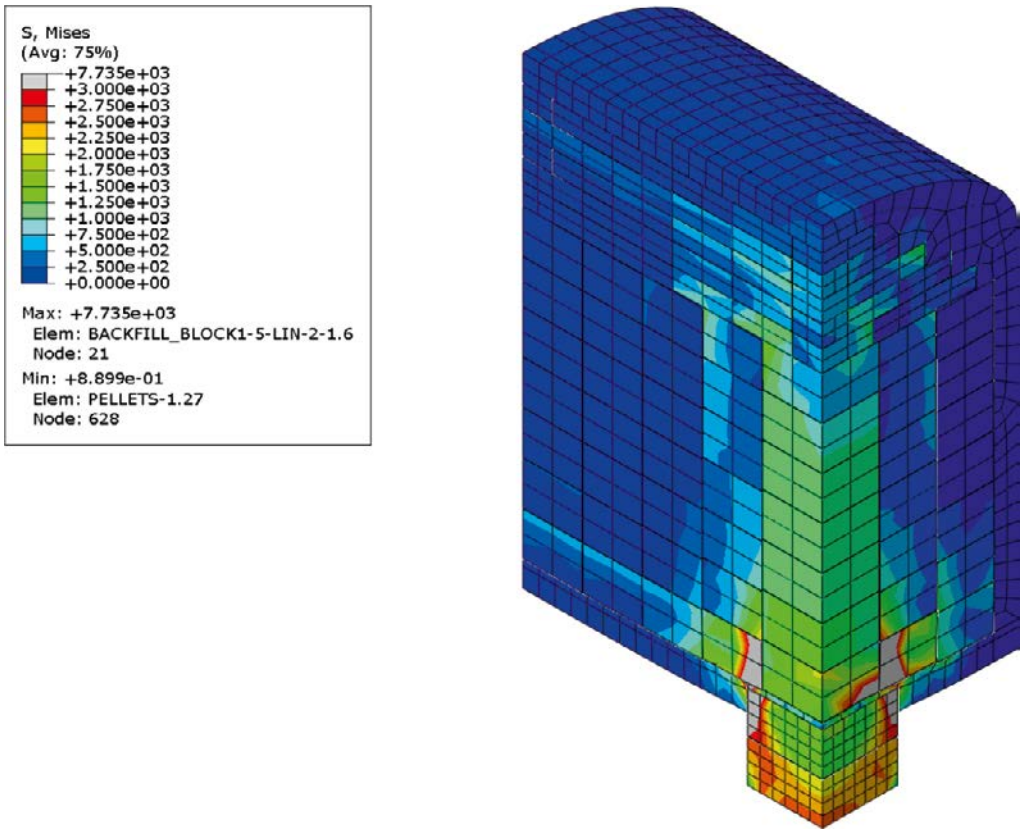

Mises stresses in the backfill (kPa)

Figure 8-9. *Von Mises' stresses in the backfill after completed swelling.*

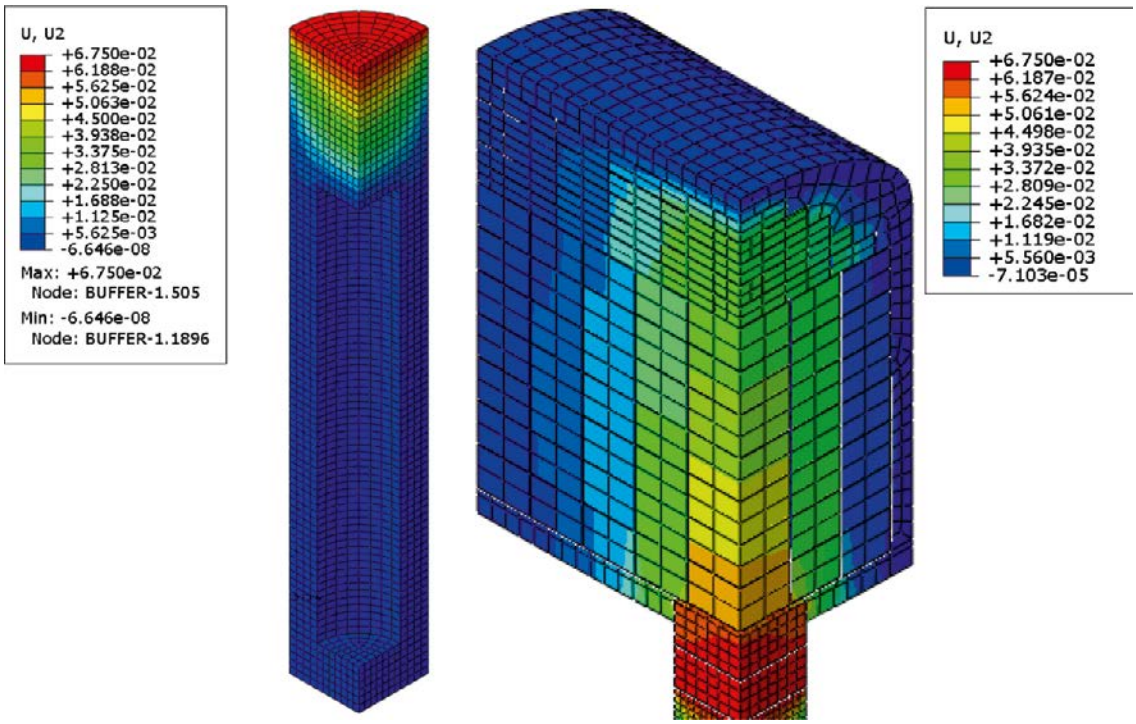

Vertical displacements (m) in the buffer

Vertical displacements (m) in the backfill

Figure 8-10. *Total vertical displacements after equilibrium.*

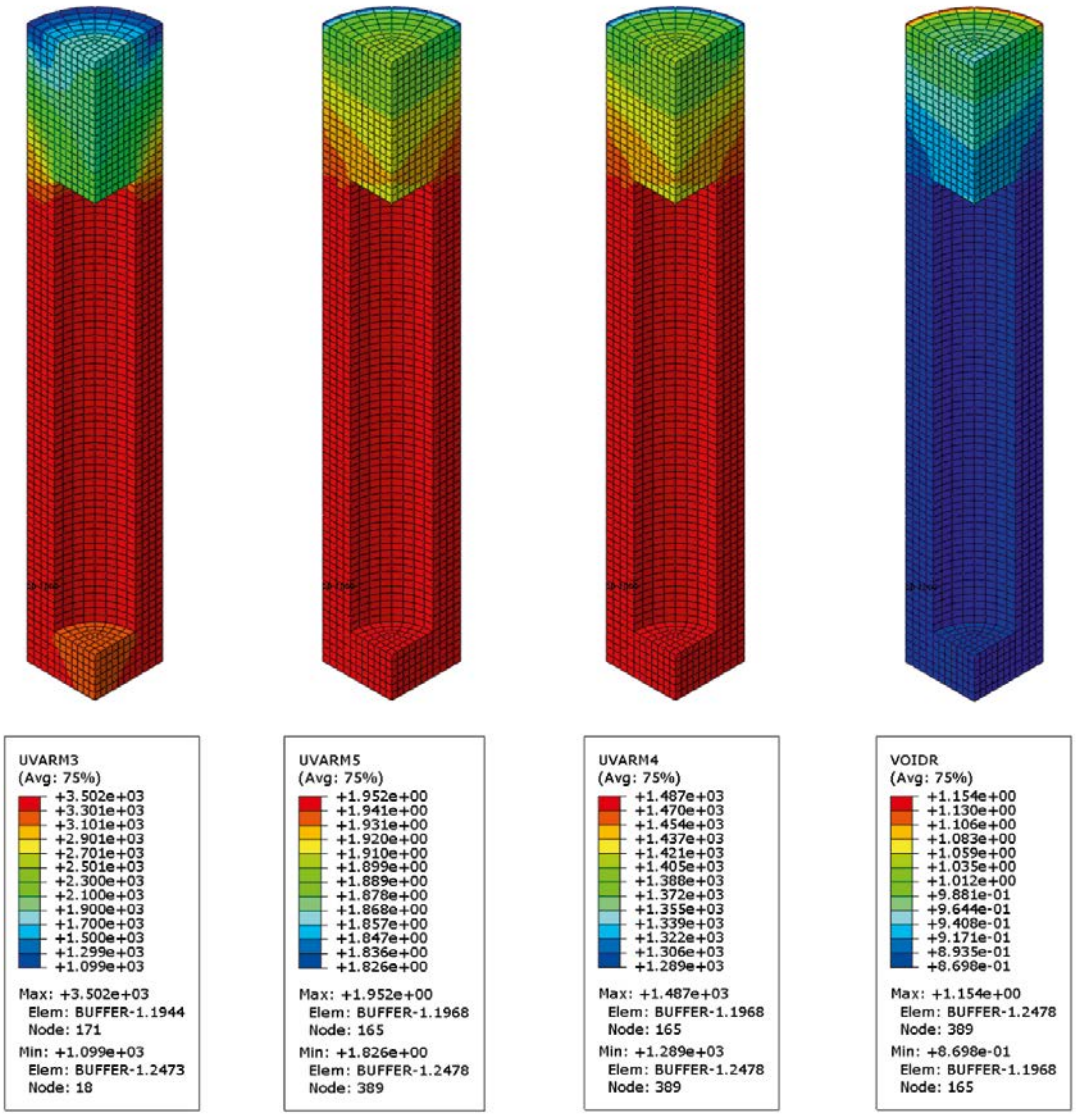

Figure 8-11. *Final state of the buffer after completed swelling.*

8.8 Conclusions and uncertainties

There will be a significant upwards swelling at the extreme case of a completely water saturated buffer material and a completely un-wetted backfill. The geometry modelled was shown in Figure 8-2. It has a degree of block filling of about 76% and a pellets filled slot at the roof of 30 or 55 cm. The important results of the three calculations are summarised in Table 8-4.

The modelled cases represent an extreme wetting situation and have a rather large pellets filled slot at the roof. Most important for the upwards swelling are the horizontal joints between the backfill blocks. The properties of those joints are not known and the stress-strain relation used is estimated.

The results show that there is a loss in density of the buffer above the canister but the resulting lowest density at water saturation at the canister/buffer contact at the initial density 2,000 kg/m^3 is 1,960 kg/m^3, which is good. If the initial density is only 1,950 kg/m^3 the corresponding density is 1,920 m^3, but the swelling pressure is 2.1 MPa so this result should also be acceptable. The results also show that there may locally, in some backfill blocks on the floor, be Mises' stresses that are higher than the compressive strength and thus may cause local crushing of the blocks. This is not expected to yield any problems.

Table 8-4. Summary of results.

Variable	Model 1	Model 2	Model 3
Density at saturation	*2,000 kg/m^3*	*2,000 kg/m^3*	*1,950 kg/m^3*
Pellets filled slot	*30 cm*	*55 cm*	*55 cm*
Max buffer upwards swelling	96 mm	102 mm	68 mm
Canister heave	4.8 mm	5.0 mm	3.2 mm
Buffer density at top of canister	1,960 kg/m^3	1,960 kg/m^3	1,920 kg/m^3
Average axial swelling pressure at top of canister	3.8 MPa	3.6 MPa	2.1 MPa

Uncertainties

There are mainly three uncertainties:

1. The buffer is modelled as completely water saturated and homogenised from start, which may affect the results. This means that the friction force between the buffer and the rock is mobilized early in the swelling process. In the real case there is a pellet filling with very low density between the bentonite blocks and the rock, with an intially rather low swelling pressure and thus low friction force. The result of this difference is that the modelled density gradient between the canister and the backfill probably is larger than if a heterogeneous unsaturated buffer was modelled. The homogenisation modelling in Sections 5.10–5.19 confirms this.
2. The mechanical behaviour of the horizontal contacts between the backfill blocks has not been measured. The relation used assumes that there is a slot of 4 mm that is closed at the pressure 10 MPa, which is probably conservative.
3. The effect of local crushing of the blocks that may occur close to the floor is not included in the model.

Another uncertainty is the how the blocks are piled. It is assumed that the blocks are not overlapping each other, which means that the there will be no lateral spreading of the pressure. The swelling is expected to be smaller if the blocks are piled with overlaps like masonry.

9 Canister sinking

9.1 Introduction

Canister settlement consists mainly of four different processes:

1. Consolidation/swelling caused by the canister weight.
2. Volumetric creep caused by the canister weight.
3. Deviatoric creep caused by the canister weight.
4. Stress changes caused by upwards swelling of the buffer/backfill interface.
   a) Consolidation/swelling
   b) Volumetric creep
   c) Deviatoric creep

The fourth process can thus be divided into the same processes as the first three processes but the consolidation and creep is caused by the swelling pressure from the buffer on the backfill instead of the weight of the canister.

The calculations include two stages, where the first stage models the swelling and consolidation that takes place in order for the buffer to reach force equilibrium. This stage takes place during the saturation phase and the subsequent consolidation/swelling phase. The second stage models the deviatoric creep in the buffer during 100,000 years.

The modelling that has been performed and is reported here takes into account all processes except volumetric creep, which thus may cause a slight underestimation of the canister displacement. The motive for excluding volumetric creep is that a canister settlement caused by volumetric creep will not change the total mass of bentonite under the canister but will only increase the density and is thus not judged to be a problem. Moreover, volumetric creep can be included in the consolidation process by decreasing the stiffness of the buffer. The volumetric creep is of the same order of magnitude as the deviatoric and since the deviatoric creep turns out to be insignificant for the function of the buffer the influence of volumetric creep has not been further dealt with.

9.2 Creep theory

9.2.1 General

The definition of creep is according to normal soil mechanics terminology a strain that will increase with time at a constant load and constant pore water pressure. The latter requirement is necessary in order to distinguish creep from consolidation. The rate of creep is thus controlled by viscosity related deformations in the structure while consolidation is controlled by the rate of the pore water flux out from (or into) the soil pore system. Creep processes take place also when the material is volumetrically confined and will at constant volume yield a change in stress with time (stress relaxation).

Creep at constant stress can be divided into two main processes, namely volumetric creep and deviatoric creep with the following symbols:

Volumetric creep strain: ε_{cv}
Volumetric creep rate: $\dot{\varepsilon}_{cv} = d\varepsilon_{cv}/dt$
Deviatoric creep strain: ε_{cd}
Deviatoric creep rate: $\dot{\varepsilon}_{cd} = d\varepsilon_{cd}/dt$

Deviatoric creep is developed after a change in deviatoric stress at constant average stress, while volumetric creep rate is caused by a change only in average stress. Only deviatoric creep is considered in the creep model as motivated in Section 9.1.

9.2.2 Deviatoric creep

Creep theory and the creep tests made for validating the theory and evaluation of the parameters are described by /Börgesson et al. 1995/. Creep theory states that the creep rate can be modelled according to Equation (9-1), which is taken from an expression suggested and shown to be valid for natural clays by /Singh and Mitchell 1968/.

$$\dot{\varepsilon}_{cdt} = \dot{\varepsilon}_{cdo} \cdot e^{\alpha D_r} \cdot e^{-\alpha D_{ro}} \cdot \left[\frac{t}{t_o}\right]^{-n} \qquad (9\text{-}1)$$

where

$\dot{\varepsilon}_{cdt}$ = deviatoric creep rate ($d\varepsilon_{cd}/dt$) at any time
$\dot{\varepsilon}_{cdo}$ = deviatoric creep rate ($d\varepsilon_{cd}/dt$) at $t=t_0$
t = time
t_o = reference time
e = 2.7183
D_r = degree of mobilised strength $(\sigma_1-\sigma_3)/(\sigma_1-\sigma_3)_f$
$(\sigma_1-\sigma_3)$ = deviatoric stress
$(\sigma_1-\sigma_3)_f$ = deviatoric stress at failure
D_{ro} = reference degree of mobilised strength $(\sigma_1-\sigma_3)_o/(\sigma_1-\sigma_3)_f$
α = inclination of the relation between $\dot{\varepsilon}_{cdo}$ and D_r plotted in a semi-logarithmic diagram
n = inclination of the relation between $\dot{\varepsilon}_{cdt}$ and t plotted in a double-logarithmic diagram

The reference parameters are

t_o = 10,000 s
D_{ro} = 0.5

The validity of Equation (9-1) rests on two observations. The first one is that the relation between $\dot{\varepsilon}_{cdo}$ and D_r is a straight line in a semi-logarithmic diagram. As indicated in Figure 9-1 this is not true for low values of D_r and of course not for D_r=0. It is neither true for high values of D_r. and of course not for D_r=1. Instead the relation shown in Figure 9-1 is used. The second observation is that the relation between $\dot{\varepsilon}_{cdt}$ and t is a straight line in a double-logarithmic diagram. Figure 9-2 shows an example of measurements that confirm this for MX-80. See also /Börgesson et al. 1995/.

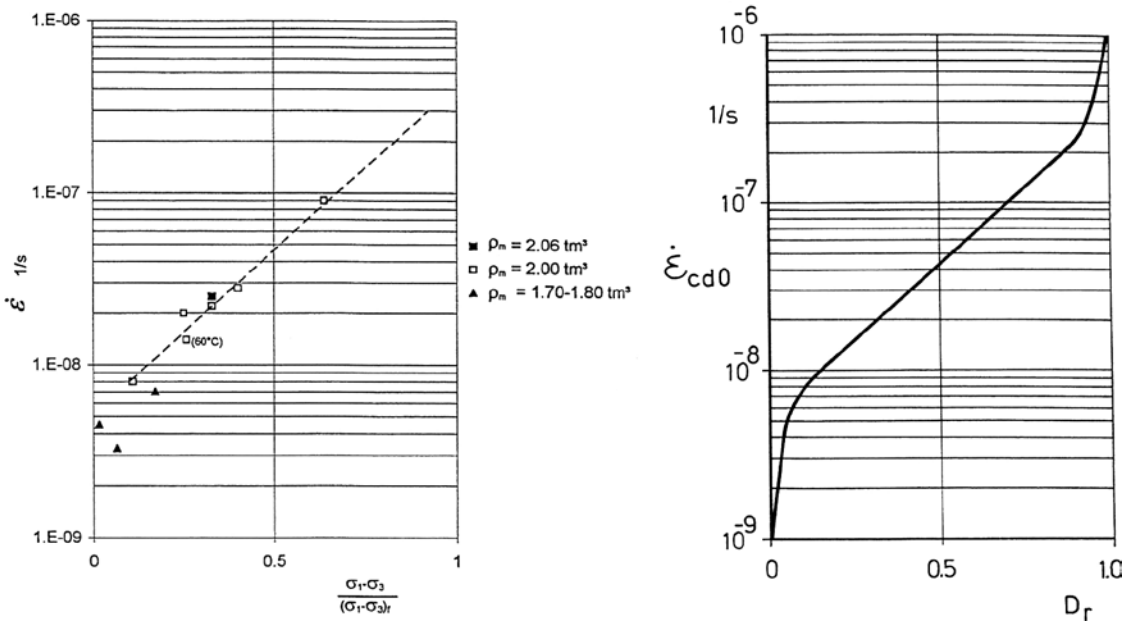

Figure 9-1. *Measured relation between creep rate $\dot{\varepsilon}_{cdt}$ and degree of mobilised strength D_r for MX-80 at different densities (left) and used in the model (right).*

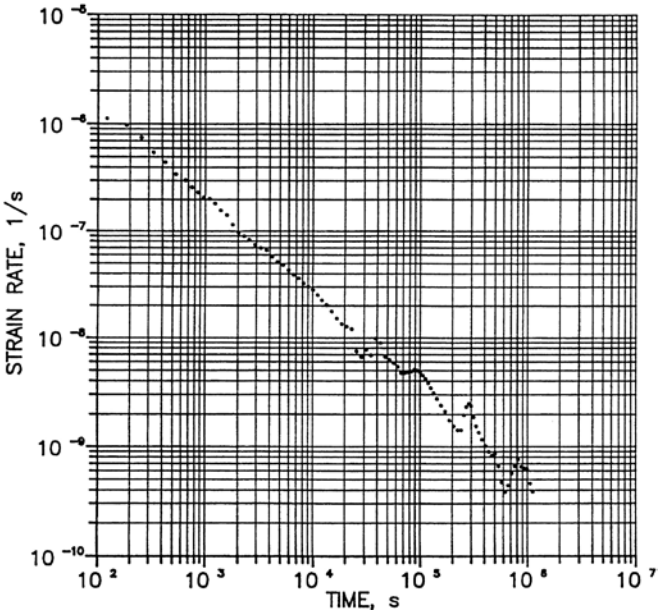

Figure 9-2. *Example of measured creep rate of a sample of MX-80 as a function of time. Sample density at saturation ρ_m=1.99 t/m³, cell pressure σ_3=4.83 MPa, initial pore water pressure u_i=0.75 MPa, degree of mobilised strength D_r=0.40.*

Parameters for Equation (9-1)

$0.1 < D_r < 0.9$

The following values were found for Equation (9-1) and the reference parameters:

$\dot{\varepsilon}_{cdo} = 4.4 \cdot 10^{-8}$ 1/s
$\alpha = 4.15$
$n = 0.91$

Equation (1-1) is thus only valid for $0.1 < D_r < 0.9$ and another relation is required outside this range.

$D_r < 0.1$

The following equation based on Figure 9-1 and Equation (9-1) is used:

$$\dot{\varepsilon}_{cdt} = A \cdot D_r^{\,a} \cdot \left[\frac{t}{t_o}\right]^{-n} \qquad (9\text{-}2)$$

with the following parameters

$t_o = 10{,}000$ s
$n = 0.91$
$A = 8.0 \cdot 10^{-8}$ 1/s
$a = 1.0$

$D_r > 0.9$

The following equation based on Figure 9-1 and Equation (9-1) is used:

$$\dot{\varepsilon}_{cdt} = B \cdot \left[1 - D_r\right]^{-b} \cdot \left[\frac{t}{t_o}\right]^{-n} \qquad (9\text{-}3)$$

with the following parameters

t_o = 10,000 s
n = 0.91
B = $2.3 \cdot 10^{-8}$ 1/s
b = 1.0

9.2.3 Abaqus application

The creep theory has been implemented in Abaqus. Since the theory according to Equations (9-1) to (9-3) is derived in two dimensions it assumes that the intermediate principle stress σ_2 is equal to the minimum principle stress σ_3, which is the case for the triaxial tests. In the 3D space, which is treated by Abaqus, σ_2 usually differs from the two other principle stresses. The deviatoric stress D is more generally expressed with von Mises' stress q that takes the intermediate principal stress into account according to Equation (9-4).

$$q=(((\sigma_1-\sigma_3)^2 + (\sigma_1-\sigma_2)^2 + (\sigma_2-\sigma_3)^2)/2)^{1/2} \quad (9\text{-}4)$$

If $\sigma_2=\sigma_3$ Mises stress will be equal to the deviatoric stress ($q=D$)

In Abaqus the degree mobilized deviatoric strength D_r is exchanged for the degree of mobilized Mises' strength Q_r.

$Q_r=q/q_f$

where

q = actual Mises' stress
q_f = Mises' stress at failure

9.3 Finite element code and finite element models

9.3.1 General

The finite element code Abaqus was used for the calculations. The creep subroutines according to Equations (9-1) to (9-3) have been coded and verified. For the swelling and consolidation processes Abaqus Standard has been used.

9.3.2 Element mesh

The element mesh of the deposition hole is shown in Figure 9-3. The mesh is axisymmetric around the vertical centre line of the deposition hole. The elements in the buffer are about 3×3 cm^2 and in the backfill about 5×5 cm^2. The approximate number of elements in the buffer are 4,300 and in the backfill 5,000.

Contact surfaces were applied at the rock surface in some calculations.

9.3.3 Creep properties of the buffer

The creep model was only used for the buffer and not for the backfill.

- Equation (9-1) was used for $0.1 \leq D_r \leq 1$
- Equation (9-2) was used for $D_r \leq 0.1$

Equation (9-3), simulating the rapid increase in creep rate when failure approaches, was not used due to problems with convergence. This simplification is thus non-conservative but justified because high values of mobilised strength were for all calculation cases only present close to the backfill in the calculations that included buffer/backfill interaction due to the friction against the rock and thus not relevant for the canister settlement with fixed buffer/backfill interface.

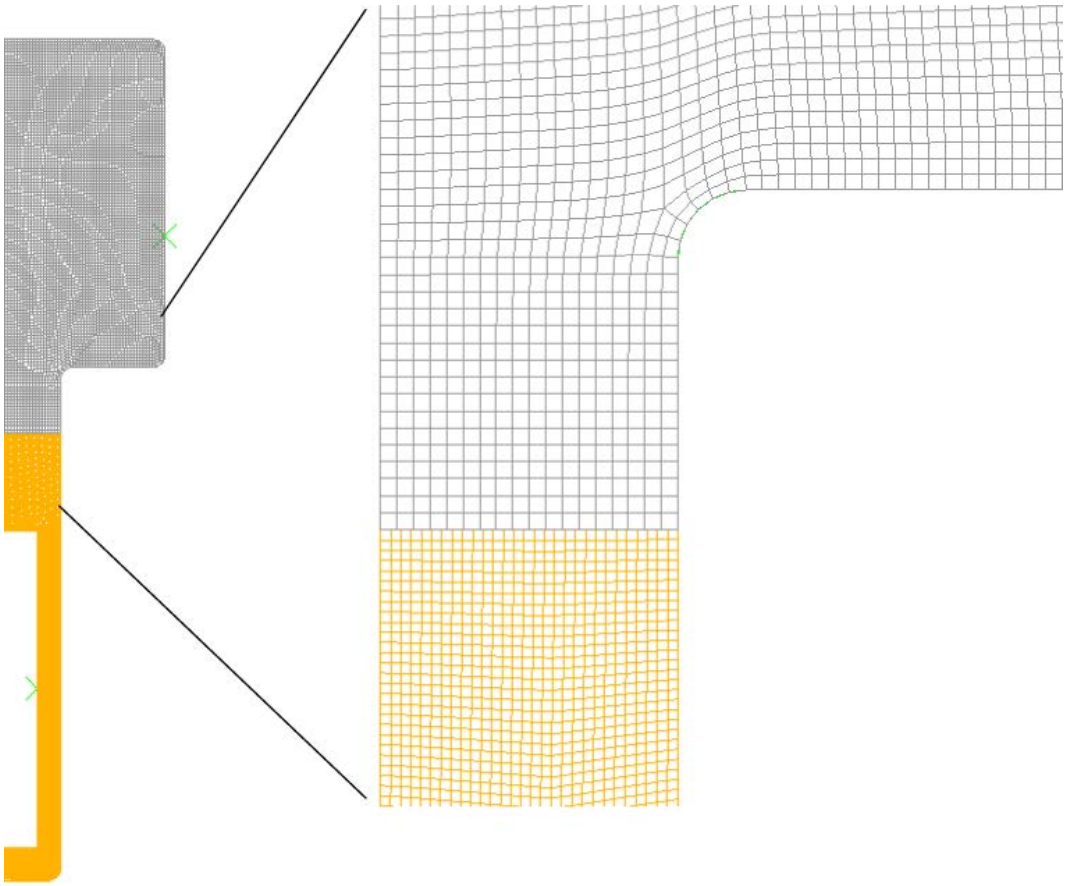

Figure 9-3. *Entire element mesh (left) and enlargement of the upper part of the deposition hole. The mesh is axially-symmetric around the left boundary.*

High values of mobilised strength appear during the consolidation calculation that precedes the creep calculation. Since the consolidation calculation was done with Drucker-Prager plasticity the high shear stresses were limited due to plastization and stress-rearrangement. In this way the consequences were limited and failure simulated.

The creep parameters shown in Section 9.2 were used.

9.3.4 Mechanical properties of the buffer and backfill

Each creep calculation was preceded by a consolidation calculation where the mechanical response of the weight of the canister and in some calculations the upwards swelling of the buffer were considered.

Buffer

The mechanical properties of the buffer controlling the consolidation phase preceding the creep are based on the models and properties derived for MX-80 by /Börgesson et al. 1995/.

The *Porous Elastic Model* implies a logarithmic relation between the void ratio e and the average effective stress p according to Equation (9-5).

$$\Delta e = \kappa \Delta \ln p \qquad (9\text{-}5)$$

where κ = porous bulk modulus.

Poisson's ratio ν is also required.

Drucker Prager Plasticity model contains the following parameters:

β = friction angle in the p-q plane
d = cohesion in the p-q plane
ψ = dilation angle
q = $f(\varepsilon^d_{pl})$ = yield function

The yield function is the relation between Mises' stress q and the plastic deviatoric strain ε^d_p at a specified stress path. The dilation angle determines the volume change during shear.

The following data has been derived and used for the *Porous Elastic* model (valid for e<1.5):

κ = 0.21
v = 0.4

The following data has been derived for the *Drucker Prager Plasticity* model

β = 16°
d = 100 kPa
ψ = 2°
yield function: see Table 9-1

The mentioned properties are the basic properties of the buffer. However, these properties were only used in the consolidation calculations not in the creep calculations, since the Drucker Prager model and Porous Elastic cannot be combined with the creep routine. Instead a linear elastic model was used in the creep calculations with elasticity adapted to the Porous Elastic behaviour based on the results of the consolidation calculation. Since a number of calculations were done with different initial swelling pressure the properties had to be changed and adapted to the stress level at each calculation. The data are shown in connection with presentation of the respective calculation.

Backfill

The backfill was considered linear elastic with properties that makes the backfill rather soft. The reason for making the backfill soft is to clearly illustrate the influence of the backfill and the difference between this case and the case where the backfill is excluded (no upwards displacements), which correspond to a backfill with identical properties as the buffer. These two cases can be considered extremes. The influence of the stiffness of the backfill on the upwards swelling of the buffer is further investigated in Chapter 8 and other reports (see e.g. /Börgesson and Hernelind 2009/).

The following elastic properties were applied for the backfill:

E = 30 MPa
v = 0.3

The swelling pressure of the backfill applied as initial conditions of the average stress p was the following

p = 300 kPa

Table 9-1. Yield function.

q (kPa)	ε_{pl}
1	0
50	0.005
100	0.02
150	0.04
200	0.1

9.3.5 Canister and rock properties

The canister was modelled as a rigid body with a weight of 200 kN, which corresponds to the weight under water since hydrostatic water pressure was not included.

The rock was modelled as a rigid surface. Surface elements were applied at the rock surface between the rock and the buffer and the rock and the backfill.

9.3.6 Properties of surface elements

The interface between the rock and the buffer and the rock and the backfill was modelled with surface elements. These elements define a surface that

1. has friction,
2. prevents movements perpendicular to the surface past the surface,
3. allows movements from the surface (lost contact).

The following friction angles have been used for the surface elements

- Rock/buffer interface: $\phi = 10$ degrees
- Rock/backfill interface: $\phi = 30$ degrees

9.4 Calculations

9.4.1 General

Two types of calculations have been performed. In the first type only consolidation and creep in the buffer caused by the weight of the canister was considered, i.e. the boundaries to the rock and the backfill were fixed. In the second type the interaction with the backfill and the rock was included, resulting in an upwards swelling of the buffer and subsequent rising of the canister.

There have been a lot of calculation problems especially for the second type, due to lack of convergence and mismatching material models. E.g. the creep model cannot be combined with the Porous Elastic model and neither with the Drucker-Prager model. This yields no problem for the first type of calculations with fixed buffer boundaries since there is no change in volume, which means that a linear elastic model for the consolidation phase is acceptable and since there is no high shear stresses against the rock wall.

However, the second type of calculations, which includes interaction with the rock and backfill, involves large volume change at the backfill interface and high shear stresses at the rock wall for the cases with high density and thus high swelling pressure. A proper consolidation (swelling) calculation thus requires both Porous Elastic and Drucker-Prager plasticity. Since the creep calculation requires other simpler models and a change of material model cannot be done, the only way forward was to map the stresses from the consolidation results to a new model.

9.4.2 Calculations with fixed boundaries buffer/backfill and buffer/rock

General

The main concern is the question of how the weight of the canister affects the buffer. How much will the canister sink as a consequence of the creep movements in the buffer caused by the stresses generated by the weight of the canister? A number of calculations have been performed with the purpose to isolate the settlement and creep caused by only the weight of the canister and thus do not consider the effect of the interaction with the backfill and resulting upwards swelling.

As mentioned in Section 9.3.3 only the two creep functions according to Equations (9-1) and (9-2) have been used for all degrees of mobilised shear strengths in the entire interval $0 < D_r < 1.0$.

Since creep driven by Mises stress cannot be combined with Porous Elastic or Drucker-Prager plasticity a linear elastic relation with no plastic strains has been used in the creep calculation as mentioned in Section 9.4.1.

Scope and specification of the calculations

The main determinant of the creep rate is the magnitude of the degree of mobilised shear strength. However, the shear strength decreases with decreasing swelling pressure. In order to study the sensitivity of the canister displacement to changes in properties of the buffer eight calculations with different assumed swelling pressure of the buffer have been performed. The swelling pressure has been varied from 7,000 kPa down to 80 kPa.

By changing the other properties (mainly the stiffness) of the buffer accordingly the variation simulates a change in density at saturation of the buffer from $\rho = 2{,}000$ kg/m^3 (swelling pressure 7,000 kPa) to $\rho = 1{,}500$ kg/m^3 (swelling pressure 80 kPa) in non-saline conditions.

The following properties are thus required at each density for these calculations:

- Swelling pressure
- Deviator (Mises') stress at failure
- Modulus of elasticity

The other properties are the same as given in Sections 9.2 and 9.3.

The relation between **swelling pressure and failure stress** is taken from Figure 9-4 /Börgesson et al. 1995/. The relation can be expressed according to Equation (9-6).

$$q_f = q_0 (p / p_0)^b \tag{9-6}$$

where

p = average stress (swelling pressure)
p_0 = reference average stress (swelling pressure)
q_f = deviator (Mises') stress at failure
q_0 = reference deviator (Mises') stress at p_0
b = constant

For MX-80 at non-saline condition:

p_0 = 1,000 kPa
q_0 = 500 kPa
b = 0.77

which yields

$$q_f = 2.45 p^{0.77} \tag{9-7}$$

The relation between **swelling pressure and elasticity** can be evaluated from the porous elastic relation, which in turn is derived from the relation between void ratio and swelling pressure according to Figure 9-5 /Börgesson et al. 1995/, which can be expressed according to Equation (9-8).

$$e = e_0 \left(\frac{p}{p_0} \right)^{\beta} \tag{9-8}$$

where

e = void ratio
e_0 = reference void ratio
p = average stress (swelling pressure)
p_0 = reference average stress (swelling pressure) at e_0

According to Figure 9-5 the parameter values for MX-80 at non-saline condition and $e < 1.5$ are

$p_0 = 1{,}000$ kPa
$e_0 = 1.1$
$\beta = -0.19$

which yields

$$e = 4.09 \cdot p^{-0.19} \tag{9-9}$$

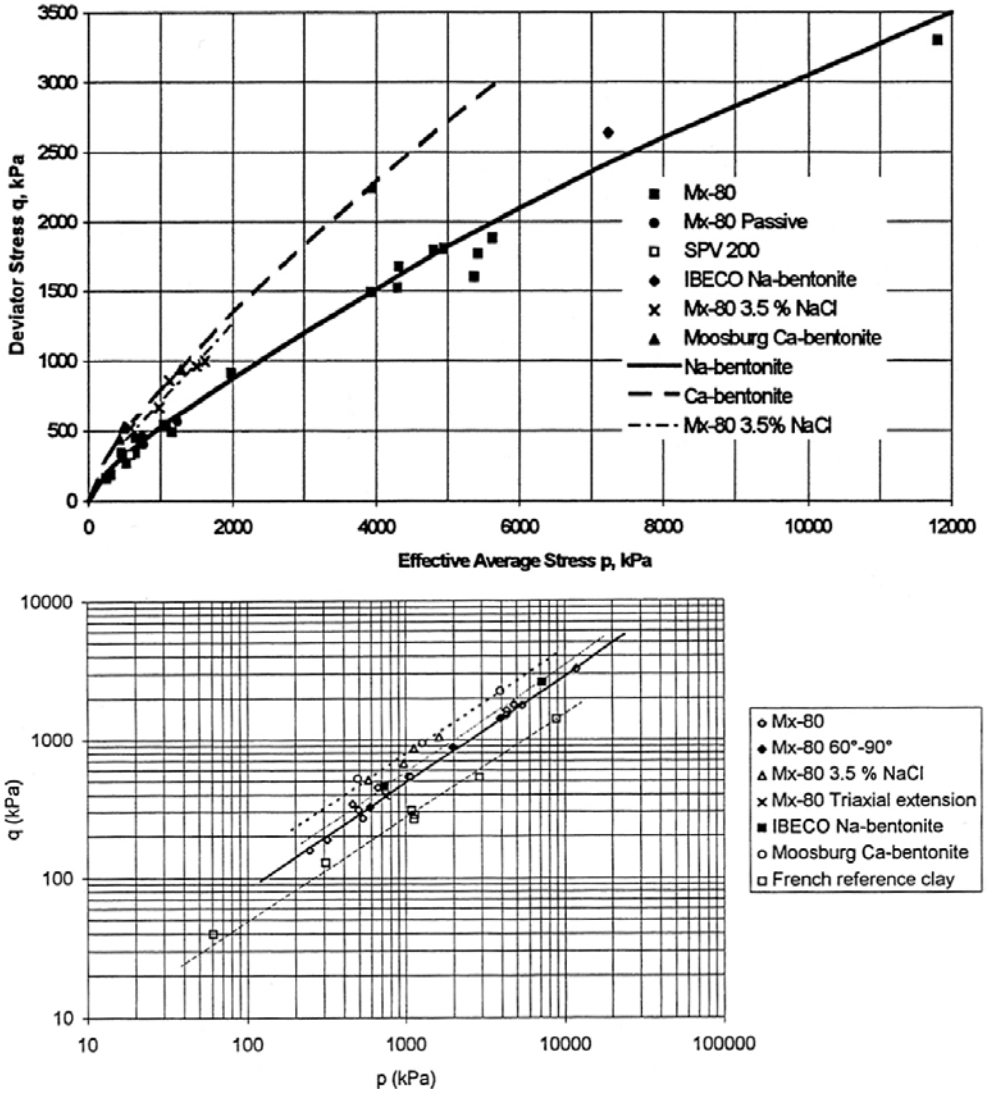

Figure 9-4. *Measured relation between deviator stress at failure q and effective average stress p (swelling pressure) in linear and double logarithmic diagrams.*

Equation (9-8) can be transformed to an E-modulus, which is a function of the swelling pressure according to Equations (9-10) to (9-13).

Derivation of Equation (9-8) yields

$$de / dp = \frac{e_0}{(p_0)^{\beta}} (p)^{\beta-1} \tag{9-10}$$

A change in void ratio can be expressed as a change in volumetric strain ε_v according Equation (9-11).

$$\varepsilon_v = \frac{\Delta e}{1 + e_0} \tag{9-11}$$

which yields

$$d\varepsilon_v / dp = \frac{e_0}{(1 + e_0) \cdot (p_0)^{\beta}} (p)^{\beta-1} = 1 / K \tag{9-12}$$

where

K = compression modulus.

The relation between K and E is

$$E = 3(1 - 2v)K \tag{9-13}$$

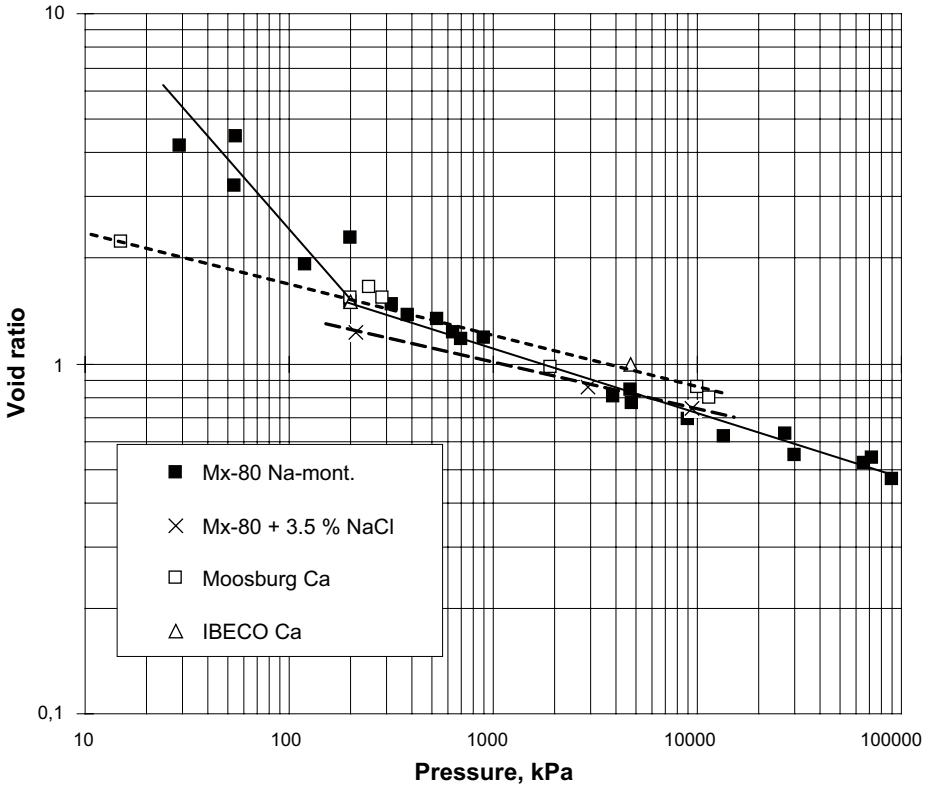

Figure 9-5. *Measured relation between swelling pressure and void ratio.*

The E-modulus is thus a tangent modulus derived from a non-linear relation and used with a constant value that is valid for the average stress as an approximation.

Table 9-2 shows derived data that needs to be used in the different calculations using Equation (9-7) for calculating the deviator stress at failure and Equations (9-12) and (9-13) for calculating the E-modulus.

Table 9-2. Mises' stress at failure and Young's modulus as functions of the swelling pressure derived according to Equations (9-7), (9-12) and (9-13).

Calculation No	Void ratio *e*	Density at saturation ρ_m (kg/m^3)	Swelling pressure *p* (kPa)	Mises' stress at failure q_f (kPa)	Young's modulus *E* (kPa)
1 (base case)	0.76	2,010	7,000	2,238	33,000
2	0.87	1,950	3,500	1,312	16,500
3	0.99	1,890	1,750	770	8,250
4	1.13	1,840	875	451	4,125
5	1.29	1,780	438	265	2,063
6	1.47	1,720	219	155	1,031
7	1.59 (1.8)[1]	1,690 (1,640)[1]	160	122	751[2]
8	1.88 (2.8)[1]	1,620 (1,470)[1]	80	72	376[2]

[1] Actual values of void ratio and density at saturation since e >1.5.

[2] Overestimated since e >1.5.

Calculation sequence

The calculation is divided into the following six main steps:

1. Establishment of initial conditions in the structure. The reference node for the canister is fixed with all nodes locked. No friction is applied between the buffer or backfill and the rock.
2. Friction between the buffer or backfill and the rock is activated. Release of the vertical displacement of the reference node of the canister.
3. The canister weight is applied. The calculations of the first three steps are done with the Porous Elastic and Drucker-Prager Plastic models. The calculation yields the expected consolidation settlement due to the weight of the canister, but the time history is not included. The stresses in the buffer are saved for the creep calculation.
4. The properties of the buffer are changed from Porous Elastic to Elastic. The stresses in the buffer are saved and applied as initial conditions. All nodes are locked.
5. The canister weight is applied and all nodes in the buffer and the canister released (except for the boundary to the backfill)
6. The creep calculation is performed for 100,000 years

Results

The main results are the canister displacement after consolidation, the canister creep during 100,000 years and the final total displacement of the canister for the 8 different calculation cases. The displaced element mesh after 100,000 years and the stresses in the buffer are also of interest.

Figure 9-6 shows the Mises stresses at the two extreme cases 1 and 8. The figure shows that these stresses are rather alike in spite of the difference in swelling pressure. The maximum Mises stress is 50–60 kPa in stress-concentrations at the corners of the canister but the overall Mises stress along the canister surface, that determines the creep rate, is only about 15 kPa.

Figure 9-7 shows the corresponding pictures for the degree of mobilized strength Q_r (called *qkp* in the pictures). Q_r determines the creep rate and the pictures show that the maximum value in stress-concentrations at the corners of the canister is about 0.7 in case 8 with the swelling pressure 80 kPa and only about 0.02 in case 1 with the swelling pressure 7 MPa. Along the canister surface D_r is about 0.24 for case 8 and only about 0.007 for case 1.

The creep that follows after consolidation is plotted as function of time in Figure 9-8 for all cases. In Figure 9-9 all results are collected in one diagram showing the consolidation alone and the sum of the consolidation and creep as a function of the swelling pressure. The total settlement varies between 0.4 mm for case 1 and 2.2 cm for case 8.

Finally Figure 9-10 shows the deformed mesh after consolidation and creep for case 8.

The results show that the settlement and creep are very small for case 1, which corresponds to the reference case. With reduced swelling pressure the settlement increases but is for the case of only 80 kPa swelling pressure not more than 2.2 cm, whereof only about 4 mm is creep.

9.4.3 Calculations that include buffer/backfill interaction

General

If the swelling pressure of the buffer is higher than the swelling pressure of the backfill there will be an upwards swelling of the buffer and corresponding compression of the backfill. In order to have full understanding of the canister displacements this process must be included although it means that the canister will rise instead of sink for some of the cases.

As mentioned in Section 9.3.4 the backfill has been made rather soft and without swelling pressure in order to illustrate the influence of the backfill and to frame the behaviour with two extremes.

These calculations have been more complicated due to the strong interaction with the backfill and the rock surface.

Left figure:

Mises stress at
σ_s=7 MPa

Scale (kPa)

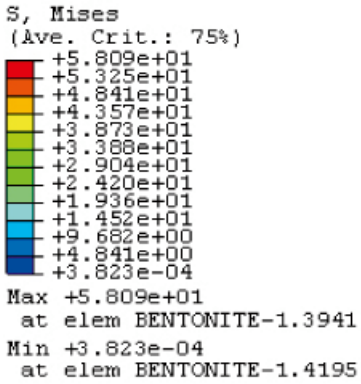

Right figure:

Mises stress at
σ_s=80 kPa

Scale (kPa)

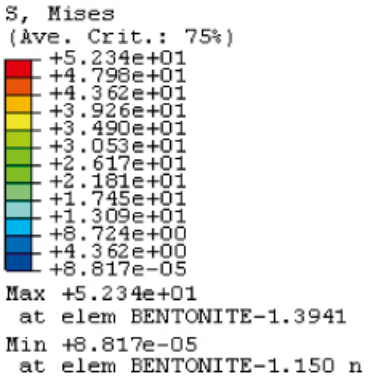

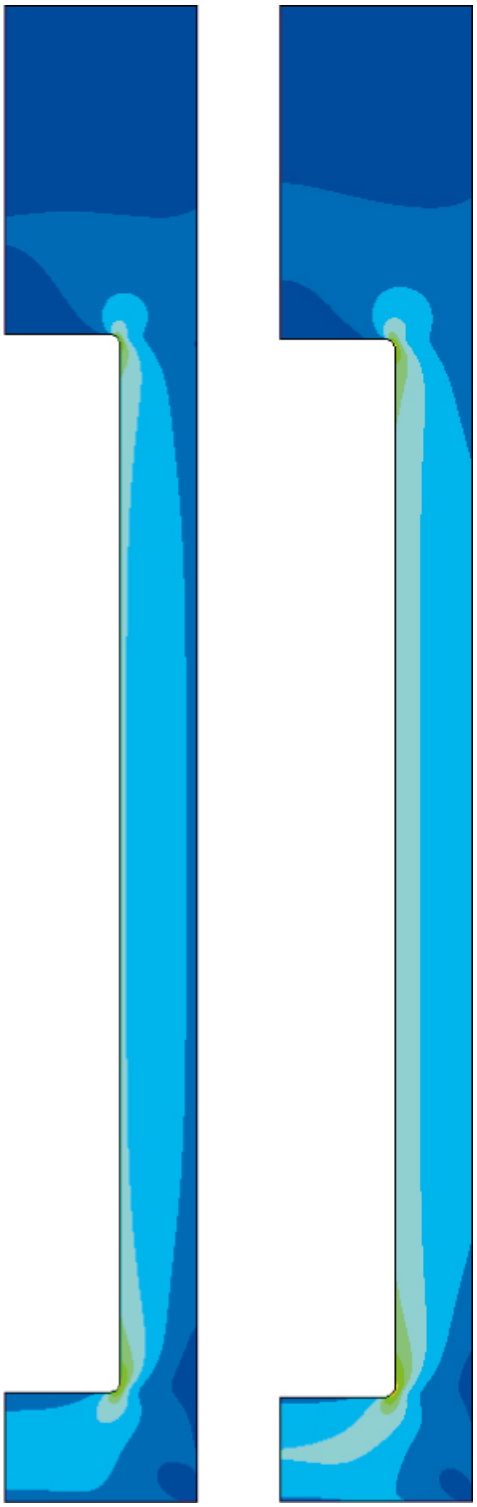

Figure 9-6. *Mises stresses in the buffer after 100,000 years creep in case 1 (σ_s=7 MPa) to the left and in case 8 (σ_s=80 kPa) to the right. No backfill.*

Left figure:

Q_r at
σ_s=7 MPa

Scale

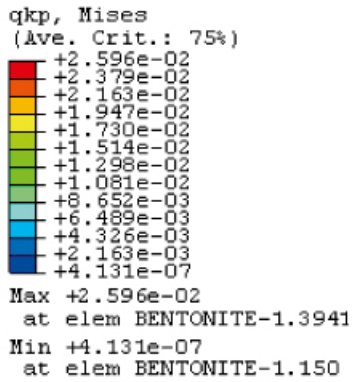

Right figure:

Q_r at
σ_s=80 kPa

Scale

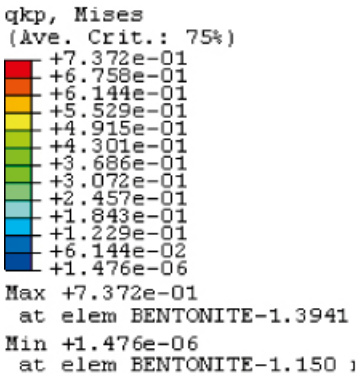

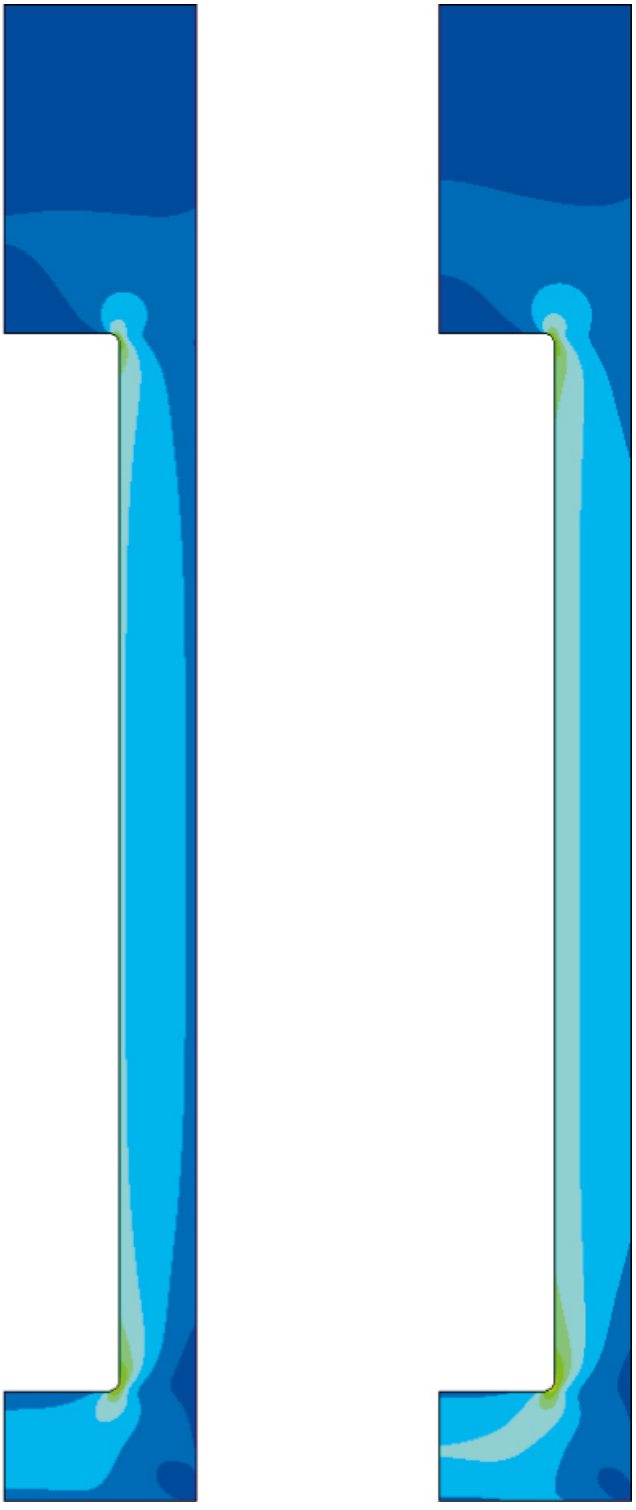

Figure 9-7. *Degree of mobilized strength Q_r in the buffer after 100,000 years creep in case 1 (σ_s=7 MPa) and in case 8 (σ_s=80 kPa). No backfill. Observe the difference in scale.*

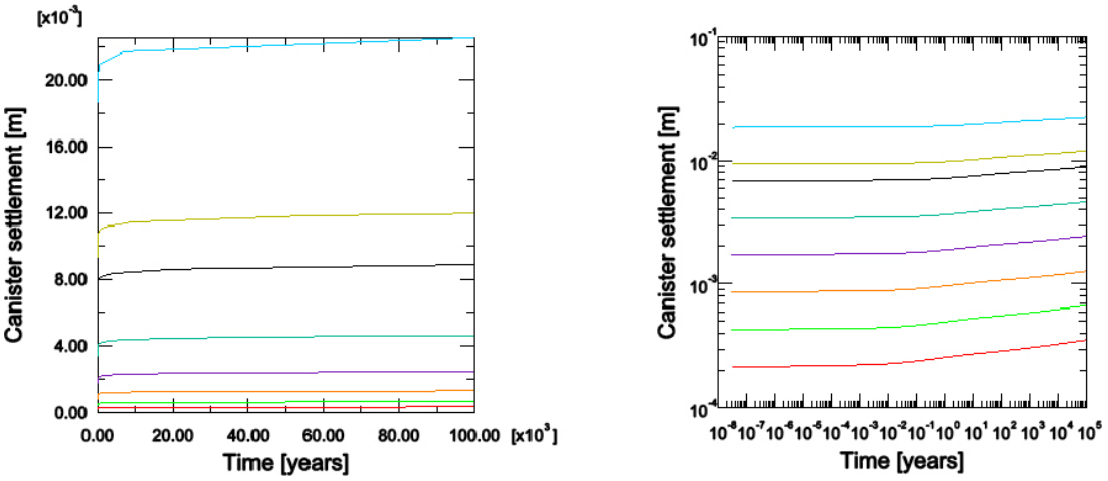

Figure 9-8. *Canister creep as a function of time for all 8 cases in linear and double logarithmic diagrams, with case 1 yielding the smallest creep (red line) and case 8 the largest (blue line). No backfill.*

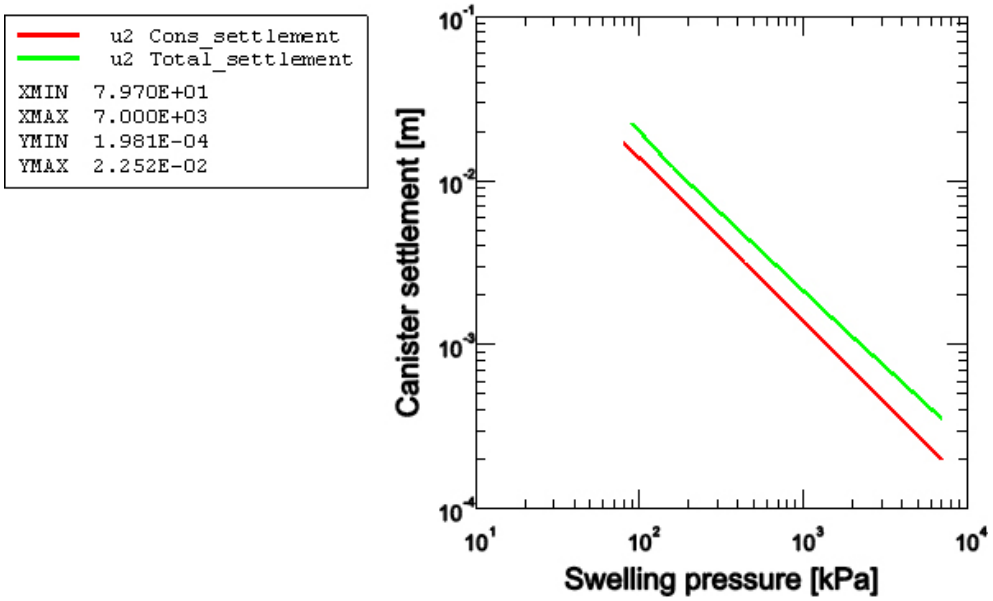

Figure 9-9. *Canister settlement for all cases with no backfill. Red line: only consolidation. Green line: consolidation + creep for 100,000 years.*

Also for these calculations only the creep models according to Equations (9-2) and (9-3) have been used, which is non-conservative for the high stresses between the rock and the buffer close to the backfill in some cases since the creep rate is underestimated. However, the effect on the creep of the canister is insignificant as concluded in Section 9.3.3.

Scope and specification of the calculations

The same material models have been used as in the calculations with fixed boundaries. These models are described in Sections 9.3.4 and 9.4.2. The set of calculations and material properties described in Table 9-2 have also been used for these calculations i.e. the swelling pressure of the buffer has been varied from 7 MPa to 80 kPa.

The differences between the calculations that include the interaction with the backfill and the rock and the calculations that don't are that the nodes between the buffer and the backfill have been released and allowed to move and the contact elements at the rock surface have been activated.

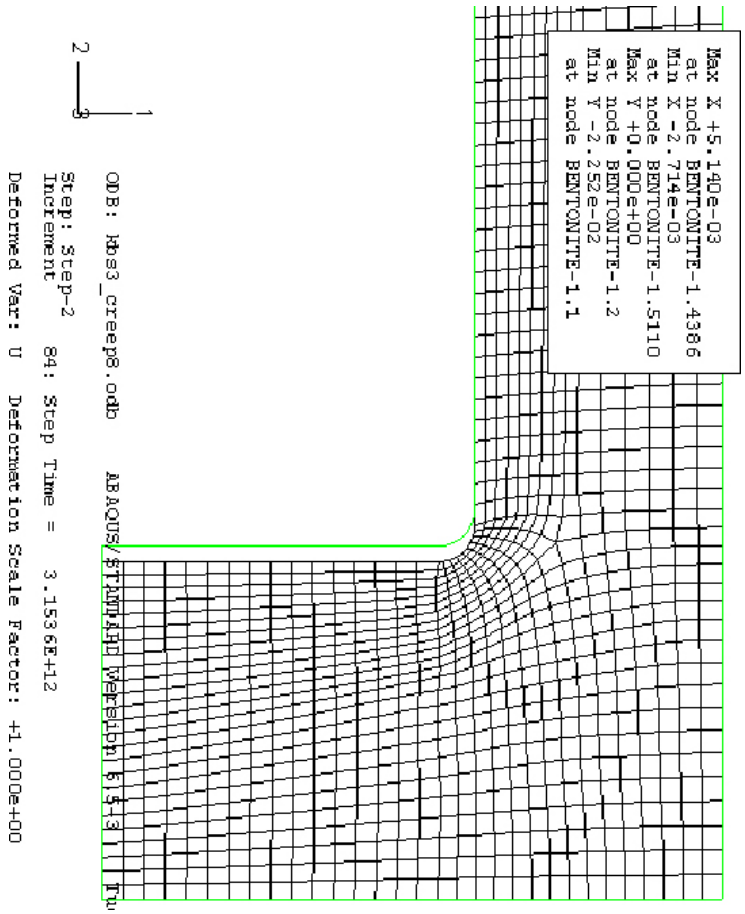

Figure 9-10. *Deformed mesh for case 8 after 2.2 cm total settlement. The green contour line indicates the original position of the canister. No backfill.*

Results

The results of most of the 8 calculations that include the backfill differ significantly from the results with locked boundary between buffer and backfill due to the strong interaction between the buffer and the backfill at least for the calculations with high swelling pressure in the buffer. The results will be illustrated with the results from the base case (that is the case with 7 MPa swelling pressure of the buffer) followed by comparison with the results of the other 7 cases.

Base case

Figure 9-11 shows two displacement plots of the base case. One refers to the vertical displacements caused by only the creep, showing that the maximum creep displacement takes place in the buffer between the canister and the backfill and is 1.4 cm upwards. The canister moves ~ 2 mm upwards by the creep. The other plot refers to the total displacement or the sum of the consolidation and creep, showing that the maximum total displacement takes place at the interface between the buffer and the backfill and is 10.7 cm upwards. The total canister displacement is too small to be observed in this scale.

Figure 9-12 shows the creep heave of the canister as a function of time.

The *heave of the canister* from the different phases is the following:

Heave from only swelling: 2.7 mm
Heave from only creep: 2.0 mm
Total heave (swelling + creep): 4.7 mm

The canister displacement during the creep phase, shown in Figure 9-12, is overestimated, since the creep in the calculation starts at the time 1 second and the creep is about 0.5 mm after 10^5 seconds. Since the values used for the shear strength and Young's modulus are based on tests with duration of

Vertical displacements

Left figure:

Creep displacements

Scale (m)

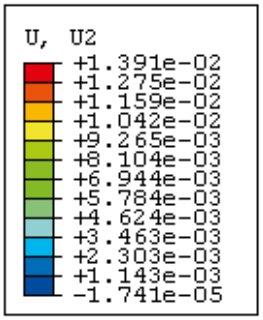

Right figure:

Total displacements (cons. + creep)

Scale (m):

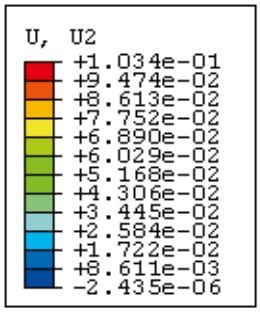

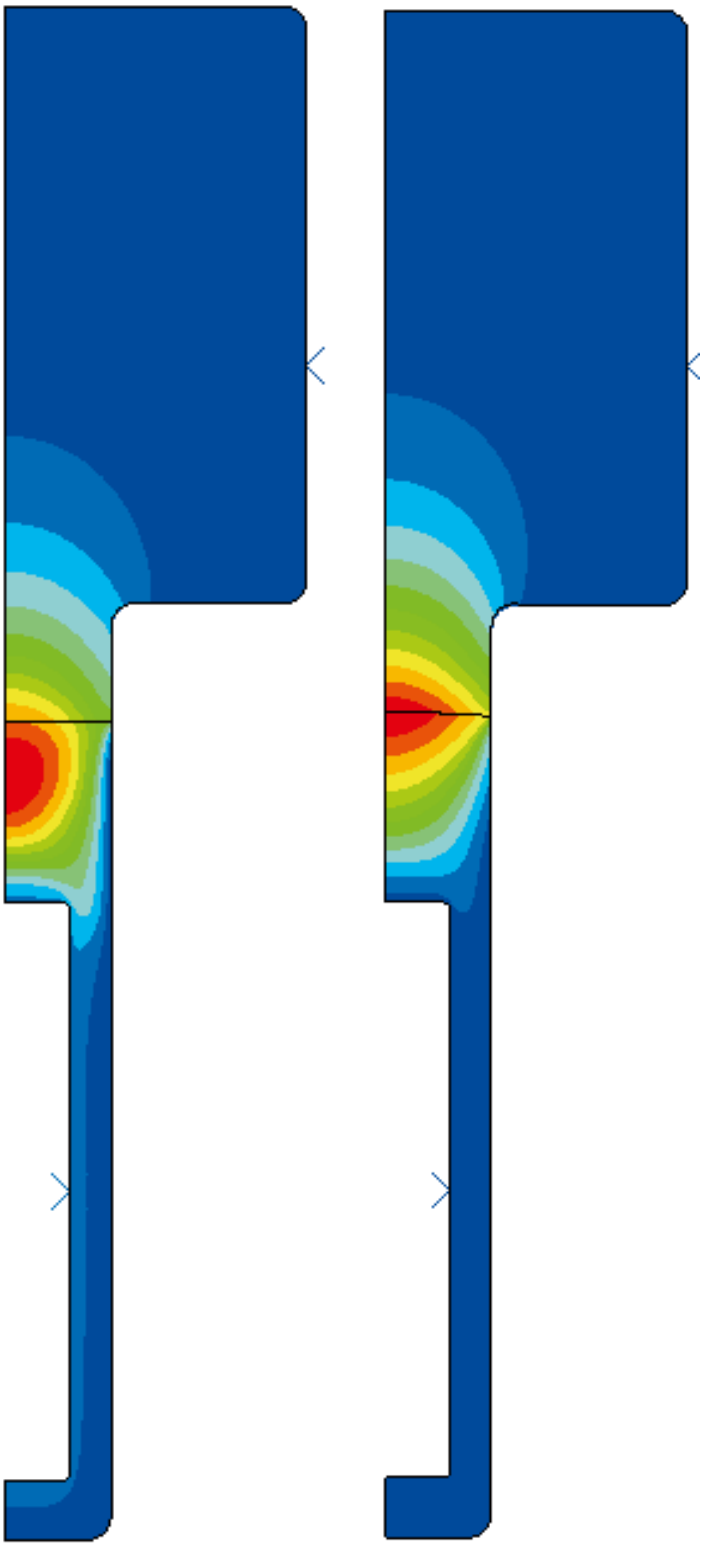

Figure 9-11. *Plots of the vertical displacements (m) upwards in the base case caused by only the creep (left) and the total displacements. Observe the difference in scale.*

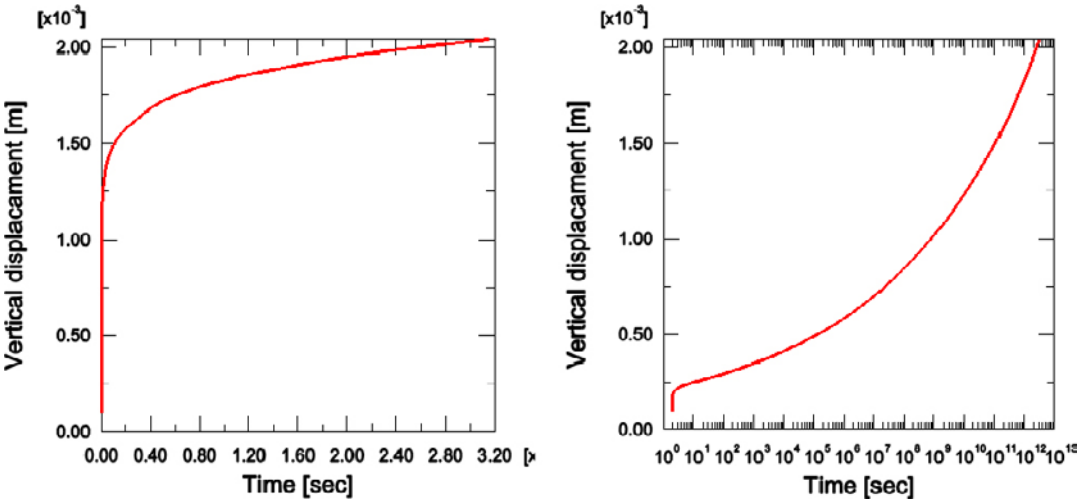

Figure 9-12. *Creep displacement of the canister as a function of time for the reference case plotted both in linear and logarithmic scale.*

between 1 and 10 days this creep is already included in the consolidation model and the calculated creep should actually start after that time. However, since this overestimation is conservative (yields too large creep deformation) and the actual start point is not well defined the results have not been corrected.

The effect of the upwards swelling is much stronger in the consolidation phase than in the creep phase and the upwards movement of the buffer/backfill interface dominates the behaviour over the influence of the weight of the canister.

Figure 9-13 shows the heave of the interface between the buffer and the backfill and the creep displacement of the interface. The difference in total heave and creep in the different parts of the interface is caused by the friction against the rock surface.

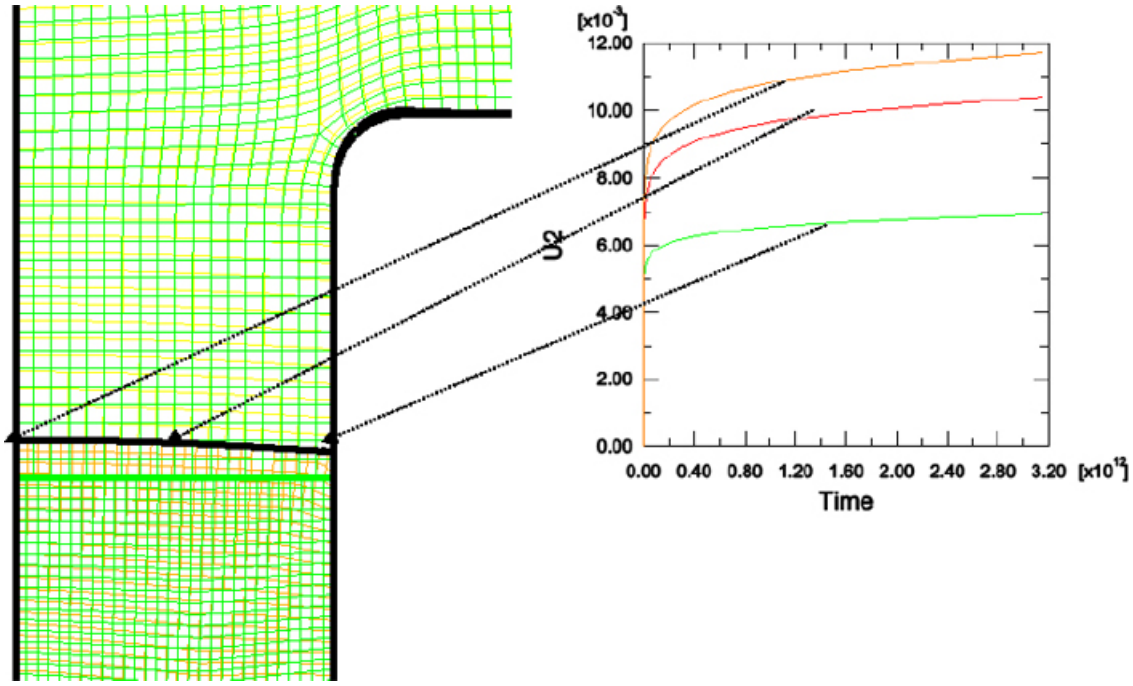

Figure 9-13. *Deformed element mesh after swelling and creep (black contour) and the creep deformation U2 (m) of three points on the buffer/backfill interface as a function of time (s).*

The *maximum heave of the interface* in the different phases is the following:

Heave from only swelling: 95 mm
Heave from only creep: 12 mm
Total heave (swelling + creep): 107 mm

The effect of swelling, consolidation and creep on the average stress in the buffer is shown in Figure 9-14. The upwards swelling has reduced the swelling pressure of the buffer to less than half at the interface with the backfill, while the creep has not influenced the stress significantly at that interface. The influence of the creep is a slight reduction in swelling pressure of about 500 kPa above the canister.

Influence of a reduction in swelling pressure

The magnitude of the swelling pressure has a strong influence on both the canister displacement and the displacement of the buffer/backfill interface.

The same contour plots of the displacement of the buffer that were shown for the base case in Figure 9-11 are shown for case 8 (the lowest swelling pressure) in Figure 9-15. The low swelling pressure means that both the canister and the interface are sinking.

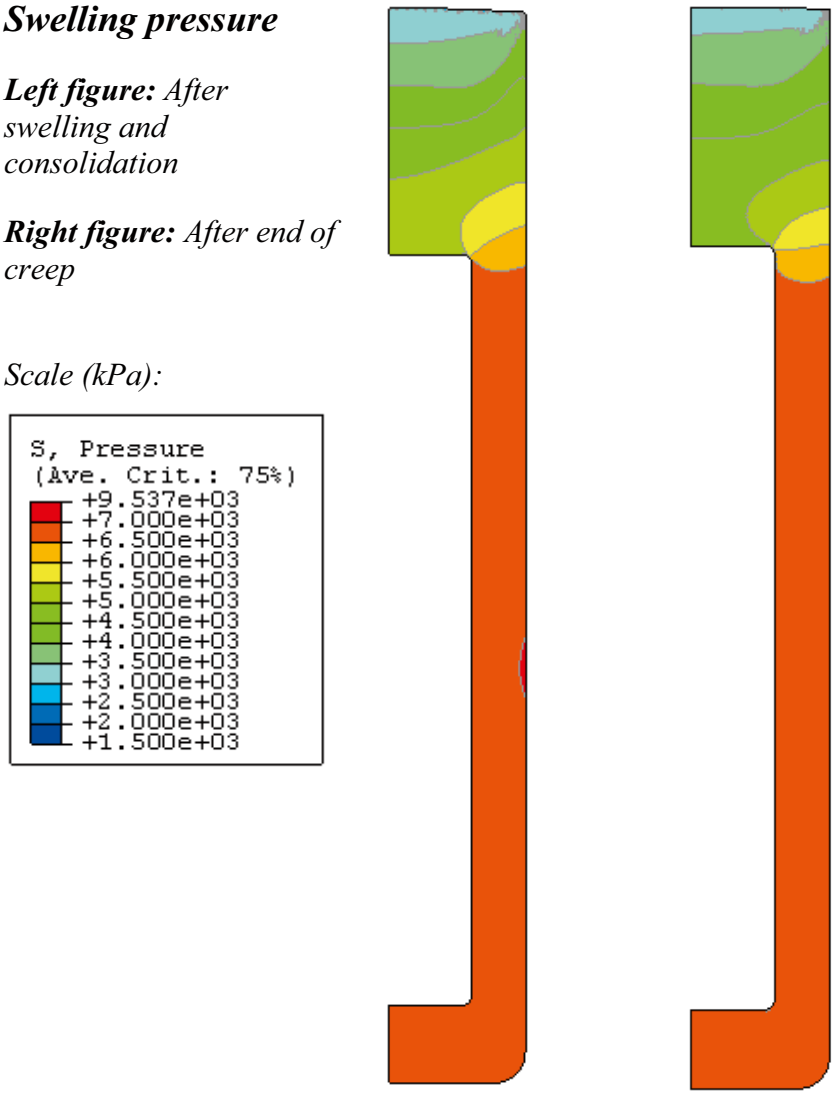

Figure 9-14. *Plots of the average stress in the buffer for the base case after only swelling and consolidation (left) and after creep as well.*

Vertical displacements

Left figure:

Creep displacements

Scale (m)

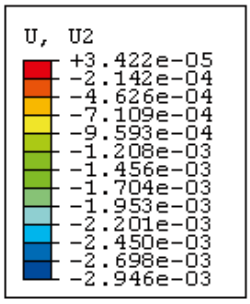

Right figure:

Total displacements (cons. + creep)

Scale (m):

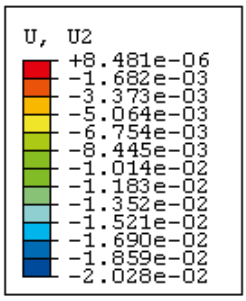

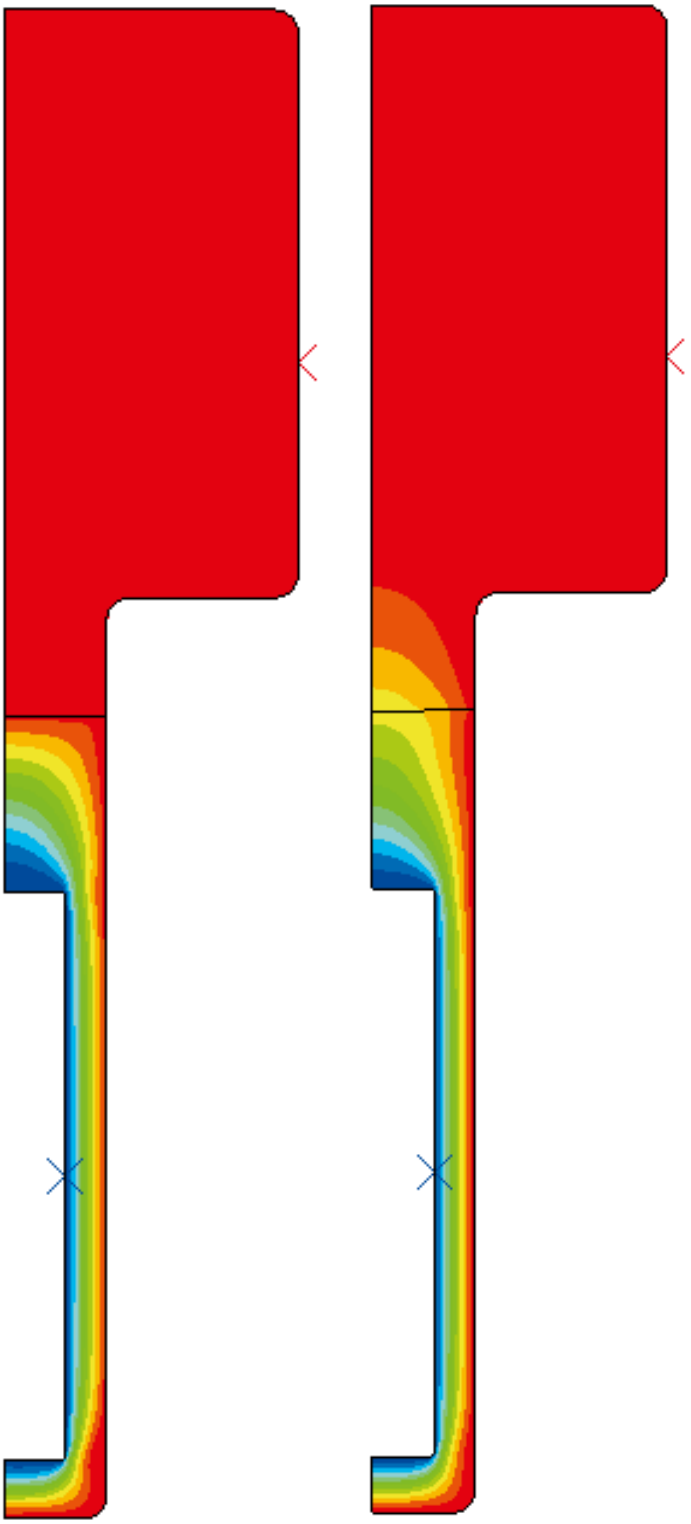

Figure 9-15. *Plots of the vertical displacements in case 8 (p=80 kPa) caused by only the creep (left) and the total displacements. Observe the difference in scale. Negative values imply sinking.*

The total *maximum sinking of the buffer/backfill interface* for case 8 and is about 6 mm.

The *sinking of the canister* from the different phases of case 8 is the following:

Canister sinking from only swelling and consolidation:	26 mm
Canister sinking from only creep:	3 mm
Total canister sinking:	29 mm

The canister creep as a function of time is shown in Figure 9-16 for all cases. The figure shows e.g. that the creep implies heave for cases 1 and 2 and (slightly) for case 3 (p >1,700 kPa) and sinking for the other cases (p < 1,700 kPa).

The swelling pressure after consolidation and creep is shown in Figure 9-17 for cases 4 and 8. For case 8 the behaviour is different to the behaviour in case 1 since the pressure is increased below the canister and in the contact zone at the backfill while case 4 behaves more like case 1 with a reduced pressure with increased vertical distance from the canister above the canister. The reason is of course that the swelling pressure is higher in the backfill than in the buffer for case 8.

The creep rate is governed by the degree of mobilized strength Q_r. Figure 9-18 shows a comparison of Q_r for some cases. In case 1 with the high swelling pressure the mobilized strength is rather high (> 0.4) in almost the entire buffer above the canister due to the strong upwards swelling of the buffer. Along the canister surface Q_r is slightly higher than 0.1. In case 3 Q_r is much lower above the canister and also much lower along the canister surface (< 0.03) than in case 1. The reason for this reduction in mobilized strength with reduced swelling pressure is of course the reduced upwards swelling of the buffer.

As illustrated by cases 6 and 8 the mobilized strength is very low above the canister while it increases with decreasing swelling pressure along the canister, where Q_r is about 0.1 for case 6 and about 0.2 for case 8. The reason for that Q_r increases again with decreasing swelling pressure is the influence of the weight of the canister that dominates for these low swelling pressures. Rather high values are also noted close to the corners of the canister lids for case 8.

Figure 9-19 shows the relaxation of the stresses, expressed as mobilized strength, which takes place due to the creep. For the reference case the relaxation is rather strong above the canister where the mobilized strength is high while it is insignificant in the other parts. For the extreme case 8 the relaxation is small everywhere.

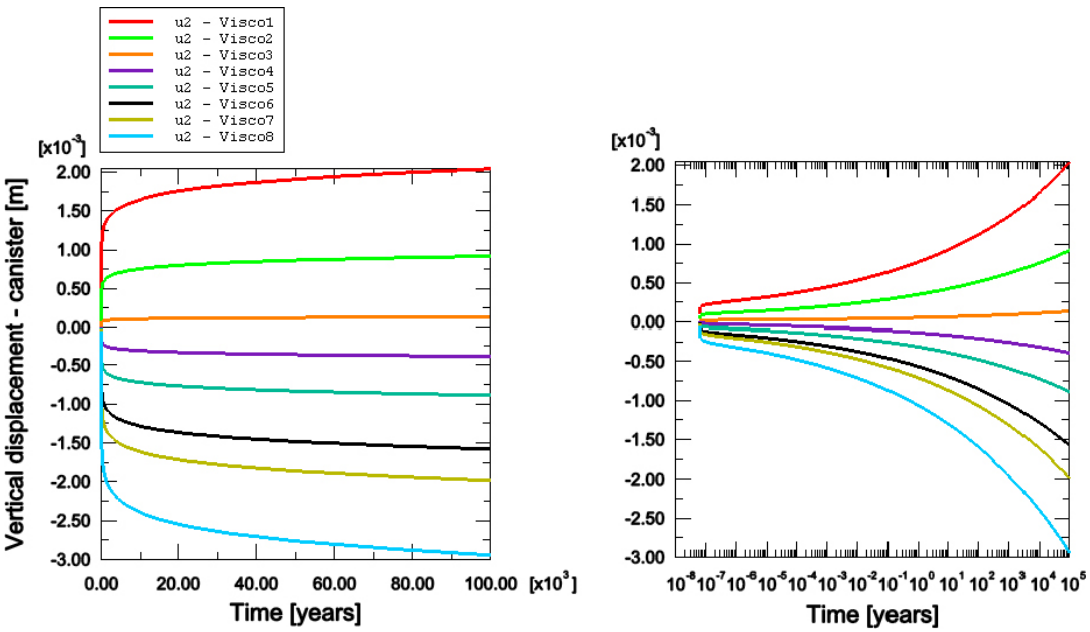

Figure 9-16. *Creep displacement of the canister as a function of time for all cases. Plotted both in linear and logarithmic scale. Visco1 refers to case 1 etc.*

Swelling pressure

Left figure:

Case 8 (p=80 kPa)

Scale (kPa)

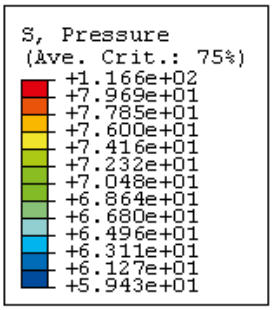

Right figure:

Case 4 (p=875 kPa)

Scale (kPa):

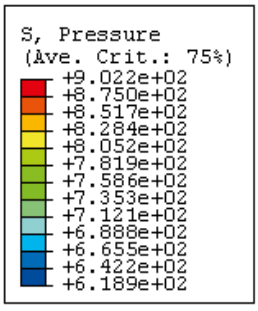

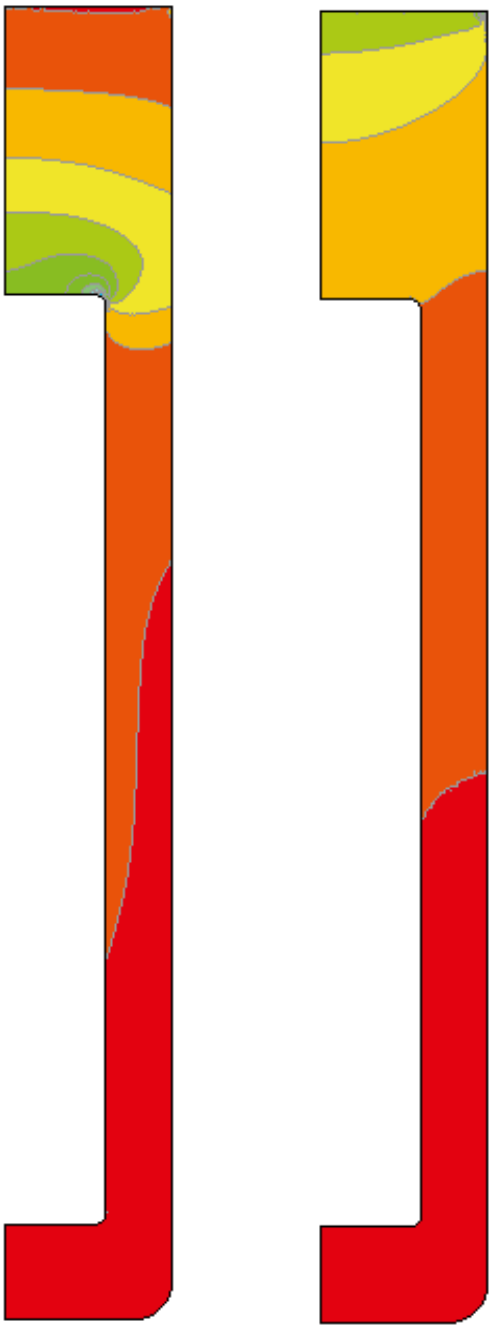

Figure 9-17. *Plots of the average stress in the buffer after consolidation and creep for cases 8 and 4. Observe the difference in scale.*

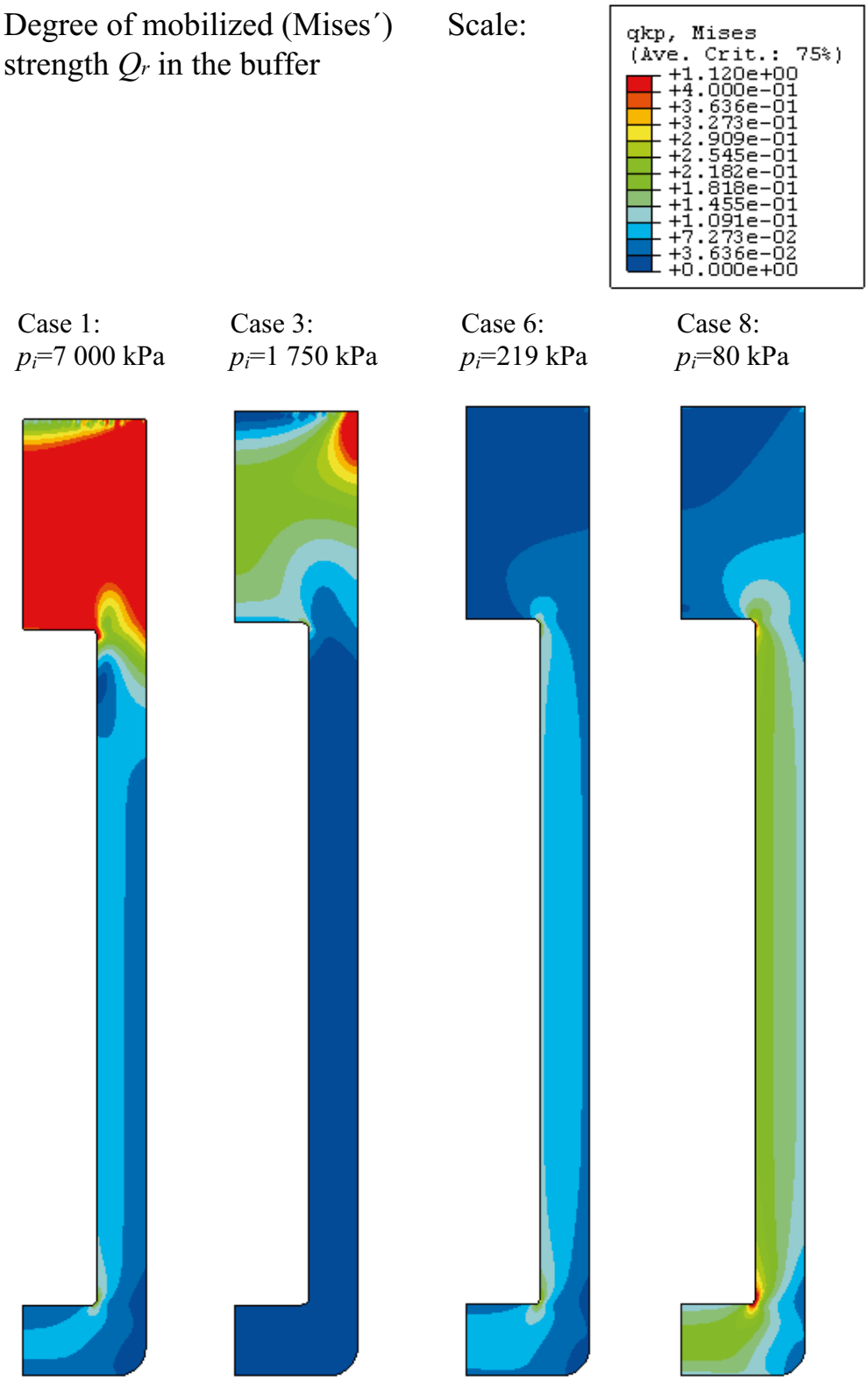

Figure 9-18. *Degree of mobilized shear strength in the buffer before creep for four different cases.*

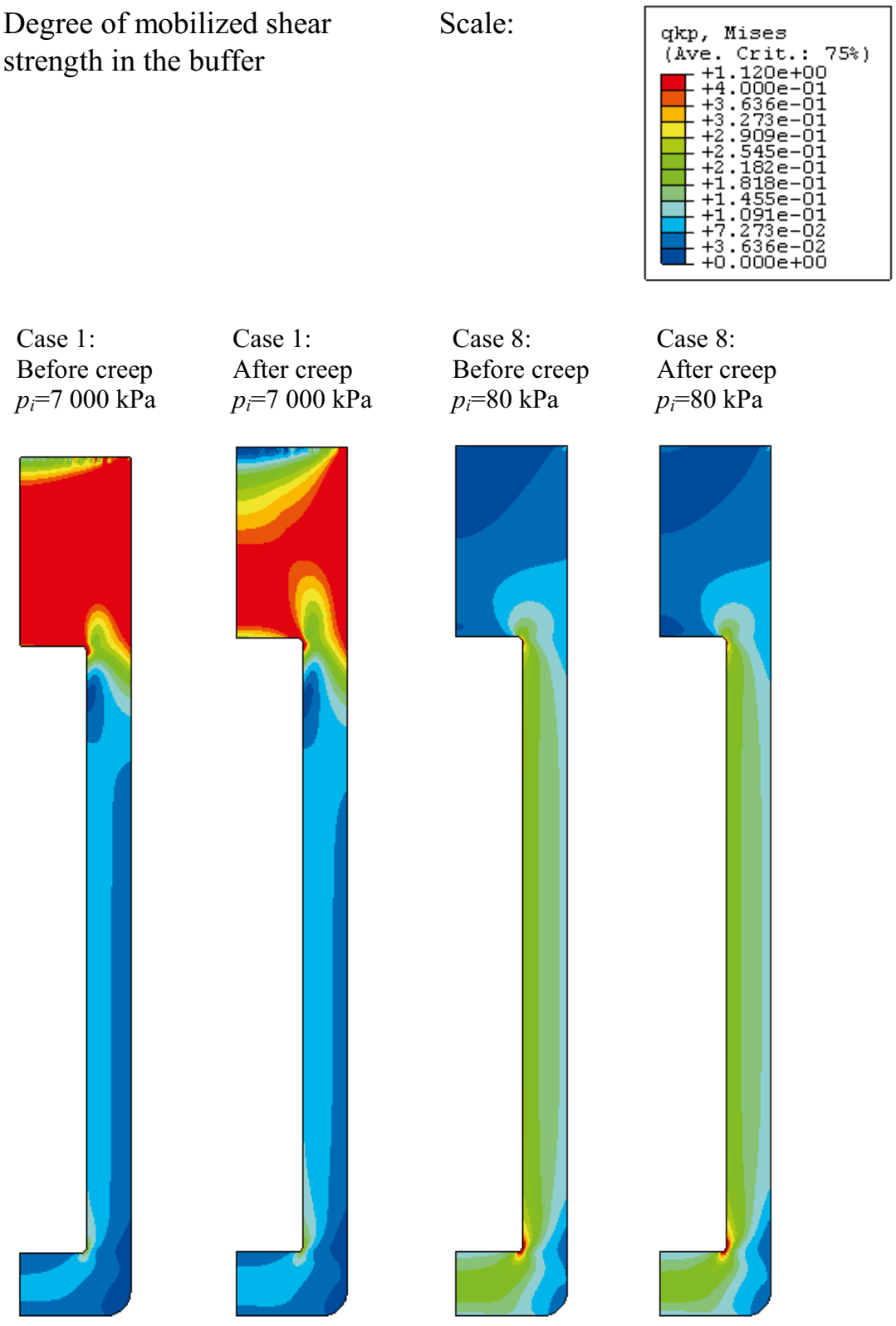

Figure 9-19. *Relaxation of the shear stress after 100,000 years creep. The degree of mobilized shear strength is shown before and after creep for two cases.*

In Figure 9-20 all results of canister displacements are collected in one diagram showing the consolidation/swelling alone and the sum of the consolidation/swelling and creep as a function of the swelling pressure. The total displacement varies between a settlement of 20 mm for case 8 and a heave of 4.7 mm for the reference case 1. The figure shows that the consolidation/swelling process that takes place before the creep dominates the displacement of the canister. It also shows that at the swelling pressure 1.2 MPa there is no displacement of the canister neither during the consolidation/ swelling phase or the creep phase indicating equilibrium stresses on the canister. At higher swelling pressure the canister is heaving and at lower the canister is sinking. At swelling pressure values below 1.2 MPa the canister settlement is rather similar to the canister settlement derived when the buffer/backfill boundary was fixed.

Figure 9-21 shows the displacement of the interface between the buffer and backfill as a function of the swelling pressure of the buffer. Three different points on the interface are shown. As expected the displacement changes from heave to settlement at the swelling pressure 300 kPa since that corresponds to the swelling pressure of the backfill.

9.5 Analyses, uncertainties and conclusions

The displacement of the canister in the KBS-3V concept has been studied in a number of consolidation and creep calculations. In one set of calculations only the consolidation and creep in the buffer without considering the interaction with the backfill was studied, which corresponds to a case where the properties of the buffer and the backfill are identical. In the other set of calculations the interaction with the backfill was included for a backfill that is rather compressible in order to illustrate the influence of the backfill and frame the behaviour. The two cases thus represent two extreme cases.

The base cases in the calculations correspond to the final average density at saturation of 2,000 kg/m^3 with the expected swelling pressure 7 MPa in a buffer. In order to study the sensitivity of the system to loss in bentonite mass and swelling pressure seven additional calculations were done with reduced swelling pressure down to 80 kPa corresponding to a density at water saturation of about 1,500 kg/m^3.

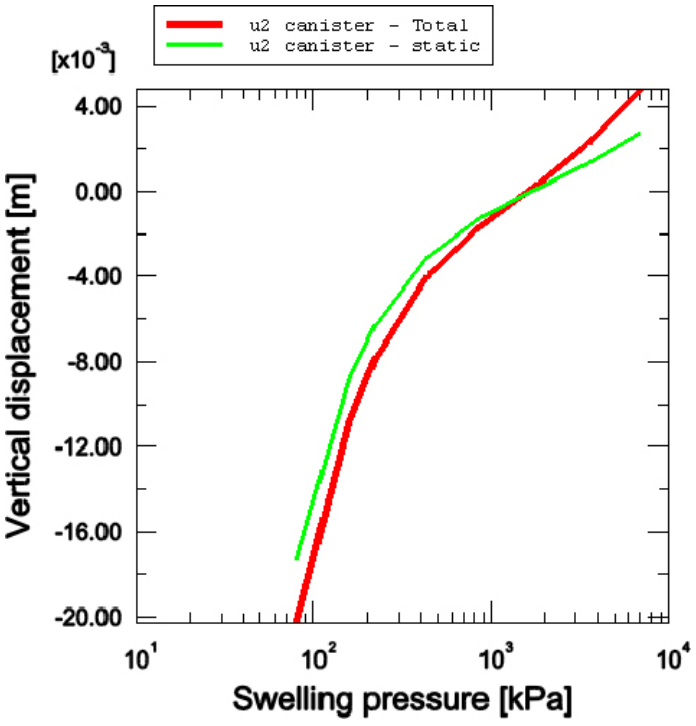

Figure 9-20. *Canister displacements (m) for all cases as a function of swelling pressure. Green line: only consolidation/swelling. Red line: consolidation + creep for 100,000 years. Negative values imply sinking.*

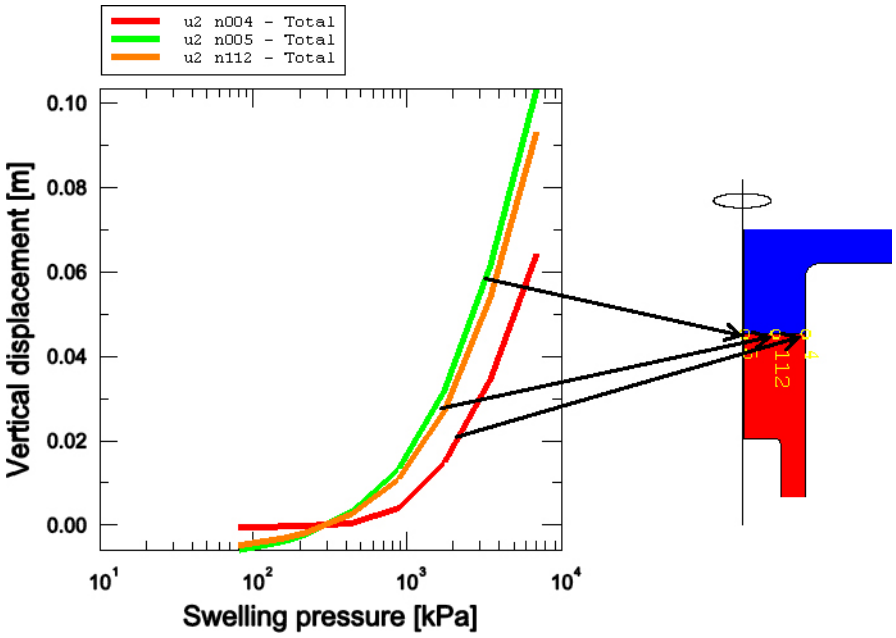

Figure 9-21. *Vertical displacement of the buffer-backfill interface as a function of the swelling pressure of the buffer.*

The calculations included two stages, where the first stage models the swelling and consolidation that takes place in order for the buffer to reach force equilibrium. This stage takes place during the saturation phase and the subsequent consolidation/swelling phase. The second stage models the deviatoric creep in the buffer during 100,000 years.

Volumetric creep is not modelled, which thus may cause a slight underestimation of the canister displacement. The motive for excluding volumetric creep is that a canister settlement caused by volumetric creep will not change the total mass of bentonite under the canister but will only increase the density and is thus not judged to be a problem. Moreover, the volumetric creep is of the same order of magnitude as the deviatoric creep, which means that the canister displacement caused by this creep will be as insignificant as the deviatoric creep.

The creep model in Equation (9-1) is based on a model presented by /Singh and Mitchell 1968/. A large number of creep tests have shown that this model is valid also for bentonite and these tests have been used for evaluating the parameters in the model /Börgesson et al. 1995/. A problem is that the laboratory tests can only be run for a limited time and the validity for 100,000 years cannot be proven.

The sensitivity of the creep has been investigated by reducing the swelling pressure and study the effect on the total creep displacement of the canister. The expected initial swelling pressure 7,000 kPa has in this study been reduced stepwise to 80 kPa, which thus corresponds to a loss in final density at saturation from 2,000 kg/m^3 to 1,500 kg/m^3. As shown in Figures 9-9 and 9-20 the canister settlement is very small even at low swelling pressure and density. The base case corresponding to the expected final swelling pressure of the buffer 7,000 kPa yields a total settlement of the canister of only 0.35 mm for the fixed boundary case, while there is a heave of the canister of about 4.5 mm at the other case due to the upwards swelling of the buffer. At reduced swelling pressure of the buffer the settlement increases but is not more than about 23 mm at the very low swelling pressure 80 kPa for both cases.

Another phenomenon that may affect the buffer is a reduction in strength or friction angle with time, which affects the critical creep parameter D_r or Q_r (degree of mobilized shear strength). A reduced friction angle will reduce the strength and thus affect the degree of mobilized strength in a similar way as a reduced swelling pressure. So the reduction in shear strength can also be considered a reduction in friction angle with retained initial density and swelling pressure. At the swelling pressure 80 kPa the deviatoric stress at failure is only 70 kPa according to Figure 9-4 and Equation (9-7).

Such a low strength at the swelling pressure 7,000 kPa corresponds to a friction angle of only 0.29 degrees, which shows that not even a strong reduction in friction angle is a threat to the canister integrity. The results of the calculations with fixed backfill boundary and the corresponding friction angle at retained initial swelling pressure are summarized in Table 9-3.

The canister settlement also includes the consolidation settlement, which takes into account that the compressibility increases when the swelling pressure decreases while a buffer with reduced friction angle with time with retained swelling pressure will not have an increased compressibility. The settlements at the presented friction angles have on this reason been recalculated as the sum of the settlement of the base case and the creep from respective creep calculation.

The conclusion is thus that the expected displacement of the canister in a deposition hole from consolidation and creep during 100,000 years is very small and for the case of a rather soft backfill actually will result in a heave of the canister. The sensitivity analyses with reduced swelling pressure corresponding to reduced density or reduced friction angle also show that the canister displacement is very insensitive to such phenomena since the total settlement will be less than a few cm even at a buffer density of 1,500 kg/m^3 or at a friction angle of 0.3°.

Table 9-3. Summary of results from the calculations with fixed buffer/backfill boundary.

Calculation No	Density at saturation ρ_m (kg/m^3)	Swelling pressure p (kPa)	Mises' stress at failure q_f (kPa)	Canister settlement (mm)	Friction angle at retained swelling pressure ϕ (°)[2]	Canister settlement at corresponding friction angle and retained swelling pressure (mm)[3]
1 (base case)	2,010	7,000	2,238	0.35	8.8	0.35
2	1,950	3,500	1,312	0.67	5.2	0.47
3	1,890	1,750	770	1.26	3.1	0.67
4	1,840	875	451	2.42	1.8	1.04
5	1,780	438	265	4.63	1.1	1.67
6	1,720	219	155	8.89	0.63	2.78
7	1,690 (1,640)[1]	160	122	12.0	0.50	3.51
8	1,620 (1,470)[1]	80	72	22.5	0.29	5.54

[1] Actual values of void ratio and density at saturation since e >1.5 and equation.

[2] $\phi = \dfrac{3}{6\,p/q_f + 1}$

[3] Derived from the consolidation in the base case (0.20 mm) + the creep from respective creep calculation.

10 Rock shear through a deposition hole

10.1 Introduction and objectives

When a fracture intersecting a deposition hole is affected by a nearby earth quake the fracture may slip and cause a shearing of the buffer and the enclosed canister. The magnitude of such a rock shear and the rate of rock shear displacement have been estimated to be at maximum 5–10 cm and 1 m/s respectively, which are stipulated as dimensioning values.

During a rock shear through a deposition hole the buffer material plays an important role to cushion the stress transfer to the canister since the buffer material is much softer than both the rock and the canister. Since stiffness and the shear strength of the buffer material is rather low the most stressed parts of the buffer close to the shear plane will plasticize and thus only transfer a small fraction of the rock displacements to the canister. However, those properties are very sensitive to the density of the bentonite and also within the relatively small density interval accepted for the buffer material ($1{,}950\ kg/m^3 < \rho_m < 2{,}050\ kg/m^3$) the stiffness and shear strength and thus also the effect on the canister can vary substantially.

Several investigations and reports regarding the consequences of a rock shear on the canister were made for SR-Can and earlier. See e.g. /Börgesson 1986, Börgesson et al. 2004, Börgesson and Hernelind 2006a/.

The rock shear calculations for SR-Site are performed in a separate project as part of the safety analyses for the canister and will be reported separately.

10.2 Approach

The material of the bentonite and the canister are modelled with von Mises' stress as a function of the strain (stress-strain model). The model is elastic-plastic with an E-modulus that determines the behaviour until the material starts yielding whereupon the plastic strain is modelled as a function of von Mises' stress and added to the elastic strain.

The rock, buffer and canister are modelled in 3D with an axisymmetry plane mirroring half the model along the canister axis. Several models with different shear plane inclinations are used. Figure 10-1 shows an example of an element model with the shear plane inclination 22.5° against the canister axis. The canister is modelled in great detail in order to catch local stresses.

The material model of the buffer is the key input to the calculations. In order to represent the worst cases the bentonite is assumed to be ion-exchanged to Ca-bentonite (MX-80Ca), which has higher shear strength than the natural Na-bentonite MX-80. The stress-strain properties used in the modelling are made a function of the strain rate as shown in the example in Figure 10-2.

The modelling is included in a project **Design analysis of the canister** and reported in a number of reports that address the response of the buffer and the canister in a KBS-3 repository to shear movements in fractures intersecting deposition holes. Figure 10-3 shows the flow of input data, modelling and evaluation of results against various criteria in the shear analysis and the relation to the design analysis. It also illustrates where the components of the analysis are reported through dashed boxes representing various reports.

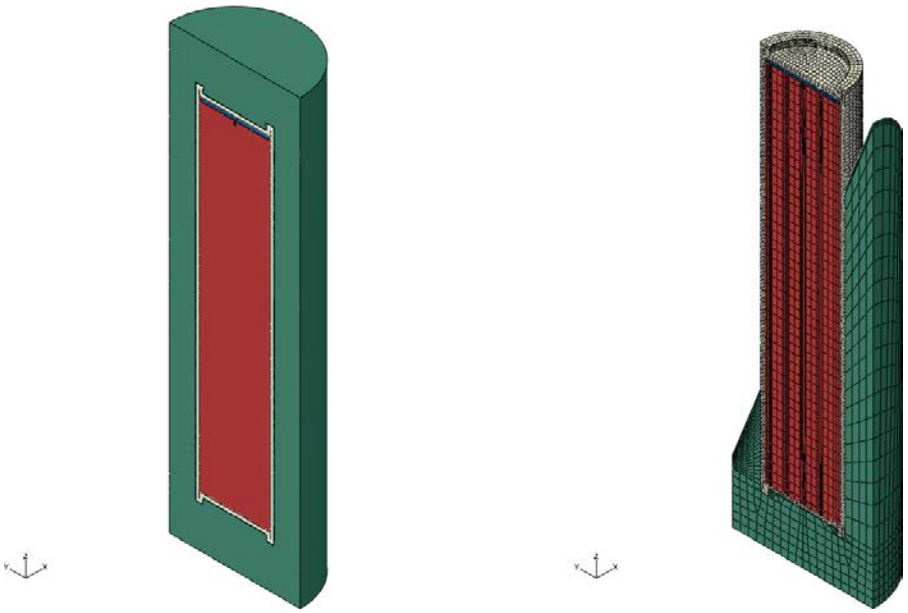

Figure 10-1. *Plot of geometry for rock shear inclined 22.5 degrees to axis of canister (left) and the element mesh with shearing part removed (right).*

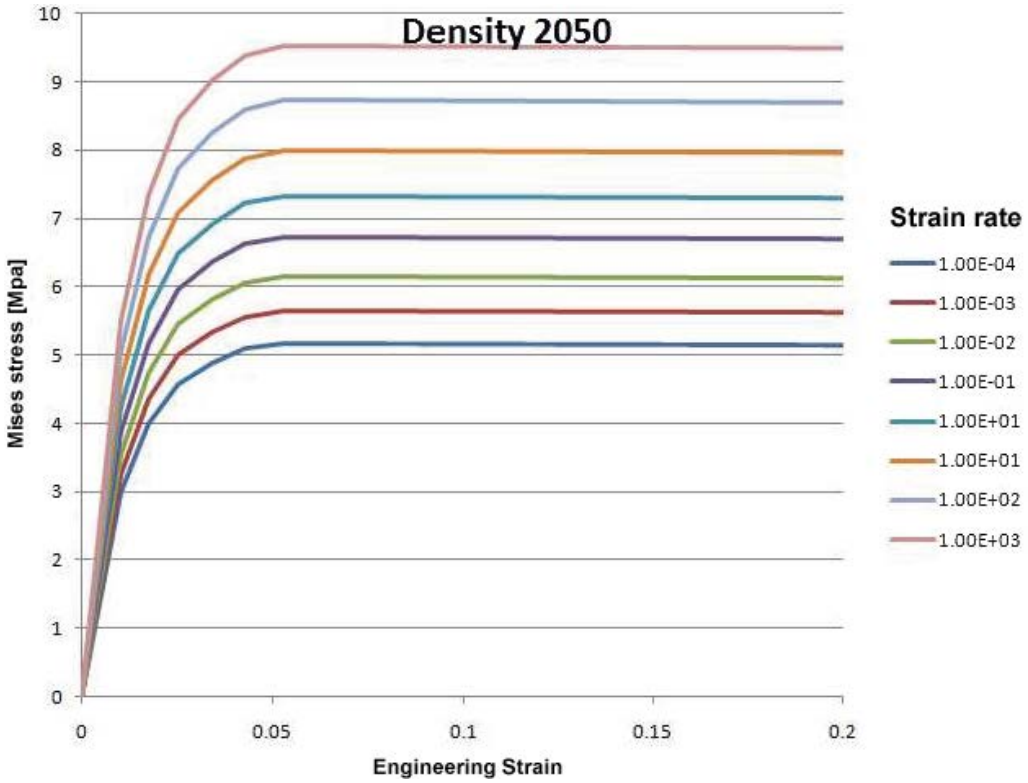

Figure 10-2. *Material model of the buffer at the density 2,050 kg/m³. The model varies with the strain rate according to the legend.*

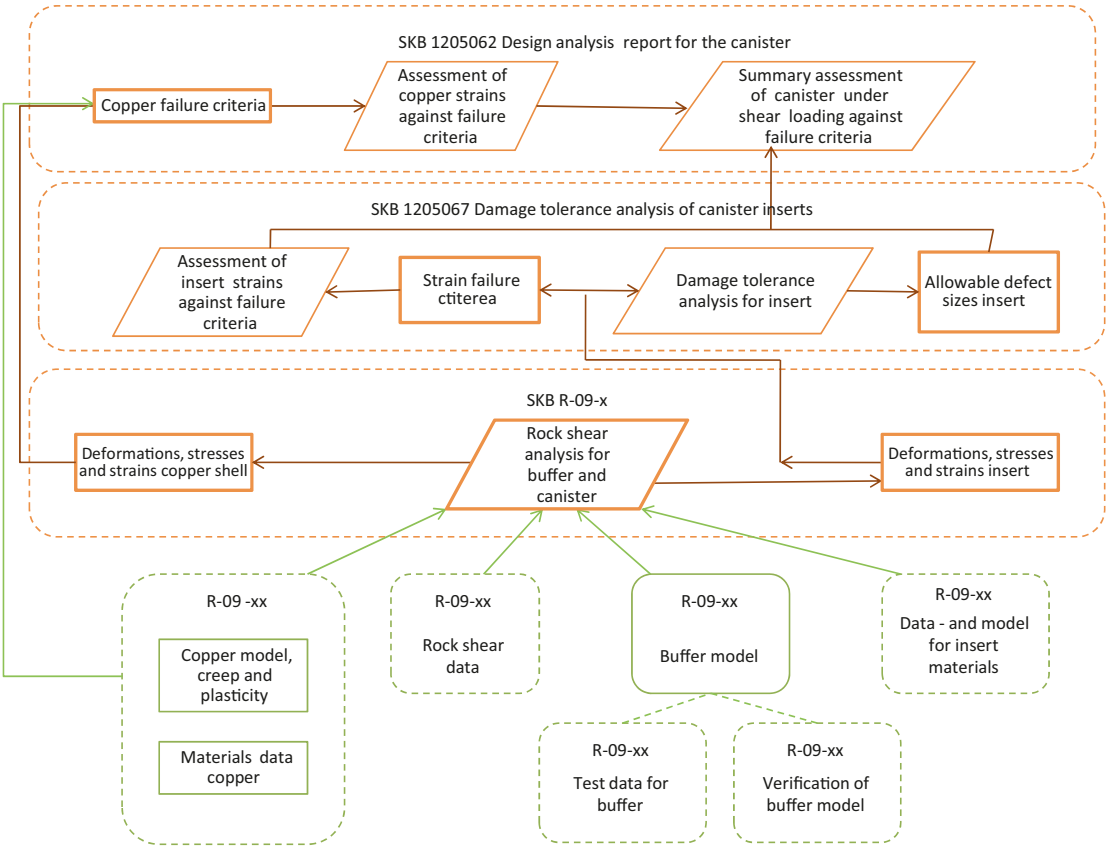

Figure 10-3. *The flow of input data, modelling and results in the shear movement analyses. The dashed boxes illustrate the reports where the various components are reported. Input data and input reports are indicated in green whilst analysis reports and flow of analysis results are indicated in brown. The model describing the buffer material is highlighted in green.*

11 Piping and erosion

11.1 Introduction

Water inflow into the deposition hole will take place mainly through fractures and will contribute to the wetting of the buffer. However, if the inflow is localized to fractures that carry more water than the swelling bentonite can adsorb, there will be a water pressure in the fracture acting on the buffer. Since the swelling bentonite is initially a gel, which increases its density with time as the water goes deeper into the bentonite, the gel may be too soft to stop the water inflow. The results may be piping in the bentonite, formation of a channel and a continuing water flow and erosion of bentonite particles. There will be a competition between the swelling rate of the bentonite and the flow and erosion rate of the buffer.

Piping will take place and the pipes remain open if the following three conditions are fulfilled at the same time:

1. the water pressure p_{wf} in the fracture, when the water flow is prevented, is higher than the sum of the counteracting total pressure from the clay and the shear resistance of the clay,
2. the hydraulic conductivity of the clay is so low that water flow into the clay is sufficiently stopped to keep the water pressure at p_{wf},
3. there is a downstream location available for the flowing water and the removal of eroded materials in order for the pipe to stay open.

Erosion will take place if the drag force on the clay particle from the water movement is higher than the sum of the friction and attraction forces between the particle and the clay structure.

Piping probably only occurs before complete water saturation and homogenisation since the swelling pressure of the buffer material is very high. Erosion can occur both as a consequence of channels caused by piping and over the long-term at the interface between the clay and the fractures in the rock. Since the water flow rate in the latter case is very low, erosion will only be important for colloids leaving the clay gel that has penetrated into the fractures.

The consequence of the piping will be a channel leading the flowing water out to dry or unfilled parts of the repository. Since the clay swells the channel will reduce in size with time but on the other hand the erosion will counteract and tear off bentonite particles and thus increase the size of the channel. There is thus a competition between swelling clay and eroding clay. If the inflow is low and the increase in water pressure slow the pipe may seal before water pressure equilibrium has been reached.

The consequence of the piping is always that there will be erosion of material that has been torn off from the pipes. That material is transported in the pipes out into either a stagnant part of e.g. the backfill where the eroded material may settle or out from the backfill into the open tunnel.

After completed water saturation and homogenisation of the buffer and backfill and re-establishment of the hydrostatic water pressure, the water pressure will be separated from the swelling pressure according to the effective stress theory. The pipes or openings caused by the erosion will thus be healed and a swelling pressure established if the density and resulting swelling pressure are high enough to overcome the internal friction. Later on there is very little risk of piping since piping requires a strong and fast increase in water pressure gradient locally in the rock at the contact with the buffer or backfill.

11.2 Problem description

There are some general understandings of how flowing water interacts with bentonite after installation at great depths that are very important for the behaviour of the buffer material in the deposition hole after exposure to the natural ground water inflow:

- The pellets filling can never stop the water inflow since the water pressure that will occur if the water inflow is stopped is in the order of several MPa and the swelling pressure of the pellets filling is initially only about 100 kPa.
- It will take several years for the buffer and even more for the backfill to generate a swelling pressure that is high enough to stop the water inflow. It has not been proven and is not sure that a large water flow can ever be stopped by self sealing of bentonite unless the high water pressure gradients that may occur at repository depth is reduced by a tight plug. The limit in water inflow rate, when the bentonite may self seal without the help from a tight plug, is not known. The limit is probably very low and it is assumed here that all inflowing water enters the deposition hole or the tunnel.
- The consequence of this is that when a plug is built in the end of a deposition tunnel the pellets slots in both the deposition holes and the tunnel will be filled with water since the pellets cannot stop the inflow but new channels that distribute the water to empty parts will steadily be formed until the slots are filled with water. When the slots are filled the water pressure in the tunnel will start to rise and the hydraulic gradients will be taken by the plug instead of by the bentonite and the inflow will be strongly reduced.
- Since the pellet filling cannot stop the water inflow there will consequently be channels in the pellet filling leading out from the deposition hole to the tunnel.
- Numerous measurements of water flowing in channels in bentonite pellets or on the surface of bentonite blocks show that the discharging water contains bentonite collected on the way through the channels due to erosion. Water flowing in channels out from the deposition hole will thus transport bentonite from the deposition hole into the backfill.

Since piping and subsequent erosion cannot be prevented by the pellets filling in the buffer or the backfill it is important to try to estimate the amount of bentonite material lost by erosion especially from the buffer in a deposition hole.

In SR-Can no calculations were done with only a brief description of the processes presented /Börgesson and Sandén 2006/. 1–10 g dry mass of bentonite per litre eroding water was used as estimate.

HM modelling of erosion processes cannot be done due to lack of models and tools. However, ongoing measurements show that limits can be set to the effect of the erosion. An empirical model of the erosion rate is under development and will be used to estimate the erosion for different cases.

As a basis for the new calculations the results of task 6 (homogenisation of erosion damages), which suggest that 100 kg of dry bentonite can be allowed to be lost from one point, have been used.

11.3 Layout and initial conditions

The layout of the tunnel and deposition hole and a possible situation, when the backfilling work will start after removal of the buffer protection, is shown in Figure 11-1.

The erosion from a deposition hole out to the tunnel and to some extent possibly out through the plug is to a large degree a function of the total volume of eroding water. If the water inflow is strong, water will at first fill up the open pore space in the pellets filling both in the buffer and in the backfill before any significant amount of water is absorbed by the buffer or backfill blocks since there is no resistance against water flow in the pellets while the very low hydraulic conductivity in the blocks limits the water uptake rate in the blocks. Thus the volume of the open pore space available for water in the pellets filling is an important parameter, but also the unsaturated voids in the blocks and the possible leakage through the plug is of relevance.

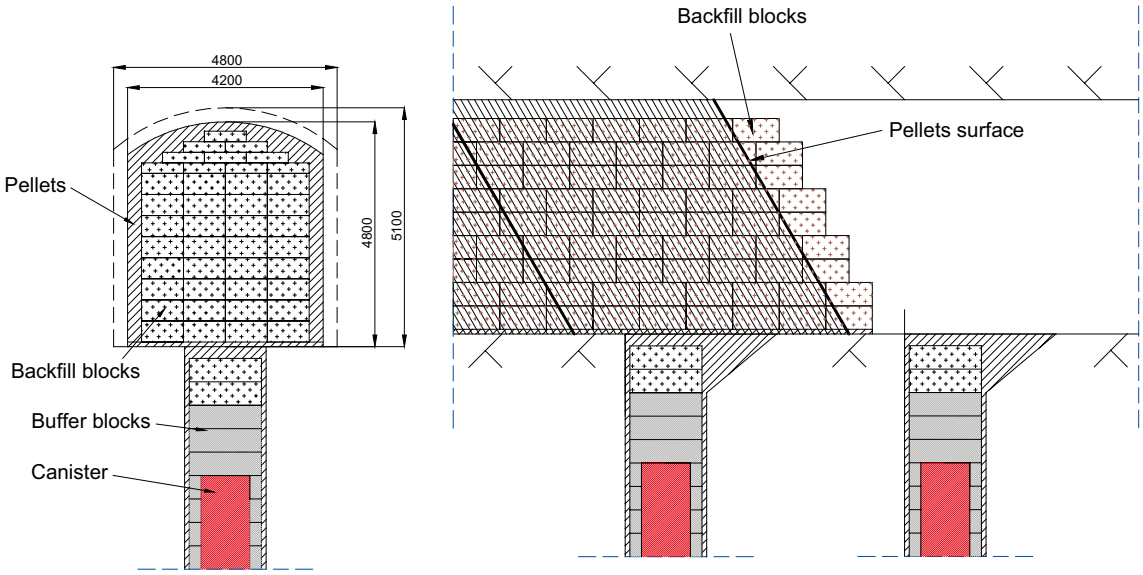

Figure 11-1. *Reference layout of the repository and illustration of the progressed backfilling just after pellets filling of the next deposition hole.*

Experiences from work with pellets filling show that the dry density of the filling will be about 1,000 kg/m^3, which yields

ρ_d = 1,000 kg/m^3
e = 1.78 (void ratio)
n = 0.64 (porosity)

The initial water content in the pellets in the backfill is planned to be w = 0.17 and in the pellets in the buffer w = 0.1.

The porosity is thus 64% but about 25% of the pore space in the backfill pellets and about 15% of the pore space in the buffer pellets are already filled with water due to the initial water content. This means that the porosity about 48% in the backfill pellets filling and about 54% in the buffer pellets is available for inflowing water.

The total pellets volume in the buffer part of the deposition hole is

9.0·0.06·1.69·π = 2.87 m^3, which yields an **empty pore volume in the buffer of the deposition hole** (V_{pd}) available for inflowing water of about

V_{pd} = 1.55 m^3

According to the backfill production line report the tunnel has a total average cross section area of 22.7 m^2 and a degree of filling of bentonite blocks of 74%. The rest of the square section (0.26×22.7 m^2 = 5.90 m^2) is filled with pellets.

The total pellets volume in the tunnel is (assuming 300 m long tunnel)

300·5.9 = 1,770 m^3, which yields an **empty pore volume of the tunnel** (V_{pt}) available for inflowing water of about

V_{pt} = 850 m^3

The **total empty volume available** is thus (using 50 deposition holes in a deposition tunnel):

V_{pt} + 50V_{pd} = 928 m^3

In addition to these empty volumes there are of course the unfilled pores in the bentonite blocks and in the slots between the blocks. The slow wetting means that only the slots between the blocks can be expected to be filled. According to the Backfill production report /SKB 2010b/ the total volume of these slots is expected to be about 2% of the total block volume, which yield that **the total volume of slots between blocks** V_{ps} is

$V_{ps} = 0.02 \cdot 0.74 \cdot 22.7 \cdot 300 = 101\ m^3$

In addition we must expect that there is some leakage through the plug, depending on the tightness of the plug. It is presently not known how tight these plugs can be made so, for the present, we assume that additionally 20% of the total volume in the tunnel will leak out through the plug. This yields a **total possible water flow into the tunnel** V_t of

$V_t \approx 1.2(V_{pt} + 50V_{pd} + V_{ps}) = 1{,}235\ m^3 \approx 1{,}250\ m^3$

11.4 Quantification of eroded bentonite

11.4.1 General

Since water inflow cannot be stopped, but piping always occurs with channel formation and subsequent erosion of bentonite in the channel, water inflow and erosion will continue until the available empty space in the pellets fillings in the deposition holes and in the tunnel is water filled.

11.4.2 Erosion model

A large number of erosion tests have been performed. Figure 11-2 shows some tests results with accumulated eroded mass plotted as a function of accumulated water flow in a double logarithmic diagram. Different materials, flow rates and flow lengths have been used for the tests but all those tests were done with horizontal flow directions. All data is limited by two straight lines with the inclination corresponding to $\alpha = 0.65$.

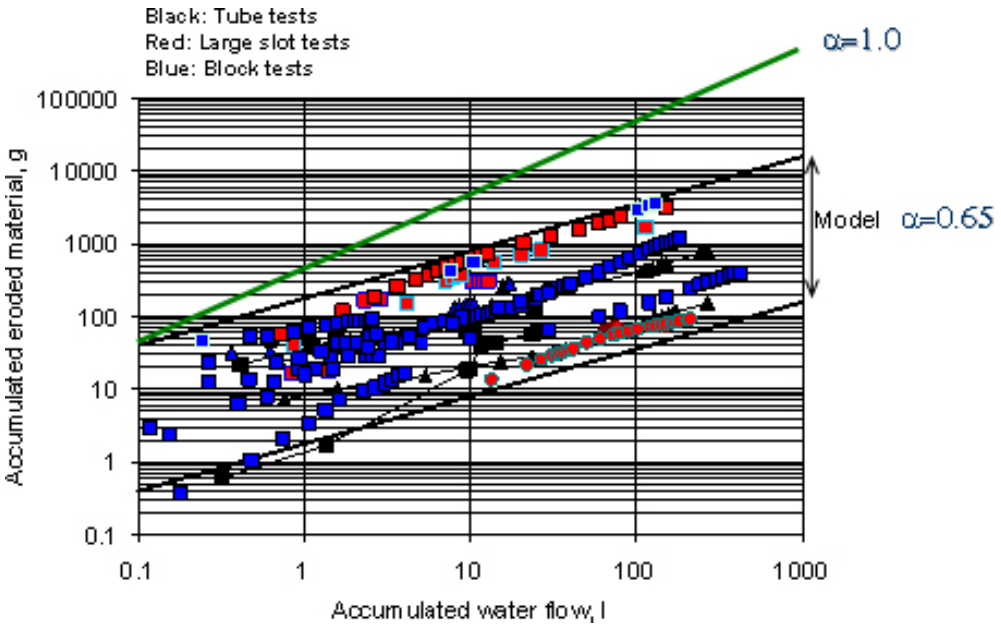

Figure 11-2. *Example of erosion results plotted in one diagram. The lower boundary line corresponds to $\beta = 0.02$ and the upper $\beta = 2.0$. The inclination corresponding to $\alpha = 0.65$ is motivated in the figure. $\alpha = 1.0$ (corresponding to constant erosion rate) is also illustrated.*

An erosion model described by Equation (11-1) has been suggested /Sandén et al. 2008/.

$$m_s = \beta \times (m_w)^{\alpha} \qquad (11\text{-}1)$$

where

m_s = accumulated mass of eroded bentonite (g)
m_w = accumulated mass of eroding water (g)
β = 0.02–2.0 = parameter defined by the level of erosion at a certain accumulated water flow
α = 0.65 = parameter defined by the inclination of the straight line relation

α = 0.65 yields a rather strong decrease in erosion rate with time and accumulated water flow. Constant erosion rate corresponding to α = 1.0 is also illustrated in the figure.

α seems not very much affected by the test material or conditions and is according to the measurements a constant with the value 0.65.

β must be measured and seems mainly dependant on the material type, the salt content, the water ratio, the geometry and (in case of water flow through a pellets filling) the pellet grain size distribution.

Results from measurements show that there is no or little influence of the flow rate and flow length, which are not included in the model although these factors may have some influence on the value of β.

A number of additional tests have recently been performed in order to simulate the erosion in a deposition hole that mainly takes place in vertical direction in pellets filling /Sandén and Börgesson 2010/. Figure 11-3 shows results of those tests included in the same diagram together with the proposed model.

Figure 11-3 shows that the new measurements are embraced by the model and that it seems as the model can be further specified for the case of vertical flow in a pellets filling. All measurements fall inside a lower limit that is characterised by the values

β = 0.02–0.2

i.e. 10 times lower upper limit than the original model.

Additional long term tests run up to a total volume of 16,000 l confirm that the model may be extrapolated /Sandén and Börgesson 2010/.

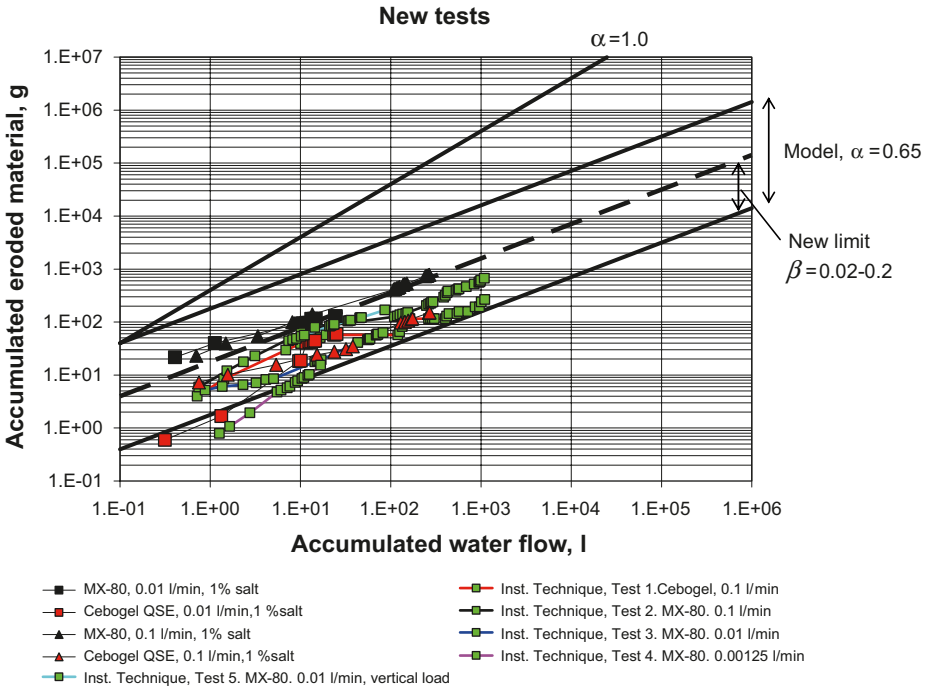

Figure 11-3. *New tests made with vertical flow in pellets filling and suggested revision of the model.*

11.4.3 Eroded mass in a deposition hole

The erosion model can be used to study the effect of water flowing from a deposition hole out to the tunnel.

As shown earlier a total volume of about 1,250 $m^3 = 1.25 \cdot 10^9$ g water is expected to flow into the tunnel before it is filled with water and sealed including possible leakage through the plug. If all water comes from one deposition hole the eroding mass of bentonite will according to Equation (11-1) and $\beta = 0.02–0.2$ be

$m_s = \beta \cdot (1.25 \cdot 10^9)^{0.65}$ g = 16.4–164 kg bentonite,

which is more than 100 kg that is proposed to be the allowable limit of local loss of bentonite from one inflow point.

Equation (11-1) can be reformulated to yield the inflow that corresponds to a certain mass of eroded material:

$$m_w = \left(\frac{m_s}{\beta} \right)^{\frac{1}{\alpha}} \qquad (11\text{-}2)$$

m_s = 100 kg yields that the total water volume that may flow from the deposition hole out to the tunnel 586 m^3 or 47% of the total volume available.

However, since the limits of the β-value found for vertical erosion needs to be further verified it is conservatively proposed that the old limits ($0.02 < \beta < 2$) are used, which yields the volume 17 m^3 or 1.4% of the total volume. If further tests confirm the finding that $0.02 < \beta < 0.2$ for vertical flow the critical total volume of inflowing water can be increased considerably.

11.5 Conclusions and uncertainties

Piping and subsequent water flow from a fracture into a deposition hole and further out into the deposition tunnel cannot be excluded if the inflow rate is higher than the rate of water absorption of the buffer material, since the pellets filling and the bentonite blocks cannot stop the water inflow until after very long time or until the deposition holes and the tunnel are water filled and the hydraulic gradient is taken by the end plug. Erosion tests have shown that the dry mass of eroded bentonite can be modelled a function of the total volume of inflowing water according to Equations (11-1) and (11-2), which yields that 17–586 m^3 of inflowing water may erode 100 kg of dry bentonite mass depending on the factor β in the equations. Until finally confirmed that upwards water flow yields a lower β-value the total allowable water inflow is conservatively suggested to be 17 m^3 or about 1.4% of the total volume space available including a total leakage of about 200 m^3 through the plug.

A weakness is that the model is purely empirical and it is difficult to theoretically derive a model. However, many geotechnical models are empirical (e.g. strength and friction angle relations) on the same reason and have successfully been used for numerous geotechnical design works.

The strengths of the model are that it refers to a volume of eroding water that has been tested and that the geometries, materials and conditions are very similar to what can be expected in reality. In addition the model used with $0.02 < \beta < 2$ has an upper erosion limit that is about 10 times larger than actually measured during vertical flow. Possible errors should be well covered with this margin and it is probable that the model in future can be proven to be valid with a lower upper boundary.

12 Analysis of time-scale of tunnel plug hydration

12.1 Introduction and objectives

The objective of this task is to analyze the time-scale to saturate the tunnel plug.

12.2 Approach

The time-scale to saturate the tunnel plug in general, and the seal in particular, is expected to be complex and dependent on piping and the frequency and transmissivity of fractures along the tunnel upstream the seal and the plug. The time-scale from the filling of the filter to the full saturation of the seal is, on the other hand, a fairly simple and well-defined problem.

The chosen approach is therefore to calculate the time to saturate the seal, given that the filter has been filled. This is basically a plane 1D hydraulic problem if the pellet-filled slot is neglected. If the pellets filling of the seal will seal quickly, then the hydration would only occur from one side. If, on the other hand, there would be a sustained piping through the pellets filling, then the hydration would be two sided. This is analyzed with small axisymmetric 2D models which only include the seal. Results are compared with results from two larger axisymmetric 2D models.

12.3 Model description

Geometries and densities are modelled in accordance with the Backfill production line report (Figure 12-1). Parameter data for backfill blocks, pellets and rock materials are used in accordance with the Buffer THM Data report /Åkesson et al. 2010/. Fracture transmissivities are used in accordance with the representation described in Section 2.3.

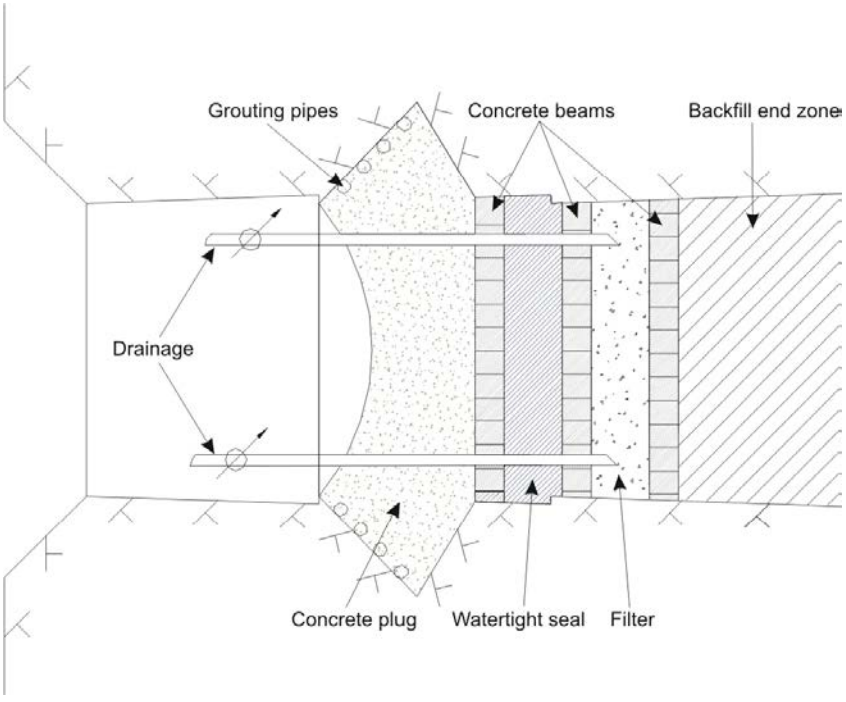

Figure 12-1. *Schematic section of the reference design of the plug (from Production line report).*

12.3.1 Geometry and mesh

Two different geometries were used: an axisymmetric 2D geometry (Figure 12-3) of the plug seal, representing basically a 1D problem; and an axisymmetric 2D geometry with 7 m tunnel and rock (Figure 12-2). This larger geometry also includes a representation of a fracture. The mesh for each model is shown in Figure 12-2 and Figure 12-3. The number of nodes and elements in the small plug seal model was 232 and 196, respectively. The corresponding numbers for the larger geometry was 1,819 and 1,632 respectively.

12.3.2 Initial and boundary conditions

The models are purely hydraulic, and therefore are only the liquid pressure specified in the initial (Figure 12-4) and the boundary conditions (Figure 12-5). The initial liquid pressure for all backfill materials were –45.9 MPa. The initial liquid pressure for the rock materials (matrix and fracture) in the 2D axisymmetric models was set to a linear distribution from 0.1 to 0.8 MPa with increasing radius, and linear from 0.8 to 4.6 MPa along the cylindrical fracture.

In the plug seal model, atmospheric boundary pressures were applied to one or both circular faces (Figure 12-5). The larger 2D axisymmetric models were fed with 4.6 MPa at the outer boundary of the cylindrical fracture (Figure 12-4). The boundaries towards the transport tunnel were kept at atmospheric pressure with a negative leakage coefficient, thereby prohibiting water inflow.

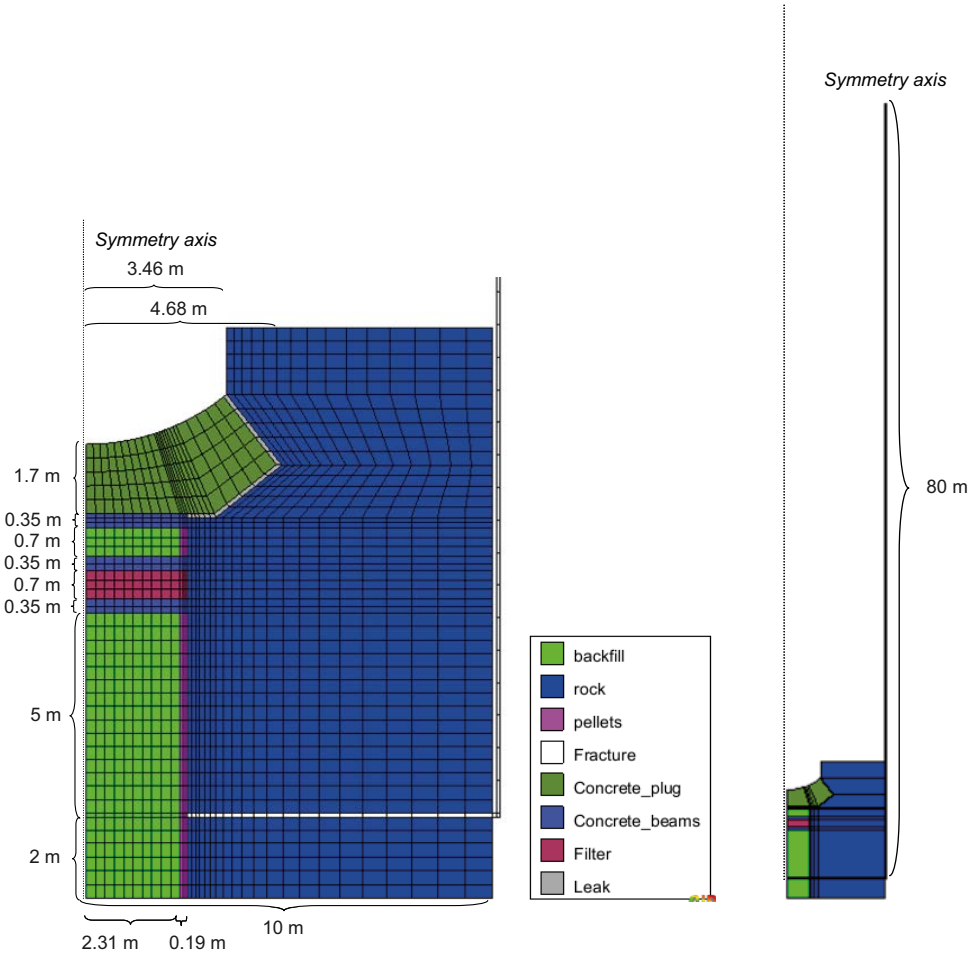

Figure 12-2. *Tunnel plug model. Geometry 1: 2D axisymmetric with representation of rock and feeding fracture.*

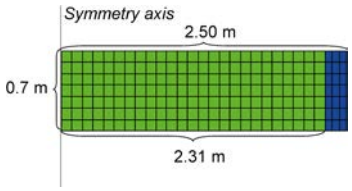

Figure 12-3. *Plug seal model. Geometry 2. 2D axisymmetric with only representation of seal blocks and pellets.*

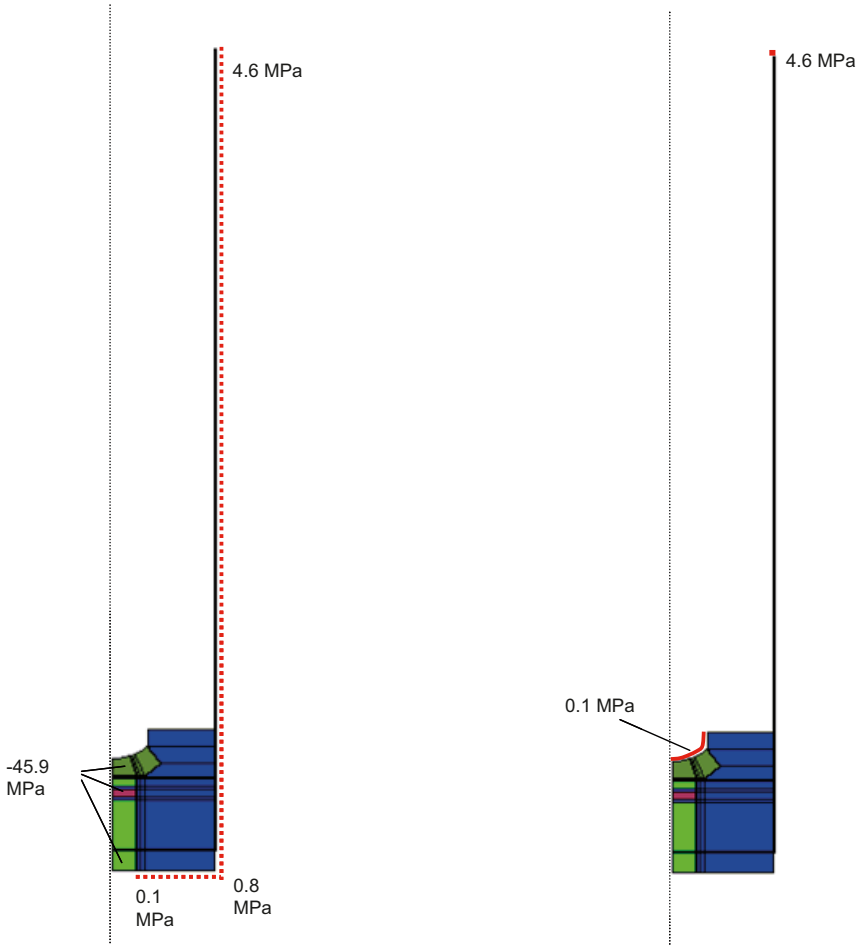

Figure 12-4. *Tunnel plug models. Initial (left) and boundary (right) conditions. Dotted red lines show initial linear distributions.*

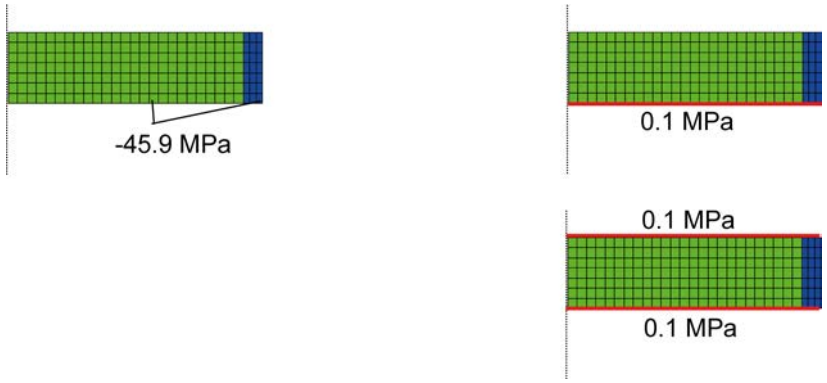

Figure 12-5. *Plug seal models: Initial (left) and boundary (right) conditions.*

12.3.3 Material properties

The properties for all modelled material are compiled in Table 12-1 and Table 12-2. Data were generally taken from the Buffer THM Data report /Åkesson et al. 2010/, but with one exception: In the larger geometry the pellets material was modelled with an alternated representation with the aim to mimic the phenomena of piping. With this approach the pellets were modelled with significantly higher flow coefficients ($k = 1E{-}15$ m^2; $k_r = 1$) throughout the calculation.

A fracture transmissivity of 5E–9 m^2/s was adopted, i.e. the same as used in the larger fractures in Chapter 2. The same transmissivity was used to represent the plug rock interface.

12.3.4 Variations

According to the plans, a drain will be installed in the filter, and with this there is an option to artificially supply the seal with water. In one variation (T12G1ap2), this has been addressed through addition of a hydraulic boundary with atmospheric pressure in the entire filter.

12.4 Model results

History plots of the degree of saturation in the nodes with the slowest hydration in the plug seal are shown in Figure 12-6 and Figure 12-7. Evaluated time scales for the hydration are compiled in Table 12-3.

In the small plug seal models, it can be noticed that the time needed for saturation is four times as high in the model with hydration from only one side. To reach 99% saturation in the blocks the time needed is 20 years for one-sided hydration, whereas it is 5.4 years for hydration from both sides. This relation is fairly obvious, since the time-scale should be proportional to the square of the width.

The time needed to saturate the seal in the larger models is only slightly longer than the time-scale in the seal model with two-sided hydration.

Table 12-1. Material properties for modelled materials (I).

Parameter		Backfill block e=0.635 w=17%	Backfill Pellets e=1.780 w=17%	Seal block e=0.635 w=17%	Filter	Concrete beams
Porosity	n (–)	0.388	0.64	0.388	0.35	0.135
Intrinsic permeability	k (m^2)	2.1E–21	1E–15* / 5.2E–19	2.1E–21	1E–15	1E–15**
Relative permeability	k_r (–)	S_r^3	1* / S_r^3	S_r^3	1	S_r^3
Water retention curve	P_0 (MPa) λ (–)	37.2 0.34	0.162 0.19	37.2 0.34	0.003 0.9 S_{min}:0.01†	9 0.3

* Piping pellets – used in Geomery 1.

** Concrete beams radial k: 5e–19 m^2.

† Other than stated in data report /Åkesson et al. 2010/.

Table 12-2. Material properties for modelled materials (II).

Parameter		Concrete plug	Rock matrix	Fracture material	EDZ	Plug/rock leak material
Porosity	n (–)	0.135	0.003	0.003	0.003	0.003
Intrinsic permeability	k (m^2)	5E–19	5E–20	5E–15	1E–15	5E–15
Relative permeability	k_r (–)	S_r^3	vG: λ = 0.6	vG: λ = 0.6	vG: λ = 0.6	vG: λ = 0.6
Water retention curve	P_0 (MPa) λ (–)	9 0.3	1.74 0.6	1.74 0.6	1.74 0.6	1.74 0.6

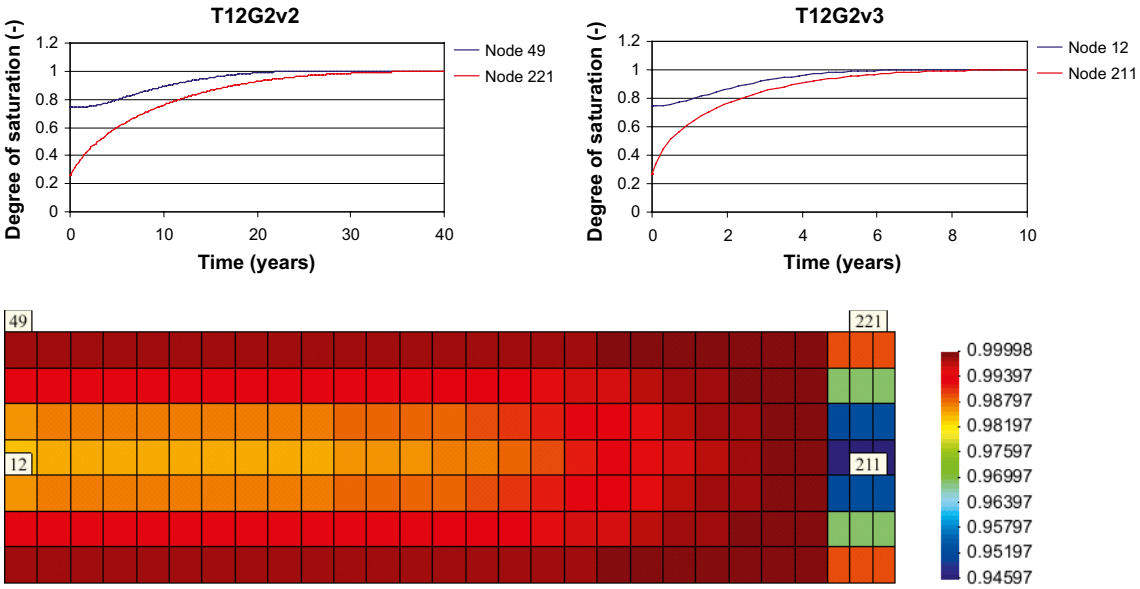

Figure 12-6. *Evolution of degree of saturation at last hydrated nodes in blocks and pellets in plug seal models. Contour plot of degree saturation after 5 years.*

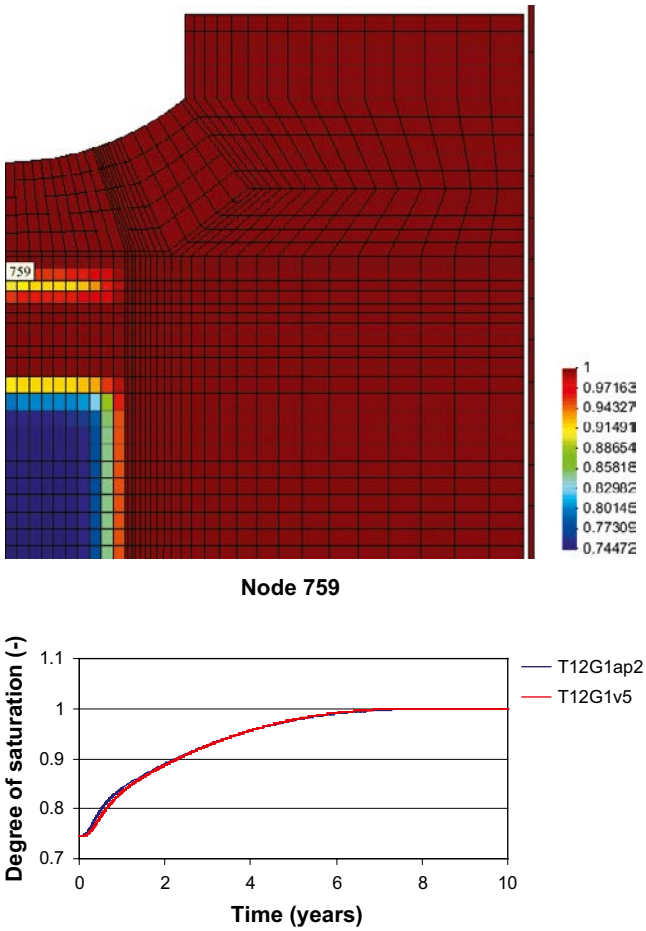

Figure 12-7. *Evolution of degree of saturation at last hydrated nodes in blocks in large tunnel plug models. Contour plot of degree saturation in 12G1v5 after 3 years.*

Table 12-3. Timescales for hydration times of plug seal (years).

Model	Seal blocks		Pellets	
	95%	99%	95%	99%
T12G2v2 – hydration from one side	15	20	23	32
T12G2v3 – hydration from two sided	3.7	5.4	5.1	7.5
T12G1v5 – hydration from fracture	3.8	5.9	–	–
T12G1ap2 – hydration from fracture and filter	3.8	6.0	–	–

12.5 Conclusions and uncertainties

Under the condition that there is good availability of water at the plug, either natural or artificial, and that piping is sustained in the pellets-filled slot, the presented analysis shows that the time to hydrate the plug seal is basically determined by the plane 1D problem of two-sided hydration of 0.7 m thick blocks. This fairly fast hydration of approx. 5 years thus relies on the piping through the pellets filled slot and the slots between the concrete beams. If, on the other hand, the pellets would seal quickly, effectively turning the problem to a one-sided hydration, then the time of hydration would increase with a factor of four and this appears to be the most realistic case.

Apart from this piping-related issue, there is the general uncertainty concerning hydraulic conductivity, the used material, slopes of retention curves and the influence of the hydro-mechanical interactions described in the Chapter 2.

It can be noted that the filter material, with its high permeability and low retention curve, implies very short time increments in the numerical model. If it would be decided that artificial water supply through the filter was to be implemented, then it would be more efficient to simplify the model and only include the seal blocks, the seal pellets and the concrete beams.

13 Hydraulic modelling of the sealing ability of the tunnel plug

13.1 Introduction and objectives

The objective of this task is to quantify the relevant properties necessary for achieving an acceptable sealing ability.

13.2 Approach

The maximum allowed cumulative leakage through the plug is considered to be a certain fraction (e.g. 10%) of the available pore volume of the pellets-filled slot in the entire tunnel. Moreover, although the seal constitutes the main resistance, it will require access to water and time to develop a high flow resistance. During this period the sealing ability will rely on the plug itself (or actually the low transmissivity between the concrete and the rock). These circumstances thus imply a relation between: i) the maximum allowed leakage, ii) the flow resistance of the plug and, iii) the time needed for the seal to become functional (Figure 13-1). In addition, the flow resistance of the pellets of the seal will increase during the water uptake and homogenisation process of this component. The characteristics of this increase are however largely unknown, and instead the current analysis was based on an approach in which the required plug resistance is calculated for different flow resistances of the seal. Analytical expressions have been derived for this reason.

13.3 Description of analytical model

The pellets-filled slot in the seal and the concrete plug rock interface are represented as two series-coupled resistances (Figure 13-2). The flow through both resistances is the same:

$$Q = \frac{h_H - h}{\varpi_s} = \frac{h}{\varpi_p} \tag{13-1}$$

Naturally, the total resistance is simply the sum of the two resistances:

$$Q = \frac{h_H}{\varpi_s + \varpi_p} \tag{13-2}$$

The resistance along the concrete plug is described as:

$$\varpi_p = \frac{L_p}{2\pi \cdot r_p \cdot T_p} \tag{13-3}$$

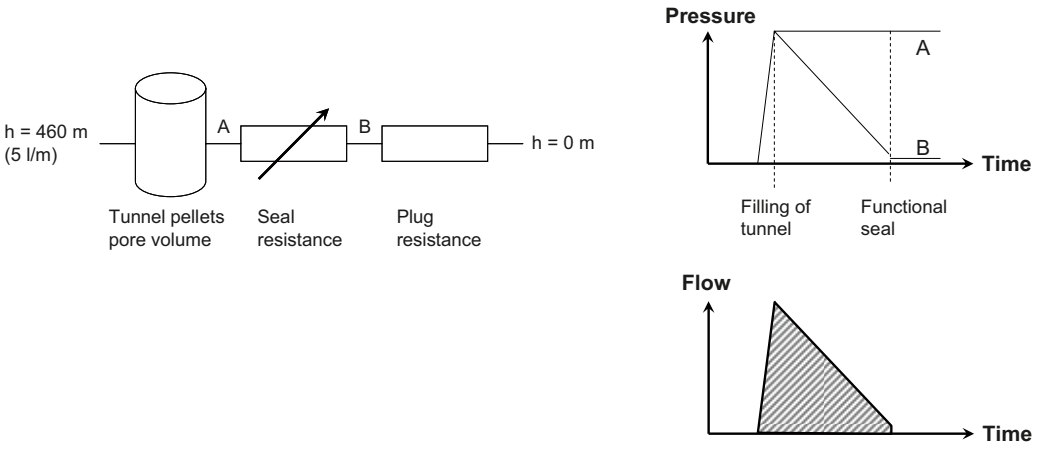

Figure 13-1. *Coupling scheme representing the main hydraulic components of the plug (left). Schematic evolution of pressures, upstream and downstream the seal, and leakage (right).*

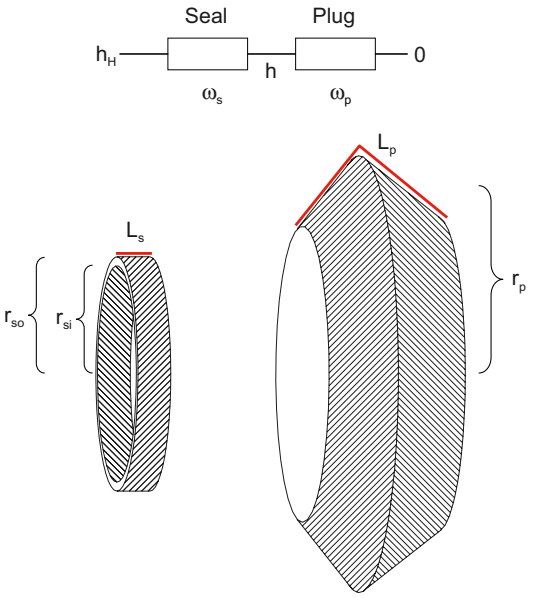

Figure 13-2. *Schematic illustration of pellets-filling in seal and concrete plug-rock interface, and used representation as two series coupled resistances.*

The relation between the transmissivity and the aperture (d) is given by /Jarsjö et al. 2001/:

$$T_p = \frac{\rho g}{\mu} \cdot \frac{d^3}{12} \tag{13-4}$$

The resistance along the pellets filling of the seal is described as:

$$\varpi_s = \frac{L_s}{\pi \cdot \left(r_{so}^{\ 2} - r_{si}^{\ 2}\right) \cdot K_s} \tag{13-5}$$

where K_s is the hydraulic conductivity of the pellets, L_s is 0.7 m, r_{so} is 2.47 m and r_{si} is 2.31 m.

The maximum allowed flow trough the plug is given as a fraction (x_V) of the available pore volume of the pellets filling along the entire tunnel (V_{pp}), and the time-needed to saturate the bentonite seal (t_{sat}).

$$Q_{\max} = \frac{x_V V_p}{t_{sat}} \tag{13-6}$$

The pore volume (V_{pp}) is approx. 1,000 m^3 (see Chapter 11) and the fraction (x_V) is set to 10%.

With this flow specified, the required resistance of the concrete plug rock interface is given by (13-2):

$$\varpi_p = \frac{h_H}{Q_{\max}} - \varpi_s \tag{13-7}$$

The used value for the hydrostatic head (h_H) is 460 m. Moreover, based on Equations (13-3) and (13-4) the following relation for the aperture can be derived:

$$d = \sqrt[3]{\frac{12 \cdot \mu \cdot L_p}{\rho g \cdot 2\pi \cdot r_p \cdot \varpi_p}} \tag{13-8}$$

where r_p is 4 m, L_p is 4.07 m, the viscosity μ is 10^{-3} Pa·s, and ρg is 9,810 Pa/m. The outcome of this representation is illustrated in Figure 13-3. The required aperture of the concrete plug rock interface is here plotted as functions of the hydraulic conductivity of the pellets filling for different saturation times of the seal.

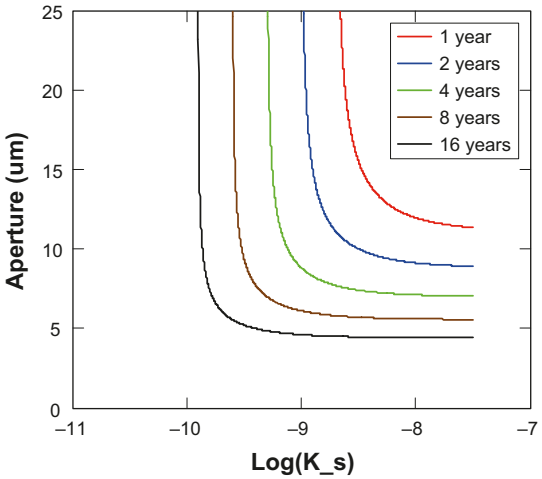

Figure 13-3. *Required aperture of the concrete plug rock interface as functions of the hydraulic conductivity of the pellets filling for different saturation times.*

13.4 Conclusions and uncertainties

The analysis reveals that a very small aperture (~ 5 µm) is required in order to obtain a sufficiently high flow resistance in the concrete plug rock interface, unless a certain hydraulic conductivity of the pellets-filled slot is included in the calculation. The required value of this conductivity is fairly high (~ 10^{-10} m/s). It can be noted that this value is much higher than the hydraulic conductivity of the expected void ratio of the homogenized seal. In Figure 13-4 (right graph) the void ratio dependence of the hydraulic conductivity is shown. This relation was presented in the Data report /Åkesson et al. 2010/. According to the calculations in Chapter 7, a final void ratio of approximately 0.9 can be expected in the outer part of a so-called "theoretical section". This density is marked in the graph.

The relation between the transmissivity and the aperture, according to Equation (13-4), is also shown in Figure 13-4. In a situation where a rock fracture would provide a path from the deposition tunnel to the transport tunnel, a similar limit would be applicable for the maximum allowed transmissivity.

Finally, two significant uncertainties should be noticed in relation to this analysis. The first point is the sealing ability of the bentonite seal in a situation where the hydraulic pressure on one side of the seal (4.6 MPa) significantly exceeds the swelling pressure (~ 2 MPa). It is currently not known if the risk of piping can be neglected in such a situation. The second point is that eroding bentonite is expected to increase the flow resistance of downstream concrete plug rock interface. This process is not well known and has not been included in the analysis.

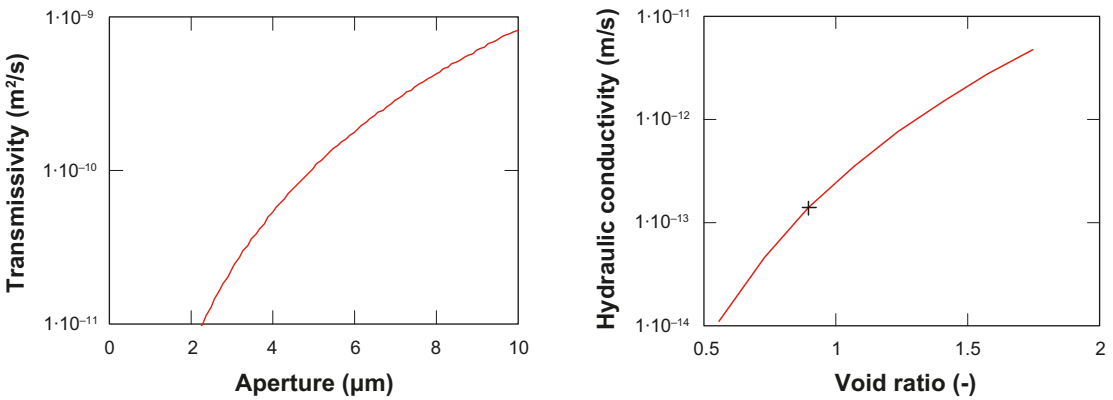

Figure 13-4. *Relations between fracture transmissivity and aperture (left); between hydraulic conductivity and void ratio (right). Expected maximum void ratio in pellets filling marked in right graph.*

14 Analysis of time scale of central area etc and top seal hydration

14.1 Introduction and objectives

The main objective of this task is to analyze the time-scale to saturate the central area and the ramp.

14.2 Approach

The chosen approach for this problem was to simplify the geometry as axisymmetric. This was a fairly obvious simplification for the central area, but for the ramp it requires some further justifications and modifications. The inflow into the ramp can be assumed to be symmetric around the ramp. If the permeability of the backfill limits the inflow, it would be relevant to model the ramp as a vertical cylinder with the same section area as the tunnel. In this case, the pore volume would only be a tenth of the inclined ramp (the inclination is 10%). If, on the other hand, the permeability of the rock limits the inflow and the pore volume of the ramp thereby influences the time-scale, then it is more relevant to increase the section area with a factor of ten.

The task was thus modelled with a number of large-scale hydraulic axisymmetric 2D models, and Code_Bright was used for this purpose. The two extremes, with a correct ramp section area or with a correct ramp volume, was investigated (Figure 14-1).

14.3 Model description

Geometries and densities are modelled in accordance with the Closure production report /SKB 2010c/ and /Brantberger et al. 2006/. Parameter data for backfill and crushed rock are used in accordance with the Data report /Åkesson et al. 2010/. The adoption of the large scale description of the rock is made in accordance with the large hydraulic model in Chapter 3.

14.3.1 Geometry and mesh

Two different geometries were used: with a true section area and with a true section volume (Figure 14-2). The excavated volume of the central area was 140.000 m^3 /Brantberger et al. 2006/. This was represented as a 6 m thick circular disk, which implies a radius of 86 m. The section area of the ramp is 33 m^2 /Brantberger et al. 2006/. This is represented in the true area model as a cylinder with a radius of 3.24 m. In the true volume model, the corresponding radius is 10.25 m.

The rock is modelled with a high permeability (see below) down to a level of 400 m, and beyond a radius 200 m from the ramp down to 600 m. The rock in the vicinity of the central area is modelled with a low permeability (see below).

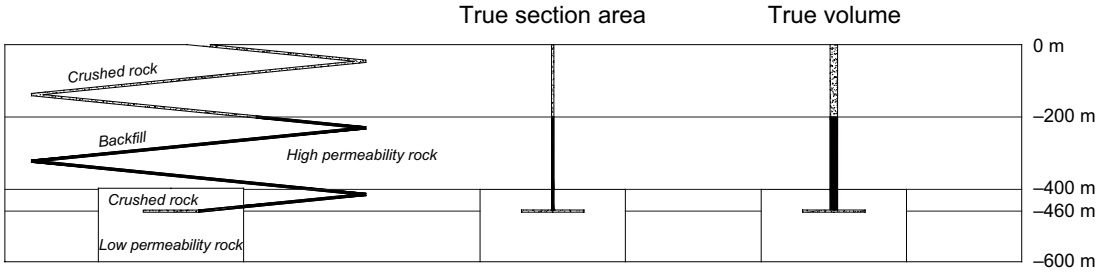

Figure 14-1. *Schematic outline of central area and ramp, and two different axisymmetric representations.*

The central area and the upper 200 m of the ramp were filled with crushed rock, whereas the lower 260 m of the ramp is filled with backfill material (following the Closure production report /SKB 2010c/).

Gravity was applied in both models, which thereby exhibit a hydrostatic pressure distribution.

The mesh is shown in (Figure 14-2). The number of nodes and elements in the true section area model was 1,653 and 1,568 respectively. The corresponding numbers for the true section volume model was 1,767 and 1,680 respectively.

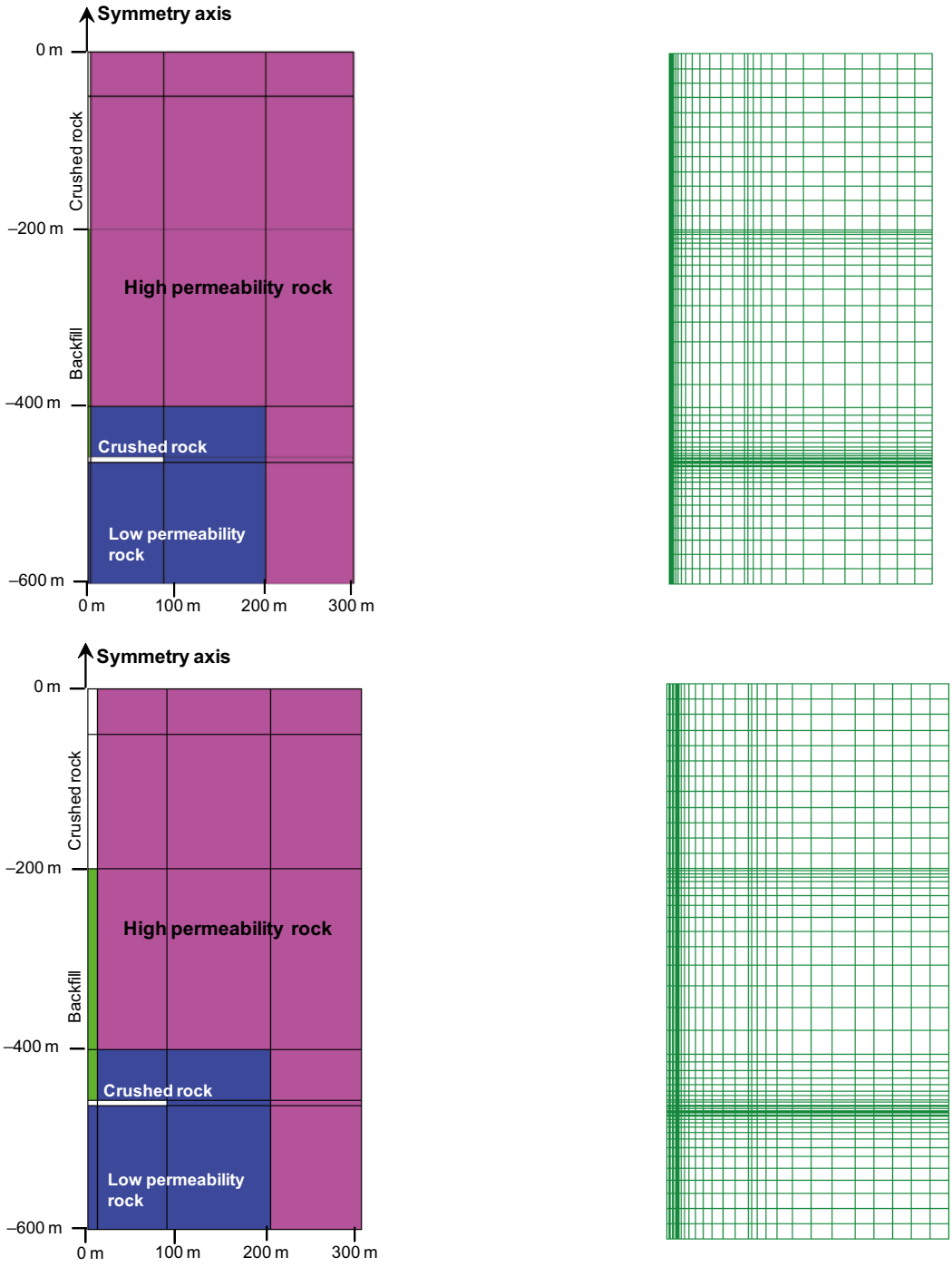

Figure 14-2. *Axisymmetric geometry and mesh for central area and ramp. True section area (upper) and true section volume (lower).*

14.3.2 Initial and boundary conditions

The models are purely hydraulic, and therefore was only the liquid pressure specified in the initial and the boundary conditions.

The initial pressure was defined as a linear distribution from 0.1 MPa at the top and 6 MPa at 600 m depth. The boundary at the ground level was kept at 0.1 MPa throughout the calculations.

During the first half year, the pressure in the central area and in the ramp was held constant at 0.1 MPa, thereby enabling a drawdown around these cavities (Table 14-1). During the subsequent half year the pressures in these materials were ramped down to 0.095 and –45.9 MPa in the crushed rock and bentonite, respectively, representing the installation of these materials. When this is completed, the actual hydration calculation begins.

14.3.3 Material properties

The properties of all modelled materials are compiled in Table 14-2. All data were in general taken from the Data report /Åkesson et al. 2010/, except for the high permeability rock, which was adopted in line with the large hydraulic model in Chapter 3.

14.4 Model results

The drawdown around the central area and the ramp is illustrated in Figure 14-3. The conditions after the initial drainage period and after the installation are shown.

Contour plots of the degree of saturation are shown for different times in Figure 14-4 and Figure 14-5. The three filling materials: crushed rock in ramp, backfill and crushed rock in central area. History plots of the saturation in the nodes with the slowest hydration are shown in Figure 14-6. Time scales for the different material are compiled in Table 14-3.

The first material to reach saturation is the crushed rock in the ramp. The crushed rock in the central area is the second, and the backfill is the last material to get saturated. It can be mentioned that the hydration of the uppermost elements of the ramp is much slower than the elements below this row. The shown history plots are therefore taken from the third node. This is basically a numerical effect, and it can be demonstrated that the same behaviour is obtained if the uppermost element is made significantly smaller.

Table 14-1. Boundary conditions during drainage and installation periods, and during hydration.

Time period (years)	Liquid pressure (MPa) Backfilled ramp	Crushed rock in ramp and central area	Upper boundary
0 – 0.5	0.1	0.1	0.1
0.5 – 1	0.1 –> –45.9	0.1 –> 0.095	0.1
> 1	Free	Free	0.1

Table 14-2. Parameter values for different materials.

Parameter		High permeabity rock	Low permeabity rock	Crushed rock	Backfill*
Porosity	n (–)	0.003	0.003	0.18	0.476
Intrinsic permeability	k (m^2)	10^{-16}†	10^{-18}	10^{-15}	$1.5 \cdot 10^{-20}$
Relative permeability	k_r (-)	vG λ = 0.6	vG λ = 0.6	1	S_r^3
Water retention curve	P_0 (MPa) λ (-)	1.74 0.6	1.74 0.6	0.003 0.9	3.45 0.2

* Homogenized – maximum fallout.

† Not stated in the data report /Åkesson et al. 2010/.

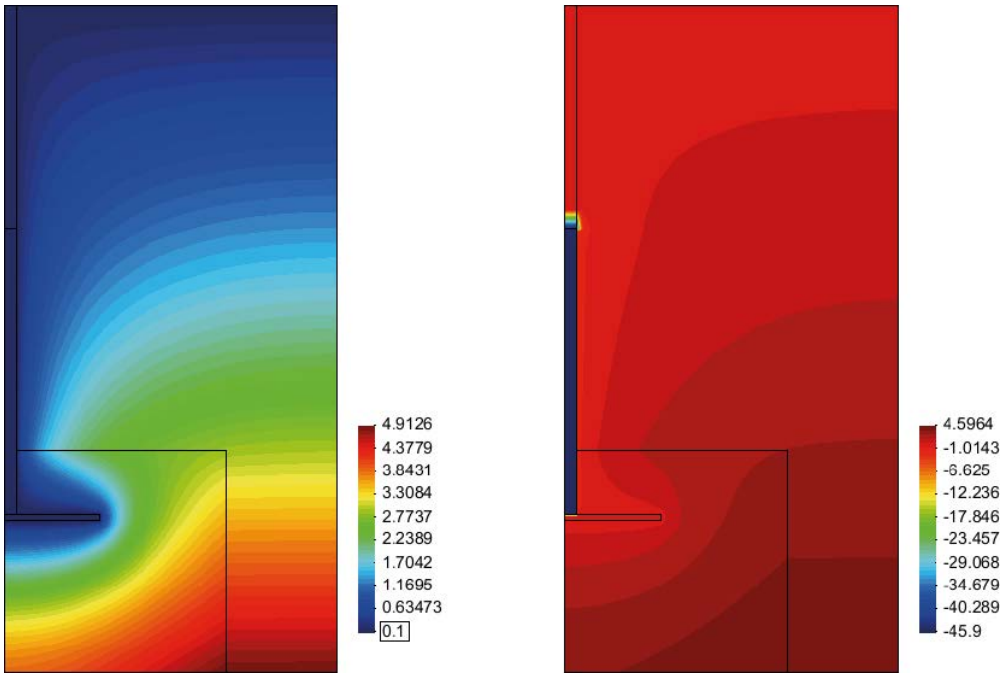

Figure 14-3. *Pressure distribution (MPa) after drainage period (left); and after installation (right).*

Table 14-3. Summary of time scales for different system components.

System component	Time scale for saturation (years)	
	True section area model	True section volume model
Crushed rock in ramp	4	18
Backfill in ramp	202	1,624
Crushed rock in central area	147	155

14.5 Discussion

According to the chosen approach, the true section area model is relevant for parts in which the filling material limits the inflow, since in this case the hydration is mainly governed by the properties of the filling material and the dimensions of the ramp section. In contrast, the true section volume model is relevant for parts in which the rock limits the inflow, since in this case the main process is basically the transfer of a specific water volume through a large rock volume. With this approach and the available results the following observations can be made:

- The time to saturate the crushed rock in the ramp is mainly governed by the rock. The most relevant time-scale for this is therefore given by the true section volume model, i.e. approx. 20 years.
- The time to saturate the crushed rock in the central area is also mainly governed by the rock. The most relevant time-scale for this is therefore also given by the true section volume model (although the difference is smaller) i.e. approx. 150 years.
- Finally, the time to saturate the backfill in ramp is mainly governed by the backfill. The most relevant time-scale for this is therefore given by the true section area model, i.e. approx. 200 years.

It should be noticed that the backfill was represented as being perfectly homogenized. It is shown in Task 2 and Task 3 that this type of representation will result in a slower hydration than if the backfill is represented with initial densities.

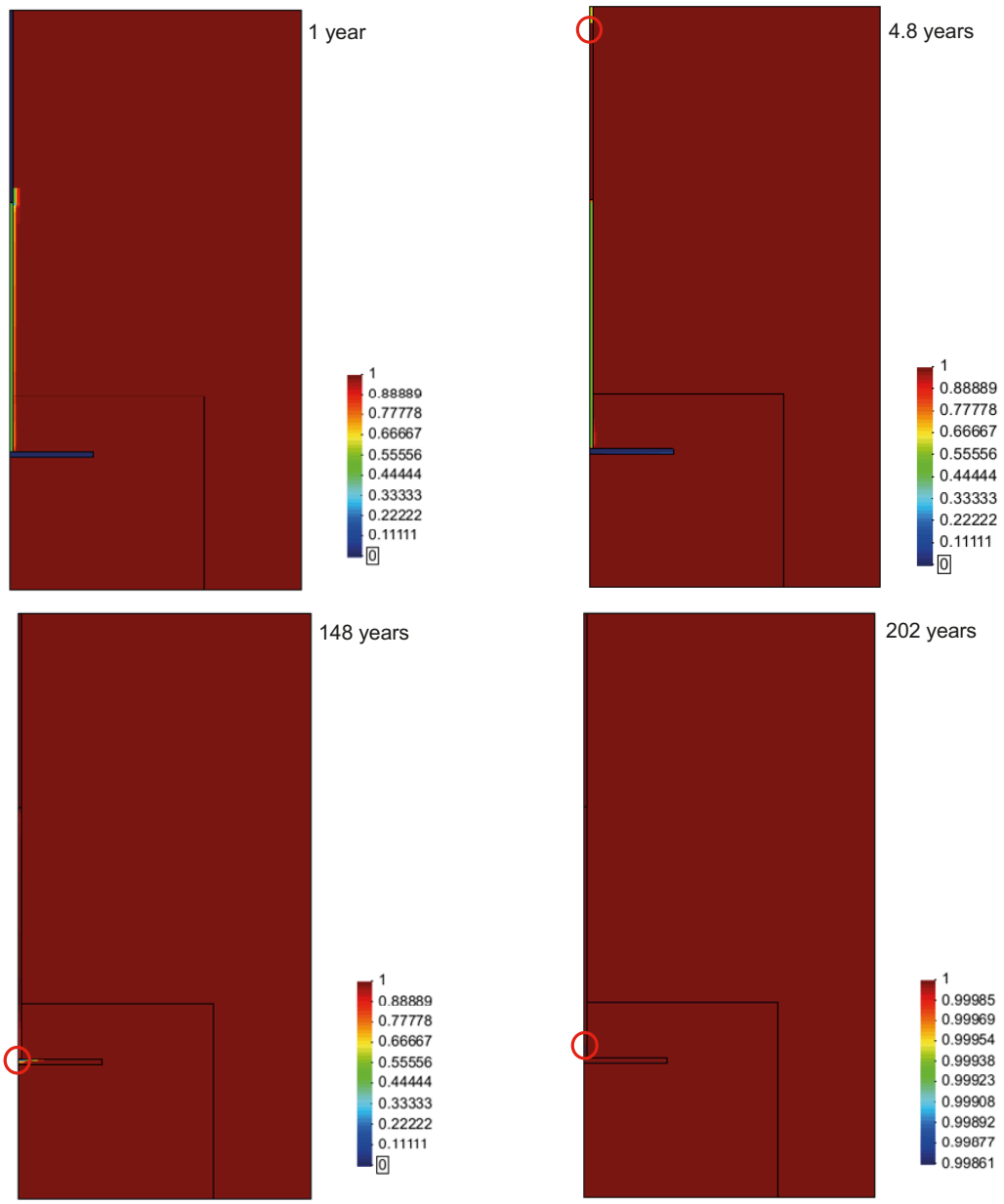

Figure 14-4. *Saturation profiles in true section area model: After installation (upper left), after saturation of crushed rock in ramp (upper right), after saturation of crushed rock in central area (lower left), and after saturation of backfill in ramp (lower right).*

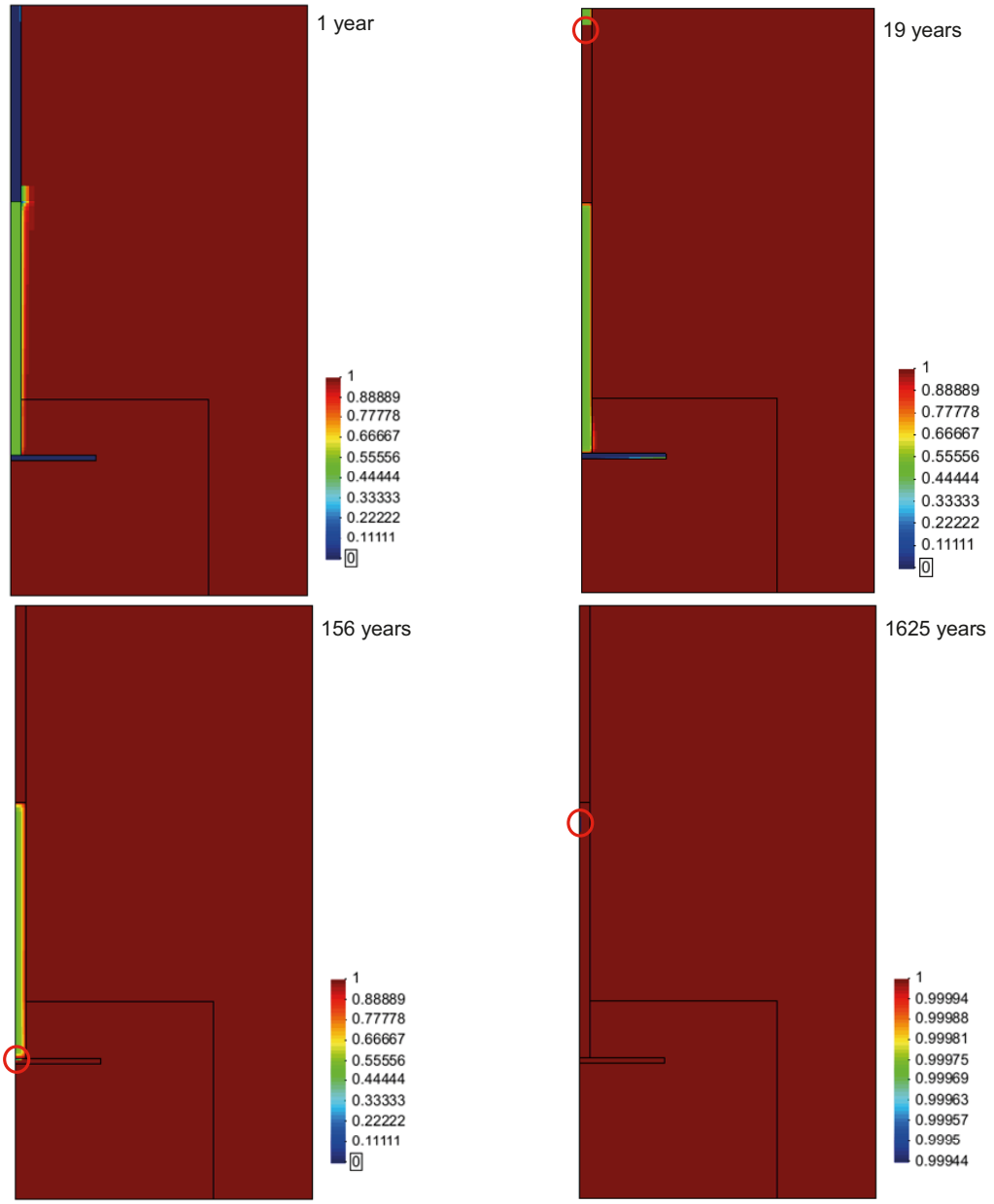

Figure 14-5. *Saturation profiles in true section volume model: After installation (upper left), after saturation of crushed rock in ramp (upper right), after saturation of crushed rock in central area (lower left), and after saturation of backfill in ramp (lower right).*

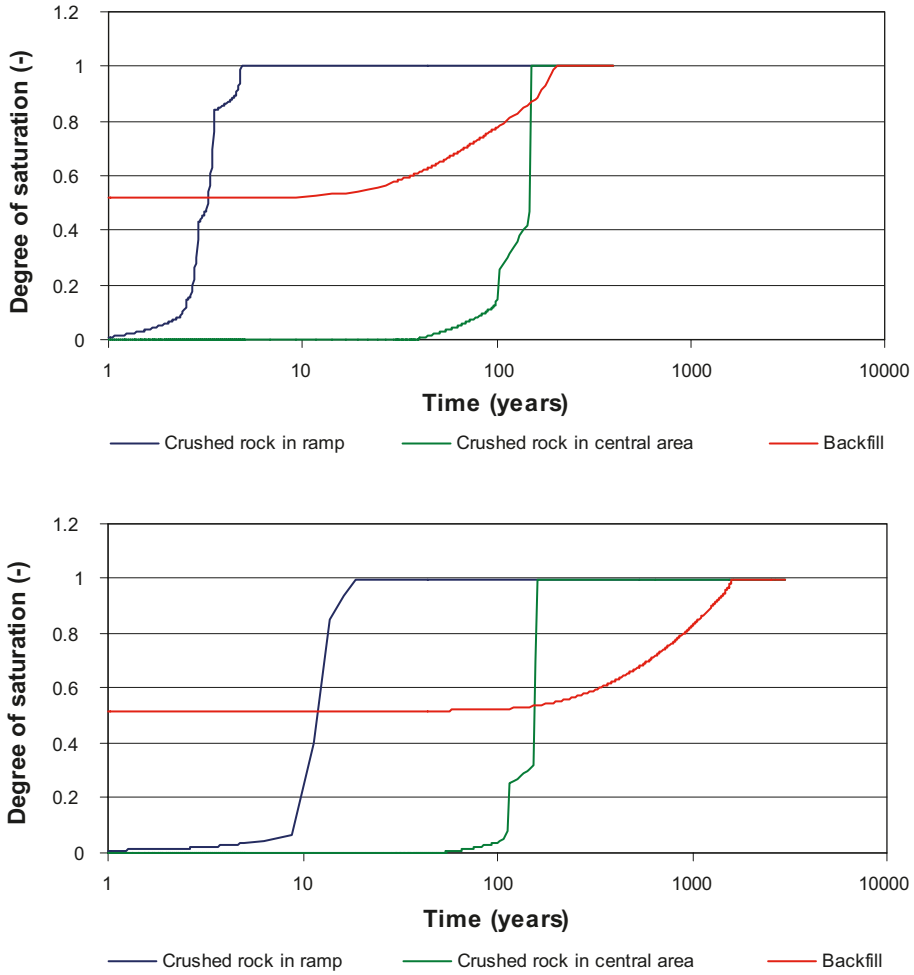

Figure 14-6. *Point analysis of degree of saturation in nodes with the slowest hydration. True section area model (upper); true section volume model (lower).*

14.5.1 Check of time-scale for central area hydration

A simple confirmation of the time-scale can be obtained through further simplification of the geometry around the central area. The cylindrical volume of rock is here simplified as a hollow sphere (see Figure 14-7).

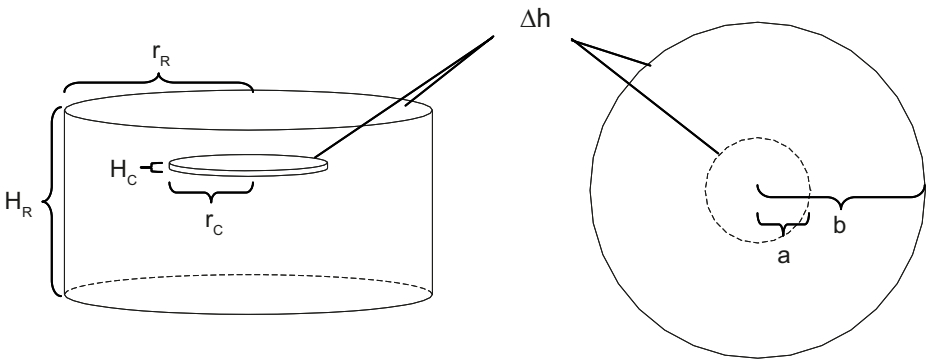

Figure 14-7. *Representation of the central area and the low permeability rock as a hollow sphere.*

The size of the sphere is chosen in such a way that the outer area of the sphere is the same as the sum of the top lateral area and circumferential area on the side of the cylinder:

$$A_R = 2\pi \cdot r_R \cdot H_R + \pi \cdot r_R^2 = 4\pi \cdot b^2 \quad (14\text{-}1)$$

In a similar way, the inner area of the sphere is the same as the total area of the cylinder representing the central area:

$$A_C = 2\pi \cdot r_C \cdot H_C + 2 \cdot \pi \cdot r_C^2 = 4\pi \cdot a^2 \quad (14\text{-}2)$$

With the following data for the cylinder of rock and the central area: $H_R = 200$ m; $r_R = 200$ m; $H_C = 6$ m; $r_C = 86$ m, this will results in the following areas: $A_R = 377{,}000$ m^2; $A_C = 50{,}000$ m^2, and the following radii of the hollow sphere: a = 63 m; b = 173 m. The inflow is given by:

$$Q = \frac{4\pi \cdot K \cdot \Delta h \cdot ab}{b - a} \quad (14\text{-}3)$$

/Carslaw and Jaeger 1959/. With a hydraulic conductivity of $K = 10^{-11}$ m/s and a head difference of $\Delta h = 460$ m the inflow will be $5.7 \cdot 10^{-6}$ m^3/s.

The time to saturate the central area is given by:

$$t = \frac{\pi \cdot r_C^{\,2} \cdot h_C \cdot n_C}{Q} \quad (14\text{-}4)$$

With a volume of 140,000 m^3 and a porosity of $n_C = 0.18$ this will give a time of 140 years. This is apparently very close to the time-scale found by the numerical models. It can be noted that the corresponding time for a very large outer radius (b) is 220 years.

14.6 Conclusions and uncertainties

The time-scale to saturate the crushed rock in the ramp was found to be approx. 20 years. The corresponding time-scale for the crushed rock in the central area was approx. 150 years. The hydration of the backfill in the ramp yielded the slowest hydration with a time-scale of approx. 200 years.

It should be remarked that the intention with this analysis was to simplify the problem as far as possible. One such simplification is the high permeability rock in the upper 400 m. In the large-scale model described in Section 3.2, this layer was divided in two: 0–200; and 200–400 m. The k-value used in this task was twice as high as the value used for the 200–400 m layer in Section 3.2, but two orders of magnitude lower than the 0–200 m layer. The only significant influence of this simplification on the result is probably the saturation of the crushed rock in the upper 50 m of the ramp. The time-scale for this process can therefore possibly be significantly shorter than the one calculated. The back-filled part is on the other hand largely determined by the backfill itself, and for this part the results are less uncertain.

The time-scale for saturating the central area is governed by the distance to hydrostatic pressure and the k-value of the low permeability rock. And a sensitivity analysis of the k-value would yield a span of time-scales similar to the results presented for the backfill hydration in Chapter 2.

It can be noted the geometry and therefore the elements are quite large. At the same time, the execution of the model is largely limited by the crushed rock (with high permeability and low retention curve) in the central area and the upper part of the ramp. The mesh dependence has therefore not been investigated.

15 Analysis of time scale of borehole seal hydration

15.1 Introduction

Carrying out site investigations for a future deep repository of spent nuclear fuel will involve drilling of a great number of deep boreholes for characterisation of the rock. These boreholes must be sealed, and a suggested technique is to fill the lower part of them (depth > 100 m) with highly compacted bentonite cylinders that are placed in perforated copper tubes to facilitate installation, see Figure 15-1. After installation of the plug, the bentonite will swell through the perforation and further out between the tube and the rock.

The swelling is coupled to the water uptake of the clay and in this task the time scale of the water saturation of the borehole plug is estimated.

15.2 Model description

In the poro-mechanical formulation Code_Bright is based on, an additive split of a material volume element, dv, in a solid volume element, dv_s, and a pore volume element, dv_p is used. Furthermore the pore volume element, dv_p, is additively split into a liquid volume element, dv^l, and a gas volume element, dv^g. The liquid volume element is divided into a liquid water volume element dv_w^l and a liquid air volume element dv_a^l (dissolved air into the liquid).

Using the defined volume elements above, or the corresponding mass elements, the following variables are defined: $w = dm_w^l/dm_s$, $S_l = dv_w^l/dv_p$, $e = dv_p/dv_s$, $n = dv_p/dv$, being the water ratio, water saturation, void ratio and porocity, respectively.

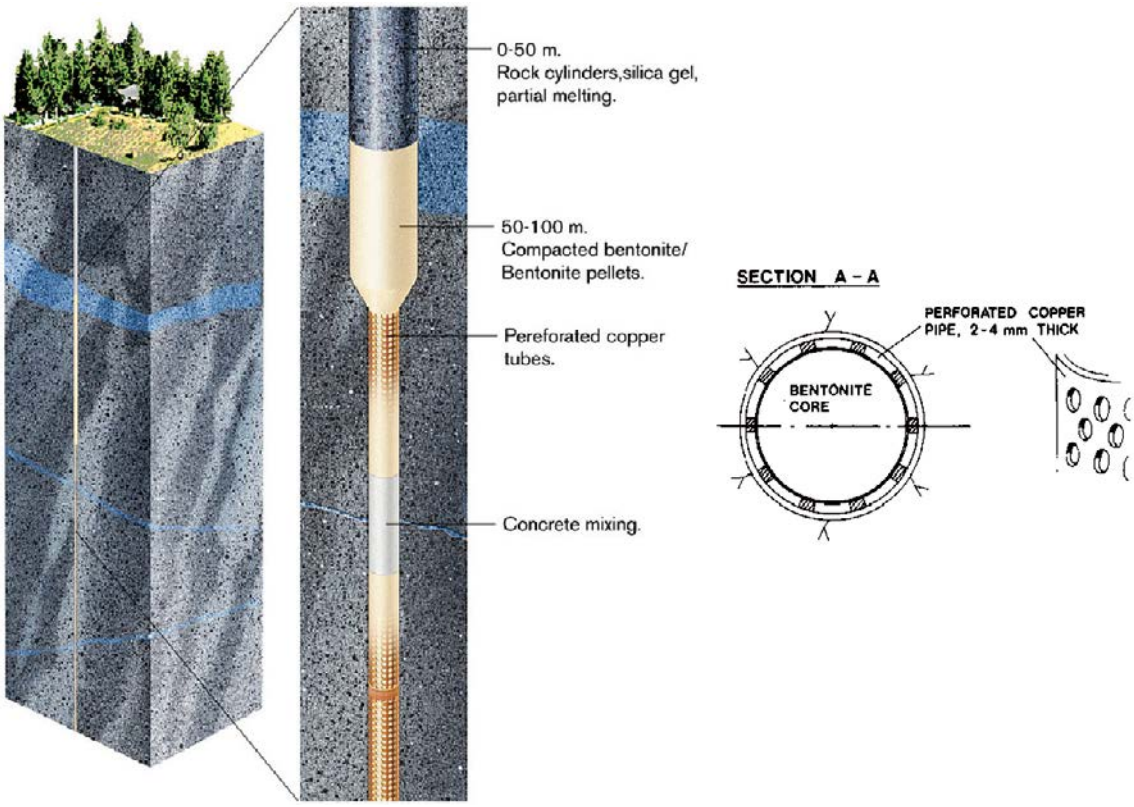

Figure 15-1. *Schematic picture of the borehole seal.*

In the THM model, balance laws of; solid mass (which gives the evolution of porosity), water mass, energy for the system and momentum for the system are considered. The gas pressure is constant, 0.1 MPa, in the model. The psycrometric law,

$$\omega_g^w = (\omega_g^w)_0 \frac{RH}{100}$$
$$(\omega_g^w)_0 = f(T) \qquad (15\text{-}1)$$
$$\frac{RH}{100} = \exp\left(\frac{-(p_g - p_l)\, M_w}{R(273.15+T)\rho_l}\right)$$

is used as an equilibrium constraint between the liquid phase and vapour phase of water.

Only axisymmetric hydraulic models, developed for the Code Bright solver, are considered, see Figure 15-2. The outer radius R, defining the boundary surface of the model, is chosen to be 600 m. The plug is represented by an inner cylinder with radius r_i = 0.045 m and an outer tube with outer radius r_o = 0.05 m. The radius r_i is thought as the location of the copper tube.

The water saturation process is studied at two different depths d = 100 m and 500 m. The representation of the problem at different depths is made by subjecting the model to different initial and boundary water pressures corresponding to the hydrostatic pressure p_h at the considered depth.

The mechanical plug representation (the porosity) is taken as the state after homogenization. The porosity adopted in the inner plug material was calculated from assuming solid mass balance between the initial and final state. The known porosities used in the solid mass balance were: the initial porosity of the inner plug (0.32) (obtained from the Closure production report /SKB 2010c/), the dimension of the initially empty outer slot ($0.045 < r < 0.05$) and adopting a porosity of 0.545 in the outer part of the plug at the final state (taken from a study of swelling and homogenization of bentonite in plugged boreholes).

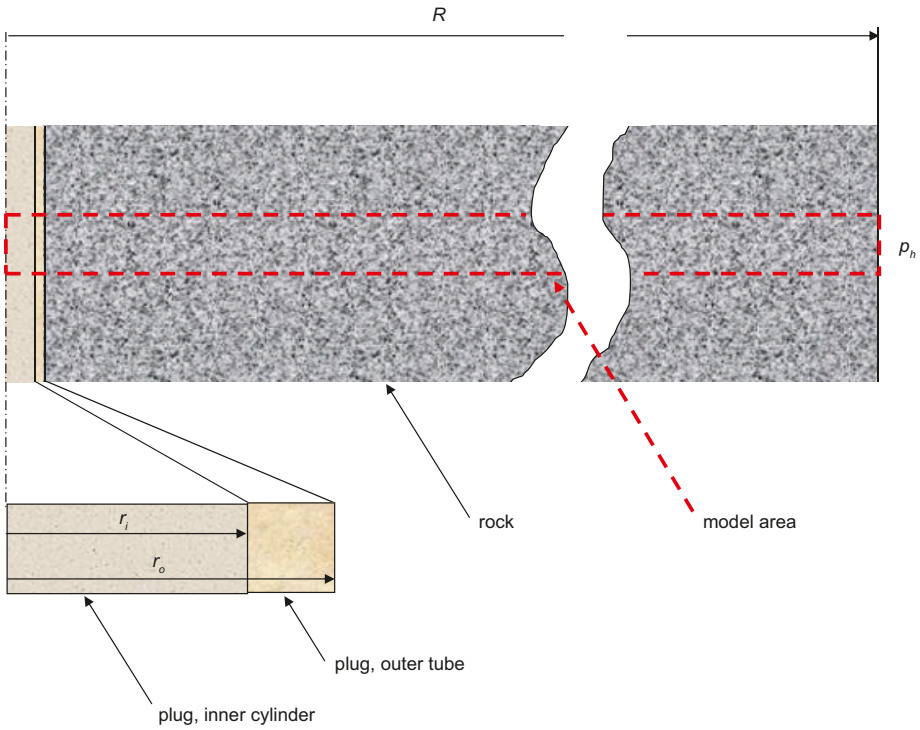

Figure 15-2. *Model geometry.*

The outer part of the plug (the tube) is taken as totally water saturated initially. To prescribe the correct amount of water in the plug initially, the inner (cylindrical) plug is divided in two parts. An inner part ($r < 0.036$) where a water saturation of 0.27 is calculated from assuming constant water mass in the cylindrical inner plug (when going from the initial to the final porosity) and a fully water saturated outer part ($r > 0.036$). The radius 0.036 m is calculated from assuming constant water mass in the entire plug (cylinder and tube).

The retention parameters of the plug materials are determined as described in the data report where the Van Genuchten model is fitted against experimental data.

The permeability of the plug materials is obtained from the void ratio dependent expression described in the data report.

Three different values of rock permeability have been used,

$k = 10^{-18}$ m^2
$k = 10^{-19}$ m^2
$k = 10^{-20}$ m^2

where the lowest permeability represent an extremely tight rock without fractures.

The constitutive laws and parameter values used in the model are shown below in Table 15-1, Table 15-2 and Table 15-3.

Table 15-1. Porosities and initial water saturation.

Parameter	Plug, inner	Plug, outer	Rock
n	0.43	0.55	0.003
S_l	= 0.27, $r < 0.036$ = 1, $r > 0.036$	1	1

Table 15-2. Retention law and parameters.

Constitutive law	Parameter	Plug, inner	Plug, outer	Rock
Retention curve	p_0 [MPa]	22.74	4	1.74
$S_l = \left(1+\left(\frac{S}{p_0}\right)^{1/(1-\lambda)}\right)^{-\lambda}$	λ	0.38	0.3	0.6
$S = p_g - p_l$				

Table 15-3. Advective water transport law and parameters.

Constitutive law	Parameter	Plug, inner	Plug, outer	Rock
Flow through porous medium	k [m^2]	$7.6\cdot10^{-21}$	$7.0\cdot10^{-20}$	10^{-18} 10^{-19} 10^{-20}
$\boldsymbol{q}_l = -\frac{kk_{rl}}{\mu_l}\nabla p_l$				
$k_{rl} = S_l^{\,3}$				
$\mu_l = 2\cdot10^{-12}\exp\left(\frac{1808.5}{273.15+T}\right)$				

15.3 Results and discussion

The resulting water saturation evolutions at the center of the plug for both rock permeability choices are shown below. In Figure 15-3 the evolutions representing 100 m depth are shown and in Figure 15-4 the evolutions obtained for the model representing 500 m depth are shown.

In the 100 m depth models a water saturation of 0.99 is reached at day 12, day 43 and day 397, for $k = 10^{-18}$ m^2, $k = 10^{-19}$ m^2 and $k = 10^{-20}$ m^2, respectively.

The 500 m depth models reach a water saturation of 0.99 at day 9, day 19, and day 153 for $k = 10^{-18}$ m^2, $k = 10^{-19}$ m^2 and $k = 10^{-20}$ m^2, respectively.

The results show that even if the rock mass is unfractured, with extremely low permeability, the models give that the plug is saturated rapidly.

15.4 Conclusions

The time until water saturation was studied for borehole seals. “Local” models at 100 m depth and 500 m depth were used. The models were equipped with three different rock conductivities 10^{-11}, 10^{-12} and 10^{-13} m/s.

The time until full water saturation (here taken as when the saturation = 0.99 in the central part of the plug) was found to be highly dependent on the rock conductivity. The obtained time until full water saturation at 100 m depth for a rock conductivity of 10^{-13} m/s was 397 days. This conductivity must be considered an extreme case at the scale considered (the outer radius of the model, where the water pressure boundary is located, is 600 m)

15.4.1 Uncertainties

The model is thought to be rather conservative in the sense that the time until water saturation is probably overestimated for the lower rock conductivity. Also, the hydraulic water pressure boundary is located quite far from the bore hole (600 m). Finally, no axial flow is allowed in the bore hole, i.e. saturated parts of the seal cannot contribute to the wetting of close unsaturated parts.

An investigation of the correctness of the FE-model has been performed by comparing the obtained inflow evolution of a FE-model, equipped with an empty borehole, with a MathCad solution of the same problem. The two solutions agreed well.

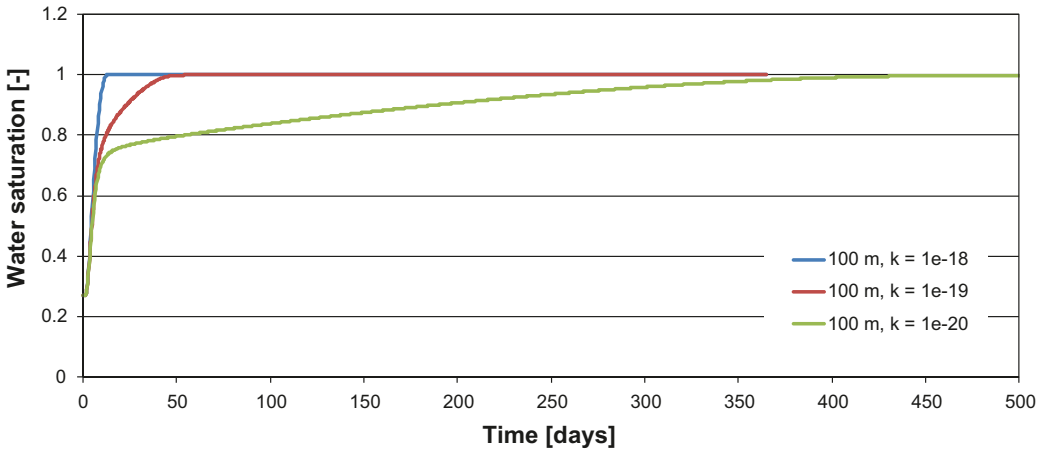

Figure 15-3. *Water saturation evolution for different rock permeability, 100 m depth model.*

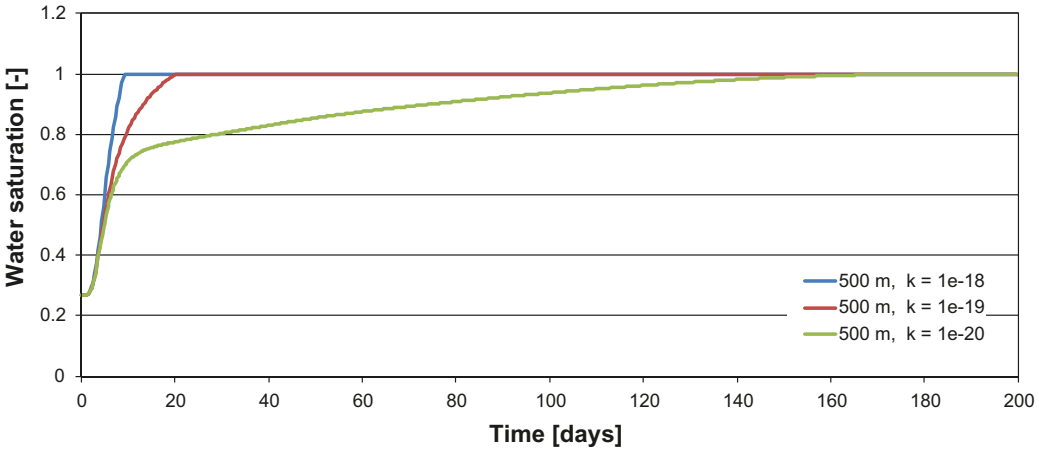

Figure 15-4. *Water saturation evolution for different rock permeability, 500 m depth model.*

16 Tunnel plug model (HM)

16.1 Introduction and objectives

The objective of this task is to analyze the homogenisation of the tunnel plug seal and to frame the conditions for achieving an acceptable swelling pressure on the plug. An analysis of the time-scale to hydrate the plug in general and the seal in particular is presented in Chapter 12.

16.2 Approach

The concrete plug is currently designed to withstand a swelling pressure of 2 MPa. The density of the backfill and the seal implies however a higher swelling pressure and the filter does therefore have to exhibit a certain thickness and compressibility. In order to provide a method which is suitable for parameter analysis, an approach was chosen to derive analytical relations for the required displacements of the interfaces toward the filter. An assumption for these relations is that the backfill and the seal exhibit a radial homogeneity. A confirmation of these relations is thereafter sought in a hydro-mechanical axisymmetric 2D model. This model is simplified in such a way that only backfill materials and filter material are included.

Two different relations between the dry density and the swelling pressure have been considered in this analysis: one based on swelling pressure measurements; and one based on retention measurements at 17% initial water content. Both curves has been evaluated on the form /Åkesson et al. 2010/:

$$\log^{10}(p_{swell}) = c_2 \cdot \rho_d{}^2 + c_1 \cdot \rho_d + c_0 \qquad (p_{swell} \text{ in } kPa) \tag{16-1}$$

The curves are shown in Figure 16-1 and the used coefficients are given in Table 16-1.

Table 16-1. Coefficients for two swelling pressure curves, derived from swelling pressure measurements and retention data, respectively.

Coefficients	p_{swell} TR-06-30 data	p_{swell} retention data
c_0	1.23	–1.74
c_1	$7.97 \cdot 10^{-4}$	$4.12 \cdot 10^{-3}$
c_2	$5.95 \cdot 10^{-7}$	$-3.94 \cdot 10^{-7}$

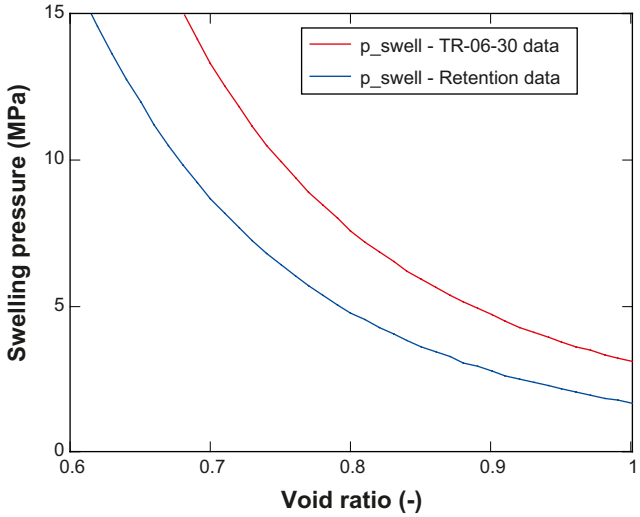

Figure 16-1. *Considered swelling pressure curves, derived from swelling pressure measurements and retention data, respectively.*

The relation derived from retention data appears to apply more correctly to swelling of compacted bentonite (see Section 7.5) and this has therefore been used in the analytical calculations. The relation derived from the TR-06-30 data was however incorporated in Code_Bright and has therefore been used in the numerical model, and in those analytical calculations that are performed for comparison.

16.3 Description of analytical model

The displacements and the stresses after homogenization of the plug are calculated through consideration of the backfill, the filter and the seal. The swelling of the backfill and the seal is assumed to follow a defined swelling pressure curve and to rely on the friction at the rock wall. A similar method was used for calculating upward swelling of buffer /Börgesson and Johannesson 2006/. Finally, the filter is assumed to exhibit an elastic behavior.

First of all, a swelling pressure curve and its inverse function are defined:

$$p_{swell}(e) \quad ; \quad e_{swell}(p) \tag{16-2}$$

The stress distribution in the part of the backfill that is affected by the swelling can be derived from the force balance (see Figure 16-2).

$$\pi \cdot r^2 \cdot (\sigma + d\sigma) + 2\pi \cdot r \cdot \tan(\phi) \cdot \sigma \cdot dz = \pi \cdot r^2 \cdot \sigma \tag{16-3}$$

From this the following differential equation can be derived:

$$\frac{d\sigma}{dz} + \frac{2 \cdot \tan(\phi)}{r} \cdot \sigma = 0 \tag{16-4}$$

The general solution to this is:

$$\sigma(z) = \sigma(0) \cdot \exp\left(-\frac{2 \cdot \tan(\phi) \cdot z}{r} \right) \tag{16-5}$$

16.3.1 Backfill

For the swelling of the backfill, the origin (z=0), is chosen at the point of unaffected swelling pressure. The stress at this point is thereby the swelling pressure of the initial void ratio:

$$\sigma(z) = p_{swell}(e_{init}) \cdot \exp\left(-\frac{2 \cdot \tan(\phi) \cdot z}{r} \right) \tag{16-6}$$

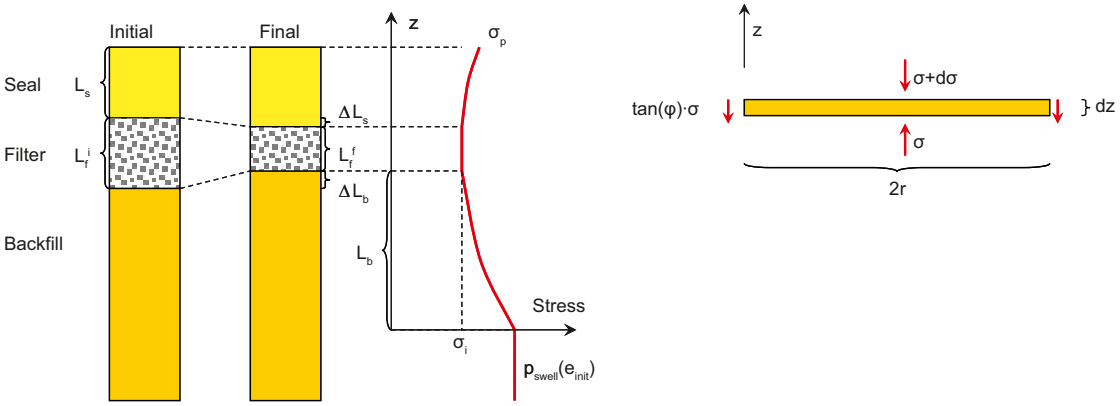

Figure 16-2. *Schematic outline of displacements and stresses in tunnel components behind the plug (left). Force balance on segment of backfill affected by swelling (right).*

The length of the affected part of the backfill is thus given by the stress (σ_i) at the interface toward the filter:

$$L_b(\sigma_i) = \ln\left(\frac{p_{swell}(e_{init})}{\sigma_i}\right)\frac{r}{2\cdot\tan(\phi)} \tag{16-7}$$

The solid mass in the affected part should be the same as in the initial length of backfill (L_b–ΔL_b):

$$(L_b - \Delta L_b)\cdot(1-n_{init}) = \int_0^{L_b} 1-n(z)\,dz \tag{16-8}$$

The porosity distribution can be calculated from the stress distribution:

$$n(z) = \frac{e_{swell}(\sigma(z))}{1+e_{swell}(\sigma(z))} \tag{16-9}$$

The displacement of the backfill (ΔL_b) is thus given by:

$$\Delta L_b(\sigma_i) = L_b(\sigma_i) - \frac{\int_0^{L_b(\sigma_i)} 1-n(z)\,dz}{1-n_{init}} \tag{16-10}$$

The porosity distribution (16-9) is substituted into (16-10) which yields:

$$\Delta L_b(\sigma_i) = L_b(\sigma_i) - \int_0^{L_b(\sigma_i)} \frac{1+e_{init}}{1+e_{swell}(\sigma(z))}\,dz \tag{16-11}$$

16.3.2 Seal

A similar approach is used for the seal, although with one difference: the initial length is known instead of the stress at one of the boundaries. The stress distribution in the seal is defined so that the origin ($z=0$) is chosen at the interface toward the filter. The stress at this point (σ_i) is thus also a variable:

$$\sigma_s(z,\sigma_i) = \sigma_i\cdot\exp\left(\frac{2\cdot\tan(\phi)\cdot z}{r}\right) \tag{16-12}$$

The final length of the seal is given by the two boundary stresses; σ_i at the interface toward the filter, and σ_p at the interface toward the plug:

$$L_{sf}(\sigma_i,\sigma_p) = \ln\left(\frac{\sigma_p}{\sigma_i}\right)\frac{r}{2\cdot\tan(\phi)} \tag{16-13}$$

The solid mass of the seal should be the same prior to and after swelling:

$$L_s\cdot(1-n_{init}) = \int_0^{L_{sf}(\sigma_i,\sigma_p)} 1-n(z)\,dz \tag{16-14}$$

The stress at the interface toward the plug can be calculated through root solving of the function:

$$F_s(\sigma_i,\sigma_p) = \frac{L_s}{1+e_{init}} - \int_0^{L_{sf}(\sigma_i,\sigma_p)} \frac{1}{1+e_{swell}(\sigma_s(z,\sigma_i))}\,dz \tag{16-15}$$

With a known $\sigma_p(\sigma_i)$ function, the displacement can be calculated as:

$$\Delta L_s(\sigma_i) = \ln\left(\frac{\sigma_p(\sigma_i)}{\sigma_i}\right)\frac{r}{2\cdot\tan(\phi)} - L_s \tag{16-16}$$

16.3.3 Filter

The compression of the filter is given by:

$$\Delta L_f(\sigma_i) = \frac{\sigma_i}{M} L_f^i \tag{16-17}$$

The equilibration stress (σ_{eq}) can finally be found by the condition that the sum of the displacements is zero:

$$F(\sigma_{eq}) = \Delta L_b(\sigma_{eq}) + \Delta L_s(\sigma_{eq}) - \Delta L_f(\sigma_{eq}) = 0 \tag{16-18}$$

16.3.4 Results

Results for twelve cases are presented in Table 16-2. Calculations have been made for four different void ratios, two different M modules, and two different filter lengths. The identification of the equilibration stress is illustrated in Figure 16-3 together with stress profiles. Both graphs correspond to case 1 in Table 16-2.

It can be noted that the lowest void ratio, 0.69, which represents the remaining minimum void ratio in a theoretical tunnel section (see Chapter 7) yields the highest stress on the plug (σ_p in Table 16-2). Different modifications (lower modulus of filter and longer filter) have therefore been analyzed in order to investigate how much the pressure on the plug can be reduced.

Table 16-2. Equilibration stresses for different geometries and material properties.

Case	e_b (–)	e_s (–)	L_s (m)	L_f (m)	M (kPa)	ϕ (°)	r (m)	σ_p (kPa)
1	0.69	0.69	0.7	0.7	67,000	10	2.5	7,058
2	0.74	0.74	0.7	0.7	67,000	10	2.5	5,466
3	0.83	0.83	0.7	0.7	67,000	10	2.5	3,496
4	0.91	0.91	0.7	0.7	67,000	10	2.5	2,388
5	0.69	0.69	0.7	0.7	22,000	10	2.5	5,573
6	0.74	0.74	0.7	0.7	22,000	10	2.5	4,424
7	0.83	0.83	0.7	0.7	22,000	10	2.5	2,944
8	0.91	0.91	0.7	0.7	22,000	10	2.5	2,071
9	0.69	0.69	0.7	1.4	22,000	10	2.5	4,599
10	0.74	0.74	0.7	1.4	22,000	10	2.5	3,712
11	0.83	0.83	0.7	1.4	22,000	10	2.5	2,539
12	0.91	0.91	0.7	1.4	22,000	10	2.5	1,825

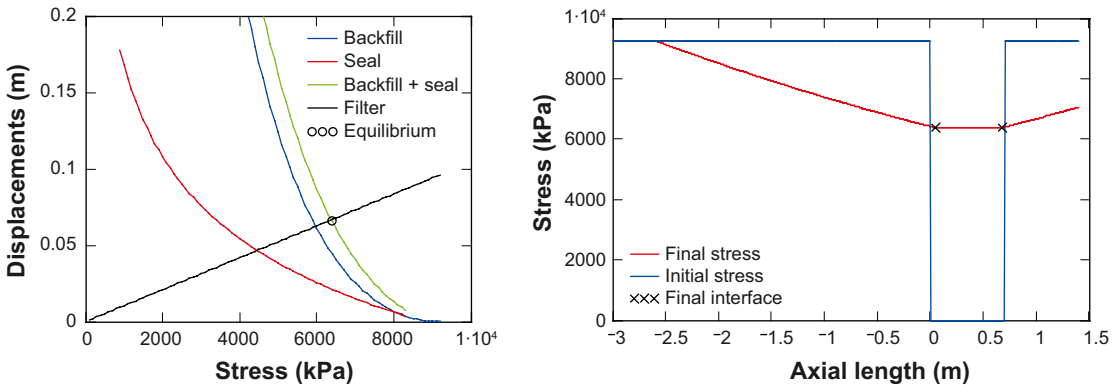

Figure 16-3. *Illustration of identification of equilibration stress (left); and initial and final stress profiles (right).*

16.4 Description of numerical model

Geometries and densities are modelled in accordance with the Backfill production line report. Parameter data for backfill blocks, pellets and filter material are used in accordance with the Buffer THM Data report /Åkesson et al. 2010/.

16.4.1 Geometry and mesh

Only one geometry was used: an axisymmetric 2D geometry (Figure 16-4). The number of nodes and elements are 2,635 and 2,520, respectively.

16.4.2 Initial and boundary conditions

The initial liquid pressure was set to –45.9 MPa, while the initial value of all principal stress was set to –0.11 MPa corresponding to a net mean stress of 0.01 MPa (at a constant gas pressure of 0.1 MPa).

Roller boundaries were applied to all mechanical boundaries, except for the outer boundary. The hydraulic boundary was implemented as a surface boundary over the pellets filling, except for the innermost elements and the filter (Figure 16-5). This boundary was increased from –45.9 to 0.1 MPa during the first 0.01 years, which corresponds to water filling of the pellets-filling. The reason for this approach is to avoid irreversible displacements within the pellets filling which otherwise would affect the final density profiles. The model was run at a constant temperature of 20°C and a constant gas pressure of 0.1 MPa.

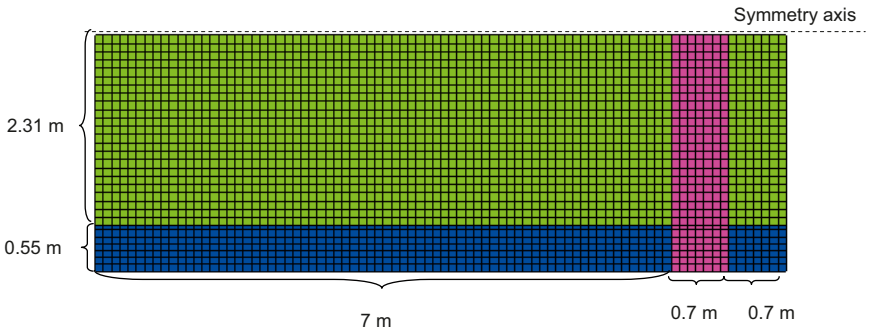

Figure 16-4. *Geometry of 2D axisymmetric model.*

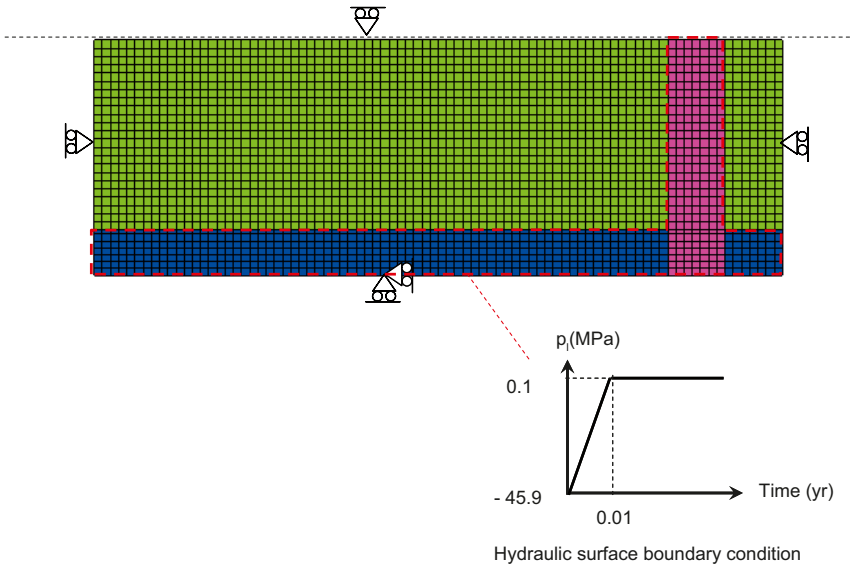

Figure 16-5. *Hydraulic and mechanical boundary conditions.*

16.4.3 Material properties

The properties of all modelled materials are compiled in Table 16-3 and Table 16-4. The geometry corresponds to a target void ratios of 0.91 (maximum fallout). All data were taken from the data report /Åkesson et al. 2010/.

16.5 Results from numerical model

Contour plots for axial displacement, axial stress and porosity are shown in Figure 16-6 and scan-lines for similar variables are shown in Figure 16-7. It can be noticed that the void ratio in the tunnel at some distance from the filter displays the same extent of remaining heterogeneity as in the "maximum fallout" model in Chapter 7, with values between 0.8 and slightly above 1.0. There is also a marked drop in axial stress at the filter along the centre of the tunnel; from 9 to 6 MPa. The displacement at the bentonite/filter interfaces is in the order of 20 to 40 mm.

Table 16-3. Parameter values used for bentonite materials.

		Backfill block e=0.635; w=17%	**Backfill pellets e=1.780; w=17%**
Intrinsic permeability	k_0 (m^2)	2.1E–21	5.2E–19
	n_0 (–)	0.388	0.64
	b (–)	21.3	21.3
Relative permeability	k_r (–)	S_r^3	S_r^3
Water retention curve,	P_0 (MPa)	37.2	0.162
	λ (–)	0.34	0.19
Target void ratio		0.91	0.91
Porous elasticity	κ_{i0} (–)	0.14	0.15
	α_i	–0.02	–0.02
	α_{ils}	0	0
	K_{min} (MPa)	20	1
Swelling modulus	κ_{s0} (–)	0.3	0.3
	α_{ss} (–)	0	0
	α_{sp}	*)	*)
	p_{ref} (MPa)	1	0.1
Poisson's ratio	ν (–)	0.2	0.2
Plastic stress strain modulus	λ_0 (–)	0.182	0.367
	r (–)	0	0
	β (MPa^{-1})	0	0
Critical state line parameter	M (–)	0.27	0.55
Tensile strength	p_{s0} (MPa)	1.5	0.05
	k (MPa^{-1})	0	0
Non-associativity parameter	α (–)	0.5	0.5
Pre-consolidation stress	p_0* (MPa)	10	0.88
	p_c (MPa)	1	1

*) The α_{sp}-parameter is replaced with an inbuilt swelling pressure relation.

Table 16-4. Parameter values used for filter material.

		Filter material (n=0.35)
Intrinsic permeability	k_0 (m^2)	1E–15
Relative permeability	k_r (–)	1
Water retention curve	P_0 (MPa)	0.003
	λ (–)	0.9
Elastic parameters	E (MPa)	60
	ν (–)	0.2

Results from the analytical calculations have been added to the scan-lines in Figure 16-7. It should be noted that these are based on the same swelling pressure relation as used in the FEM code, but different than the one used in the calculation presented in Table 16-2. Calculations are presented for two different void ratios: 0.79 and 0.91, where the latter value represents the completely homogenized void ratio, while the former is based on the remaining minimum void ratio in the tunnel. It can be seen that the lower value gives a fairly good agreement with the results along the centre line in the numerical model, concerning all three variables in Figure 16-7, and it is therefore concluded that the analytical method should be based on the expected density in the centre of the tunnels if the maximum stress is requested.

The radial distribution of axial stresses along the boundary representing the plug is shown for different times in Figure 16-8.

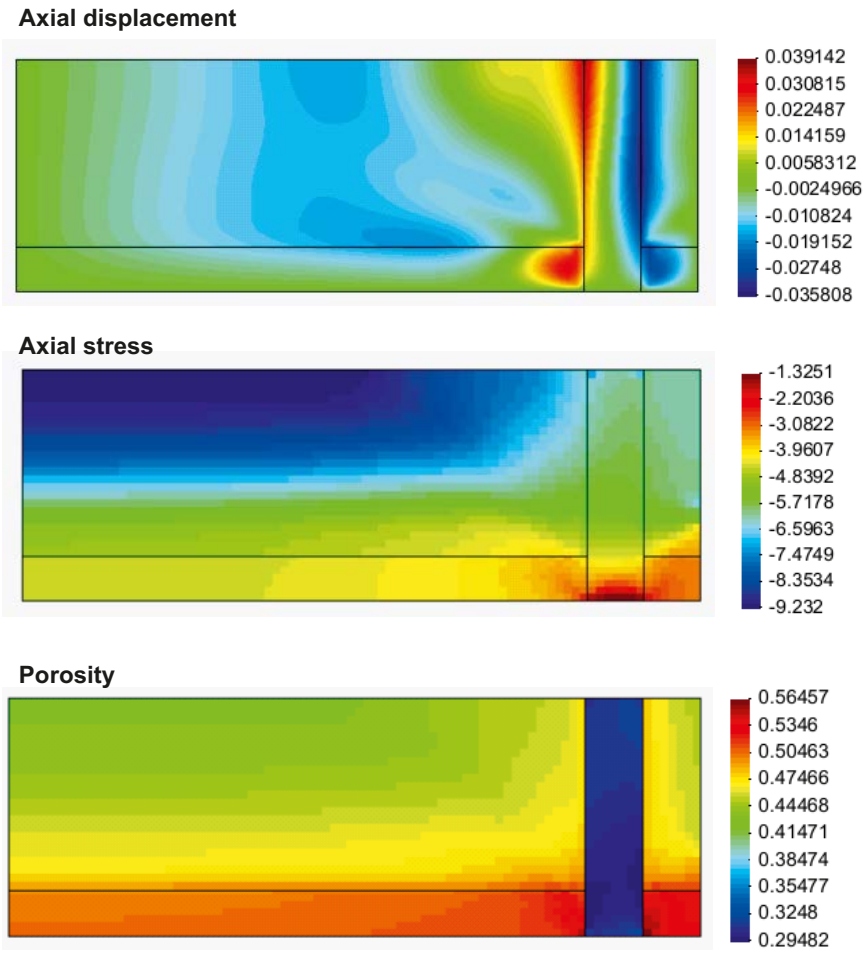

Figure 16-6. *Contour plots of final distribution of axial displacement (m), axial stress (MPa) and porosity (–).*

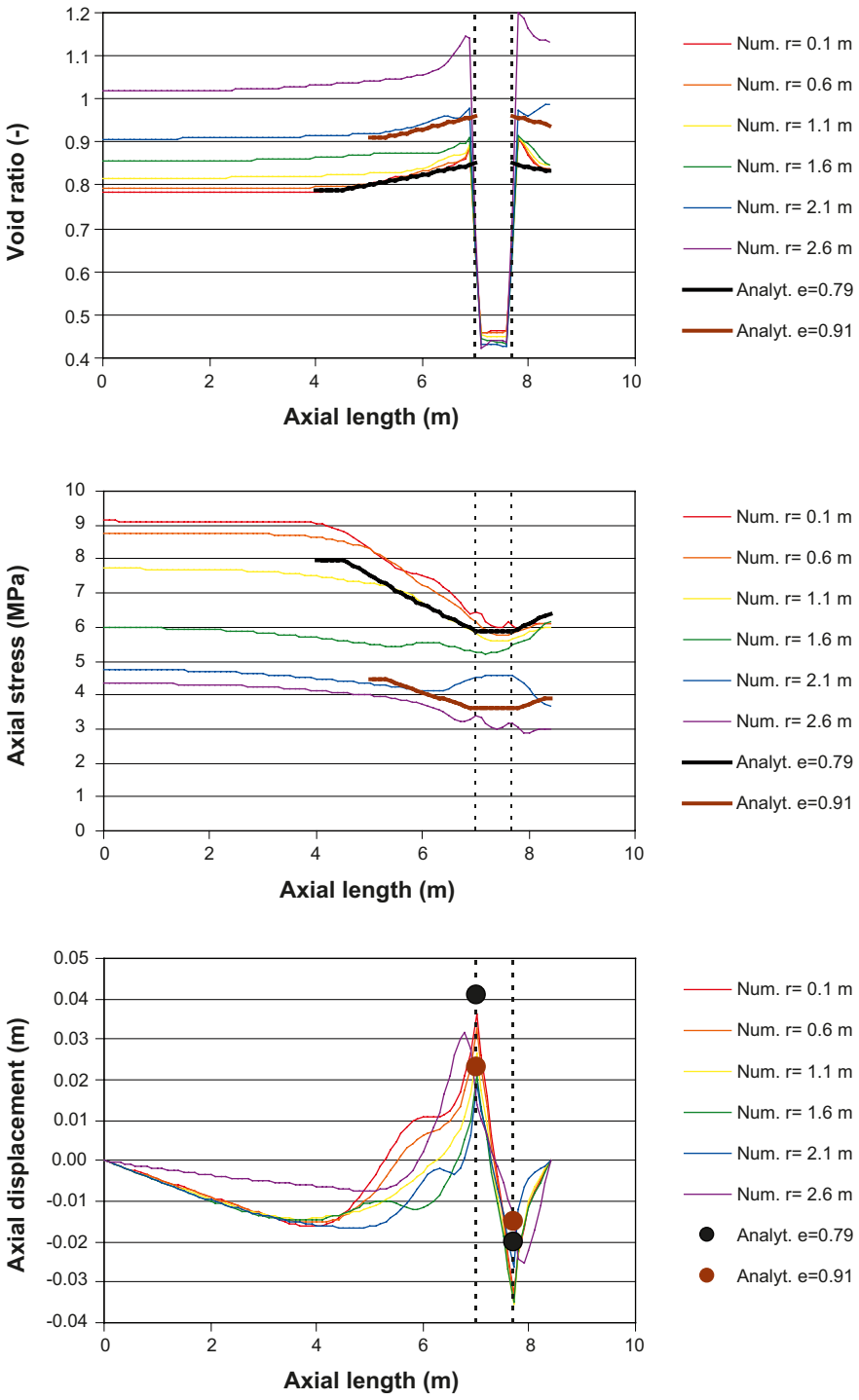

Figure 16-7. *Scan-lines of void ratio, axial stress and axial displacements from numerical model and results from analytical solution for two different void ratios.*

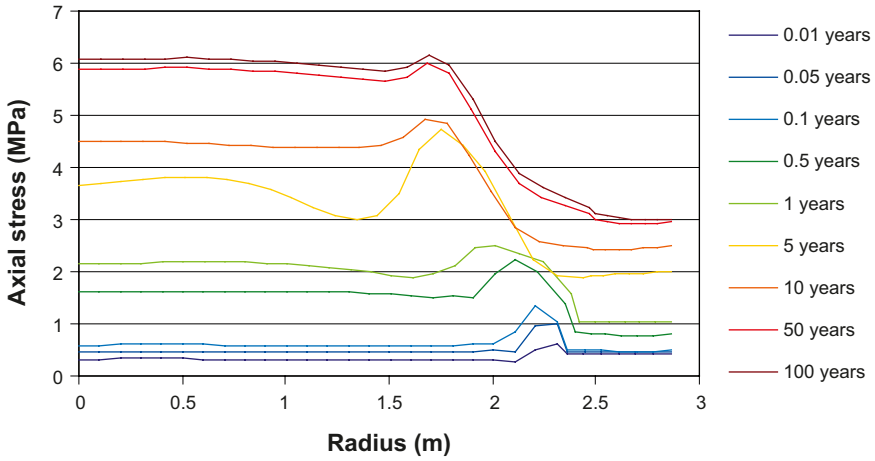

Figure 16-8. *Radial stress distribution along the plug at different times (the nodal radius is modified for displacement).*

16.6 Conclusions and uncertainties

The presented analyses illustrate that the proposed analytical method is a useful tool for testing different designs of the plug, and it should be remarked that this process is still ongoing. More specifically, it has been shown that the analytical method should be based on the expected density in the centre of the tunnels, rather than a completely homogenized density if the maximum stress is sought. An application of this finding reveals that the final pressure at the centre of the plug will be significantly higher than 2 MPa unless the seal and the outer part of the backfill are designed to yield lower stresses.

The uncertainties associated with this analysis are generally the same as those described in Chapter 7. In addition to this, it can be noted that the concrete beams have not been included in the model.

17 Backfill swelling after tunnel plug disintegration 1 – including filling outside the plug

17.1 Introduction

All deposition tunnels will be temporarily sealed with a plug at the end of the tunnel. The main purpose of the plug is to mechanically support the backfill inside the plug and hydraulically prevent leakage and subsequent erosion of bentonite past the plug until the backfill outside the plug has been placed and is saturated with water. The function of the plug is thus only required for a time of about 100 years.

The design of the plug is still ongoing but the present reference plug consists of three main parts; the concrete plug, the clay seal and a sand filter. The layout is shown in Chapter 12.

With time the cement and other substances in the concrete plugs may be dissolved and transported away, which means that the stiffness and strength of the plugs will be dramatically reduced. This disintegration will affect the backfill material on both sides of the plug. When the plug cannot withstand the swelling pressure of the backfill it will be compressed and the backfill will swell, which leads to a loss in density and swelling pressure of the backfill. Since there is friction against the rock surface the loss in density may be significant close to the plug but will be reduced with distance from the plug. In order to understand how this affects the backfill and the location of the first deposition hole a number of FE calculations have been done.

A special study of the consequences of missing backfill outside the plug has been done. This may be the resultof a very long interruption in depositing or backfilling followed by a failure to close the repository.

17.2 Problem description

The main purpose of this task is to find how much the backfill density can been reduced in order to put a limit for how close to the plug the deposition hole can be located. Since no detailed knowledge of the plug status after disintegration is required only a very simplified model of the plug needs to be done. Therefore the whole plug including the clay and sand seal is modelled as a unit with a compressibility corresponding to different plug designs. If the results appear to be critical a more detailed model will be done.

The backfill is modelled as completely homogenised and water saturated but at different initial states that correspond to the expected variation in density caused mainly by the variation in rock contour. After release of initial locking the swelling of the backfill and compression of the plug will be modelled with reversed consolidation as function of time until full equilibrium is reached. The interaction between the rock and the backfill/plug has been modelled with contact elements with different friction angle.

According to the production line report for the backfill, the average dry density of the backfill must be higher than 1,240 kg/m^3 (void ratio lower than 1.22) above a deposition hole in order not to allow too much upwards swelling of the buffer. The effect of the disintegration of the plug must not allow the swelling of the backfill to cause a decrease in dry density to below 1,240 kg/m^3 at the position of the first deposition hole.

17.3 Finite element model

The finite element program Abaqus is used for the calculations. The plug and the backfill on each side of the plug are simplified and modelled with an axisymmetric element mesh as shown in Figures 17-1 and 17-2.

The contact between the backfill and the rock and between the plug and the rock is modelled with contact elements.

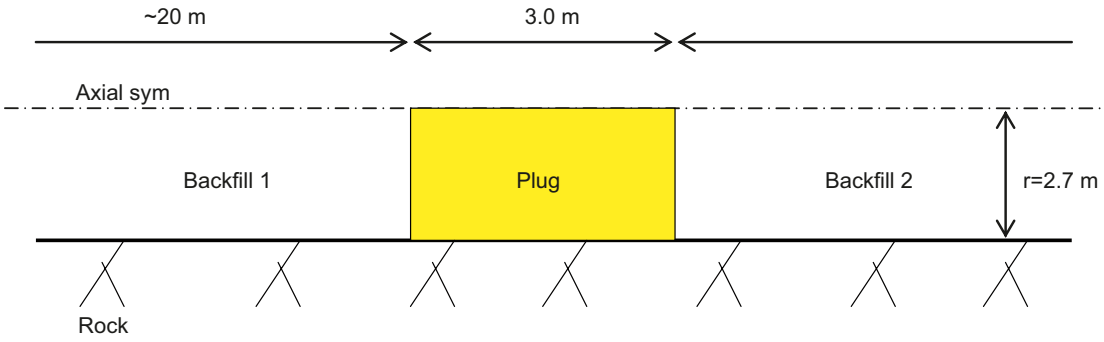

Figure 17-1. *Schematic drawing of the model. Backfill 1 is located inside the plug and Backfill 2 outside.*

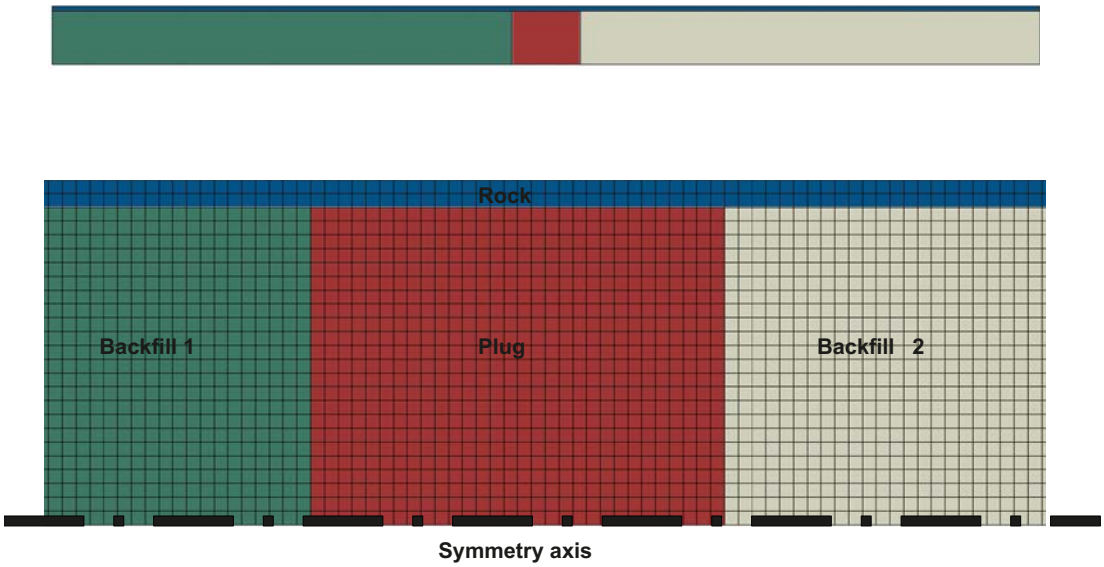

Figure 17-2. *Element mesh. The entire mesh (upper) and enlargement of the region around the plug.*

17.4 Material properties

The backfill inside the plug (Backfill 1) is modelled as a porous elastic material with Drucker-Prager plasticity with pore pressure elements, while the backfill outside the plug (Backfill 2) either is identical to Backfill 1 or is modelled as a linear elastic material with Drucker-Prager plasticity with pore pressure elements representing crushed rock. Two different densities of the backfill have been used representing the extreme average densities. The plug has been modelled in the same way as the crushed rock, to represent different types of disintegration.

17.4.1 Backfill 1

The **mechanical model** of the backfill inside the plug is identical to the model with properties derived for MX-80 by /Börgesson et al. 1995/. This model is still considered to be sufficiently good for these types of calculations and has therefore also been used in this and similar calculations for SR-Site.

Porous Elasticity combined with *Drucker Prager Plasticity* has been used for the swelling/consolidation mechanisms, while *Darcy's law* is applied for the **water flux** and the *Effective Stress Theory* is applied for the **interaction pore water and structure**.

Mechanical properties

The *Porous Elastic Model* implies a logarithmic relation between the void ratio e and the average effective stress p according to Equation (17-1).

$$\Delta e = \kappa/(1+e_0)\Delta \ln p \qquad (17\text{-}1)$$

where κ = porous bulk modulus, e_0 = initial void ratio.

Poisson's ratio v is also required.

Drucker Prager Plasticity model contains the following parameters:

β = friction angle in the p-q plane
d = cohesion in the p-q plane
ψ = dilation angle
$q = f(\varepsilon^d_{pl})$ = yield function

The yield function is the relation between Mises' stress q and the plastic deviatoric strain ε^d_p at a specified stress path. The dilation angle determines the volume change during shear.

The following data has been derived and used for the *Porous Elastic* model (valid for $e < 1.5$):

$\kappa = 0.21$
$v = 0.4$

The following data has been derived for the *Drucker Prager Plasticity* model

$\beta = 17°$
$d = 100$ kPa
$\psi = 2°$
yield function: See Table 17-1

Hydraulic properties

The hydraulic conductivity is a function of the void ratio as shown in Table 17-2.

Table 17-1. Yield function.

q **(kPa)**	ε_{pl}
113	0
138	0.005
163	0.02
188	0.04
213	0.1

Table 17-2. Relation between hydraulic conductivity and void ratio.

e	***K*** **(m/s)**
0.45	$1.0 \cdot 10^{-14}$
0.70	$8.0 \cdot 10^{-14}$
1.00	$4.0 \cdot 10^{-13}$
1.5	$2.0 \cdot 10^{-12}$
2.00	$1.0 \cdot 10^{-11}$
3.00	$2.0 \cdot 10^{-11}$
5.00	$7.0 \cdot 10^{-11}$
10.00	$3.0 \cdot 10^{-10}$
20.00	$1.5 \cdot 10^{-9}$

Interaction pore water and structure

The effective stress theory states that the effective stress (the total stress minus the pore pressure) determines all the mechanical properties. It is modelled by separating the function of the pore water and the function of the particles. The density ρ_w and bulk modulus B_w of the pore water as well as the density ρ_s and the bulk modulus of the solid particles B_s are required parameters. The following parameters are used for Na-bentonite:

Pore water

ρ_w = 1,000 kg/m^3 (density of water)
$B_w = 2.1 \cdot 10^6$ kPa (bulk modulus of water)

Particles

ρ_s = 2,750 kg/m^3 (density of solids)
$B_s = 2.1 \cdot 10^8$ kPa (bulk modulus of solids)

Initial conditions

The initial average dry density of the backfill determines the initial conditions required for the modelling. Depending on the look-out angle for the blasting boreholes and the over-break caused by blasting the cross section area and thus the dry density of the backfill can vary between ρ_d=1,450 kg/m^3 (corresponding to ρ_m=1,928 kg/m^3 at water saturation) and ρ_d=1,600 kg/m^3 (corresponding to ρ_m = 2,024 kg/m^3 at water saturation), which yield a swelling pressure between 3,000 kPa and 10,000 kPa.

For ρ_d = 1,450 kg/m^3 the initial conditions are

u_0 = 0 kPa (pore pressure)
p_0 = 3,000 kPa (average effective stress)
e_0 = 0.90 (void ratio)

For ρ_d = 1,600 kg/m^3 the initial conditions are

u_0 = 0 kPa (pore pressure)
p_0 = 10,000 kPa (average effective stress)
e_0 = 0.74 (void ratio)

17.4.2 Backfill 2

The backfill outside the plug is either the same as inside i.e. Milos backfill, which yields identical properties and initial conditions, or crushed rock. If Milos backfill is used the material model and the initial conditions are the same as for Backfill 1. If crushed rock is used the material model is as follows:

The **mechanical model** of the crushed rock is in principle the same as for the Milos backfill with the difference that a linear elastic model is used instead of porous elastic. Two different E-modules have been used, the higher one corresponding to the stiffness of crushed rock after compaction to about 90% Modified Proctor and the lower one corresponding to rather poor compaction.

Mechanical properties

Linear elasticity with the following E-modulus and Poissons ratio:

E = 37,000 kPa (3,700 kPa for the poorly compacted)
ν = 0.3

The following data has been derived for the *Drucker Prager Plasticity* model

β = 45°
d = 200 kPa
ψ = 5°
yield function: See Table 17-3

Table 17-3. Yield function.

q (kPa)	ε_{pl}
213	0
238	0.005
263	0.02
288	0.04
313	0.1

Hydraulic properties

The following constant hydraulic conductivity has been used:

$K = 1.0 \cdot 10^{-6}$ m/s

Interaction pore water and structure

Pore water

$\rho_w = 1{,}000$ kg/m^3 (density of water)

$B_w = 2.1 \cdot 10^6$ kPa (bulk modulus of water)

Particles

$\rho_s = 2{,}700$ kg/m^3 (density of solids)

$B_s = 2.1 \cdot 10^8$ kPa (bulk modulus of solids)

Initial conditions

$u_0 = 0$ kPa (pore pressure)

$p_0 = 1$ kPa (average effective stress)

$e_0 = 0.30$ (void ratio)

17.4.3 Plug

The properties of the plug after disintegration were not known when these calculations were performed. The plug has been assumed to have lost its concrete properties and turned into non-cemented particles with properties similar to crushed rock. Two different E-modules have been used and the resulting compression of the plug is rather high, which indicate that the plug model probably is conservative and yields too much expansion of the backfill.

The same properties of the plug as the properties of crushed rock for Backfill 2 (see above) have been used.

17.4.4 Boundary conditions

Mechanical

The boundaries between the backfill and the rock and between the plug and the rock are modelled with contact elements, which can slide. The elements have the following friction angles:

Bentonite backfill/rock: ϕ=10°

Crushed rock backfill/rock: ϕ=30°

Plug/rock: ϕ=30°

Hydraulic

Free access to water at the rock surface is modelled by applying constant water pressure of 0 kPa.

17.5 Calculations and results

Table 17-4 shows the different calculations.

The calculations with names beginning with Plug1 thus have bentonite backfill on both sides of the plug while calculations with names beginning with Plug2 have crushed rock outside the plug. Suffix –2 refers to calculations with the high dry density $\rho_d = 1{,}600$ kg/m^3 and high swelling pressure of the bentonite backfill, while the names without suffix refer to calculations with the low dry density $\rho_d = 1{,}450$ kg/m^3 and low swelling pressure.

Typical examples of results from calculations marked yellow in Table 17-4 are shown in Figures 17-3 to 17-8. They represent extremes regarding disintegration of the plug and swelling of the backfill. The calculations have been run to 10^{10} seconds, which correspond to 317 years. As shown in the figures the swelling is completed in about half that time period for case *Plug1*, which only swells 7 cm while for cases *Plug2b* and *Plug2b-2*, which yield swelling of 0.5 m and 1.0 m respectively, the swelling is not completely finished. However, the time sequence modelled is merely arbitary since the actual disintegration will take much longer time.

The results show that case *Plug1* yields a swelling of only 7 cm, which is the smallest swelling of the investigated cases due to the low initial swelling pressure of the backfill and the high E-modulus of the plug. The entire swelling corresponds to a compression of half the plug since the same backfill is assumed to be outside the plug. The void ratio and the swelling pressure are only changed marginally except for at a small zone at the rock/plug/backfill contact.

Case *Plug2b-2* shown in Figures 17-5 and 17-6 is the case that yields the largest swelling, due to the high initial swelling pressure of the backfill, the low E-modules of the plug and the outer backfill. The axial swelling in the centreline of the tunnel is about 1 m of which 0.5 m is compression of the plug and 0.5 m is compression of the outer backfill. The void ratio of the backfill increases to 1.18 at the plug surface, which yields a decrease in swelling pressure to about 1.5 MPa.

Case Plug2b shown in Figures 17-7 and 17-8 is the case that yields the highest void ratio, although the swelling is only 0.5 m. The reason is that the initial void ratio is higher and corresponds to the highest void ratio that is expected in the tunnel (or lowest dry density). The highest void ratio at the plug surface is 1.19, which yields an average swelling pressure of about 1 MPa.

Table 17-5 is a compilation of the most important results of the different calculations.

Table 17-4. Designation of the plug calculations and the mechanical properties of the different parts. Results are shown for the models marked yellow.

Model	Backfill 1	Backfill 2	Plug
Plug1	e=0.92, p=3 MPa	e=0.92, p=3 MPa	e=0.3, p=1 kPa, E=37 MPa
Plug1b	e=0.92, p=3 MPa	e=0.92, p=3 MPa	e=0.3, p=1 kPa, E=3.7 MPa
Plug1-2	e=0.74, p=10 MPa	e=0.74, p=10 MPa	e=0.3, p=1 kPa, E=37 MPa
Plug1b-2	e=0.74, p=10 MPa	e=0.74, p=10 MPa	e=0.3, p=1 kPa, E=3.7 MPa
Plug2	e=0.92, p=3 MPa	e=0.3, p=1 kPa, E=37 MPa	e=0.3, p=1 kPa, E=37 MPa
Plug2b	e=0.92, p=3 MPa	e=0.3, p=1 kPa, E=3.7 MPa	e=0.3, p=1 kPa, E=3.7 MPa
Plug2-2	e=0.74, p=10 MPa	e=0.3, p=1 kPa, E=37 MPa	e=0.3, p=1 kPa, E=37 MPa
Plug2b-2	e=0.74, p=10 MPa	e=0.3, p=1 kPa, E=3.7 MPa	e=0.3, p=1 kPa, E=3.7 MPa

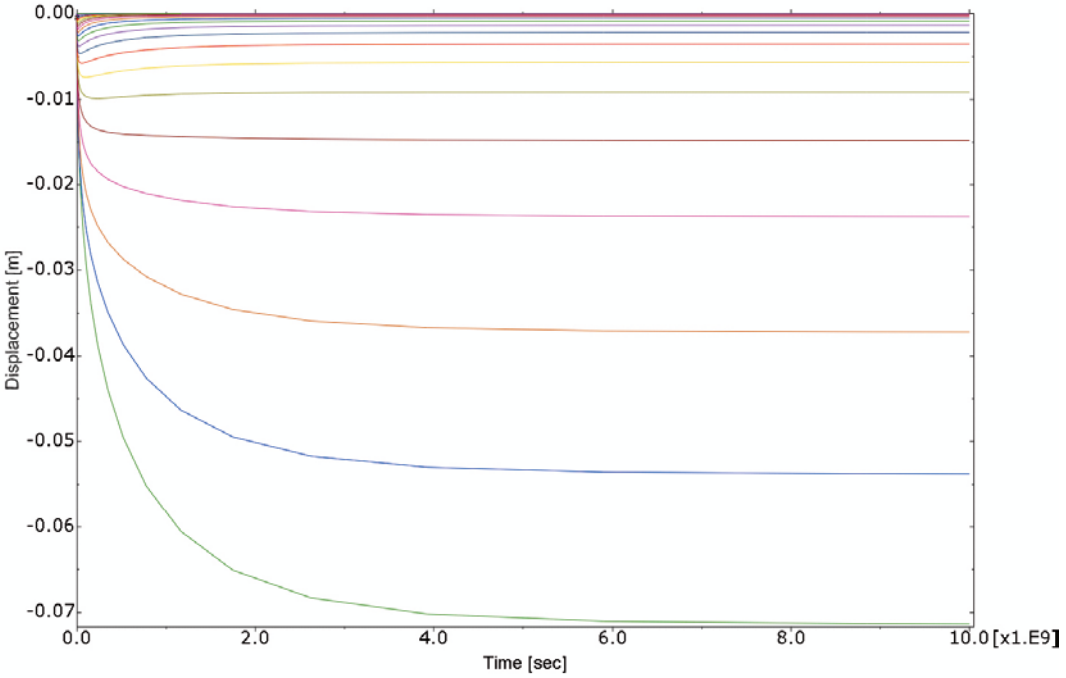

Figure 17-3. *Plug1. Axial displacements of the centre nodes in Backfill 1 as a function of time. The lower curve represents the contact backfill/plug etc.*

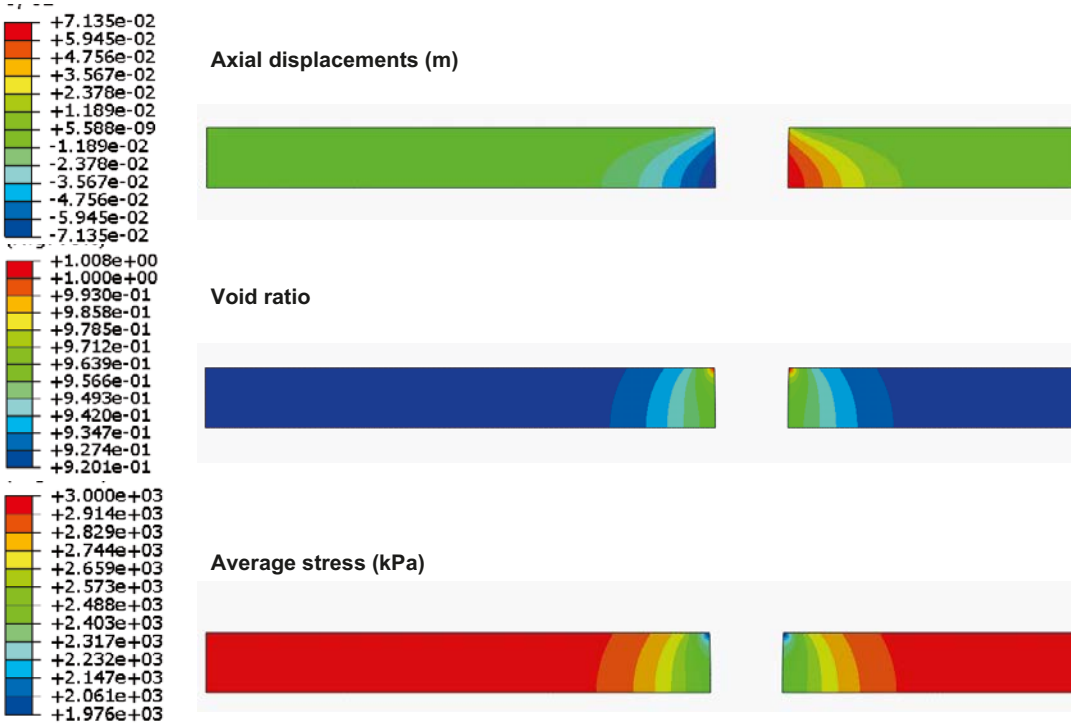

Figure 17-4. *Plug1. Contour plots of axial displacements, void ratio and average swelling pressure in the backfill.*

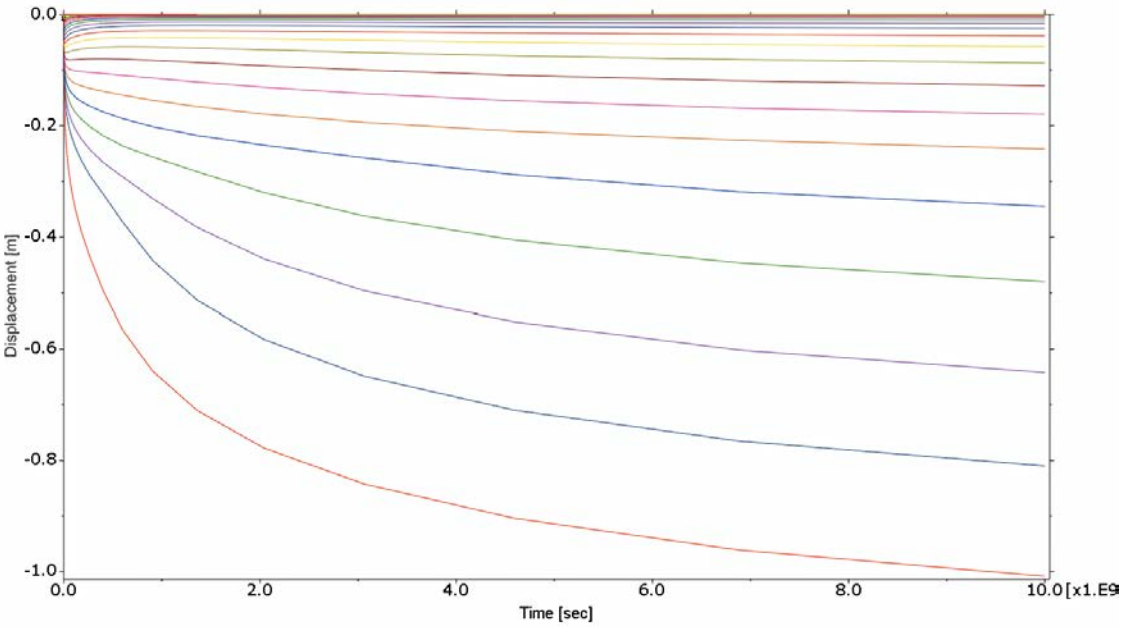

Figure 17-5. *Plug2b-2. Axial displacements of the centre nodes in Backfill 1 as a function of time. The lower curve represents the contact backfill/plug etc.*

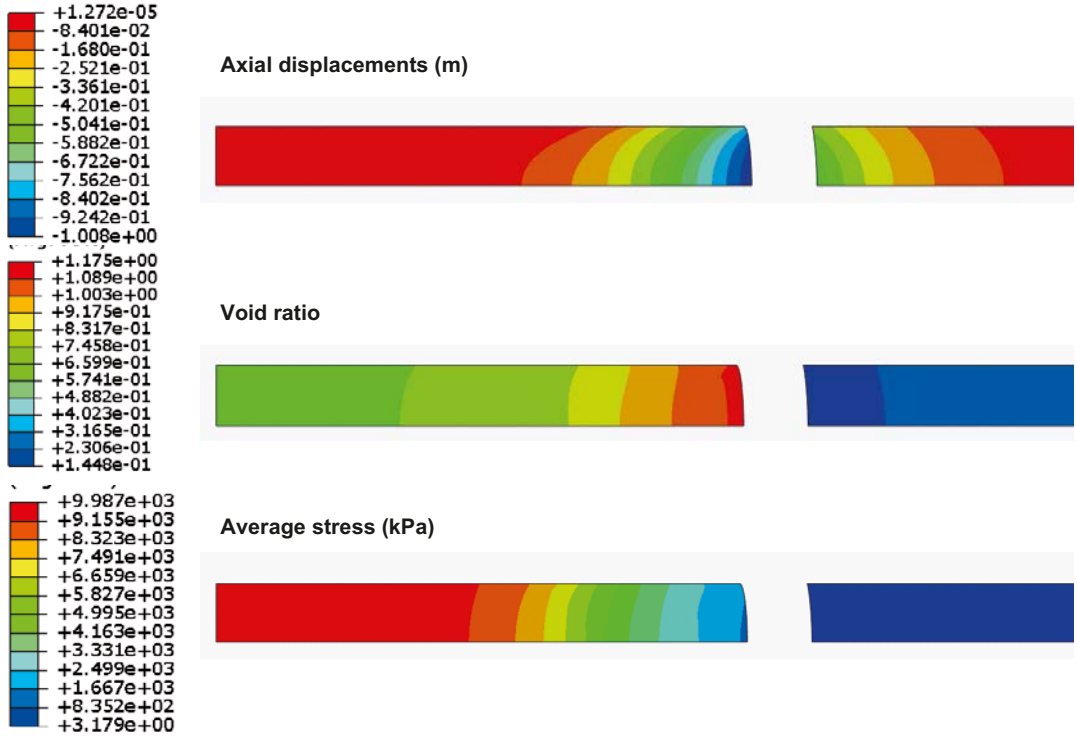

Figure 17-6. *Plug2b-2. Contour plots of axial displacements, void ratio and average swelling pressure in the backfill.*

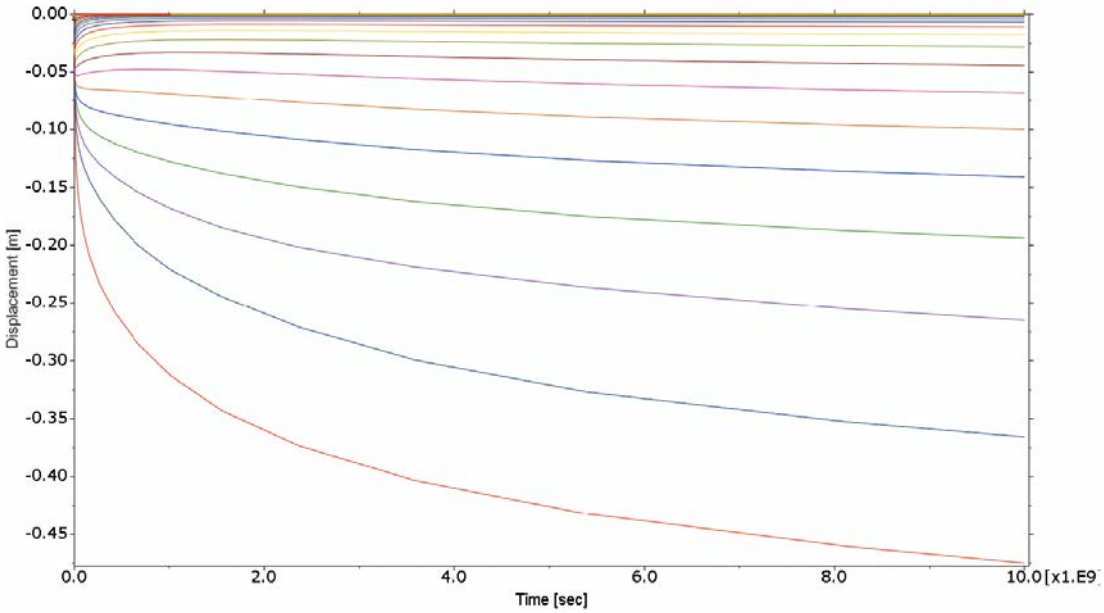

Figure 17-7. *Plug2b. Axial displacements of the centre nodes in Backfill 1 as a function of time. The lower curve represents the contact backfill/plug etc.*

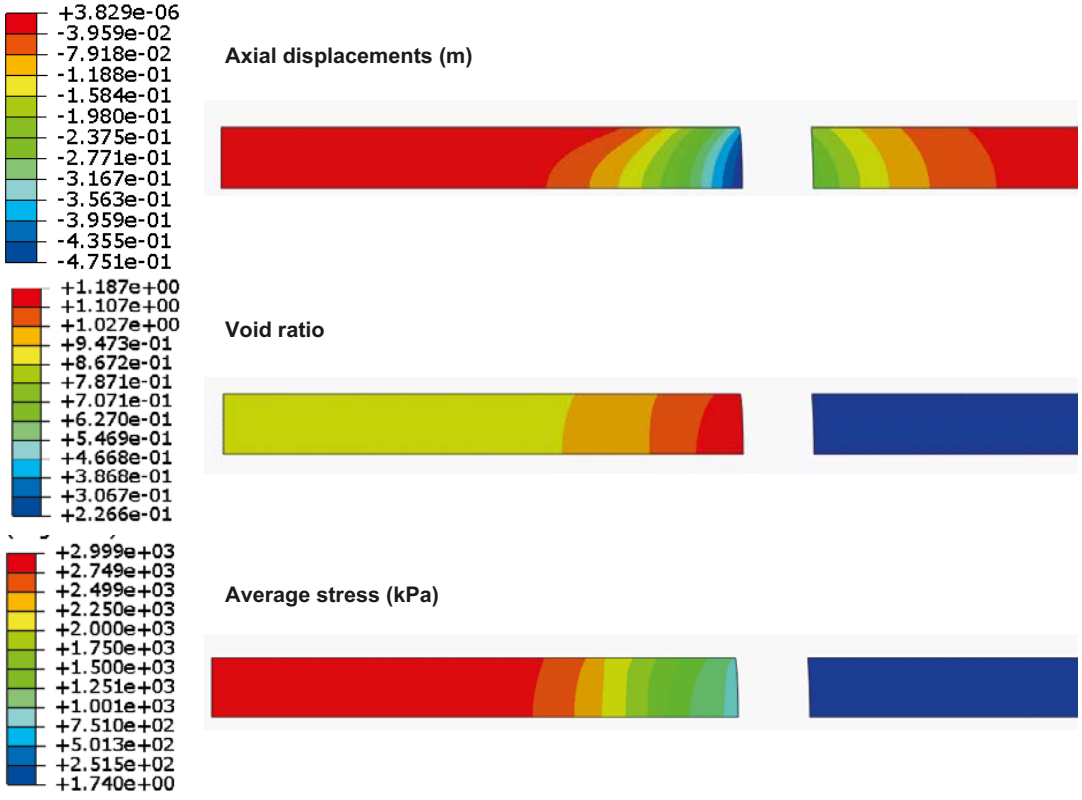

Figure 17-8. *Plug2b. Contour plots of axial displacements, void ratio and average swelling pressure in the backfill.*

Table 17-5. Compilation of results.

Calculation	Displacements (m) Backfill1/ plug	Backfill2/ plug	Maximum void ratio	Minimum swelling pressure (MPa)	Remarks
Plug1	0.03–0.07	–(0.03–0.07)	1.0	2.0	Locally at corner
Plug1b	0.15–0.27	–(0.15–0.27)	1.1	1.3	
Plug1-2	0.08–0.17	–(0.08–0.17)	0.86	5.7	
Plug1b-2	0.30–0.58	–(0.30–0.58)	0.99	3.0	
Plug2	0.10–0.15	0.05–0.07	1.1	1.7	
Plug2b	0.35–0.50	0.20–0.28	1.2	0.8	
Plug2-2	0.24–0.32	0.13–0.17	0.98	3.0	Locally at corner
Plug2b-2	0.70–1.05	0.40–0.58	1.2	1.0	

17.6 Conclusions and uncertainties

The highest resulting void ratio at the backfill/plug interface is 1.19. Since this is still within the limits set for the backfill above a deposition hole (e<1.22) the conclusion from the calculations is that the disintegration of the plug has no detrimental effect on the backfill above the first deposition hole and no restrictions caused by plug disintegration on the location of the first deposition hole is needed.

There are of course several uncertainties regarding especially the data of the plug after disintegration but also regarding the initial density and properties of the backfill. However, the properties of the plug are very conservatively set and in spite of this the results are far from critical for the buffer in the first deposition hole.

18 Bottom plate 1 – lifting of package

18.1 Introduction and objectives

The objective of this task is to analyse the potential lifting of the buffer and canister package during the period from the termination of the drainage to the installation of the backfill, if a water-bearing fracture intersects the deposition hole beneath the bottom plate. In the Process report, it was observed that the contact zones between the concrete and both the copper plate and the rock is not tight, and that this implies that a water pressure can act on the entire surface area.

This is a complex process which is highly related to the phenomenon of piping and a key issue is how fast the build-up of the swelling pressure can be. The assumption that pellets cannot stop inflowing water until all slots are filled due to piping is pessimistic in other cases, such as for the tunnel plug, but it disregards the build-up of pore pressure upstream. So in this case it is optimistic since such a build-up is unfavorable. For the present analysis, a tailored solution has been developed which is based on the following four assumptions:

- The hydration is treated as varying with time and height. The hydration of the pellets-filled slot is vertical and takes place as a distinct front, whereas the hydration of the block is radial and described by a simple exponential model. The hydration of blocks at a certain height starts when the slot hydration reaches this height.
- The build-up of swelling pressure is proportional to the extent of block hydration. This assumption is replaced by an explicit function of the swelling pressure evolution with time in a refined model in Section 18.5.
- The water pressure beneath the package equals the swelling pressure at the bottom of the blocks. Higher water pressures are assumed to imply piping, and would thereby not be possible to develop. This pressure corresponds to a lifting force.
- Concurrently with the build-up of the lifting force is the build-up of the frictional force along the rock wall. The package will be lifted if the lifting force exceeds the sum of the frictional force along the rock-wall and the weight of the package.

18.2 Model framework

The hydration of the pellets slot and the buffer is schematically illustrated in Figure 18-1. The buffer hydration at a certain height begins when the slot hydration reaches this height. For simplicity, the rate of hydration is here described as proportional to the remaining pore space.

$$\frac{d(A_b - A_{sat})}{dt} = -k \cdot (A_b - A_{sat}) \qquad (18\text{-}1)$$

A_b is the initially available pore space per unit height in the buffer, and A_{sat} is the hydrated pore space per unit height. For simplicity, the canister is disregarded. A_b is thus 0.122 m^2. The rate constant (k) is set to correspond to a "half-life" of 0.1 year. This is a very low value in comparison to the time scales of buffer hydration presented in Chapter 3. It is however quite realistic on a short-term time scale, especially if the build-up of swelling pressure is considered. This is described in Section 18.4 below.

A general function for A_{sat} can be formulated by introducing a function $t_0(z)$ which represents the rising front in the pellets:

$$A_{sat}(z,t) = \Phi(t - t_0(z)) \cdot A_b \cdot (1 - e^{-k(t-t_0(z))}) \qquad (18\text{-}2)$$

Φ is the Heaviside step function. The inverse function to $t_0(z)$, i.e. z(t), is derived in the next paragraph. The radial inflow into the buffer (q) is given as a time derivative of A_{sat}.

$$q(z,t) = \Phi(t - t_0(z)) \cdot A_b \cdot k \cdot e^{-k(t-t_0(z))} \qquad (18\text{-}3)$$

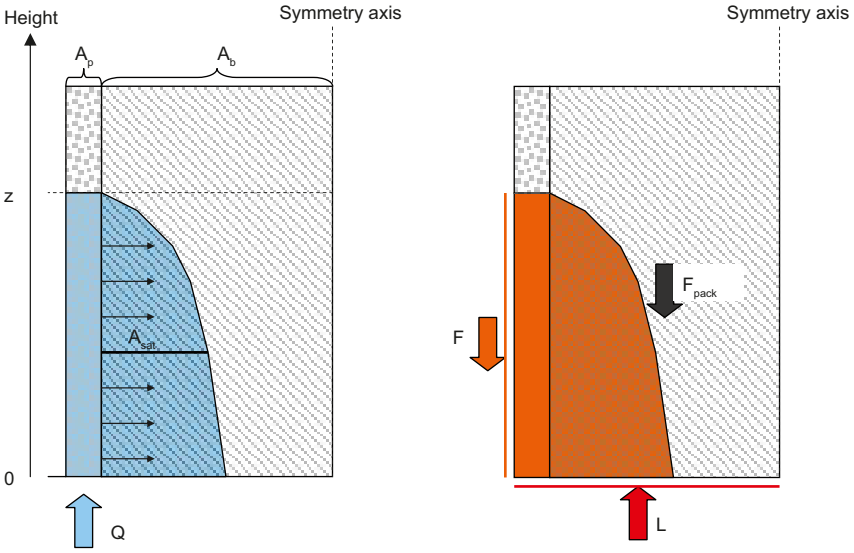

Figure 18-1. *Schematic representation of hydration of pellets slot and buffer (left) and forces acting on the package (right).*

18.3 Moving front – z(t)

The total volume of water that has entered the pellets slot and the buffer at time t is equal to Q·t:

$$Q \cdot t = A_p \cdot z + \int_0^z A_{sat}(\varsigma, t)\, d\varsigma \tag{18-4}$$

Q is the inflow into the pellets slot, A_p is the initially available pore space per unit height in the pellets slot (= 0.145 m²) and z is the current height of the saturated front (see Figure 18-1). The time derivative of this volume can, together with Equation (18-1), be expressed as:

$$Q = A_p \cdot z' + \int_0^z k(A_b - A_{sat}(\varsigma, t)) \cdot d\varsigma \tag{18-5}$$

Taking Equation (18-4) into account leads to the following differential equation:

$$z' + k\left(\frac{A_b}{A_p} + 1\right) \cdot z = \frac{Q}{A_p} \cdot (1 + k \cdot t) \tag{18-6}$$

This has the following solution (given that z = 0 when t = 0):

$$z(t) = \frac{Q \cdot A_b \left(1 - e^{-k\left(1 + \frac{A_b}{A_p}\right)t}\right)}{(A_p + A_b)^2 \cdot k} + \frac{Q \cdot t}{(A_p + A_b)} \tag{18-7}$$

An example of this front is shown in Figure 18-2. With this function in place, although the inverse has to be treated through numerical means, the extent of the hydration can be elucidated by calculating the A_{sat}/A_b-ratio:

$$\frac{A_{sat}(z,t)}{A_b} = \Phi(t - t_0(z)) \cdot (1 - e^{-k(t - t_0(z))}) \tag{18-8}$$

Examples of this function are also shown in Figure 18-2.

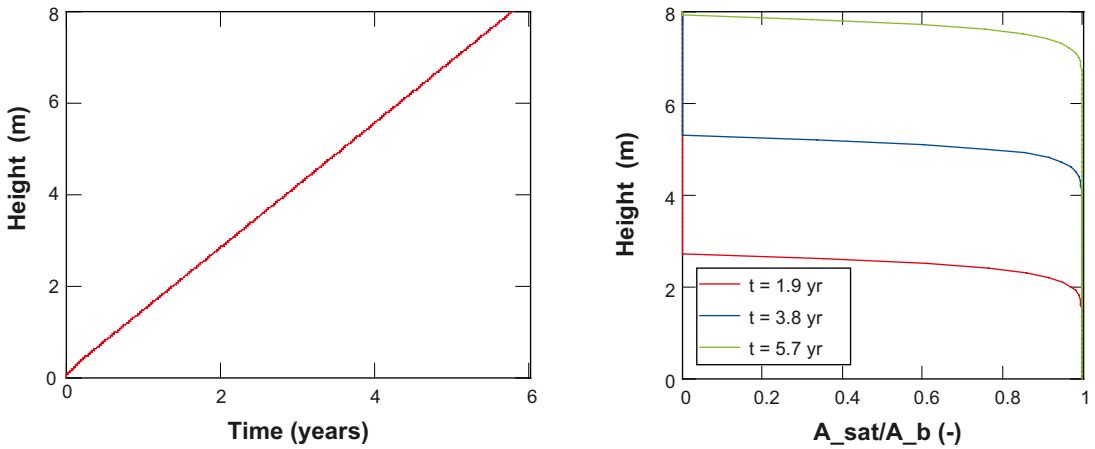

Figure 18-2. *Example of function for moving front (left) and extent of hydration for three points in time (right). (Q = 1 l/d).*

18.4 Force balance

The build-up of swelling pressure is assumed to be proportional to the extent of hydration in Equation (18-8):

$$P(z,t) = P_{\max}\frac{A_{sat}}{A_b} = \Phi(t - t_0(z)) \cdot P_{\max} \cdot \left(1 - e^{-k(t-t_0(z))}\right) \qquad (18\text{-}9)$$

The maximum swelling pressure (P_{max}) is assumed to be 8 MPa. The build-up of swelling pressure at z = 0 is illustrated in Figure 18-3. It can be noticed that a value of 5 MPa is reached after approximately 50 days. This is basically was has been observed in full-scale experiments (Protoype: Hole 1: Cylinder 1; see /Goudarzi and Börgesson 2002/), and this was the motive for choosing the high value of the rate constant.

The swelling pressure at z = 0 represents the lifting pressure, and the corresponding lifting force is given by:

$$L(t) = A_{tot} \cdot P(0,t) \qquad (18\text{-}10)$$

Of course, the lifting pressure can not exceed the hydrostatic pressure (4.6 MPa), but this level will not be reached until day 45 with the adopted rate constant, and will not have any effect on the final evaluation. This limit in lifting pressure is therefore neglected. The frictional force is calculated by

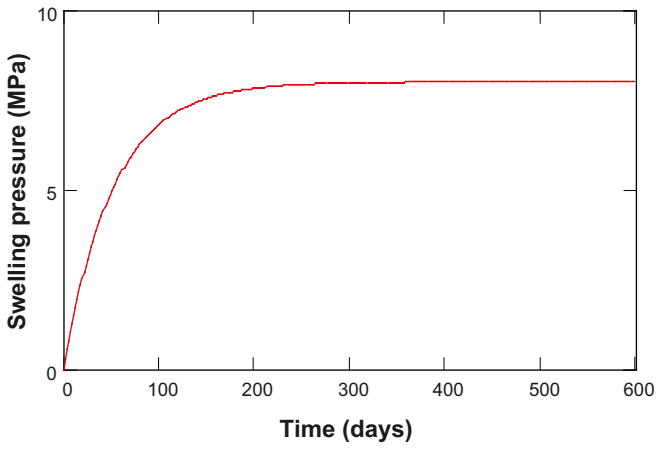

Figure 18-3. *Evolution of swelling pressure at the bottom of the buffer.*

integrating the pressure along the rock wall surface and by assuming a specific friction angle ($\phi = 8°$) and a rock wall radius (r = 0.875 m):

$$F(t) = 2\pi \cdot r \cdot \tan(\phi) \cdot \int_0^{z(t)} P(\varsigma, t) d\varsigma \qquad (18\text{-}11)$$

The height z(t) should not exceed the depth of the deposition hole, i.e. 8 m.

An example of the evolution of these two forces is shown in Figure 18-4. It can be noticed that the frictional force exceeds the lifting force with margin during the main part of the evolution. However, at the beginning the lifting force is slightly higher than the frictional force. This temporary force difference (F_{diff}) can be defined as:

$$F_{diff}(t) = L(t) - F(t) \qquad (18\text{-}12)$$

If this difference exceeds the weight of the package, i.e. approx. 0.4 MN, then the package can be lifted. In Figure 18-5 (left), the difference is evaluated as a function of the inflow into the borehole for four different points in time. It can be noticed that lifting conditions will be present after little more that one day. Moreover, the force increases significantly during the first week at inflows below 70 litres per day. At higher inflows however the force difference eventually tends to decrease with time.

The time needed to establish a zero force difference is shown together with the height of the front in the pellets-filled slot as functions of the inflow in Figure 18-5 (right). The time to reach this state decreases significantly with increasing inflows. At 144 litres per day (= 0.1 litres per minute) the time-scale is 6.4 days. The height of the front varies between 3 and 6 meters. These two extremes are basically given by the outer radius of the deposition hole and the friction angle: r/(2·tan(ϕ)) and r/tan(ϕ).

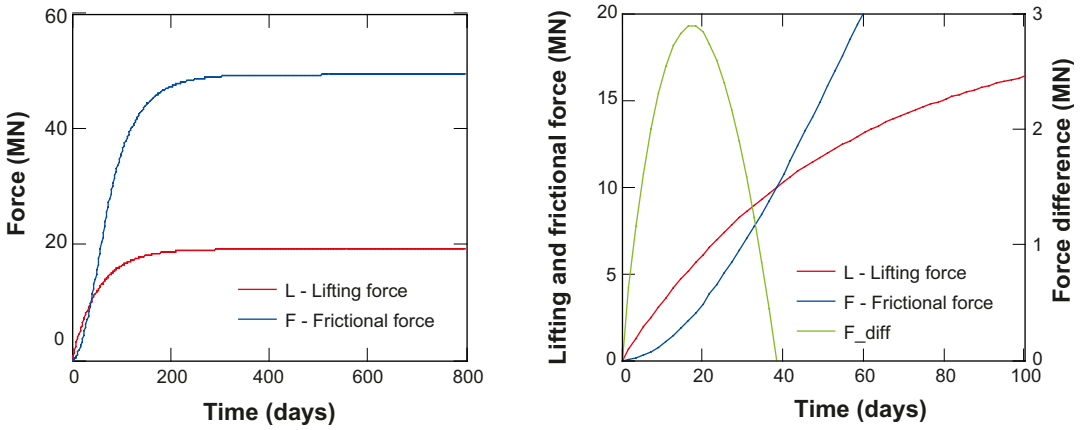

Figure 18-4. *Evolution of lifting and frictional forces. Left: the asymptotic behaviour toward the steady-state values. Right: conditions at an early stage. (Q =25 l/d).*

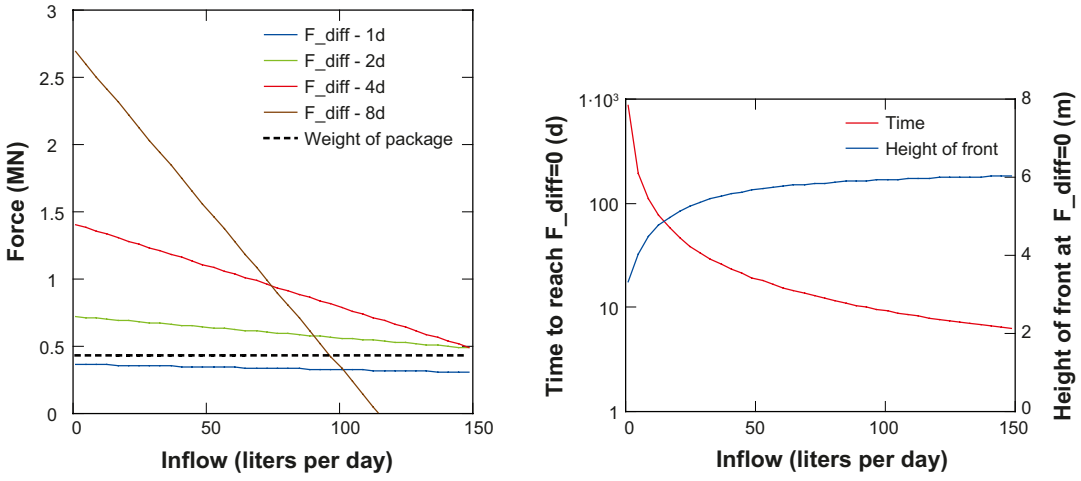

Figure 18-5. *Force difference (F_{diff}) at different times as functions of inflow and weight of package (left). Time to reach zero force difference and the height of the front in pellets-filled slot at this condition (right).*

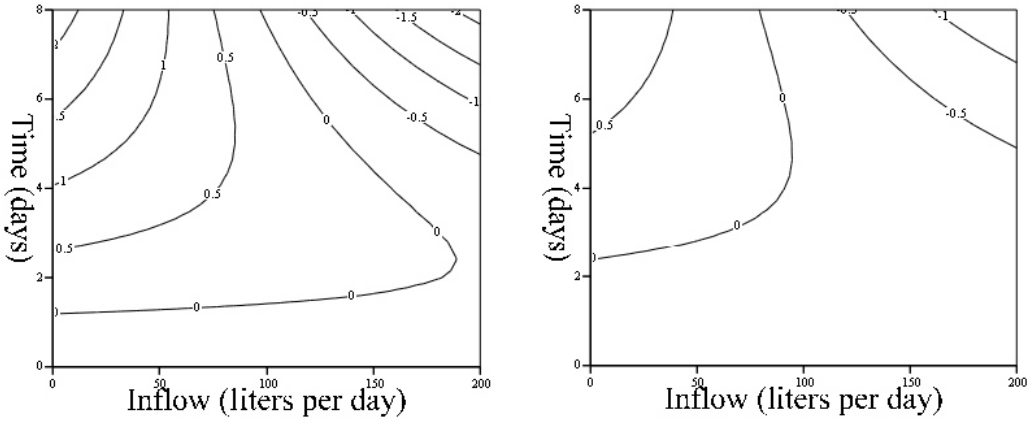

Figure 18-6. *Contour plots of net lifting force (F_{diff}-mg in MN) as a function of inflow and time. Water uptake half-life: 0.1 years (left); 0.2 years (right).*

Finally, the net lifting force (F_{diff}-mg) is shown as contour plots for different inflows and times in Figure 18-6. Moreover, calculations for two different water uptake rate constants are presented: for the original water uptake half-life (0.1 years) and twice this value. Net lifting forces higher than zero correspond to conditions which imply lifting of the package. Such conditions are found in the upper left corners of the plots.

18.5 Model refinement

During the completion of this report, it was noticed that the model presented above is sensitive to the initial buildup of swelling pressure. Moreover, the linear relation between the swelling pressure and the A_{sat}/A_b-ratio (Eq 18-9) implied that a very fast hydration rate had to be applied in order to mimic the buildup in large-scale experiments.

A more relevant representation can be made through a direct adoption of a function for the buildup of swelling pressure with time, which thereby is independent of the hydration rate. A cumulative lognormal distribution function was chosen for this purpose:

$$P_{swell}(t,\mu,\sigma) = \frac{P_{\max}}{2}\left(1+\mathrm{erf}\left(\frac{\ln(t)-\mu}{\sigma\sqrt{2}}\right)\right) \qquad (18\text{-}13)$$

μ corresponds to the time when half the maximum value is reached. In this case, μ is set to ln(40 days) in order to yield 4 MPa after 40 days. σ is set to 0.9 in order to yield approx 0.5 MPa after 10 days. These two points mimics the evolution in the Prototype experiment (Hole 1 and Cylinder 1, see /Goudarzi and Börgesson 2002/. This curve is shown in Figure 18-7 (left) together with the previously used curve for the case with a hydration rate of a 0.1 year half-life.

A more relevant hydration rate is adopted from the results in Chapter 3. An overall saturation increase from 83 to 99% in seven years corresponds to a half-life of 1.7 years. With the defined pressure evolution, an explicit relation between the swelling pressure and the A_{sat}/A_b-ratio can be derived through substituting the time t with $-k^{-1} \cdot \ln(1-A_{sat}/A_b)$ in Eq 18-13 (see Figure 18-7, right). This relation thereby replaces Eq 18-9 in the evaluation of the lifting conditions. Moreover, in this refined treatment, the following parameters were given more precise values: A_b: 0.14 m^2; A_p: 0.144 m^2 and mg: 0.46 MN. These parameter modifications have however only a minor influence on the final result. A contour plot of the net lifting force, as calculated with this refined model, is shown in Figure 18-8 for different inflows and times.

18.6 Conclusions and uncertainties

The initial calculations indicated that the conditions for lifting the package will not be present until after approximately one day regardless of the inflow, if the inflow is lower than 200 litres per day (Figure 18-6). The results thus indicated that the safety margin of a procedure with a 24 hour window from the termination of the drainage of the deposition holes to the installation of the backfill

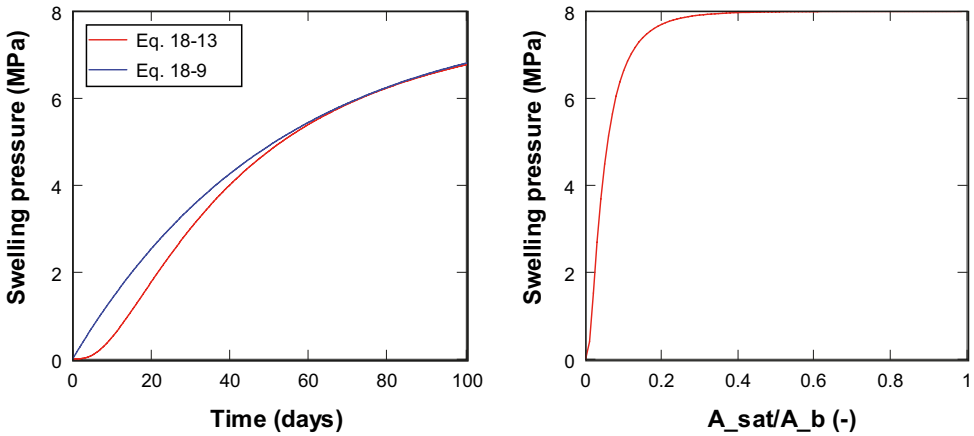

Figure 18-7. *Relations for buildup of swelling pressure with time (left), and adopted relation between the swelling pressure and the Asat/Ab-ratio (right).*

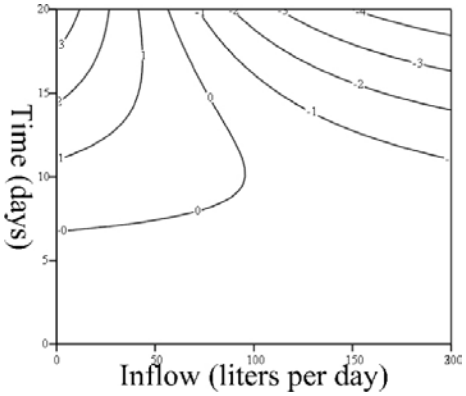

Figure 18-8. *Contour plots of net lifting force as a function of inflow and time with refined model.*

above the deposition hole was very small. The refined model indicates, in contrast, that the time to reach lifting conditions is approx. one week rather than one day. And the model also suggests that an inflow above approx. 100 litres per day will "avoid" the domain with lifting conditions in the upper left corner in Figure 18-8. The "narrowing" of this domain with time reflects the fact that the frictional force exceeds the lifting force with time. The time-scales to reach lifting conditions at low inflows are given directly by the adopted swelling pressure evolutions in Figure 18-7 (left), and the weight of the package, which corresponds to a pressure of 0.2 MPa. The swelling pressure should therefore not be allowed to reach this level as long as the backfill has not been installed.

It should be noted that the swelling pressure of the pellets-filled slot may be in this magnitude. And erosion tests with MX-80 pellets, presented by /Sandén et al 2008/, show that the pore pressure very well can reach such levels, although this can possibly be ascribed to the geometry in these tests. On the other hand, it can be remarked that the relevance of the approach is limited at very low inflows, since the disc, in which the build-up of swelling pressure takes place and in turn sets the water pressure, is very thin. Moreover, the time-scale for the water pressure to increase in the fracture should also depend on the properties of the rock, and the conditions therein, and this has not been addressed in the model.

The empirical data on the initial swelling pressure build-up in large-scale experiments (Prototype, CRT and TBT) is quite scattered. The chosen swelling pressure evolution in the refined model can nevertheless be regarded to be fairly rapid. This suggests that there should not be any risk of lifting conditions before the installation of the backfill, if a bottom plate is used in a deposition hole with a water-bearing fracture beneath. Still, due to the uncertainty in data, and to some extent also in conceptual understanding, it has not been possible to make any definitive judgment concerning the use of the bottom plate in such holes.

19 Bottom plate 2 – buffer swelling after concrete disintegration

19.1 Introduction

The cement in the thick concrete plate in the bottom of the deposition holes (see Figure 19-1) may with time be dissolved and transported away, which means that the stiffness and strength of the plate will be dramatically reduced just as for the plugs. This will cause swelling and loss of density in the buffer.

The buffer swelling after concrete disintegration has been analysed in a similar way as the models with buffer upward swelling *at saturated conditions*, i.e. with the finite element program Abaqus. This problem was not modelled in SR-Can.

The thickness of the concrete in the bottom plate depends on the evenness of the rock surface in the bottom of the deposition hole.

19.2 Problem description

Since neither the thickness of the bottom plate nor the rest product after concrete disintegration are known the problem is modelled in a pragmatic way. The concrete and the copper plate are made with a total thickness of 15 cm and the disintegration is simulated by stepwise displacement of the copper plate to a total displacement of 1.5 cm, 3.0 cm and 6.0 cm. After each step the bentonite is allowed to swell and homogenise and the pore water pressure equalise.

The same model is used as for task 8 *buffer upwards swelling*. In fact the same calculation is used but after completed upwards swelling three extra steps are added as described above. This technique can be used since the buffer between the canister and the bottom plate is insignificantly affected by the upwards swelling.

19.3 Finite element model

The finite element program Abaqus has been used for the calculations. The same 3D element model of a section of the tunnel with backfill and a deposition hole with buffer, canister and the bottom plate as for task 8 is used. Figure 19-2 shows the entire element mesh and a detail of the bottom plate.

19.4 Material properties and boundary conditions

The material properties and the boundary conditions are identical to those used in Task 8 and will not be repeated here.

The bottom plate is modelled as a rigid body.

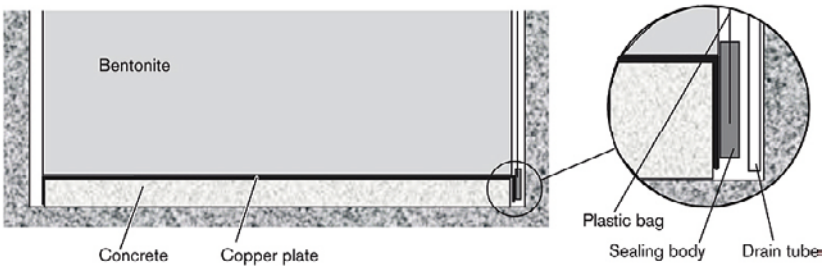

Figure 19-1. *Bottom plate.*

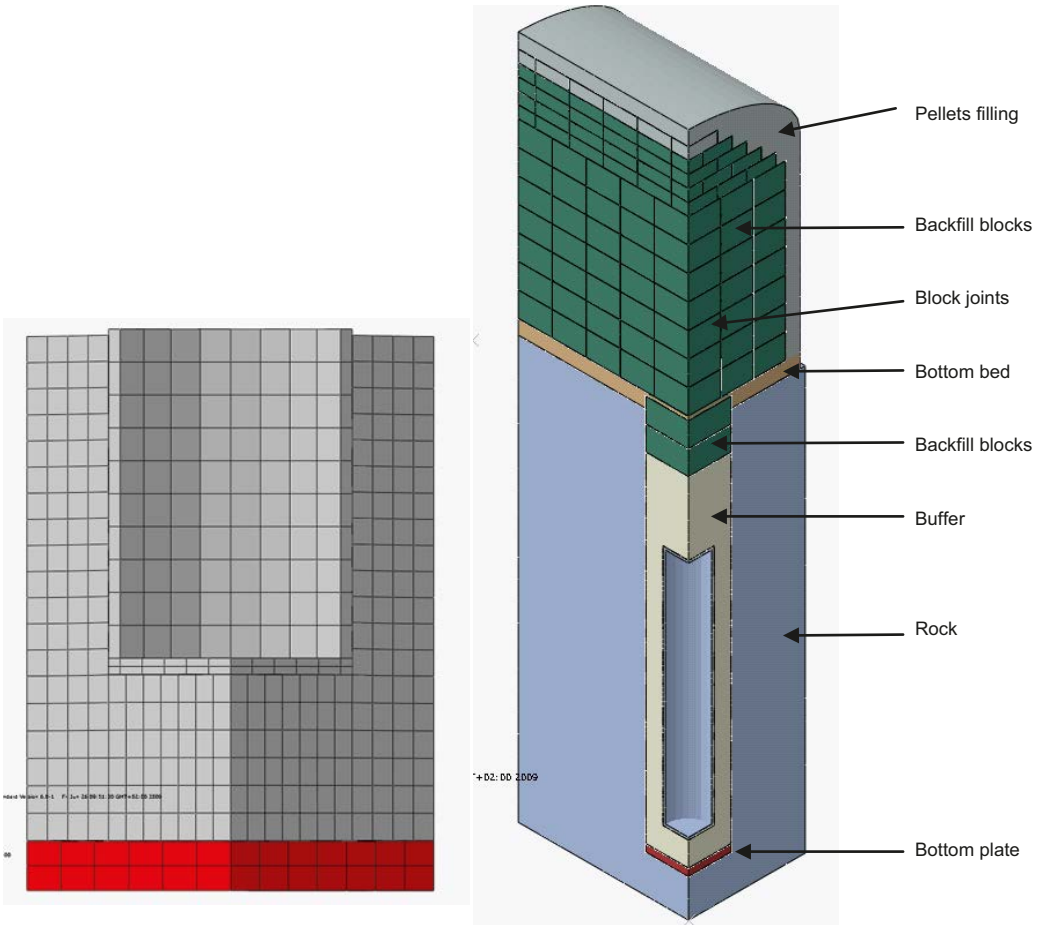

Figure 19-2. *3D element model. The left picture shows the element mesh at the bottom of the deposition hole with the bottom plate in red. The right picture shows the different property domains of the entire geometry.*

19.5 Calculation sequence

The calculations are coupled hydro-mechanical calculations. In the first step the pore water pressure in the hydraulic boundary of the buffer is stepwise increased from –7 MPa to 0 MPa during 1,000 seconds. Then the actual consolidation calculation with the upwards swelling of the buffer and compression of the backfill is run until complete pore water pressure equilibrium with pore pressure 0 MPa is reached in the entire buffer. These steps are described for Task 8.

The affect of loosing material in the concrete in the bottom plate is then modelled in the following three steps:

Step 2: 1.5 cm compression of the bottom plate.
Step 3: Additionally 1.5 cm compression of the bottom plate.
Step 4: Additionally 3.0 cm compression of the bottom plate.

For each step the calculation is run until completed pore pressure equalisation and homogenisation has occurred.

19.6 Results

The results are shown in Figures 19-3 to 19-5.

Figure 19-3 shows the vertical displacements in the lower part of the deposition hole in the three steps compared to the initial conditions, which means that the displacements after step 1 are included. The gray zone around the canister in step 2 shows that the resulting movement of the canister is still about 2 mm upwards but has been reduced from the initial 5 mm upwards movement, which was the result of step 1. In steps 3 and 4 the canister has moved downwards but less than 5 mm.

Figure 19-4 shows the axial stress (swelling pressure) in the buffer after all four steps. The figure shows that the axial stress is reduced from the initial condition 7 MPa to about 6.5 MPa below the canister already after step 1 due to the upwards movement of the canister. The swelling pressure below the canister is reduced to about 4.5 MPa, 3.0 MPa and 2.0 MPa in the following steps 2–4. However, there is no significant reduction in stress along the major part of the canister.

Figure 19-5 shows the resulting density at water saturation in all four steps. Observe that the scale is changed at step 4, due to local stress concentrations around the bottom corner of the canister. These stress concentrations are judged not to be true but caused by improper elements at the sharp corner. The density below the canister is reduced to about 1,970 kg/m^3, 1,950 kg/m^3 and 1,920 kg/m^3 after steps 2–4 but the density in the major part of the buffer between the canister and the rock remains at the density 2,000 kg/m^3.

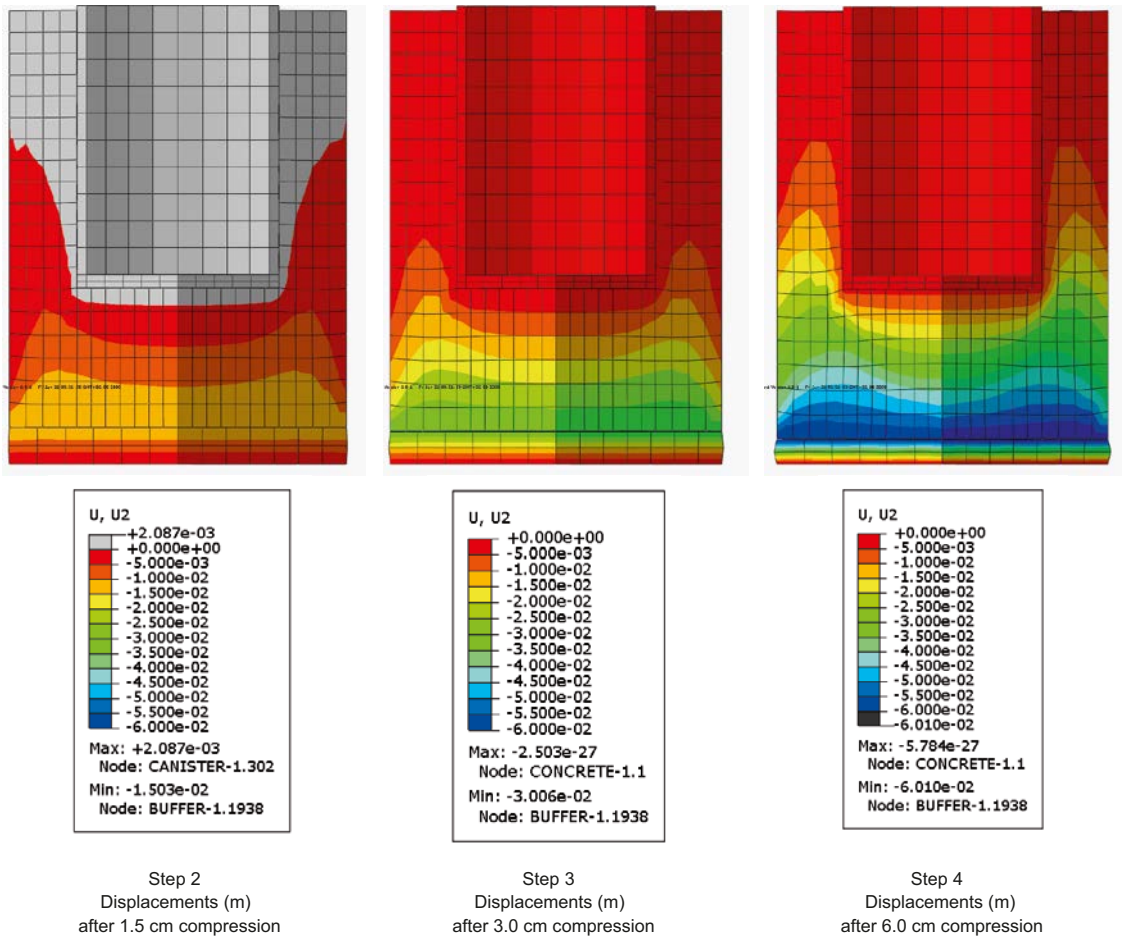

Figure 19-3. *Vertical displacements in the lower part of the deposition hole after compression of the bottom plate.*

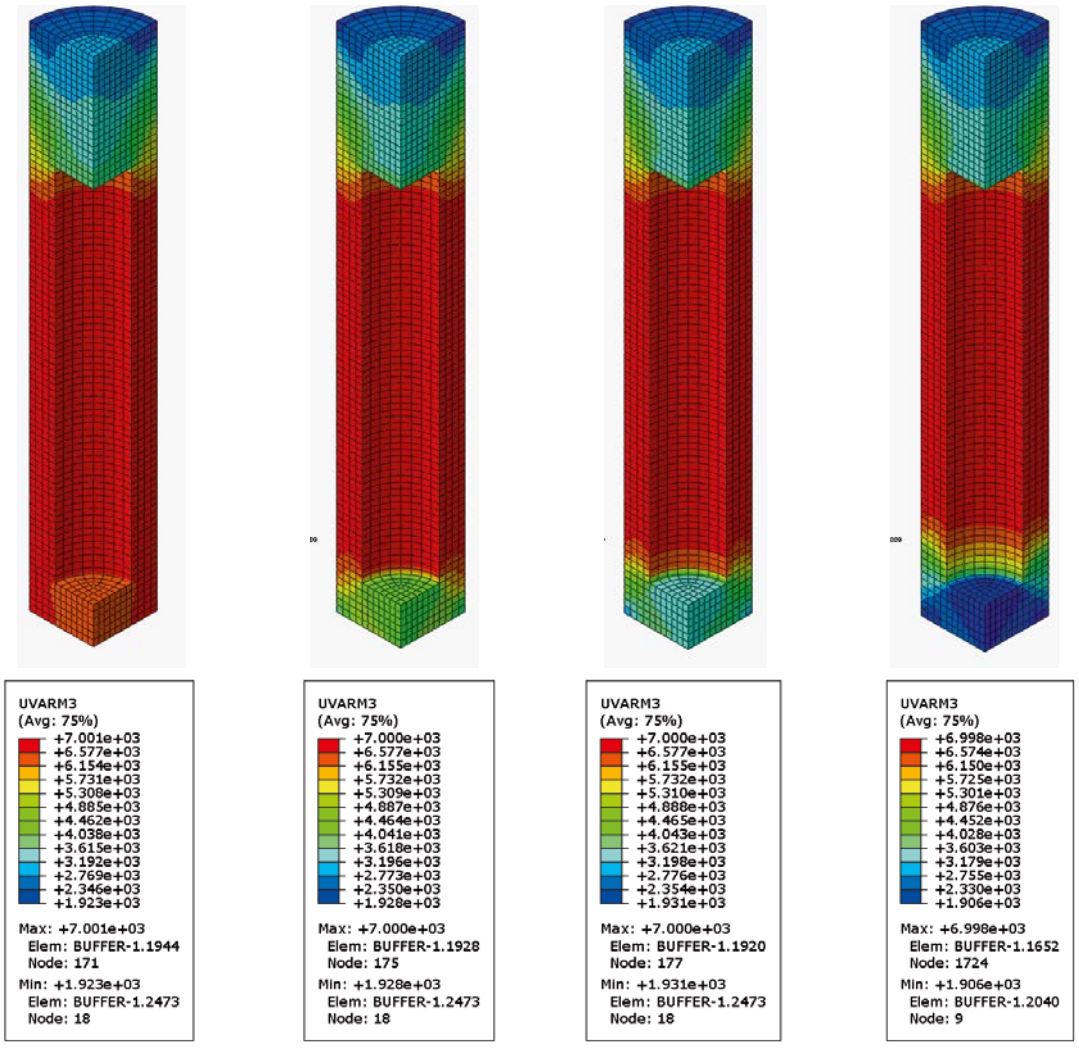

Figure 19-4. *Axial swelling pressure in the buffer after compression of the bottom plate.*

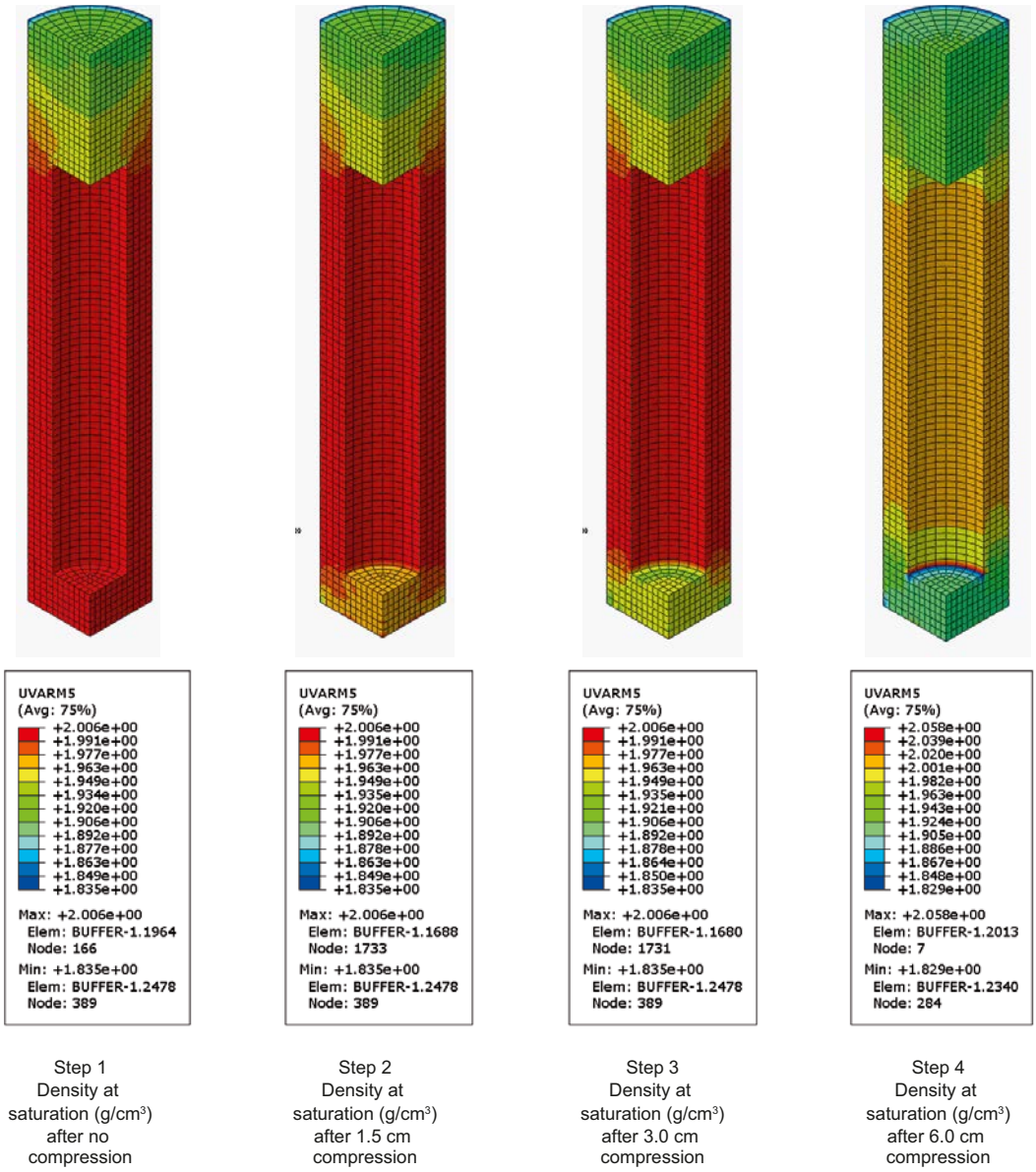

Figure 19-5. *Density at saturation in the buffer after compression of the bottom plate.*

19.7 Conclusions and uncertainties

Calculations of the mechanical effect of disintegration of the bottom plate show that the swelling pressure and density of the buffer beneath the canister as expected are reduced with increasing compression of the bottom plate. The density at saturation beneath the canister is reduced to about 1,950 kg/m^3 after 3 cm compression, which is within the tolerances. However, after 6 cm compression the loss of density seems to be too high, which means that the limit for allowable compression is about 3 cm. The bottom plate should thus be designed so that it will not be compressed more than 3 cm. However, if the initial density of the buffer beneath the canister is expected to be lower than 2,000 kg/m^3 the bottom plate should be designed accordingly.

The main uncertainty in the calculations is the compression of the bottom plate.

20 Homogenisation of borehole seals

20.1 Introduction

The suggestion is to plug boreholes with a combination of cement plugs and bentonite plugs. Only the bentonite plugs are considered in this study. The reference design of the borehole seals is to use highly compacted bentonite cylinders confined by a perforated copper tube in order to facilitate the installation. During wetting the bentonite will swell through the perforation and seal off the volume between tube and rock. Due to friction in the swelling bentonite the homogenization will be poor and the density of the bentonite outside the perforated tube lower than the average density.

The proposed design of a bentonite plug is shown in Figure 20-1. Cylindrical bentonite blocks are compacted to a height of about 5 cm and placed inside a perforated copper tube. Parcels will be made in sections of 3 meters. Several parcels will be connected and lowered into the borehole.

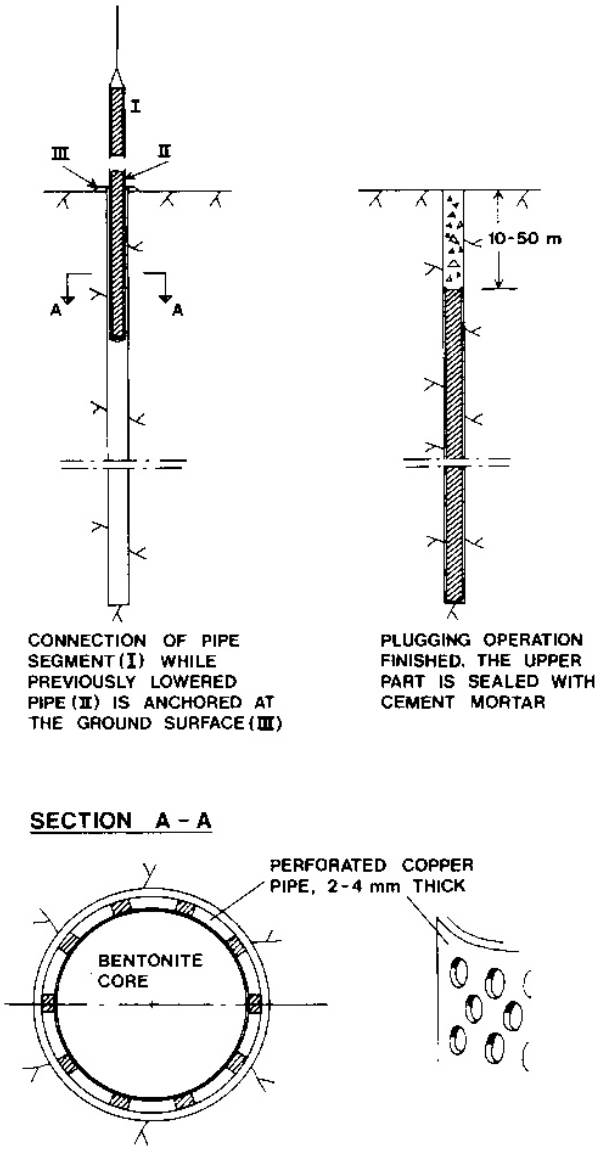

Figure 20-1. *Illustration of a bentonite borehole plug /Pusch and Ramqvist 2004/.*

In order for the plug to function properly in a bore hole the swelling ability of the bentonite must be strong enough to expand through the holes and penetrate behind the walls of the perforated tube. This expansion and penetration has been analyzed with analytical solutions and the results evaluated.

Two alternative configurations regarding the dimensions of the bore hole, the copper tube and the bentonite cylinders are considered. These alternatives are shown in Figure 20-2. Alternative 1 implies widening of the holes to 100 mm, 2.5 mm slot between the rock and the copper tube and 0.5 mm slot between the tube and the bentonite cylinders. Alternative 2 implies direct plugging of the holes and a very tight design with only 1 mm slot between the copper tube and the rock and no slot at all between the bentonite cylinders and the tube.

Alt.1		**Alt.2**	
Bentonite properties		**Bentonite properties**	
Initial values of compacted cylinders			
Bulk density, kg/m^3	2,085	Bulk density, kg/m^3	2,085
Dry density, kg/m^3	1,905	Dry density, kg/m^3	1,905
Degree of sat.%	57.2	Degree of sat.%	57.2
Void ratio	0.459	Void ratio	0.459
Average values after swelling and saturation			
Saturated density, kg/m^3	1,983	Saturated density, kg/m^3	2,086
Dry density, kg/m^3	1,533	Dry density, kg/m^3	1,692
Void ratio	0.820	Void ratio	0.649

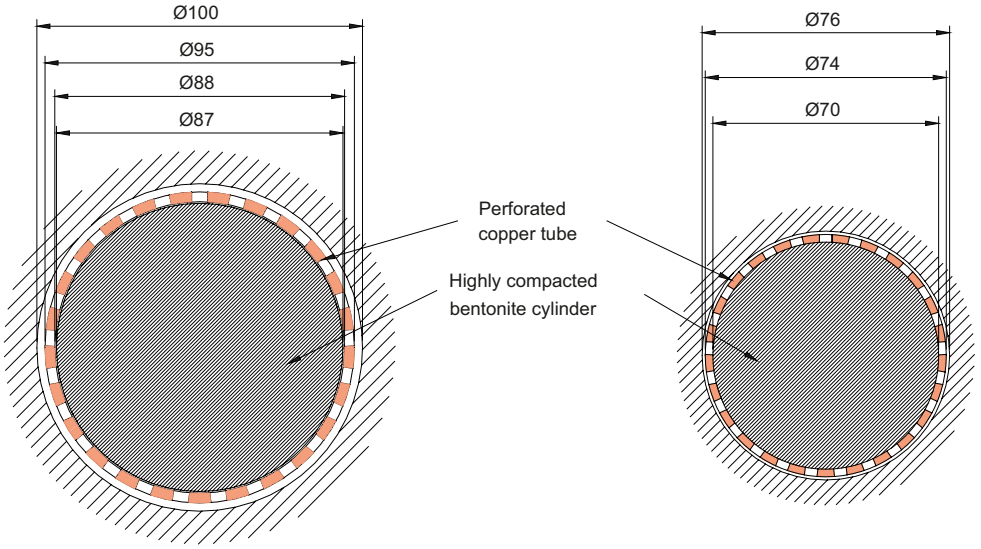

Figure 20-2. *Dimensions and properties of the two alternative borehole plugs. The table above shows the initial properties of the compacted bentonite cylinders during installation and the average properties after water saturation and swelling through the holes.*

20.2 Theoretical modelling of the interaction between the bentonite and the perforated copper tube in a plugged borehole

20.2.1 General

The bentonite will swell at first radially through the holes in the perforated copper tube and then tangentially between the copper and the rock surface (see Figure 20-3). It is important that the swelling pressure from the bentonite inside the copper tube σ_0 can be transferred to the rock with a swelling pressure σ_1 and further through the gap behind the steel with a swelling pressure σ_2, which stresses must be high enough to yield a good sealing.

The swelling and the reduction in density and swelling pressure is a function of the geometry. In order to find the best geometry of the perforation of the steel cylinder a theoretical derivation of the swelling pressures σ_1 and σ_2 have been done. σ_1 is in these formulas assumed to be the average swelling pressure between the copper tube and the rock, i.e. the swelling pressure half way between the copper tube and the rock.

The geometry of the circular holes shown in Figure 20-4 is derived from the assumption that the "degree of perforation" (that is area holes divided to total area) is $\mu = 0.5$, that all holes are equal and that the distribution is symmetric with a half hole shift.

The distance between the holes is $0.347D$ ($0.694r$) while the longest distance that the buffer must swell between the holes is $0.56r$.

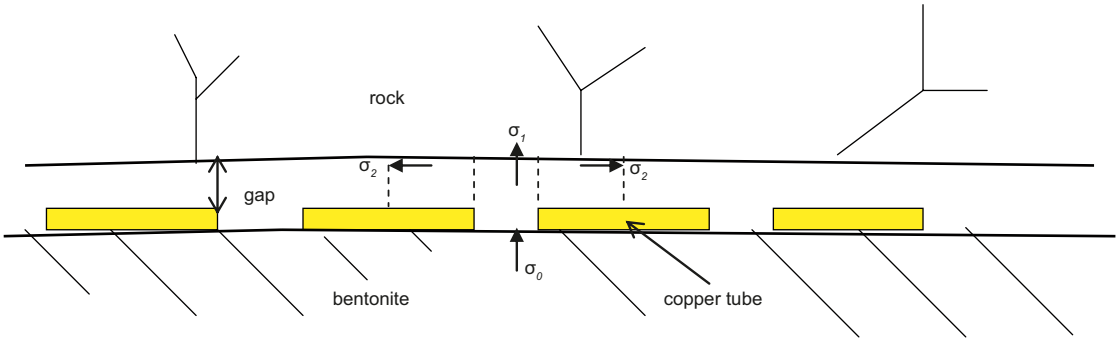

Figure 20-3. *Schematic view of the swelling of bentonite through the perforated copper tube (horizontal borehole). The original swelling pressure of the bentonite σ_0 is reduced to σ_1 when it swells through the holes to the rock and further to σ_2 when it swells behind the copper.*

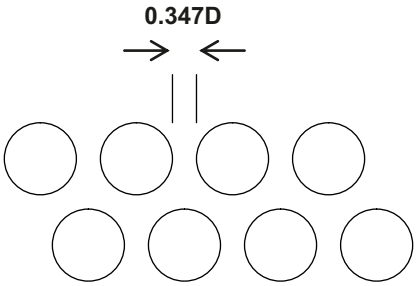

Figure 20-4. *Geometry of the circular holes with the hole diameter D.*

20.2.2 Derived model

The axial swelling can be derived from an equilibrium equation of the forces in axial swelling from σ_0 to σ_1 (Equation (20-1)), while the radial swelling can be derived from equilibrium of forces in radial direction from σ_1 to σ_2 (Equation (20-2)). The theory behind these relations is shown in Appendix G.

$$\sigma_1 = \sigma_0 \cdot e^{\frac{-2(d+z/2)\tan\phi}{r_1}} \tag{20-1}$$

$$\ln\sigma_2 = \ln\sigma_1 + K\ln\frac{r_2}{r_1} - \frac{r_2 - r_1}{z}\cdot 2\tan\phi \tag{20-2}$$

where

r_1 = hole radius
r_2 = radius at σ_2
d = tube thickness
z = slot between the copper tube and the rock

$$K = \left(\frac{\nu}{1-\nu} - 1\right)$$

ν = Poisson's ratio
ϕ = friction angle in bentonite

For the borehole plug we assume that

d = 0.0035 m
z = 0.0025 m
σ_0 = 10,000 kPa
ϕ = 20°
r_2/r_1 = 1.56

The minimum swelling pressure σ_2, which occurs between the holes at the radius $1.56r_1$ is plotted as a function of the hole radius in Figure 20-5. The extremes $K = 0$ (isotropic swelling pressure) and $K = -1$ are assumed.

If the degree of perforation is changed to μ=0.6 the longest distance that the buffer must swell between the holes will be $0.42r$. Thus the relation r_2/r_1 will change to

r_2/r_1 = 1.42

which yields Figure 20-6.

The calculations show that the optimum hole diameter is 1.0 cm if the degree of perforation is $\mu = 0.5$ and 1.1 cm if the degree of perforation is $\mu = 0.6$.

The influence of K and thus ν on the swelling pressure is a decrease in pressure of about 35% for $\nu = 0$ compared to $\nu = 0.5$. A value close to 0.5 is more likely since the bentonite is in a state of failure during the swelling process. The results from $K = 0$ (and thus $\nu = 0.5$) is used in the following evaluation.

The *minimum swelling pressure* on the rock surface is thus (for the degree of perforation $\mu = 0.5$)

σ_2 = 2,200 kPa

The *maximum swelling pressure* on the rock surface is of course in the center of the holes and can be calculated with Equation (10-1), applying that the radius of the holes is 5 mm and that the total swelling distance is 6 mm ($(d+z/2)$ in Equation (10-1))

σ_2 = 4,175 kPa

The average swelling pressure behind the copper tube will thus according to this model be about 3,200 kPa if the swelling pressure inside the tube is 10 MPa and the friction angle $\phi = 20°$. Another way to express it is to say that the average swelling pressure is reduced to 32% of the swelling pressure inside the tube.

The figure also clearly shows that the consequence of the choice of hole diameter of the perforation is very strong.

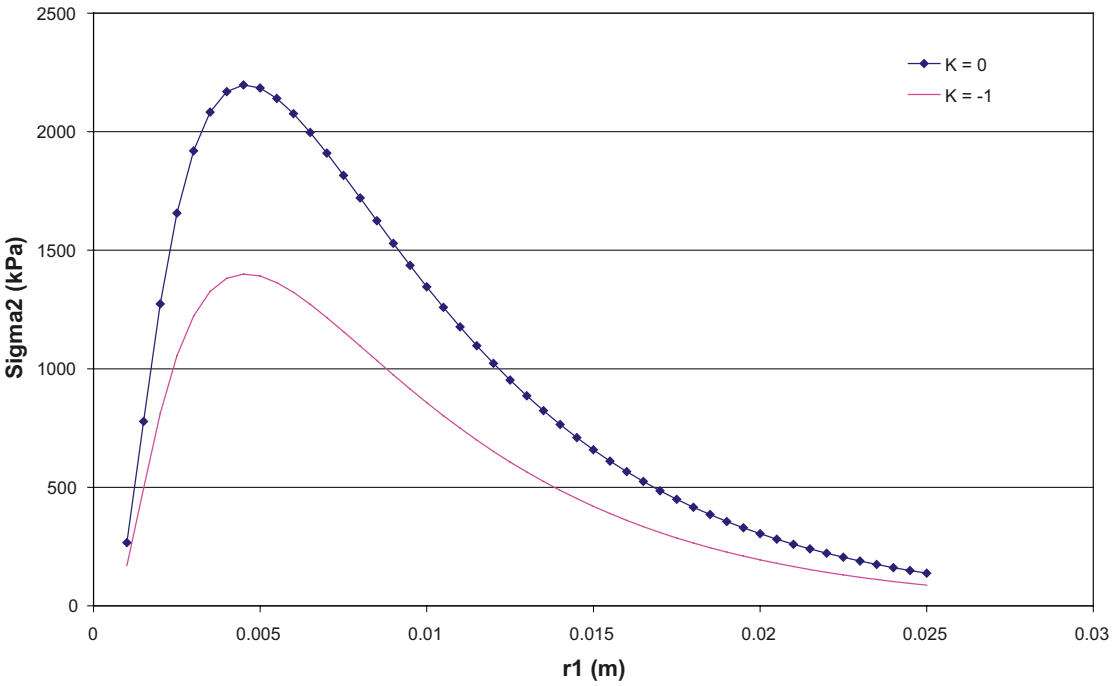

Figure 20-5. *Degree of perforation μ=0.5. Minimum swelling pressure as a function of the radius of the holes in the copper tube for two cases, where K=0 corresponds to isotropic swelling pressure. ϕ = 20°.*

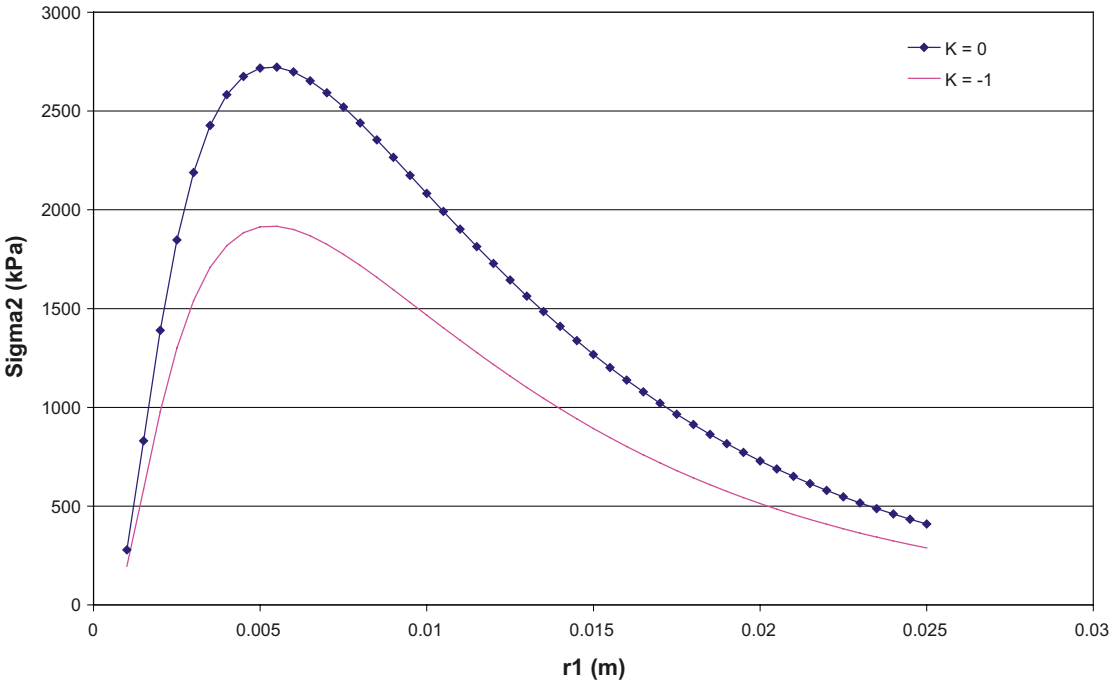

Figure 20-6. *Degree of perforation μ=0.6. Minimum swelling pressure as a function of the radius of the holes in the copper tube for two cases, where K=0 corresponds to isotropic swelling pressure. ϕ = 20°.*

20.2.3 Influence of friction angle

The swelling pressure shown in Figures 20-5 and 20-6 assumes that the average friction angle is 20 degrees. In reality the friction angle is dependant on both density and bentonite type. Figure 20-7 shows results from triaxial tests /Börgesson et al. 1995/. The deviator stress at failure is plotted as the average effective stress. The figure shows that the failure envelope is curved. The data from Figure 20-7 can be transformed to friction angle, which is shown in Table 20-1.

The calculated influence of the friction angle on the lowest swelling pressure between the copper tube and the rock surface is illustrated in Figure 20-8. The influence of an increase in friction angle from 10 to 20 degrees is very strong as shown, but if the density of the bentonite inside the tube is high enough to yield a swelling pressure of about 10 MPa, the drop in swelling pressure behind the tube is so small that the friction angle will not exceed 10 degrees. However, if the initial density is lower (due to e.g. loss of bentonite during installation), the friction angle may increase significantly and thus affect the resulting lowest selling pressure.

Table 20-1. Friction angle as function of effective average stress.

Average stress *p* (kPa)	Friction angle ϕ (degrees) Distilled water
500	17.3
1,000	13.3
2,000	11.6
5,000	9.5
10,000	8.0

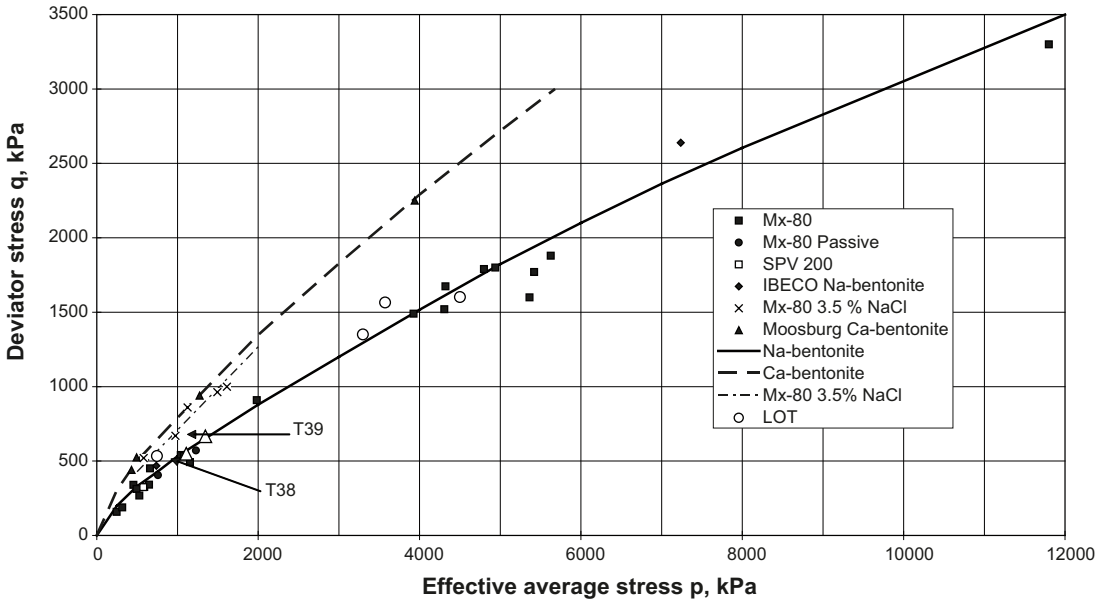

Figure 20-7. *Results from triaxial tests on MX-80.*

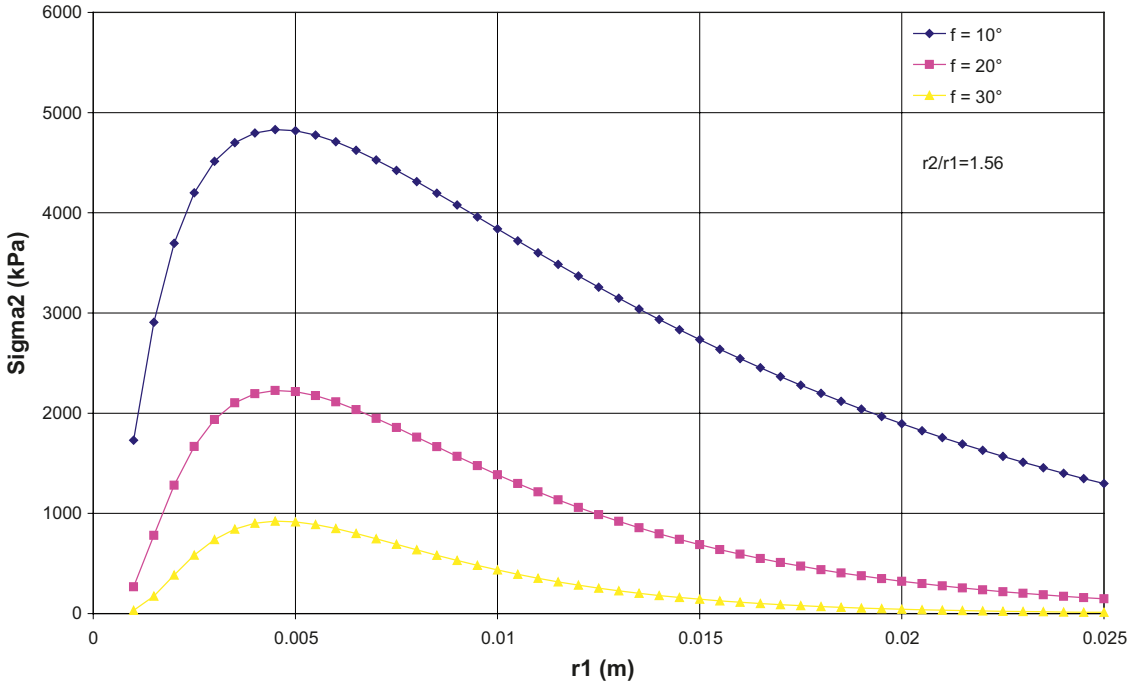

Figure 20-8. *Calculated minimum swelling pressure behind the copper tube as function of the radius of the perforation holes for different friction angles. K=0. Degree of perforation μ=0.5.*

20.3 Predicted swelling pressure on the rock

With Equations (20-1) and (20-2) and the relation between swelling pressure and friction angle the expected swelling pressure on the rock surface outside the perforated copper tube can be calculated. The average void ratio of the bentonite inside the tube has been assumed to be 0.82. The reference data for the plug is

d = 0.0035 m
z = 0.0025 m
σ_0 = 4,500 kPa (for e = 0.82)
ϕ = according to Table 3-1
K = 0
r_2/r_1 = 1.56

A stepwise calculation must be done due to the dependency of the swelling pressure on the friction angle. At first we assume a low swelling pressure since we will start with a gel that penetrates the holes. The gel then consolidates from the expansion of the bentonite inside the perforated tube. With the assumed value of the swelling pressure we can calculate the friction angle and the swelling pressure during the first expansion through the perforated holes according to Equation (20-1). Since the calculated swelling pressure does not agree with the assumed one we will have another friction angle and we can make a new calculation of the swelling pressure. We continue with these calculations until the swelling pressure used for the friction angle agrees with the calculated swelling pressure. This procedure yields σ_1. The same procedure is then repeated for the swelling between the tube and the rock surface with Equation (20-2) to yield σ_2. Finally a rough average stress behind the tube is calculated according to Equation (20-3), which is based on that 50% of the swelling pressure is equal to σ_1 (μ=50% perforation) and the rest is the average of σ_1 and the minimum stress σ_2.

$$\sigma_a = \mu \cdot \sigma_1 + (\sigma_1 + \sigma_2) \cdot (1-\mu) \qquad (20\text{-}3)$$

The stepwise calculation for the plug with distilled water is shown in Table 20-2.

Table 20-2. Stepwise calculation of σ_1 and σ_2 for distilled water.

Assumed σ_1 (kPa)	Corresponding friction angle ϕ (°)	σ_1 according to Equation (20-1) (kPa)
500	17.3	2,500
2,500	11.0	3,100
3,100	10.8	**3,140** (OK)
Assumed σ_2 (kPa)	**Corresponding friction angle ϕ (°)**	**σ_2 according to Equation (20-2) (kPa)**
500	17.3	1,570
1,570	12.5	1,910
1,910	11.8	**1,960** (OK)

Equation (20-3) then yields the average swelling pressure σ_a.

σ_a = 2,840 kPa

These results have been confirmed by laboratory tests on MX-80 bentonite in low saline water performed by Clay Technology /Pusch and Ramqvist 2007/.

20.4 Conclusions and uncertainties

A theoretical analysis of the expansion and homogenisation of the bentonite inside the perforated copper tubes in plugged boreholes has been done. The expansion through the perforation and the penetration between the tube and the rock have been analyzed. Analytical expressions of the loss in swelling pressure have been derived. The results show that the loss in swelling pressure is acceptable and yields a high enough density to fulfil the requirements of the plugs, provided that too much material is not lost during installation.

The largest uncertainty is the analytical models, which

1. assume isotropic swelling pressure,
2. are derived for the equilibrium state after fulfilled swelling and do not take the path into consideration.

Also the values of some parameters are uncertain. The strength of the model is that the actual swelling can and has been tested in simulated boreholes with geometry, material land conditions that are very similar to the real ones.

21 Homogenisation of borehole seals after loss of bentonite

21.1 Introduction

If bentonite in a section of a borehole seal is lost to such an extent that the hole will be empty along a certain length the swelling ability of the bentonite will make the adjacent bentonite swell and fill up the empty space. However, friction in the bentonite prevents complete homogenisation. The effect of such a loss needs to be investigated in order to secure that the seal functions properly.

The swelling process will be analysed analytically in a similar way as for Task 20. A model will be derived and the results calculated for different mass lost. This process was not analysed in SR-Can.

21.2 Problem description

The geometry of the bore holes and the installed perforated copper tube and bentonite cylinders is shown in Chapter 20. The perforated copper tube makes the geometry very complicated and it needs to be simplified in order to make calculations. For this reason the copper tube has been excluded and only the swelling inside the tube has been considered.

The diameter of the bore hole can vary between 76 and 100 mm which makes the inner diameter of the copper tube vary between 70 and 88 mm. According to Chapter 20 these variations yield a variation in final dry density of 1,533–1,692 kg/m^3 (density at water saturation 1,983–2,086 kg/m^3), which yield a swelling pressure 4.5–16 MPa. The variation that will be considered is thus

Hole diameter: $D = 70–100$ mm
Dry density: $\rho_d = 1{,}533–1{,}692$ kg/m^3
Swelling pressure: $\sigma_0 = 4.5–16$ MPa

Figure 21-1 describes the situation at a hypothetical moment when bentonite at the length L has been lost and the swelling and homogenisation not yet started. The idea is to find a state of equilibrium after completed swelling and homogenisation. Just as for the calculation in Chapter 20 the path and time until equilibrium are not considered.

The dry density before swelling at the boundary ρ_{d0} yields the swelling pressure σ_0 and after completed swelling the density and swelling pressure at the distance z from the unaffected bentonite boundary are ρ_{dz} and σ_z.

The problem is thus to find the axial density and swelling pressure distribution in the bore hole after equilibrium.

21.3 Theoretical solution

The theoretical solution is the similar to the solution of step 1 of the swelling through the perforated copper tube. Figure 21-2 shows the relation between an infinitesimal swelling distance z and the change in swelling pressure $d\sigma$. The swelling pressure is assumed to be isotropic.

r = hole radius
σ_0 = swelling pressure at $z = 0$
τ = $\sigma\tan\phi$
ϕ = friction angle (=10°–30° depending on the swelling pressure)

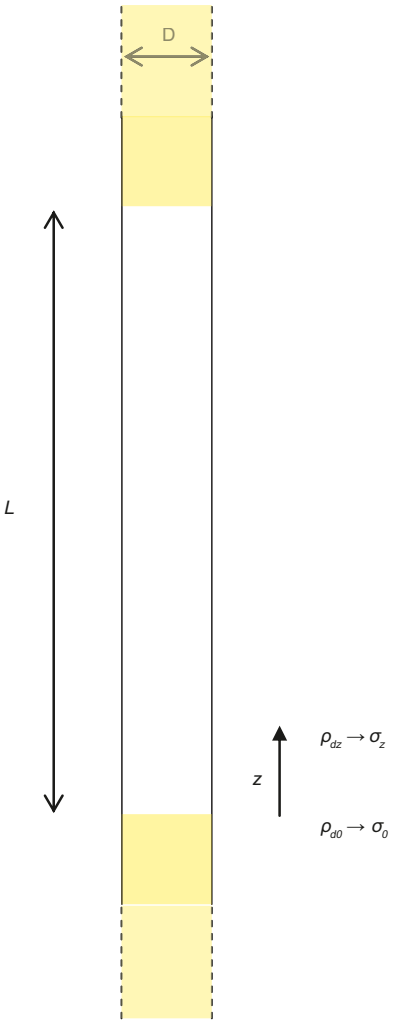

Figure 21-1. *Illustration of the plugged bore hole where bentonite at the length L has been lost.*

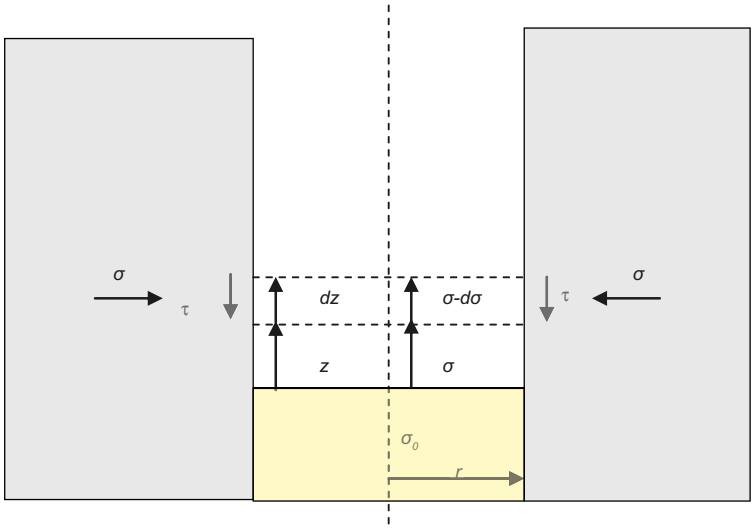

Figure 21-2. *Integration of the relation between swelling pressure σ and swelling distance z.*

Force equilibrium on the bentonite ring with the thickness dz in axial direction (disregarding gravity and internal friction):

– $d\sigma \cdot \pi r^2 = \sigma \tan\phi \cdot 2\pi r \cdot dz$

– $\frac{d\sigma}{\sigma} = \frac{2\tan\phi}{r} \cdot dz$

– $dz = \frac{r}{2\tan\phi} \cdot \frac{d\sigma}{\sigma}$

Integrating:

– $\int_0^z dz = \frac{r}{2\tan\phi} \int_{\sigma_0}^{\sigma} \frac{d\sigma}{\sigma}$

– $z = \frac{r}{2\tan\phi}(\ln\sigma - \ln\sigma_0)$

$$e^{(\ln\sigma - \ln\sigma_0)} = e^{-\frac{2z\tan\phi}{r}}$$

$$\sigma = \sigma_0 \cdot e^{\frac{-2z\tan\phi}{r}} \qquad (21\text{-}1)$$

$$z = \frac{r}{2\tan\phi} \ln\frac{\sigma_0}{\sigma} \qquad (21\text{-}2)$$

Equations (21-1) and (21-2) thus yield the relation between the swelling distance z and the swelling pressure σ.

Since the swelling takes place from both sides the minimum swelling pressure will occur half way between the upper and lower boundary at z = L/2.

However, the swelling pressure and thus density will decrease very fast and e.g. at the distance z = 1 m (corresponding to a 2 m long empty part) the swelling pressure will for the hole diameter 70 mm, the original swelling pressure 10 MPa and the friction angle ϕ = 20° be

$\sigma = 9 \cdot 10^{-3}$ Pa

which is so low that it practically corresponds to water. If 1 kPa is set as a limit where there is a gel the swelling distance will be (Equation (21-2)):

z = 0.44 m

The influence of changing different variables in Equation (21-2) is illustrated in Table 21-1.

Table 21-1. Vertical swelling calculated according to Equation (21-2) at different parameter values (deviations from the base case in yellow).

ϕ (°)	r (m)	σ (kPa)	z (m)	Comments
20	0.035	1.0	0.44	Base case
10	0.035	1.0	0.91	
30	0.035	1.0	0.28	
20	0.05	1.0	0.63	
20	0.035	0.001	0.78	
20	0.035	0.000 001	1.11	

Table 21-1 illustrates that the swelling length is not very sensitive to changes in the parameters included in Equations (21-1) and (21-2). The friction angle is the parameter that the swelling length is most sensitive to with a factor of 2 change of swelling length when the friction angle is changed from 20° to 10° or 30°. The sensitivity to swelling pressure below 1 kPa is small since the swelling length only increases with a factor 2 when the swelling pressure is reduced with a factor 10^6.

The example calculations thus indicate that the swelling will be about 0.5–1.0 m. This means that a part of the "unaffected" bore hole close to the boundary will loose in density and a part of the "empty" bore hole will increase its density. The density gradient is not linear and depends on the relation between density and swelling pressure, which has not been measured below about 10 kPa swelling pressure. A rough estimate is that 20–30% of the length z is taken from the "unaffected" part and the rest of the length z fills up the "empty" part. The remaining part of the bore hole will be unfilled or filled with a very loose sol produced by down falling bentonite particles.

The model does not take gravity into account. There will be a loss of bentonite particles from the upper bentonite surface that settles and sediments to form a sol or loose gel or sol in the water in the non-filled part of the bore hole. The dry density of this sol depends mainly on the ground water composition. It is estimated to be about $\rho_d \approx 200$ kg/m^3.

21.4 Conclusions and uncertainties

The calculations and reasoning thus show that if a bore hole sealed with bentonite looses bentonite along a length of more that 1–2 m the situation after equilibrium will be as shown in Table 21-2 and illustrated in Figure 21-3.

The calculations are based on an analytical model that has some weaknesses:

- Only the final state is considered and not the stress path to that state. In order to reach that state the swelling must either be even (i.e. steadily decreasing stress until the final state) or independent of the stress path. At least the first condition is regarded to be fulfilled.
- The swelling pressure is assumed to be isotropic. This is not always the case according to laboratory measurements. However, the deviations from that assumption can also be considered a variation or an uncertainty in the friction angle.
- The model implies that the stresses are equal along all cross section areas, which is not true but can be motivated by that average values are considered.

The uncertainties of the parameters used for these calculations are, as shown, not very important for the results. The largest uncertainty is probably the effect of gravity and thus the density of the sol or gel. However, even if the density would be much higher than the assumed density $\rho_d \approx 200$ kg/m^3 it would not influence the affected length above and below the sol very much.

Table 21-2. Illustration of expected density distribution (from bottom to top of the bore hole).

Distance (m) from original lower bentonite surface	Dry density (kg/m^3)	Comments
z<–0.05–0.2	~1,600	
From z=–0.05/–0.2 to z=+0.45/+0.8	Decreasing from 1,600 to 200	
From z=+0.45/+0.8 to z=L–0.45/–0.8	~200	A small increase in density with depth due to gravity
From z=L–0.45/–0.8 to z=L+0.05/0.2	Increasing from 200 to 1,600	
z>L+0.05/0.2	~1,600	

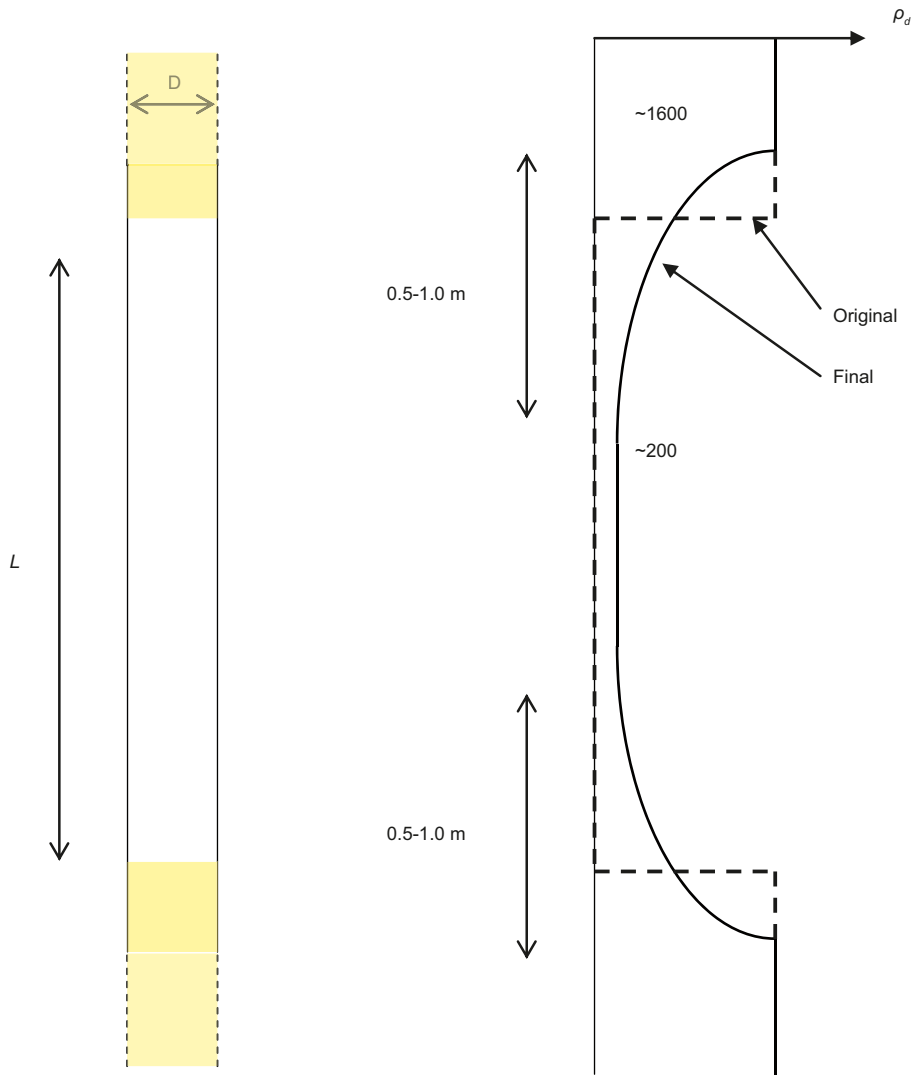

Figure 21-3. *Illustration of the density distribution in a borehole where the bentonite has been lost along the length L.*

22 Backfill swelling after tunnel plug disintegration 2 – omitted filling outside the plug

22.1 Introduction

An improbable scenario that has been considered is that the backfilling of the central area and the transport tunnels that intersect the backfilled and plugged deposition tunnels is not executed. I.e. the plugs that end the backfilled deposition tunnels are left without any support for large parts of the life time of the repository. The consequence will be that the repository will be water filled, the plugs disintegrated and the backfill will swell without resistance from any backfill outside the plug.

22.2 Problem description

After disintegration of the plug there will remain a substantial part of the components of the plug since both the sand filter and the concrete ballast material will not dissipate but is expected to remain as a soil heap. However, since it is likely that the lack of support from a backfill outside the plug will make the particles fall down to some kind of angle of repose, there may be a large opening in the upper part of the plug where bentonite freely may swell out into the transport tunnel. Since the size of this opening is difficult to predict it is conservatively assumed that the entire plug is lost.

The result of a free swelling of the backfill out of the deposition tunnel and into the transport tunnel will be driven by the swelling pressure of the backfill and counteracted by the friction between the backfill and the rock surface and the swelling of backfill from the other tunnels. The swelling is assumed to be similar from the other tunnels and thus stopped halfway between the deposition tunnels, i.e. the backfill cannot swell more than 20 m into the transport tunnel since the distance between the tunnels is 40 m.

There are two ways to tackle the problem. It can either be analysed in a simplified way with analytical solutions like the one used for tasks 20 and 21 or it can be modelled with FE. Attempts to do FE-calculations have encountered large problems caused by the extremely large swelling, large decrease in density and large element deformations, which lead to numerical problems and lack of convergence. Since no good results have been reached so far, these calculations will not be reported.

The geometry of the tunnels outside the plug where the swelling will take place is shown on Figure 22-1.

22.3 Simplified analytical solution

Equations (21-1) and (21-2) derived in Chapter 21 will be used to estimate the final equilibrium state after completed swelling.

$$\sigma = \sigma_0 \cdot e^{\frac{-2z\tan\phi}{r}} \tag{21-1}$$

$$z = \frac{r}{2\tan\phi}\ln\frac{\sigma_0}{\sigma} \tag{21-2}$$

Equations (21-1) and (21-2) describe the relation between the swelling distance z and the swelling pressure σ. The geometry will be simplified to the geometry shown in Figure 22-2. The two tunnels will be modelled with circular square section with radiuses yielding the same sectional area. The following geometrical basic data is used:

- Distance between tunnels ≈ 40 m
- Distance from backfill to transport tunnel ≈ 15 m
- Cross section area of transport tunnel ≈ 70 m^2 → r = 4.7 m
- Cross section area of deposition tunnels ≈ 23 m^2 → r = 2.7 m

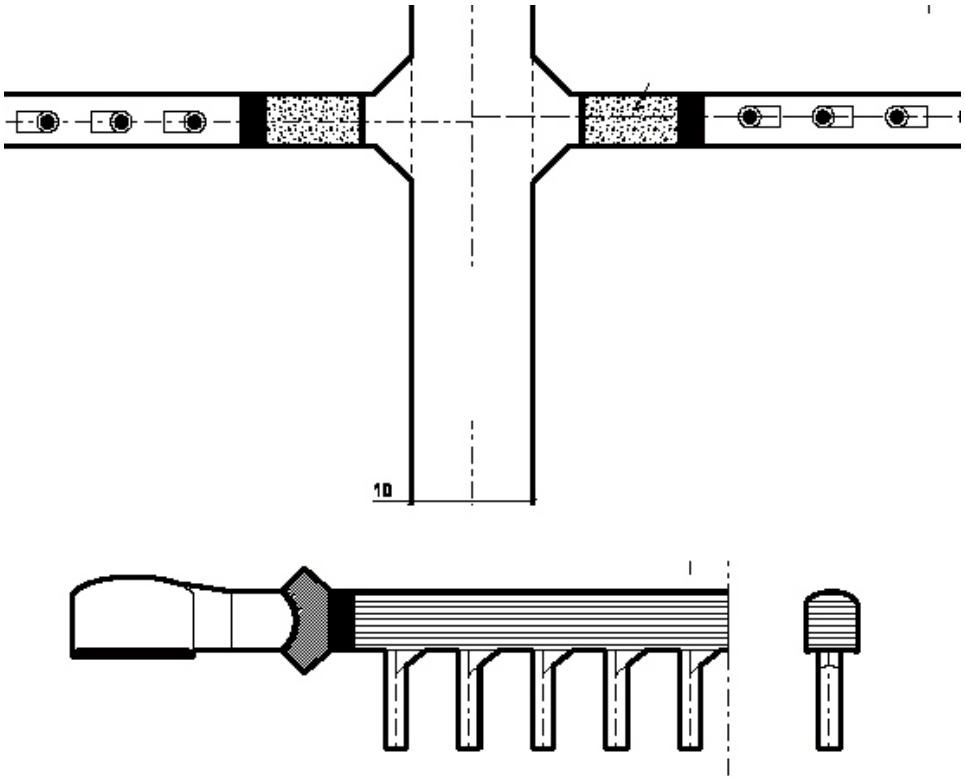

Figure 22-1. *Schematic view of the geometry of the tunnels neighbouring the plugs. Two types of plugs are illustrated.*

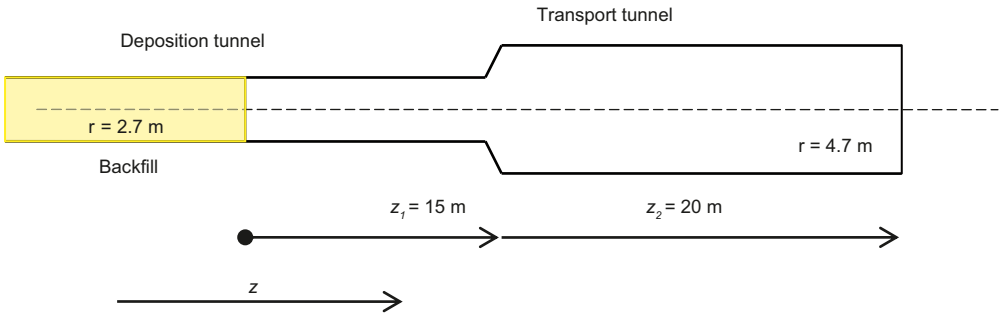

Figure 22-2. *Simplified geometry used for the analytical calculation.*

The backfill thus swells out of the deposition tunnel and into the transport tunnel that is simplified modelled as a continuation of the deposition tunnel with larger radius. In Figure 22-2 the distance z in Equation (21-2) represents the distance from the unaffected backfill with the initial swelling pressure σ_0 to the location where the swelling pressure is σ.

Backfill with a swelling pressure of 10 MPa

Using the friction angles $\phi = 20°$ and $\phi = 10°$ and the initial swelling pressure in the backfill $\sigma_0 = 10$ MPa in Equation (21-1) we will have a swelling pressure distribution along the tunnel axis as shown in Figure 22-3.

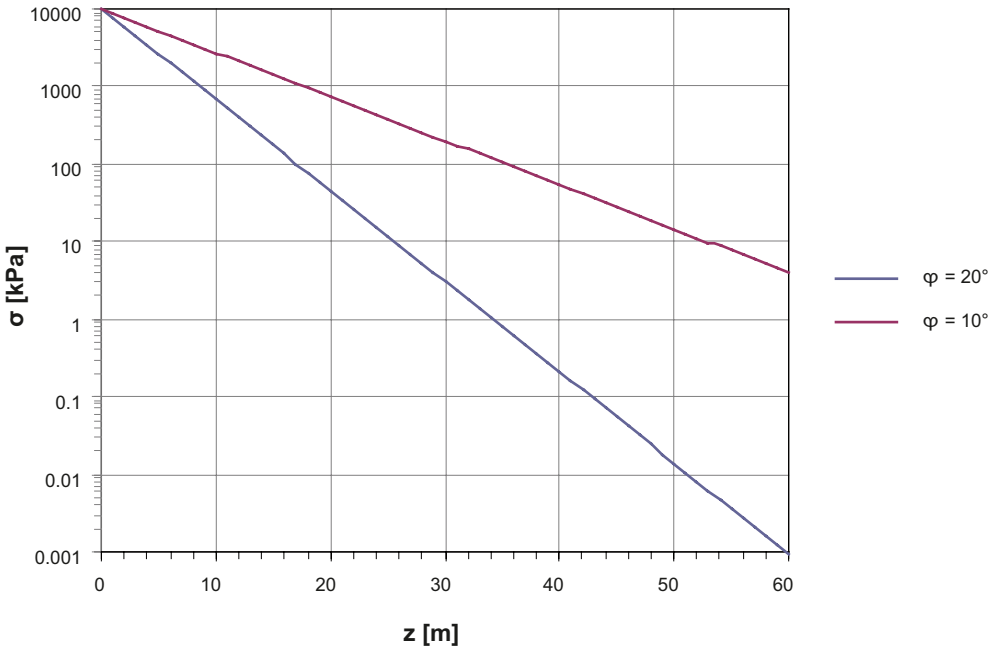

Figure 22-3. *Calculated swelling pressure as a function of the distance to the unaffected backfill front, where the swelling pressure is 10 MPa.*

Figure 22-3 shows that the swelling pressure rapidly drops and at z = 15 m it is reduced from 10 MPa to 0.2–1.5 MPa. The dry density of the bentonite can be evaluated from the relation between dry density and swelling pressure according to Equations (22-1) /Börgesson et al. 1995/ and (22-2).

$$p = p_0 \left(\frac{e}{e_0} \right)^{\frac{1}{\beta}} \tag{22-1}$$

where

e = void ratio
e_0 = reference void ratio (=1.1)
p = swelling pressure (at e)
p_0 = reference swelling pressure (at e_0) (=1,000 kPa)
β = –0.19

$$\rho_d = \frac{\rho_s}{1+e} \tag{22-2}$$

where

ρ_s = dry density
e = void ratio
ρ_s = density of solids = 2,778 kg/m^3

Figure 22-4 shows the corresponding relation between the distance to the unaffected backfill front and the dry density evaluated according to Equations (22-1) and (22-2).

If the diameter of the transport tunnel had the same diameter as the deposition tunnel Figure 22-4 could be used to calculate the density distribution and the distance to the unaffected backfill front by a mass balance view. The loss of mass inside the initial front must be equal to the mass swelled outside the front.

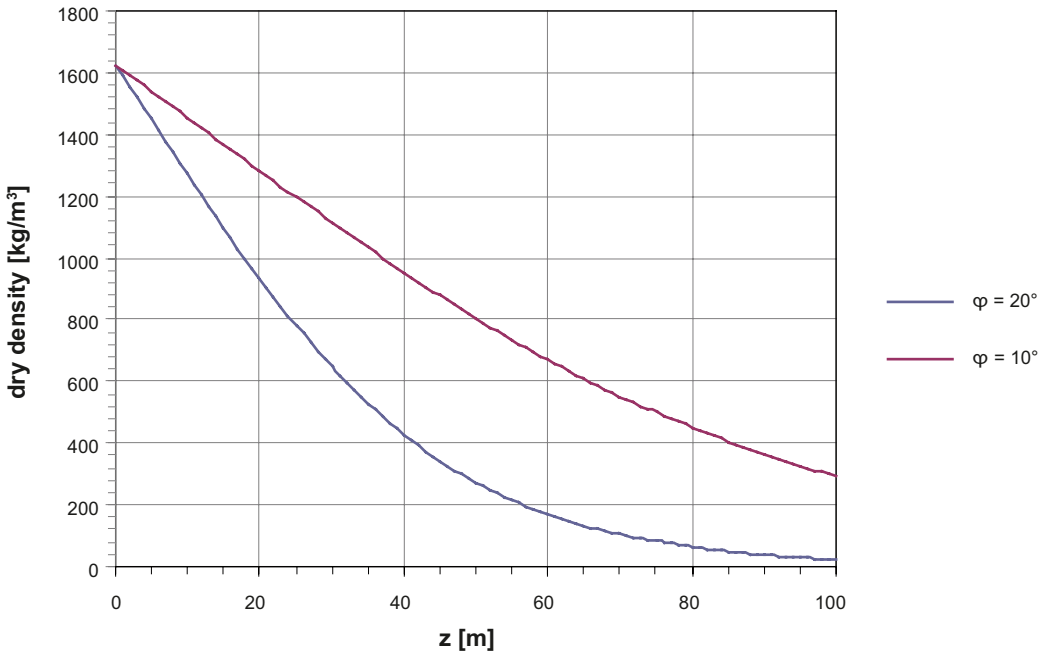

Figure 22-4. *Relation between dry density and the distance to the unaffected backfill front.*

However, this yields an underestimation of the mass lost from the deposition tunnel, since the diameter of the transport tunnel is about 4.7 m instead of 2.7 and since we have two swelling directions in the transport tunnel. The cross section area of the transport tunnel is about 3 times larger than that of the deposition tunnel, which means that the total volume is 6 times larger. If we on the other hand consider the normal situation that there is another deposition tunnel opposite the one considered, as in Figure 22-1, the total volume will only be half i.e. 3 times larger.

By trial calculations the situation illustrated in Figure 22-5 can be derived.

The dashed line in Figure 22-5 from $z = 0$ to $z = 60$ m (corresponding to a friction angle between 10 and 20 degrees) is used as the relation between the distance from the swelling front and the dry density in the deposition tunnel. The initial backfill front is at $z = 45$ m and the dry mass lost over the length Δz is

$$\Delta m = A\Delta z(\rho_i - \rho_a)$$

where

Δm = dry mass lost over the length Δz
A = cross section area
ρ_i = initial dry density
ρ_a = actual dry density

The dry mass lost inside the initial backfill front represented by area 1 marked yellow in Figure 22-5 is

$$\Delta m = \pi \cdot 2.7^2 \cdot 45 \cdot (1{,}600 - 600)/2 = 5.15 \cdot 10^5 \text{ kg}$$

The dry mass expanded into the rest of the deposition tunnel represented by area 2 marked green in Figure 22-5 (45 m < z < 60 m) is

$$\Delta m = \pi \cdot 2.7^2 \cdot 15 \cdot (600 + 230)/2 = 1.43 \cdot 10^5 \text{ kg}$$

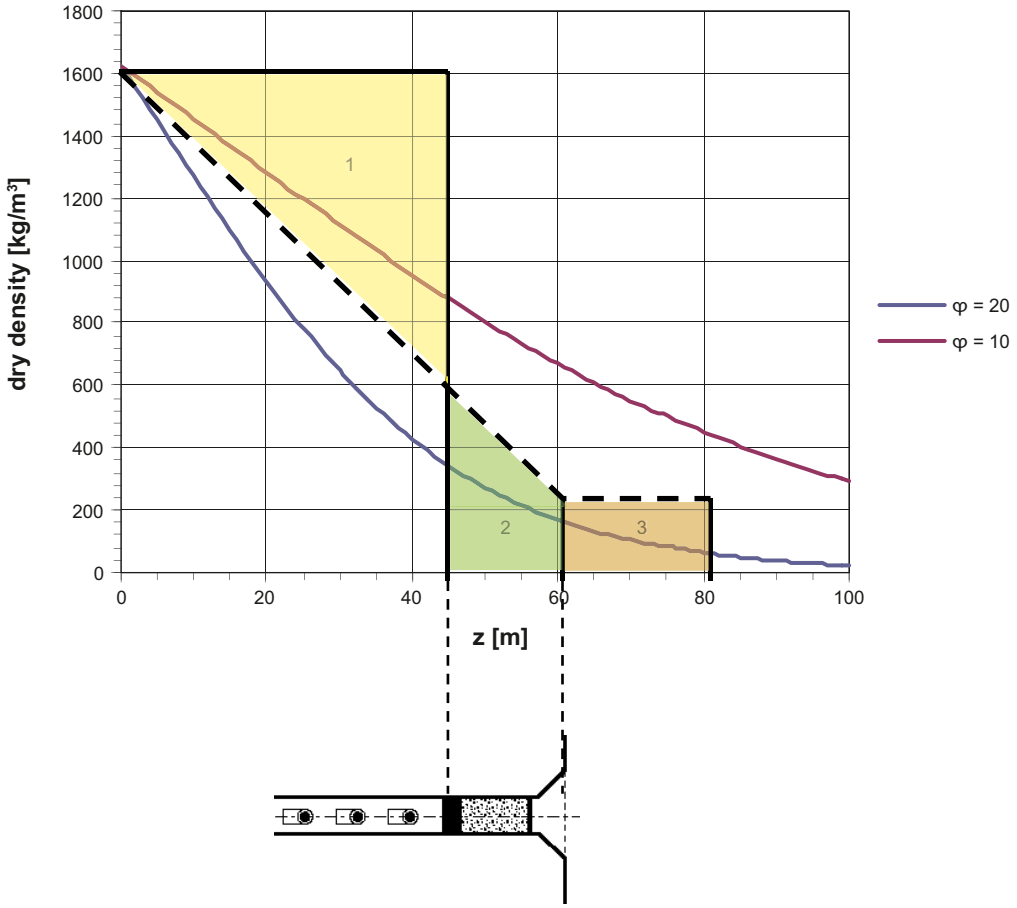

Figure 22-5. *Relation between dry density and the distance to the unaffected backfill front and the areas referred to for estimating the mass balance situation for the case of 10 MPa swelling pressure of the backfill.*

The dry mass expanded into the transport tunnel is represented by area 3 marked brown in Figure 22-5. It is conservatively assumed that there is no loss in density along the transport tunnel due to the large cross section area of the tunnel. The dry density is thus assumed to be 230 kg/m^3 in the entire tunnel. This corresponds to a water ratio of 400%, which is higher than the liquid limit of a Ca-bentonite and thus more like a liquid than a gel.

The dry mass in the transport tunnel is

$\Delta m = 3 \cdot \pi \cdot 2.7^2 \cdot 20 \cdot 230 = 3.16 \cdot 10^5$ kg

The sum of the dry mass expanded into the rest of the deposition tunnel and into the transport tunnel is $4.49 \cdot 10^5$ kg, which is close enough to the mass lost inside the initial backfill front ($5.15 \cdot 10^5$ kg) in order fulfil the mass-balance criteria.

The bentonite loss is thus according to this solution reaching 45 m into the deposition tunnel from the plug. The acceptance criteria of the backfill dry density 1,240 kg/m^3, which according to Figure 22-5 implies that the density is unacceptably low at about $z > 20$ m, which means that deposition holes located closer to the plug/backfill interface than 25 m will be covered with a backfill with unacceptably low dry density.

Backfill with a swelling pressure of 3 MPa

If the backfill has a lower swelling pressure e.g. 3 MPa the swelling will be less but the effect more severe since the starting density is lower. Figure 22-6 shows the relation between swelling pressure and the distance from the unaffected backfill front for this case (corresponding to Figure 22-3). The swelling can be calculated in an identical way as for the case with 10 MPa. Figure 22-7 shows the resulting figure for evaluating the mass balance (corresponding to Figure 22-5).

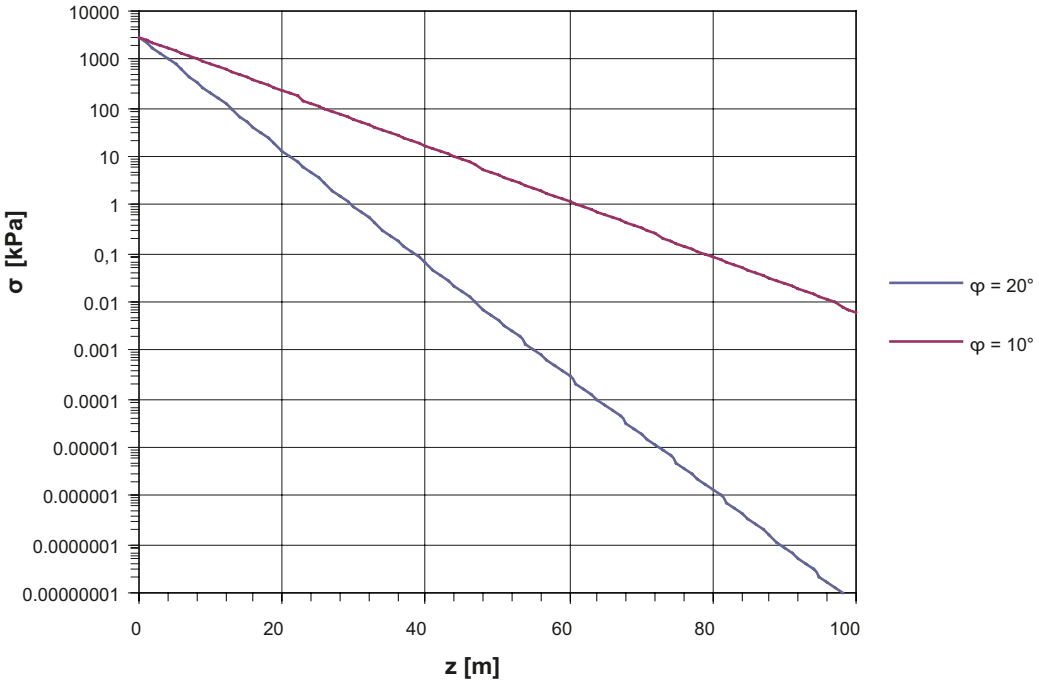

Figure 22-6. *Calculated swelling pressure as a function of the distance to the unaffected backfill front, where the swelling pressure is 3 MPa.*

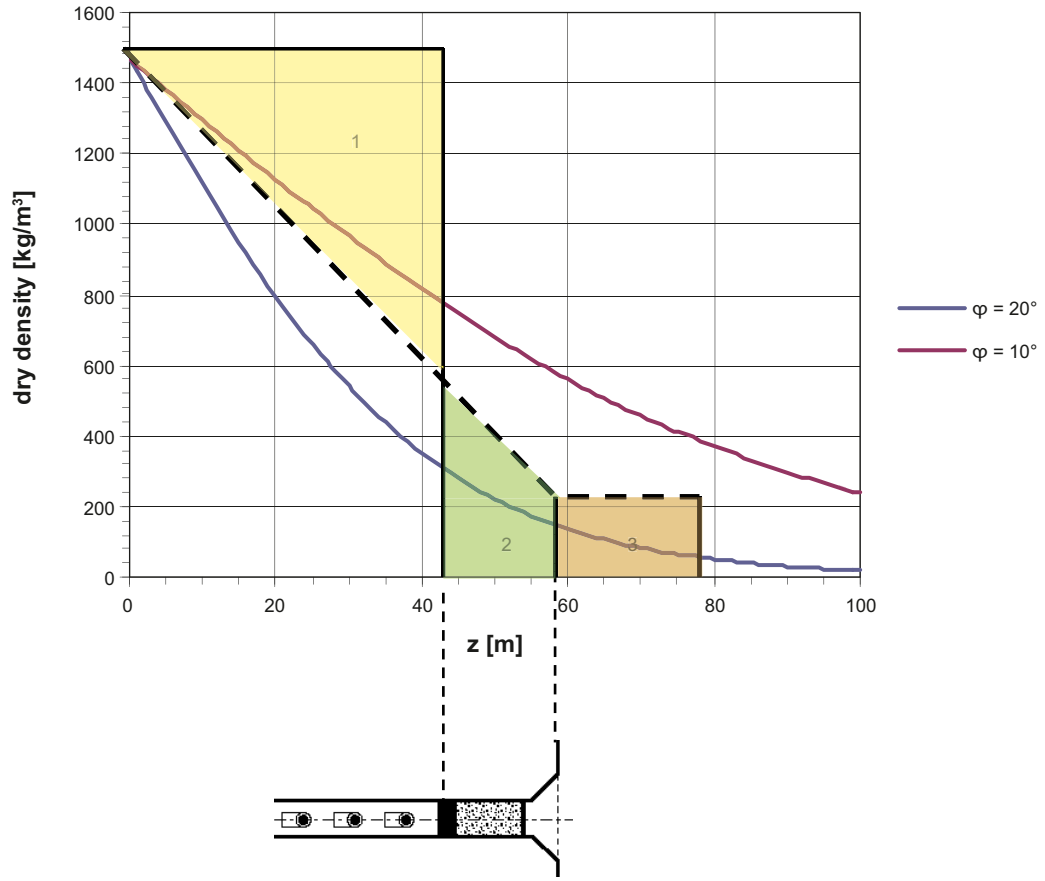

Figure 22-7. *Relation between dry density and the distance to the unaffected backfill front and the areas referred to for estimating the mass balance situation for the case of 3 MPa swelling pressure of the backfill.*

The dry mass lost inside the initial backfill front represented by area 1 marked yellow in Figure 22-7 is

$\Delta m = \pi \cdot 2.7^2 \cdot 43 \cdot (1{,}470–540)/2 = 4.58 \cdot 10^5$ kg

The dry mass expanded into the rest of the deposition tunnel represented by area 2 marked green in Figure 22-7 (43 m < z < 58 m) is

$\Delta m = \pi \cdot 2.7^2 \cdot 15 \cdot (540+220)/2 = 1.33 \cdot 10^5$ kg

The dry mass expanded into the transport tunnel is represented by area 3 marked brown in Figure 22-7. It is conservatively assumed that there is no loss in density along the transport tunnel due to the large cross section area of the tunnel. The dry density is thus assumed to be 220 kg/m^3 in the entire tunnel.

The dry mass in the transport tunnel is

$\Delta m = 3 \cdot \pi \cdot 2.7^2 \cdot 20 \cdot 220 = 3.02 \cdot 10^5$ kg

The sum of the dry mass expanded into the rest of the deposition tunnel and into the transport tunnel is $4.35 \cdot 10^5$ kg, which is close enough to the mass lost inside the initial backfill front ($4.58 \cdot 10^5$ kg) in order fulfil the mass-balance criteria.

The bentonite loss is thus according to this solution reaching 43 m into the deposition tunnel from the plug. The acceptance criteria of the backfill dry density 1,240 kg/m^3, which imply according to Figure 22-7 that the density is unacceptably low at about z > 11 m, which means that deposition holes located closer to the plug/backfill interface than 32 m will be covered with a backfill with unacceptably low dry density.

22.4 Conclusions and uncertainties

The analytical calculations of the backfill swelling out from the deposition tunnel to the transport tunnel show for the backfill initial dry density 1,470–1,600 (corresponding to a swelling pressure of 3–10 MPa) that

- the backfill inside the plug is affected to the distance 40–50 m from the plug/backfill interface,
- the density of the backfill is unacceptably low 25–35 m from the plug/backfill interface,
- the backfill will swell out into the transportation tunnel but the density will be very low there (ρ_d < 230 kg/m^3 corresponding to a water ratio of more than 400%).

However, the uncertainties are rather large:

- The analytical model entails some weaknesses (see Section 21.4).
- The friction angle is a function of the swelling pressure and increases with decreasing swelling pressure. The values at low swelling pressure are not well known. However, the calculations have used friction angle values between 10 and 20 degrees that increase with decreasing density as illustrated by the used dashed line relation in Figure 22-7.
- Laboratory measurements /Börgesson et al. 1995/ indicate that
  - the friction angle is higher than 20 degrees at low density,
  - the lateral stresses (corresponding to the normal stresses towards the rock surface) are higher than the stress in the swelling direction.

Both these factors mean that the resisting force from the friction is probably larger than that modelled, which means that the results probably are conservative in the sense that the swelling and thus density loss is smaller than modelled.

References

SKB's (Svensk Kärnbränslehantering AB) publications can be found at www.skb.se/publications.

Abaqus Manuals, 2008. Dassault Systemes Simulia Corp.

Brantberger M, Zetterqvist A, Arnbjerg-Nielsen T, Olsson T, Outters N, Syrjänen P, 2006. Final repository for spent nuclear fuel. Underground design Forsmark, Layout D1. SKB R-06-34, Svensk Kärnbränslehantering AB.

Börgesson L, 1986. Model shear tests of canisters with smectite clay envelopes in deposition holes. SKB TR 86-26, Svensk Kärnbränslehantering AB.

Börgesson L, Fredriksson A, Johannesson L-E, 1994. Heat conductivity of buffer materials. SKB TR 94-29, Svensk Kärnbränslehantering AB.

Börgesson L, Johannesson L-E, 1995. Thermo-hydro-mechanical modelling of water unsaturated buffer material – status 1995. SKB Arbetsrapport 95-32, Svensk Kärnbränslehantering AB.

Börgesson L, Johannesson L-E, Sandén T, Hernelind J, 1995. Modelling of the physical behaviour of water saturated clay barriers. Laboratory tests, material models and finite element application. SKB TR 95-20, Svensk Kärnbränslehantering AB.

Börgesson L, Hernelind J, 1999. Coupled thermo-hydro-mechanical calculations of the water saturation phase of a KBS3 deposition hole – influence of hydraulic rock properties on the water saturation phase. SKB TR-99-41, Svensk Kärnbränslehantering AB.

Börgesson L, Johannesson L-E, Hernelind J, 2004. Earthquake induced rock shear through a deposition hole. Effect on the canister and the buffer. SKB TR-04-02, Svensk Kärnbränslehantering AB.

Börgesson L, Hernelind J, 2006a. Earthquake induced rock shear through a deposition hole. Influence of shear plane inclination and location as well as buffer properties on the damage caused to the canister. SKB TR-06-43, Svensk Kärnbränslehantering AB.

Börgesson L, Hernelind J, 2006b. Canister displacement in KBS-3V – a theoretical study. SKB TR-06-04, Svensk Kärnbränslehantering AB.

Börgesson L, Hernelind J, 2006c. Consequences of loss or missing bentinite in a deposition hole. A theoretical study. SKB TR-06-13, Svensk Kärnbräsnlehantering AB.

Börgesson L, Johannesson L-E, 2006. Consequences of upwards swelling from a wet deposition hole into a dry tunnel with backfill made of blocks. A preliminary study. SKB TR-06-12, Svensk Kärnbränslehantering AB.

Börgesson L, Fälth B, Hernelind J, 2006. Water saturation phase of the buffer and backfill in the KBS-3V concept – Special emphasis given to the influence of the backfill on the wetting of the buffer. SKB TR-06-14, Svensk Kärnbränslehantering AB.

BörgessonL, Sandén T, 2006. Piping and erosion in buffer and backfill materials. Current knowledge. SKB R-06-80, Svensk Kärnbränslehantering AB.

Börgesson L, Hernelind J, 2009. Mechanical interaction buffer/backfill. Finite element calculation of the upward swelling of the buffer against both dry and saturated backfill. SKB R-09-42, Svensk Kärnbränslehantering AB.

Carslaw H S, Jaeger J C, 1959. Conduction of heat in solids. Oxford University Press.

Croney D, Coleman J D, Black W P M, 1958. Movement and Distribution of Water in Soil in Relation to Highway Design and Performance. Highway Research Board, Special Report, 40, pp 226–252.

Dueck A, 2004. Hydro-mechanical properties of a water unsaturated sodium bentonite. Laboratory study and theoretical interpretation. Doctoral Thesis, Department of Building and Environmental Technology, Division of Soil Mechanics and Foundation Engineering, Lund University.

Dueck A, Börgesson L, 2007. Model suggested for an important part of the hydro-mechanical behaviour of a water unsaturated bentonite. Engineering Geology, 92, pp 160–169.

Finsterle S, Pruess K, 1995. Solving the estimation-identification problem in two-phase flow modeling. Water Resour. Res., 31(4), pp 913–924.

Follin S, Levén J, Hartley L, Jackson P, Joyce S, Roberts P, Swift B, 2007. Hydrogeological characterisation and modelling of deformation zones and fracture domains, Forsmark modelling stage 2.2. SKB R-07-48, Svensk Kärnbränslehantering AB.

Fredlund D G, Rahardjo H, 1993. Soil Mechanics for unsaturated soils, John Wiley & Sons Inc., ISBN 0-471-85008-X, Chapter 4.

Goudarzi R, Börgesson L, 2002. Prototype repository. Sensors data report (Period: 010917-020301) Report nr:1. SKB IPR-02-22, Svensk Kärnbränslehantering AB.

Goudarzi R, Börgesson L, Röshoff K, Edelman M, 2006. Canister retrieval test – Sensors data report (Period: 001026-060501), Report no. 12. Äspö Hard Rock Laboratory. SKB IPR-06-35, Svensk Kärnbränslehantering AB.

Hedin A, 2004. Integrated near-field evolution model for a KBS-3 repository. SKB R-04-36, Svensk Kärnbränslehantering AB.

Hökmark H, Lönnquist M, Kristensson O, Sundberg J, Hellström G, 2009. Strategy for thermal dimensioning of the final repository for spent nuclear fuel. SKB R-09-04, Svensk Kärnbränslehantering AB.

Hökmark H, Lönnqvist M, Fälth B, 2010. T-H-M issues in repository rock. Thermal, mechanical, thermo-mechanical and hydro-mechanical evolution of the rock at the Forsmark and Laxemar sites. SKB TR-10-23, Svensk Kärnbränslehantering AB.

Jarsjö J, Destouni G, Gale J, 2001. Groundwater degassing and two-phase flow in fractured rock: Summary of results and conclusions achieved during the period 1994-2000. SKB TR-01-13, Svensk Kärnbränslehantering AB.

Jarsjö J, Prieto C, Destouni G, 2009. Estimation of characteristic relations for unsaturated flow through rock fractures in the Forsmark area. SKB P-15-17, Svensk Kärnbränslehantering AB.

Johannesson L-E, Nilsson U, 2006. Deep repository – engineered barrier systems. Geotechnical behaviour of candidate backfill materials. Laboratory tests and calculations for determining performance of the backfill. SKB R-06-73, Svensk Kärnbränslehantering AB.

Johannesson L-E, 2007. Canister Retrieval Test - Dismantling and sampling of the buffer and determination of density and water ratio. Äspö Hard Rock Laboratory. SKB IPR-07-16, Svensk Kärnbränslehantering AB.

Johannesson L-E, 2008. Backfilling and closure of the deep repository. Phase 3- pilot tests to verify engineering feasibility. Geotechnical investigations made on unsaturated backfill materials. SKB R-08-131, Svensk Kärnbränslehantering AB.

Kahr G, Kraenbuehl F, Stoeckli H F, Müller-Vonmoos M, 1990. Study of the Water_Bentonite System by Vapour Adsorption, Immersion Calorimetry and X-ray Techniques: II. Heats of Immersion, Swelling Pressures and Thermodynamic Properties. Clay Minerals, 25, pp 499–506.

Kassiff G, Ben Shalom A, 1971. Experimental Relationship between Swell Pressure and Suction. Géotechnique, 21(3), pp 245–255.

Low P F, Anderson D M, 1957. Osmotic Pressure Equations for Determining Thermodynamic Properties of Soil Water. Soil Science, 86, pp 251–253.

Pusch R, Ramqvist G, 2004. Borehole sealing, preparative steps, design and function of plugs – basic concept. SKB IPR-04-57, Svensk Kärnbränslehantering AB.

Pusch R, Ramqvist G, 2007. Borehole project – Final report of Phase 3. SKB R-07-58, Svensk Kärnbränslehantering AB.

Rutqvist J, Tsang C, 2008. Review of SKB's Work on Coupled THM Processes Within SR-Can. SKI Report 2008-08, Statens Kärnkraftinspektion (Swedish Nuclear power Inspectorate).

Sandén T, Börgesson L, Dueck A, Goudarzi R, Lönnqvist M, 2008. Erosion and sealing processes in tunnel backfill materials investigated in laboratory. Deep repository – Engineered barrier system. SKB R-08-135, Svensk Kärnbränslehantering AB.

Sandén T, Börgesson L, 2010. Early effects of water inflow into a deposition hole. Laboratory test results. SKB R-10-70, Svensk Kärnbränslehantering AB.

Singh A, Mitchell J K, 1968. General stress-strain-time function for soils. American Society of Civil Engineers, Proceedings, Vol. 94, No SM1.

SKB, 2010a. Design, production and initial state of the buffer. SKB TR-10-15, Svensk Kärnbränslehantering AB.

SKB, 2010b. Design, production and initial state of the backfill and plug in deposition tunnels. SKB TR-10-16, Svensk Kärnbränslehantering AB.

SKB, 2010c. Design, production and initial state of the closure. SKB TR-10-17, Svensk Kärnbränslehantering AB.

Thomas H R, Cleall P J, Chandler N, Dixon D, Mitchell H P, 2003. Water infiltration into a large-scale in-situ experiment in an underground research laboratory. Geotechnique, 53, 207–224.

Thorsager P, Börgesson L, Johannesson L-E, Sandén T, 2002. Canister Retrieval Test – Report on installation. Äspö Hard Rock Laboratory. SKB IPR-02-30, Svensk Kärnbränslehantering AB.

Wadsö L, Svennberg K, Dueck A, 2004. An experimentally simple method for measuring sorption isotherms. Drying Technology, 22(10), pp 2427–2440.

Åkesson M, Börgesson L, Kristensson O, 2010. SR-Site Data report. THM-modelling of buffer, backfill and other system components. SKB TR-10-44, Svensk Kärnbränslehantering AB.

Appendix A

Large hydraulic repository model

When deciding upon suitable hydraulic boundary conditions for the deposition hole model a large axisymmetric hydraulic model of the entire repository were developed.

Geometry

In the cylindrical large scale hydraulic model, with dimensions depth = 1,000 m or 520 m and radius = 3,057 m, the repository is represented by a disc centered at –460 m depth with a height of h_r = 6 m (approximately the tunnel height) and the radius r_r = 1,000 m. As indicated, the model is axisymmetric, thus, X is the radial coordinate, Z is the tangential coordinate and Y the vertical coordinate. The disk material represents the repository in a homogeneous way, where the backfilled tunnels and the surrounding rock are averaged. Since we have assumed axisymmetry the tunnels are concentric tori.

A volume element dV of the repository is expressed as $dV = X\,dX\,dZ\,dY$. The radial dimension of the volume element dX consists of a rock element dX_r and a backfill component dX_{bf}.

Rock hydraulic conductivities

The hydraulic conductivity of the rock was prescribed according to the values shown in Table A-1. The values in Table A-1 correspond to field-measurements from Forsmark /Follin et al. 2007/.

The position of the conductivities in the two used models is shown in Figure A-2. As can be seen in Figure A-2 the rock allotted with the "intermediate" conductivity is surrounding the rock with low conductivity above and outside the repository in the 1,000 m high model. To be conservative this is not the case in the 520 m high model.

Table A-1. Rock conductivities used in the large hydraulic model.

Rock conductivity m/s	Position m
$K = 1.44 \cdot 10^{-7}$	depth < 200
$K = 5.18 \cdot 10^{-10}$	depth > 200 and radius > 1,600
$K = 6.04 \cdot 10^{-12}$	depth > 400 and radius < 1,600

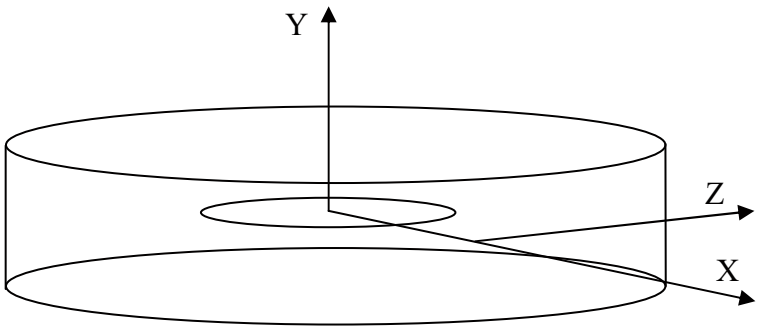

Figure A-1. *Repository model geometry.*

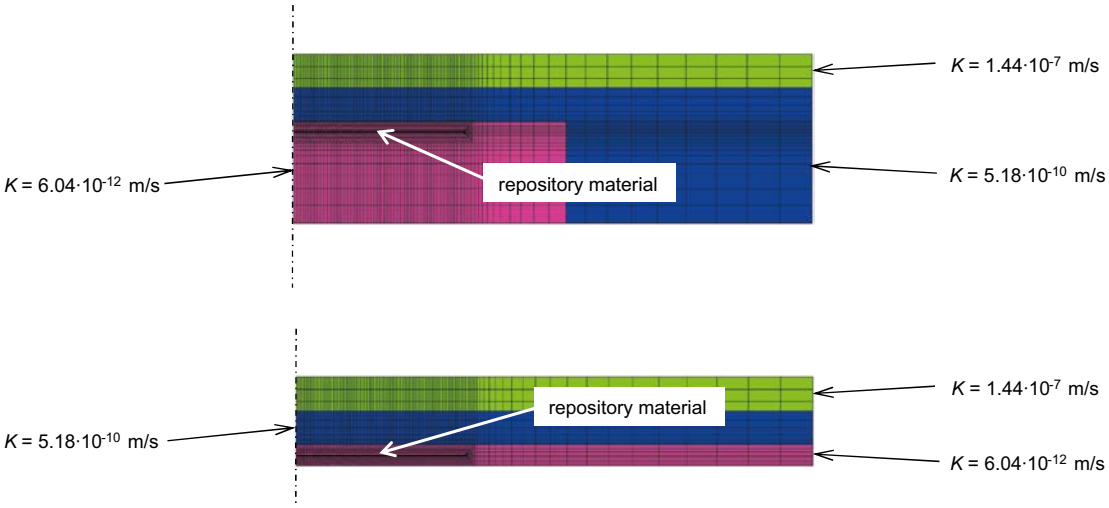

Figure A-2. *The geometry and hydraulic conductivity positions for the 1,000 m and 520 m deep model.*

Homogenized repository representation

Porosity

The backfill has a homogenized porosity $n_{bf} = 0.44$ and the rock porosity is taken as $n_r = 0.003$.

$$n_{bf} = \frac{dV_{bf}^{\ p}}{dV_{bf}} = 0.44$$
$$n_r = \frac{dV_r^{\ p}}{dV_r} = 0.003 \qquad \text{(A-1)}$$

In /Brantberger et al. 2006/ the excavated rock volume for the 400 m alternative is estimated to 1,813 000 m^3 if the ramp and shafts is not included. A "Large scale porosity", expressing how much of the disc that consist of tunnels, may be defined:

$$n_L = \frac{V_{bf}}{V} = 0.097 \qquad \text{(A-2)}$$

where $V_{bf} = 1{,}813\ 000$ m^3 and $V = h_r\, \pi\, r_r^2$. The total porosity of the disc is defined as

$$n = \frac{V^p}{V} = \frac{V_{bf}^{\ p}}{V} + \frac{V_r^{\ p}}{V} = n_{bf} n_L + n_r (1 - n_L) = 0.045 \qquad \text{(A-3)}$$

It is assumed that all porosity fields are homogeneous.

Water saturation and retention

The water saturation in the backfill and rock are defined

$$S_{lbf} = \frac{dV_{bf}^{\ w}}{dV_{bf}^{\ p}}$$
$$S_{lr} = \frac{dV_r^{\ w}}{dV_r^{\ p}} \qquad \text{(A-4)}$$

The water saturation of the disc is

$$S_l = \frac{dV^w}{dV^p} = \frac{dV_{bf}{}^w + dV_r{}^w}{ndV} = \frac{\left(S_{l\,bf} n_{bf} n_L + S_{l\,r} n_r (1-n_L)\right) dV}{ndV} =$$
$$= \frac{S_{l\,bf} n_{bf} n_L + S_{l\,r} n_r (1-n_L)}{n} \qquad \text{(A-5)}$$
$$= 0.94 S_{l\,bf} + 0.06 S_{l\,r}$$

Retention curves modelling the backfill $S_{lbf} = S_{lbf}(p_{lbf})$ and rock $S_{lr} = S_{lr}(p_{lr})$ may be inserted into the relation above. This gives that $S_l = S_l(p_{lbf}, p_{lr})$. A new retention curve $S_l{}^* = S_l{}^*(p_l)$ may be fitted to $S_l = S_l(p_{lbf}, p_{lr})$. The fitted parameters for the Van Genuchten model are $p_0 = 5.5$ MPa and $\lambda = 0.2$. The new retention curve defines a repository material water pressure p_l.

Permeability

The water flow in the backfill and rock is given by,

$$\boldsymbol{q}_{bf} = -\rho_l \frac{\boldsymbol{k}^{bf} k_{rl}}{\mu_l} \nabla p_l{}^{bf}$$
$$\boldsymbol{q}_r = -\rho_l \frac{\boldsymbol{k}^{r} k_{rl}}{\mu_l} \nabla p_l{}^{r} \qquad \text{(A-6)}$$

where the intrinsic permeability tensors $\boldsymbol{k}^{bf}$ and $\boldsymbol{k}^{r}$ are assumed to be isotropic. The water flux in the repository as a whole is assumed to be able to be represented by,

$$\boldsymbol{q} = -\rho_l \frac{\boldsymbol{k} k_{rl}}{\mu_l} \nabla p_l \qquad \text{(A-7)}$$

where the ingoing parameters refers to the properties of the homogenized repository material.

In the vertical direction (here aligned with the Y-coordinate) the rock and backfill material are assumed to be a "parallel system" where,

$$(\nabla p_l{}^{bf})_Y = (\nabla p_l{}^{r})_Y = (\nabla p_l)_Y$$
$$dA q_Y = dA_{bf} q_{Ybf} + dA_r q_{Yr} \quad \Rightarrow \quad q_Y = n_L q_{Ybf} + (1-n_L) q_{Yr} \qquad \text{(A-8)}$$

which gives

$$q_Y = -\rho_l \frac{k_{rl}}{\mu_l} \left(n_L k^{bf} + (1-n_L) k^{r}\right) (\nabla p_l)_Y \qquad \text{(A-9)}$$

Since the tunnels are assumed to be oriented along the Z-coordinate, once again a "parallel system" is obtained. Thus,

$$q_Z = -\rho_l \frac{k_{rl}}{\mu_l} \left(n_L k^{bf} + (1-n_L) k^{r}\right) (\nabla p_l)_Z \qquad \text{(A-10)}$$

In the horizontal direction perpendicular to the tunnel direction (aligned with the X-coordinate) the backfill material and rock are assumed to be a "serial system". Thus, in this direction,

$$(\nabla p_l)_X = \frac{dp_l}{dX} = \frac{dp_l{}^{bf} + dp_l{}^{r}}{dX} = \frac{dX_{bf} (\nabla p_l{}^{bf})_X + dX_r (\nabla p_l{}^{r})_X}{dX} \qquad \text{(A-11)}$$
$$q_X \approx q_{Xbf} \approx q_{Xr}$$

where the approximations hold if the tunnel dimension in the radial direction is small as compared to the repository radial dimension. Since the tunnels are assumed to be directed horizontally along the Z coordinate,

$$n_L = \frac{dV_{bf}}{dV} = \frac{XdX_{bf}dZdY}{XdXdZdY} = \frac{dX_{bf}}{dX}, \quad 1-n_L = \frac{dX_r}{dX} \tag{A-12}$$

Together with the expression for the fluxes we obtain,

$$\begin{gathered}(\nabla p_l)_X = n_L \frac{-q_X}{\rho_l \frac{k^{bf} k_{rl}}{\mu_l}} + (1-n_L)\frac{-q_X}{\rho_l \frac{k^r k_{rl}}{\mu_l}} \\ \Downarrow \\ q_X = -\rho_l \frac{k_{rl}}{\mu_l} \frac{1}{\frac{n_L}{k^{bf}} + \frac{1-n_L}{k^r}} (\nabla p_l)_X\end{gathered} \tag{A-13}$$

Thus, the non-zero components of the permeability tensor are,

$$\begin{aligned} k_{XX} &= \frac{1}{\frac{n_L}{k^{bf}} + \frac{1-n_L}{k^r}} \\ k_{YY} &= n_L k^{bf} + (1-n_L)k^r \\ k_{ZZ} &= k_{YY} \end{aligned} \tag{A-14}$$

Boundary conditions

The boundary conditions used for the two models are shown in Figure A-3.

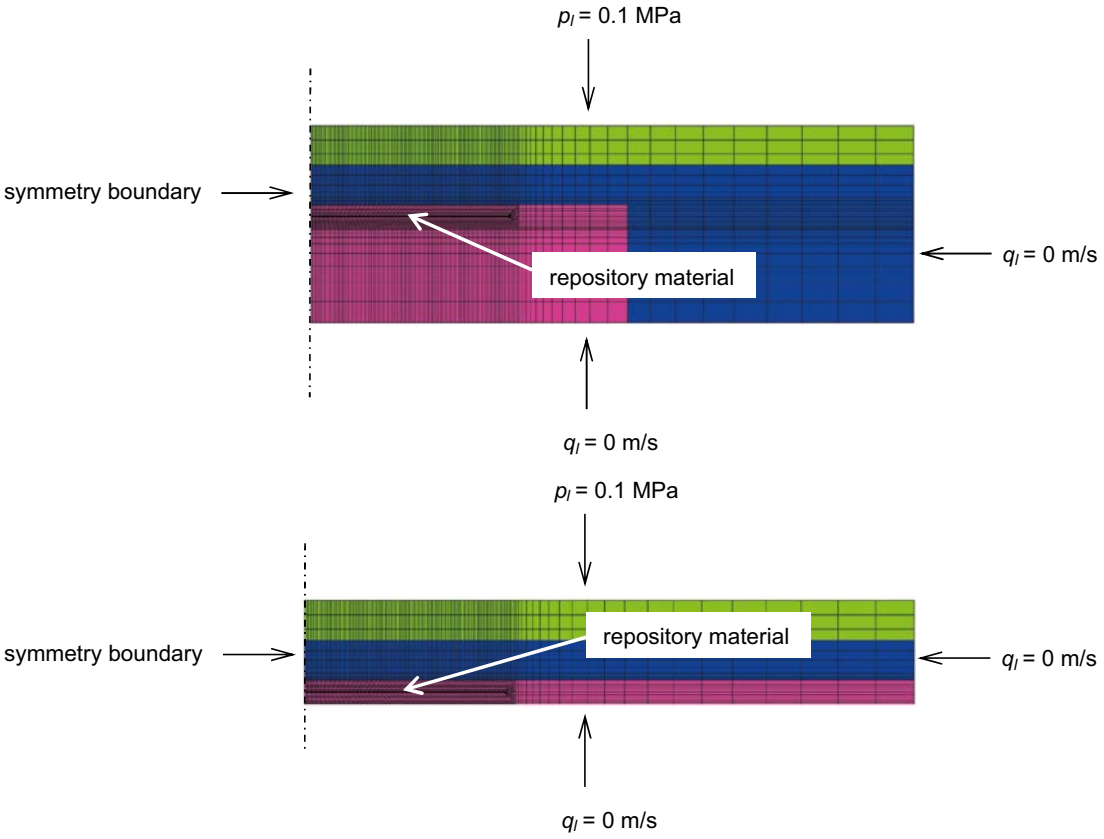

Figure A-3. *Boundary conditions of the large hydraulic axisymmetric repository models.*

Results

First the evolution of water pressure at 400 m depth (60 m above the repository) and close to the symmetry axis is studied. Figure A-4 shows that the water pressure is not significantly changed from it's initial value of 4 MPa during the saturation process. Therefore the upper hydraulic boundary condition is taken as 4 MPa in the smaller TH-model of the deposition hole.

Next, the difference of having a zero flux boundary at 1,000 m depth or 520 m depth on the water saturation evolution is investigated. As Figure A-5 shows there is an insignificant effect on the water saturation process in the repository close to the symmetry axis. This indicates that a zero flux boundary condition may be used in the smaller TH-model of the deposition hole at the lower boundary 60 m below the tunnel floor.

Fracture transmissivity

The objective is to calibrate a fracture transmissivity by setting the inflow of the fracture $Q = A_f\, q$ = 0.1 l/min. An expression of the inflow from a water bearing fracture into an open deposition hole in an axisymmetric model is derived. The fracture is assumed to have the geometry shown in the figure below, where (r_0,z_1) are the coordinates of the fracture outlet into the deposition hole, and (r_1,z_0) are the position where the fracture is pressurized.

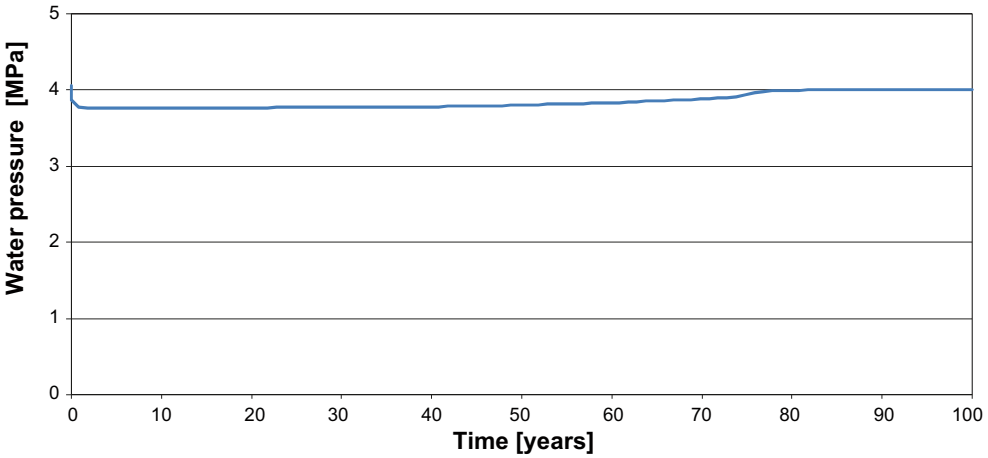

Figure A-4. Water pressure evolution at 400 m depth and close to the symmetry axis.

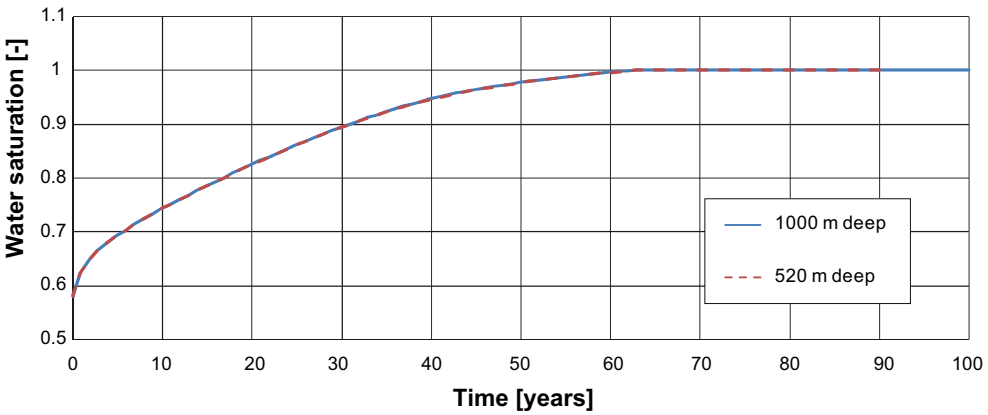

Figure A-5. Water saturation in the repository close to the symmetry axis for the 1,000 m and 520 m deep model.

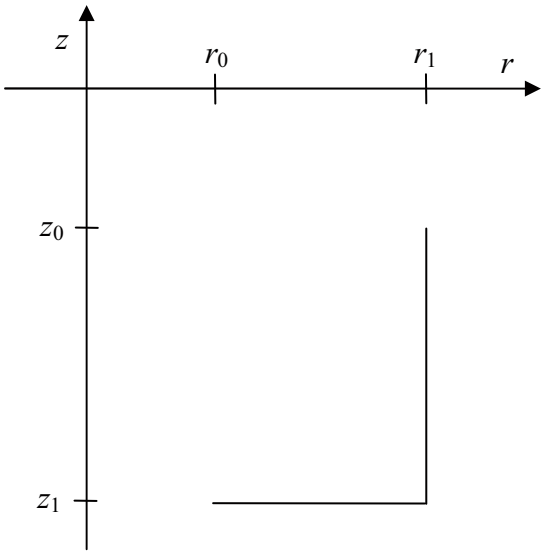

Figure A-6. *Fracture geometry.*

The transmissivity T in a fracture with a width w is coupled to a corresponding conductivity K according to,

$$T = Kw \tag{A-15}$$

In the constitutive law for the water flow that is used in Code_Bright,

$$\boldsymbol{q} = -\frac{\boldsymbol{k}k_r}{\mu}\left(\frac{\partial p}{\partial \boldsymbol{x}} + \rho g \boldsymbol{e}_z\right) \tag{A-16}$$

the flux of water $\boldsymbol{q}$ is coupled to the gradient of the water pressure p. When expressing the same process using the conductivity, the water pressure is given in water head h. The water head is given by $h = p / \rho g$. Thus,

$$\begin{aligned} &\boldsymbol{q} = -\boldsymbol{K}\left(\frac{\partial h}{\partial \boldsymbol{x}} + \boldsymbol{e}_z\right) \\ &\boldsymbol{K} = \frac{\boldsymbol{k}k_r}{\mu}\rho g \end{aligned} \tag{A-17}$$

This applied on the horizontal fracture section where the flow is radial gives,

$$\begin{aligned} &q_r = -K_r \frac{\partial h}{\partial r} \\ &A(r)q_r(r) = A(r_0)q_r(r_0) \\ &A(r) = w2\pi r \end{aligned} \quad \Rightarrow \quad q_r(r) = \frac{r_0}{r}q_r(r_0) \tag{A-18}$$

The equations above give

$$\begin{aligned} &\int_{r_0}^{r_1} q_r(r_0)\frac{r_0}{r}dr = -\int_{h(r_0)}^{h(r_1)} K_r dh \\ &\Downarrow \\ &q_r(r_0)r_0 \ln\left(\frac{r_1}{r_0}\right) = -K_r(h(r_1) - h(r_0)) \end{aligned} \tag{A-19}$$

In the vertical fracture section where the flow is axial the relations are,

$$q_a = -K_a\left(\frac{\partial h}{\partial z}+1\right)$$
$$q_a(z) = q_a(z_0) \tag{A-20}$$

The equations above gives

$$\int_{z_0}^{z_1}\left(\frac{q_a(z_1)}{K_a}+1\right)dz = -\int_{h(z_0)}^{h(z_1)} dh$$
$$\Downarrow \tag{A-21}$$
$$\left(\frac{q_a(z_1)}{K_a}+1\right)(z_1 - z_0) = -(h(z_1) - h(z_0))$$

With a combined axial and radial oriented fracture we also have the compatibility conditions:

$$q_a(z_1) = q_r(r_1)$$
$$h(z_1) = h(r_1) \tag{A-22}$$

Now, since we have five unknowns ($q_r(r_0)$, $q_r(r_1)$, $q_a(z_1)$, $p(r_1)$, $p(z_1)$) and five equations , we may solve the equation system for $q_r(r_0)$.

$$q_r(r_0) = \left(\frac{r_0}{r_1}\frac{z_1 - z_0}{K_a} - \frac{r_0}{K_r}\ln(\frac{r_1}{r_0})\right)^{-1}\left(h(z_0) - h(r_0) - z_1 + z_0\right) \tag{A-23}$$

Inserting the geometry of the model together with the boundary pressures $p(h(z_0)) = 4$ MPa, $p(h(r_0)) = 0.1$ MPa and choosing $K_a = K_r = 4.2 \cdot 10^{-8}$ m/s gives an inflow of $Q = 0.1$ l/min. The corresponding transmissivity and permeability are $T = 5.25 \cdot 10^{-9}$ m^2/s and $k = 4.31 \cdot 10^{-15}$ m^2, respectively.

Appendix B

Thermal simulation of the area around the CRT and TBT experiments

Here a short presentation of the model which has been used when solving this problem is shown.

Geometry

Figure B-1 shows a 3D model of the CRT and TBT experimental geometry containing:

A. surrounding rock
B. steel lid
C. concrete plug
D. engineered buffer (averaged properties of all constituents)
E. canister/heaters

Loads, boundary conditions and initial conditions

Heat load

Measured canister power from CRT and TBT.

Boundary conditions

Convection conditions have been prescribed in the tunnel where a heat transfer coefficient of $\gamma = 10$ W/(°C·m^2) and a tunnel air temperature of 15°C has been used.

On the outer boundary surface, adiabatic conditions are used.

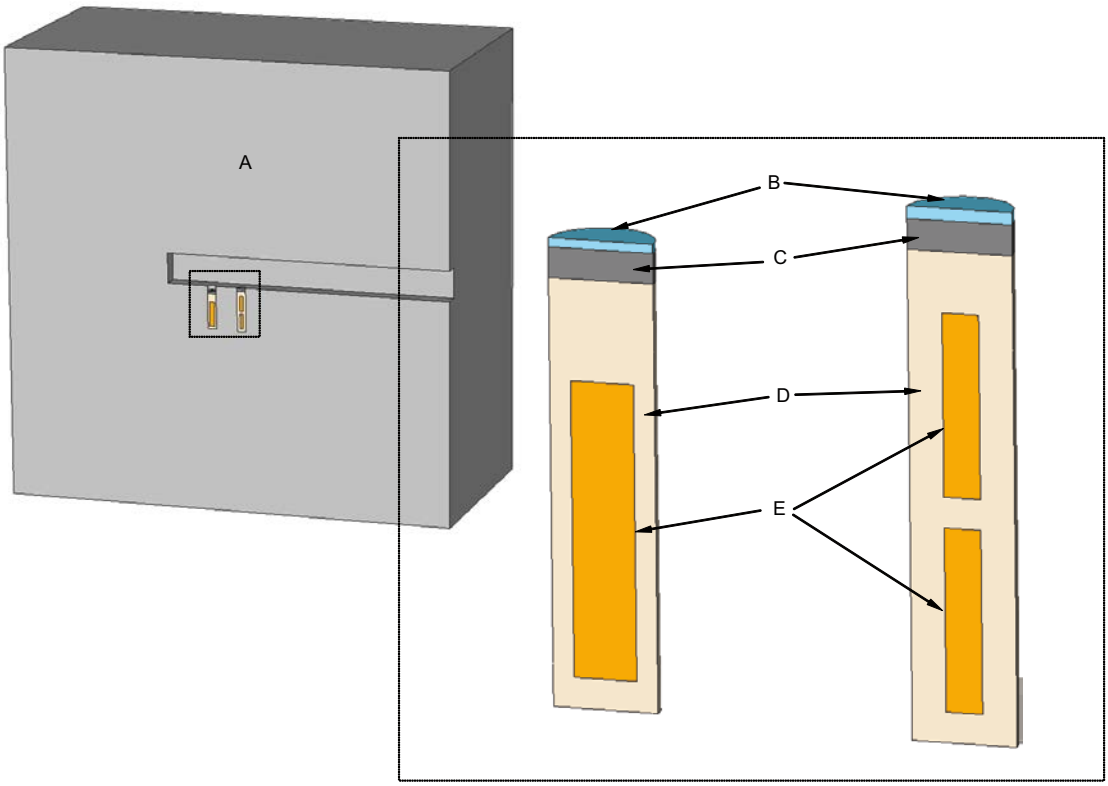

Figure B-1. *Geometry of a 3D model used for thermal simulation of the CRT and TBT environment.*

Initial conditions

Temperature: 17°C

Material properties

In Table B-1 the material properties used in the thermal 3D model are shown.

Spatial average estimates of the parameters have been used for representing the buffer and the canisters. When it comes to the buffer, the used value of conductivity is also an average in time in the sense that the conductivity is dependent on water saturation. In order to get an estimate of this effect an alternative value of conductivity has also been used for the buffer.

Sensors to check with

Figure B-2 shows the position and name of the sensors measuring the temperature in the rock and canister which the model results is verified against.

Results

The comparison between the rock temperature measured by the chosen sensors and the temperature obtained by the simulation is given in Figure B-3. In Figure B-4 the experimental and simulated temperatures of the canister temperature are shown.

The buffer conductivity does not affect the temperature evolution in the rock significantly. Therefore the results in Figure B-3 are obtained using the base case value of buffer thermal conductivity only. The simulated temperatures agree well with the measured.

Table B-1. Material properties used in the model.

Material	ρ [kg/m³]	c [J/(kg·K)]	λ W/(m·K)]	n [–]
Rock	2,770	770	2.6	0
Steele lid	7,840	460	47	0
Concrete plug	2,400	770	2.7	0
Buffer	2,780	800 (of solid)	1.2 (1.0)	0.4
Canisters	8,000	450	100	0

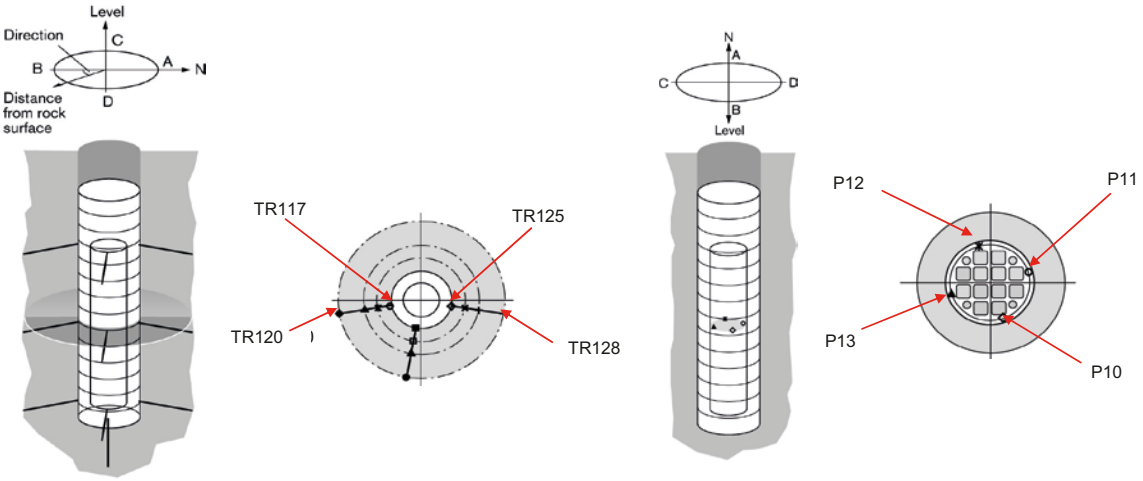

Figure B-2. *Rock and canister temperature sensor positions and names.*

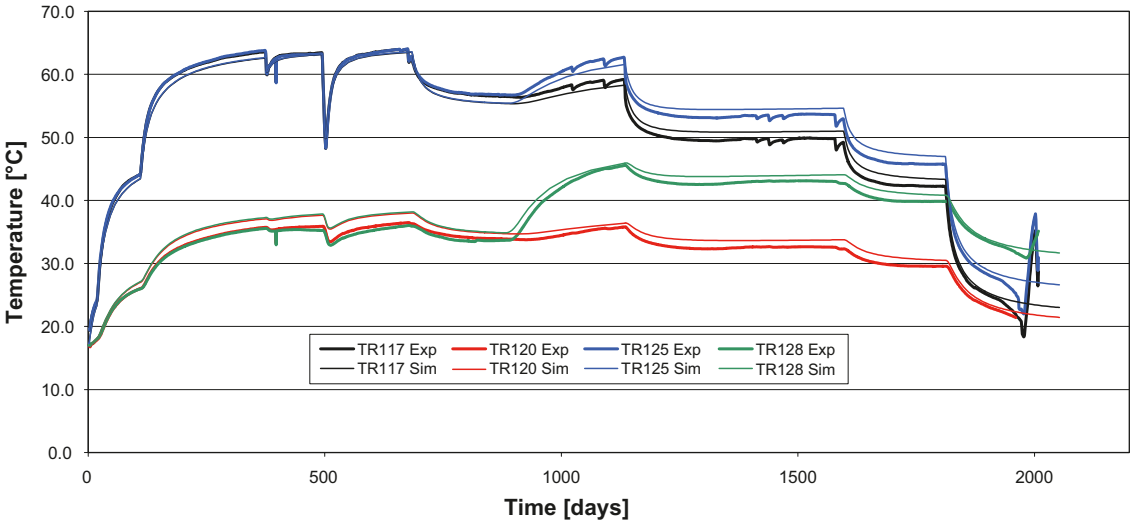

Figure B-3. *Experimental and simulated rock temperatures at canister mid-height.*

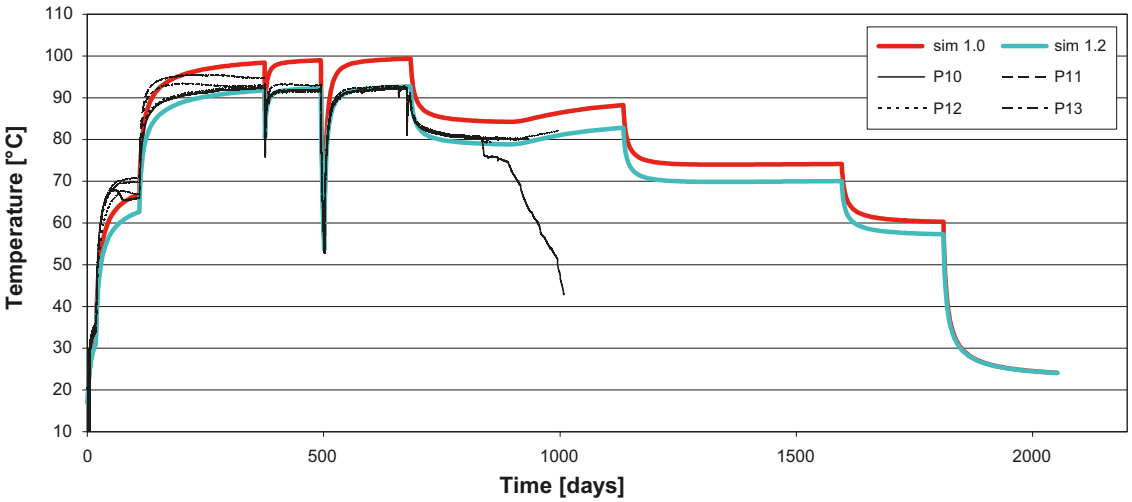

Figure B-4. *Experimental and simulated canister surface temperatures at canister mid-height.*

When the canister surface temperatures were simulated, both base case and alternative buffer conductivity were used in order to evaluate the effect of the water saturation process in the buffer on the canister temperatures. The "true" temperature evolution is considered to go from the temperature curve obtained from using the lower value of conductivity (= dry conditions) towards the curve obtained using the higher value of thermal conductivity (= wet conditions). Figure B-4 shows that the simulated temperatures fit well to the measured temperature evolution when "in thought" considering the water saturation process.

The obtained horizontal component of the canister surface heat flux as a function of height at day 375 and day 1,063 is shown in Figure B-5. The heat flux profile is shown for a vertical cut through the canister in the tunnel direction, i.e. the heat flux along the indicated canister boundary in Figure B-5. The rugged appearance of the curves comes from the approximate representation of the field in the model. However, the difference in heat flux at the two different times is clear. The overall difference in magnitude comes from changes in canister power. The unsymmetrical appearance of the heat flux curves at the opposite sides of the canister at day 1,063 comes from that the TBT canisters are activated at this time and as a consequence the heat flux field around CRT therefore gains some in the opposite direction.

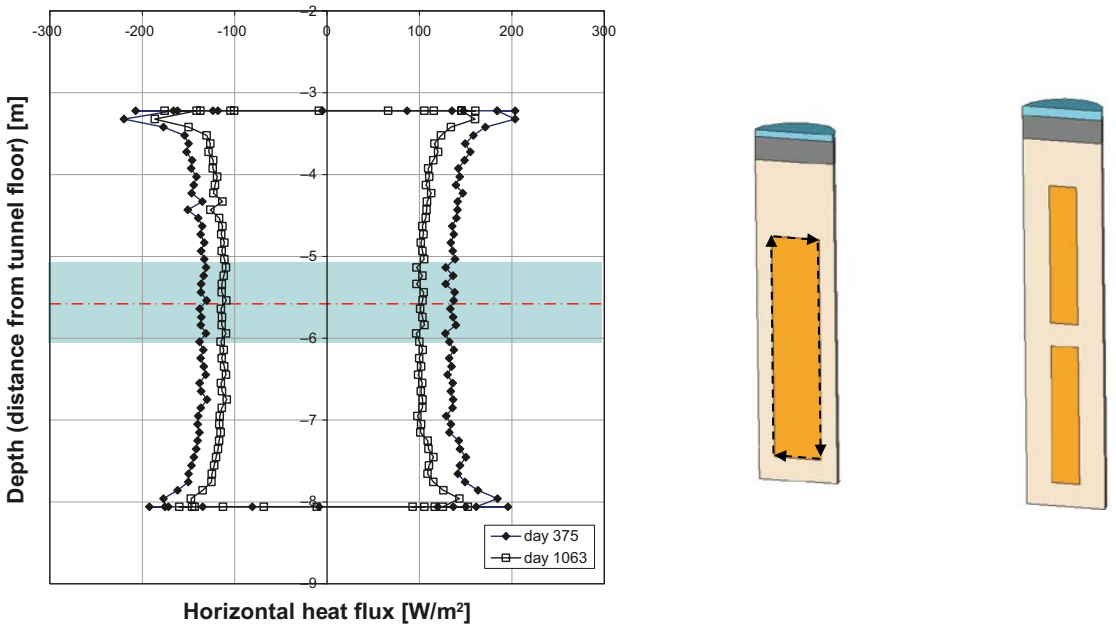

Figure B-5. *The horizontal component of the canister surface heat flux profile at day 375 and 1,063 along the scan-line indicated with the dashed line. The mid-height is shown together with the interval where the heat flux is averaged.*

In the forthcoming an axisymmetric representation of the CRT experiment is used to simplify the models somewhat. In order to obtain a heat flux history at the canister mid-height which can be used in the axisymmetric representation, an average of the horizontal heat flux is calculated for the histories shown above at canister mid-height ± 0.5 m. The result is shown in Figure B-6.

Note that if the heat flux is to be used as a boundary condition together with adiabatic conditions at the horizontal boundaries, the radial dimension of the model has to be small as compared to the canister height. A suitable model could start at the canister surface and end at the hole wall.

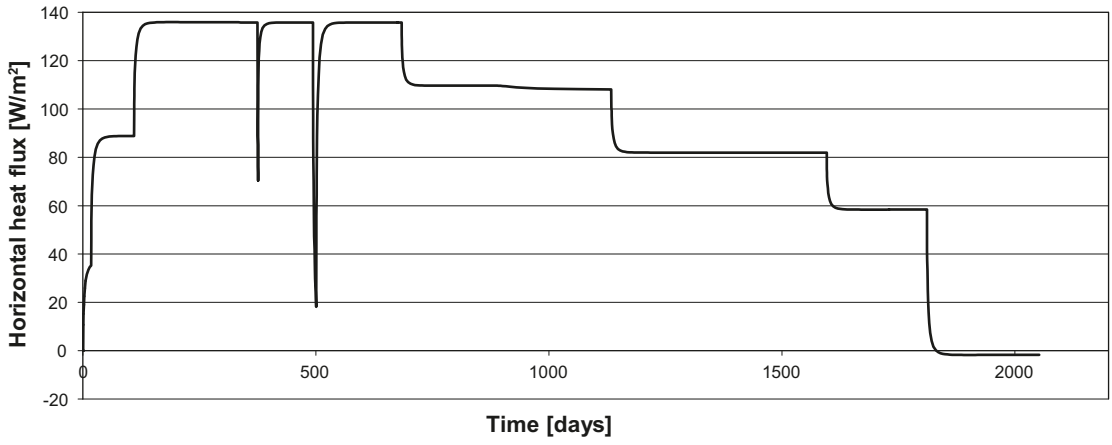

Figure B-6. *Horizontal heat flux average formed at canister mid-height ± 0.5 m.*

Appendix C

Swelling modulus κ_s dependent on swelling pressure curves

A new function governing the swelling modulus κ_i in the hydraulic strain increment of BBM, (C-1), has been implemented in Code Bright in order to mimic the behaviour of bentonite clay.

$$d\varepsilon_v^{\ h} = \frac{\kappa_s(p',e)}{(1+e)(s+p_{atm})}ds \tag{C-1}$$

The idea behind the new expression is to utilize a swelling pressure curve (the pressure obtained at full water saturation under confined conditions) obtained from analyzing experimental data. The adopted function has following form,

$$\kappa_s(p',e) = \kappa_{s0} f(p',e)$$

$$f(p',e) = \begin{cases} 1 & \text{if } p' < p_{ref} \\ 10^{-20} & \text{if } p' > p_{swell}(e) \\ 1 - \dfrac{\ln p' - \ln p_{ref}}{\ln(p_{swell}(e)) - \ln p_{ref}} & \text{otherwise} \end{cases} \tag{C-2}$$

$$p_{swell}(e) = 10^{\left[-4.741+4.117\cdot10^{-3}\frac{\rho_s}{1+e}-3.94\cdot10^{-7}\left(\frac{\rho_s}{1+e}\right)^2\right]}$$

In Figure C-1 the pressure dependence of the normalized function (κ_i / κ_{i0}) is shown for two constant void ratios. When the pressure, p', is less than the referential pressure, p_{ref}, the function equals the referential value κ_{i0}. Thus, the upper "knee" occurs when $p' = p_{ref}$. When $p' = p_{swell}(e)$ the function equals zero (or rather 10^{-20} to avoid division by zero). I.e., swelling may occur until the pressure equals the swelling pressure at the current void ratio.

The void ratio dependence is shown in Figure C-2 below where the normalized modulus is given for three constant pressures. The void ratio is normalized against the void ratio, e_s, that give the specified pressure when inserted in the swelling pressure function. As can be seen, the modulus decreases with increasing void ratio.

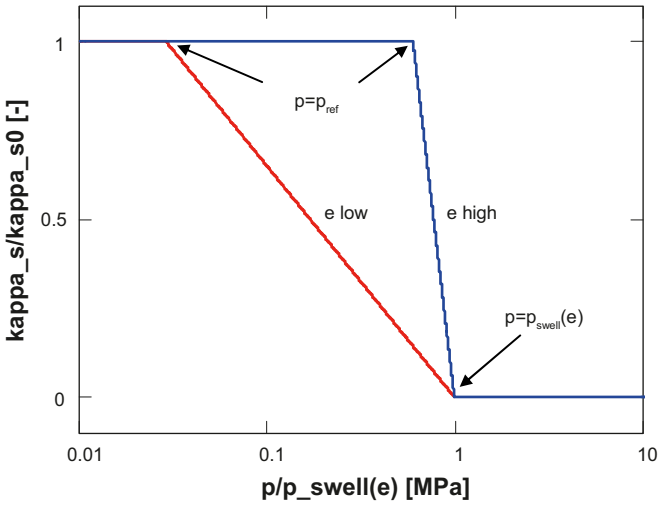

Figure C-1. *Pressure dependence of the normalized swelling modulus.*

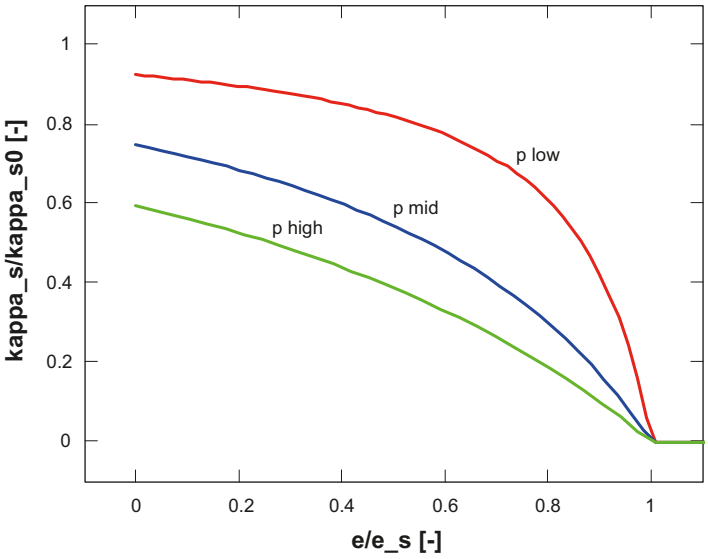

Figure C-2. *Void ratio dependence of the normalized swelling modulus*

Test and validation

In the following some simple elastic and isotropic examples are studied using MathCad and the CodeBright implementation. Thus, only states inside the yield surface during wetting are considered. At the higher void ratios used this is probably not a very suitable representation, but this exercise is only performed to study the performance of the modulus-function and the implementation in CodeBright.

Wetting under constant pressure

First, wetting under constant pressure is investigated when using the modulus function. The unsaturated clay sample can be thought of being contained within a soft membrane that is subjected to an outer constant pressure p'. When water is added to the clay, the specimen should swell until the swelling pressure equals the outer prescribed pressure.

The parameters used are:

- $\kappa_{s0} = 0.3$
- $p_{ref} = 1$ MPa
- $\rho_s = 2{,}780$ kg/m^3
- $p_{atm} = 0.1$ MPa

The initial states are given by $e = 0.57$ and $p' = \{2,5,10,15\}$ MPa.

In the normalized responses, shown in Figure C-3 below, obtained from using MathCad, it can be seen that the void ratio obtained at full water saturation, e_s, is given by $p_{swell}(e_s) = p'$, exactly as expected for a correct implementation.

To check the CodeBright implementation the results obtained from using MathCad and CodeBright are compared in Figure C-4. The agreement between the solutions is very good.

Wetting under constant void ratio (confined swelling)

The next simple case that is studied is wetting under constant void ratio e (confined swelling). Two different void ratios are used. Here, the final pressure p', at full water saturation, should match the swelling pressure curve so that $p' = p_{swell}(e)$.

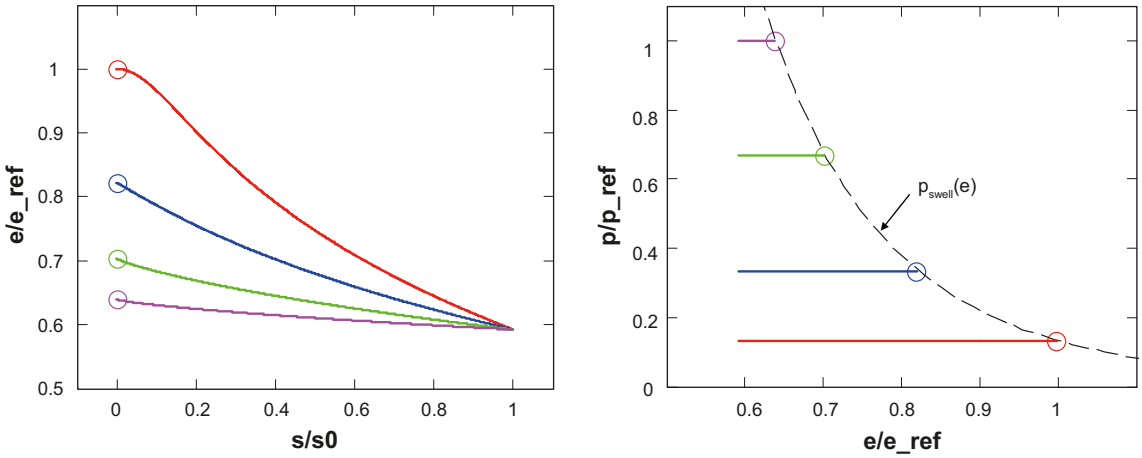

Figure C-3. *MathCad responses for wetting under constant pressure.*

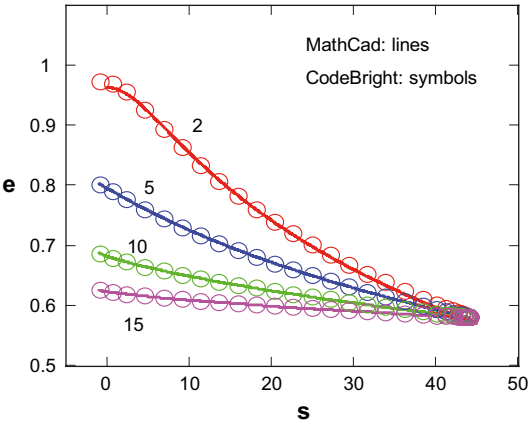

Figure C-4. *MathCad and CodeBright responses for wetting under constant pressure. The net mean stress used is indicated close to the corresponding response curve.*

In this example, also the elastic part of BBM comes into play, where the elastic modulus K is present, see (C-3). For the two different void ratios the parameters in K have been kept the same.

$$d\varepsilon_v^{\,e} = \frac{dp'}{K}$$

$$K = \max\left\{\frac{(1+e)p'}{\kappa_i(s)}, K_{\min}\right\} \qquad \text{(C-3)}$$

$$\kappa_i(s) = \kappa_{i0}\left[1+\alpha_i s\right]$$

The parameters used are:

- $\kappa_{s0} = 0.3$
- $p_{ref} = 1$ MPa
- $\rho_s = 2{,}780$ kg/m^3
- $p_{atm} = 0.1$ MPa
- $\kappa_{i0} = 0.13$
- $\alpha_i = -0.02$
- $K_{min} = 13$ MPa

The initial states are given by $e = \{0.57, 0.8\}$ and $p' = 0$ MPa.

As can be seen in Figure C-5, the MathCad results from using the modulus function follow the adopted swelling pressure curve.

To check the CodeBright implementation the results obtained from using MathCad and CodeBright are compared in Figure C-6. The agreement between the solutions is very good.

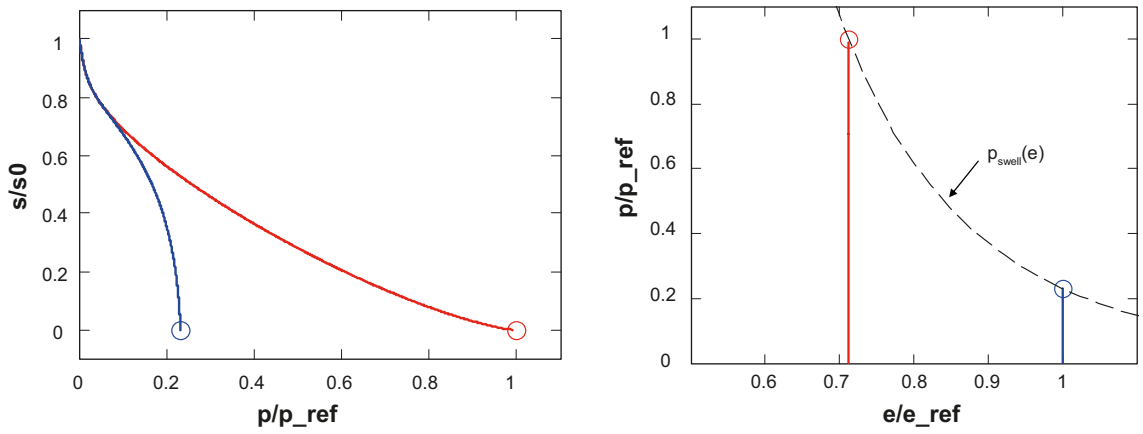

Figure C-5. *MathCad responses for confined wetting.*

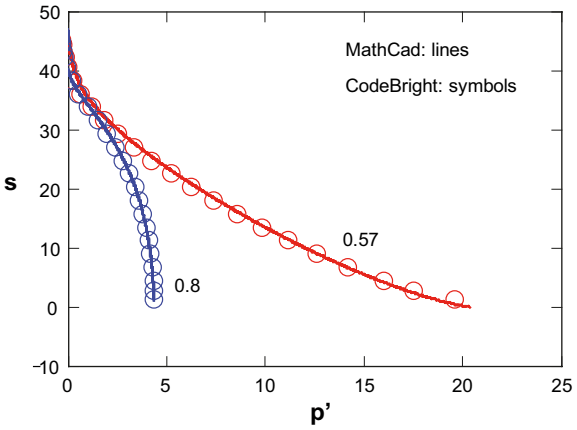

Figure C-6. *MathCad and CodeBright responses for confined wetting. The void ratio used is indicated close to the corresponding response curve.*

Appendix D

Incorporation of a varying critical state line slope parameter M in BBM

The underlying idea with this modification is to incorporate a dependence of M (representing the slope of the critical state line) in the plastic part of BBM (D-1) so that an experimentally validated expression of the type $q_f = q_f(p')$ that are found for bentonite clay are fulfilled.

$$
\begin{aligned}
&d\boldsymbol{\varepsilon}^p = d\Lambda \frac{\partial g}{\partial \boldsymbol{\sigma}} \\
&f = q^2 - M^2 (p' + p_s)(p_0 - p') \\
&g = \alpha q^2 - M^2 (p' + p_s)(p_0 - p') \\
&M = M(p_0, p_s) \\
&p_0(s, p_0^*) = p^c \left(\frac{p_0^*}{p^c} \right)^{\frac{\lambda_0 - \kappa_{i0}}{\lambda(s) - \kappa_{i0}}} \\
&\lambda(s) = \lambda_0 \\
&dp_0^* = \frac{1+e}{\lambda_0 - \kappa_{i0}} p_0^* d\varepsilon_v^p
\end{aligned}
\tag{D-1}
$$

In BBM the deviatoric failure stress q_f occurs at the mid-point pressure $p'_{\text{mid}} = (p_0 - p_s)/2$ of the yield surface f. When failure occurs the material model behaves plastic, i.e. $f = 0$. The obtained expression reads,

$$f = q_f^{\,2} - M^2 (p'_{mid} + p_s)(p_0 - p'_{mid}) = 0 \tag{D-2}$$

The parameter M may accordingly be expressed as,

$$M = \frac{q_f(p'_{mid})}{\frac{p_0 + p_s}{2}} \tag{D-3}$$

The experimentally validated $q_f = q_f(p')$ expression reads,

$$q_f(p') = ap'^b \tag{D-4}$$

where no cohesion is present. Since the presence of p_s means that the BBM model includes cohesion, the original expression of q_f has been altered to

$$q_f(p') = a(p' + p_s)^b \tag{D-5}$$

If this altered expression is used in the expression of the variable M we obtain,

$$M(p_0, p_s) = \frac{q_f\left(\frac{p_0 - p_s}{2}\right)}{\frac{p_0 + p_s}{2}} = a\left(\frac{p_0 + p_s}{2}\right)^{b-1} \tag{D-6}$$

Contributions to the stiffness tensors

Below the new relation $M = M(p_0, p_s)$ is introduced into the BBM framework and the new contributions are shown. A von Mises type yield surface is considered (meaning that it is independent of Lode's angle) and the temperature dependence is omitted.

The differential of the yield surface becomes,

$$df = \frac{\partial f}{\partial \boldsymbol{\sigma}} \cdot d\boldsymbol{\sigma} + \frac{\partial f}{\partial s} ds + \frac{\partial f}{\partial \varepsilon_v^{\ p}} d\varepsilon_v^{\ p} \tag{D-7}$$

where the new dependency of M will have an effect on the last two partial derivatives since $p_0 = p_0(s, \varepsilon_v^p)$ and $p_s = p_s(s)$. The additional contributions can be seen when evaluating the partial derivatives below.

$$\begin{aligned}
\frac{\partial f}{\partial s} &= \frac{\partial f}{\partial p_0}\frac{\partial p_0}{\partial s} + \frac{\partial f}{\partial p_s}\frac{\partial p_s}{\partial s} = \left(\left.\frac{\partial f}{\partial p_0}\right|_{dM=0} + \frac{\partial f}{\partial M}\frac{\partial M}{\partial p_0} \right)\frac{\partial p_0}{\partial s} + \left(\left.\frac{\partial f}{\partial p_s}\right|_{dM=0} + \frac{\partial f}{\partial M}\frac{\partial M}{\partial p_s} \right)\frac{\partial p_s}{\partial s} \\
\frac{\partial f}{\partial \varepsilon_v^{\ p}} &= \frac{\partial f}{\partial p_0}\frac{\partial p_0}{\partial \varepsilon_v^{\ p}} = \left(\left.\frac{\partial f}{\partial p_0}\right|_{dM=0} + \frac{\partial f}{\partial M}\frac{\partial M}{\partial p_0} \right)\frac{\partial p_0}{\partial \varepsilon_v^{\ p}}
\end{aligned} \tag{D-8}$$

Since the partial derivatives above now have additional terms, there will be contributions to the elastoplastic stiffness tensors $\boldsymbol{C}^{ep}$ and $\boldsymbol{c}^{ep}$.

$$d\boldsymbol{\sigma} = \boldsymbol{C}^{ep} d\boldsymbol{\varepsilon} + \boldsymbol{c}^{ep} ds \tag{D-9}$$

$$\boldsymbol{C}^{ep} = \boldsymbol{C}^{e} - \frac{1}{A}\left(\boldsymbol{C}^{e} \frac{\partial g}{\partial \boldsymbol{\sigma}} \right) \otimes \left(\boldsymbol{C}^{e} \frac{\partial f}{\partial \boldsymbol{\sigma}} \right) \tag{D-10}$$

$$\boldsymbol{c}^{ep} = \boldsymbol{c}^{e} - \frac{1}{A}\frac{\partial f}{\partial s}\boldsymbol{C}^{e}\frac{\partial g}{\partial \boldsymbol{\sigma}} - \frac{1}{A}\frac{1}{3K^{h}}\left(\left(\boldsymbol{C}^{e} \frac{\partial g}{\partial \boldsymbol{\sigma}} \right) \otimes \left(\boldsymbol{C}^{e} \frac{\partial f}{\partial \boldsymbol{\sigma}} \right) \right) \boldsymbol{I} \tag{D-11}$$

$$A = -\frac{\partial f}{\partial \varepsilon_v^{\ p}}\frac{\partial g}{\partial p'} + \frac{\partial f}{\partial \boldsymbol{\sigma}} \cdot \left(\boldsymbol{C}^{e} \frac{\partial g}{\partial \boldsymbol{\sigma}} \right) \tag{D-12}$$

The additional terms in (D-8) are here specified in the variables and parameters used

$$\begin{aligned}
\frac{\partial f}{\partial M} &= -2M(p' + p_s)(p_0 - p') \\
\frac{\partial M}{\partial p_0} &= \frac{a(b-1)}{2}\left(\frac{p_0 + p_s}{2} \right)^{b-2} \\
\frac{\partial M}{\partial p_s} &= \frac{a(b-1)}{2}\left(\frac{p_0 + p_s}{2} \right)^{b-2}
\end{aligned} \tag{D-13}$$

Test and validation

The implementation in CodeBright is tested below for a case where a loose clay specimen is first subjected to an increasing hydrostatic stress state which is followed by a “triaxial test” stress state (shearing), where two of the principal stresses are held constant and the third is increased (compressively). Drained hydraulic conditions prevail during the process. A case with a constant M and the new varying M are used to investigate the differences of the two formulations. The shearing begin at two different levels of hydrostatic pressure in order to investigate the behaviour of the models for different stress evolutions and validate that the final stress state coincides with $q_f = q_f(p')$ for the variable M implementation.

The parameters used in the mechanical model are:

Elastic strain increment

- $\kappa_{i0} = 0.15$
- $\alpha_i = -0.02$
- $K_{min} = 2$ MPa

Plastic strain increment

- $\lambda_0 = 0.18$
- $p_{s0} = 0.05$ MPa
- $p^c = 1$ MPa
- M = (5) (with a = 0.5 and b = 0.77) or M = 0.589
- $\alpha = 0.5$
- $p_0^* = 0.242$ MPa

Hydraulic strain increment

- $\kappa_{s0} = 0.2$
- $p_{ref} = 0.1$ MPa
- $\rho_s = 2{,}780$ kg/m^3
- $p_{atm} = 0.1$ MPa

The initial states are given by $e = 1.78$, $p = 0.2$ MPa and $p_l = 0.1$ MPa.

λ_0 is set to correspond to the void ratio e at the start of shearing at the higher level of hydrostatic stress. This has been done in order to enable evaluation against the closely related experimental conditions of experiment T17 in /Börgesson et al. 1995/. The used swelling pressure curve is utilized for obtaining a value of λ_0.

$$\lambda(e) = \left[\frac{\mathrm{d}\ln\left(p_{swell}(e)\right)}{\mathrm{d}e}\right]^{-1}$$
$$p_{swell}(e) = 10^{\left[-4.741+4.117\cdot10^{-3}\frac{\rho_s}{1+e}-3.94\cdot10^{-7}\left(\frac{\rho_s}{1+e}\right)^2\right]} \qquad \text{(D-14)}$$

As can be seen in Figure D-1 the responses obtained using the variable M implementation are much more in agreement with the T17 data as compared to the constant M implementation. It can also be seen that both stress states for the variable M simulation coincide with the $q_f(p')$ expression. This indicates that the CodeBright implementation is correct.

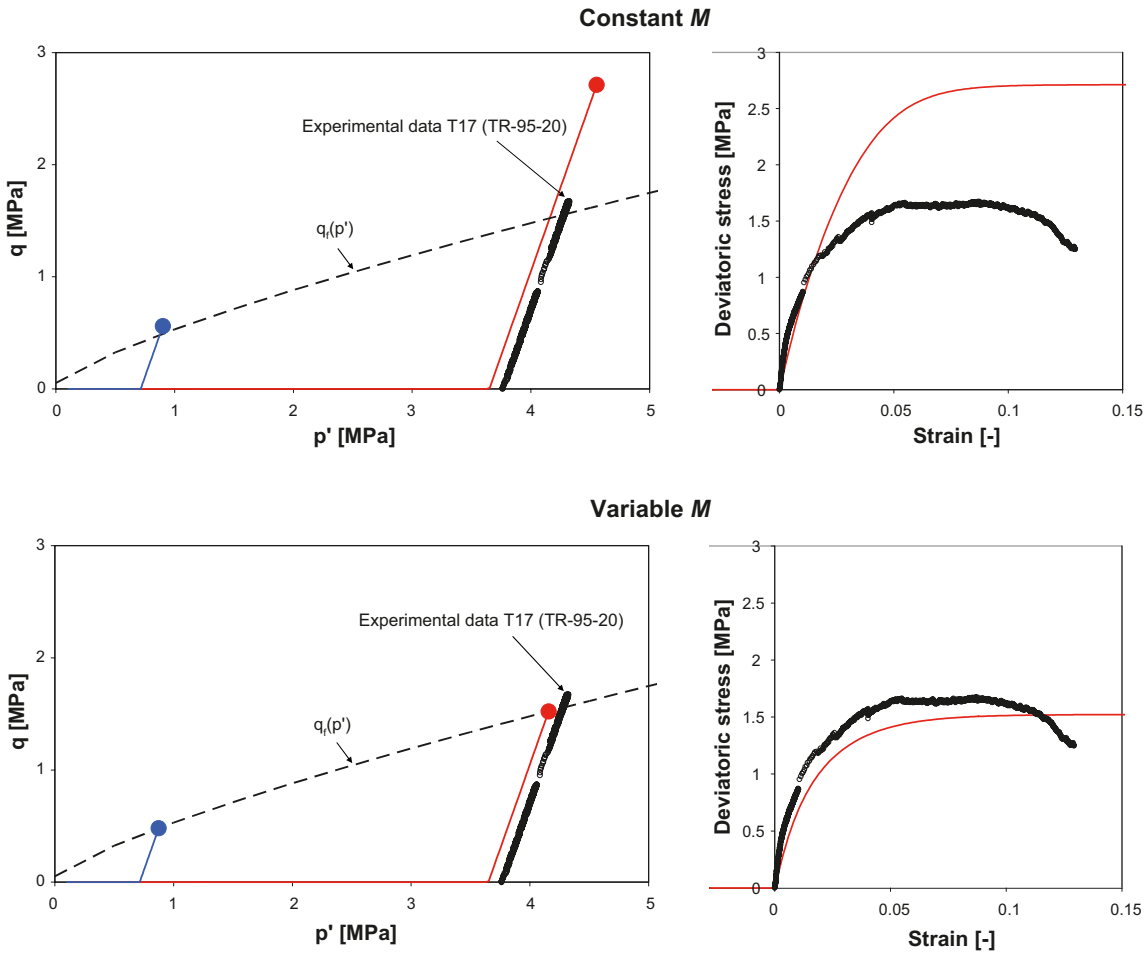

Figure D-1. *Stress state (left) and q – strain relation (right) for the constant M (top) and variable M (bottom) models.*

Appendix E

Generation of retention curves for the three bentonite block types in CRT

General

The relation between water content and suction describes the main driving force for the saturation process. The relation is often called the retention curve. One application of the retention curve is as input data to material models used for prediction and evaluation of large field tests.

The retention curve can be determined as water contents w (the mass of water divided by the mass of solids) in equilibrium with a series of relative humidity at free swelling conditions. The appearance of this retention curve depends to some extent on the initial water content (e.g. /Dueck 2004/). The retention curve determined under free swelling condition and starting with an initial water content deviating from 0% is called the specific retention curve.

When the retention curve is used as input data to material models the so called confined retention curve is also needed. This curve can be based on the specific retention curve but is valid for a confined volume. The retention curve used for modelling purpose is often expressed as suction versus degree of saturation. Equation (E-1) is the definition of suction ψ according to /Fredlund and Rahardjo 1993/. The degree of saturation S_r is calculated according to Equation (E-2).

$$\psi = -\frac{R \cdot T \cdot \rho_w}{\omega_v} \cdot \ln\left(\frac{p}{p_{sat}}\right) \tag{E-1}$$

$$S_r = \frac{w \cdot \rho_s}{e \cdot \rho_w} \tag{E-2}$$

In Equation (E-1) T is the temperature (K), R the universal gas constant (8.31432 J/(mol K)) and ω_v the molecular mass of water vapor (0.018 kg/mol). The relative humidity is defined as $RH = 100 \cdot (p/p_s)$ where p is the partial pressure of pore-water vapor and p_s is the saturation pressure of water vapor over a flat surface of pure water at the temperature T. In Equation (E-2) ρ_s is the particle density, ρ_w is the density of water and e is the void ratio.

Material

The material is a commercially available sodium bentonite with a quality symbol MX-80 from American Colloid Co. The bentonite has montmorillonite as the dominating smectite clay mineral. The particle density ρ_s = 2,780 kg/m^3 and water density ρ_w = 1,000 kg/m^3 were used for evaluation of void ratio and degree of saturation from measured variables /Börgesson et al. 1995/.

Specific retention curves for MX-80

Specific retention curves with different initial water contents were determined with a method described by /Wadsö et al. 2004/ using 10g samples placed in pans hanging from lids in glass jars. The sample weight was monitored by below balance weighing. Measurements were carried out at seven different RH values (11%, 33%, 59%, 75%, 85%, 93%, 98%). The jars were placed at laboratory room climate with a temperature of 20±0.5°C. According to /Dueck 2004/ the final water contents for the initial water contents 7.5% and 17.5% were (2.7, 7.2, 10.5 15.5, 18.4, 23.1, 33.5) and (3.3, 9.3, 15.4, 17.7, 20.2, 24.3, 34.6), respectively.

A continuous formulation of the specific retention curve according to Equation (E-3) was used with different constants (B, b) to coincide with the measured values representing the different initial water contents; 7.5% (–0.0007, –0.319) and 17.5% (–0.00013, 0.28). The relation and the constants valid for relative humidity from 75% to 98% were presented by /Dueck 2004/ and /Dueck and Börgesson 2007/.

$$w = \left[B \cdot \ln\left(\frac{RH_{ret}}{100}\right) \right]^b \tag{E-3}$$

Model for the development of confined stress at constant volume conditions

The model includes mainly two equations, Equations (E-4) and (E-5), which relate the variables stress, relative humidity, water content and void ratio. It was proposed by /Dueck 2004/ and mainly based on tests with constant volume conditions. The included relationships are further described by /Dueck and Börgesson 2007/.

Equation (E-4) describes the relation between the mean stress P, the actual relative humidity RH_{act} in the sample and the relative humidity according to the retention curve at actual water content RH_{ret}. The retention curve is derived from Equation (E-3) with the constants B and b corresponding to the appropriate initial water content.

$$P(RH_{act}, w) = -\frac{R \cdot T \cdot \rho_w}{\omega_v} \cdot \ln\left(\frac{RH_{ret}(w)}{RH_{act}}\right) \quad \text{(E-4)}$$

Equation (E-5) describes the relation between the mean stress and the degree of saturation S_r at a specified void ratio e. The initial degree of saturation of the unloaded sample $S_{r,ini}$ is included. The swelling pressure at saturation P_{ret} can be calculated from the retention curve (E-6) which includes the void ratio e and the water content at saturation w_s (E-7).

$$P(S_r, e) = \frac{S_r - S_{r,ini}}{1 - S_{r,ini}} \cdot P_{ret}(e) \quad \text{(E-5)}$$

$$P_{ret}(e) = -\frac{R \cdot T \cdot \rho_w}{\omega_v} \cdot \ln\left(\frac{RH_{ret}(w_s)}{100}\right) \quad \text{(E-6)}$$

$$w_s = 100 \cdot \frac{e \cdot \rho_w}{\rho_s} \quad \text{(E-7)}$$

Retention curves ψ(Sr) at specific conditions

Three specific conditions were considered. The void ratio and the initial water content (e, w_{ini}) for the three conditions were (0.56, 17.1%), (0.636, 17.1%) and (0.72, 16.5%).

The retention curve consists in this description of two main parts and a transition in between. In the dry part of the curve no influence of confinement was considered and the specific retention curve was used. In the wet part, starting from the specified initial degree of saturation $S_{r,ini}$ the confined retention curve was used. Between the specific and the confined curves an intermediate curve was drawn.

Specific retention curve

In the dry part (70 MPa < ψ < 300 MPa) the specific retention curve was used and the measurements from the conditions RH = 11%, 33 and 59% were used. Since the appearance of the retention curve depends on the initial water content, the final water contents used were linearly interpolated between the measured values mentioned above. Suction was calculated from Equation (E-1) and the degree of saturation was calculated from Equation (E-2) with the specified void ratio.

Confined retention curve

In the wet part (0.1 MPa < ψ < 37 MPa) the confined retention curve $\psi_{confined}$ was used. From Equations (E-4) to (E-7) a relation between suction and degree of saturation was explicitly expressed according to Equation (E-8). Since the retention curve depends on the initial water content the constants B and b from Equation (E-3) were linearly interpolated between the given values above to correspond to the specified initial water content.

$$\psi_{confined} = -\frac{R \cdot T \cdot \rho_w}{\omega_v} \cdot \left[\left((S_r \cdot e \cdot \rho_w / \rho_s)^{1/b} \right) / B - \frac{S_r - S_{r,ini}}{100 - S_{r,ini}} \cdot \left((100 \cdot e \cdot \rho_w / \rho_s)^{1/b} \right) / B \right] \quad \text{(E-8)}$$

Intermediate curve

The intermediate curve, between the specific and the confined retention curves, was made with a best fit line between the final point from the specific curve and the first points of the confined curve. The shape of Equation (E-9) was found suitable for this intermediate curve and for each specified condition the constants (K, L) were determined.

$$\psi = K \cdot \ln(S_r) + L \qquad \text{(E-9)}$$

Input data to the modelling

The resulting retention curves for the three conditions considered for modelling purpose are plotted in Figure E-1.

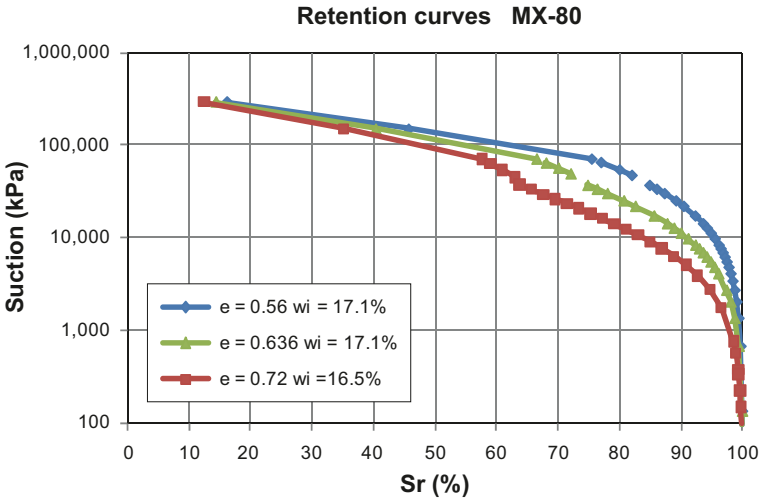

Figure E-1. *Retention curves for three conditions considered for modelling purpose.*

Appendix F

Backfill material lost by colloid erosion – estimation of critical loss

Background

If a fracture intersects the entire perimeter of the backfilled tunnel there will be no deposition hole at that location, which means that such fractures do not intersect deposition holes. However, it is expected that there will be several such fractures crossing the tunnel close to deposition holes. Since these fractures are hydraulically active they may expose the backfill to colloid erosion under certain conditions after a glaciation while leaving the buffer in the deposition hole little affected. This appendix aims at investigating how much backfill can be lost via colloid erosion before the buffer swells so much to make up for the material loss that it results in the buffer losing its sealing ability, although such massive amounts of backfill can only be lost under very conservatively assumed specific circumstances.

This swelling and homogenisation process is difficult to model with FE-methods since the geometry is complicated and since the swelling is very strong and goes from a high swelling pressure down to very low swelling pressure. In order to be able to estimate this process several simplifications must be done and only analytical solutions have been used.

Problem description

The buffer material is considered to completely have completely lost its sealing ability when the average swelling pressure between the canister and the rock has become lower than 100 kPa because at about that swelling pressure the transport of species will be dominated by advection instead of diffusion. Since the swelling of the buffer takes place upwards into the tunnel where the backfill is lost the swelling pressure will be lower on top of the canister than further down into the deposition hole. The criteria for loss of sealing ability will thus be when the swelling pressure on top of the canister is 100 kPa.

Due mainly to friction between the buffer and the rock the swelling pressure is likely to be lower at the opening of the hole than on top of the canister. However, for some of the cases simulated it is assumed that the swelling pressure will be 100 kPa in the entire upper 2.5 m of the deposition hole above the canister. The assumption is conservative (underestimates the mass of bentonite that may be lost) since a swelling pressure of 100 kPa at the top of the deposition hole will result in a higher swelling pressure at tha top of the canister. The effect of this had also been studied in some of the cases examined.

In the tunnel the swelling pressure for most cases studied is also assumed to be 100 kPa in the entire square section above the deposition hole. This is also somewhat conservative since the self-weight of the backfill will cause an effective stress of about 30 kPa at the density that yields a swelling pressure of 100 kPa.

The aim of the calculations is to study how much backfill can be lost under a range of conditions where a swelling pressure 100 kPa is still maintained on top of the canister.

Prerequisites

The initial conditions and geometries of the system are set in accordance with the production line reports as follows:

Deposition hole:

- Radius = 0.875 m.
- Distance from canister top to tunnel floor: 2.5 m.
- Dry density of buffer and backfill in the deposition hole: 1,560 kg/m^3. (The upper meter is called backfill but will be made of buffer blocks identical to the ones used in the buffer.)

Backfilled tunnel:

- Average tunnel square section area: A = 22.7 m^2
- Average dry density: 1,504 kg/m^3
- Distance between deposition holes: L = 6.0 m

The tunnel geometry is simplified to be a circular tube with the diameter 5.4 m, which yields a square section area of A = 22.9 m^2.

Except for the initial average density, the properties of the buffer and the backfill have been assumed to be the same in accordance with the other calculations in this report.

Studied cases

General

Four main cases have been studied, which are all simplified final stages. All these four cases assume a swelling pressure of 100 kPa in the deposition hole in level with the floor. In addition two more cases that also consider the shear resistance to upwards swelling have been included in the study. Only case 6 considers the residue after erosion.

100 kPa swelling pressure above the canister of course results in upwards swelling of the buffer between the canister and the rock and lifting of the canister. The following simple estimation can be done:

The relation between swelling pressure and dry density can for MX-80 be described by Equations (F-1) and (F-2) /Börgesson et al. 1995/.

$$p = p_r \left(\frac{e}{e_r} \right)^{\frac{1}{\beta}} \qquad \text{(F-1)}$$

where

e = void ratio
e_r = reference void ratio (= 1.1)
p = swelling pressure (at e)
p_r = reference swelling pressure (at e_0) (= 1,000 kPa)
β = –0.19

$$\rho_d = \frac{\rho_s}{1+e} \qquad \text{(F-2)}$$

where

ρ_s = dry density
e = void ratio
ρ_s = density of solids = 2,780 kg/m^3

The worst case of canister lifting is that the entire buffer below the canister swells to yield the same swelling pressure and density as the buffer above the canister. Swelling pressure 100 kPa yields according to Equations (F-1) and (F-2) the dry density ρ_d = 1,030 kg/m^3. The buffer below the canister will thus swell from

ρ_d = 1,560 kg/m^3

to

ρ_d = 1,030 kg/m^3

This change in density is directly proportional to the change in volume, which corresponds to the same change in distance between the bottom of the deposition hole and the canister. This distance will thus increase a factor 1,560/1,030 = 1.515 or from 50 cm to 76 cm. The maximum lifting of the canister is thus 26 cm and will actually be smaller due to the weight of the canister and the shear resistance in the buffer.

Equations (F-1) and (F-2) also settles the full swelling pressure of the undisturbed backfill with the average dry density ρ_d = 1,030 kg/m^3 to p = 3,900 kPa.

Altogether six different cases have been studied and will briefly be described below.

Case 1

In case 1 the erosion takes place above the deposition hole so that the backfill has disappeared in a 2 m long section above the deposition hole to yield a swelling pressure is of 100 kPa in this part. This is the most unfavourable location. Figure F-1 describes case 1.

Case 2

In case 2 the erosion takes place half way between two deposition holes and the backfill has disappeared on both sides all the way to the neighbouring deposition holes yielding a 8 m long section to yield a swelling pressure of 100 kPa in this part. This is the most favourable location. Figure F-2 describes case 2.

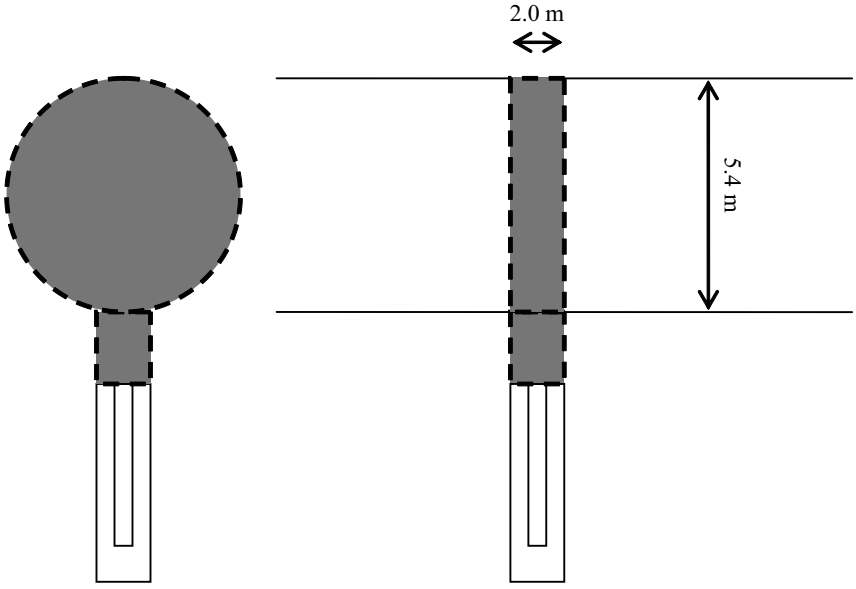

Figure F-1. *Case 1.The grey area has lost mass to yield a swelling pressure of 100 kPa.*

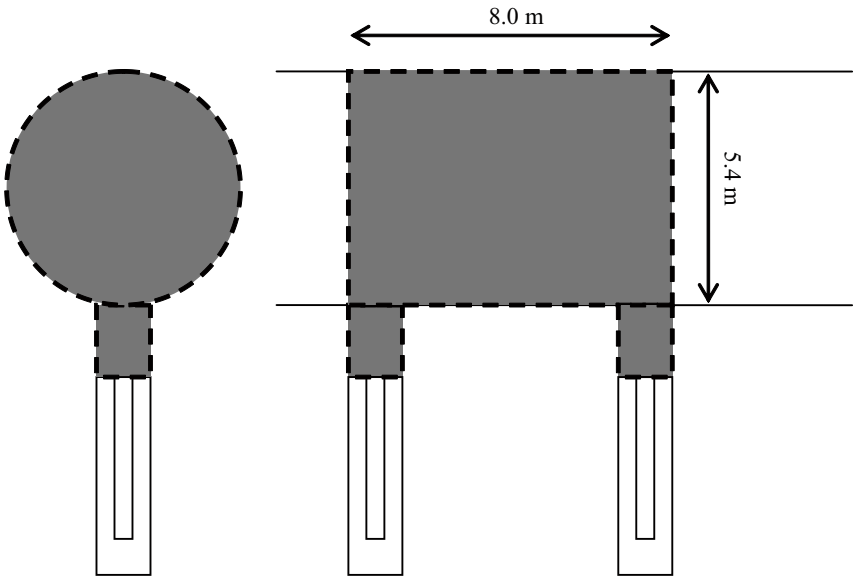

Figure F-2. *Case 2.The grey area has lost mass to yield a swelling pressure of 100 kPa.*

Case 3

In case 3 the erosion takes place above the deposition hole so that the backfill has disappeared in a 2 m long section above the deposition hole to yield a swelling pressure is 100 kPa in this part. This is identical to case 1 but in addition the backfill swelling from adjacent parts of the tunnel has been considered. Figure F-3 describes case 3.

The successive swelling from the backfill in the tunnel to the erosion zone yields a density gradient and resulting axial gradient in swelling pressure from 100 kPa to full swelling pressure 3.9 MPa at the axial distance L from the zone. This is also illustrated in Figure F-3.

Case 4

In case 4 the erosion takes place between two deposition holes and the backfill has disappeared on both sides all the way to the neighbouring deposition holes yielding a 8 m long section so that the swelling pressure is 100 kPa in this part. This is identical to case 2 but in addition the backfill swelling from adjacent parts of the tunnel has been considered. Figure F-4 describes case 4.

Cases 5 and 6

In case 5 and 6 the upwards swelling in the deposition hole is considered in the same way as the axial swelling in cases 3 and 4 i.e. the loss in swelling pressure and thus density is taken into account, which will result in a swelling pressure in the tunnel that is considerably lower than 100 kPa. Figure F-5 describes cases 5 and 6.

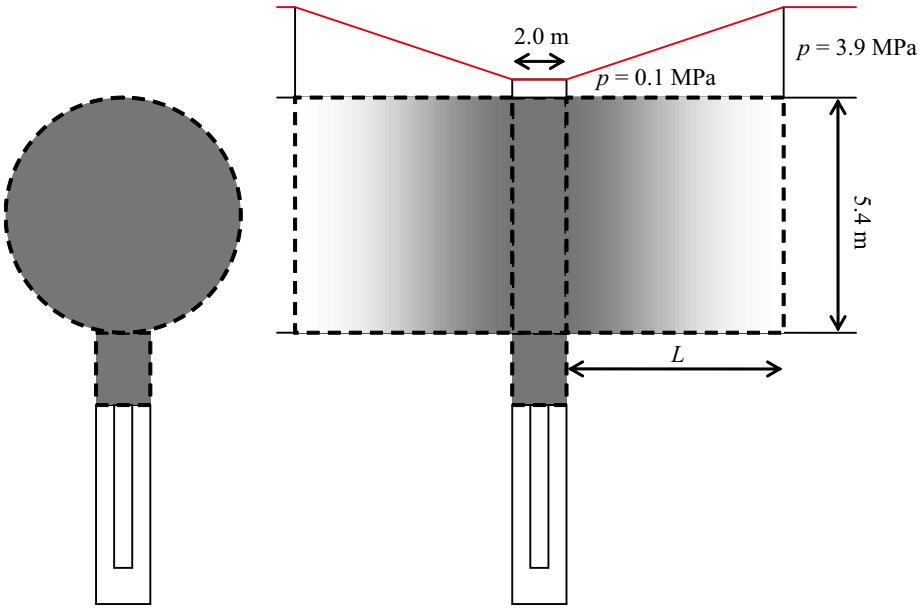

Figure F-3. *Case 3.The dark grey area has lost mass to yield a swelling pressure of 100 kPa. The successive transition from dark grey to white illustrates the decrease in loss of bentonite resulting in an increase in swelling pressure from 100 kPa to 3.9 MPa. The swelling pressure variation is also illustrated by the red lines above the tunnel.*

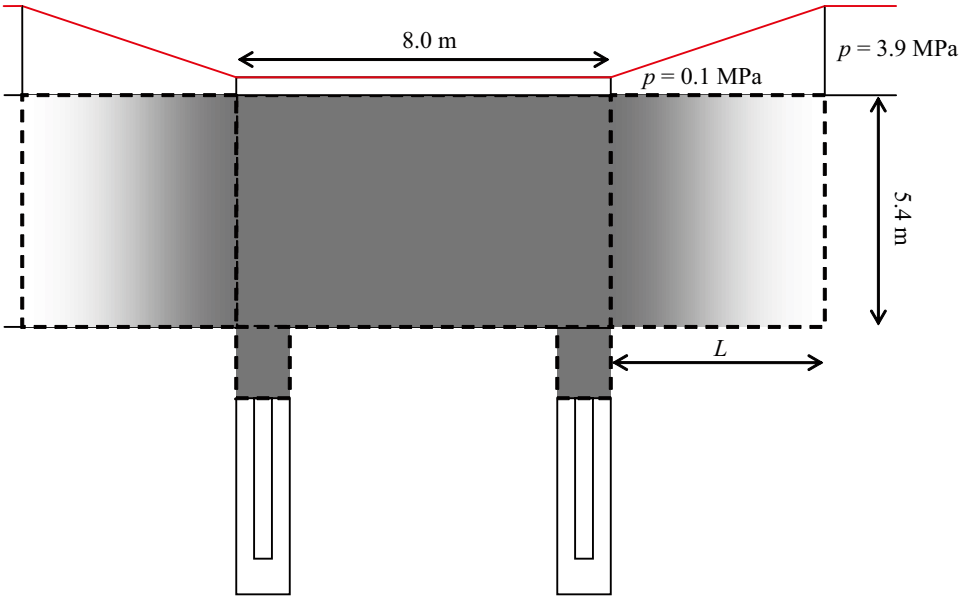

Figure F-4. *Case 4.The dark grey area has lost mass to yield a swelling pressure of 100 kPa. The successive transition from dark grey to white illustrates the decrease in loss of bentonite resulting in an increase in swelling pressure from 100 kPa to 3.9 MPa. The swelling pressure variation is also illustrated by the red line above the tunnel.*

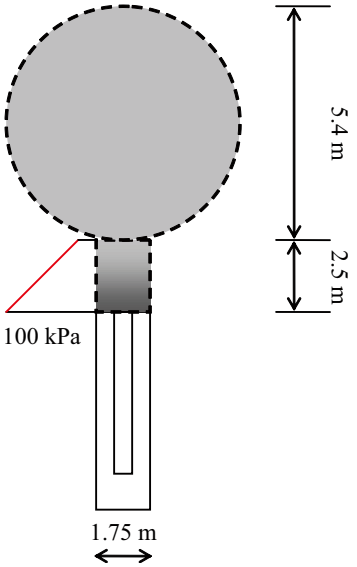

Figure F-5. *Cases 5 and 6. The dark grey area has lost mass to yield a swelling pressure of 100 kPa. The successive transition from dark grey to light grey illustrates the decrease in swelling pressure and density. The final swelling pressure in level with the floor will be studied. The swelling pressure variation in the upper part of the deposition hole is shown by the red line.*

Calculations

General

The calculations of the mass lost are made by calculating the dry density distribution and deduct it from the initial dry density distribution. The dry density distribution can be calculated from the swelling pressure distribution by combining Equations (F-1) and (F-2) with the following Equations (F-3) and (F-4) that describe the axial swelling pressure as a function of the axial distance from the unaffected bentonite at equilibrium after completed swelling in a circular tube (see Section 21.3).

$$p = p_0 \cdot e^{\frac{2z\tan\phi}{r}} \tag{F-3}$$

$$z = \frac{r}{2\tan\phi}\ln\frac{p}{p_0} \tag{F-4}$$

where

z = axial distance from the border of the unaffected bentonite
r = radius
p = swelling pressure at z
p_o = swelling pressure at $z = 0$
ϕ = friction angle (= 10°–30° depending on the swelling pressure)

Mass lost in the deposition hole in cases 1–4

The density in the upper 2.5 m above the canister in the deposition hole is decreased from ρ_{d1} = 1,560 kg/m^3 to ρ_{d2} = 1,030 kg/m^3 in cases 1–4, which yields the following masses:

$$M_{S1} = \rho_{d1}\pi r^2 L \tag{F-5}$$

$$M_{S2} = \rho_{d2}\pi r^2 L \tag{F-6}$$

$$\Delta M_S = M_{S1} - M_{S2} = \pi r^2 L(\rho_{d1} - \rho_{d2}) \tag{F-7}$$

where

M_{S1} = Dry mass before (kg)
M_{S2} = Dry mass after (kg)
$\Delta M_S = 6.01\cdot(1{,}560–1{,}030) = 3{,}187$ kg

The total loss of dry bentonite in the deposition hole will thus be 3.2 t for cases 1–4.

Case 1

See Figure F-1 describing case 1. The scenario corresponds to a situation where the erosion takes place in a square section above a deposition hole. The mass lost in the 2 m long part of the tunnel with the radius 2.7 m can be calculated with Equations (F-5) to (F-7).

$\Delta M_S = 45.80\cdot(1{,}504–1{,}030) = 21{,}711$ kg

The total loss of dry bentonite in case 1 will thus be the sum of the loss in the deposition hole and the loss in the tunnel or 21.7 t +3.2 t = 24.9 t.

Case 2

See Figure F-2 describing case 2. The scenario corresponds to that the erosion takes place in a square section half way between two deposition holes. The mass lost in the 8 m long part of the tunnel with the radius 2.7 m can be calculated with Equations (F-5) to (F-7).

$\Delta M_S = 183.20\cdot(1{,}504–1{,}030) = 86{,}844$ kg

The total loss of dry bentonite in case 1 will thus be the sum of the loss in the deposition hole and the loss in the tunnel or 86.8 t +3.2 t = 90.0 t.

Case 3

See Figure F-3 describing case 3. The scenario corresponds to case 1 but takes also into account swelling from the neighbouring tunnel sections. The swelling can be modelled according to Equations (F-1) to (F-3). Combining the expressions in Equations (F-1) and (F-3) for the swelling pressure yields Equation (F-8).

$$p_r\left(\frac{e}{e_r}\right)^{\frac{1}{\beta}} = p_0 \cdot e^{\frac{2z\tan\phi}{r}} \tag{F-8}$$

Applying Equation (F-2) for the relation between void ratio and dry density and

e_r = 1.1 = reference void ratio
p_r = 1,000 kPa = reference swelling pressure at e_r = 1.1
p_0 = 100 kPa = swelling pressure at z = 0

yield Equation (F-9):

$$1000 \cdot \left(\frac{\left(\frac{\rho_s}{\rho_d}\right)-1}{1.1}\right)^{\frac{1}{\beta}} = 100 \cdot e^{\frac{2z\tan\phi}{r}} \tag{F-9}$$

$$\frac{\frac{\rho_s}{\rho_d}-1}{1.1} = \left(\frac{e^{\frac{2z\tan\phi}{r}}}{10}\right)^{\beta} \tag{F-10}$$

$$\frac{\rho_s}{\rho_d} = 1.1 \cdot \frac{e^{\frac{2z\tan\phi}{r}\beta}}{10^{\beta}} + 1 \tag{F-11}$$

Applying β = –0.19, r = 2.7 m and ρ_s = 2.78 t/m^3 yields

$$\frac{2.78}{\rho_d} = 1.704 \cdot e^{-\frac{0.38 \cdot z \cdot \tan\phi}{2.7}} + 1 \tag{F-12}$$

$$\rho_d = \frac{2.78}{1.704 \cdot e^{-0.141 \cdot z \cdot \tan\phi} + 1} \tag{F-13}$$

The dry mass over an axial length of dz of the tunnel will be

$$dm_{S2} = \rho_d \cdot \pi r^2 dz = \frac{2.78}{1.704 \cdot e^{-0.141 \cdot z \cdot \tan\phi} + 1} \tag{F-14}$$

$$dm_{S2} = \frac{2.78\pi 2.7^2 dz}{1.704 \cdot e^{-0.141 \cdot z \cdot \tan\phi} + 1} = \frac{63.67}{1.704 \cdot e^{-0.141 \cdot z \cdot \tan\phi} + 1} dz$$
$$dm_{S2} = \frac{37.4}{e^{-0.141 \cdot z \cdot \tan\phi} + 0.587} dz \tag{F-15}$$

In order to calculate the total mass M_{S2} we have to integrate the mass from $z = 0$ to $z = L$, but at first we change Equation (F-15) to Equation (F-16):

$$dm_{S2} = \frac{a}{e^{b \cdot z} + c} dz \tag{F-16}$$

where

$a = 37.4$

$b = -0.141 \cdot \tan\phi$

$c = 0.587$

Integration yields the total mass M_{S2}

$$M_{S2} = \int_{z=0}^{z=L} dm_{S2} = \int_{z=0}^{z=L} \frac{a}{e^{b \cdot z} + c} dz \tag{F-17}$$

$$M_{S2} = \frac{aL}{c} - \frac{a}{bc} \ln(c + e^{bL}) + \frac{a}{bc} \ln(c + 1) \tag{F-18}$$

We thus have a general expression for the total dry mass in the tunnel section after erosion when the backfill increases its dry density from ρ_d = 1,030 kg/m^3 (with the swelling pressure 100 kPa) to the density that corresponds to the axial length of the affected backfill L.

The initial dry mass of bentonite over the length L is

$$M_{S1} = \rho_d \pi r^2 L = 1.504 \cdot \pi \cdot 2.7^2 \cdot L = 34.44L \tag{F-19}$$

The loss is thus

$$\Delta M_S = M_{S1} - M_{S2} \tag{F-20}$$

The net loss is a function of the friction angle ϕ and the total distance of affected bentonite L, which in turn is a function of the friction angle according to Equation (F-4). The result of the calculations at different friction angles are shown in Table F-1. The total loss including the other parts is the loss calculated for case 1 (24.9 t) + 2·ΔM_S.

Case 4

See Figure F-4 describing case 4. The case is identical to case 3 with the exception that case 2 is added instead of case 1. The total loss is thus 90 t + 2·ΔM_S. Table F-2 summarises the results.

Table F-1. Summary of calculations for case 3.

ϕ (°)	L (m)	M_{S1} (t)	M_{S2} (t)	ΔM_S (t)	Total loss (t)
10	28.0	964	811	153	331
20	13.6	468	394	74	173
30	8.57	295	248	47	119

Table F-2. Summary of calculations for case 4.

ϕ (°)	L (m)	M_{S1} (t)	M_{S2} (t)	ΔM_S (t)	Total loss (t)
10	28.0	964	811	153	396
20	13.6	468	394	74	238
30	8.57	295	248	47	184

Case 5

During swelling not only in the tunnel but especially in the deposition hole the counteracting friction between the bentonite and the rock surface will limit the swelling and cause a swelling pressure gradient and corresponding density gradient, just as illustrated in cases 3 and 4. Equation (F-4) can be used to calculate the drop in swelling pressure as a function of the distance from the canister surface z, which yields Equation (F-21).

$$p = p_0 \cdot e^{-\frac{2z\tan\phi}{r}} = 100 \cdot \exp(-2z\tan\phi/0.875) \qquad \text{(F-21)}$$

Figure F-6 shows the relation for three different friction angles.

Tests have shown /Börgesson et al. 1995/ that the friction angle is higher than 20° when the swelling pressure is below 100 kPa. Using $\phi = 20°$ yields the swelling pressure

$p = 12.5$ kPa at $z = 2.5$ m and
$p = 28.7$ kPa at $z = 1.5$ m.

These low values of swelling pressure can be used to calculate corresponding allowable loss in backfill material as for cases 1–4. This would mean additionally 50%–60% of the axial swelling length L in the backfilled tunnel, which in turn would increase the allowable mass of erosion by doubling the value of ΔM_S in Equation (F-20), or with between 50 and 150 tons.

Case 6

Another discourse on the problem is the following:

The montmorillonite content in MX-80 is about 80%, which means that about 20% will not be colloids that are transported away and lost from the backfill. 20% of the mass above a deposition hole will thus always remain although it will have no swelling properties and exert no swelling pressure. However, the mass of particles will settle on the floor and with its own weight exert a pressure on the bentonite in the deposition hole.

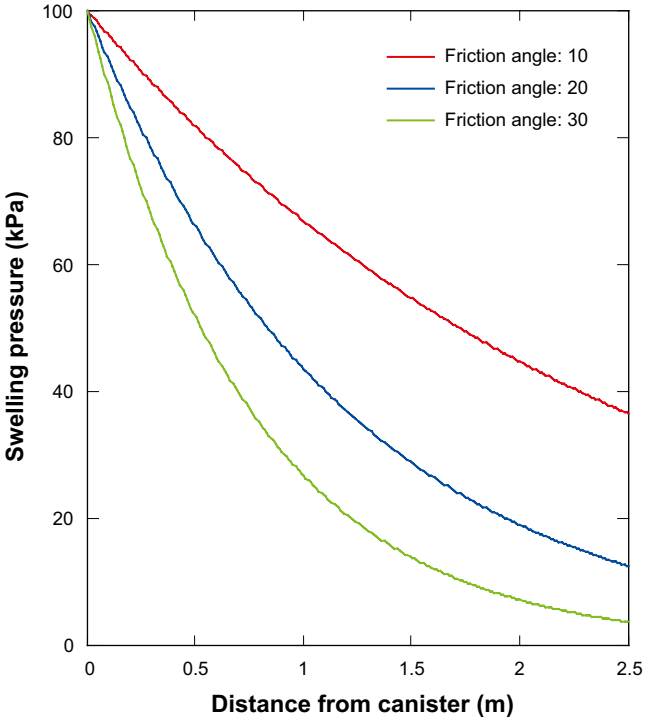

Figure F-6. *Relation between swelling pressure and axial distance from the canister lid for different friction angles (°).*

The effective pressure p from these non-montmorillonite particles on the tunnel floor will be according to Equation (F-22).

$$P = Hg(\rho_m - \rho_w) \quad \text{(F-22)}$$

where

H = height (m)
g = acceleration of gravity (9.81 m/s^2)
p_m = density at saturation (t/m^3)
p_w = density of water (t/m^3)

The dry density of the backfill 1.504 t/m^3 yields for this case a remaining dry density of 0.3 t/m^3 or ρ_m = 1.19 t/m^3. Inserting this value and the height of the tunnel H=5 m yields

p = 5.0g (1.19–1.0) = 9.3 kPa

The effective pressure from the remaining non-montmorillonite particles in MX-80 will thus not be enough to keep the swelling pressure at the canister surface at 100 kPa since 12.5 kPa was required. However, the nominal design of the backfill is according to the production line report 50–60% montmorillonite. If 60% is used the pressure will instead be

p = 18.6 kPa,

which is more than the required 12.5 kPa if the entire 2.5 m of the deposition hole up to the floor level is included. If only the buffer part (1.5 m) is included the extra metre will increase the counteracting pressure to

p = 22.4 kPa,

which is lower than the required 28.7 kPa.

The results of the calculations for case 6 are thus that if the non-montmorillonite particles in the backfill are included in the modelling, the remaining pressure on the top of the deposition hole is high enough to ensure that the swelling pressure at the top of the canister will remain higher than 100 kPa even if all montmorillonite disappears in the backfill under the conditions that the montmorillononite content is lower than about 70% and the upper metre of the deposition hole is included in the model (no chase in the floor).

The problem with this result is of course that the hydraulic conductivity of the remaining backfill will be high and that the density of the backfill will be so low that there will be an open slot between the backfill and the roof.

Uncertainties

A number of simplifications have been made in order to make a reasonable estimation of the amount of dry bentonite that may erode from the backfill in the deposition tunnel before so much of the buffer on top of the canister is lost that the buffer can be considered to have lost its barrier function. These simplifications create the following uncertainties that will be briefly analysed.

- The geometry – a cylindrical tunnel has been assumed.
- The initial density distribution before erosion is assumed to be constant and set to the average values.

These are reasonable simplications that should have very little influence

- The critical density of the buffer (ρ_d = 1,030 kg/m^3) is assumed to prevail in the entire deposition hole above the canister (cases 1–4).

This is a conservative assumption. If the same theory leading to Equation (F-3) is used for the upwards swelling in the deposition hole (case 5) the swelling pressure in level with the floor would be 10–30 kPa when the swelling pressure is 100 kPa at the top of the canister. This would mean

additionally 50–60% of axial swelling length L in the tunnel, which in turn would increase the allowable mass of erosion by doubling the value of ΔM_s, or with between 50 and 150 tons.

- Equation (F-3) is based on simplified force equilibrium after completed swelling and the validity has not been proven.

This is a basic uncertainty that remains to be discarded. However, the successive extremely slow reduction in swelling pressure that takes place due to colloid erosion speaks in favour of the validity since the bentonite mass is always in equilibrium.

- The friction angle is assumed to not change considerably over long times.

This is an uncertain factor. However, cases 3 and 4 will favour from decreased friction angle with time, while cases 5 and 6 will suffer from it.

- The backfill has been considered a uniform mass that has an unchanged composition after far advanced erosion (cases 1–5).

This simplification needs to be further investigated. When the dry density of the backfill has been reduced from ρ_{d1} = 1,504 kg/m^3 to ρ_{d2} = 1,030 kg/m^3 (as assumed in cases 1–5) about 32% of the mass is lost. However, at colloid erosion only the montmorillonite particles are lost, which means that the remaining montmorillonite content is decreased and will be as follows.

$$m_{m1} = c_{m1} \cdot \rho_{d1} \cdot V \tag{F-23}$$

$$m_{m2} = c_{m2} \cdot \rho_{d2} \cdot V \tag{F-24}$$

where

m_{m1} = mass of montmorillonite before erosion
m_{m2} = mass of montmorillonite after erosion
c_{m1} = montmorillonite content before erosion
c_{m2} = montmorillonite content after erosion
V = volume

Equations (F-23) and (F-24) yield

$$c_{m2} = c_{m1} \frac{\rho_{d1}}{\rho_{d2}} - \frac{m_{m1} - m_{m2}}{V \cdot \rho_{d2}} \tag{F-25}$$

Applying V = 1 m^3 the mass of lost montmorillonite m_{m1}–m_{m2} will be 474 kg since all material lost is montmorillonite.

Equation (F-25) yields the results shown in Table F-3.

The consequences of such changes are not well known. Probably the swelling pressure will be reduced and the friction angle increased, which both could tend to reduce the allowable mass lost, although the changes are not expected to be very strong unless the initial montmorillonite content is low.

- In case 6 all the non-montmorillonitic particles have been assumed to stay in their initial place in the tunnel and not be moved along the tunnel.

Table F-3. Change in montmorillonite content caused by colloid erosion.

Montmorillonite content before erosion	Montmorillonite content after erosion
50%	27%
60%	42%
70%	56%
80%	71%

This is probably a conservative incorrect assumption since the axial swelling of the backfill will move these particles towards the section where the erosion takes place and increase the density of this non-swelling material above the deposition hole. So this is positive for the density of the residue close to the erosion zone and negative for the density of the residue far away from the erosion zone.

Conclusions

Case 1 with only loss of bentonite to a swelling pressure of 100 kPa in a zone above the deposition hole and no account taken to the swelling of the adjacent backfill yields that only about 25 t can be lost. However, this case must be considered too conservative and unrealistic since there can never be a sharp transition in swelling pressure in the backfill from 100 kPa to 3.2 MPa.

When account is taken to the swelling of the adjacent backfill as described by **Case 3** the allowable mass lost will be much higher (between119 t and 331 t), and dependant on the friction angle between the rock and the backfill. However, this case is also deemed to be conservative since no account is taken to the resistance to upwards swelling in the deposition hole.

If proper account is taken to include the friction in the deposition hole in the calculations as in **Case 5** there will be an additional 50–150 t backfill that may be lost in addition to that estimated in Cases 3 and 4 without compromising the minimum swelling pressure limits for the buffer.

Cases 2 and 4 with the erosion zone located between two deposition holes are of course more favourable and yield additionally about 65 t.

Case 6 with all montmorillonite lost in the zone above the deposition hole is an interesting case. Simple calculations show that there will be a sufficient counter pressure on top of the deposition hole by the own weight of the material in order to prevent too much swelling of the backfill if the backfill has a montmorillonite content lower than about 70% and if the entire deposition hole is included in the calculation i.e. there is no chase in the floor. However, the result will probably be an open slot at the roof, which may be unacceptable.

Appendix G

Simplified calculation of the swelling of bentonite through the holes of the perforated copper tube

Round holes are considered. Only the stage after completed swelling and homogenisation is considered. The calculation is made in two steps. The first step regards the stresses after swelling through the holes and considers a state of equilibrium in only the direction perpendicular to the rock surface (axial direction in relation to the holes in the container). The second step regards the stresses after swelling into the slot between the tube and the rock and considers a state of equilibrium in only the direction parallel to the rock surface (radial direction in relation to the holes in the container).

Step 1. Equlibrium after swelling through the holes

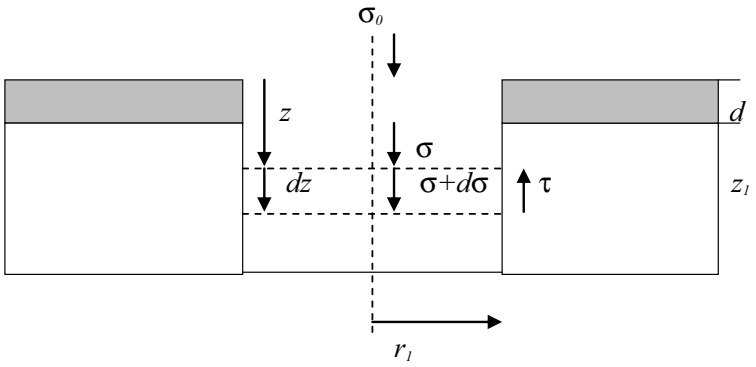

d = container thickness
z_1 = distance between container and the rock
r_1 = hole radius
σ_0 = swelling pressure at $z = 0$

Force equilibrium in axial direction (the swelling pressure is assumed to be isotropic):

$$d\sigma \cdot \pi r_1^2 = \sigma \tan\phi \cdot 2\pi r_1 \cdot dz$$

$$\frac{d\sigma}{\sigma} = \frac{2\tan\phi}{r_1} \cdot dz$$

$$dz = \frac{r}{2\tan\phi} \cdot \frac{d\sigma}{\sigma}$$

Integrating:

$$\int_0^z dz = \frac{r_1}{2\tan\phi} \int_{\sigma_0}^{\sigma} \frac{d\sigma}{\sigma}$$

$$z = \frac{r_1}{2\tan\phi}\left(\ln\sigma - \ln\sigma_0\right)$$

σ_1 = average swelling pressure in the slot (at $z = d+z_1/2$)

$$e^{(\ln\sigma_1 - \ln\sigma_0)} = e^{-\frac{2z\tan\phi}{r_1}}$$

$$\sigma_1 = \sigma_0 \cdot e^{\frac{-2(d+z_1/2)\tan\phi}{r_1}} \qquad \text{(G-1)}$$

Step 2a. Equilibrium after swelling into the slot without considering in-plane stresses

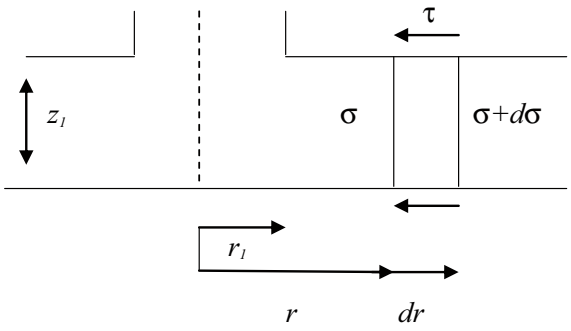

Force equilibrium in radial direction:

$$\sigma \cdot 2\pi r z_1 - (\sigma + d\sigma)2\pi (r + dr) z_1 = \left[\pi (r + dr)^2 - \pi r^2\right]\left(\sigma + \frac{d\sigma}{2}\right) \cdot \tan\phi \cdot 2$$

$$-\sigma dr - r d\sigma = \sigma r dr \cdot \frac{2\tan\phi}{z_1}$$

$$-\frac{dr}{r} - \frac{d\sigma}{\sigma} = dr \frac{2\tan\phi}{z_1}$$

Integrating from r_1 to a specified maximum distance between the holes r_2:

$$-\int_{\sigma_1}^{\sigma_2} \frac{d\sigma}{\sigma} = \int_{r_1}^{r_2} \frac{dr}{r} + \frac{2\tan\phi}{z_1} \int_{r_1}^{r_2} dr$$

$$\ln\sigma_1 - \ln\sigma_2 = \ln\frac{r_2}{r_1} + (r_2 - r_1)\frac{2\tan\phi}{z_1}$$

$$\ln\sigma_2 = \ln\sigma_1 - \ln\frac{r_2}{r_1} - \frac{r_2 - r_1}{z_1} \cdot 2\tan\phi \qquad \text{(G-2)}$$

Step 2b. Equilibrium after swelling into the slot (general case)

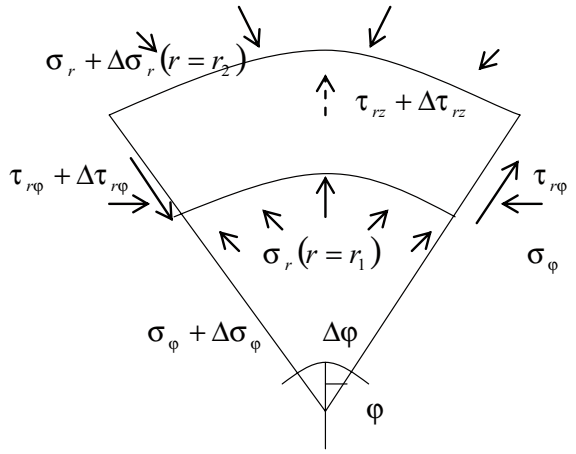

$$P_1 - (\sigma_r + \Delta\sigma_r)(r + \Delta r)\Delta\varphi \cdot \Delta z + \sigma_r \cdot r\Delta\varphi\Delta z + \tau_{r\varphi} \cdot \Delta r \cdot \Delta z - (\tau_{r\varphi} + \Delta\tau_{r\varphi}) \cdot \Delta r\Delta z + \cdot$$
$$(\sigma_\varphi + \sigma_\varphi + \Delta\sigma_\varphi) \cdot \Delta r \cdot \Delta z + \frac{\Delta\varphi}{z} + [(\tau_{rz} + \Delta\tau_{rz}) - \tau_{rz}] \cdot \Delta\varphi \cdot \left[\frac{(r+\Delta r)^2}{2} - \frac{r^2}{2}\right] = 0$$

$$-\sigma_r r\Delta\varphi\Delta z - \sigma_r \Delta r\Delta\varphi\Delta z - \Delta\sigma_r r\Delta\varphi\Delta z - \Delta\sigma_r \Delta r\Delta\varphi\Delta z + \sigma_r r\Delta\varphi\Delta z - \Delta\tau_{r\varphi}\Delta r\Delta z + \sigma_\varphi \Delta r\Delta z\Delta\varphi +$$
$$\Delta\sigma_\varphi \Delta r \frac{\Delta\varphi}{2} \cdot \Delta z + \Delta\tau_{rz} \cdot \Delta\varphi\left(r \cdot \Delta r + \frac{\Delta r^2}{2}\right) = 0$$

$$(\sigma_\varphi - \sigma_r) - \Delta\sigma_r\left(\frac{r}{\Delta r} + 1\right) + \Delta\sigma_\varphi / 2 - \frac{\Delta\tau_{r\varphi}}{\Delta\varphi} + \frac{\Delta\tau_{rZ}}{\Delta z}\left(r + \frac{\Delta r}{2}\right) = 0$$

$$\Delta\sigma_\varphi = 0$$
$$\frac{\Delta\tau_{r\varphi}}{\Delta\varphi} = 0$$
$$\Delta\tau_{rZ} = -2\sigma_r \cdot \tan\phi$$

$\Rightarrow$

$$(\sigma_\varphi - \sigma_r) - \Delta\sigma_r \frac{r}{\Delta r} - \frac{2\sigma_r \tan\phi}{\Delta z} \cdot r = 0 \qquad \text{(G-3)}$$

Assuming isotropic swelling pressure

$$\sigma_r = \sigma_\varphi$$

$$\Rightarrow$$

$$-\Delta\sigma_r \frac{r}{\Delta r} - \frac{2\sigma_r \tan\phi}{\Delta z} \cdot r = 0$$

$$-\frac{d\sigma_r}{\sigma_r}\Delta z = 2\tan\phi \cdot \Delta r$$

$$-\left(\ln\frac{\sigma_2}{\sigma_1}\right)\cdot z_1 = 2\tan\phi\left(r_2 - r_1\right)$$

$$\sigma_2 = \sigma_1 \cdot e^{-\frac{2\tan\phi\left(r_2 - r_1\right)}{z_1}} \qquad \text{(G-4)}$$

Assuming unisotropic swelling pressure

$$\sigma_\varphi / \sigma_r = \nu/(1-\nu) \Rightarrow$$

$$\sigma_\varphi - \sigma_r = \sigma_r\left(\frac{\upsilon}{1-\upsilon} - 1\right)$$

$$K = \left(\frac{\nu}{1-\nu} - 1\right) \Rightarrow$$

$$\sigma_\varphi - \sigma_r = \sigma_r \cdot K \qquad \text{(G-5)}$$

Equation (G-5) applied to Equation (G-3) yields

$$-\Delta\sigma_r \frac{r}{\Delta r} + \sigma_r\left(+K - \frac{2\tan\phi}{\Delta z}\cdot r\right) = 0$$

$$\frac{d\sigma_r}{\sigma_r}\Delta z = \left(K\frac{dr}{r}\Delta z - 2\tan\phi dr\right)$$

$$\left(\ln\frac{\sigma_2}{\sigma_1}\right)z_1 = K\cdot z_1 \cdot \ln\frac{r_2}{r_1} - 2\tan\phi\left(r_2 - r_1\right)$$

$$\frac{\sigma_2}{\sigma_1} = \cdot e^{K\ln\left(\frac{r_2}{r_1}\right) - 2\tan\phi\left(\frac{r_2 - r_1}{z_1}\right)}$$

$$\ln\sigma_2 = \ln\sigma_1 + K\ln\frac{r_2}{r_1} - \frac{r_2 - r_1}{z_1}\cdot 2\tan\phi \qquad \text{(G-6)}$$

ν	K
0	–1
0.3	–0.57
0.5	0

Thus $\nu = 0$ in Equation (G-6) yields Equation (G-2) and $\nu = 0.5$ yields Equation (G-4).